



**THÈSE DE DOCTORAT**  
**DE L'UNIVERSITÉ PSL**

Prepared at Paris Observatory - CNRS

**The Cepheid distance scale:  
From the local Gaia calibration to distant galaxies**

Defended by

**Louise BREUVAL**

on October 15th 2021

Doctoral school n°127

**Astronomie et  
Astrophysique  
d'Île-de-France**

Specialty

**Astronomy and  
Astrophysics**

**Thesis committee:**

Françoise COMBES <i>LERMA, Observatoire de Paris</i>	President
Lucas MACRI <i>Texas A&amp;M University, USA</i>	Reviewer
Gisella CLEMENTINI <i>INAF, Bologna, Italy</i>	Reviewer
Massimo MARENGO <i>Iowa State University, USA</i>	Examinator
Adam RIESS <i>Johns Hopkins University, STScI, USA</i>	Invited
Grzegorz PIETRZYŃSKI <i>Warsaw University, Poland</i>	Invited
Pierre KERVELLA <i>LESIA, Observatoire de Paris</i>	Supervisor





*"She had the happy, joyful, faculty of appreciating all that was worthy and lovable in others, and was possessed of a nature so full of sunshine that, to her, all of life became beautiful and full of meaning."*

Solon I. Bailey, about Henrietta S. Leavitt

# Acknowledgements

First, I would like to thank my advisor Pierre Kervella for giving me the opportunity to carry out my PhD thesis in his team and to work on such an inspiring project: studying the Cepheid distance scale at the time of *Gaia* DR2 and EDR3 is a great privilege. Pierre is a thoughtful and passionate scientist, his kindness, trust and support helped me to overcome the difficulties throughout the three years of my thesis and to continue my growth as a scientist and as a person.

I would like to thank my thesis committee members, Françoise Combes, Lucas Macri, Gisella Clementini, Massimo Marengo, Adam Riess and Grzegorz Pietrzyński for accepting to review my work and for providing constructive comments on my results.

It was also a great pleasure to work alongside the members of the Araucaria Project. I am very grateful to Wolfgang Gieren for his constant support and kindness and for reminding me that the world is beautiful outside of my computer screen. I would also like to thank Antoine Mérand and Nicolas Nardetto for sharing with me their expertise in interferometry, for supporting me throughout my thesis and for helping me to improve my thesis manuscript. I will always remember the very nice discussion I had with Alexandre Gallenne at Cerro Calan in Santiago in February 2020 and I am thankful to him for taking me to Paranal Observatory for the first time in May 2017. I am happy to have met Behnam Javanmardi who is a wonderful colleague and also a good friend. I am grateful to Grzegorz Pietrzyński, Jesper Storm, Giuseppe Bono and Piotr Wielgórski for their support and for their contribution to my research. A special thanks to Vincent Houdé and Eric Lagadec for organizing a surprise for my birthday in Cloudcroft in 2019.

During these three years I also had the pleasure of interacting with other scientists who have helped me, inspired me and supported me. I am deeply grateful to Adam Riess for carefully checking each step of my re-evaluation of the Hubble constant in my first paper and for patiently helping me to improve my research. I would like to thank Richard I. Anderson for our insightful discussions in New Mexico and in Croatia and for his very useful advice. I am thankful to Frédéric Arenou for teaching me all the secrets of the *Gaia* satellite and for his very kind support during the last months of my thesis. I will always remember the day I met Wendy Freedman and Barry Madore at the Cosmic Controversies conference in Chicago in October 2019: I am very grateful to both of them for offering me their support and for our nice discussion by the river. I am grateful to Brigitte Rocca-Volmerange for being a wonderful and inspiring internship supervisor during my bachelor studies in 2016, and for convincing me to pursue a career in astrophysics. I would like to thank Keegan Thomson-Paressant for patiently reading my entire manuscript and for pointing out all the English mistakes, but also for being a great office neighbor. I am grateful to Vincent Coudé du Foresto for his kind support. I would like to thank Ghislaine Sapena, Nicolas Wipf, Yohan Loquais, Pascal Girault and Alain Abergel for being very good teachers and for allowing me to discover the beauty of the universe through their math, physics and chemistry classes. I have loved studying and learning, and I will always do. It was a pleasure to work at building 5 in Meudon, where I have spent very good times and coffee breaks

with my colleagues and friends. Finally, I would never have come this far without Joanne Breithfelder who gave me Pierre's email address in 2016 when I was looking for a master internship.

During my thesis I had the amazing opportunity to spend six weeks at Cerro Armazones Observatory in the Atacama desert in Chile: I would like to thank Bartek Zgirski, Darek Graczyk, Mikołaj Kałuszyński and Marek Górski for their very nice company on top of the mountain, for driving me to Paranal on Saturdays, for walking with me on the foundations of the ELT building site, for taking me to the city of Taltal for a lunch and a few piscos, and for the beautiful trips to the ocean and to the desert.

My friends have always believed in me and I have always felt supported and loved. For this reason I would never have made it without Marie Wolfer, who is my friend since our childhood in Cuvry, Barbara Mazzilli-Ciraulo and François Caillet who I consider as my family, Κατερίνα Παππα my Greek sister, my friends from Orsay, Aurélien Stcherbinine, Dany Galarraga, Natalia Zambrana, Guillaume Thiam, but also Pierre Guiot and Gabriel Pelouze who have been inspiring mentors and showed me the way to become a successful scientist like them, my friends from Chile, Maxime Lombart, Kevin Dehondt and Hélène Gaudin, and finally my friends from high school and college, Marvin Dupuis, Pauline Aimi, Juliette Gabrion, Julia Schmitt, Anaïs Scipioni, Camille La Loggia and Johanna Alonso.

My parents, my sister and my family have always accepted and supported my choices, they have allowed me to study in Paris and to travel the world, even if it means that I don't see them as much as I would like. I owe my success to them and to the education they gave me.

Finally, I would like to thank my life partner, best friend and closest colleague, Boris Trahin, who has supported me everyday during my thesis, but who has also discussed and understood in detail each point of my work. I am deeply grateful for his help, his patience and his love. I could not dream of a better person to spend my life with.

# Table of contents

<b>1</b>	<b>The distance scale</b>	<b>10</b>
1.1	History of the distance scale . . . . .	11
1.1.1	From Henrietta Leavitt to Edwin Hubble . . . . .	11
1.1.2	Early tensions . . . . .	13
1.1.3	The standard model of cosmology . . . . .	16
1.1.4	The tension on the Hubble constant . . . . .	16
1.2	Measuring astronomical distances . . . . .	21
1.2.1	Trigonometric parallaxes . . . . .	21
1.2.2	Eclipsing binaries . . . . .	22
1.2.3	Pulsating stars . . . . .	24
1.2.4	The Tip of the Red Giant Branch . . . . .	25
1.2.5	Type Ia supernovae . . . . .	26
1.2.6	Water masers in NGC 4258 . . . . .	27
1.2.7	Other methods for distance determination . . . . .	28
1.2.7.1	The Tully-Fisher relation . . . . .	28
1.2.7.2	The fundamental plane method . . . . .	28
1.2.7.3	The Surface Brightness Fluctuation method . . . . .	28
1.3	Cepheids as distance indicators . . . . .	29
1.3.1	Properties of Cepheid stars . . . . .	29
1.3.2	The place of Cepheids in the distance scale . . . . .	32
<b>2</b>	<b>Calibration of the Cepheid Leavitt Law in the Milky Way</b>	<b>36</b>
2.1	Calibration of the Cepheid Leavitt Law before <i>Gaia</i> . . . . .	37
2.1.1	The P-L relation with Hipparcos parallaxes . . . . .	37
2.1.2	Improvements with the <i>Hubble</i> Space Telescope . . . . .	39
2.1.2.1	HST Fine Guidance Sensor Parallaxes . . . . .	39
2.1.2.2	Parallaxes from HST Wide Field Camera 3 spatial scanning . . . . .	41
2.1.3	Other methods . . . . .	44
2.2	Cepheids with <i>Gaia</i> . . . . .	45
2.2.1	The <i>Gaia</i> mission . . . . .	45
2.2.2	Parallaxes from <i>Gaia</i> Data Release 2 . . . . .	49
2.2.3	Parallaxes from <i>Gaia</i> Early Data Release 3 . . . . .	53
2.3	Calibration of the P-L relation with <i>Gaia</i> parallaxes . . . . .	56
2.3.1	Sample of Cepheids companions . . . . .	56
2.3.2	Sample of Open Cluster Cepheids . . . . .	61
2.3.2.1	Open Cluster mean parallaxes and uncertainties . . . . .	62
2.3.2.2	Open Cluster Cepheids from <i>Gaia</i> DR2 and <i>Gaia</i> EDR3 . . . . .	63
2.3.2.3	Open Cluster Cepheids from the literature . . . . .	68
2.3.3	Photometry . . . . .	71

2.3.4	Extinction . . . . .	73
2.3.5	Pulsation modes . . . . .	75
2.3.6	Method and results . . . . .	76
2.4	Implications for the Hubble constant . . . . .	84
2.5	Conclusion on the calibration of the Leavitt law . . . . .	87
2.5.1	Summary of the study . . . . .	87
2.5.2	Limitations . . . . .	88
2.5.3	Perspectives . . . . .	89
2.6	Publication: <i>The Milky Way Cepheid Leavitt law based on Gaia DR2 parallaxes of companion stars and host open cluster populations</i> , Breuval et al. 2020, A&A 643 A115 . . . . .	90
<b>3</b>	<b>The effect of metallicity on the Leavitt Law</b>	<b>105</b>
3.1	The metallicity effect: definition and values from the literature . . . . .	107
3.2	Photometry . . . . .	111
3.2.1	Photometry for Milky Way Cepheids . . . . .	111
3.2.2	Photometry for Large Magellanic Cloud Cepheids . . . . .	113
3.2.3	Photometry for Small Magellanic Cloud Cepheids . . . . .	114
3.3	Distances . . . . .	115
3.3.1	Gaia EDR3 parallaxes of Milky Way Cepheids . . . . .	115
3.3.2	Distance to Large Magellanic Cloud Cepheids . . . . .	117
3.3.3	Distance to Small Magellanic Cloud Cepheids . . . . .	118
3.4	Metallicity . . . . .	120
3.4.1	Metallicity for Milky Way Cepheids . . . . .	120
3.4.2	Metallicity for LMC and SMC Cepheids . . . . .	122
3.5	Calibration of the P-L relation in the Milky Way and Magellanic Clouds . . . . .	122
3.5.1	Method . . . . .	123
3.5.1.1	From distances and apparent magnitudes to the P-L coefficients . . . . .	123
3.5.1.2	Extinction law and Wesenheit indices . . . . .	123
3.5.1.3	Width of the instability strip . . . . .	124
3.5.1.4	Period cut . . . . .	124
3.5.2	Results . . . . .	124
3.6	Deriving the metallicity effect on the Leavitt law . . . . .	128
3.6.1	The metallicity term in the Milky Way . . . . .	128
3.6.2	The metallicity term from Milky Way and Magellanic Cloud Cepheids . . . . .	131
3.6.2.1	Method . . . . .	131
3.6.2.2	Results . . . . .	133
3.6.2.3	The effect of CO absorption on <i>Spitzer</i> bands . . . . .	134
3.6.2.4	The dependence of the metallicity effect with wavelength, comparison with the literature . . . . .	135
3.6.2.5	Influence of the radius around the SMC center . . . . .	137
3.7	Conclusion on the metallicity effect . . . . .	139
3.7.1	Summary of the data, method and results . . . . .	139
3.7.2	Limitations and perspectives . . . . .	141
3.8	Publication: <i>The Influence of Metallicity on the Leavitt Law from Geometrical Distances of Milky Way and Magellanic Cloud Cepheids</i> , Breuval et al. 2021, ApJ 913 38 . . . . .	142

<b>4</b>	<b>Conclusions and perspectives</b>	<b>163</b>
4.1	Results of the thesis . . . . .	164
4.2	Main limitations in the Cepheid distance scale . . . . .	165
4.3	Perspectives . . . . .	166
4.3.1	Cluster Cepheid photometry in HST system . . . . .	166
4.3.2	Uncrowding extragalactic Cepheids in SN Ia hosts with JWST . . . . .	167
4.3.3	Other perspectives . . . . .	169
	<b>Bibliography</b>	<b>171</b>
<b>A</b>	<b>Contribution to Trahin et al. (2021), accepted in A&amp;A</b>	<b>183</b>
<b>B</b>	<b>Contribution to Javanmardi et al. (2021), ApJ, 911, 12</b>	<b>187</b>
<b>C</b>	<b>List of publications</b>	<b>192</b>
<b>D</b>	<b>Oral presentations, conferences, seminars</b>	<b>194</b>
<b>E</b>	<b>List of acronyms</b>	<b>198</b>

# Introduction

Cepheids are yellow giant and supergiant pulsating stars that undergo regular radial pulsations with periods between 2 and  $\sim 100$  days. They are present in the Milky Way as well as in other galaxies and are very bright stars. The particularity of Cepheids is that their pulsation period is directly related to their intrinsic brightness through the period-luminosity (P-L) relation, discovered by Henrietta Leavitt in 1908 and also called the Leavitt law. Thanks to this remarkable property, Cepheids are the most important standard candles, that is, astronomical objects that have a known absolute magnitude. By comparing the observed apparent brightness of standard candles to their known absolute magnitude, astronomers can deduce their distance.

Distances are probably the most difficult parameter to measure in astronomy. While Cepheids can be observed in nearby galaxies, they are too faint to be detected at larger distances. Therefore, in order to measure distances to the most remote galaxies, one needs to combine several distance indicators covering different ranges: this is what astronomers call the *distance scale*.

The first step of the distance scale usually consists in determining geometric distances to nearby distance indicators such as Cepheids, for example by measuring their trigonometric parallax. The parallax of a star is the angle described by the apparent change of its position in the sky during one year due to the movement of the Earth around the Sun. These geometric distances constitute the basis for the calibration of the Cepheid period-luminosity relation. The second step of the distance ladder is the calibration of type Ia supernovae (SNe Ia) luminosity using Cepheid distances: to this aim, Cepheids must be observed together with SNe Ia in nearby host galaxies, but such associations are relatively rare and only a few dozen were observed. Finally, once SN Ia brightness is calibrated, the distance to remote galaxies hosting SN Ia can be derived, especially at large distances where the velocities of galaxies are dominated by the expansion of the Universe. This region of the Universe (at  $z > 0.025$ ) is called the *Hubble flow*.

The Universe is in accelerated expansion and its current expansion rate is called the Hubble constant and is noted  $H_0$ . The Hubble-Lemaître law states that galaxies appear to be moving away from the Earth at speeds proportional to their distance, the ratio between velocity and distance being the Hubble constant. This cosmological parameter is of major importance to understand the nature and evolution of our Universe, and for this reason, measuring precise distances is paramount.

The Cepheid - SN Ia method was used by several teams to measure the Hubble constant empirically and mostly resulted in  $H_0 \approx 73$  km/s/Mpc. A second independent approach to estimate this parameter is from the Cosmic Microwave Background (CMB) observed by the *Planck* satellite. This *Planck* estimate, recently measured to  $H_0 \approx 67$  km/s/Mpc, is called the *early* measurement of the Hubble constant, as opposed to the *late* one from Cepheids and SN Ia, and is based on the standard model of cosmology, called the  $\Lambda$ -Cold Dark Matter ( $\Lambda$ -CDM) model. Comparing the early  $H_0$  value with the direct measurement at the present time is a powerful test of the cosmological model.

The early and late measurements of the Hubble constant are currently estimated with a very good precision on both sides and differ by more than  $4\sigma$ : this discrepancy between the direct (late) and model-dependent (early) determinations is often called the *Hubble tension*. If it is confirmed at a higher level of precision, such a strong discrepancy between both measurements would imply that the  $\Lambda$ -CDM model may need to be refined or adapted, for example by including new physics or exotic particles.

Cepheids play a key role in estimating extragalactic distances and therefore in the  $H_0$  controversy, although they are observed in our nearby environment. The P-L relation must be calibrated extremely carefully with precise and accurate distances of a large number of Cepheids and is sensitive to several systematic effects which must be understood. This calibration has long been limited by the lack of precise distances. In past decades, the *Hipparcos* satellite was the first mission dedicated to astrometry: for the first time, it provided parallaxes for a large sample of Cepheids, however the precision of these measurements remained limited. The *Hubble* Space Telescope (HST) was later used to measure Cepheid distances with a better precision but for a small number of stars. The true astrometric revolution was enabled by the launch of the *Gaia* satellite. This astrometric mission has measured high-quality parallaxes for 1.5 billion stars: these measurements are essential for the calibration of the P-L relation and are expected to improve the Hubble constant value close to a 1% precision. However, *Gaia* parallaxes are subject to a zero-point offset which introduces substantial systematics in the P-L calibration. Additionally, Cepheid parallaxes are affected by saturation due to their brightness and by potential chromaticity issues due to their change of color during their pulsation cycle. These limitations must be overcome in order to fully exploit the *Gaia* parallaxes. Furthermore, it has been demonstrated that the chemical composition of Cepheids impacts their intrinsic brightness. The difference in Cepheid metallicity between galaxies in which the P-L relation is calibrated and the galaxies hosting supernovae must be taken into account by including a corrective term in the P-L relation.

The aim of this thesis is to take advantage of the *Gaia* Data Release 2 (DR2) and Early Data Release 3 (EDR3) to improve the calibration of the P-L relation and to reduce the systematic effects that limit its accuracy. The present work is limited to the Cepheid P-L relation, the principal first anchor of the distance scale, but other distance indicators are of course necessary to obtain a final and more precise value of the Hubble constant. The thesis is structured as follows.

Chapter 1 gives an overview of the history of the calibration of the distance scale, from the early XX<sup>th</sup> century to the current tension on the Hubble constant. Several distance indicators are described such as eclipsing binaries, type-Ia supernovae and the tip of the red giant branch. Chapter 1 concludes with the important place of Cepheids in the distance scale.

Chapter 2 recalls previous calibrations of the P-L relation before *Gaia* with *Hipparcos* and the *Hubble* Space Telescope. I then describe the functioning of the *Gaia* satellite and the improvements on the Cepheid distance scale enabled by the *Gaia* data. This chapter highlights that *Gaia* DR2 parallaxes of Cepheids can be subject to unwanted noise and are occasionally unreliable due to saturation and variability. In order to avoid these issues, I developed a new method based on companion stars and open clusters hosting Cepheids. The *Gaia* DR2 astrometric solution of fainter and stable neighbour companions of Cepheids is more reliable than that of their parent variable star. Open clusters are also interesting for similar reasons: their numerous member stars allow us to derive an average value of the cluster parallax, which provides an alternative way to measure a precise distance to the Cepheids they host. I show that in *Gaia* EDR3, the noise and unreliability of Cepheid parallaxes due to their variability were significantly alleviated, thanks to the larger time coverage of the observations.



Finally, I also investigate the impact of the P-L relation on the distance scale by deriving a revised value for the Hubble constant.

In Chapter 3, I perform a calibration of the metallicity effect by comparing the P-L calibration in the Milky Way, where Cepheids are metal-rich, with the P-L relation in the Magellanic Clouds where Cepheids are more metal-poor than in our galaxy. Distances to Galactic Cepheids are adopted from the *Gaia* EDR3 catalog while distances to Magellanic Cloud Cepheids are derived from detached eclipsing binaries. I also discuss the dependence of the metallicity effect with wavelength by performing the same calibration in optical, near infrared and mid infrared bands.

Finally, in Chapter 4, I conclude by describing the ongoing efforts to reduce the systematics of the Cepheid distance scale, using the HST and *James Webb* Space Telescope as well as ground-based instruments. I discuss future projects and perspectives to improve our knowledge on astronomical distances and the expansion rate of the Universe.

Two additional studies are included in Appendix, they describe my contribution to two recent papers. In Appendix A, I discuss the calibration of the Cepheid projection factor with a view to apply the parallax-of-pulsation method to derive Cepheid distances. Using the recent *Gaia* EDR3 parallaxes, we implemented the SPIPS algorithm to derive physical parameters for a sample of Milky Way Cepheids and we evaluate the accuracy of the parallax-of-pulsation technique (Trahin et al. 2021). In Appendix B, the Cepheid distance to the SN Ia host galaxy NGC 5584 is examined ([Javanmardi et al. 2021](#)). We inspect each step of the SH0ES team procedure in an independent analysis. While intentionally employing systematically different tools and methods for the data reduction and analysis, we derive a distance to NGC 5584 that is consistent with the SH0ES estimate.

# Chapter 1

## The distance scale

---

<b>1.1</b>	<b>History of the distance scale . . . . .</b>	<b>11</b>
1.1.1	From Henrietta Leavitt to Edwin Hubble . . . . .	11
1.1.2	Early tensions . . . . .	13
1.1.3	The standard model of cosmology . . . . .	16
1.1.4	The tension on the Hubble constant . . . . .	16
<b>1.2</b>	<b>Measuring astronomical distances . . . . .</b>	<b>21</b>
1.2.1	Trigonometric parallaxes . . . . .	21
1.2.2	Eclipsing binaries . . . . .	22
1.2.3	Pulsating stars . . . . .	24
1.2.4	The Tip of the Red Giant Branch . . . . .	25
1.2.5	Type Ia supernovae . . . . .	26
1.2.6	Water masers in NGC 4258 . . . . .	27
1.2.7	Other methods for distance determination . . . . .	28
1.2.7.1	The Tully-Fisher relation . . . . .	28
1.2.7.2	The fundamental plane method . . . . .	28
1.2.7.3	The Surface Brightness Fluctuation method . . . . .	28
<b>1.3</b>	<b>Cepheids as distance indicators . . . . .</b>	<b>29</b>
1.3.1	Properties of Cepheid stars . . . . .	29
1.3.2	The place of Cepheids in the distance scale . . . . .	32

---

## 1.1 History of the distance scale

### 1.1.1 From Henrietta Leavitt to Edwin Hubble

Born in 1868, Henrietta Swan Leavitt was an American astronomer at Harvard College Observatory. She worked as a "woman computer" under the supervision of Edward Charles Pickering and was in charge of analysing thousands of photographic plates of the Large Magellanic Cloud (LMC) and Small Magellanic Cloud (SMC), two neighbour galaxies to the Milky Way. Her duty, for which she worked for free and later for thirty cents an hour, was to classify the magnitudes of stars. By comparing the size of the points on photographic plates taken at different times, she could see if the stars had a constant brightness or if they were varying in time. In 1908, Henrietta Leavitt published a catalog of 1777 variable stars that she identified in the SMC ([Leavitt 1908](#)). She noticed for the first time that the brighter Cepheids of her sample had the longer periods:

*"It is worthy of notice that in Table VI the brighter variables have the longer periods."*

A second paper, published in 1912 and signed by the name of Pickering ([Leavitt & Pickering 1912](#)), explicitly reveals their discovery: since all the stars of the SMC are approximately located at the same distance, the intrinsic luminosity of Cepheid stars is linearly correlated with the logarithm of its period (see Fig. 1.1), which makes Cepheids potential distance indicators. This period-luminosity (P-L) relation (Eq. 1.1) will later be called the Leavitt law to honor her work:

$$M = a \log P + b \quad (1.1)$$

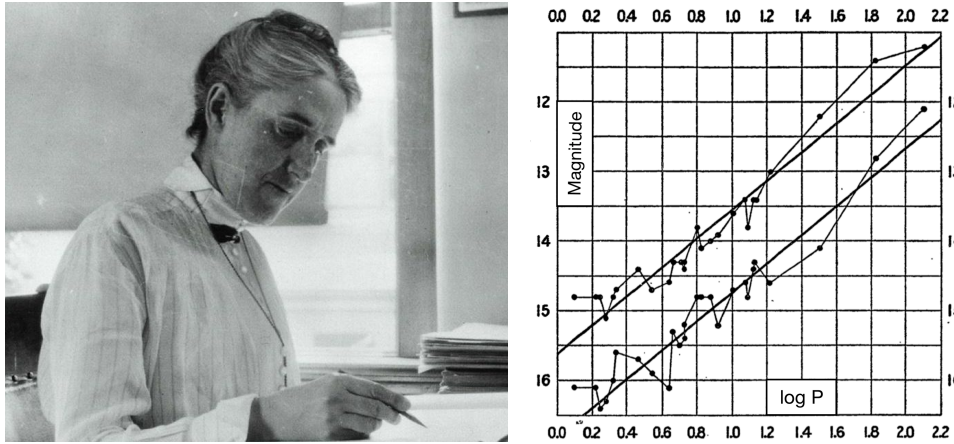


Figure 1.1: **Left:** Photography of Henrietta Swan Leavitt (Credit: The Harvard College Observatory). **Right:** First relation between magnitude and period established by Henrietta Leavitt from 25 variable stars in the SMC ([Leavitt & Pickering 1912](#)).

At the time of Henrietta Leavitt's discovery, it was generally conceived that our entire Universe was limited to the Milky Way. Our Galaxy was represented as a lens-shaped disk of 25,000 light years wide, known as the Kapteyn representation of the Universe, from the name of the dutch astronomer who had estimated its size. However, new ideas started to emerge on that matter, questioning the current belief. Several astronomers started to use Leavitt's results in order to study the structure of the Milky Way, and ultimately to estimate the distance of the nebulae they observed in the sky. In 1913, Ejnar Hertzsprung performed the first calibration of the P-L relation and derived the distance to the SMC ([Hertzsprung 1913](#)), followed by Henry Norris Russell on the same year.

In 1914, Vesto Slipher discovered how to estimate the speed of distant nebulae based on the Doppler effect (Slipher 1914): measuring the spectral shifts of fifteen "spiral nebulae" (galaxies), Slipher found them to be travelling at outstanding velocities. This work, although independent from Leavitt's research, would lead a few years later to another important discovery. Today, this spectral shift in the wavelength of distant galaxies is called the redshift and is noted  $z$ , defined as:

$$z = \frac{\lambda_{\text{obs}} - \lambda_0}{\lambda_0} \quad (1.2)$$

where  $\lambda_{\text{obs}}$  is the observed wavelength and  $\lambda_0$  is the emitted wavelength. It is still used to measure the recessional velocity of galaxies in the Hubble flow. In 1918, with the 60-inch telescope at Mount Wilson Observatory, Harlow Shapley measured the magnitudes and colors of Cepheids in 69 globular clusters (Shapley 1918a). Using Leavitt's relation, he derived the distances to these objects (Shapley 1918b). Noticing that globular clusters are not distributed evenly in the sky but appear to be concentrated in the Sagittarius constellation, he concluded that this region must be the center of the galaxy, and that Earth is located at the periphery. He revised the size of the Milky Way to 300,000 light-years, more than ten times larger than Kapteyn's estimate: he understood that if all the spiral nebulae observed in the sky were the size of the Milky Way, then the Andromeda nebula should be at enormous distance, given its apparent diameter.

In 1920, Heber Curtis confronted Shapley in the Great Debate, where they argued about the nature of our Universe. Curtis defended the idea of "island universes", later called galaxies, and claimed that Andromeda was one of them (Curtis 1920). He placed this nebula at 500,000 light-years of distance, and other spirals at more than 10 million light-years, from the novae he had used as distance indicators. On the other side, Shapley thought that our entire Universe was contained in the Milky Way (Shapley 1919).

In 1921, Henrietta Leavitt took the lead of the stellar photometry department at Harvard College Observatory, taking over from Pickering. However, she suffered from a lack of recognition, since scientists initially did not give credit to her for the discovery of the P-L relation. At that time, as a woman, she was not expected to investigate stars, but only to catalogue them meticulously, and she was not even allowed to operate telescopes. She started to progressively lose her hearing after travelling to Europe in her thirties, and became deaf eventually. She was also prone to illness and spent many years in her bed at home or at the hospital.

In 1926, the Swedish committee for the Nobel Prize in Physics considered nominating Henrietta Leavitt for her outstanding work and discovery on variable stars. Unfortunately, she had died from cancer five years earlier, in December 1921. Her groundbreaking contribution marked the beginning of a century of active research and major discoveries, that will deeply impact our knowledge of astrophysics and cosmology. In his book *The Realm of the Nebulae* (Hubble 1936), Edwin Hubble himself calls her finding "*a new feature of extraordinary significance*".

In 1929, Edwin Hubble used Leavitt's relation to measure the distance to Cepheids in the Andromeda nebula and understood that it is another galaxy beyond the Milky Way, hence confirming Curtis hypothesis and putting an end to the Great Debate. He also used the period-luminosity relation to measure the distances to variable stars located in several spiral nebulae and, combining those distances with their velocities derived from Vesto Slipher's method, Hubble discovered that the most distant nebulae have larger recessional velocities than nearby ones (see Fig. 1.2, Hubble 1929). Two years earlier, Georges Lemaître had already predicted that the Universe was expanding, however his paper was written in French and was therefore ignored by the specialists of the field (Lemaître 1927).

This linear relationship is now known as the Hubble-Lemaître law:

$$v = H_0 d \quad (1.3)$$

In this equation,  $v$  represents the recessional velocity of a galaxy, measured by spectroscopy as  $v = cz$ , and  $d$  is the distance of the galaxy in Mpc, derived from Cepheids and supernovae located in distant galaxies. The parameter  $H_0$ , named after Edwin Hubble and called the Hubble constant, describes the expansion rate of the Universe. The index 0 indicates the present time. The debates around the Hubble constant's value are extensively discussed in Sections 1.1.2, 1.1.4 and in the following chapters.

The Cepheid period-luminosity relation, discovered by Henrietta Leavitt, now serves as a primary distance indicator. Cepheids can be detected in nearby galaxies but are too faint to be seen in the Hubble flow ( $z \sim 0.1$ ), where the expansion of the universe dominates over gravitational attraction between galaxies. Cepheids are used as essential calibrators for secondary methods such as Type Ia supernovae (SN Ia), that can be observed to larger distances.

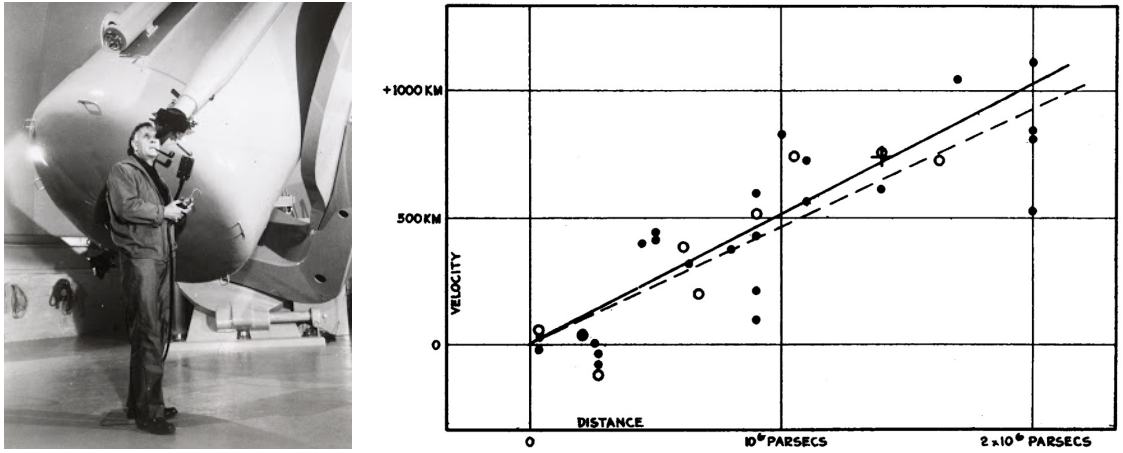


Figure 1.2: **Left:** Edwin Hubble at the Schmidt telescope, Palomar Observatory (Credit: Mt. Wilson Archive, Carnegie Institution of Washington). **Right:** Velocity of extra-galactic nebulae represented as a function of their distance (Hubble 1929).

### 1.1.2 Early tensions

After Hubble and Lemaître discovered that the Universe is expanding, astronomers tried to estimate the value of its expansion rate  $H_0$ . Lemaître (1927) was the first to propose a value for this parameter with 625 km/s/Mpc, while Hubble (1929) derived a similar but slightly lower value of 500 km/s/Mpc (Fig. 1.2). The Hubble constant remained very high with the study by de Sitter (1930) based on 54 galaxies in the Coma cluster that concluded with  $H_0 = 461$  km/s/Mpc.

In the fifties,  $H_0$  started to decrease: Sandage (1954) summarized four years of observations with the Hale 200-inch telescope and concluded with  $125 < H_0 < 276$  km/s/Mpc. Four years later, he became the first to derive a Hubble constant of 75 km/s/Mpc (Sandage 1958), which is extremely close to the current estimate. He was followed by Holmberg (1958) and Van Den Bergh (1960) with values around  $\sim 110$  km/s/Mpc. By 1962, most authors agreed that the value of  $H_0$  was located somewhere between 70 and 150 km/s/Mpc (Fig. 1.3).

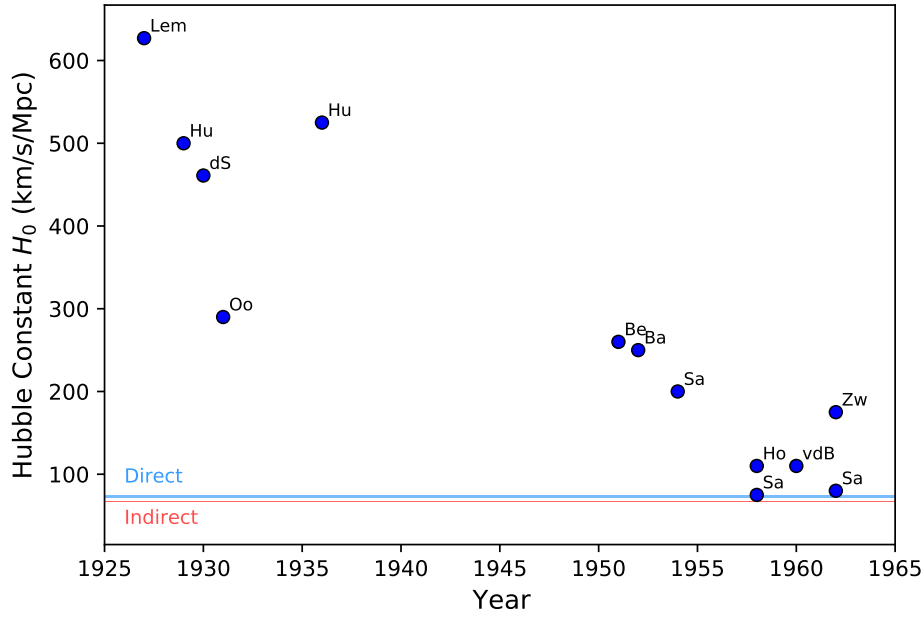


Figure 1.3: Determinations of  $H_0$  from 1927 to 1962. The two horizontal colored lines represent the most recent direct and indirect  $H_0$  values (Riess et al. 2021b; Planck Collaboration et al. 2020). The other references are: (Lem): Lemaître (1927), (Hu): Hubble (1929, 1936), (dS): de Sitter (1930), (Oo): Oort (1931), (Be): Behr (1951), (Ba): Baade (1948), (Sa): Sandage (1954, 1958, 1962), (Ho): Holmberg (1958), (vdB): Van Den Bergh (1960), (Zw): Zwicky (1962).

However, a disagreement between different authors emerged in the seventies, with some values around 55 and others closer to 100 km/s/Mpc (Fig. 1.4). The leader astronomers in favour of a low value for the Hubble constant were Allan Sandage and Gustav Tammann: for example, Sandage & Tammann (1975) derived  $H_0 = 55 \pm 5$  km/s/Mpc based on a sample of 36 spiral galaxies. In this paper, the largest contribution to the error budget of the Hubble constant is attributed to the calibration of the Cepheid PL relation. Gérard de Vaucouleurs took part of both sides of the debate, first deriving  $H_0 = 50$  km/s/Mpc from bright clusters (de Vaucouleurs 1970) but revising the value to the double with  $H_0 = 100 \pm 10$  km/s/Mpc a few years later (de Vaucouleurs 1977).

Sandage confirmed a  $H_0$  value as low as 50 km/s/Mpc several times in the following years in Sandage & Tammann (1982) and Sandage (1996). Although this early tension was gradually alleviated in the nineties with the increasing apparition of papers claiming a Hubble constant of  $\sim 70$  km/s/Mpc (Van Den Bergh 1988; Gouguenheim et al. 1990), many authors still defended low values around 50 km/s/Mpc (Terndrup 1988; Tammann & Leibundgut 1990; Sandage 2002) or values as high as 109 km/s/Mpc (de Vaucouleurs & Peters 1986). In 1996, a conference held in Washington, entitled "The scale of the Universe", opposed Tammann and Sidney Van den Bergh, who debated about this early tension (clearly visible in Fig. 1.4).<sup>1</sup>

At the end of the XX<sup>th</sup> century, a large survey of distant supernovae was carried out by the High-z Supernova Search Team (Schmidt et al. 1998; Garnavich et al. 1998; Riess et al. 1998b). In order to measure the deceleration parameter ( $q_0$ ) of the Universe by looking at the spectral shift of galaxies hosting SN Ia, the observations must be taken at sufficiently large distance so that the peculiar motion of galaxies is negligible (typically  $v \sim 10^4$  km/s, which corresponds to  $z \sim 0.03$ ),

<sup>1</sup> This short summary of the research on the value of  $H_0$  from  $\sim 1930$  to  $\sim 2000$  was inspired by Tammann (2006), we refer the reader to this thorough report for more details and additional references.

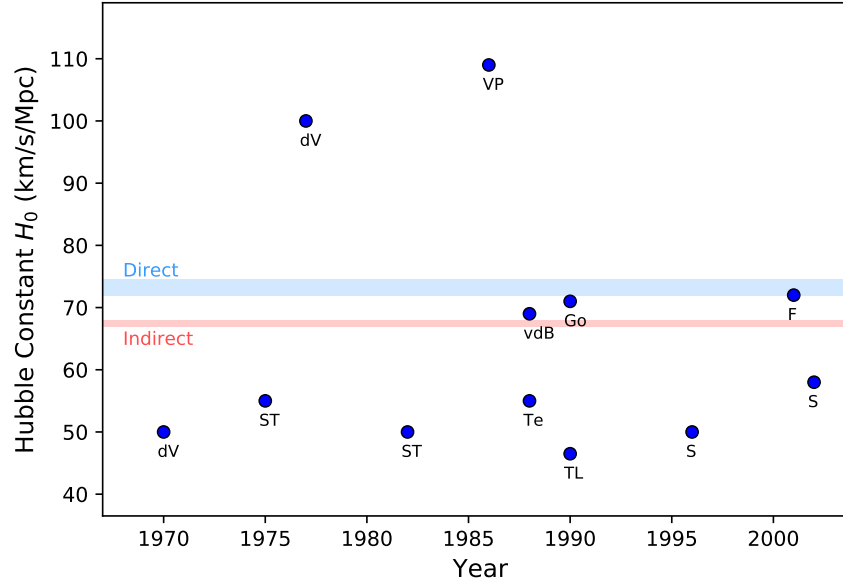


Figure 1.4: Determinations of  $H_0$  from 1970 to 2002. The two horizontal colored regions represent the most recent direct and indirect  $H_0$  values (Riess et al. 2021b; Planck Collaboration et al. 2020). The other references are: (dV): de Vaucouleurs (1970, 1977), (ST): Sandage & Tammann (1975, 1982), (VP): de Vaucouleurs & Peters (1986), (vdB): Van Den Bergh (1988), (Go): Gouguenheim et al. (1990), (Te): Terndrup (1988), (TL): Tammann & Leibundgut (1990), (S): Sandage (1996, 2002), (F): Freedman et al. (2001).

which was the aim of this survey. Riess et al. (1998a) published the redshifts and light curves of 16 high-redshift SN Ia ( $0.16 < z < 0.97$ ), obtained with ground-based telescopes such as Keck and the 3.6m at the ESO La Silla Observatory, combined with 34 nearby supernovae: this work provided strong evidence for a positive cosmological constant ( $\Omega_\Lambda > 0$ ) and a negative deceleration parameter ( $q_0 < 0$ ), which means an accelerating expansion of the Universe (see Sect. 1.1.3). The Supernova Cosmology Project published the same conclusion one year later in Perlmutter et al. (1999), from 42 high redshift supernovae. The Nobel Prize in Physics was awarded to Saul Perlmutter, Brian Schmidt and Adam Riess in 2011 for this discovery.

The launch of the NASA Hubble Space Telescope (HST) in 1990 was a major turning point in the history of the Hubble constant, and of astronomy in general. This new space observatory provided precise optical and near infrared (NIR) photometry for Cepheids and other standard candles. After decades of ground-based observations, astronomers could finally get rid of atmospheric turbulence and observe the stars without relying on weather conditions. However, the HST does not benefit from the protection of the Earth atmosphere and receives about 100 times more cosmic rays than ground-based telescopes, which contaminates space observations.

In 2001, the HST Key Project on the Extragalactic Distance Scale published their final results (Freedman et al. 2001): thanks to the high resolving power of HST, they used Cepheids to calibrate several independent distance indicators such as Type Ia supernovae, the Tully-Fisher relation or surface brightness fluctuations. Combining the results obtained from the different methods, which were in good agreement, they derived a final value of  $H_0 = 72 \pm 8$  km/s/Mpc. The Key Project was one of the major studies of  $H_0$  based on the first HST data, with a goal of 10% precision. Similarly, Sandage et al. (2006) used independent HST observations and published a lower estimate of  $H_0 = 62.3 \pm 5.2$  km/s/Mpc from the Cepheid-calibrated luminosity of Type Ia supernovae.



### 1.1.3 The standard model of cosmology

The standard model of cosmology, as it is admitted currently, describes the Universe in which we live on large scales. According to this model, the Universe is homogenous, isotropic, flat, and in accelerating expansion. It contains three main components: ordinary baryonic matter (e.g. stars, planets, gas, dust) with an energy density of  $\Omega_B \sim 0.049$ , a cold dark matter (CDM) that is non-baryonic, collisionless, stable and does not interact with light, at the amount of  $\Omega_M \sim 0.265$ , and finally a dark energy described by the cosmological constant  $\Lambda$ , with a total energy density of  $\Omega_\Lambda \sim 0.68$ . This last component, first introduced by Einstein in his theory of General Relativity in order to describe a closed and static Universe, was confirmed by the discovery of the accelerated expansion of the Universe (Riess et al. 1998a; Perlmutter et al. 1999). Dark energy acts like a repulsive gravity, and causes the negative pressure to dominate over matter's attractive gravity. It is mathematically equivalent to an energy density associated to the vacuum. The energy density budget also includes a small contribution from the radiation of the Cosmic Microwave Background (CMB),  $\Omega_R \sim 0.005$ , which used to be significant in the early Universe but is negligible today. These quantities must verify the relation:

$$\Omega_B + \Omega_M + \Omega_R + \Omega_\Lambda = 1 \quad (1.4)$$

The standard cosmological model, which is also called the  $\Lambda$  Cold Dark Matter ( $\Lambda$ CDM) model, is described by the Friedmann equations:

$$H^2 = \frac{8\pi G\rho}{3} - \frac{k}{a^2} + \frac{\Lambda}{3} \quad (1.5)$$

and:

$$\frac{\ddot{a}(t)}{a(t)} = -\frac{4\pi G}{3}(\rho + 3P) + \frac{\Lambda}{3} \quad (1.6)$$

where  $H$  is the Hubble parameter,  $\rho$  is the average density of matter,  $G = 6.67 \cdot 10^{-11} \text{ m}^3 \text{ kg}^{-1} \text{ s}^{-2}$  is the gravitational constant,  $a$  is the scale factor,  $k$  is the spatial curvature of the Universe and  $P$  is the pressure. The curvature  $k$  can be equal to 1 (positive curvature, closed universe), to -1 (negative curvature, hyperbolic) or to 0 (flat universe). The deceleration parameter  $q_0$ , mentioned in Sect. 1.1.2, is defined as:  $q_0 = \Omega_M/2 - \Omega_\Lambda$ . Its evolution over time is related to the Hubble parameter through the equation:  $\dot{H}/H^2 = -(1 + q)$ . The energy density associated with dark energy is connected to the Hubble constant by the relation:  $\Omega_\Lambda = \Lambda/3H_0^2$ . The scale factor  $a(t)$  can be expressed as a function of the redshift as:

$$1 + z = \frac{a_0}{a(t)} \quad (1.7)$$

The expression of the evolution of the Hubble parameter with time as a function of the scale factor  $a(t)$  is, by definition:

$$H(t) = \frac{\dot{a}(t)}{a(t)} \quad (1.8)$$

In cosmology, the knowledge of  $H_0$ , the present expansion rate, is essential to estimate the fundamental parameters of the Universe: for example, the inverse of the Hubble constant,  $H_0^{-1}$ , sets the age  $t_0$  of the Universe and the size of the observable universe  $R_0 = ct_0$ .

### 1.1.4 The tension on the Hubble constant

Besides empirical measurements of the local Hubble constant based on Cepheid distances of SN Ia (Sect. 1.1.1 and 1.1.2), it is also possible to predict  $H_0$  from the angular scale of the fluctuations in the power spectrum of the CMB. This different approach provides a picture of the very young Universe, 380,000 years after the Big Bang and is considered an "early" measurement. This  $H_0$  prediction from



the CMB is not a direct measurement, in the sense that it involves assumptions about the cosmological model and the physics in the early universe. Local measurements made in the present day do not depend on these assumptions: therefore, comparing the early and late measurements of the Hubble constant is a powerful test of the standard cosmological model (Verde et al. 2019). The Cosmic Background Explorer (COBE) satellite, launched in 1989, the Wilkinson Microwave Anisotropy Probe (WMAP), launched in 2001, and later the Planck satellite (ESA), mapped the CMB in the finest details and allowed to improve, year after year, the precision of the Hubble constant in the early Universe in a  $\Lambda$ CDM context.

In the mean time, Cepheids and supernovae measurements became increasingly more precise. The SH0ES team (Supernova  $H_0$  for the Equation of State), led by Adam Riess, observed a large number of Cepheids in SNe Ia host galaxies with the HST Wide Field Camera 3 (WFC3, Riess et al. 2009, 2011) and derived  $H_0 = 73.8 \pm 2.4$  km/s/Mpc. This result was still in good agreement ( $\sim 1.2\sigma$ ) with the estimate from the CMB observed by WMAP in 2011 ( $70.4 \pm 1.4$  km/s/Mpc, Jarosik et al. 2011). However, the next values measured from the CMB started to become lower and progressively inconsistent with the estimates derived from the Cepheid-SN Ia method (Fig. 1.5).

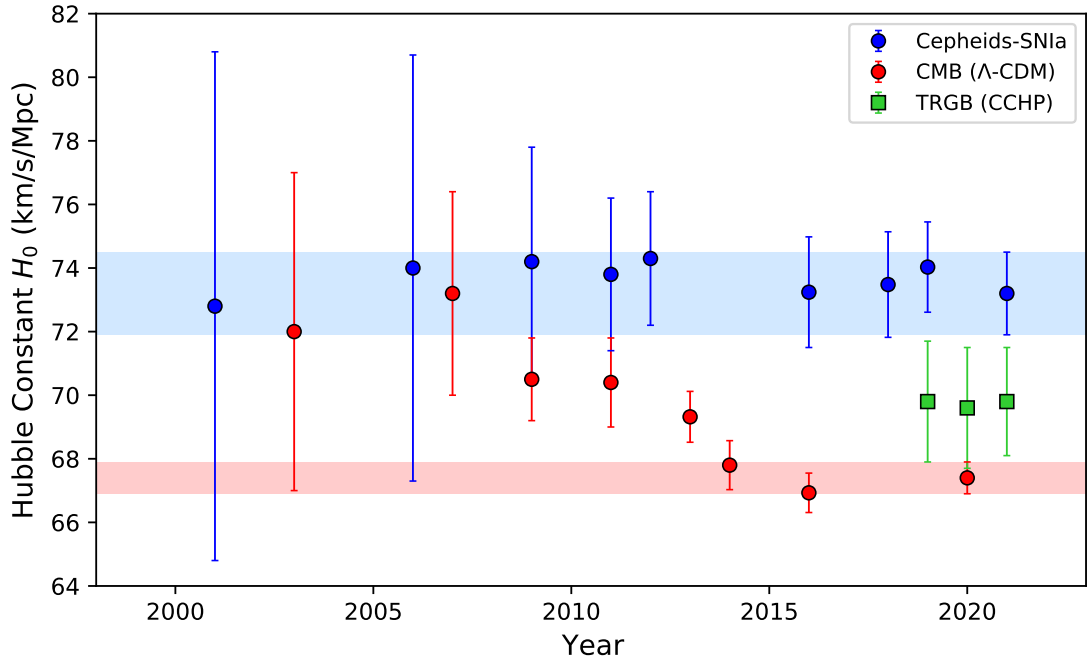


Figure 1.5: Determinations of  $H_0$  from 2001 to 2021. The two horizontal colored regions represent the most recent direct and indirect  $H_0$  values (Riess et al. 2021b; Planck Collaboration et al. 2020). The Cepheid-SNIa measurements (blue points) are, from left to right: Freedman et al. (2001), Macri et al. (2006), Riess et al. (2009), Riess et al. (2011), Freedman et al. (2012), Riess et al. (2016), Riess et al. (2018a), Riess et al. (2019a), Riess et al. (2021b). The CMB measurements (red points) are, from left to right: WMAP1 (Spergel et al. 2003), WMAP3 (Spergel et al. 2007), WMAP5 (Hinshaw et al. 2009), WMAP7 (Jarosik et al. 2011), WMAP9 (Bennett et al. 2013), Planck Collaboration et al. (2014), Planck Collaboration et al. (2016), Planck Collaboration et al. (2020). The TRGB measurements (green points) are, from left to right: Freedman et al. (2019), Freedman et al. (2020), Freedman (2021).

The local  $H_0$  value measured empirically remained relatively stable during the last decade, regardless of the adopted method. From an infrared calibration of the Cepheid P-L relation with the Spitzer telescope, [Freedman et al. \(2012\)](#) derived  $74.3 \pm 2.1$  km/s/Mpc. A few years later, [Riess et al. \(2016\)](#) combines four anchors in a robust 2.4% determination of the Hubble constant: water masers in NGC 4258, detached eclipsing binaries in the LMC, Milky Way Cepheids with HST and *Hipparcos* parallaxes, and finally eclipsing binaries in the Andromeda galaxy. They find  $H_0 = 73.24 \pm 1.74$  km/s/Mpc. The same year, [Planck Collaboration et al. \(2016\)](#) publishes a new value of  $66.93 \pm 0.62$  km/s/Mpc from the CMB, showing a  $2.8\sigma$  discrepancy with the recent local estimate.

Various methods were employed in order to test the reliability of the Cepheid-SN Ia method and to understand if it is responsible for this troubling disagreement, but the tension persisted. Using HST/WFC3 spatial scanning, [Riess et al. \(2018a\)](#) measure the parallaxes of seven long-period Cepheids and derives  $H_0 = 73.48 \pm 1.66$ , a value precise to 2.3% and still  $3\sigma$  away from Planck.

In 2019, the publication of a new distance of  $49.59 \pm 0.55$  kpc to the LMC, estimated by [Pietrzyński et al. \(2019\)](#) from 20 detached eclipsing binary systems (DEB), provides another improvement in the calibration of the local distance scale. This LMC distance was used as a strong anchor by [Riess et al. \(2019a\)](#) who publish a revised value of  $74.03 \pm 1.42$  km/s/Mpc. Finally, the recent data release (EDR3) of the *Gaia* astrometric mission (ESA) provided distances with a great level of precision for Milky Way Cepheids: combining HST/WFC3 photometry with *Gaia* EDR3 parallaxes for 75 Milky Way Cepheids, [Riess et al. \(2021b\)](#) finds  $H_0 = 73.2 \pm 1.3$  km/s/Mpc, the most precise local value to date for the Hubble constant. The latest result from [Planck Collaboration et al. \(2020\)](#) increases the tension to  $4.2\sigma$  with the extremely precise estimate of  $H_0 = 67.4 \pm 0.5$  km/s/Mpc. Recent values of the Hubble constant, derived empirically in the local universe or from CMB observations, are listed in Table 1.1.

The empirical work by the SH0ES team and others has greatly advanced the investigations on the Hubble constant over the last decade. In particular, the SH0ES calibration of the distance scale is performed using the same HST instruments and in a consistent photometric system from Milky Way Cepheids to distant supernovae. These homogeneous observations have the advantage of reducing the systematic errors due to calibration effects. The wavelengths adopted by the SH0ES team in their studies (Wesenheit and NIR bands) are also very weakly affected by extinction and by the choice of reddening law. In order to make SH0ES results compatible with early universe measurements, it would take a systematic bias of at least  $\sim 0.1$  mag in the intercept of the Cepheid P-L relation, in the sense that SH0ES Cepheids would have to be too bright, which is unexpected. [Javanmardi et al. \(2021\)](#) performed a fully independent reanalysis of the Cepheid calibration of the SN Ia host galaxy NGC 5584 implemented by [Riess et al. \(2016\)](#) and [Hoffmann et al. \(2016\)](#). By systematically adopting different tools and methods for each step, [Javanmardi et al. \(2021\)](#) find no systematic difference with the SH0ES paper.

Alternative methods have been developed where Cepheids are replaced by other stars acting as standard candles. The Tip of the Red Giant Branch (TRGB) is a good example of such primary calibrators (the method is described in Sect. 1.2.4). Using this technique, [Freedman \(2021\)](#) derived a Hubble constant value of  $69.8 \pm 1.7$  km/s/Mpc from TRGB stars, in agreement within  $\sim 1.5\sigma$  with both estimates from SH0ES and from the Planck CMB. A revisited value of  $71.5 \pm 1.8$  km/s/Mpc was recently published by [Anand et al. \(2021\)](#) from a slightly different sample of host galaxies.

Mira stars are also an interesting alternative to Cepheids for the calibration of SNe Ia luminosities. They are variable stars that belong to an older population than Cepheids and have a longer

Table 1.1: Recent estimates of the Hubble constant  $H_0$  (in km/s/Mpc) based on local measurements and from the CMB observation assuming a  $\Lambda$ -CDM model.

$H_0$	Method and reference
Local values	
$72 \pm 8$	Key Project: HST Cepheid-SN Ia method ( <a href="#">Freedman et al. 2001</a> )
$74 \pm 6.7$	Cepheid-SN Ia method ( <a href="#">Macri et al. 2006</a> )
$74.2 \pm 3.6$	SH0ES Team: HST Cepheid-SN Ia method ( <a href="#">Riess et al. 2009</a> )
$73.8 \pm 2.4$	SH0ES Team: HST Cepheid-SN Ia method ( <a href="#">Riess et al. 2011</a> )
$74.3 \pm 2.1$	Key Project: Cepheids + Spitzer ( <a href="#">Freedman et al. 2012</a> )
$73.24 \pm 1.74$	SH0ES Team: NGC 4258 + LMC + MW + M31 ( <a href="#">Riess et al. 2016</a> )
$73.48 \pm 1.66$	SH0ES Team: HST/WFC3 spatial scanning ( <a href="#">Riess et al. 2018a</a> )
$69.8 \pm 1.9$	Carnegie-Chicago Hubble Program: TRGB ( <a href="#">Freedman et al. 2019</a> )
$74.03 \pm 1.42$	SH0ES Team: NGC 4258 + MW + LMC DEB distance ( <a href="#">Riess et al. 2019a</a> )
$72.0 \pm 1.9$	NGC 4258 megamaser ( <a href="#">Reid et al. 2019</a> )
$69.6 \pm 1.9$	Carnegie-Chicago Hubble Program: TRGB ( <a href="#">Freedman et al. 2020</a> )
$76.0 \pm 2.5$	Tully-Fisher relation ( <a href="#">Kourkchi et al. 2020</a> )
$73.3 \pm 4.0$	SH0ES Team: Mira variables ( <a href="#">Huang et al. 2020</a> )
$73.3 \pm 1.8$	H0LiCOW: Gravitational lensing ( <a href="#">Wong et al. 2020</a> )
$73.9 \pm 3.0$	Megamaser host galaxies ( <a href="#">Pesce et al. 2020</a> )
$71.1 \pm 4.2$	Surface Brightness Fluctuations ( <a href="#">Blakeslee et al. 2021</a> )
$73.20 \pm 1.30$	SH0ES Team: HST/WFC3 + <i>Gaia</i> EDR3 ( <a href="#">Riess et al. 2021b</a> )
$69.8 \pm 1.7$	Carnegie-Chicago Hubble Program: TRGB ( <a href="#">Freedman 2021</a> )
$71.5 \pm 1.8$	Independent re-evaluation of CCHP TRGB distances ( <a href="#">Anand et al. 2021</a> )
CMB values	
$72 \pm 5$	WMAP 1 ( <a href="#">Spergel et al. 2003</a> )
$73.2 \pm 3.2$	WMAP 3 ( <a href="#">Spergel et al. 2007</a> )
$70.5 \pm 1.3$	WMAP 5 ( <a href="#">Hinshaw et al. 2009</a> )
$70.4 \pm 1.4$	WMAP 7 ( <a href="#">Jarosik et al. 2011</a> )
$69.32 \pm 0.80$	WMAP 9 ( <a href="#">Bennett et al. 2013</a> )
$67.80 \pm 0.77$	Planck 2013 results ( <a href="#">Planck Collaboration et al. 2014</a> )
$66.93 \pm 0.62$	Planck 2016 results ( <a href="#">Planck Collaboration et al. 2016</a> )
$67.40 \pm 0.50$	Planck 2018 results ( <a href="#">Planck Collaboration et al. 2020</a> )

pulsation period, greater than 100 days. [Huang et al. \(2018\)](#) provide a calibration of the Mira period-luminosity relation in the water maser host galaxy NGC 4258. Applying this calibration to the SN Ia host galaxy NGC 1559, [Huang et al. \(2020\)](#) derive a Hubble constant of  $73.3 \pm 4.0$  km/s/Mpc. Finally, the H0LiCOW collaboration uses quasar images that appear gravitationally lensed due to foreground galaxies in the line of sight, measuring the differences in path lengths. This independent approach, although model-dependent, provides a value of  $73.3 \pm 1.8$  km/s/Mpc for the Hubble constant ([Wong et al. 2020](#)). Other measurements of the Hubble constant in the late universe, using for example gravitational waves, should continue to improve in precision in the near future and provide complementary results to better understand the Hubble tension.<sup>2</sup>

This significant discrepancy between the Planck prediction from the CMB, assuming a  $\Lambda$ -CDM cosmology, and the local measurements of the Hubble constant is now commonly called the Hubble

<sup>2</sup> A detailed review of the Hubble constant tension and the various solutions suggested are presented in [Di Valentino et al. \(2021\)](#).

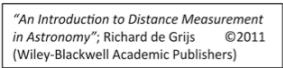


Figure 1.6: Various methods used to measure astronomical distances, from the nearest indicators (bottom) to the most distant (top). The methods discussed in the present thesis are highlighted in red. (Source: [De Grijs 2011](#), *An Introduction to Distance Measurement in Astronomy*).

tension. If confirmed with improved precision, it would provide a strong evidence for a failure in the standard cosmological model and may reveal the existence of new physics. Some suggestions to solve or to alleviate this puzzling tension were postulated: they include new relativistic particles, exotic dark energy, dark matter or neutrino interactions, modified gravity and non-zero curvature, among other ideas.

## 1.2 Measuring astronomical distances

This section aims at describing several methods used to measure astronomical distances. The geometrical method of the parallax, applicable to nearby stars, is described in Sect. 1.2.1. Then, the capabilities of eclipsing binaries as distance indicators are discussed in Sect. 1.2.2. Distance measurements based on pulsating stars, and in particular on Cepheids, are mentioned in Sect. 1.2.3 but are detailed throughout the following chapters. Tip of the Red Giant Branch stars can also be used as an alternative to Cepheids for the calibration of Type-Ia supernovae luminosity, both methods are described in Sect. 1.2.4 and 1.2.5 respectively. Finally, Sect. 1.2.7 provides three additional methods applicable in distant galaxies, but which rely on the prior calibration of primary distance indicators. This section only provides a non-exhaustive list of methods used to measure distances. Many other techniques are represented in Fig. 1.6, taken from [De Grijs \(2011\)](#).

### 1.2.1 Trigonometric parallaxes

The trigonometric parallax is the most geometric and the most direct method to measure the distance of the stars in our close environment. The parallax of a star is measured by observing its position in the sky at different times of the year: since the Earth is revolving around the Sun with a period of one year, the movement of the star described in the sky during six months can be linked to the distance  $d$  using a simple trigonometry relation, knowing the diameter  $2R$  of the Earth's orbit (Fig. 1.7):  $\tan \alpha = R/d$ . Since  $\alpha \ll 1$ , the distance is simply:  $d = R/\alpha$  with  $R = 1$  AU. The background stars, which are far enough to be considered motionless, are used as a reference. By definition, a star at a distance of 1 kpc has a parallax of 1 milliarcsec (mas).

The parallax method is one of the most robust approaches to calibrate the P-L relation with a sample of nearby Cepheids. Parallaxes are now measured with a good precision within the Milky Way thanks to the *Gaia* satellite (see Chapters 2 and 3). The *Gaia* Data Release 2 (DR2), published in 2018, provides parallaxes of Cepheids up to 10 kpc ( $\sim 0.1$  mas) in the Milky Way, with a precision of about 10%. This precision was improved to 5% with the Early Data Release 3 (EDR3). In comparison, Cepheid parallaxes measured by the HST Fine Guidance Sensor (FGS) about fifteen years ago were precise to 8% ([Benedict et al. 2007](#)), and the parallaxes obtained by spatial scanning with HST/WFC3 are precise to 10% ([Riess et al. 2018a](#)).

This last technique was recently used by the SH0ES Team and consists in slewing the space telescope during the observation, which results in long trails described by each source on the detector: the light of each star is spread over a large number of pixels, allowing a larger signal to noise ratio to be achieved, and contains thousands of individual position measurements in the direction opposite to the trail. This method can provide Cepheid parallaxes up to a distance of 5 kpc with a precision of  $\sim 30 \mu\text{as}$ . It was also used to measure Cepheid photometry and allowed for bypassing the saturation for bright stars ([Riess et al. 2018b](#)). Although this method has proven to be powerful, HST can only measure individual distances to a limited sample of Cepheids, whereas the *Gaia* satellite is fully dedicated to distance measurements and has observed more than 9,500 Cepheids.

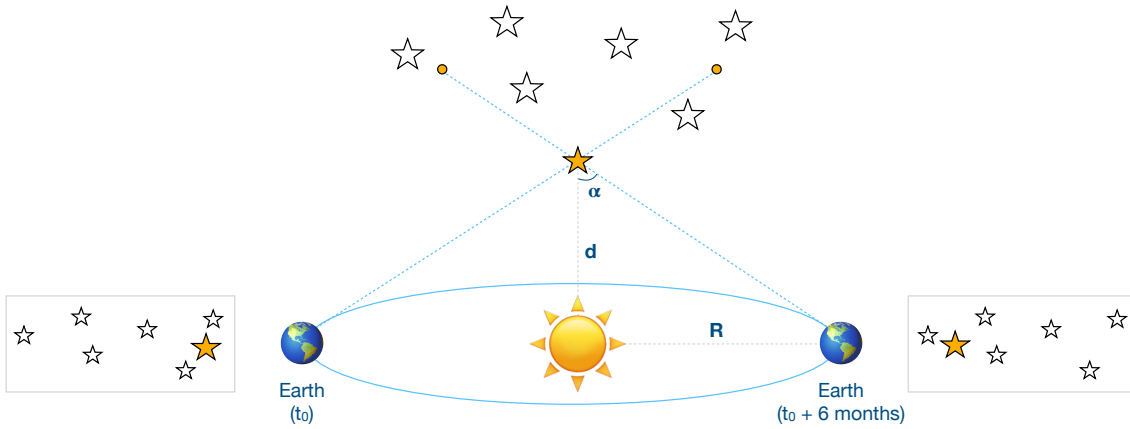


Figure 1.7: Representation of the parallax method. The large empty stars are background distant point-like sources, they have a constant position, and the orange star is the one that is observed and for which the parallax is measured. The two orange dots represent the projected position of the orange star at time  $t_0$  and  $t_0 + 6$  months.

### 1.2.2 Eclipsing binaries

Eclipsing binaries are systems of two stars orbiting around each other, which happen to have their orbit plane parallel to our line of sight. They are widely used to measure distances to the galaxies of the Local Group, and especially to the LMC and the SMC. They are a key indicator used by the Araucaria Project<sup>3</sup> (PIs: Grzegorz Pietrzyński and Wolfgang Gieren) in order to improve the precision of the distance scale. Eclipsing binaries belong to the class of variable stars: when one component of the system orbits around the other, it eclipses its light, so the brightness of the system changes with time. However they should not be confused with pulsating stars, discussed in Sect. 1.2.3: the variability of eclipsing binaries is not due to intrinsic changes of the stars.

The method, described by Lacy (1977), is geometric: the comparison between the angular diameter  $\theta$  of one component and its linear size  $R$  gives a direct estimate for the distance of the eclipsing binary system through the relation:

$$\tan \theta = \frac{2R}{d} \sim \theta \quad (1.9)$$

where the distance  $d$  is in the same unit as  $R$ , and the angular diameter  $\theta$  is in radians. The angular diameter is derived from surface brightness-color relations previously calibrated using interferometric measurements, and the linear size  $R$  is obtained from the analysis of the photometric and radial velocity curves (Guinan et al. 1998; Fitzpatrick et al. 2003).

The precision of this technique is mostly limited by the use of surface brightness color relations and by the photometric zero point between different sets of data. Pietrzyński et al. (2019) provides an improved calibration of this relation with a precision of 0.8%, using 41 red clump giant stars. These

<sup>3</sup> <https://araucaria.camk.edu.pl/>



stars are in the core helium burning phase of stellar evolution, therefore the relation is particularly suited to determine distances to eclipsing binaries, which are composed of helium-burning giant stars. Various surface brightness color relations have been implemented so far, but strong discrepancies in terms of precision and accuracy still exist in the literature (Salsi et al. 2021). From angular diameters measured by interferometry with the PIONIER instrument at the Very Large Telescope Interferometer (VLTI), they derive a relation between the surface brightness  $S_V$  and the  $(V - K)$  color (Fig. 1.8):

$$S_V = 1.330_{\pm 0.017} [(V - K)_0 - 2.405] + 5.869_{\pm 0.003} \text{ mag} \quad (1.10)$$

The index 0 indicates that the magnitudes are corrected for extinction. The angular diameter  $\theta$  is then directly obtained from the definition of the surface brightness:  $S_V = V_0 + 5 \log(\theta)$ .

The LMC and the SMC contain a large number of variable stars, and thus have become the best anchors to calibrate the extragalactic distance scale. Recently, Pietrzyński et al. (2019) determined an improved distance to the LMC from a sample of 20 late-type detached eclipsing binary systems. They derive a distance of  $49.59 \pm 0.09$  (stat.)  $\pm 0.54$  (syst.) kpc, which converts to a distance modulus  $\mu = m - M = 18.477 \pm 0.004 \pm 0.026$  mag. This new LMC distance led Riess et al. (2019a) to derive a revised value for the Hubble constant, anchored to the LMC.

While the LMC has a simple and well-studied structure, the SMC has a more complex geometry and in particular a large extension along the line of sight, which makes its distance difficult to measure with precision. Similarly to the LMC study, Graczyk et al. (2020) used 10 new late-type detached eclipsing binaries in the SMC, in addition to 5 other systems previously published in Graczyk et al. (2014). They find a final distance of  $62.44 \pm 0.47$  (stat.)  $\pm 0.81$  (syst.) kpc to the core region of the SMC, precise to 2%, which converts into a distance modulus of  $18.977 \pm 0.016 \pm 0.028$  mag.

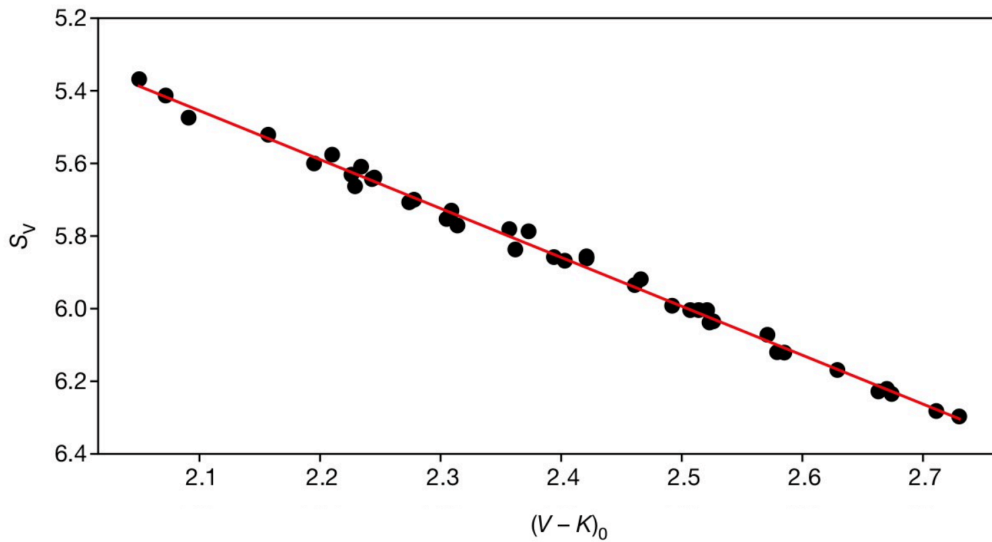


Figure 1.8: Surface brightness-color relation calibrated by Pietrzyński et al. (2019) using angular diameters of 41 red clump stars measured by interferometry with VLTI/PIONIER. This relation has a dispersion of 0.018 mag and provides a 0.8% precision in the derived stellar angular diameters.

Early-type eclipsing binaries are brighter and easier to detect than late-type systems, but the precision on the surface brightness color relation for this type of stars has been very limiting. It was however improved recently to 8% precision by Challouf et al. (2014) and to 2% by Salsi et al. (2021)

thanks to the CHARA/VEGA instrument, offering a new possibility to measure angular diameters. The late-type binaries are, on the other hand, much scarcer and more difficult to detect, but when observed, they provide a robust tool for distance determination.

### 1.2.3 Pulsating stars

Pulsating stars are among the most direct, empirical and well-established standard candles to measure distances. This approach relies on the P-L relation, discovered by Henrietta Leavitt ([Leavitt & Pickering 1912](#), see Sect. 1.1.1):

$$M = a \log P + b \quad (1.11)$$

The pulsation period  $P$  of a star can be easily obtained by collecting measurements of its brightness during the pulsation: the time between successive maxima defines the period. Once the coefficients  $a$  and  $b$  are precisely calibrated, for example using parallaxes for a sample of pulsating stars, this law provides the absolute magnitude  $M$  of a star of period  $P$ . Finally, taking the flux-average of the light curve gives the mean apparent magnitude  $m$  of the star. The comparison between apparent and intrinsic brightness gives the distance  $d$  of the star in kpc:

$$M = m - 5 \log d - 10 \quad (1.12)$$

Among pulsating stars, Cepheids provide the most precise and homogeneous distances, with periods ranging from 2 to  $\sim 100$  days (see Sect. 1.3). With their brightness reaching 100 000 solar luminosities, they can be observed to a distance of tens of megaparsecs, in remote galaxies hosting type Ia supernovae. The Cepheid P-L relation was extensively studied and calibrated in various wavelengths ([Madore & Freedman 2012](#); [Groenewegen 2018](#); [Riess et al. 2019a](#); [Clementini et al. 2019](#); [Breuval et al. 2020](#); [Ripepi et al. 2020](#); [Chown et al. 2021](#)). It has improved significantly in the past few years thanks to the publication of new precise geometric distances, such as the *Gaia* parallaxes for a large number of Milky Way Cepheids and the distance to the LMC and SMC from eclipsing binary systems. However, remaining systematic effects are still limiting the application of the Leavitt law: for example, optical bands are strongly affected by reddening, the effect of metallicity on the P-L relation is still poorly calibrated, and the presence of a circumstellar envelope of ionized gas around Cepheids may introduce a bias on the measurements ([Hocdé et al. 2020](#)). The aim of this thesis is to improve the calibration of the Cepheid P-L relation and to examine its dependences, in order to reduce the error budget of the Hubble constant.

Besides Cepheids, other pulsating stars are also used to derive distances (Fig. 1.9). RR Lyrae stars have shorter periods, from a few hours to slightly more than a day, they are fainter than Cepheids ( $\sim 50 L_{\odot}$ ) and less massive ( $\sim 0.7-0.8 M_{\odot}$ ) but widely distributed in nearby galaxies and in the Milky Way. They are also core helium burning stars. Compared to Cepheids, they are more metal-poor and also older than Cepheids ( $> 10$  Gyr). RR Lyrae are good tracers of old stellar populations. They can be observed close to the galactic center, in the halo and in globular clusters. While RR Lyrae follow a P-L relation in the infrared ([Longmore et al. 1986](#); [Madore et al. 2013](#); [Marconi et al. 2015](#); [Neeley et al. 2017](#), and references therein), in optical wavelengths they follow a Luminosity-Metallicity relation ([Clementini et al. 2003](#); [Muraveva et al. 2018](#), and references therein). Many RR Lyrae are subject to the Blazhko effect, which appears as periodic amplitude and phase modulations of the light curve. The physics behind this phenomenon is not fully understood. Finally, the distances reached by RR Lyrae are limited to about 4 Mpc due to their lower luminosity, about ten times closer than Cepheids. For these reasons, they are very interesting astronomical objects and promising standard candles, but are still not competitive with Cepheids as distance indicators for the measurement of  $H_0$ .



On the other hand, Mira stars are highly-evolved asymptotic giant branch stars with low mass and longer periods, from 80 to 1,000 days. They are more common than Cepheids and can be found in all galaxies, which makes them excellent substitutes for measuring the distance to supernovae host galaxies where primary distance indicators are missing, enlarging the small number of SNe Ia available through Cepheid distances only. Their position in the Hertzsprung-Russell (HR) diagram is distinct from that of Cepheids and their pulsation mechanism is also different, but Mira stars are a promising independent distance indicator. They are once to twice brighter than Cepheids and their amplitude can reach 2 magnitudes in optical bands, which makes them detectable to large distances and their pulsation easy to study. They can be divided in two categories: oxygen-rich (O-rich) Miras, which follow a well-defined P-L relation (Whitelock et al. 2008; Yuan et al. 2017), and carbon-rich (C-rich) Miras, which can be distinguished from the first category with color information. The Mira P-L relation calibrated by Huang et al. (2020) led to a new calibration of SN Ia luminosity, and to a Hubble constant of  $73.3 \pm 4.0$  km/s/Mpc.

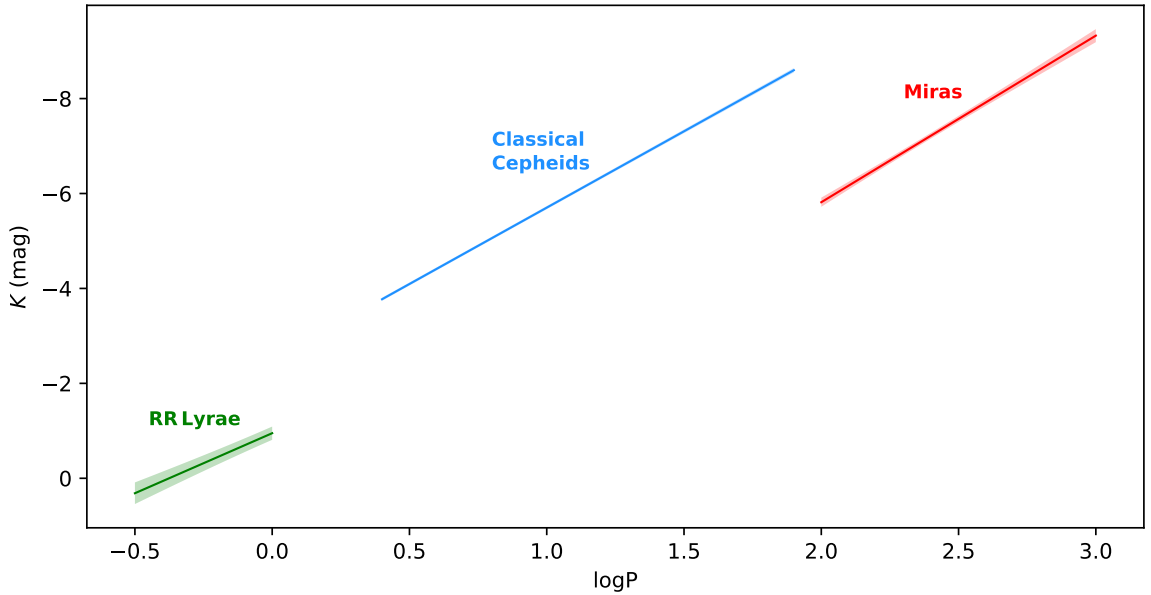


Figure 1.9: Period-luminosity relations in the near infrared  $K$  band for RR Lyrae stars (Muraveva et al. 2015), Classical Cepheids (Breuval et al. 2021) and Mira stars (Whitelock et al. 2008).

#### 1.2.4 The Tip of the Red Giant Branch

The Tip of the Red Giant Branch (TRGB) refers to a region of the Hertzsprung-Russell (HR) diagram where red and low-mass stars become abruptly fainter and move to the horizontal branch. This transition starts by the helium flash, where the triple-alpha reaction produces a large amount of energy because of its extreme sensitivity to temperature. It initiates the combustion of helium in the core. Then, red giant stars continue to burn helium and the hydrogen-burning zone moves to a surrounding shell. At this stage, the star inflates and becomes brighter and bluer. This sequence of stellar evolution marks an upper boundary for the luminosity of RGB stars. This limit is well understood empirically (McQuinn et al. 2019; Freedman et al. 2020) and theoretically (Serenelli et al. 2017).

Since the helium flash depends on the temperature, stars reach the TRGB at a known intrinsic luminosity that can be calibrated. In the  $I$ -band, the TRGB luminosity has a very small dependency

on the age and metallicity of the stars, which makes it a useful distance indicator. It was calibrated at  $M_I^{\text{TRGB}} = -4.047 \pm 0.022 \text{ (stat)} \pm 0.039 \text{ (syst)} \text{ mag}$  by [Freedman et al. \(2020\)](#). Fig.1.10 represents the color-magnitude diagram in the  $I$  band for the outer region of the LMC taken from [Freedman et al. \(2019\)](#), showing a discontinuity at the apparent magnitude of 14.595 mag.

Red giant branch stars can be found in the halo of galaxies of all morphological types, where the background noise due to crowding is lower, as well as the reddening. In other bands than  $I$ , where a dependence of the TRGB luminosity with metallicity is significant, it can be identified by its color. This dependence was precisely calibrated ([Jang & Lee 2017](#)) and is easily accounted for as a correction. Although this method is well established, RGB stars are up to 2.5 mag fainter than Cepheids in the optical, limiting the applicability of this method to a distance of  $\sim 30 \text{ Mpc}$ , in the nearby galaxies, where few SNe Ia are identified.

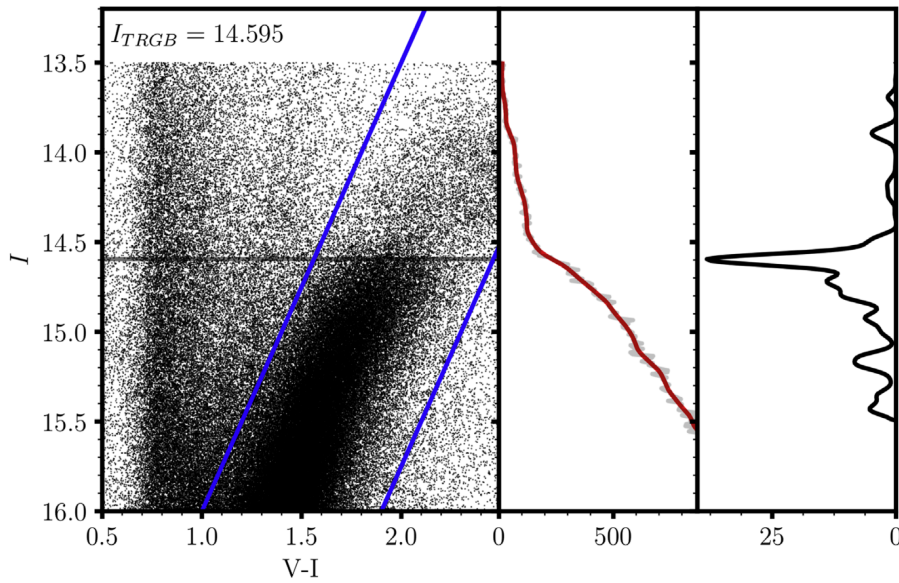


Figure 1.10: Color-magnitude diagram for the outer region of the LMC in the  $I$ -band, luminosity function and edge-detection response to a filter. (Source: [Freedman et al. 2019](#)).

### 1.2.5 Type Ia supernovae

A type Ia supernova results from the explosion of a white dwarf in a binary system, where the parent star is accreting the material of a companion star. Once the white dwarf reaches the Chandrasekhar mass ( $1.4 M_{\odot}$ ), the equilibrium between gravitation and electron pressure in the star is broken: the core enters a carbon-burning phase that produces so much energy that the star is torn apart and explodes in a cataclysmic blast: a type Ia supernova explosion.

The brightness of a SN Ia is comparable to that of an entire galaxy and can reach billions of solar luminosities, making them observable up to a distance of hundreds of megaparsecs. Type Ia supernovae serve as powerful distance indicators thanks to a remarkable property: the intrinsic peak luminosity correlates with the rate at which the light decreases after reaching the peak ([Phillips 1993](#)). Therefore, bright supernovae see their luminosity decrease slower than the fainter ones. Examples of SN Ia light curves in various wavelengths are provided in Fig. 1.11.

Type Ia supernovae are secondary distance indicators, which means that we cannot perform direct measurements of their distance, but their brightness must be calibrated using other standard candles such as Cepheids or the TRGB. To obtain the distance of a SN Ia, one needs to measure the rise, the peak and the dimming of the brightness to derive the intrinsic luminosity, and finally compare it with the apparent brightness.

The advantage of supernovae is that they can be observed on a large range of distances, and that nearby and high redshift supernovae show very similar light curves. At high redshifts, they are excellent tracers of the expansion rate of the Universe when it was younger, while their nearby counterparts show the current expansion rate: comparing supernovae observed at various distances can teach us the evolution of this quantity over time.

The main limitation to this method is the rarity of SNe Ia in the local universe. Only 19 are observed in nearby galaxies hosting Cepheids (Riess et al. 2016) but this sample should be doubled in the coming months. Moreover, as for Cepheids and many other astronomical objects, the brightness of supernovae is severely affected by the dust in their host galaxies and on the line of sight, which dims their light and reddens their color.

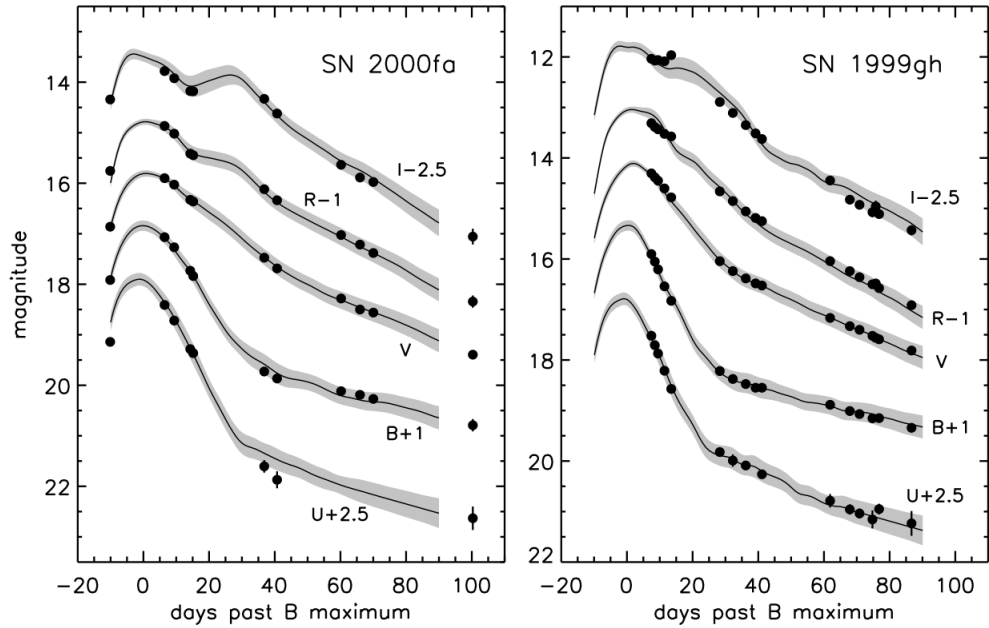


Figure 1.11: Example of SN Ia light curves in different wavelengths. (Source: Jha et al. 2007).

### 1.2.6 Water masers in NGC 4258

In the nearby galaxy NGC 4258, water masers orbit the central black hole of  $4 \times 10^7 M_{\odot}$  in a sub-parsec scale accretion disk. The Keplerian motion of the masers was observed by mapping and spectral monitoring using very long baseline interferometry (VLBI) in order to derive their position, velocities, and angular and linear accelerations. A geometric distance of NGC 4258 is directly obtained by fitting the positions, velocities and combined line-of-sight accelerations of the maser features (Humphreys et al. 2013).

Combining 18 VLBI epochs, [Reid et al. \(2019\)](#) derives a distance of  $7.576 \pm 0.082$  (stat.)  $\pm 0.076$  (sys.) Mpc to this galaxy. Using this distance as the unique source of calibration of the Cepheid-SN Ia distance scale, they obtain a Hubble constant of  $H_0 = 72.0 \pm 1.9$  km/s/Mpc. Combining the NGC 4258 water maser distance with geometric distances of Milky Way Cepheids and LMC eclipsing binaries yields  $H_0 = 73.5 \pm 1.4$  km/s/Mpc. It agrees within  $1\sigma$  with each anchor estimate by [Riess et al. \(2019a\)](#). Similarly, the work by [Pesce et al. \(2020\)](#) also confirms the Hubble tension with a value of  $73.9 \pm 3.0$  km/s/Mpc from the combination of several megamaser host galaxies. The megamaser approach is particularly interesting because the method is purely geometric and independent of any other calibration. This distance to NGC 4258 from [Reid et al. \(2019\)](#) is used to calibrate the P-L relation of its Cepheids. However, its major limitation is the rarity of such maser systems, making the measurement difficult to replicate.

### 1.2.7 Other methods for distance determination

In this section, a few additional methods of distance determination are described. They are secondary distance indicators, which means that they must be calibrated by direct methods such as Cepheids or TRGB. They can be adopted as substitutes to SNe Ia for measuring extragalactic distances on large scales, and they are often used as independent checks of the recent precise measurements. However, they are not competitive with the Cepheid–SN Ia method in terms of precision and accuracy.

#### 1.2.7.1 The Tully-Fisher relation

The Tully-Fisher method ([Tully & Fisher 1977](#)) is based on the empirical relation between the total brightness of spiral galaxies and their maximum rotation rate. These two quantities are highly correlated: the brighter spiral galaxies, which are also the more massive, have a higher rotation speed that compensates gravitational attraction. The rotation speed can be easily measured by spectroscopy, using the neutral hydrogen line. The most recent calibration of the Tully-Fisher relation was established by [Kourkchi et al. \(2020\)](#) from a sample of  $\sim 600$  spiral galaxies observed in optical and infrared wavelengths, they derive a Hubble constant of  $76.0 \pm 2.5$  km/s/Mpc.

#### 1.2.7.2 The fundamental plane method

Similarly to the Tully-Fisher relation, which applies to spiral galaxies, the fundamental plane method is based on the correlation between the average surface brightness, the radius and the velocity dispersion of elliptical galaxies. This approach is described by [Gudehus \(1973\)](#). The relationship between intrinsic luminosity and radius is straightforward: the brighter elliptical galaxies have a larger effective radius. When applying this method, as well as the Tully-Fisher relation, the quantities must be corrected for the inclination of the galaxy.

#### 1.2.7.3 The Surface Brightness Fluctuation method

Finally, one last technique that will be described here is the surface brightness fluctuation method ([Tonry & Schneider 1988](#)). When a galaxy is observed through a telescope, the light received by each pixel of the camera corresponds to the sum of the light of all the stars, and the fluctuations of the light received pixel by pixel depend on the distance of the galaxy. For example, the image of a distant galaxy contains more stars per pixel than a nearby galaxy (the amount of stars per pixel

increases as  $\propto d^2$ ), but the stars of a distant galaxy are also fainter than the stars of a closer galaxy (the apparent brightness follows  $\propto d^{-2}$ ). Therefore, the flux received is independent of the distance. However, the variations of the flux between two pixels increase as  $d^{-1}$ , which means that it can be used to derive the distance. The more distant is a galaxy, the smoother will be its surface brightness. This method relies on the assumption that the galaxy has a homogeneous stellar content, which is not always verified for spiral galaxies. However, elliptic galaxies are particularly well-suited for this approach. The most recent study based on surface brightness fluctuations is by [Blakeslee et al. \(2021\)](#): from HST/WFC3 imaging of 63 bright galaxies out to a distance of 100 Mpc, they calibrate the method using both Cepheids and TRGB stars and derive a Hubble constant of  $71.1 \pm 4.2$  km/s/Mpc.

## 1.3 Cepheids as distance indicators

### 1.3.1 Properties of Cepheid stars

Among the various distance indicators described in the previous section, Cepheids are the best-established and most precise technique to derive distances. They are bright yellow giant or supergiant stars, with a mass ranging from 4 to 15  $M_{\odot}$ . Their luminosity is as high as 100,000  $L_{\odot}$  and their brightness variation can reach 2 magnitudes in optical bands, which makes them easy to detect in the Local Group and in distant galaxies out to 50 Mpc. Being up to  $\sim 8$  mag brighter than RR Lyrae, Cepheids are the primary distance indicator that can reach the most distant SN Ia host galaxies.

In the HR diagram, Cepheids are located in a well-defined region called the "instability strip" (Fig. 1.12), which also contains other pulsating stars such as RR Lyrae, Type II Cepheids and  $\delta$  Scuti variables. In this thesis, only Type I Cepheids, also called Classical Cepheids (CCs), are considered for the calibration of the P-L relation. Type II Cepheids are also interesting and are distributed in various subclasses depending on their period (BL Herculis, W Virginis, RV Tauri). They are generally less massive than Cepheids and follow their own P-L relation.

[Eddington \(1917\)](#) was the first to propose the existence of a dense external layer blocking the radiation of the star as an explanation for Cepheid pulsation. He describes a more detailed theory on regions of partial ionization of hydrogen in [Eddington \(1941\)](#). Cepheids are stars that have depleted the hydrogen in their core by thermonuclear fusion reaction and have started to burn helium. These new conditions cause significant changes in the internal physics, these stars no longer dissipate the energy created in the core efficiently enough and the hydrostatic equilibrium is then broken. Its structure starts to expand and contract periodically thanks to a self-sustaining mechanism. This stage marks the entrance of the star in the instability strip. It starts burning helium in the core, turning it into a combination of inert carbon and oxygen.<sup>4</sup>

The mechanism that drives Cepheid pulsation comes from the change in the opacity of the ionized zone under the photosphere of the star, for this reason it is known as " $\kappa$  mechanism". The rise in temperature resulting from the fusion of helium in a small volume increases the electronic pressure and therefore ionizes helium, creating a dense layer of helium under the photosphere of the star. This helium layer blocks the energy emitted inside the star and prevents the radiation from moving to the surface. Radiative flux becomes insufficient to release the energy, then radiation pressure increases in the outer layers and overcomes gravitational pressure: the star enters an expansion phase. While the radius of the star is expanding, electrons are recombined in the external helium layer. The important

<sup>4</sup> The detailed report by [Bhardwaj \(2020\)](#) describes the different evolutionary stages of a Cepheid and the successive crossings of the instability strip.

amount of energy stored under the layer is finally released, opacity decreases and radiative flux raises. Finally, gravitation starts to dominate over radiation pressure, which contracts the Cepheid and results in the reionization of the external helium layer. This contraction starts a new cycle of pulsation. This pulsation mechanism was later studied in detail by [Baker & Kippenhahn \(1962\)](#), [Cox \(1963\)](#) and [Zhevakin \(1963\)](#).

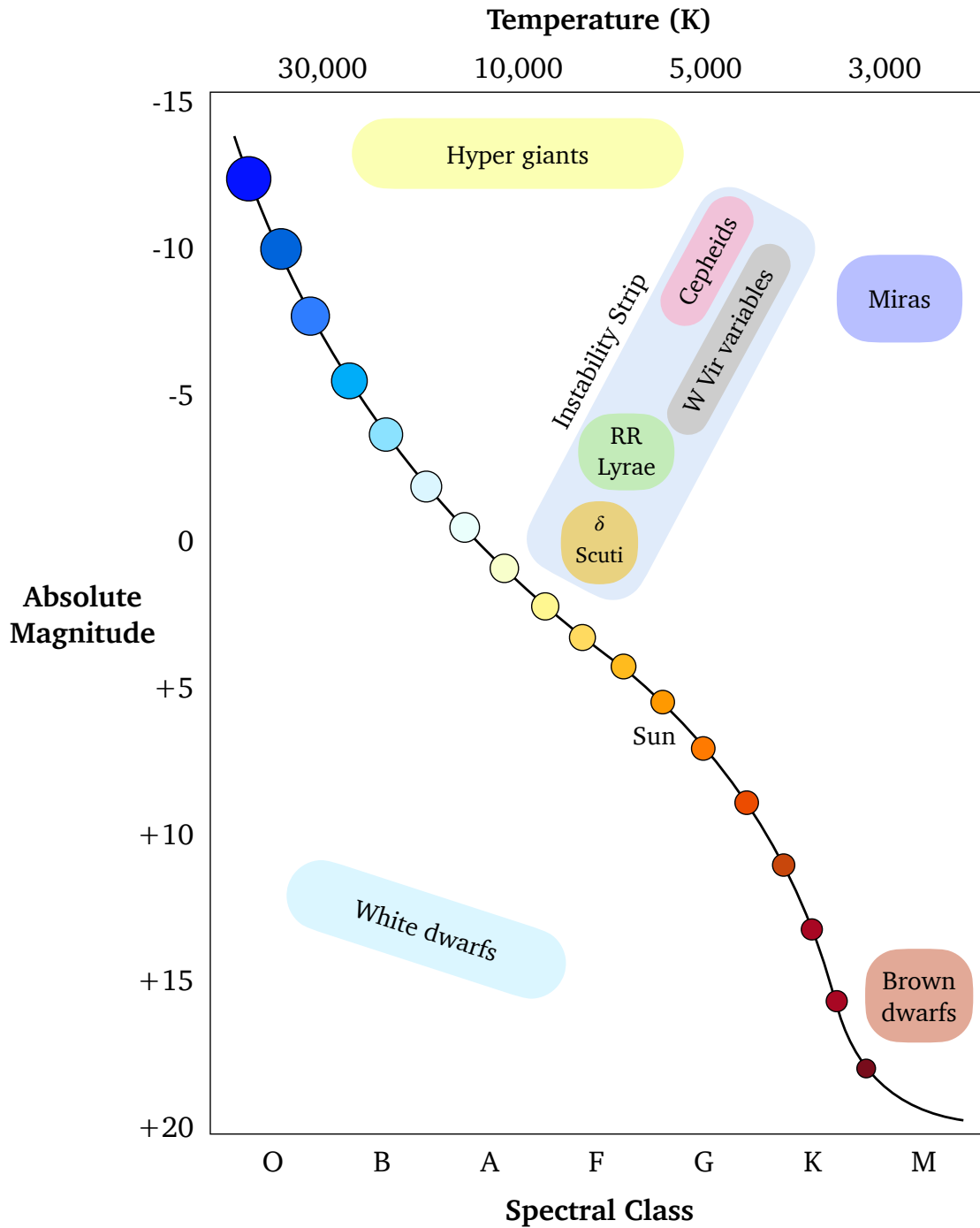


Figure 1.12: Position of the instability strip in the Hertzsprung-Russell diagram.

Considering a Cepheid as a homogeneous pulsating sphere of gas of period  $P$ , density  $\rho$ , mass  $M$  and radius  $R$ , Ritter's relation gives:

$$P \propto \frac{1}{\sqrt{\rho}} \propto \left(\frac{R^3}{M}\right)^{1/2} \quad (1.13)$$

Substituting the mass and radius in Eq. 1.13 using the mass luminosity relation

$$M \propto L^{1/\alpha} \quad (1.14)$$

and the Stefan-Boltzmann law

$$R \propto \left(\frac{L}{T_{\text{eff}}^4}\right)^{1/2} \quad (1.15)$$

yields:

$$P \propto \frac{L^{3/4-2\alpha}}{T_{\text{eff}}^3} \quad (1.16)$$

Taking the logarithm of Eq.1.16 gives:

$$\log P = A \log L + B \log T_{\text{eff}} + C \quad (1.17)$$

which is equivalent to the period-luminosity-color relation:

$$\log P = A' \times M + B' \times (\text{color}) + C' \quad (1.18)$$

where  $M$  is the absolute magnitude of the star. The color term  $B'$  is small because Cepheids are relatively similar in color due to the narrow width of the instability strip. This term can be neglected at the expense of a slightly higher scatter of the P-L relation.

Long period Cepheids have the higher masses, and high-mass Cepheids also have a shorter life time. It is therefore more likely to observe short period Cepheids than long period ones. This can be limiting since long period Cepheids are observable to larger distance and are also essential to calibrate the slope of the P-L relation.

Cepheids pulsate radially and different pulsation modes can be observed. If all parts of the star pulsate in a synchronized way, the Cepheid has a fundamental pulsation mode. However, a significant number of Cepheids have higher oscillation modes. For example, first-overtone mode Cepheids (FO) have lower amplitudes and very symmetrical light curves. They usually have shorter periods (from 1 to 4 days) than fundamental mode Cepheids and follow a parallel P-L relation. In some works, FO Cepheids are included in the fundamental P-L relation by means of a simple conversion of their period (see next chapter). This transformation seems reliable in the sense that it brings FO Cepheids exactly on the fundamental P-L relation without increasing the dispersion, but this transformation is not always recommended since first-overtone and higher mode Cepheids may introduce additional systematics.

Circumstellar envelopes have been discovered and detected around Cepheids using near infrared and mid infrared interferometry (Kervella et al. 2006; Mérand et al. 2006, 2007; Kervella et al. 2009; Gallenne et al. 2013; Hocdé et al. 2020). They are likely due to the mass-loss of the stars and produce an infrared excess on the Cepheid brightness, which can affect the Leavitt law and is likely to introduce dispersion. They also represent a potential source of bias in interferometric measurements of Cepheid angular diameters. It is therefore crucial to understand the physics behind circumstellar



envelopes and mass loss in order to limit the possible systematics on the Hubble constant.

Additionally, distances to pulsating stars can be estimated through a totally different method: the parallax-of-pulsation technique (PoP). The comparison between the variation in angular diameter and the variation in linear diameter of a star provides its distance. Angular diameters can be measured by interferometry, or alternatively by applying surface brightness color relations (e.g. Eq. 1.10). In the latter case, the method is referred to as the Baade-Wesselink (Baade 1948; Wesselink 1946) technique, although it was first suggested by (Lindemann 1918). On the other hand, the variation of the star's linear diameter is derived by integration of the pulsation velocity. The current limitation of this method relies on the transformation between the observed spectroscopic radial velocities and the true pulsation velocity of the star. Indeed, the real pulsation velocity is obtained by multiplying spectroscopic radial velocities, integrated over the surface of the stellar disk, by a parameter called the projection factor (hereafter  $p$ -factor, Nardetto et al. 2004, 2007, 2009, 2017). The parallax-of-pulsation technique was extensively studied (e.g., by Mérand et al. 2015; Breifelder et al. 2015, 2016; Kervella et al. 2017; Gallenne et al. 2017; Trahin 2019, Trahin et al. 2021), but these various studies have not yet provided a precise calibration of the Cepheid  $p$ -factor. The method as well as the calibration of the projection factor and its dependencies are detailed in Appendix A.

### 1.3.2 The place of Cepheids in the distance scale

The distance is certainly the most difficult parameter to measure in astronomy. It has only been one hundred years that we are able to do it precisely for distant galaxies. Thanks to Leavitt's work, Cepheids became the first standard candles, a class of astronomical objects that can be used to derive distances thanks to their physical properties.

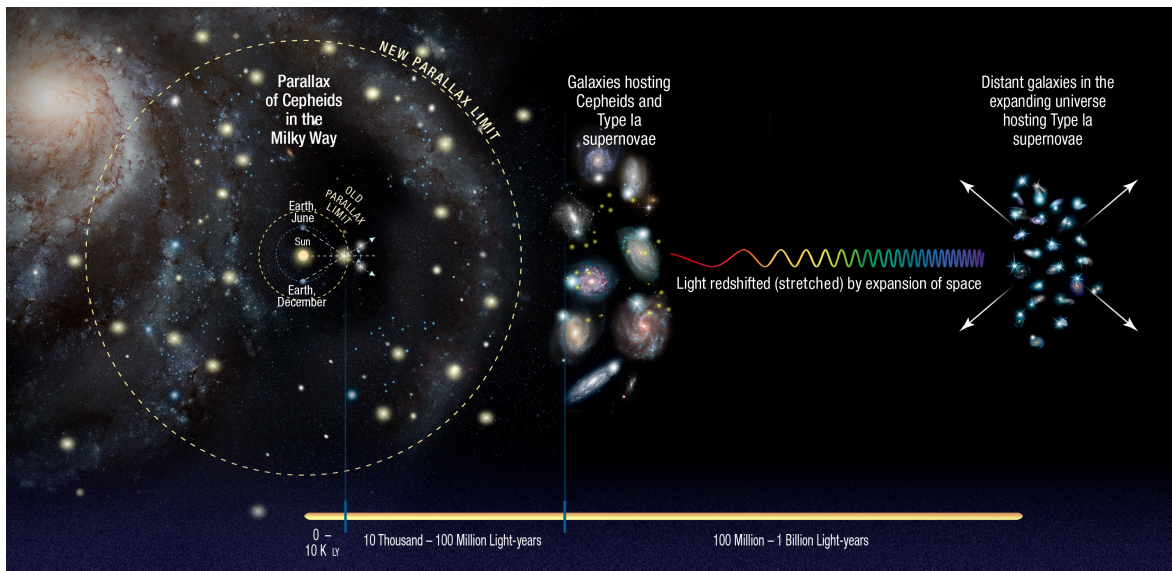


Figure 1.13: The three steps of the cosmic distance scale. Credit: NASA, ESA, A. Feild (STScI), and A. Riess (STScI/JHU).

The strongest distance ladder is based on nearby geometrical distances, the Cepheid Leavitt law and SN Ia in distant galaxies. The three steps are represented in Fig. 1.13. First, the distance to the closest Cepheids are estimated through the method of the parallax (see Sect. 1.2.1), mainly in



the Milky Way, or using eclipsing binaries in the Magellanic Clouds. These geometric distances are used as a basis to calibrate the Cepheid P-L relation. Secondly, Cepheids must be detected in galaxies hosting other distance indicators such as Type Ia supernovae (see Sect. 1.2.5). The P-L relation can be directly applied to calibrate these second standard candles. Finally, SNe Ia are observed in distant galaxies whose velocity is set by the Hubble flow: they trace the expansion of the Universe and provide a value for the Hubble constant.

For a set of supernovae of redshift  $z$  and apparent magnitude  $m_x^0$ , the absolute magnitude  $M_x^0$  and the intercept  $a_x$  of the SN Ia magnitude-redshift diagram (Fig. 1.14) determines the Hubble constant by means of the following equation (Riess et al. 2016):

$$5 \log H_0 = M_x^0 + 5a_x + 25 \quad (1.19)$$

Absolute SN Ia magnitudes  $M_x^0$  are obtained from apparent magnitudes  $m_x^0$  based on a Cepheid calibration, previously established.

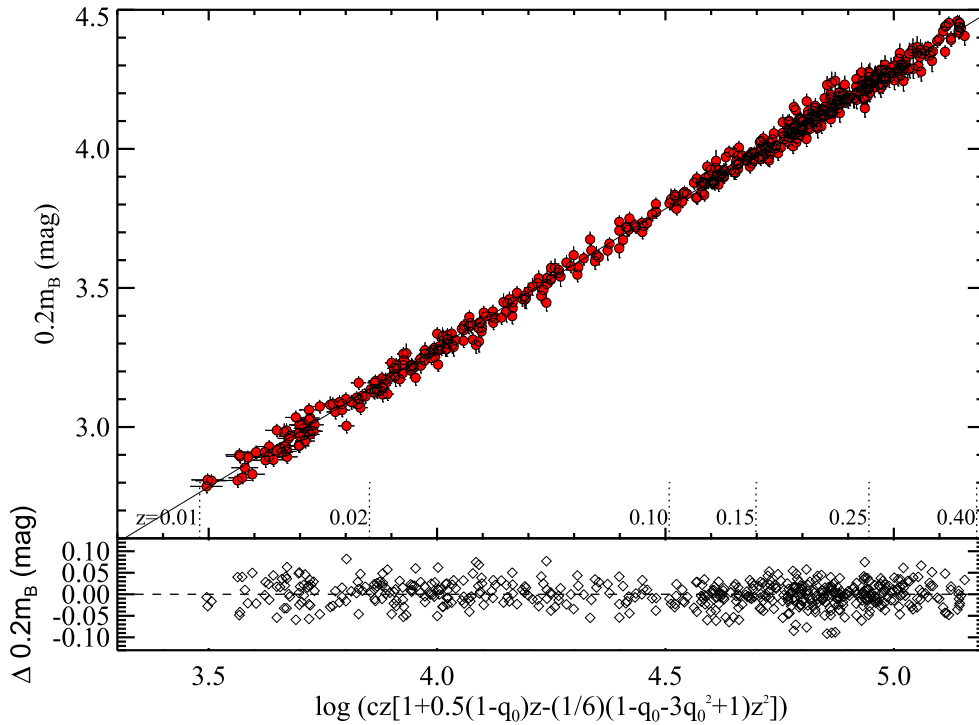


Figure 1.14: SN Ia Hubble diagram for more than 600 supernovae. The intercept of this plot determines the term  $a_x$  (Source: Riess et al. 2016).

A poor calibration of the Cepheid P-L relation in the Milky Way and in nearby galaxies would significantly affect the resulting SNe Ia absolute luminosities and distances. For this reason, the local calibration of the Cepheid distance scale is of paramount importance and should be treated with the greatest care.

The largest contributors to the  $H_0$  error budget are first, the local calibration of the Cepheid P-L relation, and especially its zero-point, and secondly the number of SN Ia available to calibrate the second rung of the distance ladder. Each supernova is currently precise to about 6%, but the number of SNe Ia calibrated by Cepheid distances is still limited, due to the small number of nearby galaxies

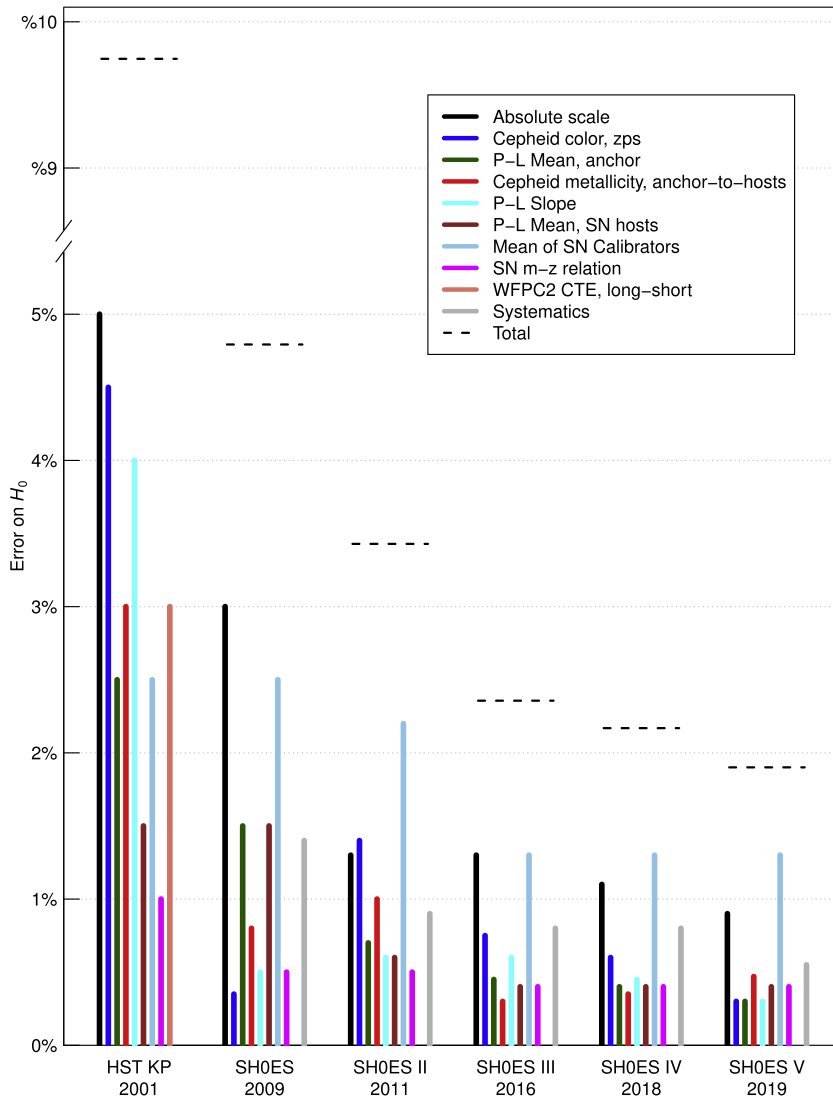


Figure 1.15: Evolution of the error budget on  $H_0$ : comparison of the HST Key Project results (Freedman et al. 2001) and the recent results by the SH0ES team (Source: Riess et al. 2019a).

that are both hosting SNe Ia and within reach of the best telescopes for measuring Cepheid distances. The evolution of the various contributors to the  $H_0$  error budget over the past 20 years is displayed in Fig. 1.15, taken from Riess et al. (2019a).

In this thesis, I will focus on the improvements of the Cepheid distance scale in the Milky Way and in the Magellanic Clouds. Decades of research on the P-L relation still have not resulted in a precise and accurate calibration. Even in the *Gaia* era, various systematics are still affecting the Leavitt law and limiting its precision. The effect of chemical composition on Cepheid magnitudes is still poorly understood and likely introduces a bias on the P-L zero point. This point is discussed in details in Chapter 3.

Additionally, interstellar dust obscures the light of Cepheids and makes the objects appear redder than they actually are. This effect is called "extinction" and should be corrected when measuring apparent magnitudes. It also contributes to the scatter of the P-L relation, especially in the optical

where it is particularly strong. For this reason, near infrared (NIR) bandpasses are more advantageous for the P-L calibration: Cepheids have lower systematics and the intrinsic width of the instability strip is also narrower at longer wavelengths, which mitigates color dependences.

Nearby Cepheids and those located in distant galaxies have very different fluxes, which makes it difficult to observe them with the same instruments. This constitutes an additional limitation: the combination of various photometric systems introduces a systematic zero point uncertainty on the derived magnitudes. The work led by the SH0ES team has reached a refined precision thanks to the consistent use of HST photometry in the NIR for nearby and distant Cepheids.

Finally, Cepheids in distant galaxies are affected by crowding: the large number of background stars in the field of view of the telescope biases the true luminosity of the Cepheid and makes it difficult to measure precise photometry ([Anderson & Riess 2018](#); [Javanmardi et al. 2021](#)). This crowding can be estimated and corrected by using artificial star simulations ([Hoffmann et al. 2016](#)). In the very near future, the powerful resolving capabilities of the *James Webb Space Telescope* (JWST) will allow to separate Cepheids from the photometric background noise by an order of magnitude compared with HST, and remove this source of uncertainty from the P-L relation (See Cycle 1 JWST Proposal: [Riess et al. 2021a](#), and Appendix B). Additionally, observing Cepheids in the periphery of galaxies may help to reduce the effect of crowding as well as reddening.

## Chapter 2

# Calibration of the Cepheid Leavitt Law in the Milky Way

---

<b>2.1</b>	<b>Calibration of the Cepheid Leavitt Law before Gaia</b>	<b>37</b>
2.1.1	The P-L relation with Hipparcos parallaxes	37
2.1.2	Improvements with the <i>Hubble</i> Space Telescope	39
2.1.2.1	HST Fine Guidance Sensor Parallaxes	39
2.1.2.2	Parallaxes from HST Wide Field Camera 3 spatial scanning	41
2.1.3	Other methods	44
<b>2.2</b>	<b>Cepheids with <i>Gaia</i></b>	<b>45</b>
2.2.1	The <i>Gaia</i> mission	45
2.2.2	Parallaxes from <i>Gaia</i> Data Release 2	49
2.2.3	Parallaxes from <i>Gaia</i> Early Data Release 3	53
<b>2.3</b>	<b>Calibration of the P-L relation with <i>Gaia</i> parallaxes</b>	<b>56</b>
2.3.1	Sample of Cepheids companions	56
2.3.2	Sample of Open Cluster Cepheids	61
2.3.2.1	Open Cluster mean parallaxes and uncertainties	62
2.3.2.2	Open Cluster Cepheids from <i>Gaia</i> DR2 and <i>Gaia</i> EDR3	63
2.3.2.3	Open Cluster Cepheids from the literature	68
2.3.3	Photometry	71
2.3.4	Extinction	73
2.3.5	Pulsation modes	75
2.3.6	Method and results	76
<b>2.4</b>	<b>Implications for the Hubble constant</b>	<b>84</b>
<b>2.5</b>	<b>Conclusion on the calibration of the Leavitt law</b>	<b>87</b>
2.5.1	Summary of the study	87
2.5.2	Limitations	88
2.5.3	Perspectives	89
<b>2.6</b>	<b>Publication: <i>The Milky Way Cepheid Leavitt law based on Gaia DR2 parallaxes of companion stars and host open cluster populations</i>, Breuval et al. 2020, A&amp;A 643 A115</b>	<b>90</b>

---

Trigonometric parallaxes are the most direct technique to calibrate the Cepheid P-L relation. The *Gaia* mission is dedicated to measure this parameter for more than a billion stars in our galaxy. However, parallax measurements are complex and the first two data releases suffer from issues limiting the applicability of *Gaia* parallaxes, especially for Cepheids. Pending the next data releases which are expected to provide more precise astrometry, I propose in this chapter an alternative and original method to bypass the problems that may affect variable stars and especially Cepheids. To this end, I adopt the parallaxes of stars located in the neighbourhood of Cepheids, such as resolved companions and members of open clusters hosting Cepheids.

First, in Sect. 2.1, I present several P-L calibrations determined prior to the publication of *Gaia* parallaxes. Sect. 2.2 introduces the *Gaia* mission, describes the characteristics of the satellite and gives the main properties of *Gaia* DR2 and *Gaia* EDR3 data. Two samples of Milky Way Cepheids are presented in Sect. 2.3: Cepheids with resolved companions and Cepheids in open clusters. The period-luminosity relation is calibrated with these stars, allowing to bypass issues affecting Cepheid parallaxes, such as variability or saturation. Finally, a revised value of the Hubble constant anchored to Milky Way Cepheids is derived from this sample in Sect. 2.4.

## 2.1 Calibration of the Cepheid Leavitt Law before Gaia

### 2.1.1 The P-L relation with Hipparcos parallaxes

The *Hipparcos* satellite of the European Space Agency (ESA) was launched in 1989 with the aim to precisely measure the position, parallax and proper motion of stars in our galaxy (ESA 1997). As the predecessor of *Gaia*, it was the first mission dedicated to measuring astrometric parameters for a large number of stars. It provided parallaxes to a mean precision of 1 mas, with 10% precision for more than 20,000 stars and with 20% precision for almost 50,000 stars, and could observe stars up to an apparent magnitude of 12 mag. *Hipparcos* was of course not competitive with the current *Gaia* data, but its parallaxes served as a first basis for the calibration of the P-L relation based for the first time on a significant sample of Cepheid distances: previous calibrations were using important surveys of LMC Cepheids, for example, but all calibrators were assigned the same distance.

From a sample of 26 bright and nearby Milky Way Cepheids, Feast & Catchpole (1997) calibrated the P-L relation in the *V* band. Adopting the slope from a prior work on LMC Cepheids they find:

$$M_V = -2.81 \log P - 1.43_{\pm 0.10} \quad (2.1)$$

Lanoix et al. (1999) reanalyzed this paper and inspected the weighting of the individual distance measurements, deriving a very similar relation in *V*:

$$M_V = -2.77 \log P - 1.44_{\pm 0.05} \quad (2.2)$$

They also extended this study to the *I* band and published the following equation:

$$M_I = -3.05 \log P - 1.81_{\pm 0.09} \quad (2.3)$$

This paper also raised the question of the Lutz-Kelker bias (Lutz & Kelker 1973) as modified by Hanson (1979) (hereafter LKH bias). This bias originates from the fact that if a sample is selected based on the measured parallaxes, each parallax is more likely to be overestimated than underestimated, due to the non-uniform distribution of the parallaxes. For example, let us assume that a given sample of stars is selected on the basis of their parallaxes with a minimum value of  $\varpi_{\text{lim}}$ . Among the stars

observed at a parallax  $\varpi_{\text{lim}}$ , some of them will actually have a true parallax that is lower than  $\varpi_{\text{lim}}$ , and others will have a true parallax larger than  $\varpi_{\text{lim}}$ . Assuming that stars are uniformly distributed in space, the number of stars per parallax interval varies as  $1/\varpi^4$ , so there are more stars outside the region of radius  $d_{\text{lim}} = 1/\varpi_{\text{lim}}$  than inside of it. As a consequence, the average true parallax of stars with a measured parallax of  $\varpi_{\text{lim}}$  is smaller than  $\varpi_{\text{lim}}$ . In summary, this systematic bias causes observed parallaxes to be too large, and in turn, absolute magnitudes derived from these observed parallaxes to be too faint. Therefore, absolute magnitudes obtained from observed trigonometric parallaxes should be corrected.

The LKH bias was widely discussed in the literature. For example, [Lanoix et al. \(1999\)](#) showed that excluding negative parallaxes (which are present in *Hipparcos* data) results in underestimating distances, and that a selection based on the ratio  $\sigma_{\varpi}/\varpi$  leads to a similar issue. Known for decades ([Eddington 1913](#); [Dyson 1926](#)), this bias could not be empirically calibrated due to the lack of data available for an independent external verification. Following the publication of *Hipparcos* parallaxes, careful attention was given to this issue. [Koen & Laney \(1998\)](#) demonstrated that the *Hipparcos* parallaxes used by [Feast & Catchpole \(1997\)](#) were not subject to the LKH bias. However, [Oudmaijer et al. \(1998\)](#) found that for certain samples, this issue has significant consequences on the calibration of the P-L relation and suggested a calculation in order to correct the inferred absolute magnitudes.

The most straightforward approach to bypass this problem is first to adopt a sample of Cepheids without applying any cut based on parallaxes. A second way to avoid issues associated to the LKH bias is to remain in the space of parallaxes, as opposed to that of distances, by using astrometric based luminosities (ABL) ([Feast & Catchpole 1997](#); [Arenou & Luri 1999](#); [Lanoix et al. 1999](#)). The ABL method consists in substituting the absolute magnitudes by a proxy that is linearly dependent on the parallax, as explained in Sect. 2.3.6.

The parallaxes measured by *Hipparcos* were very unprecise. For example, among the sample of 26 Cepheids chosen by [Feast & Catchpole \(1997\)](#), 11 stars differ by more than 0.5 mas from the *Gaia* EDR3 parallax (the most recent and most precise to date, see Sect. 2.2). The mean precision of this sample is 60% and the parallaxes are precise to 0.7 mas on average. This sample contains the brightest and closest Cepheids, with the highest signal-to-noise ratio, so their parallaxes are expected to be very good compared with more distant stars.

Later, [Groenewegen & Oudmaijer \(2000\)](#) adopted a larger sample of 236 Cepheids with *Hipparcos* parallaxes and discussed the P-L calibration in optical and NIR bands. They also derived the LMC distance modulus based on the multi-band P-L relation. Similarly, [Madore & Freedman \(1998\)](#) compared the Milky Way P-L relation obtained using *Hipparcos* parallaxes in *B*, *V*, *I*, *J*, *H*, *K* bands (Fig. 2.1), with a previous calibration in the LMC ([Madore & Freedman 1991](#)). They concluded that *Hipparcos* parallaxes were in good agreement with previous calibrations but that they were still not accurate enough to provide a significant improvement to the Cepheid distance scale. Indeed, some outliers with important error bars are present in each panel, which means that the parallaxes are responsible for biased absolute magnitudes. Finally, ten years after the first *Hipparcos* data release, [van Leeuwen \(2007\)](#) published a new reduction of the *Hipparcos* astrometry, improving by up to a factor 4 the accuracy of the data from the original catalog.

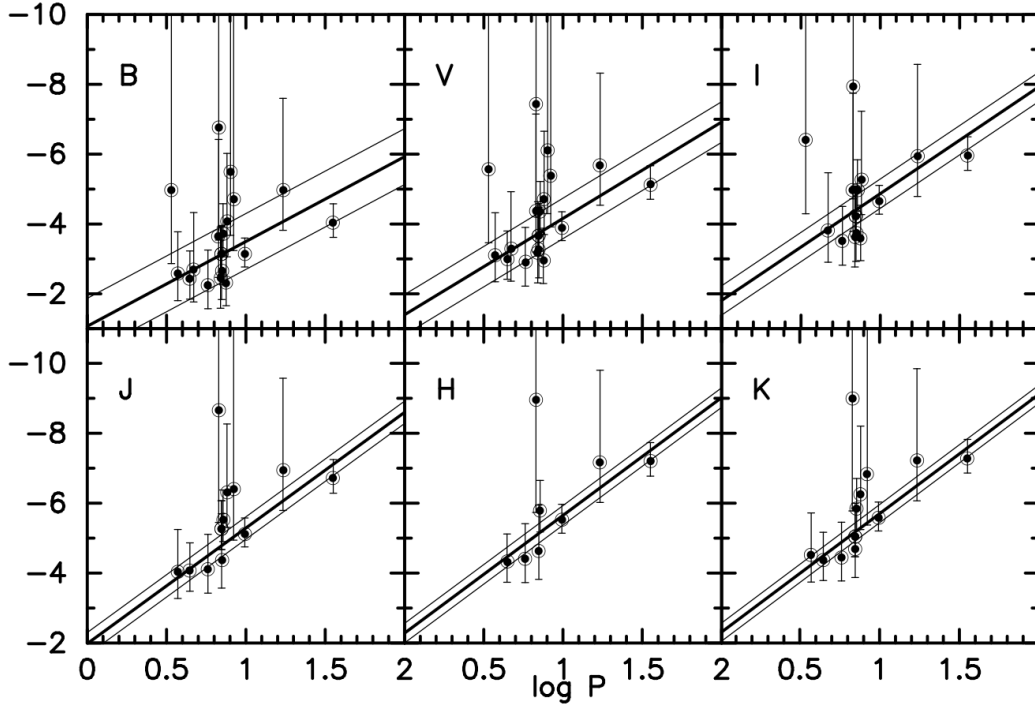


Figure 2.1: Multi wavelength P-L relation for Cepheids with *Hipparcos* parallaxes taken from [Madore & Freedman \(1998\)](#). The thick line represents the fit from [Madore & Freedman \(1991\)](#) and the thin lines are the  $2\sigma$  width of the instability strip.

### 2.1.2 Improvements with the *Hubble* Space Telescope

This section presents the parallax measurements of Milky Way Cepheids obtained with two different instruments of the *Hubble* Space Telescope: the Fine Guidance Sensor (FGS) and the Wide Field Camera 3 (WFC3).

#### 2.1.2.1 *HST* Fine Guidance Sensor Parallaxes

The prototype star  $\delta$  Cep was the first individual Cepheid parallax measured with the FGS, a white-light interferometer on the *Hubble* Space Telescope ([Bradley et al. 1991](#); [Nelán 2001](#); [Benedict et al. 1999](#)). The parallax of this bright and nearby Cepheid is measured at  $3.66 \pm 0.15$  mas, with a precision of 4 % ([Benedict et al. 2002](#)), better than the most accurate Cepheid parallax from *Hipparcos*. As a comparison, the *Hipparcos* parallax of  $\delta$  Cep is  $3.32 \pm 0.58$  mas, which is consistent within  $1\sigma$  with the HST/FGS value but is only precise to 17 %.

The parallax of  $\delta$  Cep is obtained by measuring its position relatively to five other reference stars. In order to determine the parallax of the target star, the parallaxes of the reference stars must be estimated too. Spectra are used to determine the temperature and luminosity class of each reference star, and they are combined with photometric measurements to obtain their visual extinction. The absolute magnitude is estimated from the spectral type of each source. The spectrophotometric estimate of the parallax of a reference star is then:

$$\pi_{\text{abs}} = 10^{-(V-M_V+5-A_V)/5} \quad (2.4)$$

where  $V$  and  $M_V$  are respectively the apparent and absolute magnitudes, and  $A_V$  is the extinction in the  $V$  band. Seven sets of data were acquired for  $\delta$  Cep and the reference stars, spanning a total of 127 measurements over a period of 2.5 years. For each data set, the position of the stars are measured multiple times to correct for intra-orbit drift of the telescope. The parallaxes of 9 additional nearby Milky Way Cepheids were later measured by [Benedict et al. \(2007\)](#) using the same technique with HST/FGS, with an individual precision of  $\sim 8\%$ . Their main parameters are listed in Table 2.1.

Table 2.1: Parameters of the 10 Cepheids measured with HST/FGS ([Benedict et al. 2002, 2007](#)): logarithm of the period, HST/FGS and *Hipparcos* parallaxes, apparent  $K$  magnitude, reddening and LKH correction.

Cepheid	$\log P$ (days)	$\pi_{\text{FGS}}$ (mas)	$\pi_{\text{Hip}}$ (mas)	$m_K$ (mag)	$E(B - V)$ (mag)	LKH (mag)
$\ell$ Car	1.551	$2.01 \pm 0.20$	$2.06 \pm 0.27$	1.071	0.170	-0.08
$\zeta$ Gem	1.006	$2.78 \pm 0.18$	$2.71 \pm 0.17$	2.097	0.018	-0.03
$\beta$ Dor	0.993	$3.14 \pm 0.16$	$3.64 \pm 0.28$	1.944	0.044	-0.02
W Sgr	0.880	$2.28 \pm 0.20$	$2.59 \pm 0.75$	2.796	0.111	-0.06
X Sgr	0.846	$3.00 \pm 0.18$	$3.39 \pm 0.21$	2.557	0.197	-0.03
Y Sgr	0.761	$2.13 \pm 0.29$	$3.73 \pm 0.32$	3.582	0.205	-0.15
$\delta$ Cep	0.730	$3.66 \pm 0.15$	$3.81 \pm 0.20$	2.310	0.092	-0.01
FF Aql	0.650	$2.81 \pm 0.18$	$2.05 \pm 0.34$	3.465	0.224	-0.03
T Vul	0.647	$1.90 \pm 0.23$	$2.31 \pm 0.29$	4.187	0.064	-0.12
RT Aur	0.572	$2.40 \pm 0.19$	$-0.23 \pm 1.01$	3.925	0.051	-0.05

In this study, a correction for the Lutz-Kelker bias is included in the derived absolute magnitudes (it is proportional to  $\sigma_\pi/\pi$ ), as well as a correction for the reddening. The P-L relation in the  $V$  band based on the 10 Cepheid parallaxes from HST/FGS ([Benedict et al. 2002, 2007](#)) is the following:

$$M_V = -2.43_{\pm 0.02} \log P - 1.62_{\pm 0.03} \quad (2.5)$$

The zero-point agrees to  $1.8\sigma$  with the relation by [Feast & Catchpole \(1997\)](#) and to  $3\sigma$  with the one revised by [Lanoix et al. \(1999\)](#), both based on *Hipparcos* parallaxes. The precision of the zero-point reaches 2% thanks to HST/FGS parallaxes. The  $K$ -band P-L relation is represented in Fig. 2.2: the blue points and the solid line are derived after correcting for the Lutz-Kelker bias, and the corresponding equation is:

$$M_K = -3.32_{\pm 0.12}(\log P - 1) - 5.71_{\pm 0.03} \quad (2.6)$$

When the Lutz-Kelker correction is ignored, the equation becomes:

$$M_K = -3.35_{\pm 0.08}(\log P - 1) - 5.67_{\pm 0.02} \quad (2.7)$$

and is represented by the dashed line in Fig. 2.2. The green symbols represent the positions of the same points if HST/FGS parallaxes are replaced by *Hipparcos* parallaxes ([van Leeuwen 2007](#)). Adopting the HST/FGS parallaxes gives a dispersion of 0.11 mag around the P-L relation (solid line, including Lutz-Kelker correction), while *Hipparcos* parallaxes yield a 0.58 mag dispersion, five times larger.

This first sample of 10 HST/FGS Cepheid parallaxes represents a significant improvement in terms of quality compared with the *Hipparcos* catalog. It was used by [Riess et al. \(2016\)](#) as the Milky Way anchor for the determination of the Hubble constant and led to a local value of  $76.18 \pm 2.37$



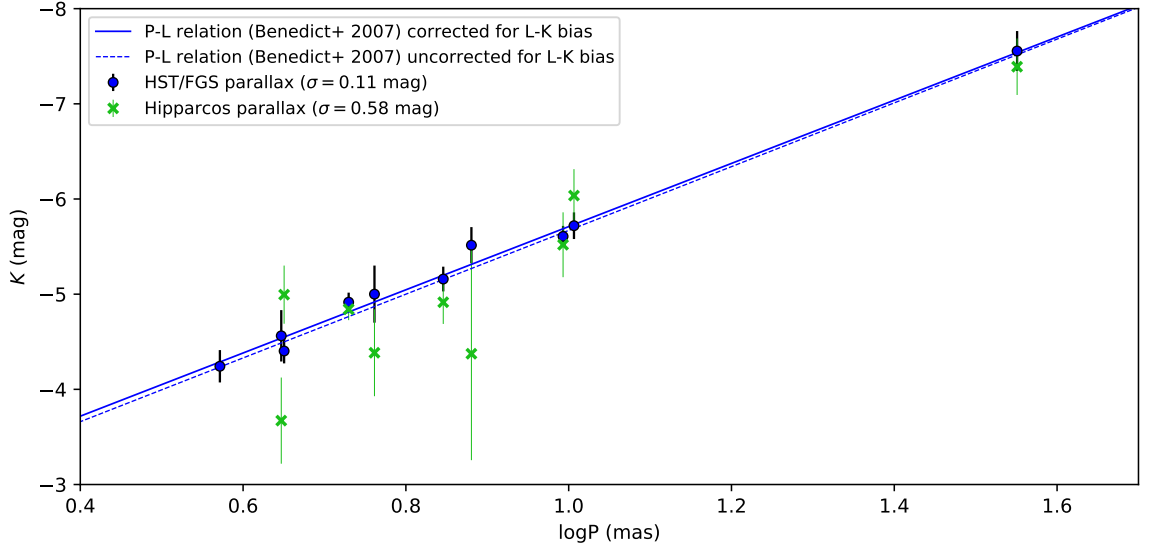


Figure 2.2: Period-Luminosity relation in the  $K$  band (CIT system) based on 10 Cepheid parallaxes measured by HST/FGS (Benedict et al. 2002, 2007). The solid line represents the fit when the correction for the Lutz-Kelker bias is included (Eq. 2.6) and the dotted line is without this correction (Eq. 2.7). The green markers correspond to the absolute magnitudes obtained with *Hipparcos* parallaxes. The Cepheid RT Aur, with the shortest period, has a negative *Hipparcos* parallax so it is not represented in green.

km/s/Mpc. However, the accuracy of  $H_0$  obtained with this sample was still limited by different factors. The number of parallaxes available via this method remained limited, the distances reached did not exceed 500 pc, and the periods of the Cepheids in this sample were shorter than those of the extragalactic Cepheids in SN Ia hosts. Finally, the Cepheids of this sample are too bright to obtain HST photometry with the same instrument, introducing an additional systematic uncertainty in the distance scale.

#### 2.1.2.2 Parallaxes from HST Wide Field Camera 3 spatial scanning

As described in Sect. 1.2.1, trigonometric parallaxes can be measured by spatial scanning with the Wide Field Camera 3 instrument on the HST, under FGS control. This method was developed in 2011 to obtain photometry during exoplanet transits. It was recently implemented by the SH0ES team in order to complement the sample of HST/FGS parallaxes measured by Benedict et al. (2007). The telescope is drifted along one direction, which creates trails of the stars on the detector. These trails contain a great density of astrometric information in only one image: by comparing pixel by pixel the separation between two stars (i.e. two trails) in the same frame, and after removing the noise due to the jitter of the telescope by subtracting two scan lines, the average position of the Cepheid is measured with a precision of 20 to 40  $\mu$ as. The annual movement of a Cepheid is obtained by repeating these scans during several years.

A parallax of  $0.428 \pm 0.054$  mas was first obtained using this technique by Riess et al. (2014) for the Cepheid SY Aur, with a precision of 12 %. It was followed by the measurement of SS CMa parallax to  $0.348 \pm 0.038$  mas by Casertano et al. (2016), with an 11% precision. The same method was applied to 7 additional Cepheids in Riess et al. (2018a). This sample was focused on long period Cepheids, with periods between 10 days and 68 days ( $1 < \log P < 1.85$ ): they are particularly rare

in our nearby environment and are paramount in the calibration of the P-L relation, and especially its slope. Additionally, the WFC3 sample contains Cepheids located at much larger distances compared with the [Benedict et al. \(2007\)](#) sample. While the Cepheids of the HST/FGS sample were confined within a distance of 500 pc, the SH0ES sample reached 3 kpc.

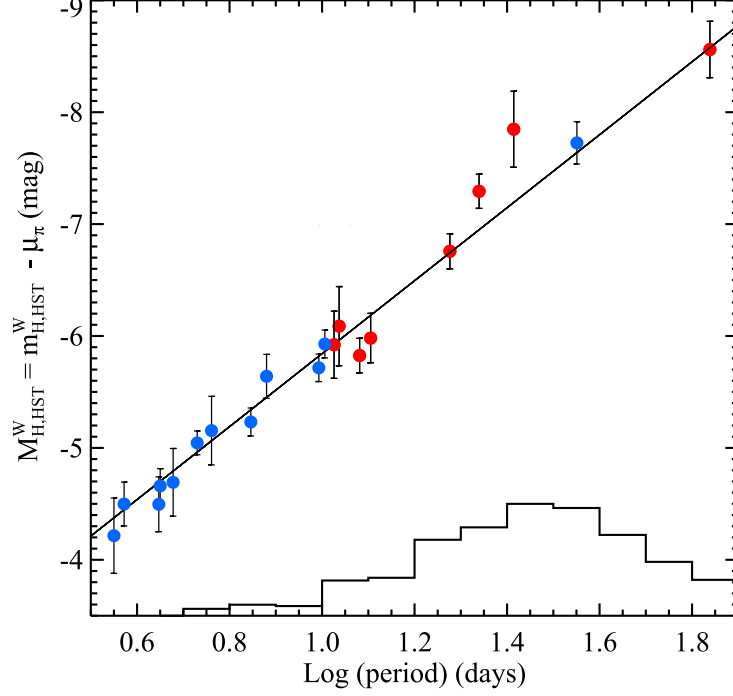


Figure 2.3: Period-Luminosity relation in the Wesenheit  $W_H$  band based on Cepheid parallaxes using HST/FGS and Hipparcos parallaxes (blue points, [Benedict et al. 2007](#); [van Leeuwen 2007](#)) and HST/WFC3 spatial scanning parallaxes (red points, [Riess et al. 2014, 2018b](#); [Casertano et al. 2016](#)). The histogram represents the quantity of extragalactic Cepheids for a given period. (Source: [Riess et al. 2018a](#)).

By combining these new Cepheid parallaxes with HST/WFC3 photometry in a consistent way, [Riess et al. \(2018a\)](#) calibrated the Leavitt law in the reddening-free Wesenheit index  $W_H$ , defined as:

$$m_W^H = F160W - 0.368(F555W - F814W) \quad (2.8)$$

The Wesenheit P-L relation in Fig. 2.3, taken from [Riess et al. \(2018a\)](#)<sup>1</sup>, is based on HST/FGS, *Hipparcos* and HST/WFC3 spatial scanning parallaxes (red points, [Riess et al. 2018b](#)). This figure shows the excellent agreement between the parallaxes previously available and the new spatial scanning measurements. The P-L relation associated with these parallaxes is:

$$W_H = -3.26(\log P - 1) - 5.85 \quad (2.9)$$

The *Hipparcos* counterparts of the red points are not represented because they are often very far from the expected values due to the large distance of these stars: the parallax uncertainties are sometimes very important ( $> 1$  mas) and the parallax values can be negative. This period-luminosity relation was used to calibrate the MW Cepheid anchor in the Hubble constant determinations by [Riess et al. \(2016\)](#),

<sup>1</sup> A correction for the count rate non-linearity effect (CRNL) was included in this calibration, it will be explained later in this chapter.

2018a, 2019a). The HST measurements allowed to reach a  $\sim 10\%$  precision in Cepheid parallaxes, to a distance up to 10 times larger than those reached by *Hipparcos*.

In Fig. 2.4 are represented the distances reached by different instruments or surveys with a 10% precision, as a function of the *V* band apparent magnitude (Casertano et al. 2016). Spatial scanning with HST/WFC3 increased this distance up to 3 kpc. The capabilities of the *Gaia* satellite at the end of the mission are expected to reach a 10% precision up to 10 kpc for stars brighter than 12 mag, and a similar precision on faint stars down to 19 mag up to a distance of 1 kpc.

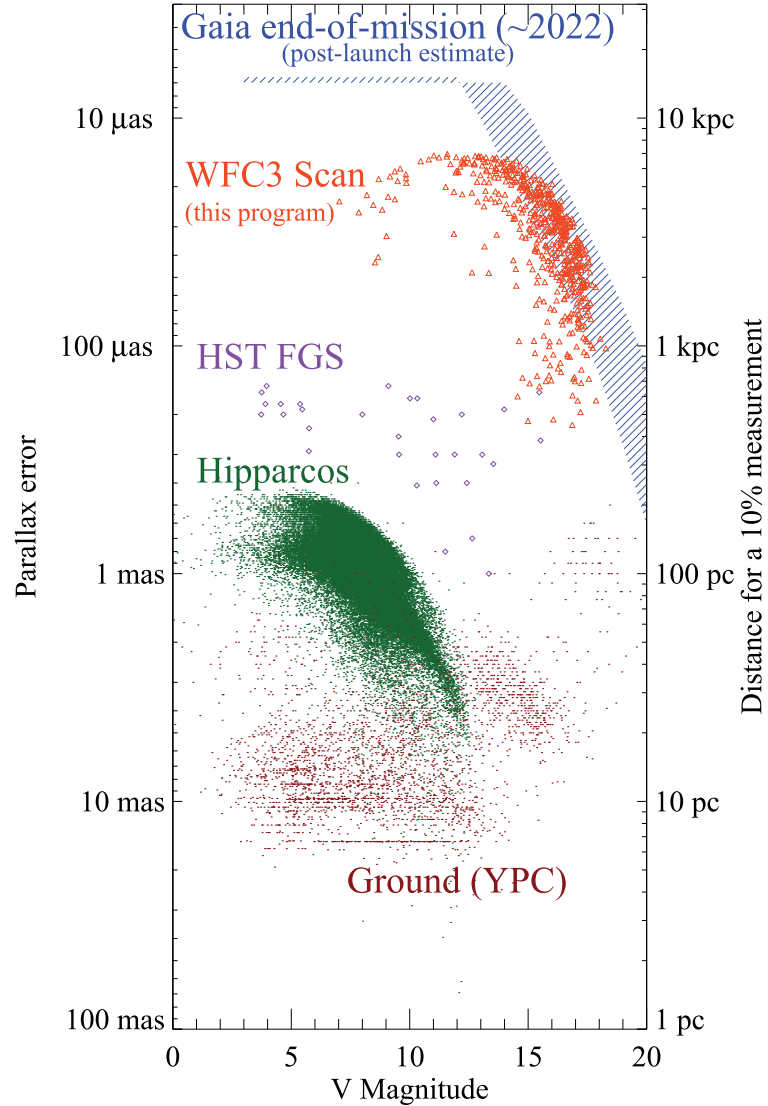


Figure 2.4: Precision of parallax measurements as a function of apparent brightness. Brown stars at the bottom of the figure are from the Yale Parallax Catalog (YPC, van Altena et al. 1995), green stars are from *Hipparcos*, purple stars are from HST/FGS (MacConnell et al. 1997; Hershey & Taff 1998; Benedict et al. 2000, 2001, 2002, 2007, 2009, 2011; Nelan & Bond 2013), orange stars are from HST/WFC3 (Riess et al. 2014; Casertano et al. 2016). (Source: Casertano et al. 2016).

### 2.1.3 Other methods

Before the launch of the *Gaia* satellite (see next section), the only direct and competitive parallax measurements for Galactic Cepheids were obtained by the *Hubble* Space Telescope (see previous section). Additionally, indirect techniques were also developed to measure Cepheid distances in the Milky Way. A few of them are mentioned in this section.

Open clusters (OC) can be used as very powerful distance indicators. By fitting the main sequence of a stellar cluster on a color-magnitude diagram, one can easily derive their distance since the absolute magnitude of a star on the main sequence is known with a relatively good precision. [An et al. \(2007\)](#) used this technique to derive the distance to 7 open cluster Cepheids. This work was followed by similar studies based on this method. [Turner \(2010\)](#) recalibrated the P-L relation using open cluster Cepheids. [Anderson et al. \(2013\)](#) analyzed the membership of Cepheids in clusters and derived a sample of 23 bona fide associations. [Chen et al. \(2015\)](#) also investigated memberships and obtained 19 cluster Cepheids that they use to derive the NIR P-L relation. Finally, [Chen et al. \(2017\)](#) updated their previous OC study and provided a sample of 31 high-confidence associations, leading to an improved calibration of the NIR P-L relation from OC Cepheids. Milky Way open clusters are particularly interesting because of the important number of stars they contain, being all at the same distance. The average parallax of all cluster members provides a robust and accurate estimate for the distance of the Cepheids they host. This approach is used with *Gaia* data and is described in Sect. 2.3.

A second technique, the parallax-of-pulsation (PoP) method, already mentioned in Sect. 1.3.1, is often used to derive the distance to pulsating stars independently of parallax measurements ([Fouqué & Gieren 1997](#); [Kervella et al. 2004](#); [Fouqué et al. 2007](#); [Mérand et al. 2015](#); [Breitfelder et al. 2015](#); [Trahin 2019](#)). This approach is explained in more detail in Appendix A, which describes my contribution to the paper by Trahin et al. (2021) on the calibration of the Cepheid projection factor. However this method is limited by the small angular size of Cepheids, even for the closest ones, and directly depends on the projection factor which transforms observed radial velocities into the real pulsation velocity of the star ([Nardetto et al. 2004](#); [Mérand et al. 2005](#), and references therein). In [Fouqué et al. \(2007\)](#), the value of this parameter is derived from a previously established period- $p$ -factor relation, whose calibration is still largely discussed ([Nardetto et al. 2007, 2009](#); [Groenewegen 2013](#); [Kervella et al. 2017](#)) and relies on approximations of various effects. The  $p$ -factor contains, in a single value, the complex physics of the formation of hundreds of absorption lines, in a pulsating atmosphere, integrated over the surface of the star, which results in a difficulty to model this parameter. As a consequence, many period- $p$ -factor relations available in the literature are not consistent with each other. The presence of circumstellar envelopes around most Cepheids ([Kervella et al. 2006](#); [Hocdé et al. 2020](#); [Gallenne et al. 2021](#)) can also strongly impact this method and the resulting P-L relation. Various studies are based on Cepheid distances estimated using this method, although their precision is limited. [Storm et al. \(2011a\)](#) and [Breitfelder et al. \(2016\)](#) used the existing HST/FGS parallaxes to calibrate this period- $p$ -factor relation and to derive distances to a larger sample of Cepheids. The distances derived by [Fouqué et al. \(2007\)](#) were adopted by [Marengo et al. \(2010\)](#) to calibrate the mid-infrared P-L relation, in combination with HST and *Hipparcos* parallaxes. The PoP technique and its limitations for the calibration of the distance scale are discussed in Appendix A.

Due to the limited sample of accurate individual distances to Galactic Cepheids, the calibration of the P-L relation was often based on Large Magellanic Cloud Cepheids. An average distance modulus of  $\sim 18.5$  mag was generally assumed for the LMC, although a precise distance determination was not yet established. For example, [Freedman et al. \(2008\)](#), [Ngeow & Kanbur \(2008\)](#) and [Madore et al. \(2009\)](#) improved the mid-infrared calibration of the Leavitt law in the LMC using photometry from the *Spitzer* Space Telescope.

Other original methods were established to measure individual distances to Cepheids. One interesting example is described in [Kervella et al. \(2014\)](#): the light echoes of the Cepheid RS Pup propagate in the surrounding dust nebula and provide an independent distance indicator (see Fig. 2.5).

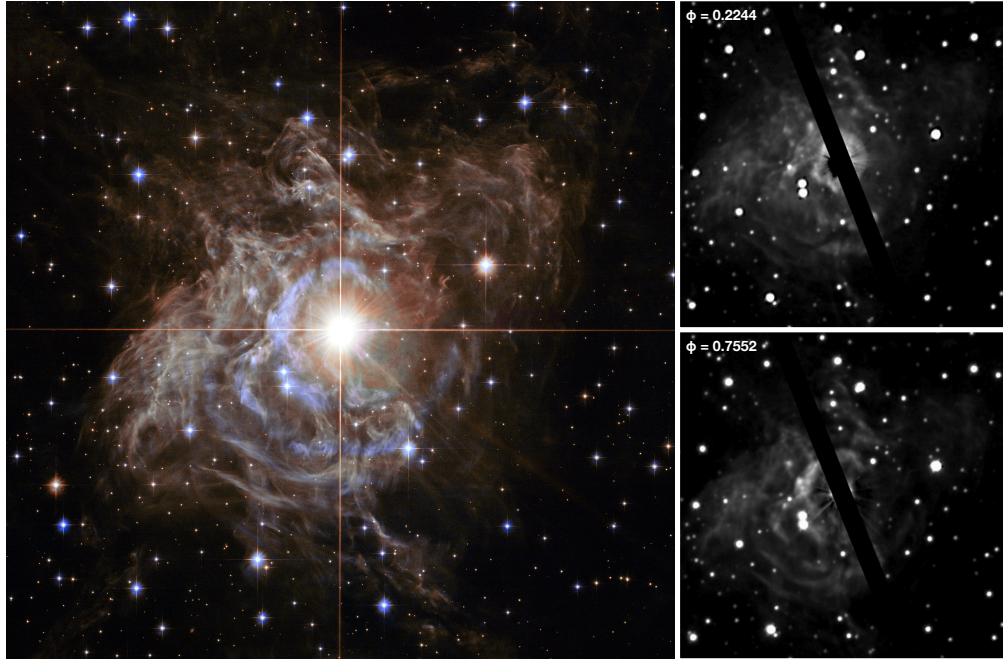


Figure 2.5: **Left:** Color composite view of the circumstellar nebula of RS Pup assembled from ACS WFC images in the F435W and F606W filters (Source: NASA, ESA, Hubble Heritage Team). **Right:** Propagation of RS Pup light echos observed at two different pulsation phases (Source: [Kervella et al. 2008](#)).

## 2.2 Cepheids with *Gaia*

### 2.2.1 The *Gaia* mission

*Gaia* is an astrometric mission dedicated to studying the Milky Way. It is expected to measure, by the end of the mission, the distance to more than 2 billion stars and to provide the most accurate map of our Galaxy. The spacecraft was developed by the European Space Agency (ESA) as the successor of *Hipparcos* and was launched on December 19th 2013. It is placed in orbit around the Earth and is located at the second Lagrange point (L2) of the Sun-Earth-Moon system, at 1.5 million km from Earth.

*Gaia* is a double telescope: with its two rectangular mirrors of 1.45 m by 0.50 m (M1 and M'1 on Fig. 2.6), it observes simultaneously in two directions separated by an angle of  $106.5^\circ$ . As a comparison, the *Hipparcos* mirror was only 29 cm in diameter. Each telescope observes a field of view of  $1.7^\circ$  by  $0.6^\circ$  on the sky. They are both combined in the focal plane where a single integrated instrument lies, which comprises three major functions: astrometry, photometry, and spectrometry. It is made of 106 CCDs, forming a billion pixel mosaic (Fig. 2.7). With a physical dimension of 0.5 m by 1 m, it is the largest camera ever flown in space.



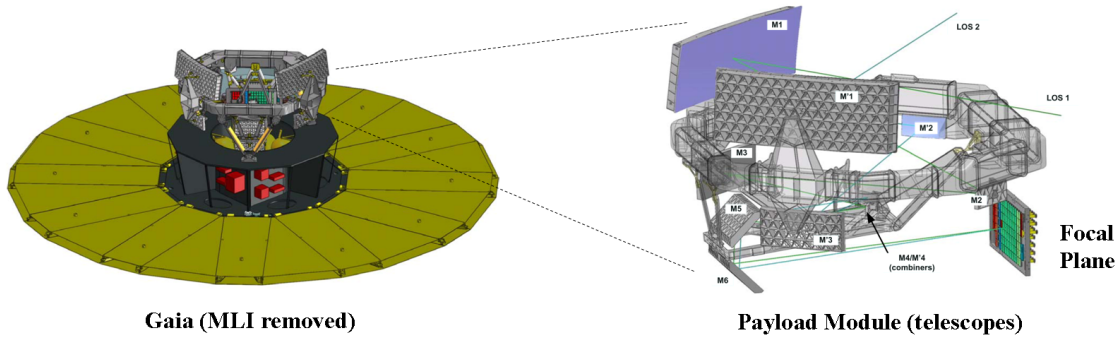


Figure 2.6: Schematic of the structure of *Gaia*. The left-hand diagram represents the *Gaia* satellite without the multi-layer solar insulation (MLI). The right-hand diagram shows the position of the main mirrors (M1 and M'1), of the secondary mirrors and of the focal plane inside the payload module. (Credit: ESA, Alexander Short)

*Gaia* slowly spins so that the two telescopes successively cover the same region of the sky with an angular speed of 60 arcsec by second of time, repeatedly observing all objects in the sky with a magnitude brighter than  $G = 21$  mag. This uniform revolving scanning ensures an excellent astrometric accuracy as well as a homogeneous sky coverage. A complete observation of the sky takes approximately six months. Initially, *Gaia* was expected to observe each target 70 times on average by the end of a five-year mission. It has already been in operation during seven years (two years longer than the estimated length of the mission) and is expected to last at least three more years.

The light of the sources observed by *Gaia* crosses several regions of the detector successively (from left to right in Fig. 2.7). It first enters a CCD column made of a wavefront sensor, used to measure the quality of the image in each field of view, and two basic angle monitors (BAM) used to calibrate the angle between the two telescopes. The two following columns of 7 CCDs are the Sky Mapper: they identify which one of the two telescopes is observing the source and communicate the nature of the sources and their position to the next columns.

The large array of 9 columns of 7 CCDs forms the main astrometric field: it measures the angular position of the stars with a precision better than 50 to 100 times that of HST or *Hipparcos*. The data collected in these 9 columns will serve to determine the five-parameter astrometric solution (the coordinates  $\alpha$  and  $\delta$ , the parallax  $\varpi$  and the proper motion  $\mu_\alpha$  and  $\mu_\delta$ ). The parallax of each star is derived by analyzing their movement in the sky, precisely recorded by *Gaia*. The first column is also used to identify false-detections due to cosmic rays. The large size of the two mirrors and the extreme stability of the spacecraft ensure a large precision in the position measurements. However, the astrometric precision obtained on these 9 columns depends on the brightness of the sources, on their color (the CCDs are more sensitive in the red domain) and on the latitude (there are more observations per star at ecliptic latitudes). The middle CCD of the 9th column is a second wavefront sensor.

After the astrometric field, the light is scattered by two prisms and passes through two successive vertical columns of 7 CCDs: the blue (BP) and red photometers (RP). They provide spectrophotometric measurements of each object with a low resolution over the wavelength ranges 320 – 660 nm and 650 – 1000 nm for the BP and RP photometers respectively. A third photometric measurement is obtained from the astrometric field in the broad band  $G$ , which covers the wide wavelength range from 330 nm to 1050 nm. The photometric measurements provide important information, such as the

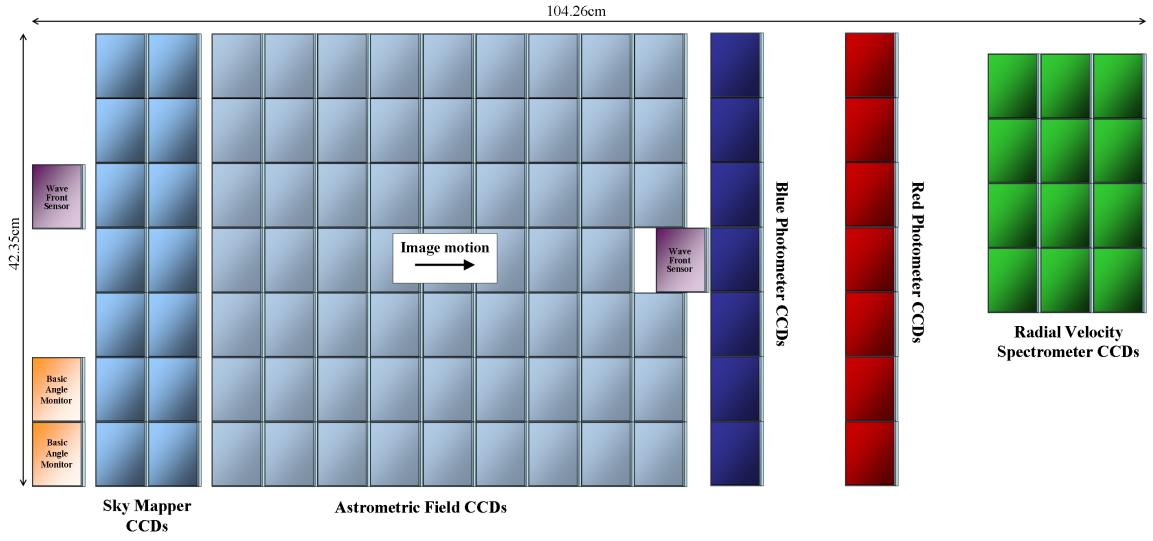


Figure 2.7: Diagram of the focal plane of *Gaia*, and the function of each CCD column. (Credit: ESA, Alexander Short)

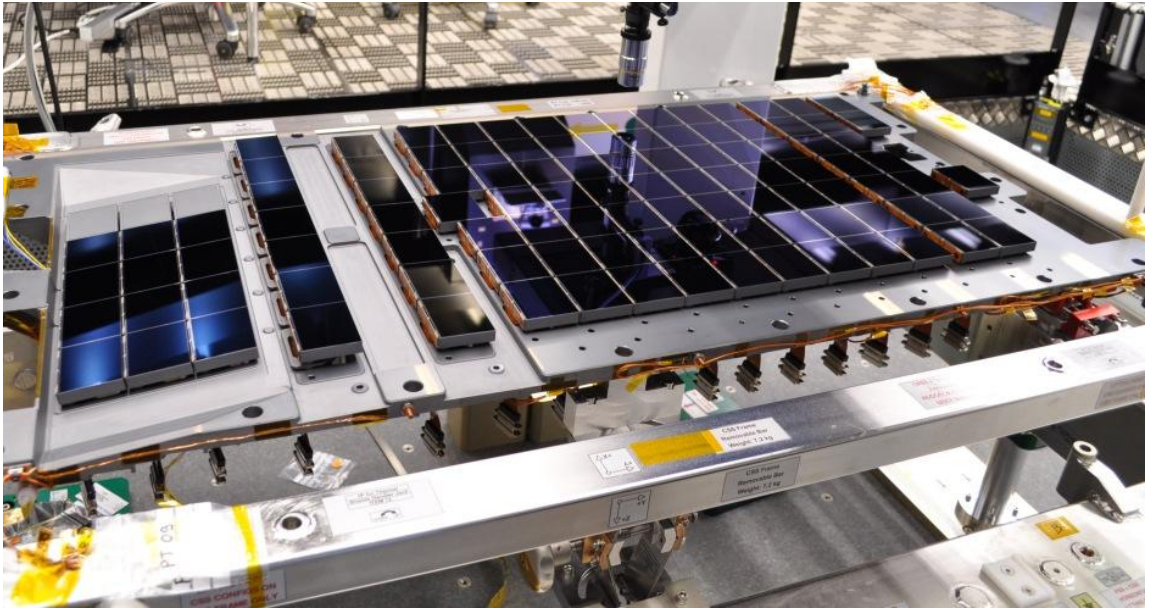


Figure 2.8: Picture of the focal plane of *Gaia*. The orientation is reversed compared with Fig. 2.7. (Credit: ESA, Astrium France)

color, that are used to reduce the astrometric data. They are also helpful to classify and characterize the objects observed by *Gaia*, for example they serve for the detection of variable stars, the measurement of interstellar extinction and for the determination of stellar types. The expected precision at the end of the mission is between 0.2 and 3.7 milli-magnitude in the *G* band and between 1 and 100 milli-magnitude in *BP* and *RP* bands. It depends on the brightness and on the spectral type of the stars.

Finally, the Radial Velocity Spectrograph (RVS) is composed of 3 columns of 4 CCDs and analyzes the spectra of each object brighter than  $G_{RVS} = 17$  mag. It operates in a narrow range of wavelength between 845 and 872 nm, with a high spectral resolution of  $\sim 11500$ . The precision of

the radial velocity measurements was expected to reach 0.5 km/s for very bright stars and  $\sim 15$  km/s for fainter sources at the end of a five-year mission. The photometric and spectroscopic data are used to measure key physical properties of each star such as its brightness, chemical composition and temperature.<sup>2</sup>

The main goal of the *Gaia* mission is to create a 3D map of the Milky Way in order to study its structure, the kinematics of its various components and help us understand the mechanisms behind the formation and evolution of our galaxy. Besides the stars of our galaxy, it also observes extragalactic objects such as quasars and distant galaxies, and many objects in the Solar System like comets and asteroids.

Since the first publication in 2016, the *Gaia* data are progressively published in successive data releases. The first *Gaia* Data Release (DR1) was published on September 14th 2016, it was based on 14 months of observations and contains the positions and magnitudes in the *G* band for 1.1 billion stars (about 1% of our galaxy's stellar content) based on *Gaia* data only. Combined with the Tycho-Gaia Astrometric Solution (TGAS), the *Gaia* DR1 catalogue provided the positions, parallaxes and proper motions for more than 2 million stars (Lindegren et al. 2016), and contains light curves for about 3000 variable stars. Due to the limited precision of the DR1 data, this first release is not discussed in this thesis. The *Gaia* Data Release 2 (DR2) was made available on April 25th 2018, it is described and discussed in Sect. 2.2.2 and served as a first basis for my research on the P-L calibration. The third *Gaia* Data Release (DR3) is expected in 2022, but the first installment of the DR3 catalog called "Early Third Data Release" (EDR3) was made available on December 3rd 2020. It is detailed in Sect.2.2.3.



Figure 2.9: Picture of *Gaia* before launch. (Credit: ESA, Astrium France)

<sup>2</sup> For more information, see the *Gaia* website: <https://www.cosmos.esa.int/web/Gaia>



### 2.2.2 Parallaxes from *Gaia* Data Release 2

The *Gaia* Second Data Release (hereafter DR2) was published on April 25th 2018 (Gaia Collaboration et al. 2018). It is based on data collected spanning a period of 22 months (between July 2014 and May 2016), compared with the 14 months initially covered by the *Gaia* Data Release 1 (DR1). *Gaia* DR2 provided positions and *G* magnitudes for nearly 1.7 billion stars and a 5 parameter (5-p) astrometric solution (i.e. position, proper motion and parallax) for 1.3 billion sources, in a magnitude range  $3 < G < 21$  mag, compared with 2 million sources in *Gaia* DR1. A total of  $\sim 550,000$  variable stars, including 9500 Cepheids and 140,000 RR Lyrae, were detected in *Gaia* DR2, with an average of 30 epochs per light curve (Clementini et al. 2019). Cepheids were classified by type and pulsation modes on the basis of their light curve shape, and reclassified later by Ripepi et al. (2019). The typical precision reached by *Gaia* DR2 is listed for different ranges of magnitudes in Table 2.3 (Sect. 2.2.3) and is compared with the precision obtained with *Gaia* EDR3.

One important limitation of *Gaia* DR2 parallaxes is that they are affected by a zero-point ( $ZP_{DR2}$ ) offset. It was estimated by various teams based on different sources, but provided various estimations: no uniform value was found for this parameter. Table 6 in Breuval et al. (2020) gives a short list of the determinations of this parameter. It ranges between  $-0.029$  mas based on distant and faint quasars (Lindgren et al. 2018) and  $-0.082$  mas from eclipsing binaries (Stassun & Torres 2018). A median value of  $-0.046$  mas was derived by Riess et al. (2018b) using Milky Way Cepheids, and similarly an offset of  $-0.049$  mas is found by Groenewegen (2018). While this zero-point only weakly impacts the parallax of nearby stars, it has a significant effect on distant stars, which have a smaller parallax. The *Gaia* DR2 parallax zero-point is suspected to depend on the position on the sky and on the brightness of the sources, which is particularly limiting. In the following of this chapter and in my first paper (Breuval et al. 2020), a uniform and constant zero-point of  $-0.046$  mas is adopted with an uncertainty of  $0.015$  mas, which covers almost all the range of values derived in the literature.

A good indicator of the quality of an astrometric solution is the Renormalized Unit Weight Error (RUWE). It evaluates the quality of the astrometry of a source compared with stars of the same type (color, brightness). It is defined by:

$$RUWE = \frac{\sqrt{\chi^2/(N-5)}}{u_0(G, BP - RP)} \quad (2.10)$$

where  $\chi^2$  indicates the quality of the fit,  $N$  is the number of good CCD transits,  $u_0$  is a normalization factor that can be computed using the lookup table on the ESA DR2 Known issues web page.<sup>3</sup> Lindgren (2018c) suggests that well-behaved astrometric solutions verify  $RUWE < 1.4$ . I adopt this selection criterion in the following studies. While there are certainly unresolved binaries with  $1 < RUWE < 1.4$ , their impact on the parallaxes is expected to be very limited, except in the (rare) case of a period close to one year. We will see that filtering Cepheid parallaxes using this RUWE parameter is a powerful test to detect and remove outliers.

An additional limitation of this second data release is that bright stars are affected by saturation. As a consequence, sources brighter than  $G = 6$  mag have a poor quality astrometric solution, large uncertainties and possibly additional systematic errors (Lindgren et al. 2018; Drimmel et al. 2019; Lindgren 2020). Figure 2.10 shows the different regimes for *Gaia* DR2 parallaxes. Stars brighter than  $G = 3$  mag (regime A) are too bright for precise astrometric measurements and fully saturate the detector. Between  $G = 3$  and  $G = 6$  mag (regime B), the sources are still partly saturated

<sup>3</sup> ESA DR2 Known issues web page: <https://www.cosmos.esa.int/web/gaia/dr2-known-issues>

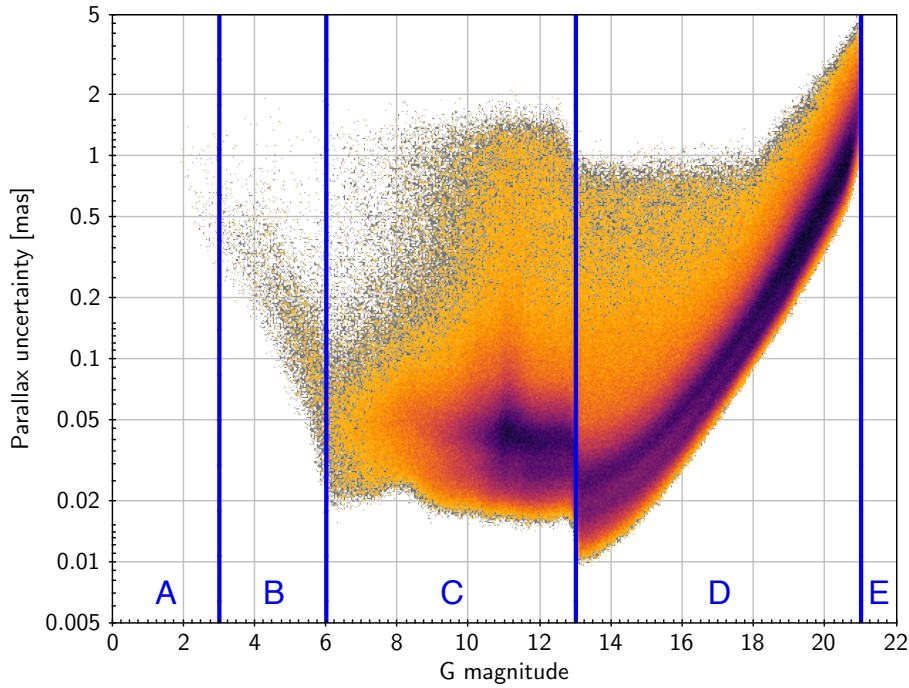


Figure 2.10: Gaia DR2 parallax uncertainty represented as a function of the  $G$  magnitude (Source: [Lindgren 2018a](#)).

and the resulting astrometric solutions are unreliable. Between  $G = 6$  and  $G = 21$  mag (regime C and D), the optimal precision is obtained, although the parallax uncertainties start to become limiting ( $\sigma_{\varpi} > 0.1$  mas) for faint stars below  $G = 18$  mag. In regime C, the stars which should be saturated are observed with a reduced integration time and suffer from calibration issues: since bright stars are less common than faint ones, the instruments are insufficiently calibrated in the bright regimes. Finally, sources with magnitudes  $G > 21$  mag are too faint for detection with Gaia.

Cepheids are intrinsically very bright stars: the closest and brightest sources, which have the largest parallaxes and are therefore less sensitive to the effect of the parallax zero-point, have potentially unreliable parallaxes due to saturation. A comparison between HST/FGS, HST/WFC3 and *Gaia* DR2 parallaxes is represented in Fig. 2.11. The 10 Cepheids observed by [Benedict et al. \(2002, 2007\)](#) with HST/FGS (left panel) are all in the range  $3 \text{ mag} < G < 6 \text{ mag}$ . Almost all of these stars have a large RUWE parameter (indicated by a red square), sometimes even a negative parallax, and *Gaia* DR2 parallaxes which can differ by more than 3 mas from the expected value. The prototype star  $\delta$  Cep has an exceptionally high RUWE of 20.9. Additionally, almost all Cepheids on the left panel of Fig. 2.11 have a *Gaia* DR2 parallax smaller than their HST/FGS parallax. The dispersion around the identity line is of  $\sim 2$  mag which is very high.

On the other hand, Cepheids observed by spatial scanning with HST/WFC3 (right panel, [Riess et al. 2014, 2018b; Casertano et al. 2016](#)) are below the saturation limit, with magnitudes in the range  $7 \text{ mag} < G < 10 \text{ mag}$ . They are therefore less affected by saturation and all have a RUWE parameter below 1.4, which indicates that their astrometric solution is reliable. The *Gaia* DR2 parallaxes are close to the expected value and in general good agreement with the HST/WFC3 measurements ( $\sigma = 0.08$  mag), except one star, SS CMa, which differs by  $3\sigma$  from the WFC3 parallax.

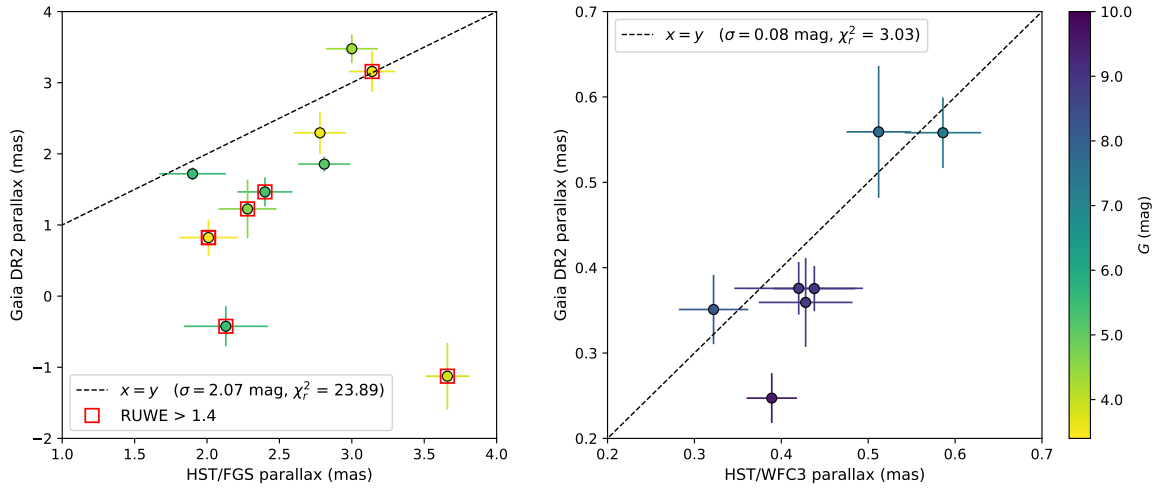


Figure 2.11: **Left:** Comparison between HST/FGS parallaxes (Benedict et al. 2002, 2007) and *Gaia* DR2 parallaxes. **Right:** Comparison between HST/WFC3 spatial scanning parallaxes (Riess et al. 2014, 2018b) and *Gaia* DR2 parallaxes. The color map represents the apparent *G* magnitude. *Gaia* parallaxes are corrected by a zero-point of  $-0.046 \pm 0.015$  mas.

Besides saturation, Cepheids also suffer from an additional effect due to their variation in color during a pulsation cycle. The parallax of a star is measured by the movement it describes on the sky during one year. It thus depends on the exact position where the light of the star hits the detector each time it is observed. However, due to the diffraction of the light through the prisms, the position where the light hits the detector depends on the wavelength of the light, and thus on the color of the star. Since Cepheids show variations in color up to 0.5 mag during a pulsation cycle (Gaia Collaboration et al. 2019, Fig. 11), it affects the position of the star on the detector. For this reason, chromaticity corrections should be applied on each epoch data. However, *Gaia* DR2 parallaxes have been derived assuming a constant color and brightness.

This effect is very rarely discussed in the literature but affects Cepheid DR2 parallaxes. Mowlavi et al. (2018) raised this issue for long period variable stars in *Gaia* DR2, and Pourbaix et al. (2003) mention that for *Hipparcos* parallaxes, the use of a single chromaticity correction was not sufficient to obtain reliable parallaxes of long period variables. This effect is not a bias in the sense that it does not change the parallax values in a particular direction, but it increases the dispersion of the measurements and it is responsible for an additional noise that is not included in *Gaia* DR2 error bars. This chromaticity effect is difficult to quantify, as we have no access to *Gaia* DR2 raw data, but it can be seen on the dispersion of the P-L relation obtained with *Gaia* DR2 parallaxes of Cepheids, as discussed in Breuval et al. (2020).

Many studies of the Cepheid P-L relation based on *Gaia* DR2 parallaxes were published, although the chromaticity effect was neglected. Given the large number of calibrating Cepheids used in these papers, this effect is likely averaged but may still be responsible for residual noise. Groenewegen (2018) adopted a sample of 452 Milky Way Cepheids to calibrate the P-L relation in *V*, *K* and *W<sub>VK</sub>* bands. The sample of individual distances is significantly increased, however, one limitation of this study is the use of single-point photometry from the literature, which may increase the scatter of the P-L relation. Based on 9 Cepheids with accurate *Gaia* and non-*Gaia* parallaxes, a zero-point of  $-0.049$  mas is derived. A distance modulus of 18.7 mag to the LMC is also obtained, which is 0.2 mag larger than the expected value. This study shows that the calibration of the P-L relation strongly de-

depends on the *Gaia* DR2 parallax zero-point, and finds no evidence for a metallicity term in the Leavitt law. [Groenewegen \(2018\)](#) concluded the paper with a strong statement, that *Gaia* DR2 parallaxes do not allow to improve on the current distance scale based on Milky Way Cepheids, with a remaining uncertainty of the order of 0.15 mag, mostly due to the parallax zero-point.

[Clementini et al. \(2019\)](#) described the validation procedure of Cepheids and RR Lyrae in the *Gaia* DR2 variability catalog, using the Specific Objects Study (SOS) pipeline. They defined a Wesenheit index  $W(G, G_{RP})$  based on *Gaia* passbands:

$$W(G, G_{RP}) = G - 0.08193 - 2.98056(G - G_{RP}) - 0.21906(G - G_{RP})^2 - 0.6378(G - G_{RP})^3 \quad (2.11)$$

and provide the P-L distribution of fundamental mode Cepheids and other pulsating stars in the Milky Way, LMC and SMC, in the  $G$  band and Wesenheit index. One limitation of these P-L relations is that they do not include reddening corrections. The SOS Cep&RRL pipeline results in a final number of 140,784 RR Lyrae and 9,575 Cepheids.

[Ripepi et al. \(2019\)](#) reanalyzed the sample of Cepheids identified by [Clementini et al. \(2019\)](#) and reclassified them into classical, anomalous and Type-II Cepheids, using information from the literature, *Gaia* DR2 astrometry, the position of each star in the P-L diagram, and by performing a visual inspection of each light curve. They defined a Wesenheit index based on the 3 *Gaia* passbands:

$$W(G, G_{BP}, G_{RP}) = G - 1.90(G_{BP} - G_{RP}) \quad (2.12)$$

and derived new calibrations of the P-L relation in the *Gaia* bands and Wesenheit index, for all types of Cepheids in the Milky Way, LMC and SMC. A total of 1,257 stars were reclassified as Cepheids and 84 stars as RR Lyrae. They derived a parallax zero-point of  $-0.070$  mas (slightly higher than other estimates from the literature) and find a weak metallicity dependence of the P-L relation in *Gaia* bands. The paper concludes that *Gaia* DR2 parallaxes of MW Cepheids are still too uncertain to allow for a significant improvement in the precision of  $H_0$ , confirming [Groenewegen \(2018\)](#) conclusion.

In [Riess et al. \(2018b\)](#), *Gaia* DR2 parallaxes are used simultaneously with HST photometry for a sample of 46 Galactic Cepheids. The authors used the P-L relation calibrated in [Riess et al. \(2016\)](#) in the HST system to compute the expected photometric parallaxes. The comparison between *Gaia* DR2 parallaxes and the photometric parallaxes yielded a zero-point of  $-0.046 \pm 0.006$  mas. This value is slightly larger (in the absolute sense) than the one derived by [Lindgren et al. \(2018\)](#) from quasars, suggesting that this quantity may depend on magnitude, color and position in the sky. For this sample of Cepheids with magnitudes in the range  $6 < G < 12$  mag, *Gaia* DR2 parallaxes are generally in good agreement with the expected values. However, due to the remaining uncertainty on the zero-point, the improvement in the precision of the distance scale reached by *Gaia* DR2 is still limited.

Many studies have been published based on the *Gaia* DR2 data. Among them, we can mention the catalog of Milky Way open clusters assembled by [Cantat-Gaudin et al. \(2018\)](#) and their mean parameters, especially distances, derived from all the cluster members and based on *Gaia* DR2 data alone. This catalog is extremely useful for obtaining precise Cepheid distances and is used later in this chapter.

### 2.2.3 Parallaxes from *Gaia* Early Data Release 3

The *Gaia* Early Data Release 3 (EDR3) was published on December 3rd 2020 ([Gaia Collaboration et al. 2021](#); [Lindgren et al. 2021b](#)). It is the first installment of the *Gaia* DR3 catalog, expected to be released in 2022. It provides a 5-parameter astrometric solution for 1.467 billion sources, compared with 1.3 billion in *Gaia* DR2, and a 2-parameter astrometric solution (positions) for 1.811 billion sources in total. An additional 6th parameter is fitted: it corresponds to the pseudo-color and was included for stars with high-quality color information. A total of 882 million sources have a 6-parameter solution, with an astrometric precision slightly inferior to that of 5-parameter solutions. The number of parameters fitted are given by `astrom_params_solved`, which is equal to 3 for 2-p solutions, 31 for 5-p solutions and 95 for 6-p solutions. Note that the  $G$ ,  $G_{BP}$ ,  $G_{RP}$  filter transmission curves adopted in *Gaia* EDR3 are slightly different from the passbands used in *Gaia* DR2.

Contrary to the second data release, the RUWE parameter (Eq. 2.10) is now directly available in the EDR3 catalog. It is still recommended to adopt the criterion  $\text{RUWE} < 1.4$  to eliminate contaminated sources. Other parameters can be used to detect potential outliers. The Goodness-of-Fit (GoF) parameter is similar to the RUWE, and the well-behaved sources generally verify  $\text{GoF} < 8$ . The parameter `ipd_frac_multi_peak` gives the fraction of observations where more than one peak is detected on the CCD, which can suggest resolved binary sources. If `ipd_frac_multi_peak`  $> 2$ , the quality of the parallax can be degraded. Additionally, the parameter `ipd_gof_harmonic_amplitude` indicates the level of asymmetry in the astrometric image. A value above 0.1 strongly suggests the presence of a partially resolved double star. The contents of *Gaia* DR1, DR2 and EDR3 are listed in Table 2.2.

Table 2.2: Contents of *Gaia* DR1, *Gaia* DR2 and *Gaia* EDR3.

	DR1	DR2	EDR3
Total sources (positions)	1.142 billion	1.692 billion	1.811 billion
5-parameter astrometric solutions	2 millions	1.331 billion	1.467 billion
6-parameter astrometric solutions	0	0	882 millions
Variable stars	3000	550000	-
Time coverage	14 months	22 months	34 months

A major improvement provided in *Gaia* EDR3 is the possibility to estimate an individual parallax zero-point offset for each source, using the code developed by [Lindgren et al. \(2021a\)](#).<sup>4</sup> This parallax offset of a few tens of microarcseconds depends on the magnitude, the color and the position of the sources. For the sample of Cepheids with HST/FGS or HST/WFC3 parallaxes described in Sect. 2.2.2 and represented in Fig. 2.11, the *Gaia* EDR3 parallax zero-point ranges between  $4\mu\text{as}$  and  $43\mu\text{as}$ . An uncertainty of a few micro arcseconds is recommended for this quantity. [Fabricius et al. \(2021\)](#) indicate a residual offset of  $6\mu\text{as}$  for Cepheid parallaxes after applying the correction by [Lindgren et al. \(2021a\)](#), which means that  $6\mu\text{as}$  should be subtracted to the corrected parallaxes to obtain their true values. Similarly, from a sample of 75 MW Cepheids, [Riess et al. \(2021b\)](#) derive a residual parallax offset of  $-14 \pm 6\mu\text{as}$ , in the sense that the [Lindgren et al. \(2021a\)](#) corrections are too negative and that resulting parallaxes are over corrected: one should remove  $14\mu\text{as}$  from the

<sup>4</sup> The Python tool developed by [Lindgren et al. \(2021a\)](#) to correct for individual *Gaia* EDR3 parallax zero-points is available at: <https://www.cosmos.esa.int/web/gaia/edr3-code>.



Table 2.3: Mean precision reached by *Gaia* DR2 and *Gaia* EDR3 for parallaxes and magnitudes.

Parameter	Magnitude range	Average uncertainty	
		DR2	EDR3
Parallax	$G < 15$ mag	0.020 – 0.040 mas	0.020 – 0.030 mas
	$G \sim 17$ mag	0.100 mas	0.070 mas
	$G \sim 20$ mag	0.700 mas	0.500 mas
	$G \sim 21$ mag	2.000 mas	1.300 mas
$G$ -photometry	$G < 13$ mag	0.3 mmag	0.3 mmag
	$G \sim 17$ mag	2 mmag	1 mmag
	$G \sim 20$ mag	10 mmag	6 mmag
$BP$ -photometry	$G < 13$ mag	2 mmag	0.9 mmag
	$G \sim 17$ mag	10 mmag	1.2 mmag
	$G \sim 20$ mag	200 mmag	108 mmag
$RP$ -photometry	$G < 13$ mag	2 mmag	0.6 mmag
	$G \sim 17$ mag	10 mmag	6 mmag
	$G \sim 20$ mag	200 mmag	52 mmag

corrected parallax. Based on red-giant branch stars, [Zinn \(2021\)](#) obtain a similar conclusion with an overcorrection of  $15 \pm 3 \mu\text{as}$ . Finally, [Lindgren et al. \(2021a\)](#) note that the Python procedure proposed in their paper is not definitive and that further tests and investigations should be carried out to refine the parallax zero-point offset. Very recently, [Groenewegen \(2021\)](#) developed an alternative procedure to the [Lindgren et al. \(2021a\)](#) code to derive the *Gaia* EDR3 zero-point as a function of position and magnitude, based on a large sample of quasars. For simplicity, only the [Lindgren et al. \(2021a\)](#) correction is considered in this chapter.

The correction of the chromaticity effect for parallaxes of variable stars is still not implemented in *Gaia* EDR3, which can lead to potentially unreliable Cepheid parallaxes. However, the *Gaia* EDR3 release covers 34 months of observations (compared with 22 months for *Gaia* DR2) so it is reasonable to expect that the noise due to the chromaticity effect is averaged and does not impact significantly the quality of Cepheids parallaxes in *Gaia* EDR3. The influence of this effect on the P-L calibration is discussed later in this chapter.

The uncertainties on *Gaia* EDR3 parallaxes are represented in Fig. 2.12 as a function of the  $G$ -band magnitude. The precision reached by *Gaia* EDR3 for the parallaxes and for the photometry is reported in Table 2.3 and is compared with *Gaia* DR2. Stars brighter than  $G = 15$  mag are expected to have a parallax precise to  $30 \mu\text{as}$  at least. Figure 2.12 suggests that the optimal precision for parallaxes is reached for  $9 < G < 13$  mag. However, in this range of magnitudes, stars are still relatively bright: for their observation, only small patches called "windows" of the CCD images around the detected point sources are transmitted. Depending on the brightness of the source, different sampling schemes are adopted, such as the window size or the pixel binning. To avoid pixel saturation, the integration time can be reduced by means of gates around  $G = 13$  mag and  $G = 11$  mag ([Crowley et al. 2016](#)). This process is known as time delayed integration (TDI) gating (see [Lindgren et al. 2021a](#)). Finally, bright stars are less common than faint ones, for this reason the number of bright calibrating sources is smaller.

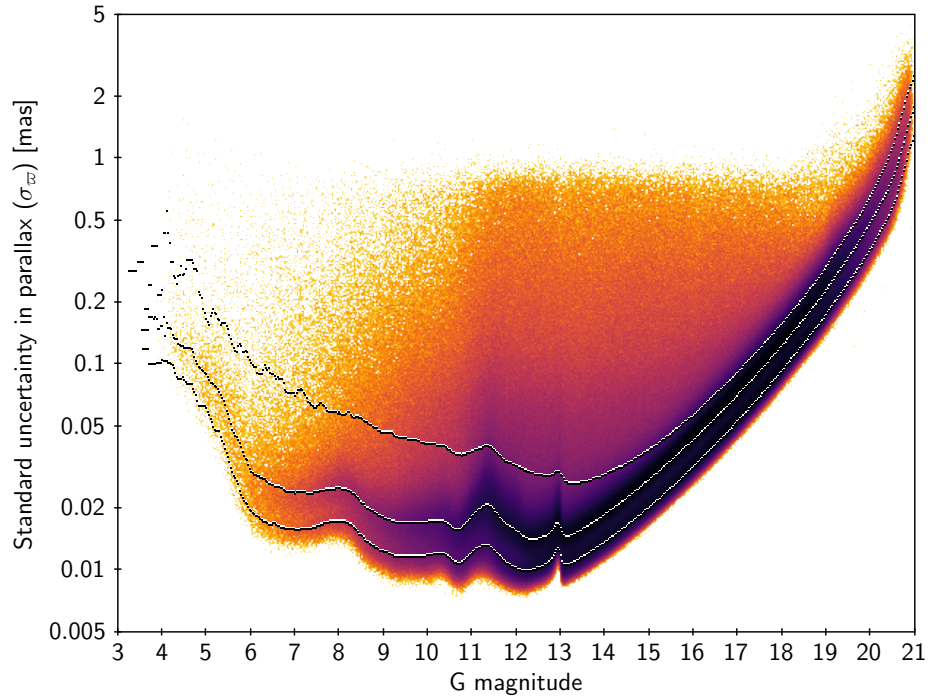


Figure 2.12: Uncertainties in *Gaia* EDR3 parallax as a function of the *G*-band magnitude for 5-parameter solutions. The three curves show the 10<sup>th</sup>, 50<sup>th</sup>, and 90<sup>th</sup> percentiles of the distribution at a given magnitude. The figure is taken from [Lindegren et al. \(2021b\)](#).

The HST/FGS and HST/WFC3 parallaxes already discussed in Sect. 2.2.2 are compared with their *Gaia* EDR3 counterparts in Fig. 2.13. The very bright Cepheids observed with the HST/FGS are still saturated in the *Gaia* EDR3 catalog: seven out of ten have a RUWE parameter larger than 1.4 (Fig. 2.13, left panel). However, all of them now have a physical parallax value (i.e. positive), and the maximum RUWE value for this sample is 6.4 (compared with a RUWE of 20.9 obtained for  $\delta$  Cep in *Gaia* DR2). The largest difference is of 0.9 mas and is obtained for the Cepheid FF Aql with  $\varpi_{\text{HST}} = 2.81 \pm 0.18$  mas and  $\varpi_{\text{EDR3}} = 1.94 \pm 0.07$  mas (including the zero-point correction). *Gaia* EDR3 parallaxes are on average twice more precise than HST/FGS parallaxes measured by [Benedict et al. \(2002, 2007\)](#). Out of 10 Cepheids, 8 have a larger parallax from HST/FGS than in *Gaia* EDR3 catalog, and the dispersion is of  $\sigma = 0.40$  mag which is considerably smaller than with *Gaia* DR2. On the right panel of Fig. 2.13, the sample of HST/WFC3 parallaxes is found to be in good agreement with the *Gaia* EDR3 values. In this range of magnitudes, Cepheids are not saturated: each parallax has a RUWE lower than 1.4 and the difference between HST/WFC3 and EDR3 parallaxes do not exceed 0.1 mas, with a dispersion of  $\sigma = 0.08$  mag. On average, *Gaia* EDR3 parallaxes are 2.7 times more precise than spatial scanning measurements.

So far, few papers making use of *Gaia* EDR3 parallaxes for the calibration of the distance scale have been published. The SH0ES team ([Riess et al. 2021b](#)) combined parallaxes of 75 Milky Way Cepheids with HST photometry to derive a 1.8% value of the Hubble constant:  $H_0 = 73.2 \pm 1.3$  km/s/Mpc. [Soltis et al. \(2021\)](#) adopted *Gaia* EDR3 parallaxes to derive a 2.2% distance to the massive globular cluster  $\omega$  Centauri and obtained an improved calibration of the Tip of the Red Giant Branch in this cluster. Finally, in my paper [Breuval et al. \(2021\)](#), I used *Gaia* EDR3 parallaxes to calibrate the Leavitt law, and more precisely the effect of Cepheid metallicity on this relation. This work is described in Chapter 3.

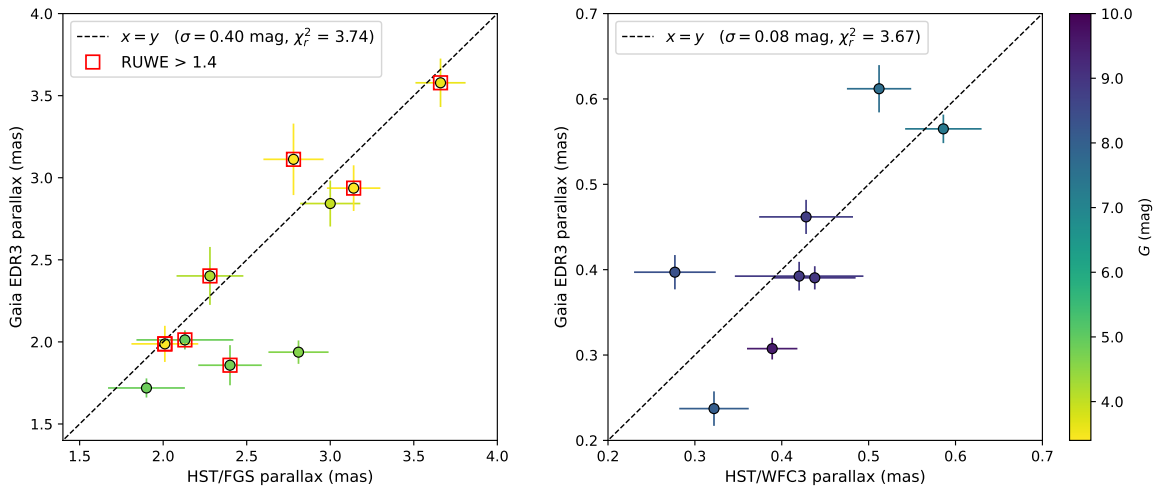


Figure 2.13: **Left:** Comparison between HST/FGS parallaxes (Benedict et al. 2002, 2007) and *Gaia* EDR3 parallaxes. **Right:** Comparison between HST/WFC3 spatial scanning parallaxes (Riess et al. 2014, 2018b) and *Gaia* EDR3 parallaxes. The color map represents the apparent  $G$  magnitude. *Gaia* parallaxes are corrected by the individual zero-points (Lindgren et al. 2021a).

## 2.3 Calibration of the P-L relation with *Gaia* parallaxes

The analysis carried out in this section is described in my first paper, Breuval et al. (2020) (hereafter B20), based on *Gaia* DR2 parallaxes. Since the publication of this paper, the new *Gaia* EDR3 catalog provided more precise parallaxes for Milky Way Cepheids. In this thesis, I therefore extend and improve this preliminary study: I include recent references and I adopt the new *Gaia* EDR3 parallaxes. The samples and the method are mentioned in B20 but I will describe each step in detail in the following sections.

The first motivation of the B20 paper is to use *Gaia* parallaxes of Milky Way Cepheids in order to precisely and accurately calibrate the Leavitt law with a large number of stars. However, as mentioned in Sect. 2.2.2, *Gaia* DR2 parallaxes of variable stars were subject to the chromaticity effect, which produces additional noise in their parallax measurements.

In Sect. 2.3.1, I select a sample of Cepheids with resolved companion stars. Using the companions, which are fainter than Cepheids and not variable, as a proxy for the Cepheid parallaxes, allows to bypass the saturation issue and the chromaticity effect. In Sect. 2.3.2, I perform a census of Milky Way Cepheids in Open Clusters (OCs): averaging the parallaxes of their numerous member stars provides a precise estimate for the distance of the Cepheids they host. The photometry, reddenings and pulsation modes are discussed in Sect. 2.3.3, 2.3.4 and 2.3.5 respectively. Finally, the method and the results are provided in Sect. 2.3.6.

### 2.3.1 Sample of Cepheids companions

A sample of 28 Cepheids with wide spatially resolved companions was published by Kervella et al. (2019b). They are identified by the similarity of their *Gaia* DR2 parallax, by the difference in tangen-



Table 2.4: Milky Way Cepheids and their respective resolved companions from [Kervella et al. \(2019b\)](#). *Gaia* DR2 parallaxes are corrected by a zero-point of  $-0.046$  mas and *Gaia* EDR3 parallaxes are corrected by the individual zero-point from [Lindgren et al. \(2021a\)](#). Bold font indicates a RUWE  $> 1.4$ , in this case the parallax should not be used. For Cepheids with multiple companions, the star symbol (★) indicates which companion is adopted. *G*-band apparent mean magnitudes are taken from *Gaia* EDR3.

Source / <i>Gaia</i> DR2 Id.	$\log P$	Gaia DR2		Gaia EDR3		
		$\varpi$	RUWE	$\varpi$	RUWE	<i>G</i>
TV CMa 3044483895574944512	0.669	$0.360 \pm 0.034$ $0.472 \pm 0.050$	0.888 1.096	$0.420 \pm 0.015$ $0.448 \pm 0.036$	1.195 1.013	10.224 15.802
ER Car 5339394048386734336	0.888	$0.842 \pm 0.035$ $0.935 \pm 0.208$	0.853 1.079	$0.869 \pm 0.015$ $0.796 \pm 0.144$	0.824 1.099	6.577 18.422
DF Cas 465719182408531072	0.583	$0.353 \pm 0.028$ $0.413 \pm 0.101$	0.884 1.153	$0.374 \pm 0.014$ $0.317 \pm 0.076$	1.049 1.058	10.472 17.230
V0659 Cen 5868451109212716928	0.750	$0.530 \pm 0.154$ $1.401 \pm 0.448$	<b>4.116</b> 1.041	$0.905 \pm 0.052$ $0.878 \pm 0.344$	<b>2.990</b> 1.026	6.475 19.692
$\delta$ Cep 2200153214212849024	0.730	$-1.126 \pm 0.468$ $3.410 \pm 0.050$	<b>20.908</b> 1.292	$3.578 \pm 0.147$ $3.483 \pm 0.051$	<b>2.713</b> <b>1.415</b>	3.851 6.300
AX Cir 5874031027625742848	0.722	$1.791 \pm 0.345$ $1.771 \pm 0.527$	<b>8.014</b> 1.132	$1.979 \pm 0.248$ $0.904 \pm 0.422$	<b>7.805</b> 1.050	5.658 19.793
BP Cir 5877472464676660480	0.380	$1.041 \pm 0.040$ $1.542 \pm 0.262$	1.045 1.056	$1.043 \pm 0.022$ $1.083 \pm 0.206$	1.050 0.995	7.327 18.877
R Cru 6054935874780531328	0.765	$-1.077 \pm 0.219$ $1.124 \pm 0.116$	<b>4.568</b> <b>2.805</b>	$1.078 \pm 0.028$ $0.892 \pm 0.060$	1.161 <b>1.443</b>	6.585 15.754
X Cru 6059762524642419968	0.794	$0.570 \pm 0.046$ $0.655 \pm 0.056$	0.863 1.132	$0.654 \pm 0.019$ $0.649 \pm 0.042$	0.947 1.082	8.172 16.034
VW Cru 6053622508133367680	0.721	$0.829 \pm 0.045$ $0.725 \pm 0.028$	0.934 0.892	$0.738 \pm 0.016$ $0.751 \pm 0.018$	0.854 0.986	9.076 14.063
V0532 Cyg 1971721839529622272	0.516	$0.607 \pm 0.033$ $0.665 \pm 0.027$	0.750 0.896	$0.624 \pm 0.013$ $0.643 \pm 0.018$	0.943 0.987	8.700 14.664
V1046 Cyg 2060460708575795712	0.694	$0.312 \pm 0.029$ $0.373 \pm 0.069$	1.132 <b>1.514</b>	$0.295 \pm 0.016$ $0.439 \pm 0.051$	1.087 1.324	11.609 15.848
CV Mon 3127142224816361600 3127142327895572352★	0.731	$0.528 \pm 0.041$ $0.584 \pm 0.038$ $0.554 \pm 0.025$	1.096 1.031 0.963	$0.601 \pm 0.015$ $0.566 \pm 0.017$ $0.565 \pm 0.015$	1.100 1.040 1.227	9.701 13.555 13.479
RS Nor 5932812740361508736	0.792	$0.467 \pm 0.046$ $0.495 \pm 0.038$	0.918 1.026	$0.472 \pm 0.017$ $0.465 \pm 0.023$	0.938 1.036	9.611 14.535
SY Nor 5884729035245399424 5884729035255068800★	1.102	$0.446 \pm 0.035$ $0.460 \pm 0.053$ $0.455 \pm 0.079$	1.040 1.260 0.980	$0.258 \pm 0.027$ $0.533 \pm 0.088$ $0.357 \pm 0.070$	<b>1.552</b> <b>2.607</b> 0.912	9.041 12.143 17.022
QZ Nor 5932565899990412672	0.578	$0.520 \pm 0.038$ $0.498 \pm 0.130$	0.908 1.011	$0.484 \pm 0.020$ $0.447 \pm 0.113$	1.032 0.994	8.624 17.923
AW Per 174489098011144960	0.810	$1.088 \pm 0.064$ $1.092 \pm 0.348$	1.019 1.068	$1.093 \pm 0.029$ $0.460 \pm 0.138$	1.156 1.063	7.086 17.439
RS Pup 5546476755539995008	1.618	$0.630 \pm 0.026$ $0.549 \pm 0.045$	0.902 0.987	$0.581 \pm 0.017$ $0.601 \pm 0.035$	1.157 1.062	6.638 16.246

...

**Table 2.4** (continued)

Source / <i>Gaia</i> DR2 Id.	$\log P$	<i>Gaia</i> DR2		<i>Gaia</i> EDR3		
		$\varpi$	RUWE	$\varpi$	RUWE	$G$
U Sgr	0.829	$1.506 \pm 0.045$	0.898	$1.605 \pm 0.022$	0.853	6.429
4092905066374437760*		$1.551 \pm 0.074$	0.998	$1.520 \pm 0.020$	0.680	10.146
4092905203841177856		$1.507 \pm 0.038$	0.920	$1.502 \pm 0.018$	0.671	11.141
V0350 Sgr	0.712	$1.032 \pm 0.047$	0.794	$0.810 \pm 0.062$	<b>2.427</b>	7.249
4080121319521641344*		$1.061 \pm 0.048$	1.096	$1.014 \pm 0.018$	0.993	12.259
4080121521343969024		$1.156 \pm 0.198$	<b>2.265</b>	$1.125 \pm 0.151$	<b>2.029</b>	17.051
V0950 Sco	0.529	$0.886 \pm 0.052$	0.994	$0.942 \pm 0.022$	0.807	7.069
5960623340819000192		$0.939 \pm 0.065$	0.980	$0.939 \pm 0.040$	1.015	15.274
CM Sct	0.593	$0.422 \pm 0.065$	1.001	$0.444 \pm 0.017$	0.835	10.546
4253603428053877504		$0.564 \pm 0.051$	0.931	$0.474 \pm 0.031$	0.982	14.712
EV Sct	0.490	$0.543 \pm 0.054$	0.952	$0.526 \pm 0.018$	1.009	9.644
4156513016572003840		$0.527 \pm 0.034$	1.014	$0.491 \pm 0.019$	0.985	13.608
SX Vel	0.980	$0.455 \pm 0.041$	0.893	$0.501 \pm 0.019$	1.022	8.121
5329838158460399488		$0.478 \pm 0.083$	0.934	$0.444 \pm 0.062$	0.982	17.009
CS Vel	0.771	$0.211 \pm 0.030$	1.036	$0.272 \pm 0.013$	0.905	11.188
5308893046071732096		$0.268 \pm 0.045$	0.925	$0.286 \pm 0.033$	0.944	16.194
DK Vel	0.395	$0.255 \pm 0.025$	0.940	$0.266 \pm 0.011$	0.992	10.403
5311599390863537408		$0.419 \pm 0.115$	0.987	$0.334 \pm 0.090$	0.966	18.072

tial velocity between the Cepheid and the field star, and by their separation projected along the line of sight. The companion stars are photometrically stable and have a constant color, unlike Cepheids, hence they are not subject to the chromaticity effect mentioned in Sect. 2.2.2. Cepheids are usually very bright stars and their companions are fainter, which also allows to circumvent the saturation issue. Moreover, some Cepheids have no valid parallax in *Gaia* DR2 (e.g.  $\delta$  Cep, R Cru), likely due to saturation, while their companions all have a physical parallax value. Assuming that both components of the binary system share the same parallax, the companion provides a reliable and accurate estimate for the Cepheid parallax. The binaries are classified in three categories: bound binaries (based on the escape velocity), unbound binaries, and nearby companion (within 50,000 au). In the following, only the binary systems flagged as "bound" are selected, in order to ensure that the Cepheids and their respective companions are at the same distance. The selected binary Cepheids and their companions are listed in Table 2.4.

Two stars were excluded from this catalog. First, the Cepheid CE Cas A: it is in a binary system with CE Cas B, which is also a variable star. Moreover, the separation between the two stars is of only 2.47 arcsec, which is very small compared with other systems of this sample (see [Kervella et al. 2019b](#), Table A1). Additionally, the two stars are often confused in the literature and many catalogs provide the same parameters for both components. Therefore, it is safer to discard this association from the sample. Secondly, the very nearby star  $\alpha$  UMi is extremely bright ( $V \sim 2$  mag,  $K \sim 0.5$  mag) and saturates most detectors. Its pulsation mode is debated and its nature as a Cepheid is also discussed ([Anderson 2018](#)). For these reasons this star is excluded from the sample.

A potential limitation of using faint companion parallaxes is the possible contamination from the bright neighbour Cepheid. However, the separation between the two components of the system is generally larger than 10 arcsec, and given the brightness of the Cepheids of this sample, this separation is large enough to prevent flux contamination. Moreover, the difference of flux between Cepheids

and their companions is not sufficient to induce a significant contamination: the Cepheids have magnitudes between  $G = 3.8$  mag and  $G = 11.6$  mag, while the companions are between  $G = 6.3$  mag and  $G = 19.8$  mag. The RUWE parameter accounts for this possible flux contamination and increases when a parallax is not reliable. Only companions with a RUWE below 1.4 were selected in order to carefully avoid this type of contamination. The mean RUWE of Cepheids is 1.48 and the mean RUWE of companions is 1.12 (for this sample and in *Gaia* EDR3 catalog), showing that Cepheids are more affected by biases and by saturation than companions, and that companion parallaxes are generally reliable.

A second issue that can arise when using this approach is the effect of binarity on the proper motion of the system. Since the Cepheid and its companion are gravitationally bound, their motion is mutually influenced, as the system moves around the center of mass. For this reason, the influence of the Cepheid on the astrometric solution of the companion can be questioned. Nevertheless, this effect is limited to the systems with an orbital period close to one year. The mean separation of the systems is  $\sim 20$  kAU and the masses of the Cepheids range from 4 to 10 solar masses, so the orbital periods are of the order of tens of thousands of years. This implies that the impact of binarity is negligible for the parallaxes of this sample.

Fig. 2.14 shows the  $G$ -band magnitudes of the Cepheids and of the companions, as a function of the *Gaia* EDR3 parallax. Nearby Cepheids ( $\varpi > 1$  mas) are usually brighter than distant ones and are close to the saturation limit. While several Cepheids in the sample are below or close to the saturation limit (e.g. ER Car, V0659 Cen,  $\delta$  Cep, AX Cir, U Sgr), their companions are on average 7 mag fainter. This diagram clearly shows that the companions belong to the best dynamical range for *Gaia*'s detector, and therefore are suitable for the calibration of the Leavitt law.

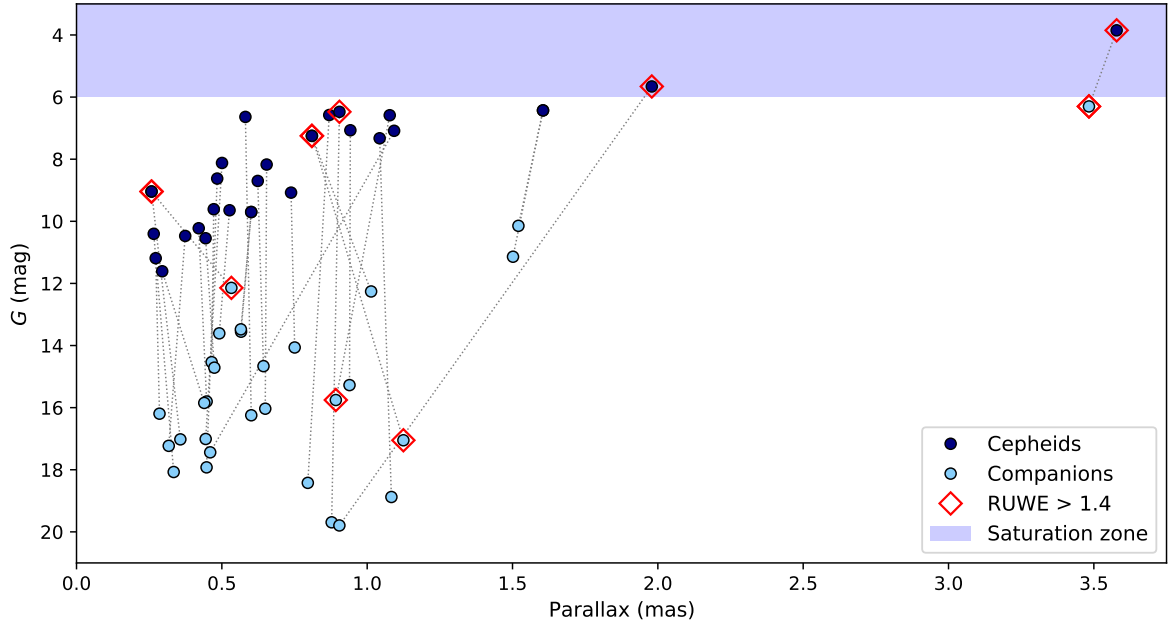


Figure 2.14:  $G$ -band magnitudes of Cepheids (dark blue points) and their companions (light blue points) as a function of the *Gaia* EDR3 parallax. Red markers represent a RUWE parameter larger than 1.4. The blue region is the saturation zone, where the magnitude is brighter than  $G = 6$  mag.

Among the binary systems detected by [Kervella et al. \(2019b\)](#), four Cepheids are found with multiple companions: CV Mon, SY Nor, U Sgr and V0350 Sgr. Using the parallaxes of two companions for the same Cepheid in the calibration of the Leavitt law would introduce unwanted correlations, therefore only one companion is retained for each Cepheid.<sup>5</sup>

- CV Mon has two companions: *Gaia* DR2 3127142224816361600 (comp. 1) and *Gaia* DR2 3127142327895572352 (comp. 2). Both have parallaxes that agree at  $1\sigma$  in *Gaia* DR2 and EDR3. They both have RUWE parameters lower than 1.4 and are not saturated. However, comp. 2 has a slightly more precise parallax so it is preferred as the companion star of CV Mon, and comp. 1 is discarded.
- SY Nor has two companions: *Gaia* DR2 5884729035245399424 (comp. 1) and *Gaia* DR2 5884729035255068800 (comp. 2). They have consistent parallaxes in *Gaia* DR2, however their *Gaia* EDR3 parallaxes differ by 0.241 mas ( $2.1\sigma$ ). Comp. 1 has a RUWE of 2.6 in *Gaia* EDR3, which can be explained by contamination from the Cepheid due to the small separation ( $2.5''$ ) between the two components, while comp. 2 has a RUWE of 0.9. Additionally, the parallax of comp. 2 is the most precise and is also closer to the Cepheid parallax: comp. 2 is selected as the companion of SY Nor.
- U Sgr has two companions: *Gaia* DR2 4092905066374437760 (comp. 1) and *Gaia* DR2 4092905203841177856 (comp. 2). They are both very similar in terms of parallax value, precision, RUWE and brightness. Comp. 1 is finally selected because its *Gaia* EDR3 parallax is closer to the Cepheid parallax, while Comp. 2 differs by almost 0.1 mas from the Cepheid.
- V0350 Sgr has two companions: *Gaia* DR2 4080121319521641344 (comp. 1) and *Gaia* DR2 4080121521343969024 (comp. 2). Comp. 2, which is relatively faint ( $G \sim 17$  mag), has a RUWE  $> 2$  in both catalogs and has large parallax uncertainties. Comp. 1 has an acceptable RUWE and a parallax in good agreement with that of the Cepheid, therefore it is adopted as the companion star of V0350 Sgr.

The left-hand panel of Fig. 2.15 compares Cepheid and companion parallaxes from *Gaia* DR2. The agreement is globally correct but a small trend is observed: companion parallaxes are slightly larger than Cepheid parallaxes. In this figure, Cepheids with a RUWE parameter larger than 1.4 are indicated by a blue square and companions with a RUWE larger than 1.4 are indicated by a red square. Two companions are found in the latter case and should not be considered for the calibration of the Leavitt law: the companions of R Cru and V1046 Cyg. Two Cepheids have a negative parallax value, whereas all companions have a physical value (i.e. positive), which shows that for this sample and in *Gaia* DR2, companion parallaxes are more reliable than Cepheid parallaxes. On average, parallaxes of companions are precise to 0.115 mas while parallaxes of Cepheids are precise to 0.075 mas. This is due to the faint magnitudes of some companions, compared with Cepheids which are relatively bright.

The right-hand panel of Fig. 2.15 compares the parallaxes of Cepheids and companions from *Gaia* EDR3, after including the zero-point correction from [Lindgren et al. \(2021a\)](#). Contrary to *Gaia* DR2, all Cepheids and companions of this sample have a positive value. Five Cepheids have a RUWE larger than 1.4 while only two companions are in this case: the companions of  $\delta$  Cep and R Cru. These two stars are therefore discarded for the calibration of the P-L relation (Sect. 2.3.6). The companions of V0659 Cen and AX Cir both have a good RUWE but also have very large parallax uncertainties ( $0.878 \pm 0.344$  mas, 39 % and  $0.904 \pm 0.422$  mas, 47 %, respectively) due to their

<sup>5</sup> Adopting the average parallax of the two companions would give very similar results.

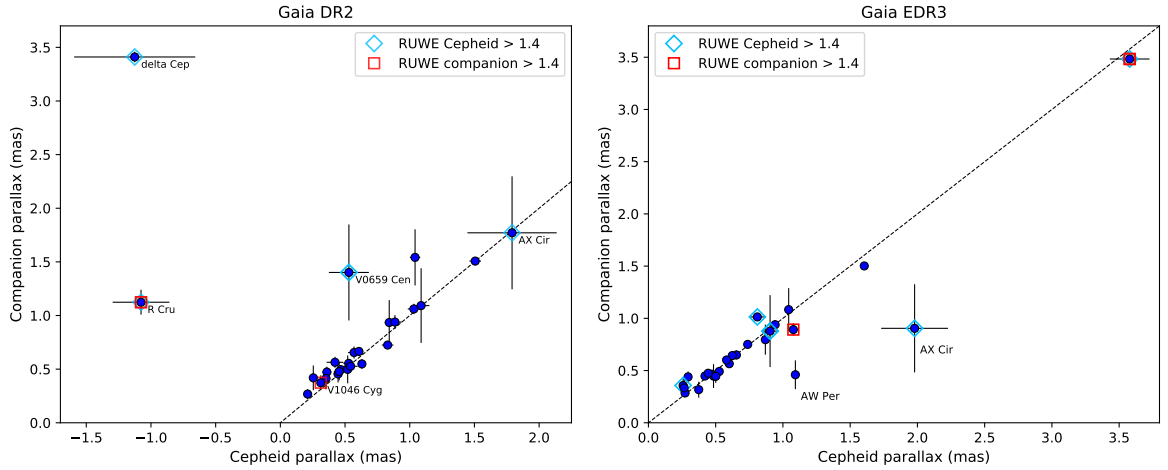


Figure 2.15: **Left:** *Gaia* DR2 parallax of Cepheids against *Gaia* DR2 parallax of the respective companions, both corrected by a zero-point of  $-0.046$  mas. **Right:** *Gaia* EDR3 parallax of Cepheids against *Gaia* EDR3 parallax of their respective companions, both corrected by the [Lindgren et al. \(2021a\)](#) zero-point. Blue squares indicate a Cepheid with a RUWE larger than 1.4 and red squares indicate that the parallax of the companion has a RUWE larger than 1.4.

particularly faint magnitude ( $G = 19.69$  mag and  $G = 19.79$  mag). They should be treated carefully in the calibration of the Leavitt law. *Gaia* EDR3 parallaxes of Cepheids are precise to  $0.035$  mas on average, compared with a mean precision of  $0.082$  mas for companions. The precision of companion parallaxes is significantly improved in this third data release. Additionally, the large time coverage of 34 months included in *Gaia* EDR3 as well as the good agreement between most Cepheids and their respective companions suggest that the chromaticity issue is averaged and can be neglected. This assumption will be tested in Sect. 2.3.6.

The distance of RS Pup was measured to  $1910 \pm 80$  pc ( $\varpi = 0.524 \pm 0.022$  mas) by [Kervella et al. \(2014\)](#) using the propagation of the light echoes through the surrounding gas nebula. In *Gaia* EDR3, the companion of this Cepheid has a parallax of  $0.601 \pm 0.035$  mas while RS Pup itself has a parallax of  $0.581 \pm 0.017$  mas. Both Cepheid and companion parallax are compatible to  $2\sigma$  or better with the light echo estimate. This example shows the consistency of *Gaia* measurements with other distance determinations and the high potential of Cepheid companions for calibrating the Leavitt law.

### 2.3.2 Sample of Open Cluster Cepheids

Open clusters (OCs) are open stellar groups, their member stars were formed at the same time, from the same molecular gas cloud, and therefore have a similar chemical composition. Due to their membership to the cluster, they share a common average position, proper motion, distance and age. OCs are detected by the isochrone pattern they describe in the color-magnitude diagram. They are numerous in the Milky Way and have been used extensively for calibrating the Cepheid P-L relation (e.g. [An et al. 2007](#); [Anderson et al. 2013](#); [Chen et al. 2015, 2017](#); [Zhou & Chen 2021](#); [Medina et al. 2021](#)). Similarly to the sample of Cepheid companions described in the previous section, OCs provide a reliable estimate for the distance of the Cepheids they host. The large majority of the member stars are fainter than Cepheids and are not variable, hence their parallax is not affected by the change of color and by saturation. However, the number of confirmed open cluster Cepheids is still limited ( $\sim 30$ ).

Averaging the parallaxes over the numerous members of the OC gives a particularly precise parallax for the cluster. However, one limitation of using clusters to derive the distance to Cepheids is that the parallaxes of the members are strongly correlated due to their small angular separation in the sky: this effect must be included in the estimation of the error of the cluster mean parallax. The detailed calculation of the uncertainties of a mean cluster parallax is given in Sect. 2.3.2.1. The sample of cluster Cepheids adopted in B20 is re-analyzed in Sect. 2.3.2.2 with *Gaia* EDR3 data, and additional associations of Cepheids and OCs from the literature are finally discussed in Sect. 2.3.2.3.

### 2.3.2.1 Open Cluster mean parallaxes and uncertainties

The total uncertainty of the mean parallax for a cluster hosting  $N$  member stars is defined by [Lindgren \(2018b\)](#) as:

$$\sigma_{\text{total}}^2 = \frac{1}{N} \left[ k^2 \langle \sigma_i^2 \rangle + V_{\varpi}(0) \right] + \frac{N-1}{N} \langle \langle V_{\varpi}(\theta_{ij}) \rangle \rangle \quad (2.13)$$

where  $k$  is an overestimation factor,  $\sigma_i$  are the statistical errors on each individual parallax from the *Gaia* catalog,  $\theta_{ij}$  is the separation between each couple of member stars and  $V_{\varpi}(\theta_{ij})$  is the spatial covariance function. The operator  $\langle \rangle$  represents the sum over the  $N$  cluster members and the operator  $\langle \langle \rangle \rangle$  is the sum over the  $N(N-1)/2$  non-redundant pairs of member stars. The first term of Eq. 2.13 strongly depends on the number of member stars  $N$  and on their magnitude  $G$ , while the second term depends on the spatial distribution of the sources.

For *Gaia* DR2, the spatial covariance function was provided in  $\mu\text{as}^2$  on the ESA DR2 *Known issues* webpage<sup>6</sup>. [Lindgren \(2018b\)](#) gives  $k = 1.08$  for the overestimation factor, and  $V_{\varpi}(0) = \sigma_s^2$  is the variance of the systematic error, with  $\sigma_s = 0.043$  mas for  $G > 13$  mag and  $\sigma_s = 0.021$  mas for  $G < 13$  mag.

For *Gaia* EDR3, the multiplicative constant  $k$  was computed by [Fabricius et al. \(2021\)](#) and is represented in their Fig. 19. For 5-parameter solutions, it can be approximated by the following expression:

$$\left\{ \begin{array}{ll} k = 1.6 & G < 12 \\ k = 1.8 & 12 < G < 13 \\ k = 1.4 & 13 < G < 14 \\ k = 1.3 & 14 < G < 16 \\ k = 1.2 & 16 < G \end{array} \right.$$

It is slightly higher for 6-parameter solutions, however in the clusters of this study the number of stars with 6-parameters solutions is close to zero. A similar expression for  $k$  is provided in [Maíz Apellániz et al. \(2021\)](#) and yields smaller  $k$  values (Fig. 2.16), but the conservative estimate by [Fabricius et al. \(2021\)](#) is adopted for safety.

Regarding the spatial covariance function  $V_{\varpi}(\theta)$  for *Gaia* EDR3 parallaxes, no official table is available on the *Gaia* website so far, but several papers attempted to derive an analytical expression for this function. Based on faint and distant quasars, [Lindgren et al. \(2021b\)](#) obtain for  $0.5^\circ < \theta < 80^\circ$ :

$$V_{\varpi}(\theta) = (142 \mu\text{as}^2) \times \exp(-\theta/16^\circ) \quad (2.14)$$

This relation cannot be applied for the clusters of this study since the cluster radii range between  $0.05^\circ$  and  $0.3^\circ$ . For a zero separation, they obtain  $V_{\varpi}(0) = 700 \mu\text{as}^2$ , which is relatively high. On the other

<sup>6</sup> *Gaia* Known issues webpage: <https://www.cosmos.esa.int/web/gaia/dr2-known-issues>



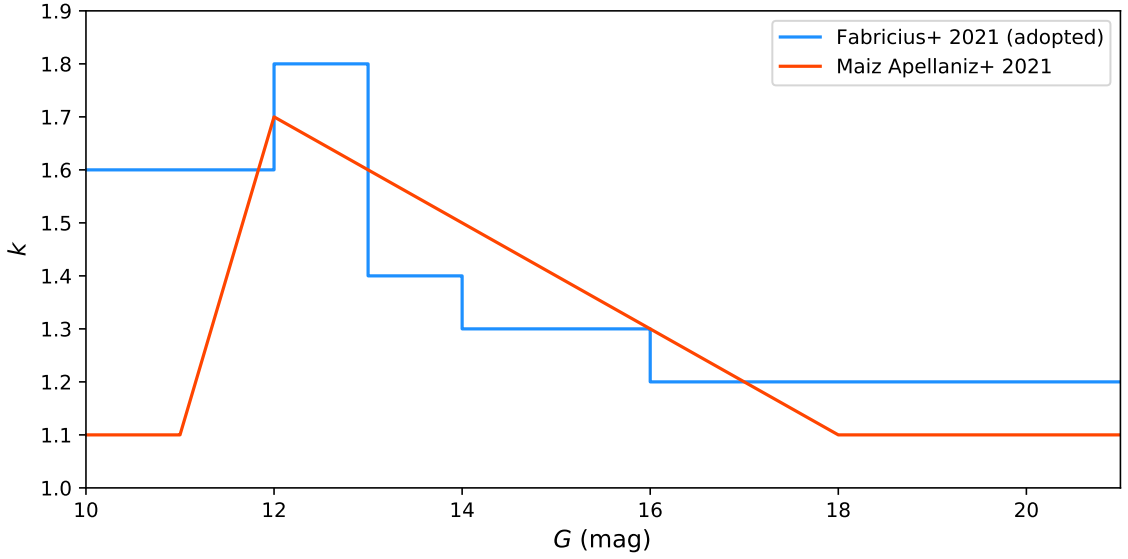


Figure 2.16: Values of the  $k$  parameter of Eq. 2.13 as a function of  $G$  magnitude, according to Maíz Apellániz et al. (2021) and Fabricius et al. (2021).

hand, Maíz Apellániz et al. (2021) use bright sources in the LMC and derive in the range  $0^\circ < \theta < 4^\circ$ :

$$V_{\varpi}(\theta) = V_{\varpi}(0) \left[ a e^{-\theta/1.4} + (1-a) \frac{\cos(2\pi\theta/\lambda + \phi)}{\cos(\phi)} \left( b e^{-(\theta/0.35)^{0.8}} + 1 - b \right) \right] \quad (2.15)$$

with  $V_{\varpi}(0) = 46.2 \mu\text{as}^2$ ,  $a = 0.6$ ,  $b = 0.94$ ,  $\lambda = 1.05^\circ$  and  $\phi = -5\pi/18$ . For the typical separation of the clusters considered below,  $V_{\varpi}(\theta)$  vary between 46 (at most) and  $15 \mu\text{as}^2$ , which is more optimistic than the Lindegren et al. (2021b) evaluation. However this expression is derived only from LMC stars, all located in the same limited area in the sky. Finally, Vasiliev & Baumgardt (2021) complement these recent estimates with dense globular clusters observed in various directions in the sky and obtain:

$$V_{\varpi}(\theta) = \left[ \frac{50}{1 + \theta/0.3^\circ} + 70 \exp\left(-\theta/30^\circ - (\theta/50^\circ)^2\right) \right] \times \max(G - 17, 1) \quad (2.16)$$

where  $G$  is the brightest star of the pair, which yields  $V_{\varpi}(\theta)$  values between 90 and  $120 \mu\text{as}^2$ . This formula includes correlations at small separations, estimated based on clusters, and also correlations at larger spatial scales from Lindegren et al. (2021b) calibrated on quasars. Fig. 3 of Vasiliev & Baumgardt (2021) shows that the spatial covariance function only reaches a maximum of  $\sim 50 \mu\text{as}$  at zero separation and for  $13 < G < 18$ , because large-scale correlations cancel out. Therefore, adopting Eq. 2.16 is conservative in the sense that the parallax uncertainties may be overestimated by this formula.

### 2.3.2.2 Open Cluster Cepheids from Gaia DR2 and Gaia EDR3

In Breuval et al. (2020), I crossmatched the Ripepi et al. (2019) reclassification of *Gaia* DR2 Cepheids (575 fundamental-mode and 204 first-overtone Cepheids) with the catalog of 1229 open clusters with mean *Gaia* DR2 parallaxes by Cantat-Gaudin et al. (2018). The crossmatch was based on 6 parameters: the positions ( $\alpha$ ,  $\delta$ ), the proper motions ( $\mu_\alpha^*$ ,  $\mu_\delta$ ), the parallaxes ( $\varpi$ ) and the ages ( $\log t$ ). A preliminary sample of 11 OC Cepheids is derived from this crossmatch. However, some Cepheids are

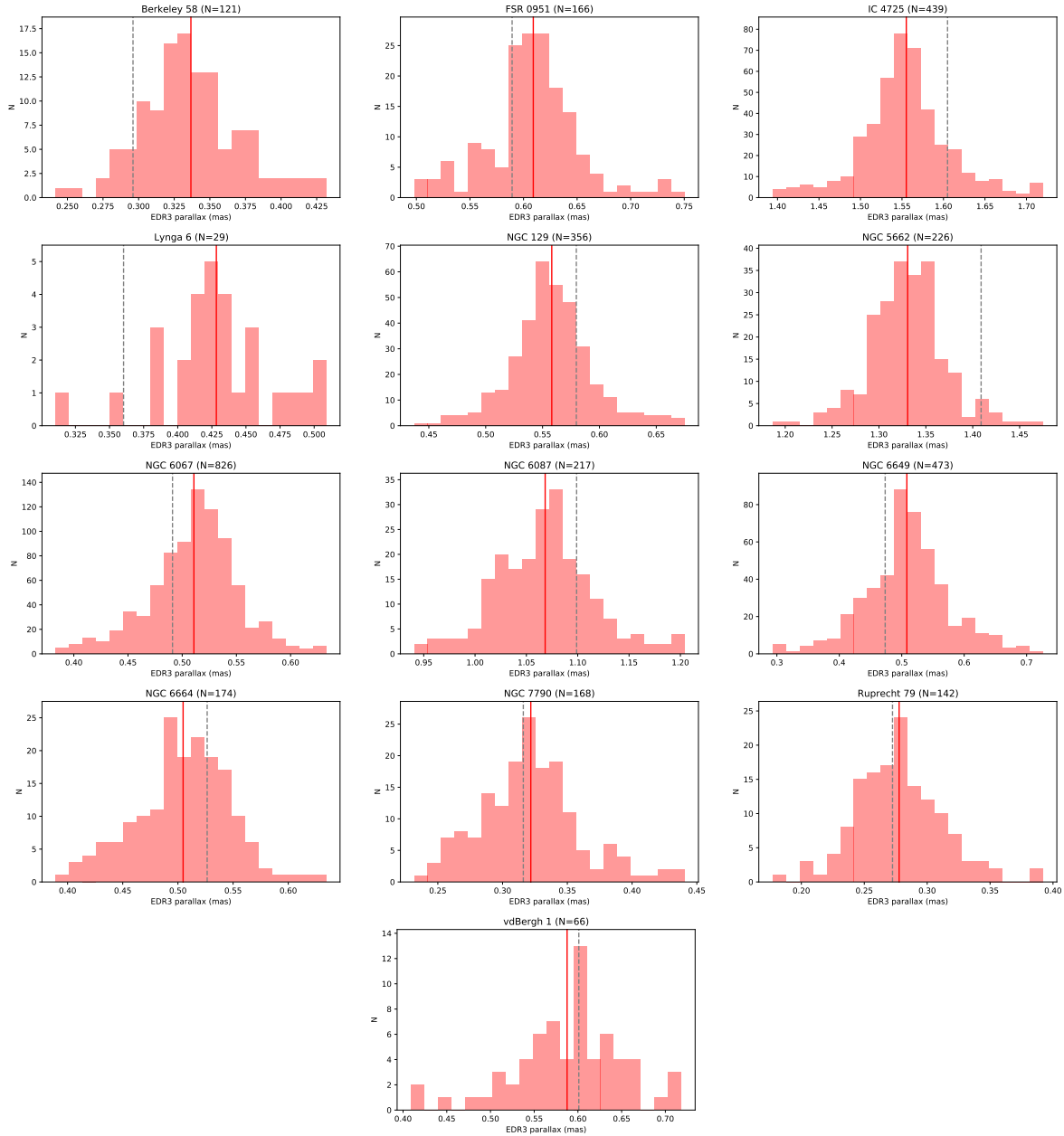


Figure 2.17: Histograms of the *Gaia* EDR3 parallaxes of the members of the open clusters used in B20. The red line shows the mean cluster parallax while the dashed grey line indicates the Cepheid parallax from *Gaia* EDR3, corrected for the zero-point.

missing from the [Ripepi et al. \(2019\)](#) reclassification, therefore I searched the literature for additional associations (e.g. [Anderson et al. 2013](#); [Chen et al. 2015](#)) and I verified the agreement of their parameters in *Gaia* DR2. A final number of 14 cluster Cepheids is adopted in B20, after rejecting some associations due to unprecise or single-point photometry for the Cepheid. Among this sample, two Cepheids were found in the same cluster (NGC 6067) so it leaves 14 Cepheids and 13 open clusters in total.

In this section, I re-examine the sample of OC Cepheids selected in B20 by using *Gaia* EDR3 parallaxes in place of DR2 parallaxes. So far, no catalog of open clusters based on *Gaia* EDR3 has



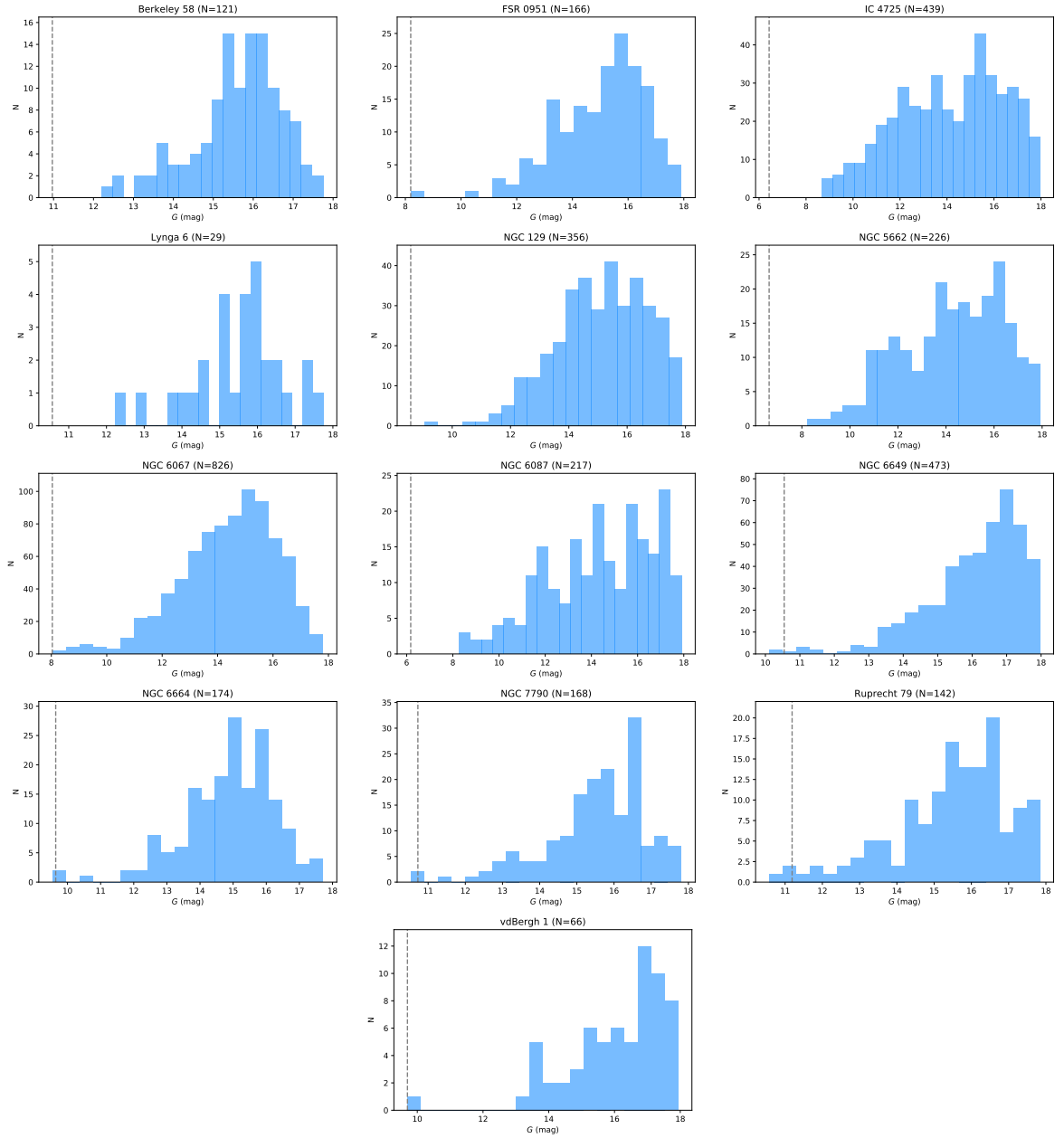


Figure 2.18: Histograms of the  $G$ -band magnitudes of the members of the open clusters used in B20. The dashed grey line shows the apparent magnitude of the Cepheid.

been published: I did not repeat the Cantat-Gaudin analysis with *Gaia* EDR3 parallaxes, because it represents a very detailed and thorough work. However, I tested the validity of the Cepheid memberships with *Gaia* EDR3 data and derived a final mean EDR3 parallax for each cluster. The first step of this analysis was to collect the name of each member of the 13 open clusters in the catalog by Cantat-Gaudin et al. (2020). This study, based on *Gaia* DR2, is a detailed census of cluster members and provides average parallaxes and proper motions for about 2000 clusters. Additional parameters such as age, extinction and distance are also estimated. I collected *Gaia* EDR3 parallaxes of each cluster member and corrected them of the zero-point (Lindgren et al. 2021a). For each of the 13 clusters, I applied a  $3\sigma$  clipping procedure on the parallaxes of the members to reject non-member stars that were misidentified in the original Cantat-Gaudin et al. (2018) catalog. Only a few sources

Table 2.5: Sample of Open Cluster Cepheids adopted in B20 and corresponding parallaxes, proper motion and ages. The  $i^{\text{th}}$  Cepheid (top part of the table) is in the  $i^{\text{th}}$  cluster (bottom part of the table). All parallaxes are corrected from the zero-point. Parallaxes are all from *Gaia* EDR3, as well as Cepheid proper motions. Open cluster proper motions are from Cantat-Gaudin et al. (2020), they are based on *Gaia* DR2 data. Cepheid ages are derived from a period-age relation and cluster ages are from Cantat-Gaudin et al. (2020).

Cepheid	$\log P$ (days)	$\varpi$ (mas)	$\mu_{\alpha}^*$ (mas/yr)	$\mu_{\delta}$ (mas/yr)	Age (log[yr])
DL Cas	0.903	$0.580 \pm 0.027$	$-2.706 \pm 0.025$	$-1.189 \pm 0.027$	$7.94 \pm 0.79$
S Nor	0.989	$1.099 \pm 0.022$	$-1.608 \pm 0.025$	$-2.136 \pm 0.020$	$7.89 \pm 0.79$
V Cen	0.740	$1.409 \pm 0.022$	$-6.697 \pm 0.016$	$-7.068 \pm 0.018$	$8.04 \pm 0.80$
V340 Nor	1.053	$0.491 \pm 0.025$	$-2.066 \pm 0.027$	$-2.634 \pm 0.021$	$7.85 \pm 0.79$
U Sgr	0.829	$1.605 \pm 0.022$	$-1.795 \pm 0.025$	$-6.127 \pm 0.017$	$7.99 \pm 0.80$
EV Sct	0.643	$0.526 \pm 0.018$	$-0.209 \pm 0.018$	$-2.546 \pm 0.015$	$8.10 \pm 0.81$
CS Vel	0.771	$0.272 \pm 0.013$	$-4.567 \pm 0.014$	$3.131 \pm 0.014$	$8.02 \pm 0.80$
CF Cas	0.688	$0.316 \pm 0.012$	$-3.240 \pm 0.012$	$-1.766 \pm 0.012$	$8.07 \pm 0.81$
TW Nor	1.033	$0.360 \pm 0.020$	$-1.891 \pm 0.021$	$-2.806 \pm 0.017$	$7.86 \pm 0.79$
V367 Sct	0.799	$0.473 \pm 0.020$	$0.082 \pm 0.021$	$-0.273 \pm 0.019$	$8.00 \pm 0.80$
CV Mon	0.731	$0.601 \pm 0.015$	$0.349 \pm 0.016$	$-0.666 \pm 0.014$	$8.04 \pm 0.80$
QZ Nor	0.732	$0.484 \pm 0.020$	$-1.896 \pm 0.023$	$-3.848 \pm 0.019$	$8.04 \pm 0.80$
CG Cas	0.640	$0.296 \pm 0.014$	$-3.241 \pm 0.013$	$-1.673 \pm 0.015$	$8.10 \pm 0.81$
RS Ori	0.879	$0.589 \pm 0.030$	$0.196 \pm 0.036$	$0.005 \pm 0.028$	$7.96 \pm 0.80$
Cluster		$\varpi$ (mas)	$\mu_{\alpha}^*$ (mas/yr)	$\mu_{\delta}$ (mas/yr)	Age (log[yr])
NGC 129		$0.558 \pm 0.010$	$-2.605 \pm 0.099$	$-1.096 \pm 0.099$	$8.11 \pm 0.81$
NGC 6087		$1.068 \pm 0.010$	$-1.567 \pm 0.138$	$-2.411 \pm 0.148$	$8.00 \pm 0.80$
NGC 5662		$1.331 \pm 0.010$	$-6.427 \pm 0.160$	$-7.243 \pm 0.187$	$8.30 \pm 0.83$
NGC 6067		$0.511 \pm 0.010$	$-1.907 \pm 0.123$	$-2.586 \pm 0.120$	$8.10 \pm 0.81$
IC 4725		$1.555 \pm 0.010$	$-1.688 \pm 0.208$	$-6.117 \pm 0.242$	$8.05 \pm 0.81$
NGC 6664		$0.505 \pm 0.011$	$-0.089 \pm 0.109$	$-2.561 \pm 0.103$	$8.35 \pm 0.84$
Ruprecht 79		$0.278 \pm 0.011$	$-4.631 \pm 0.090$	$2.995 \pm 0.088$	$7.79 \pm 0.78$
NGC 7790		$0.322 \pm 0.011$	$-3.276 \pm 0.096$	$-1.677 \pm 0.092$	$8.11 \pm 0.81$
Lynga 6		$0.428 \pm 0.015$	$-1.866 \pm 0.144$	$-2.757 \pm 0.098$	$6.49 \pm 0.65$
NGC 6649		$0.508 \pm 0.011$	$-0.007 \pm 0.178$	$-0.055 \pm 0.182$	$7.85 \pm 0.78$
vdBergh 1		$0.588 \pm 0.014$	$0.396 \pm 0.180$	$-0.771 \pm 0.164$	$7.61 \pm 0.76$
NGC 6067		$0.511 \pm 0.010$	$-1.907 \pm 0.123$	$-2.586 \pm 0.120$	$8.10 \pm 0.81$
Berkeley 58		$0.337 \pm 0.011$	$-3.498 \pm 0.065$	$-1.782 \pm 0.075$	$7.78 \pm 0.78$
FSR 0951		$0.609 \pm 0.011$	$0.242 \pm 0.120$	$0.070 \pm 0.105$	$8.72 \pm 0.87$

were removed during this step. I also performed a quality selection based on the RUWE parameter and discarded the sources with a RUWE larger than 1.4. Finally, member stars brighter than  $G = 8$  were excluded to avoid the use of parallaxes affected by saturation. Histograms of the parallaxes for the 13 clusters are represented in Fig. 2.17. The parallaxes of the members are homogeneously distributed around the median value and no outliers are visible. Similarly, the distributions of the  $G$ -band magnitudes of the cluster members are represented in Fig. 2.18. The range of magnitudes covered by the cluster members is generally around  $12 < G < 18$  mag, which is far from the saturation zone and is in the optimal regime of *Gaia*. The influence of the bright stars with magnitudes  $8 < G < 13$  mag on the resulting mean cluster parallaxes is discussed below.

For each cluster member, an individual  $k$  value is calculated using the distribution by Fabricius et al. (2021), represented in Fig. 2.16, and is included in the first term of Eq. 2.13. Both Eq. 2.15 by

Maíz Apellániz et al. (2021) and Eq. 2.16 by Vasiliev & Baumgardt (2021) are adopted successively: using the optimistic relation from Maíz Apellániz et al. (2021) returns very low parallax uncertainties down to  $\sim 6 \mu\text{as}$ , on the other hand, the conservative relation from Vasiliev & Baumgardt (2021) yields mean cluster parallaxes with uncertainties of the order of  $\sim 11 \mu\text{as}$ , still two to three times more precise than individual Cepheid parallaxes. For safety, the covariance function from Vasiliev & Baumgardt (2021) is adopted for deriving the cluster mean parallax uncertainties.

The parameters of Cepheids and OCs considered in this analysis are listed in Table 2.5. Cepheid and cluster parallaxes are from *Gaia* EDR3, they are all corrected for the zero-point offset (Lindgren et al. 2021a). Proper motions are taken from *Gaia* EDR3 for Cepheids and from Cantat-Gaudin et al. (2020) for clusters. Open cluster proper motions  $\mu_\alpha^*$  and  $\mu_\delta$ , taken from Cantat-Gaudin et al. (2020), are estimated based on *Gaia* DR2 data. I did not attempt to recompute their mean values with *Gaia* EDR3 individual proper motions because it is only used for the crossmatch, whereas parallaxes are useful for calibrating the P-L relation in the next section. Mean proper motions should be calculated with the same method as mean parallaxes, by taking into account the spatial correlations.

The age of Cepheids is derived from the period-age relation from Anderson et al. (2016b):  $\log t = -0.592 \log P + 8.476$  for fundamental-mode Cepheids and  $\log t = -0.633 \log P + 8.406$  for first-overtone Cepheids. Anderson et al. (2016b) recommends to adopt a 50% uncertainty on Cepheid ages if crossing numbers, position in the instability strip and the rotational histories are not known, which is the case in the present study. The age of the clusters is directly taken from Cantat-Gaudin et al. (2020), all with an uncertainty of 10%. The agreement between Cepheid and cluster parallaxes, proper motions and ages is represented in Fig. 2.19 and is listed in Table 2.6 (which is the equivalent of Table 2 of B20 with updated *Gaia* EDR3 parameters).

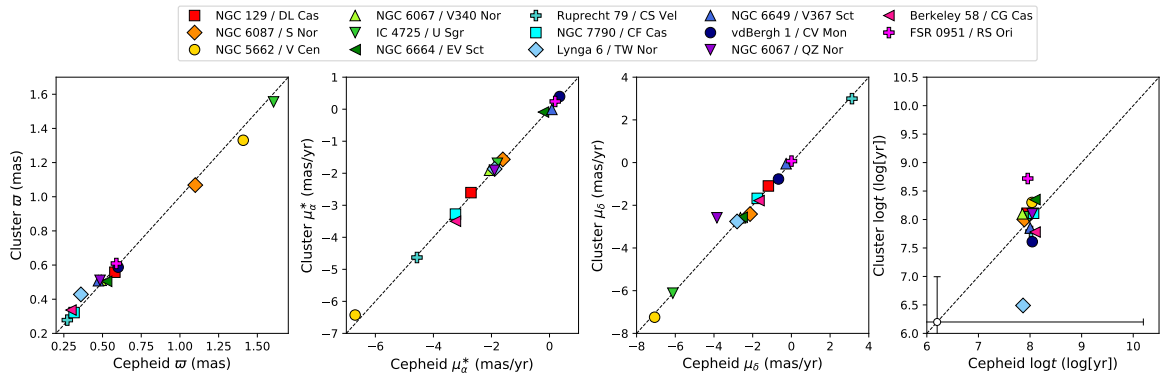


Figure 2.19: Comparison of the *Gaia* EDR3 parallaxes, proper motions and ages for Cepheids and open clusters of the B20 sample. A representative individual uncertainty on Cepheid and cluster ages is shown on the open symbol in the fourth panel.

The agreement between Cepheid and cluster parallaxes is very good, with a largest difference of  $78 \mu\text{as}$  ( $3.2\sigma$ ) between V Cen and NGC 5662. As for the proper motions, all associations are in good agreement, except QZ Nor which has a  $\mu_\delta$  value significantly different (by  $1.2 \text{ mas/yr}$ ) from its host cluster NGC 6067. However the parallaxes agree to  $1.2\sigma$ , with a difference of only  $27 \mu\text{as}$ , and this membership was studied and confirmed by Majaess et al. (2013a) and Medina et al. (2021) so it is not excluded from the sample. Finally, the ages all agree to  $1\sigma$  except TW Nor and Lynga 6 which are at  $1.3\sigma$ . On Fig. 2.19, the age of some Cepheids (e.g. RS Ori, TW Nor) seems particularly distant from the age of the cluster, which is probably due to the large uncertainties introduced by the use of

Table 2.6: Agreement between Cepheids and open clusters from the B20 sample. Filled circles indicate a  $1\sigma$  agreement.

Cepheid	Cluster	$\varpi$	$\mu_\alpha^*$	$\mu_\delta$	$\log t$	N	$r_{50}$ (arcmin)	Sep (arcmin)
CF Cas	NGC 7790	•	•	•	•	168	3.54	1.29
DL Cas	NGC 129	•	•	•	•	356	10.14	3.37
CV Mon	vdBergh 1	•	•	•	•	66	1.80	0.89
RS Ori	FSR 0951	•	•	•	•	166	9.84	1.99
CS Vel	Ruprecht 79	•	•	1.5 $\sigma$	•	142	3.12	2.16
V340 Nor	NGC 6067	•	1.3 $\sigma$	•	•	826	6.72	0.95
U Sgr	IC 4725	2.0	•	•	•	439	15.66	2.10
S Nor	NGC 6087	1.3 $\sigma$	•	1.8 $\sigma$	•	217	14.76	0.99
V Cen	NGC 5662	3.2 $\sigma$	1.7 $\sigma$	•	•	226	19.80	24.60
EV Sct	NGC 6664	1.1 $\sigma$	1.1 $\sigma$	•	•	174	6.12	2.44
TW Nor	Lynga 6	2.7 $\sigma$	•	•	1.3 $\sigma$	29	3.36	0.59
V367 Sct	NGC 6649	1.5 $\sigma$	•	1.2 $\sigma$	•	473	3.42	2.80
QZ Nor	NGC 6067	1.2 $\sigma$	•	10.4 $\sigma$	•	826	6.72	17.94
CG Cas	Berkeley 58	2.3 $\sigma$	3.9 $\sigma$	1.4 $\sigma$	•	121	3.60	5.52

a simple period-age relation. To conclude, all memberships of cluster Cepheids considered in B20 are still valid after adopting *Gaia* EDR3 parallaxes for clusters and Cepheids, as well as *Gaia* EDR3 proper motions for Cepheids. The mean cluster parallaxes derived by Cantat-Gaudin et al. (2018) based on *Gaia* DR2 and those derived in this section from *Gaia* EDR3 are in very good agreement, with a difference of  $50\mu\text{as}$  at maximum.

As mentioned previously (see Sect. 2.2.3), the precision of the astrometry for sources between  $G = 6$  and  $G = 13$  mag can be affected by the time delayed integration and the use of windows of the CCD images around the detected point source to avoid pixel saturation. When all cluster members brighter than  $G < 13$  are excluded, the mean parallaxes only change by  $2\mu\text{as}$  on average, which shows that bright sources up to  $G = 8$  can be included as cluster members without introducing any bias to the mean parallax. The right-hand term of Eq. 2.13, which includes the angular correlations, strongly dominates over the left-hand term: it contributes to 95% of the total error on the mean cluster parallax and is responsible for a threshold uncertainty of  $\sim 0.010\text{mas}$  in the cluster parallaxes listed in Table 2.5.

### 2.3.2.3 Open Cluster Cepheids from the literature

In addition to the initial sample of open cluster Cepheids adopted in B20, new associations were recently suggested and can be included to this study for the calibration of the Leavitt law. Zhou & Chen (2021) carried out a crossmatch similar to that of B20 and compared the OCs from Cantat-Gaudin et al. (2020) and the Cepheids from *Gaia* EDR3. The constraints used by Zhou & Chen (2021) to establish the memberships are the position, the proper motion, the parallax and the evolutionary state, through color-magnitude diagrams. They derive 33 OC Cepheids among which 13 are newly discovered. However, several issues can be mentioned about this paper: mean cluster parallaxes are based on *Gaia* DR2 instead of the recent and more precise *Gaia* EDR3, the brightness of cluster members is not discussed, the quality criteria for *Gaia* parallaxes (such as the RUWE parameter) are not used and the important issue of the parallax zero-point is not mentioned. Many of the new Cepheids are relatively distant from their cluster center, they could be misidentifications and require more detailed

inspection. Additionally, the information provided by [Zhou & Chen \(2021\)](#) about the memberships is limited to differences expressed in sigmas, which is not sufficient to have a precise idea of the available data.

Table 2.7: Subsample of open cluster Cepheids adopted in [Zhou & Chen \(2021\)](#) and corresponding parallaxes, proper motions and ages. All parallaxes are corrected for the zero-point offset.

Cepheid	$\log P$ (days)	$\varpi$ (mas)	$\mu_\alpha^*$ (mas/yr)	$\mu_\delta$ (mas/yr)	Age (log[yr])
WX Pup	0.951	$0.387 \pm 0.015$	$-2.164 \pm 0.010$	$+2.559 \pm 0.014$	$7.91 \pm 0.79$
CM Sct	0.593	$0.444 \pm 0.016$	$-1.064 \pm 0.015$	$-1.414 \pm 0.014$	$8.12 \pm 0.81$
X Cru	0.794	$0.654 \pm 0.019$	$-5.926 \pm 0.015$	$-0.173 \pm 0.017$	$8.01 \pm 0.80$
X Vul	0.801	$0.864 \pm 0.022$	$-1.352 \pm 0.016$	$-4.247 \pm 0.020$	$8.00 \pm 0.80$
SV Vul	1.652	$0.402 \pm 0.021$	$-2.158 \pm 0.016$	$-5.962 \pm 0.021$	$7.50 \pm 0.75$
V438 Cyg	1.050	$0.530 \pm 0.016$	$-3.324 \pm 0.017$	$-4.559 \pm 0.019$	$7.85 \pm 0.79$
V733 Cyg	0.659	$0.238 \pm 0.012$	$-2.713 \pm 0.014$	$-3.341 \pm 0.012$	$8.09 \pm 0.81$
DP Vel	0.739	$0.335 \pm 0.013$	$-4.306 \pm 0.016$	$+3.345 \pm 0.013$	$8.04 \pm 0.80$
Cluster		$\varpi$ (mas)	$\mu_\alpha^*$ (mas/yr)	$\mu_\delta$ (mas/yr)	Age (log[yr])
UBC 231		$0.361 \pm 0.012$	$-2.263 \pm 0.067$	$+2.214 \pm 0.080$	$8.07 \pm 0.81$
UBC 106		$0.442 \pm 0.010$	$-1.088 \pm 0.100$	$-1.317 \pm 0.110$	$8.20 \pm 0.82$
UBC 290		$0.645 \pm 0.010$	$-5.892 \pm 0.083$	$-0.293 \pm 0.071$	$8.28 \pm 0.83$
UBC 129		$0.881 \pm 0.010$	$-0.967 \pm 0.106$	$-4.337 \pm 0.110$	$7.72 \pm 0.77$
UBC 130		$0.427 \pm 0.011$	$-2.099 \pm 0.073$	$-5.856 \pm 0.064$	$7.44 \pm 0.74$
UBC 375		$0.597 \pm 0.011$	$-3.422 \pm 0.074$	$-5.224 \pm 0.109$	$8.03 \pm 0.80$
Kronberger 84		$0.238 \pm 0.015$	$-3.085 \pm 0.191$	$-2.908 \pm 0.131$	$8.46 \pm 0.85$
UBC 491		$0.304 \pm 0.011$	$-4.393 \pm 0.109$	$+3.322 \pm 0.098$	$8.26 \pm 0.83$

In this section, I adopt the approach described in Sect. 2.3.2.2 and apply it to a subsample of the OC Cepheids from [Zhou & Chen \(2021\)](#): 8 Cepheids are selected and are listed in Table 2.7. They have low extinction ( $A_V < 3$  mag) and a good distance precision. For each cluster, the members are taken from [Cantat-Gaudin et al. \(2020\)](#) and their individual parallaxes are collected in *Gaia* EDR3 catalog. I corrected them for their individual zero-point ([Lindgren et al. 2021a](#)), excluded sources brighter than  $G = 8$  and parallaxes with a RUWE  $> 1.4$ . Finally, a  $3\sigma$  clipping procedure is applied to the parallaxes. The uncertainties on the mean cluster parallaxes are derived using Eq. 2.13 and include spatial correlations (Eq. 2.16). Proper motions are taken from *Gaia* EDR3 for Cepheids and from [Cantat-Gaudin et al. \(2020\)](#) for clusters. The ages are derived exactly as in Sect. 2.3.2.2. The agreement between the various parameters is represented in Fig. 2.20 and listed in Table 2.8.

The associations presented by [Zhou & Chen \(2021\)](#) are mostly confirmed by the use of *Gaia* EDR3 parallaxes and proper motions. One exception is the membership of V438 Cyg in UBC 375 which can be doubtful: the parallaxes only agree to  $3.5\sigma$  and the proper motion  $\mu_\delta$  at  $6\sigma$ . All the ages agree within  $1\sigma$  but the uncertainties are high, due to the use of a period-age relation, which makes the age a weakly constraining parameter. This association should be investigated more carefully, for example by using additional constraints or by looking at its position in the P-L plane. In the case of WX Pup and UBC 231, the parameters are in correct agreement but the separation of  $25.9'$  between the Cepheid and the cluster center corresponds to more than 5 times the radius  $r_{50}$  of the cluster, which is very far. The membership of SV Vul in UBC 130 is particularly useful because of the long period of this Cepheid, which is particularly rare in the Milky Way. It was confirmed by [Negueruela et al. \(2020\)](#) and [Medina et al. \(2021\)](#). The Cepheid CM Sct and the cluster UBC 231 are in excellent

Table 2.8: Agreement between Cepheids and open clusters from the [Zhou & Chen \(2021\)](#) sample. Filled circles indicate a  $1\sigma$  agreement.

Cepheid	Cluster	$\varpi$	$\mu_\alpha^*$	$\mu_\delta$	$\log t$	N	$r_{50}$ (arcmin)	Sep (arcmin)
CM Sct	UBC 106	•	•	•	•	217	7.26	9.36
X Cru	UBC 290	•	•	$1.6\sigma$	•	226	9.06	18.86
X Vul	UBC 129	•	$3.6\sigma$	•	•	826	12.60	18.33
V733 Cyg	Kronberger 84	•	$1.9\sigma$	$3.3\sigma$	•	142	1.14	18.13
SV Vul	UBC 130	$1.1\sigma$	•	$1.6\sigma$	•	439	6.36	9.75
WX Pup	UBC 231	$1.4\sigma$	$1.5\sigma$	$4.2\sigma$	•	356	4.86	25.90
DP Vel	UBC 491	$1.9\sigma$	•	•	•	168	7.80	11.99
V438 Cyg	UBC 375	$3.5\sigma$	$1.3\sigma$	$6.0\sigma$	•	174	7.86	6.99

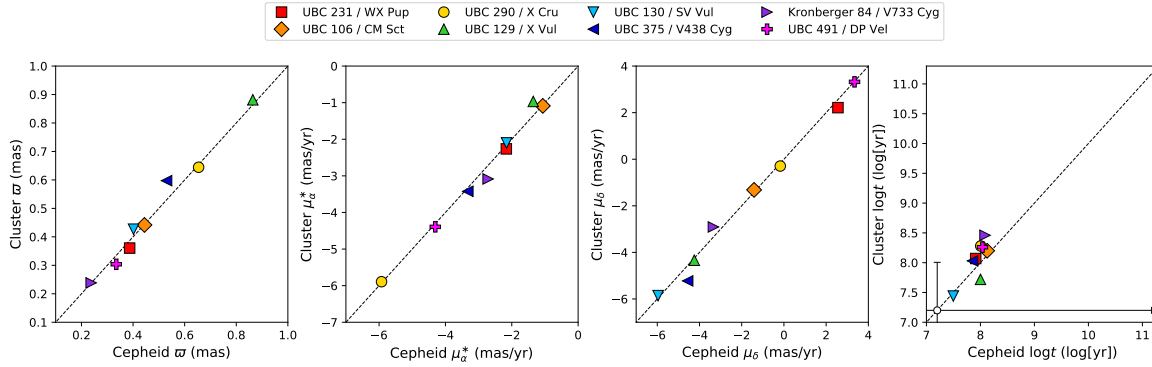


Figure 2.20: Comparison of the parallaxes, proper motions and ages for Cepheids and open clusters of the [Zhou & Chen \(2021\)](#) subsample. A representative individual uncertainty on Cepheid and cluster ages is shown on the open symbol in the fourth panel.

agreement and this membership is also confirmed by [Negueruela et al. \(2021\)](#). These associations will be tested as calibrators of the P-L relation later in this chapter.

Among this sample of OC Cepheids, seven stars also have companions and are listed in Table 2.4, in the previous section: CM Sct, X Cru, U Sgr, EV Sct, CS Vel, CV Mon and QZ Nor. In these particular cases, the companion and cluster parallaxes agree within the error bars, except for U Sgr with a small difference of  $\sim 35\mu\text{as}$  ( $\varpi_{\text{comp}} = 1.520 \pm 0.020\text{ mas}$  and  $\varpi_{\text{cluster}} = 1.555 \pm 0.010\text{ mas}$ ).

The recent paper by [Medina et al. \(2021\)](#) presents a detailed all-sky census of OC Cepheids based on a Bayesian approach inspired by [Anderson et al. \(2013\)](#), it confirms many memberships already mentioned in this chapter and reports new associations with high membership probabilities, such as V0423 CMa in *Gaia* 5, AM Vel in Gulliver 9 and V0335 Pup in UBC 229 for example. Other associations were recently discovered by [Clark et al. \(2015\)](#), [Lohr et al. \(2018\)](#), [Alonso-Santiago et al. \(2020\)](#). However, many of these Cepheids have very poor light-curve coverage, or only single-point photometry, which yields unprecise mean magnitudes and limits the use of some stars in the calibration of the P-L relation, even when the parallax is extremely precise.

This sample of confirmed cluster Cepheids from [B20](#) and cluster Cepheids from [Zhou & Chen \(2021\)](#) will be tested and used for the calibration of the P-L relation in this chapter. V733 Cyg and DP



Vel are discarded in the following analysis because of the lack of data (photometry, reddening, pulsation mode) for these stars. Together with the list of Cepheid companions introduced in Sect. 2.3.1, they are the most complete sample of Cepheids for which an independent parallax can be obtained.

### 2.3.3 Photometry

In order to calibrate the Cepheid P-L relation, apparent flux-averaged mean magnitudes are necessary. Considering that the brightness variation of Cepheids can reach 2 mag during a pulsation cycle, it is essential to use full light curves with the best possible coverage. If only a single data point is available at one extremum of the curve, then the mean magnitude can be biased by up to 1 mag. The more complete is a light curve, the more precise will be the average magnitude.

Near infrared (NIR) photometry for Galactic Cepheids can be taken from four main surveys, assembled in the recent catalog by [Groenewegen \(2018\)](#). They are listed below by order of preference:

- [Monson & Pierce \(2011\)](#) provided  $J$ ,  $H$ ,  $K$  light curves for 131 Northern fundamental-mode Cepheids, with an average of 22 measurements per star. They were measured at the University of Wyoming Red Buttes Observatory at the 0.6 m telescope with the BIRCAM NIR camera. Intensity mean magnitudes are derived with an uncertainty of 0.008 mag.
- [Laney & Stobie \(1992\)](#) observed 51 Cepheids with an average of 31 observations per stars in the  $J$ ,  $H$ ,  $K$  bands. These measurements were obtained between 1982 and 1990 at the Sutherland observing station of the South African Astronomical Observatory, with the 0.75 m telescope. By performing Fourier fits of the light curves, they derived NIR mean magnitudes in the SAAO system with a precision of 0.008 mag.
- [Barnes et al. \(1997\)](#) obtained NIR photometry for 22 bright Cepheids with the 1.3 m telescope at Kitt Peak National Observatory between 1988 and 1994. Mean magnitudes are provided in the CIT system with an uncertainty of 0.01 mag.
- [Welch et al. \(1984\)](#) give complete light curves for 23 Cepheids in the  $J$ ,  $H$ ,  $K$  bands using the 1 m Swope reflector at Las Campanas Observatory, Chile, and the Mount Wilson 0.6 m reflector. Intensity-averaged magnitudes are obtained in the CIT system with a precision of 0.01 mag.

Additionally to these four catalogs, Cepheid NIR magnitudes are also provided in other studies but are often older or less precise and the light curves are not so well-covered. For example, [Genovali et al. \(2014\)](#) adopted single-point photometry from the 2MASS catalog ([Skrutskie et al. 2006](#)) and estimated mean magnitudes using the light-curve template from [Soszyński et al. \(2005\)](#). [McGonegal et al. \(1983\)](#) and [Schechter et al. \(1992\)](#) provided additional NIR measurements in the CIT system. [Groenewegen \(2018\)](#) complemented these observations with 2MASS single point photometry and data from Laney (priv. comm.) as quoted in [Genovali et al. \(2014\)](#). A more detailed analysis is performed in Chapter 3 where light curves are fitted using Fourier series. In this work, I simply adopted the mean values from the [Groenewegen \(2018\)](#) catalog. This compilation is heterogeneous because it includes several sources in different photometric systems, estimated by various methods (e.g. Fourier fit of the light curves, template fitting from single point photometry). I converted all the NIR data from this catalog into the 2MASS system using the equations from [Monson & Pierce \(2011\)](#):

$$\begin{cases} K_{2\text{MASS}} &= K_{\text{BIRCAM}} + 0.008 (J_{\text{BIRCAM}} - K_{\text{BIRCAM}}) - 0.042 \\ J_{2\text{MASS}} &= K_{2\text{MASS}} + 1.052 (J_{\text{BIRCAM}} - K_{\text{BIRCAM}}) - 0.002 \\ H_{2\text{MASS}} &= K_{2\text{MASS}} + 0.993 (H_{\text{BIRCAM}} - K_{\text{BIRCAM}}) + 0.050 \end{cases}$$

$$\begin{cases} K_{2\text{MASS}} &= K_{\text{CIT}} &+& 0.001 (J_{\text{CIT}} - K_{\text{CIT}}) &-& 0.019 \\ J_{2\text{MASS}} &= K_{2\text{MASS}} &+& 1.068 (J_{\text{CIT}} - K_{\text{CIT}}) &-& 0.020 \\ H_{2\text{MASS}} &= K_{2\text{MASS}} &+& 1.000 (H_{\text{CIT}} - K_{\text{CIT}}) &+& 0.034 \end{cases}$$

and from [Koen et al. \(2007\)](#):

$$\begin{cases} J_{2\text{MASS}} &= J_{\text{SAAO}} &-& 0.047 (J_{\text{SAAO}} - K_{\text{SAAO}}) &-& 0.028 \\ H_{2\text{MASS}} &= H_{\text{SAAO}} &+& 0.014 \\ K_{2\text{MASS}} &= K_{\text{SAAO}} &+& 0.177 (H_{\text{SAAO}} - K_{\text{SAAO}}) &-& 0.082 (J_{\text{SAAO}} - H_{\text{SAAO}})^2 &-& 0.015 \end{cases}$$

In the optical  $V$  band, the compilation by [Groenewegen \(2018\)](#) mostly takes values from [Mel'nik et al. \(2015\)](#) and from [Berdnikov et al. \(2000\)](#) in the Johnson system, with an uncertainty of 0.008 mag. The apparent magnitudes adopted for the sample of Cepheids with companions and Cepheids in clusters are listed in Table 2.9.

In this chapter, I calibrate the Cepheid P-L relation in the optical  $V$  band and in NIR bands  $J$ ,  $H$ ,  $K$ . Additionally, Wesenheit indices can be constructed by a linear combination of apparent magnitudes as defined in [Madore \(1982\)](#):  $W(\lambda_1, \lambda_2, \lambda_3) = m_{\lambda_1} - R(m_{\lambda_2} - m_{\lambda_3})$  where  $R$  is the ratio of total-to-selective absorption:  $R = R_{\lambda_1}/(R_{\lambda_2} - R_{\lambda_3})$ . Assuming the reddening law from [Fitzpatrick \(1999\)](#) with:

$$\begin{cases} R_V &= 3.3 \\ R_J &= 0.86 \\ R_H &= 0.55 \\ R_K &= 0.37 \end{cases}$$

gives:

$$W(J, K) = K - 0.755 (J - K) \quad (2.17)$$

$$W(V, K) = K - 0.126 (V - K) \quad (2.18)$$

A Wesenheit index based on the HST passbands  $F160W$ ,  $F555W$  and  $F814W$  and noted  $W_H$  is defined in [Riess et al. \(2018a\)](#) by:

$$W_H = F160W - R(F555W - F814W) \quad (2.19)$$

with  $R = 0.386$ . Photometry in these HST bands is not available for this sample of Cepheids, however it can be reconstructed from ground-based photometry by using the following transformations:

$$\begin{cases} F160W &= H &+& 0.25 (J - H) &-& 0.030 \\ F555W &= V &+& 0.28 (J - H) &+& 0.020 \\ F814W &= V &-& 0.47 (V - H) &-& 0.035 \end{cases}$$

They were obtained by comparing the [Riess et al. \(2018a\)](#) sample with the [Groenewegen \(2018\)](#) catalogue and have a dispersion of 0.06 mag. These transformations from ground-based magnitudes to the HST system require the addition of a small correction to  $F160W$  magnitudes due to the count-rate non-linearity (CRNL) effect ([Riess et al. 2018b](#)). This correction is applied to account for the high and low fluxes received by the WFC3 detector for Milky Way Cepheids and extragalactic Cepheids respectively, it was estimated to be of 0.026 mag by [Riess et al. \(2019b\)](#).

Cepheids are located in the instability strip, which has a finite width: even with photometry of excellent precision, a Cepheid's magnitude cannot exactly predict its parallax because its position on the instability strip is unknown ([Riess et al. 2019a](#)). This effect introduces additional scatter in



the P-L relation and must be included as a systematic uncertainty in apparent magnitudes (it is not included in the photometric uncertainties in Table 2.9). For example, [Riess et al. \(2019a\)](#) describe the calculation in the Wesenheit  $W_H$  band: the width of the instability strip is obtained by taking the scatter of the P-L relation, which is 0.075 mag from their Table 3, and by subtracting quadratically the errors on photometric measurements (e.g. photometric inhomogeneities, phase corrections) which are of 0.030 mag. They obtain an intrinsic width of 0.069 mag for the instability strip. Similarly, I used the study by [Macri et al. \(2006\)](#) for the  $V$  band: in their Figure 13, the scatter of the P-L relation is 0.23 mag and in their Table 8, the errors on the photometry are 0.05 mag (systematics) and 0.03 mag (random errors), which gives a width of 0.22 mag for the instability strip in  $V$ . Finally, in  $J$ ,  $H$  and  $K$  bands, [Persson et al. \(2004\)](#) obtained a dispersion of 0.14 mag, 0.12 mag and 0.11 mag respectively and measurement errors of 0.083 mag from their Table 6, which gives a width of 0.11 mag, 0.09 mag and 0.07 mag for the NIR instability strip. This correction is equivalent to including a color term in the P-L relation. It is taken into account in many studies, for example [Groenewegen \(2018\)](#) corrects for the width of the instability strip by increasing the error on distance moduli  $M - m$ , which is equivalent to the approach adopted here.

Various references are used and data are often given in different systems. To account for this heterogeneity in the apparent magnitudes adopted in this study, a systematic uncertainty (also called the photometric zero-point) was included quadratically to the photometric errors. In the NIR, most data are taken from the four following catalogs: [Monson & Pierce \(2011\)](#), [Barnes et al. \(1997\)](#), [Welch et al. \(1984\)](#), and [Laney & Stobie \(1992\)](#). [Monson & Pierce \(2011\)](#) compared the apparent magnitudes from these four studies and found that they are in very good agreement, with residuals of 0.013, 0.010, and 0.002 mag in  $J$ ,  $H$ , and  $K$ , respectively. These values are adopted as photometric zero-point in the NIR. In the  $V$  band, apparent magnitudes are almost all from [Mel'nik et al. \(2015\)](#), who compiled data from the [Berdnikov et al. \(2000\)](#) database. The systematic uncertainties related to the photometric systems used in  $V$  can be neglected.

### 2.3.4 Extinction

Before adopting apparent mean magnitudes for calibrating the Leavitt law, they must be corrected by the extinction  $A_\lambda = R_\lambda E(B - V)$ . The reddening values  $E(B - V)$  are taken from the following references, by order of preference: [Anderson et al. \(2013\)](#), [Kovtyukh et al. \(2008\)](#), [Laney & Caldwell \(2007\)](#), [Sziládi et al. \(2007\)](#), [Acharova et al. \(2012\)](#) and [Fernie et al. \(1995\)](#), they are listed in Table 2.9. The extinction values are very inhomogeneous due to the large number of references used, but there is so far no catalog that would provide the reddening for each Cepheid of this sample. The Cepheids which have a companion or which are found in open clusters are not necessarily the most studied and the most observed ones, therefore some of them often lack data. The database assembled by [Fernie et al. \(1995\)](#) is, to date, the most complete catalog of Cepheid reddenings and is still widely used today ([Anderson et al. 2016a](#); [Gaia Collaboration et al. 2017](#); [Groenewegen 2018](#)).

Additionally, 3D maps published recently by [Lallement et al. \(2018\)](#) provide complementary estimates for MW Cepheid extinction. However they are limited to a nearby region up to  $\sim 2$  kpc, while many Cepheids are located beyond this distance. At distances larger than 1.5 kpc, the uncertainties on the reddening values are generally larger than 0.1 mag, which is limiting for the purpose of this work. For example, the three Cepheids with the largest reddening values in Table 2.9 are TW Nor, V367 Sct and V438 Cyg with reddening values of  $1.240 \pm 0.030$  mag,  $1.273 \pm 0.050$  mag and  $1.300 \pm 0.050$  mag, from [Anderson et al. \(2013\)](#), [Sziládi et al. \(2007\)](#) and [Fernie et al. \(1995\)](#) respectively. For TW Nor, located at  $\sim 2.5$  kpc, the reddening is not defined in the [Lallement et al. \(2018\)](#) 3D map beyond 2.2 kpc and the uncertainties exceed 0.25 mag after 1.6 kpc. For V367 Sct, [Lallement](#)

Table 2.9: Photometry in optical (Johnson system) and NIR (2MASS system) for the samples of Cepheids with companions and Open Cluster Cepheids. The references are: (M15): [Mel'nik et al. \(2015\)](#), (B00): [Berdnikov et al. \(2000\)](#), (M11): [Monson & Pierce \(2011\)](#), (LPC): [Laney \(priv. comm.\)](#), (G14): [Genovali et al. \(2014\)](#), (B97): [Barnes et al. \(1997\)](#), (W84): [Welch et al. \(1984\)](#), (L92): [Laney & Stobie \(1992\)](#), (2M): 2MASS ([Cutri et al. 2003](#)), (F95): [Fernie et al. \(1995\)](#), (A12): [Acharova et al. \(2012\)](#), (K08): [Kovtyukh et al. \(2008\)](#), (A13): [Anderson et al. \(2013\)](#), (LC7): [Laney & Caldwell \(2007\)](#), (Sz7): [Sziládi et al. \(2007\)](#).

Cepheid	$V$ (mag)	$\text{err}_V$ (mag)	ref	$J$ (mag)	$H$ (mag)	$K$ (mag)	$\text{err}_{\text{NIR}}$ (mag)	ref	$E(B - V)$ (mag)	err (mag)	ref
Cepheids with companions ( <a href="#">Breuval et al. 2020</a> )											
TV CMa	10.590	0.008	M15	8.022	7.582	7.364	0.008	M11	0.611	0.031	F95
ER Car	6.820	0.008	M15	5.310	5.034	4.896	0.008	LPC	0.096	0.050	A12
DF Cas	10.880	0.008	M15	8.488	8.036	7.879	0.025	G14	0.570	0.050	A12
V0659 Cen	6.620	0.008	M15	5.177	4.907	4.651	0.025	G14	0.128	0.050	A12
Delta Cep	3.950	0.008	M15	2.683	2.396	2.294	0.010	B97	0.045	0.018	K08
AX Cir	5.880	0.008	M15	4.299	3.879	3.780	0.025	G14	0.146	0.050	A12
BP Cir	7.550	0.008	M15	5.870	5.626	5.483	0.008	LPC	0.224	0.050	A12
R Cru	6.760	0.008	M15	5.211	4.945	4.808	0.008	LPC	0.183	0.050	A12
X Cru <sup>(**)</sup>	8.400	0.008	M15	6.521	6.125	6.001	0.010	W84	0.272	0.050	A12
VW Cru	9.600	0.008	M15	6.805	6.261	6.051	0.025	G14	0.643	0.050	A12
V0532 Cyg	9.090	0.008	M15	6.863	6.393	6.250	0.050	2M	0.568	0.050	K08
V1046 Cyg	12.350	0.008	M15	8.978	8.257	8.012	0.025	G14	1.143	0.050	F95
CV Mon <sup>(*)</sup>	10.310	0.008	M15	7.314	6.781	6.529	0.008	M11	0.680	0.050	A13
RS Nor	10.000	0.008	M15	7.227	6.802	6.599	0.050	2M	0.614	0.038	F95
SY Nor	9.500	0.008	M15	6.574	6.105	5.865	0.008	LPC	0.756	0.050	A12
QZ Nor <sup>(*)</sup>	8.870	0.008	M15	7.085	6.748	6.614	0.008	L92	0.307	0.021	F95
AW Per	7.480	0.008	M15	5.213	4.832	4.657	0.008	M11	0.515	0.015	K08
RS Pup	7.010	0.008	M15	4.365	3.828	3.619	0.008	L92	0.515	0.050	K08
U Sgr <sup>(*)</sup>	6.690	0.008	M15	4.506	4.100	3.912	0.008	M11	0.390	0.020	A13
V0350 Sgr	7.470	0.008	M15	5.625	5.245	5.121	0.010	W84	0.280	0.050	K08
V0950 Sco	7.310	0.008	M15	5.681	5.439	5.295	0.008	LPC	0.254	0.050	A12
CM Sct <sup>(**)</sup>	11.100	0.008	M15	8.300	7.818	7.558	0.025	G14	0.711	0.030	LC7
EV Sct <sup>(*)</sup>	10.130	0.008	M15	7.608	7.184	7.018	0.008	L92	0.737	0.050	K08
SX Vel	8.290	0.008	M15	6.500	6.133	5.991	0.008	L92	0.272	0.050	K08
CS Vel <sup>(*)</sup>	11.700	0.008	M15	8.771	8.246	8.011	0.008	L92	0.737	0.050	A12
DK Vel	10.690	0.008	M15	8.820	8.496	8.386	0.025	G14	0.287	0.050	A12
Cepheids in Open Clusters ( <a href="#">Breuval et al. 2020</a> )											
DL Cas	8.970	0.008	M15	6.550	6.101	5.892	0.008	M11	0.460	0.020	A13
S Nor	6.420	0.008	M15	4.674	4.288	4.149	0.008	L92	0.120	0.050	A13
V Cen	6.820	0.008	M15	5.019	4.642	4.498	0.008	L92	0.250	0.050	A13
V340 Nor	8.370	0.008	B00	6.211	5.745	5.573	0.008	L92	0.320	0.020	A13
CF Cas	11.140	0.008	M15	8.590	8.126	7.900	0.008	M11	0.480	0.030	A13
TW Nor	11.670	0.008	M15	7.442	6.712	6.375	0.008	L92	1.240	0.030	A13
V367 Sct	11.610	0.008	M15	7.605	6.955	6.651	0.008	L92	1.273	0.050	Sz7
CG Cas	11.380	0.008	M15	8.903	8.299	8.109	0.025	G14	0.690	0.010	A13
RS Ori	8.410	0.008	M15	6.398	6.020	5.860	0.008	M11	0.410	0.050	K08
Cepheids in Open Clusters ( <a href="#">Zhou &amp; Chen 2021</a> )											
WX Pup	9.060	0.008	M15	7.032	6.710	6.539	0.050	2M	0.303	0.030	LC7
X Vul	8.850	0.008	M15	5.912	5.424	5.194	0.008	M11	0.798	0.022	K08
SV Vul	7.230	0.008	M15	4.547	4.063	3.868	0.008	M11	0.510	0.020	K08
V438 Cyg	10.950	0.008	M15	6.780	6.074	5.723	0.008	M11	1.300	0.050	F95

(\*) = also in the sample of Open Cluster Cepheids ([B20](#)).

(\*\*) = also in the sample of Open Cluster Cepheids ([Zhou & Chen 2021](#)).

et al. (2018) find  $E(B - V) = 1.384 \pm 0.15$  which is in agreement with the estimate by Sziládi et al. (2007) but three times less precise. Finally, for the Cepheid V438 Cyg, the 3D map gives a reddening of  $0.713 \pm 0.09$  mag which is twice smaller than the value from Fernie et al. (1995) but also less precise.

### 2.3.5 Pulsation modes

Knowing the pulsation mode of Cepheids is essential for the calibration of the Leavitt law. First-overtone (FO) Cepheids belong to a sequence on the P-L diagram distinct from that of fundamental-mode Cepheids, and could contaminate the calibration by introducing unwanted dispersion if they are misidentified. FO Cepheids generally have short periods (from 2 to 5 days) and have symmetrical and sinusoidal light curves.

Several catalogs were compared to determine the pulsation mode of the Cepheids of this sample: Berdnikov et al. (2000), the Variable Star index catalogue (VSX, Watson et al. 2006), Klagyivik & Szabados (2009), Mel'nik et al. (2015), Groenewegen (2018), Luck (2018) and the reclassification of the *Gaia* DR2 by Ripepi et al. (2019). Only a few FO mode pulsators are found in this sample of Cepheids: V0532 Cyg, QZ Nor, V0950 Sco and EV Sct are confirmed FO mode Cepheids by most of the references cited above. Other stars have an unclear pulsation mode:

- V0659 Cen is identified as a fundamental pulsator by Berdnikov et al. (2000) and Luck (2018), while Ripepi et al. (2019), Groenewegen (2018), Klagyivik & Szabados (2009) and the VSX catalog classify it as a FO Cepheid.
- V0367 Sct is labelled as a double-mode Cepheid in Groenewegen (2018) and in the VSX catalog, but Anderson et al. (2013) consider it as a fundamental-mode.
- BP Cir is a FO mode Cepheid according to Klagyivik & Szabados (2009), VSX, Groenewegen (2018) and Ripepi et al. (2019) but it is classified as fundamental mode by Luck (2018).
- DK Vel has a very uncertain pulsation mode: in Berdnikov et al. (2000), Mel'nik et al. (2015), Luck (2018) and Groenewegen (2018), it is listed as fundamental mode but VSX and Ripepi et al. (2019) consider it as a FO mode Cepheid.

These particular cases must be investigated further and can be possibly excluded based on their position in the P-L relation.

In many studies, FO Cepheids are considered as fundamental-mode ones after applying a transformation relation to their period. Alcock et al. (1995) used double-mode Cepheids (or "beat" Cepheids) in the LMC and derived that the overtone period  $P_1$  of a FO Cepheid can be converted into a "fundamentalized" period  $P_0$  by the relation:

$$P_1/P_0 = 0.720 - 0.027 \log P_0 \quad (2.20)$$

Feast & Catchpole (1997) simplified this equation into:

$$P_1/P_0 = 0.716 - 0.027 \log P_1 \quad (2.21)$$

with a dispersion of order 0.002 estimated from the Alcock et al. (1995) data. Similarly, from a set of double-mode MW Cepheids, Kovtyukh et al. (2016) established a relation between the period ratio  $P_1/P_0$  and the metallicity  $[\text{Fe}/\text{H}]$ :

$$P_1/P_0 = -0.0239_{\pm 0.0031} \log P_0 - 0.0404_{\pm 0.0035} [\text{Fe}/\text{H}] + 0.7187_{\pm 0.0017} \quad (2.22)$$

At solar metallicity, this equation can be approximated to:

$$P_0 = 1.4457P_1 - 0.0744 \quad (2.23)$$

Using this formula, I obtained the fundamentalized periods ( $P_0$ ) listed in Table 2.10 for the 4 confirmed FO Cepheids of the sample. Transforming the period of FO Cepheids into a fundamentalized period is not always recommended, although it is done in many studies, because the physics behind the pulsation of first-overtone mode Cepheids may not be exactly identical to that of fundamental Cepheids. The impact of these few stars on the dispersion of the P-L relation and on the Hubble constant is discussed in next sections.

Table 2.10: Period transformation from  $P_1$  to  $P_0$  using Eq. 2.23 for confirmed and suspected first-overtone Cepheids.

Cepheid	$P_1$ (days)	$P_0$ (days)
Confirmed FO Cepheids		
EV Sct	3.0910	4.3943
V0532 Cyg	3.2836	4.6727
V0950 Sco	3.3801	4.8122
QZ Nor	3.7860	5.3990
Possible FO Cepheids		
BP Cir	2.3981	3.3925
DK Vel	2.4820	3.5138
V0659 Cen	5.6231	8.0549
V0367 Sct	6.2931	9.0235

### 2.3.6 Method and results

Calibrating the Cepheid P-L relation consists in deriving a relation between absolute magnitudes ( $M$ ) of Cepheids for which the distance is known and the logarithm of their period ( $P$ ). Absolute magnitudes can be obtained by the following relation:

$$M_\lambda = m_\lambda - 5 \log d - 10 \quad (2.24)$$

where  $d$  is the distance in kpc obtained by inverting the parallax  $\varpi$  (in mas), and apparent magnitudes  $m_\lambda$  are corrected for the reddening. However, it can be unsafe to invert parallaxes to obtain distances, especially when parallax errors are large. Additionally, samples which are truncated or selected on the basis of magnitude, parallax value or parallax error, are subject to the LKH bias (Lutz & Kelker 1973; Hanson 1979) raised in Sect. 2.1.1, which causes observed parallaxes to be overestimated. A solution to avoid this bias is to remain in the space of parallaxes, as opposed to that of distances, and to substitute the absolute magnitudes  $M$  by a proxy that is linearly dependent on the parallax. The Astrometric Based Luminosity (ABL) approach was introduced by Feast & Catchpole (1997) and Arenou & Luri (1999). I adopted the ABL function, defined as:

$$ABL = 10^{0.2M_\lambda} = \varpi 10^{0.2(m_\lambda - 10)} \quad (2.25)$$

The calibration of the P-L relation of the form  $M = a \log P + b$  is equivalent to the determination of the coefficients  $a$  and  $b$  in:

$$ABL = 10^{0.2[a(\log P - \log P_0) + b]} \quad (2.26)$$

The P-L relation can be parametrized by an additional coefficient  $\log P_0$ , which is the median value of  $\log P$  for the sample, with  $M = a(\log P - \log P_0) + b$ . For the present sample of Milky Way Cepheids,  $\log P_0 \sim 0.8$ . This formulation of the P-L relation is used to minimize correlations between the coefficients  $a$  and  $b$ .

The parallaxes listed in Table 2.4 for Cepheid companions and Table 2.5 and 2.7 for Cepheids in open clusters are assembled with the apparent mean magnitudes and the reddenings provided in Table 2.9 in order to derive the ABL function for each Cepheid. Periods are taken from the VSX catalog (Watson et al. 2006) and magnitudes are corrected for extinction using the Fitzpatrick (1999) reddening law (see Sect. 2.3.3). Equation 2.26 is fitted using the `curve_fit` function of the Python Scipy library. In order to derive the  $a$  and  $b$  coefficients and to obtain a robust estimate of their uncertainties, I applied a Monte Carlo procedure with 100,000 iterations. The statistical uncertainties are derived from the 16<sup>th</sup> and 84<sup>th</sup> percentiles of the slope and intercept distributions.

Figure 2.21 shows the P-L relation obtained using *Gaia* EDR3 parallaxes of Cepheid companions after applying the zero-point correction by Lindegren et al. (2021a). The  $K_S$  band is represented because it is the less sensitive to reddening and the width of the instability strip is expected to be narrower in this band. First-overtone Cepheids converted into fundamental pulsators are represented

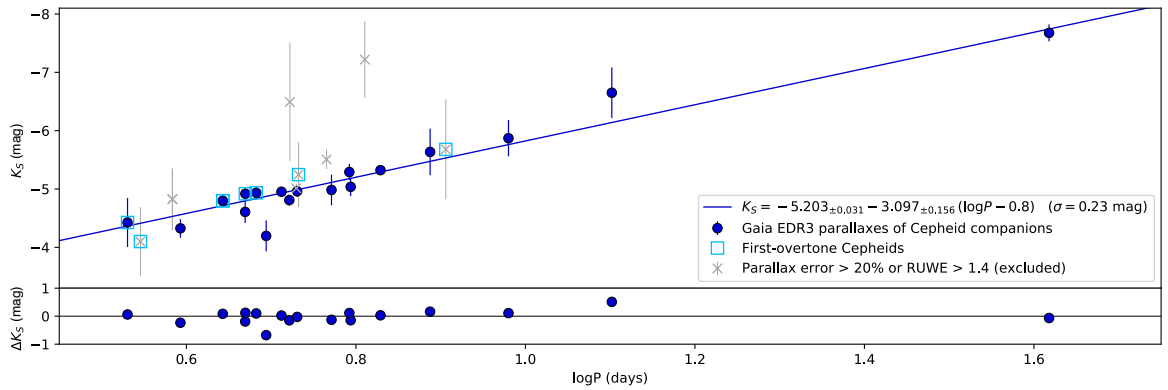


Figure 2.21: P-L relation calibrated in the  $K_S$  band with *Gaia* EDR3 parallaxes of Cepheid companions.

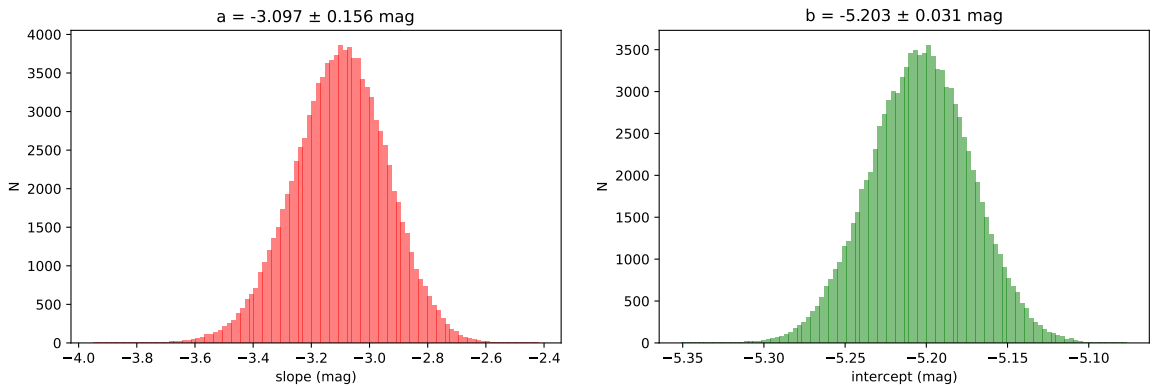


Figure 2.22: Histograms of the slopes and intercepts obtained by the Monte Carlo algorithm applied for the fit of the  $K_S$  band P-L relation represented in Fig. 2.21, based on *Gaia* EDR3 companion parallaxes.

by blue squares (after the transformation of their period) and the stars excluded due to a RUWE parameter larger than 1.4 or a parallax uncertainty larger than 20% are indicated by grey markers. Several points have a large error bar due to an unprecise parallax (generally faint companions) and were excluded. Among the remaining stars, the dispersion is 0.23 mag. The histograms of the slope and intercept values derived by the Monte Carlo algorithm are represented in Fig. 2.22. The P-L relation obtained in the  $K_S$  band with companion parallaxes is:

$$K_S = -3.097_{\pm 0.156} (\log P - 0.8) - 5.203_{\pm 0.031} \quad (2.27)$$

The most distant point from the fit, around  $\log P \sim 0.7$  and  $K \sim -4$  mag, is V1046 Cyg: the companion of this Cepheid has a parallax precise to 12% and a RUWE of 1.3, it is in the best range of magnitudes (not affected by saturation and not too faint) with  $G = 15.8$  mag and the Cepheid is pulsating in the fundamental mode. The  $K_S$ -band absolute magnitude of this point agrees within  $2.5\sigma$  with the linear fit of the P-L relation. The disagreement of this star with the P-L fit is similar in the  $J$ ,  $H$ , and  $K_S$  bands but is not present in  $V$ , which suggests that the issue is due to the NIR photometry rather than to the parallax. For V1046 Cyg, NIR mean magnitudes are taken from [Genovali et al. \(2014\)](#) and are computed by fitting template light curves to 2MASS single point photometry. This example highlights the need for complete light curves in the calibration of the Leavitt law and the issues resulting from the use of single-point photometry.

The four stars confirmed as first-overtone Cepheids in Table 2.10 agree well with the fundamental sequence after their period transformation, although they are almost all slightly brighter than the magnitude predicted by the fit: this suggests that the transformed period  $P_0$  may be slightly underestimated. The FO Cepheid QZ Nor ( $\log P \sim 0.75$ ) was discarded because the parallax of its companion is only precise to 25%.

In Sect. 2.3.5, three Cepheids of this sample were suspected to be possibly pulsating in the first-overtone mode: BP Cir, DK Vel and V0659 Cen. According to their position in the P-L relation, BP Cir (the star marked with a blue square that has the shortest period,  $\log P \sim 0.5$ ) and V0659 Cen (the star marked with a blue square that has the longest period,  $\log P \sim 0.9$ ) indeed appear as FO Cepheids. They both are placed very close to the fitted P-L relation after the conversion of their period. Further investigations based on Fourier modes and light curve analysis are still required to confirm this classification. Additionally, V0659 Cen is not considered in the fit because of the large error bar of its companion parallax. As for DK Vel, transforming its period into a fundamentalized one results in placing the point slightly below the fitted P-L relation (i.e. fainter than the predicted magnitude): The present work does not allow to confirm the pulsation mode of DK Vel. Due to its large parallax error, the companion of DK Vel is discarded from the fit.

Excluding FO Cepheids does not allow us to reduce the scatter of the P-L relation, on the contrary it raises the dispersion to 0.25 mag, which shows that in this case, they are not responsible for additional contamination in the fundamental P-L relation. After excluding FO mode Cepheids, the coefficients of the P-L relation still agree within the error bars, however they change by  $\sim 0.1$  mag for the slope and by  $\sim 0.03$  mag for the intercept. The significant change in slope indicates that these stars must be considered carefully, but can also be explained by the limited number of stars in this sample.

Finally, the Cepheid with the longest period, RS Pup, has a small error bar and constrains the slope of the P-L relation. In order to analyze the influence of this star on the fitted relation, the P-L relation is determined after excluding this Cepheid: the slope obtained in this test is consistent with the slope found in Eq. 2.27 within the error bars but is significantly steeper. Additionally, the



uncertainties on the slope and zero-point without RS Pup are twice larger than when it is included. This suggests that adding more long-period Cepheids to the sample would consequently improve the precision of the P-L coefficients. The limited number of long-period Cepheids in the Milky Way is a critical issue in the calibration of the Leavitt law and is one of the main limitations of this sample of Cepheid companions.

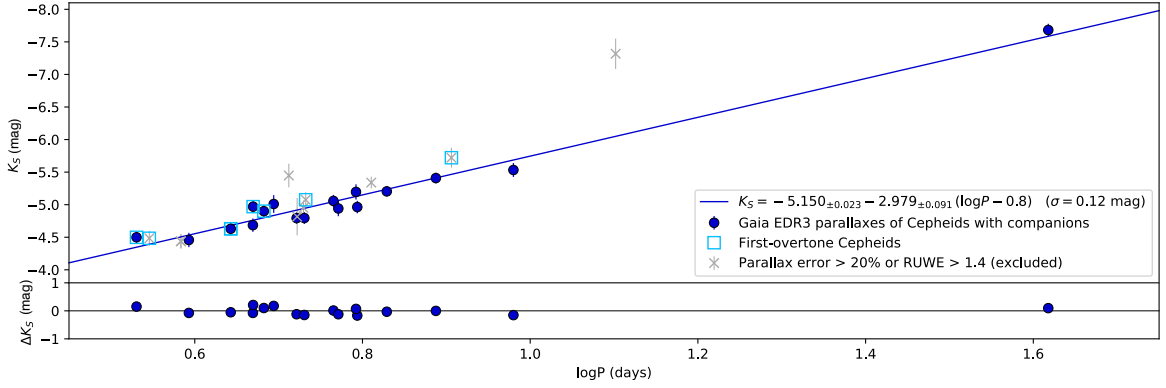


Figure 2.23: P-L relation calibrated in the  $K_S$  band for the sample of Cepheids with companions, adopting *Gaia* EDR3 parallaxes of Cepheids. First-overtone Cepheids are converted into the fundamental mode.

Fig. 2.23 represents the calibration of the P-L relation using *Gaia* EDR3 Cepheid parallaxes directly in place of companion parallaxes. A few outliers with a large RUWE parameter or a large parallax uncertainty are still present but they are ignored. The dispersion of the points around the linear fit is 0.12 mag, half of the dispersion obtained with companion parallaxes. First-overtone Cepheids are still placed on the fundamental relation, and the P-L coefficients are more precise than with companion parallaxes:

$$K_S = -2.979_{\pm 0.091} (\log P - 0.8) - 5.150_{\pm 0.023} \quad (2.28)$$

The slope and intercept change by 0.118 mag/dex and 0.053 mag respectively between Eq. 2.27 and 2.28, which is consistent within the error bars and shows that the PL calibration obtained with companions is consistent with that derived directly using Cepheid parallaxes. The long-period Cepheid RS Pup still constrains the slope significantly: removing this star from the sample yields a slope that differs by 0.4 mag/dex and is less steep.

This comparison shows that with *Gaia* EDR3 parallaxes, using companion parallaxes in place of Cepheids does not allow to improve the precision of the P-L calibration. This result also suggests that the color variation that affects Cepheids, also called the chromaticity issue, is not as limiting as in *Gaia* DR2 thanks to the more complete time coverage of *Gaia* observations. Additionally, the number of outliers among Cepheid parallaxes in Fig. 2.23 is reduced compared with *Gaia* DR2 and even Cepheids with a RUWE larger than 1.4 are located relatively close to the P-L fit. With *Gaia* EDR3 parallaxes, Cepheid companions are no longer competitive for improving the calibration of the P-L relation, though this method was particularly powerful at the time of *Gaia* DR2. It was used in B20 to obtain distances to more than 20 Cepheids without relying on their direct parallax.

Fig. 2.24 shows the  $K_S$  band P-L relation calibrated with mean *Gaia* EDR3 parallaxes of Cepheids residing in open clusters, and Fig. 2.25 gives the histograms of the slopes and intercepts derived for this sample by the Monte Carlo algorithm. The samples of OC Cepheids from B20 and Zhou & Chen (2021) were combined. Two first-overtone mode Cepheids were identified (EV Sct



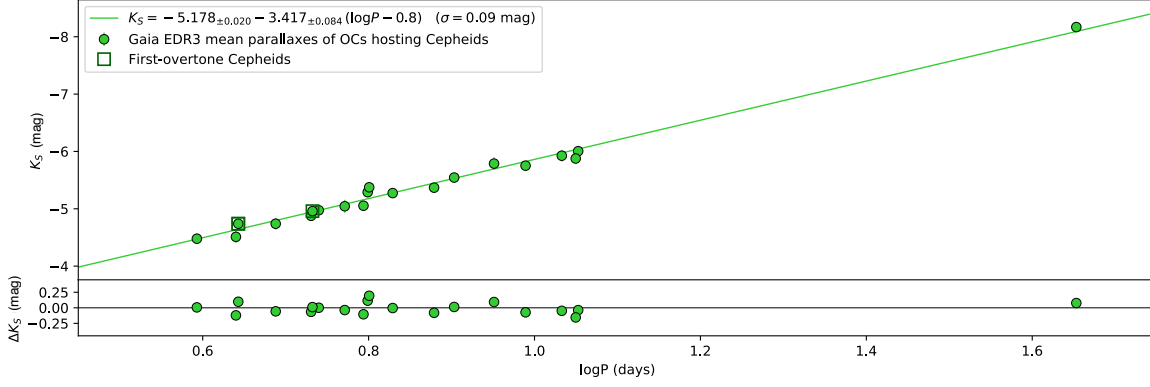


Figure 2.24: P-L relation in the  $K_S$  band calibrated with *Gaia* EDR3 mean parallaxes of OC Cepheids. First-overtone Cepheids are converted into the fundamental mode.

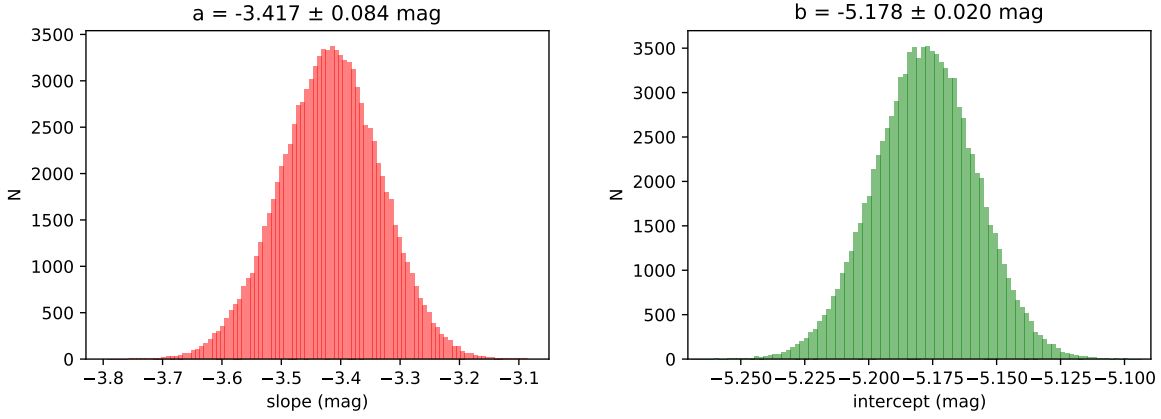


Figure 2.25: Histograms of the slopes and intercepts obtained by the Monte Carlo algorithm applied for the fit of the P-L relation in the  $K_S$  band represented in Fig. 2.24, based on *Gaia* EDR3 mean cluster parallaxes.

and QZ Nor) and are represented by green squares. Their periods were transformed using Eq. 2.23 and their positions are perfectly consistent with the fundamental sequence of the P-L relation. As discussed in Sect. 2.3.5, V367 Sct has an uncertain pulsation mode. According to its position in Fig. 2.24, it is consistent with a fundamental mode Cepheid. All clusters have a parallax more precise than 20% so all clusters are included. The scatter is remarkably low, 0.09 mag, which is very close to the intrinsic width of the instability strip. The P-L relation obtained in the  $K_S$  band is:

$$K_S = -3.417_{\pm 0.084} (\log P - 0.8) - 5.178_{\pm 0.020} \quad (2.29)$$

Similarly to the sample of Cepheid companions, only one cluster Cepheid has a period longer than  $\log P = 1.2$ , it is SV Vul. Excluding this star from the sample gives a very similar slope, consistent to  $1\sigma$  with Eq. 2.29. However, it remains necessary to enlarge the number of long-period Cepheids to improve the precision of the P-L coefficients.

The same calibration is performed using directly *Gaia* EDR3 parallaxes of Cepheids in place of open cluster mean parallaxes. It is represented in Fig. 2.26. In this case, the dispersion is slightly higher with  $\sigma = 0.13$  mag and the P-L coefficients are slightly less precise than in Eq. 2.29, with:

$$K_S = -3.588_{\pm 0.116} (\log P - 0.8) - 5.200_{\pm 0.024} \quad (2.30)$$

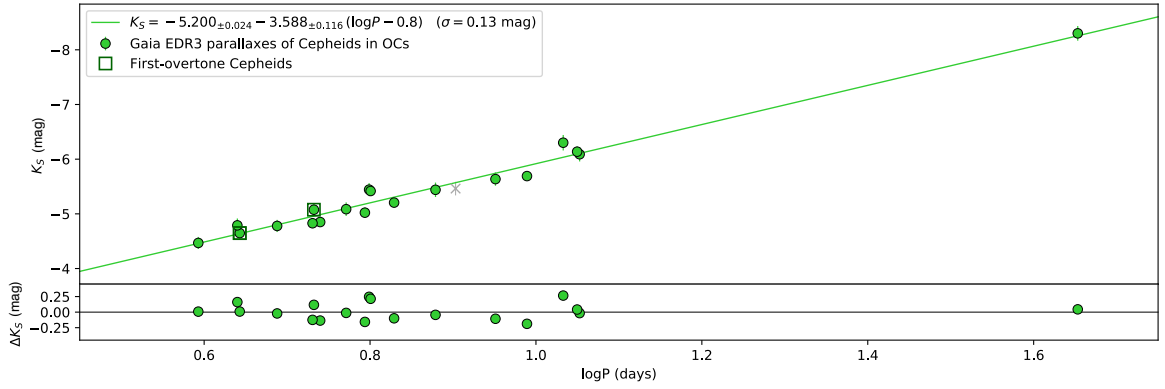


Figure 2.26: P-L relation in the  $K$  band calibrated with *Gaia* EDR3 parallaxes of Cepheids located in Open Clusters.

The intercepts obtained with mean OC parallaxes and with Cepheid parallaxes agree within the error bars with a difference of 0.022 mag, while the slopes differ by 0.171 mag/dex. The dispersion is lower and the slope and intercept are more precise when adopting mean cluster parallaxes rather than individual Cepheid parallaxes: this comparison shows that unlike the method of Cepheid companions described above, the approach of using Cepheids in OCs is very promising and allows to reach a higher level of precision in the calibration of the Leavitt law.

The P-L relations obtained with companion parallaxes (Eq. 2.27) and mean open cluster parallaxes (Eq. 2.29) are consistent to  $1.8\sigma$  and  $0.7\sigma$  in slopes and intercepts respectively. The two samples are combined in the P-L relation represented in Fig. 2.27. The linear fit performed on both samples combined gives:

$$K = -3.338_{\pm 0.071} (\log P - 0.8) - 5.191_{\pm 0.017} \quad (2.31)$$

with a dispersion of 0.17 mag. The fit is mostly dominated by the green points, which represent Cepheids in open clusters, because their precision is significantly better than that of companion parallaxes (blue points). In B20, I obtained a similar dispersion ( $\sigma = 0.14$  mag) using the equivalent of this sample with *Gaia* DR2. The combination of both samples returns a higher precision on the slope and intercept compared with taking each sample alone.

For comparison purposes, three other  $K_S$  band P-L calibrations from the literature are also represented in Fig. 2.27, in the 2MASS system. All equations are parametrized as  $M = a (\log P - 1) + b$  so that they can be directly compared. The dashed blue line is the Leavitt law from Breuval et al. (2020), derived from the same sample as in this study (Cepheid companions and OC Cepheids) but with *Gaia* DR2 parallaxes corrected by a zero-point of  $-0.046$  mas. The relation is:

$$K_S = -3.257_{\pm 0.163} (\log P - 1) - 5.844_{\pm 0.037} \quad (2.32)$$

while the equation derived in the present work with the same parametrization is given by:

$$K_S = -3.338_{\pm 0.071} (\log P - 1) - 5.859_{\pm 0.022} \quad (2.33)$$

The intercepts are in excellent agreement and the slopes are similar. The gain in precision enabled by *Gaia* EDR3 reduces the uncertainties on the P-L coefficients almost by half. The dashed orange line is the P-L relation obtained by Groenewegen (2018) from a large sample of Milky Way

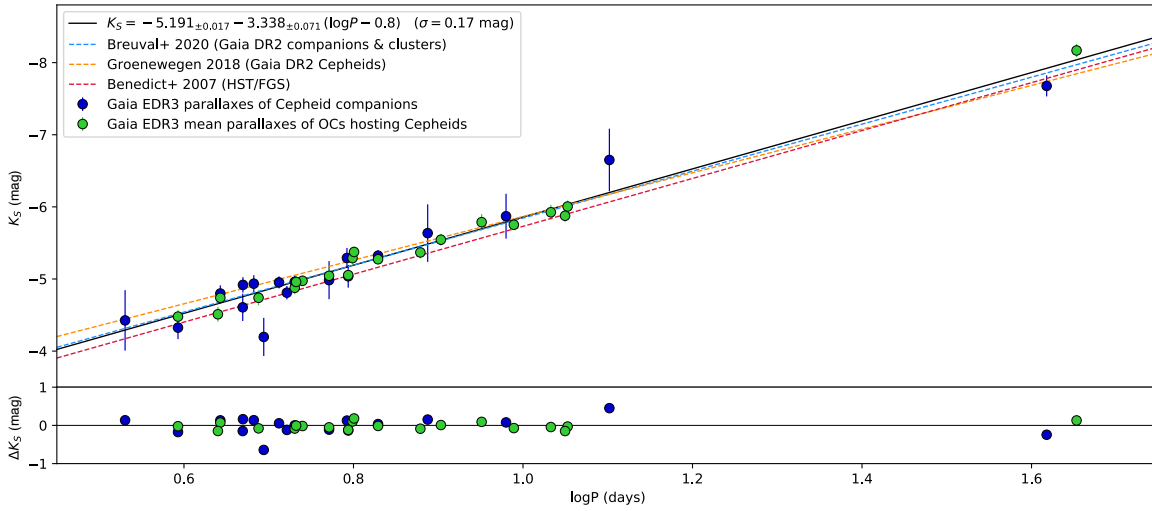


Figure 2.27: P-L relation in the  $K$  band calibrated with *Gaia* EDR3 parallaxes of Cepheid companions and mean parallaxes of Open Clusters hosting Cepheids.

Cepheids with *Gaia* DR2 parallaxes. For consistency with Eq. 2.32, the relation represented was obtained after applying a parallax zero-point of  $-0.046$  mas:

$$K_S = -3.028_{\pm 0.067} (\log P - 1) - 5.867_{\pm 0.087} \quad (2.34)$$

The slope obtained by [Groenewegen \(2018\)](#) differs by  $3\sigma$  from the present calibration. This discrepancy can be explained by the effect of chromaticity that impacts Cepheid parallaxes in *Gaia* DR2. However the zero-point at  $\log P = 1$  is consistent with my results based on *Gaia* EDR3 parallaxes. Finally, the P-L calibration by [Benedict et al. \(2007\)](#) is represented by the red dashed line. It was based on HST/FGS parallaxes of 10 nearby and bright Cepheids and gives:

$$K_S = -3.32_{\pm 0.12} (\log P - 1) - 5.73_{\pm 0.03} \quad (2.35)$$

This equation was obtained by transforming the relation provided by [Benedict et al. \(2007\)](#) from the CIT system into the 2MASS system, using the transformation from [Carpenter \(2001\)](#). It also includes a correction for the Lutz-Kelker bias, which is necessary for this sample because the 10 Cepheids were selected based on their short distance. The slope is in excellent agreement with my P-L calibration obtained with *Gaia* EDR3 but the intercept differs from it by 0.1 mag at the central period of  $\log P = 1$ . This difference in intercept is consistent with the comparison between HST/FGS and *Gaia* parallaxes, represented in Fig. 2.11 and 2.13, at the beginning of this chapter. On these two plots, HST/FGS parallaxes appear systematically larger than *Gaia* DR2 and *Gaia* EDR3 parallaxes, which results in fainter absolute magnitudes in the P-L plane. However, this comparison is limited by the extreme brightness of the Cepheids from the [Benedict et al. \(2007\)](#) sample, which have apparent magnitudes between  $G = 3$  mag and  $G = 6$  mag. Stars in this range of magnitudes are saturated in *Gaia*'s detectors and have therefore no reliable parallax.

The results of the various calibrations performed in this section are listed in Table 2.11. When both samples are fitted together, the dispersion is generally slightly lower in the case where Cepheid parallaxes are used directly. The uncertainties on the slopes and intercepts are of the same order. The most precise calibration is obtained in the  $W_{VK}$  band with companion and open cluster parallaxes combined, and the smaller dispersion ( $\sigma = 0.07$  mag) is obtained from the sample of open cluster Cepheid parallaxes in  $W_{VK}$ .

A possible break of the P-L relation around  $\log P \sim 1$  was raised in several studies (Sandage et al. 2004; Bhardwaj 2020, and references therein). It is suspected to be connected with the Hertzsprung progression (Hertzsprung 1924, 1926): it is characterized by a bump in the light curves of Cepheids which migrates in phase with increasing periods (Sandage et al. 2004; Kanbur et al. 2010) and can also be identified by a discontinuity in the amplitude Fourier coefficients at  $\log P = 1$ . Physically, it is interpreted as a resonance between the fundamental and the second overtone modes. This characteristic of the Leavitt law should be examined carefully. However, the present sample only includes two Cepheids with periods larger than  $\log P = 1.2$ , which is very limiting for this analysis. For this reason, I did not investigate this effect in this chapter.

Table 2.11: Coefficients of the Period-Luminosity relations of the form  $M = a(\log P - 0.8) + b$  for the samples of Cepheids with companions, Cepheids in Open Clusters and both samples combined. The left side gives the results obtained with indirect parallaxes (companions or OCs) and the right side gives the results obtained with Cepheid parallaxes. All parallaxes are from *Gaia* EDR3 and are corrected for the zero-point.

Band	$a$	$b$	$\sigma$	$a$	$b$	$\sigma$
	Companions			Cepheids		
$V$	$-2.625_{\pm 0.307}$	$-3.741_{\pm 0.072}$	0.30	$-2.354_{\pm 0.254}$	$-3.710_{\pm 0.066}$	0.29
$J$	$-2.951_{\pm 0.187}$	$-4.833_{\pm 0.041}$	0.27	$-2.806_{\pm 0.127}$	$-4.789_{\pm 0.033}$	0.15
$H$	$-3.058_{\pm 0.166}$	$-5.110_{\pm 0.036}$	0.23	$-2.951_{\pm 0.108}$	$-5.055_{\pm 0.027}$	0.13
$K_S$	$-3.097_{\pm 0.156}$	$-5.203_{\pm 0.031}$	0.23	$-2.979_{\pm 0.091}$	$-5.150_{\pm 0.023}$	0.12
$W_{VK}$	$-3.191_{\pm 0.133}$	$-5.409_{\pm 0.019}$	0.24	$-3.030_{\pm 0.058}$	$-5.341_{\pm 0.014}$	0.11
$W_{JK}$	$-3.245_{\pm 0.139}$	$-5.504_{\pm 0.019}$	0.21	$-3.109_{\pm 0.060}$	$-5.422_{\pm 0.014}$	0.11
$W_H$	$-3.148_{\pm 0.175}$	$-5.305_{\pm 0.035}$	0.25	$-3.034_{\pm 0.106}$	$-5.249_{\pm 0.027}$	0.12
	Open Clusters			Cepheids		
$V$	$-2.857_{\pm 0.210}$	$-3.702_{\pm 0.057}$	0.26	$-2.995_{\pm 0.239}$	$-3.775_{\pm 0.063}$	0.32
$J$	$-3.334_{\pm 0.116}$	$-4.795_{\pm 0.029}$	0.13	$-3.494_{\pm 0.145}$	$-4.829_{\pm 0.033}$	0.16
$H$	$-3.399_{\pm 0.098}$	$-5.079_{\pm 0.025}$	0.10	$-3.562_{\pm 0.129}$	$-5.109_{\pm 0.028}$	0.14
$K$	$-3.417_{\pm 0.084}$	$-5.178_{\pm 0.020}$	0.09	$-3.588_{\pm 0.116}$	$-5.200_{\pm 0.024}$	0.13
$W_{VK}$	$-3.422_{\pm 0.047}$	$-5.379_{\pm 0.008}$	0.08	$-3.652_{\pm 0.088}$	$-5.355_{\pm 0.015}$	0.13
$W_{JK}$	$-3.447_{\pm 0.049}$	$-5.477_{\pm 0.009}$	0.07	$-3.671_{\pm 0.087}$	$-5.459_{\pm 0.015}$	0.14
$W_H$	$-3.492_{\pm 0.100}$	$-5.262_{\pm 0.024}$	0.10	$-3.644_{\pm 0.130}$	$-5.287_{\pm 0.028}$	0.10
	Companions + Open Clusters			Cepheids		
$V$	$-2.776_{\pm 0.174}$	$-3.722_{\pm 0.046}$	0.28	$-2.779_{\pm 0.169}$	$-3.760_{\pm 0.046}$	0.32
$J$	$-3.219_{\pm 0.099}$	$-4.815_{\pm 0.023}$	0.21	$-3.181_{\pm 0.097}$	$-4.823_{\pm 0.023}$	0.18
$H$	$-3.304_{\pm 0.085}$	$-5.095_{\pm 0.019}$	0.17	$-3.268_{\pm 0.084}$	$-5.094_{\pm 0.020}$	0.16
$K$	$-3.338_{\pm 0.071}$	$-5.191_{\pm 0.017}$	0.17	$-3.272_{\pm 0.073}$	$-5.185_{\pm 0.017}$	0.15
$W_{VK}$	$-3.385_{\pm 0.044}$	$-5.387_{\pm 0.007}$	0.17	$-3.261_{\pm 0.050}$	$-5.356_{\pm 0.010}$	0.15
$W_{JK}$	$-3.413_{\pm 0.044}$	$-5.484_{\pm 0.008}$	0.15	$-3.324_{\pm 0.051}$	$-5.447_{\pm 0.010}$	0.15
$W_H$	$-3.390_{\pm 0.084}$	$-5.283_{\pm 0.020}$	0.18	$-3.341_{\pm 0.083}$	$-5.279_{\pm 0.019}$	0.14

## 2.4 Implications for the Hubble constant

As discussed in Chapter 1, the Cepheid P-L relation is the first rung of the extragalactic distance ladder: it is used to calibrate the luminosity of SN-Ia and to measure the current expansion rate of the Universe, called the Hubble constant and noted  $H_0$ . In this section, I evaluate the implication of my calibration of the Leavitt law, obtained with *Gaia* EDR3 parallaxes, on the value of the Hubble constant. For this purpose, I extract from the literature a Hubble constant that was derived with non-*Gaia* parallaxes, and replace them by the *Gaia* EDR3 parallaxes of my sample. The revised Hubble constant estimate is written as:

$$H_{0, \text{Gaia}} = \frac{\varpi_{\text{Gaia}}}{\varpi_{\text{predicted}}} H_{0, \text{init.}} \quad (2.36)$$

where  $\varpi_{\text{Gaia}}$  are the *Gaia* EDR3 parallaxes of the Cepheid companions and host open clusters used in this work and  $\varpi_{\text{predicted}}$  are the parallaxes predicted by the P-L relation adopted for the estimation of the Hubble constant  $H_{0, \text{init.}}$ , derived with non-*Gaia* parallaxes.

Riess et al. (2016) calculated the Hubble constant by combining several distance indicators, also called anchors, on different scales: Milky Way Cepheids, water masers in NGC 4258 and detached eclipsing binaries in the LMC and in M31. They derived a  $H_0$  value for each individual anchor and finally assembled them into a final value of  $73.24 \pm 1.74$  km/s/Mpc, associated with the global P-L relation in the Wesenheit  $W_H$  band, provided in Riess et al. (2018a):

$$M_H^W (\text{all anchors}) = -3.26 (\log P - 1) - 5.93 \quad (2.37)$$

In order to re-evaluate the Hubble constant from this work by adopting the recent *Gaia* EDR3 parallaxes, I only consider the contribution from the Milky Way anchor in Riess et al. (2016), which gives  $H_0 = 76.18 \pm 2.37$  km/s/Mpc. It was obtained using parallaxes of 15 Galactic Cepheids: 10 measured by HST/FGS (Benedict et al. 2002, 2007), three from *Hipparcos* (van Leeuwen 2007) and two Cepheids with HST/WFC3 spatial scanning parallaxes (Riess et al. 2014; Casertano et al. 2016). I adopt  $H_{0, \text{init.}} = 76.18 \pm 2.37$  km/s/Mpc. The P-L relation associated to the Hubble constant anchored only to the MW is obtained by adding an offset  $\Delta M_H^W$  to the intercept of Eq. 2.37, such that:

$$M_H^W (\text{MW Cepheids}) = -3.26 (\log P - 1) - 5.93 + \Delta M_H^W \quad (2.38)$$

Parallaxes, which vary as  $H_0$  (Eq. 2.36), are related to magnitudes by:  $\varpi \propto 10^{0.2M}$ . Therefore the offset can be derived by:

$$\frac{H_0 (\text{MW Cepheids})}{H_0 (\text{all anchors})} = 10^{0.2 \Delta M_H^W} \quad (2.39)$$

With  $H_0 (\text{MW Cepheids}) = 76.18 \pm 2.37$  km/s/Mpc and  $H_0 (\text{all anchors}) = 73.24 \pm 1.74$  km/s/Mpc, the offset is  $\Delta M_H^W = 0.085$  mag and the P-L relation associated to the MW anchor is:

$$M_H^W (\text{MW Cepheids}) = -3.26 (\log P - 1) - 5.85 \quad (2.40)$$

This relation is represented by the red line in Fig. 2.28, where it can be compared with my P-L calibration in the  $W_H$  band based on companion stars and open clusters. Although the slopes differ by 0.13 mag, it is in relatively good agreement with my calibration, especially at short periods ( $\log P < 1$ ).

For each Cepheid having either a companion star or a host open cluster, the parallax predicted by the MW Cepheid P-L relation (Eq. 2.40) is given by:

$$5 \log \varpi_{\text{predicted}} = M_H^W (\text{MW Cepheids}) - m_H^W + 10 \quad (2.41)$$

Apparent magnitudes in the Wesenheit band  $m_H^W$  are derived from the combination of ground-based magnitudes provided in Sect. 2.3.3 and are corrected for the count rate non-linearity effect, described

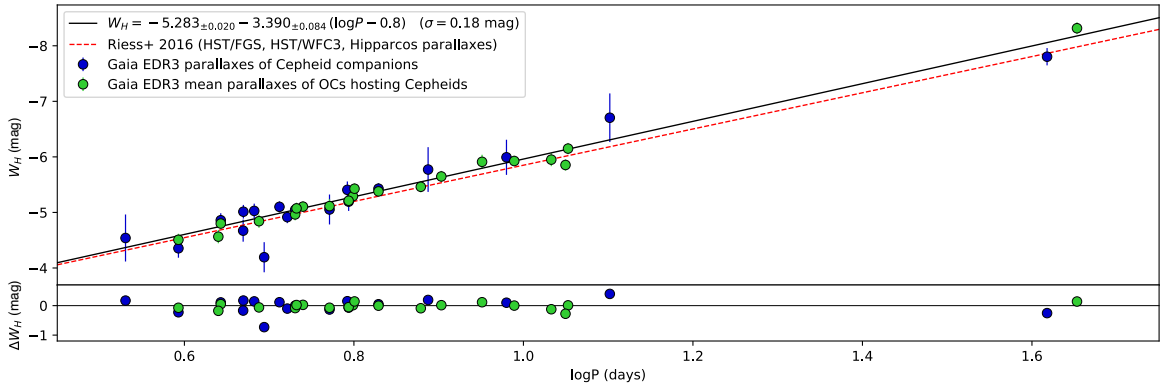


Figure 2.28: P-L relation in the  $W_H$  band calibrated with *Gaia* EDR3 parallaxes of Cepheid companions and mean parallaxes of open clusters hosting Cepheids. Comparison with the calibration by [Riess et al. \(2016\)](#), based on HST/FGS, HST/WFC3 and *Hipparcos* parallaxes (Eq. 2.40).

in the same section. To account for the width of the instability strip ( $\sigma = 0.07$  mag in the  $W_H$  band) and for the photometric transformations from ground to HST system ( $\sigma = 0.06$  mag), the apparent magnitude uncertainties are set to 0.09 mag. The choice of a reddening law in agreement with [Riess et al. \(2016\)](#) ensures the consistency of this comparison. The predicted parallaxes are represented as a function of *Gaia* EDR3 parallaxes in Fig. 2.29. Parallaxes predicted by Eq. 2.40, based on a non-*Gaia* calibration of the Leavitt law, are systematically larger than *Gaia* EDR3 counterparts. This shift is consistent with the small difference observed between the two P-L relations represented in Fig. 2.28.

For each Cepheid of the sample, the ratio  $\alpha = \varpi_{\text{Gaia}}/\varpi_{\text{predicted}}$  is computed and a Monte-Carlo algorithm is applied to the  $\alpha$  values in order to derive a final  $\alpha$  value averaged over the sample. The final error on the Hubble constant includes three terms:

$$\sigma^2 = \sigma_\alpha^2 + \sigma_{\text{photom.}}^2 + \sigma_{\text{R16}}^2 \quad (2.42)$$

where  $\sigma_\alpha$  is the standard deviation of the  $\alpha$  values obtained by the Monte Carlo procedure,  $\sigma_{\text{photom.}} = 1.5\%$  is the error on the transformations from ground-based magnitudes into the HST system and  $\sigma_{\text{R16}}$  is the uncertainty on the  $H_0$  estimate from [Riess et al. \(2016\)](#) (2.4%) after removing the subtotal error on all anchors (1.6%, see Table 6 in [Riess et al. 2019a](#)), which gives  $\sigma_{\text{R16}} = 1.8\%$ .

As mentioned above, considering first-overtone mode Cepheids in the calibration of the P-L relation does not increase its dispersion and does not raise the uncertainties on the fitted coefficients. However, there are variations among the different transformation equations found in the literature to convert the period of FO mode Cepheids into a fundamentalized period, which suggests that performing this transformation is not always recommended. In this section, the results are given in two cases: for fundamental mode Cepheids only, and with FO Cepheids included.

The first line of Table 2.12 gives the Hubble constant derived from *Gaia* EDR3 parallaxes of Cepheids directly and the last line in bold font gives the value obtained by combining companion and cluster parallaxes (i.e. indirect parallaxes for Cepheids): using direct and indirect parallaxes returns two values of  $H_0$  that differ by 1.16 km/s/Mpc, which shows that the accuracy of Cepheid parallaxes may still be limited in *Gaia* EDR3. The use of indirect parallaxes such as from open clusters is still recommended with the present release in order to avoid biases due to Cepheid brightness and variability.

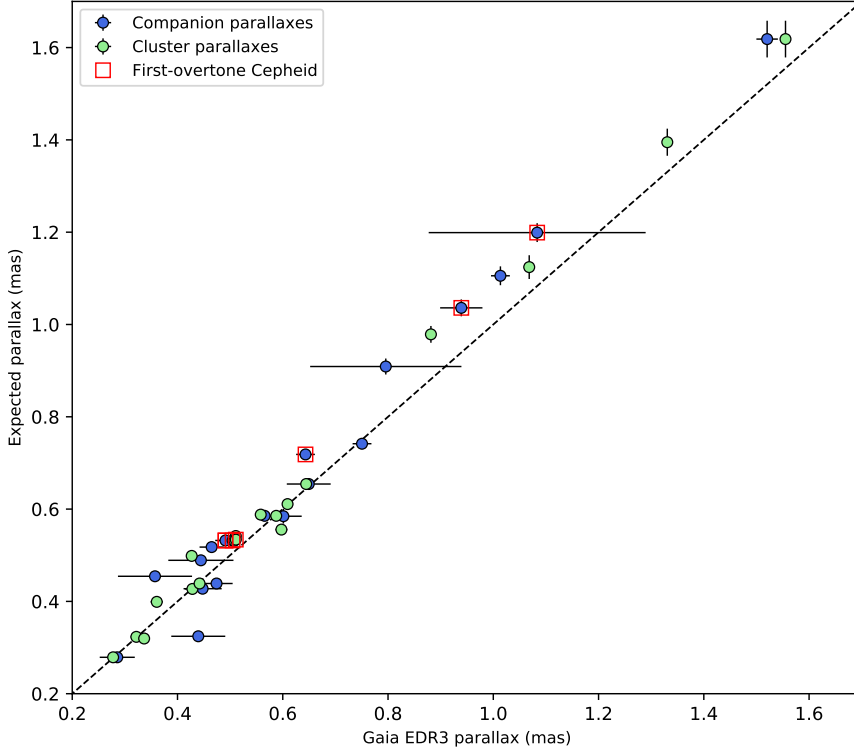


Figure 2.29: Comparison between *Gaia* EDR3 parallaxes of Cepheid companions or host open clusters and predicted parallaxes from Eq. 2.40.

The inclusion of the six FO mode Cepheids reduces  $H_0$  by 1.2 km/s/Mpc, which is significant. The Hubble constant values obtained with parallaxes of Cepheid companions and with host open clusters are in excellent agreement together when FO modes are excluded (left column). However when FO mode Cepheids are included, they differ by 1.4 km/s/Mpc (right column). Since they strongly impact  $H_0$ , it is safer to exclude these stars in order to avoid introducing additional contamination from non-fundamental mode Cepheids. They only represent six stars among a sample of 38 Cepheids and removing them does not limit the precision on the resulting Hubble constant.

Cepheids in open clusters are more numerous than Cepheids with resolved companions and their parallaxes are also significantly more precise, therefore the  $H_0$  value from cluster Cepheids is more precise than that from companions. The combination of both samples of companions and clusters gives a Hubble constant precise to 2.4%, which is similar to the result obtained by [Riess et al. \(2016\)](#). However, the uncertainties quoted in Table 2.12 are likely underestimated because they do not take into account the error due to the *Gaia* EDR3 parallax zero-point. It was greatly reduced compared with *Gaia* DR2 but should be evaluated precisely.

From an initial value of  $H_0 = 76.18 \pm 2.37$  km/s/Mpc anchored to Milky Way Cepheids with HST and *Hipparcos* parallaxes ([Riess et al. 2016](#)), a revised value of  $73.47 \pm 1.77$  km/s/Mpc is obtained by adopting 32 *Gaia* EDR3 parallaxes of fundamental mode Cepheid companions or host open clusters. This result still agrees to  $1\sigma$  with the initial value but is 2.7 km/s/Mpc lower. The new value is also in better agreement with the  $H_0$  estimates based on other anchors in [Riess et al. \(2016\)](#) (e.g. from  $72.04 \pm 2.67$  km/s/Mpc for LMC eclipsing binaries to  $74.50 \pm 3.27$  km/s/Mpc for M31 eclipsing binaries). This updated value is very close to the result obtained by applying the same



Table 2.12: Re-evaluation of the Hubble constant, starting from an initial value of  $H_0 = 76.18 \pm 2.37$  km/s/Mpc (Riess et al. 2016) and replacing the HST and *Hipparcos* parallaxes of Milky Way Cepheids by the *Gaia* EDR3 parallaxes of Cepheid companions and host open clusters.

	$H_0$ (km s <sup>-1</sup> Mpc <sup>-1</sup> )	$N_{\text{stars}}$	$H_0$ (km s <sup>-1</sup> Mpc <sup>-1</sup> )	$N_{\text{stars}}$
	FU modes only		FU + FO modes	
Cepheids	$74.63 \pm 1.81$	30	$73.43 \pm 1.77$	36
Companions	$73.13 \pm 1.94$	14	$72.04 \pm 1.86$	18
Clusters	$73.56 \pm 1.79$	18	$73.44 \pm 1.78$	20
Companions + Clusters	<b><math>73.47 \pm 1.77</math></b>	32	<b><math>73.10 \pm 1.76</math></b>	38

method with *Gaia* DR2 (Breuval et al. 2020), which was of  $72.76 \pm 1.86$  (stat. + syst.)  $\pm 1.89$  (ZP) km/s/Mpc. In the present case, the statistical and systematic uncertainties (excluding the parallax zero-point error) are of 1.77 km/s/Mpc, which is smaller than in B20 thanks to the use of *Gaia* EDR3 parallaxes instead of *Gaia* DR2 and to the addition of new cluster Cepheids. However, this time I did not attempt to estimate the systematics related to *Gaia* EDR3 parallax zero-point: it is definitively lower than 1.89 km/s/Mpc but should be derived more precisely, for example by comparing several methods. Finally, the present  $H_0$  value is consistent to  $1.5\sigma$  with the result by Freedman (2021) based on TRGB stars. The discrepancy between the revised value and the prediction from Planck Collaboration et al. (2020) assuming the  $\Lambda$ -CDM model is  $3.3\sigma$ . It is important to note that this revised value is anchored to Milky Way Cepheids only. It should be combined with other distance indicators in order to derive a final Hubble constant value.

Finally, extragalactic Cepheids have longer periods than the Cepheids considered in this study (generally  $\sim 30$  days). The extrapolation of the Milky Way Leavitt law, calibrated by short to medium period Cepheids (with mean periods around  $\sim 5$  days), to the extragalactic distance scale, may introduce additional dispersion to the results. For this reason, the search for long-period Cepheids in open clusters and the precise photometric measurements of long-period Cepheids are crucial for improving the calibration of the distance scale.

## 2.5 Conclusion on the calibration of the Leavitt law

### 2.5.1 Summary of the study

In this chapter, I first described previous calibrations of the Leavitt law determined using *Hipparcos* and HST parallaxes before the publication of the *Gaia* catalog. I also mentioned additional methods to obtain Cepheid distances in order to calibrate the P-L relation. In a second section I presented the *Gaia* spacecraft and the main characteristics of the second and early third *Gaia* data releases. The Milky Way Leavitt law is then calibrated using the parallaxes of Cepheid resolved companions and mean parallaxes of open clusters hosting Cepheids: this approach was adopted in Breuval et al. (2020) in order to avoid several issues that affect Cepheid parallaxes. First, nearby Cepheids are very bright stars and often saturated, which degrades the quality of their astrometric solution. Secondly, the variability of pulsating stars is not yet incorporated in the *Gaia* data reduction (for *Gaia* DR2 and EDR3 releases). The change in color observed during a pulsation cycle slightly changes the position of the source on *Gaia*'s detector and may result in potentially unreliable parallaxes. By adopting the

parallaxes of stars located in the close environment of Cepheids such as companions or cluster members, instead of using the Cepheid parallaxes directly, one can therefore avoid contamination due to saturation and variability.

Breuval et al. (2020) provide an original calibration of the Leavitt law in the Milky Way using this approach without relying on Cepheid parallaxes and re-evaluate the Hubble constant anchored to Galactic Cepheids based on *Gaia* DR2 parallaxes. In this thesis, I adopted the same sample of 18 Cepheid companions and 14 open cluster Cepheids, and I included 6 new associations from the literature. This chapter is an update of the study by Breuval et al. (2020) where *Gaia* DR2 parallaxes are replaced by the recent and more precise *Gaia* EDR3 parallaxes.

Contrary to *Gaia* DR2, companion parallaxes from *Gaia* EDR3 are in relatively good agreement with Cepheid parallaxes, which suggests that the longer time coverage of *Gaia* EDR3 reduces the contamination of the astrometry due to color variability. Especially, the number of outliers is considerably reduced in *Gaia* EDR3 companion parallaxes. However, companions are often faint which makes their parallax unprecise: adopting companion parallaxes instead of Cepheid parallaxes from *Gaia* EDR3 constitutes an interesting quality check but does not improve the precision of the P-L calibration.

On the other hand, mean cluster parallaxes are very close to *Gaia* EDR3 Cepheid parallaxes and are also more precise thanks to the average over a large number of stars. Using mean cluster parallaxes reduces by half the dispersion of the P-L relation compared with using direct Cepheid parallaxes. The Leavitt law calibrations derived from *Gaia* EDR3 parallaxes in this work and from *Gaia* DR2 parallaxes in Breuval et al. (2020) are consistent: the present analysis validates the method of companions and open clusters for calibrating the P-L relation and shows that it is robust and stable over both data releases.

Based on the samples of companions and host open clusters restricted to fundamental mode pulsators only, a revised value of  $73.47 \pm 1.77$  km/s/Mpc is obtained for the Hubble constant in place of the initial value of  $76.18 \pm 2.37$  km/s/Mpc derived by Riess et al. (2016). Including first-overtone Cepheids yields a slightly lower value of  $73.10 \pm 1.76$  km/s/Mpc. Although the use of *Gaia* EDR3 parallaxes reduces  $H_0$  compared with using HST parallaxes, the tension between the Planck Collaboration et al. (2020) prediction based on the  $\Lambda$ -CDM model and the present value is still significant at  $\sim 3\sigma$ . Additionally, the re-evaluated value is also in better agreement with other estimates of the Hubble constant from Riess et al. (2016) based on different distance indicators. In this chapter, I also slightly improved the precision of the Hubble constant based on this sample of Cepheids compared with Breuval et al. (2020), thanks to the use of *Gaia* EDR3 parallaxes instead of *Gaia* DR2 and to the addition of new cluster Cepheids.

### 2.5.2 Limitations

The calibration of the Leavitt law based on companion stars and host open clusters is still limited for various reasons. First, some companion stars are particularly faint and can reach  $G > 18$  mag, which yields unprecise parallaxes with a low signal-to-noise ratio. Each Cepheid of the Kervella et al. (2019b) sample has only one or two companions, therefore this sample does not benefit from the averaging effect that applies for cluster Cepheids. Resolved companions are still limited to a small number, although Kervella et al. (2019b) noted that a large majority of Cepheids are in a multiple system.

Similarly, only a few dozen of open cluster Cepheids are confirmed in the literature, which constitutes a main limitation for this method. Additionally, large angular correlations are responsible for important systematic errors of the order of  $\sim 10 \mu\text{as}$  in the mean cluster parallaxes. These systematics should be estimated carefully with a relevant covariance function.

Cepheids with resolved companions or residing in clusters are not always the most studied ones: they sometimes have poor light-curve coverage or unprecise reddening values. These stars should be studied in priority since we dispose of independent methods to calibrate their distances. While the use of companion parallaxes improved the precision of the P-L calibration with *Gaia* DR2 (Breuval et al. 2020), they are not competitive anymore with Cepheid parallaxes in *Gaia* EDR3, since the noise due to the chromaticity issue is averaged.

Finally, a large fraction of the Cepheids of this sample pulsate in the first-overtone mode, therefore excluding them substantially reduces the size of the sample. The periods of first-overtone Cepheids were converted into the fundamental mode, which may introduce a bias in the fundamental-mode PL relation, and consequently on the Hubble constant. For this reason,  $H_0$  was estimated in two cases: with and without considering first-overtone mode Cepheids. The physics behind Cepheid pulsation modes should be studied in more detail before considering these stars in the distance scale.

### 2.5.3 Perspectives

*Gaia* provides thousands of Cepheid parallaxes, which represents a considerable improvement compared with the limited number of Cepheid parallaxes measured with HST. Future releases will cover a larger period of time (the final *Gaia* Data Release is expected to cover 66 months of observations), which will improve again the quality of the astrometry. The determination of the parallax zero-point was significantly improved in *Gaia* EDR3 and its value is now reduced compared with *Gaia* DR2. It now takes into account the position, magnitude and color of the sources (Lindgren et al. 2021a). Additionally, in future *Gaia* data releases, the color variation of pulsating stars will be included and should result in more precise parallaxes for Cepheids.

Obtaining photometry for nearby and extragalactic Cepheids in a consistent and homogeneous system would also reduce the systematics on the Leavitt law and on the Hubble constant (Riess et al. 2021b). This point is discussed in Chapter 4. Finally, including long-period Cepheids ( $\log P > 1.2$ ) would considerably improve the precision on the P-L relation slope and intercept. Especially, it would also be more consistent with extragalactic Cepheids which have longer periods<sup>7</sup>.

The present study provides a powerful validation of the method adopted in Breuval et al. (2020) and of the sample of companions and open cluster Cepheids. This approach allows to bypass the saturation and the chromaticity issues that affect Cepheids. It may also be applied to RR Lyrae and Mira variables to improve the precision of their P-L relation.

---

<sup>7</sup> Cepheids observed in distant galaxies are biased toward the brightest ones, which result in an observational cut around  $\sim 20$  days (Javanmardi et al. 2021).

## **2.6 Publication: *The Milky Way Cepheid Leavitt law based on Gaia DR2 parallaxes of companion stars and host open cluster populations*, Breuval et al. 2020, A&A 643 A115**

This section presents my first paper, [Breuval et al. \(2020\)](#). It describes the calibration of the Cepheid Leavitt law using *Gaia* DR2 parallaxes. In order to avoid contamination due to saturated sources or variability, we adopted parallaxes of Cepheid resolved companions and host open clusters. A revised value of the Hubble constant is derived based on this sample.

# The Milky Way Cepheid Leavitt law based on *Gaia* DR2 parallaxes of companion stars and host open cluster populations

Louise Breuval<sup>1</sup>, Pierre Kervella<sup>1</sup>, Richard I. Anderson<sup>2</sup>, Adam G. Riess<sup>3,4</sup>, Frédéric Arenou<sup>5</sup>, Boris Trahin<sup>1</sup>, Antoine Mérand<sup>2</sup>, Alexandre Gallenne<sup>6,7,8,9</sup>, Wolfgang Gieren<sup>7</sup>, Jesper Storm<sup>10</sup>, Giuseppe Bono<sup>11,12</sup>, Grzegorz Pietrzyński<sup>7,8</sup>, Nicolas Nardetto<sup>6</sup>, Behnam Javanmardi<sup>1</sup>, and Vincent Hodge<sup>6</sup>

<sup>1</sup> LESIA, Observatoire de Paris, Université PSL, CNRS, Sorbonne Université, Univ. Paris Diderot, Sorbonne Paris Cité, 5 place Jules Janssen, 92195 Meudon, France  
e-mail: [louise.breuval@obspm.fr](mailto:louise.breuval@obspm.fr)

<sup>2</sup> European Southern Observatory, Karl-Schwarzschild-Str. 2, 85748 Garching, Germany

<sup>3</sup> Space Telescope Science Institute, 3700 San Martin Drive, Baltimore, MD 21218, USA

<sup>4</sup> Department of Physics and Astronomy, Johns Hopkins University, Baltimore, MD 21218, USA

<sup>5</sup> GEPI, Observatoire de Paris, Université PSL, CNRS, 5 place Jules Janssen, 92190 Meudon, France

<sup>6</sup> Université Côte d'Azur, Observatoire de la Côte d'Azur, CNRS, Laboratoire Lagrange, France

<sup>7</sup> Universidad de Concepción, Departamento de Astronomía, Casilla 160-C, Concepción, Chile

<sup>8</sup> Nicolaus Copernicus Astronomical Centre, Polish Academy of Sciences, Bartycka 18, 00-716 Warszawa, Poland

<sup>9</sup> Unidad Mixta Internacional Franco-Chilena de Astronomía (CNRS UMI 3386), Departamento de Astronomía, Universidad de Chile, Camino El Observatorio 1515, Las Condes, Santiago, Chile

<sup>10</sup> Leibniz-Institut für Astrophysik Potsdam (AIP), An der Sternwarte 16, 14482 Potsdam, Germany

<sup>11</sup> Department of Physics, Università di Roma Tor Vergata, Via della Ricerca Scientifica 1, 00133 Roma, Italy

<sup>12</sup> INAF-Osservatorio Astronomico di Roma, Via Frascati 33, 00040 Monte Porzio Catone, Italy

Received 10 June 2020 / Accepted 9 September 2020

## ABSTRACT

**Aims.** Classical Cepheids provide the foundation for the empirical extragalactic distance ladder. Milky Way Cepheids are the only stars in this class accessible to trigonometric parallax measurements. However, the parallaxes of Cepheids from the second *Gaia* data release (GDR2) are affected by systematics because of the absence of chromaticity correction, and occasionally by saturation.

**Methods.** As a proxy for the parallaxes of 36 Galactic Cepheids, we adopt either the GDR2 parallaxes of their spatially resolved companions or the GDR2 parallax of their host open cluster. This novel approach allows us to bypass the systematics on the GDR2 Cepheids parallaxes that is induced by saturation and variability. We adopt a GDR2 parallax zero-point (ZP) of  $-0.046$  mas with an uncertainty of  $0.015$  mas that covers most of the recent estimates.

**Results.** We present new Galactic calibrations of the Leavitt law in the  $V$ ,  $J$ ,  $H$ ,  $K_S$ , and Wesenheit  $W_H$  bands. We compare our results with previous calibrations based on non-*Gaia* measurements and compute a revised value for the Hubble constant anchored to Milky Way Cepheids.

**Conclusions.** From an initial Hubble constant of  $76.18 \pm 2.37$  km s<sup>-1</sup> Mpc<sup>-1</sup> based on parallax measurements without *Gaia*, we derive a revised value by adopting companion and average cluster parallaxes in place of direct Cepheid parallaxes, and we find  $H_0 = 72.8 \pm 1.9$  (statistical + systematics)  $\pm 1.9$  (ZP) km s<sup>-1</sup> Mpc<sup>-1</sup> when all Cepheids are considered and  $H_0 = 73.0 \pm 1.9$  (statistical + systematics)  $\pm 1.9$  (ZP) km s<sup>-1</sup> Mpc<sup>-1</sup> for fundamental mode pulsators only.

**Key words.** parallaxes – stars: distances – stars: variables: Cepheids – distance scale

## 1. Introduction

Classical Cepheids (CCs) have a historical major importance among variable stars because of the simple correlation between the pulsation period and intrinsic luminosity, also called the Leavitt law or the period–luminosity (PL) relation (Leavitt 1908; Leavitt & Pickering 1912). However, after more than a century of active research, the absolute calibration of the Leavitt law is still unsatisfactory because of the lack of precise and direct distance measurements for a sizeable sample of these stars. A careful calibration of this relation and especially of its zero-point is fundamental as it is used to establish extragalactic distances and to derive the expansion rate of the Universe, the Hubble constant  $H_0$ . The determination of  $H_0$  from the cosmic microwave background (CMB) based on the standard  $\Lambda$  cold dark matter ( $\Lambda$ CDM) model (Planck Collaboration VI 2020) is currently found to be in  $\sim 5\sigma$  tension with the empirical or direct distance ladder measurements (Riess 2019). This tension may have

important implications in cosmology, and may even point toward new physics beyond  $\Lambda$ CDM (Verde et al. 2019).

Calibrating the Leavitt law requires independent and accurate distance measurement for a sample of CCs. Unfortunately, *Gaia*'s second data release (hereafter GDR2) contains a number of systematic effects that may reduce the precision of the parallaxes of CCs (Gaia Collaboration 2018). First, CCs are bright stars, so a small number with  $G < 6$  mag are affected by saturation, making their parallaxes unreliable. In addition, CC colors cycle through many variations during the parallax cycle; the effective temperature of a Cepheid changes on average by 1000 K over a full pulsation cycle (Proxauf et al. 2018), which means  $\sim 0.5$  mag in optical bands, so this may add additional noise to their astrometry due to the chromaticity of the PSF. Future *Gaia* data releases are expected to include chromaticity corrections for variable stars and incorporate a better model of the PSF to deal with saturation. While recent analyses of *Gaia* DR2 parallaxes for CCs with  $G > 6$  mag do not appear to be

affected by excess noise (an indicator of poor quality for GDR2 astrometric data; Groenewegen 2018; Riess et al. 2018a; Gaia Collaboration 2017; Clementini et al. 2019), it is important to pursue alternative approaches to extract parallaxes from *Gaia* DR2 for CCs that are insensitive to these systematics.

Even in the absence of systematic errors, the use of open cluster parallaxes for the CCs they host can provide enhanced precision over the use of a single CC parallax. Because open cluster parallaxes are based on many stars, the increased precision from averaging and the ability to reject outliers for stars in astrometric binaries is extremely valuable.

In the present paper our aim is to calibrate the Milky Way (MW) Cepheid Leavitt law using stars that are not affected by these issues and to benefit from the gain in precision afforded by cluster average parallaxes. In Sect. 2 we introduce our sample of stars and their associated parallaxes and photometry. In Sect. 3.1 we derive calibrations of the Leavitt law in various bands. Then in Sect. 3.2 we compare our GDR2 parallaxes with the corresponding expected parallaxes from *Hubble* Space Telescope (HST) measurements, and in Sect. 3.3 we derive a value for the Hubble constant anchored to Milky Way Cepheids.

## 2. Sample

We consider two sets of parallaxes: one based on Cepheid companions and one based on average cluster parallaxes. The benefits of these samples are flux and color constancy (companions and clusters) and averaging over a large sample (clusters).

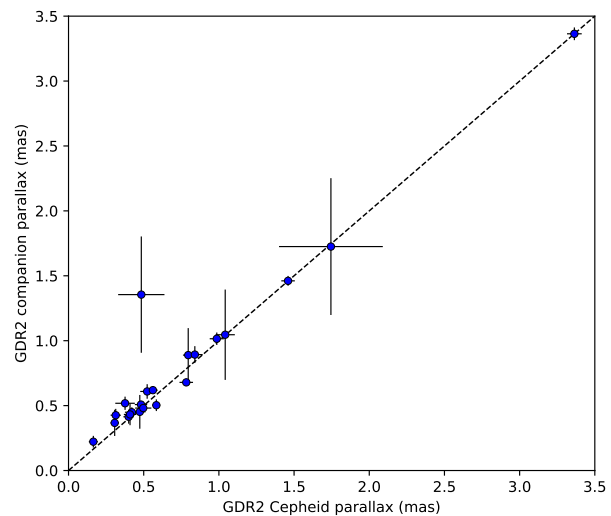
### 2.1. Parallaxes of Cepheid resolved companions

Recently, Kervella et al. (2019) presented a sample of 28 Galactic Cepheids that are members of gravitationally bound and spatially resolved stellar systems. In these systems Cepheid companions are photometrically stable stars and their GDR2 parallaxes are therefore not affected by such a strong chromatic effect as Cepheids. As the CCs and their companions share the same parallax (their relative distance is negligible compared to the distance to *Gaia*), the GDR2 parallaxes of the companions provide a natural proxy for those of the CCs. The companions' parallaxes are precise within 15%, on average. A comparison between direct GDR2 Cepheid parallaxes and the corresponding GDR2 companion parallaxes is displayed in Fig. 1.

The angular separation between the CCs and their companions is in most cases larger than 10 arcsec, which is large enough to prevent flux contamination, given the brightness of the CCs. At 10'' separation for stars hundreds to thousands of parsec distant there is no expected effect of orbital motion on parallax or proper motion measurements: the parallaxes of the CCs and companions are not sensitive to the binarity of these wide systems.

The GDR2 astrometry is generally of poor quality for very bright stars ( $G < 6$  mag), due to calibration issues and saturation (Riess et al. 2018a; Drimmel et al. 2019; Lindegren 2020). This occurs independently of the chromaticity issue raised previously, whether the star is variable or not. While several Cepheids in our sample are close to this limit, with an average  $G$  magnitude of 8 mag, their companions are on average 7 mag fainter than their parent Cepheids. The companions are therefore not as affected as CCs by the saturation issue and they are far away from the sensitivity limit. They consequently belong to the best dynamical range for *Gaia*.

For a given Cepheid, when more than one companion was found by Kervella et al. (2019), we selected the companion with the smallest uncertainty on its parallax. This selection was performed for CV Mon, SY Nor, U Sgr, and V350 Sgr.



**Fig. 1.** GDR2 parallaxes of our sample of companions as a function of the corresponding GDR2 Cepheid parallax. The dashed line corresponds to the identity line.

Various quality indicators are introduced in the second release of *Gaia* data, such as the re-normalized unit weight error (RUWE, noted  $\varrho$  in the following). It is particularly pertinent because it evaluates the quality of the parallax of a star compared to other stars of the same type. This parameter is defined by Lindegren (2018a) as

$$\varrho = \frac{\text{UWE}}{u_0(G, C)}, \quad (1)$$

where  $\text{UWE} = \sqrt{\chi^2/(N-5)}$  is the unit weight error and  $u_0$  is an empirical normalization factor that is not directly available in the *Gaia* release, but which can be computed from the lookup table on the ESA DR2 *Known issues* web page<sup>1</sup>. Following Lindegren (2018a), we estimate that a parallax is reliable if  $\varrho < 1.4$ . The Table 1 gives the RUWE for the Cepheids and the companions in our sample.

We note that some CCs from the Kervella et al. (2019) sample have no valid GDR2 parallax ( $\delta$  Cep, R Cru,  $\alpha$  UMi), while all companions have a valid parallax. In the initial Kervella et al. (2019) sample of 28 Cepheids, five of them have  $\varrho > 1.4$ , while only two companions are in this case, R Cru and V1046 Cyg, with  $\varrho = 2.80$  and 1.51, respectively. We exclude these two stars from the sample of companions in order to keep accurate parallaxes only. The star CE Cas B is a particular case because its companion CE Cas A is also a Cepheid. We exclude both stars from our sample as a precaution.

The star  $\alpha$  UMi is extremely bright, with  $K \approx 0.5$  mag. Therefore, measuring accurate photometry for this star is particularly challenging. It has no valid parallax in GDR2 and appears saturated in most catalogs (Skrutskie et al. 2006). The only accurate average magnitudes based on several pulsation cycles were found in the AAVSO database that provides  $J = 0.93 \pm 0.01$  mag and  $H = 0.67 \pm 0.01$  mag in the UKIRT system. Additionally, the uncertain pulsation mode and the age difference between the Cepheid and its companion raise questions concerning the properties of  $\alpha$  UMi and whether it should be included in PL relation fits (Anderson 2018; Bond et al. 2018;

<sup>1</sup> <https://www.cosmos.esa.int/web/gaia/dr2-known-issues>



**Table 1.** Sample of Cepheids in resolved binary systems taken from [Kervella et al. \(2019\)](#): parameters of the Cepheids and of their stable companions.

Cepheid	$\varpi_{\text{GDR2}}$ (mas)	$\varrho$	$G$ (mag)	$BP-RP$ (mag)	Companion (GDR2)	$\varpi_{\text{GDR2}}$ (mas)	$\varrho$	$G$ (mag)	$BP-RP$ (mag)
DF Cas	0.307 $\pm$ 0.028	0.98	10.43	1.50	465719182408531072	0.367 $\pm$ 0.101	1.12	17.26	2.02
CM Sct	0.376 $\pm$ 0.065	1.02	10.51	1.81	4253603428053877504	0.518 $\pm$ 0.051	0.95	14.73	1.49
EV Sct	0.497 $\pm$ 0.054	1.05	9.62	1.63	4156513016572003840	0.481 $\pm$ 0.034	1.03	13.62	0.88
TV CMa	0.314 $\pm$ 0.034	0.94	10.08	1.69	3044483895574944512	0.426 $\pm$ 0.049	1.12	15.77	1.18
V532 Cyg	0.561 $\pm$ 0.032	0.86	8.67	1.44	1971721839529622272	0.619 $\pm$ 0.027	0.93	14.67	1.04
V950 Sco	0.840 $\pm$ 0.052	1.09	7.05	1.05	5960623340819000192	0.893 $\pm$ 0.065	1.00	15.28	1.03
V350 Sgr	0.986 $\pm$ 0.047	0.92	7.25	1.26	4080121319521641344	1.015 $\pm$ 0.048	0.96	12.27	0.50
VW Cru	0.783 $\pm$ 0.045	0.98	9.01	1.85	6053622508133367680	0.679 $\pm$ 0.028	0.96	14.07	1.18
AX Cir	1.745 $\pm$ 0.345	10.3 (*)	5.63	1.15	5874031027625742848	1.725 $\pm$ 0.527	1.13	19.82	1.65
$\delta$ Cep	–	20.9 (*)	–	–	2200153214212849024	3.364 $\pm$ 0.049	0.85	6.28	–0.02
CV Mon	0.482 $\pm$ 0.041	1.16	9.61	1.78	3127142327895572352	0.508 $\pm$ 0.025	1.03	13.49	1.03
QZ Nor	0.474 $\pm$ 0.038	1.01	8.58	1.18	5932565899990412672	0.452 $\pm$ 0.130	1.02	17.93	1.29
V659 Cen	0.484 $\pm$ 0.154	4.52 (*)	6.39	1.04	5868451109212716928	1.355 $\pm$ 0.448	1.00	19.69	2.50
CS Vel	0.165 $\pm$ 0.030	1.01	11.10	1.83	5308893046071732096	0.222 $\pm$ 0.045	0.95	16.20	1.08
RS Nor	0.421 $\pm$ 0.046	0.99	9.49	1.73	5932812740361508736	0.449 $\pm$ 0.038	1.06	14.55	0.97
X Cru	0.523 $\pm$ 0.046	0.97	8.07	1.28	6059762524642419968	0.609 $\pm$ 0.056	1.16	16.04	1.11
AW Per	1.042 $\pm$ 0.064	1.06	7.05	1.97	174489098011144960	1.046 $\pm$ 0.348	1.07	17.42	1.54
U Sgr	1.460 $\pm$ 0.045	1.06	6.35	1.54	4092905203841177856	1.461 $\pm$ 0.038	0.90	11.14	0.67
ER Car	0.796 $\pm$ 0.035	0.95	6.61	1.08	5339394048386734336	0.889 $\pm$ 0.208	1.09	18.44	1.37
SX Vel	0.409 $\pm$ 0.041	1.00	7.97	1.24	5329838158460399488	0.432 $\pm$ 0.083	0.95	17.02	1.13
SY Nor	0.400 $\pm$ 0.035	1.10	8.97	1.83	5884729035245399424	0.414 $\pm$ 0.053	1.28	12.10	0.88
RS Pup	0.584 $\pm$ 0.026	0.97	6.46	1.88	5546476755539995008	0.503 $\pm$ 0.045	1.00	16.25	1.28

**Notes.** The symbol  $\varrho$  is the RUWE quality indicator from GDR2 and (\*) indicates that  $\varrho > 1.4$ .

[Groenewegen 2018](#)). We decided to exclude this star from our sample.

Finally, this selection results in a sample of 22 GDR2 parallaxes of Cepheids resolved companions, listed in Table 1.

## 2.2. Parallaxes of Cepheids in open clusters

Open clusters (OCs) contain a significant number of stars located at the same distance and are numerous in the Milky Way. Therefore, identifying Cepheids in OCs allows us to estimate their distances, with an important gain in precision by taking the average over a population compared to individual parallax measurements.

We performed a cross-match between the [Ripepi et al. \(2019\)](#) reclassification of GDR2 Cepheids and the [Cantat-Gaudin et al. \(2018\)](#) catalog of Milky Way Open Clusters. This catalog provides parallaxes for 1229 OCs, computed as the median GDR2 parallax of their member stars. Our comparison is based on five membership constraints: separation  $\theta$ , parallax  $\varpi$ , proper motion  $\mu_\alpha^*$  and  $\mu_\delta$ , and age.

Following [Anderson et al. \(2013\)](#), we start the search for potential cluster members by looking at the proximity in the sky: we selected all Cepheids located in a region of  $10r_{50}$  around each cluster (where  $r_{50}$  is the radius containing half of the members) and we find a total of 2647 couples. For these couples we compared the parallaxes, the proper motions, and the ages of the two components. Since GDR2 parallaxes of Cepheids may be affected by systematics due to the absence of chromaticity correction, we account for this effect by including 20% error in quadrature. The proper motions for Cepheids and open clusters are taken from [Ripepi et al. \(2019\)](#) and [Cantat-Gaudin et al. \(2018\)](#), respectively. The age of open clusters is provided by [Kharchenko et al. \(2013\)](#), and the age for Cepheids is derived using period–age relations from [Anderson et al. \(2016\)](#).

We also searched in the literature for additional combinations and examined whether they satisfy our membership constraints. Some Cepheids are not present in the [Ripepi et al. \(2019\)](#) reclassification, so they could not be found by means of our cross-match. [Anderson et al. \(2013\)](#) presented many of our couples and provided three additional combinations that verify our membership criteria: TW Nor, CV Mon, and V0367 Sct respectively in Lyngå 6, vdBergh 1, and NGC 6649. Other studies, such as [An et al. \(2007\)](#) and [Chen et al. \(2015\)](#), also confirm most of our cluster memberships. Recently, [Clark et al. \(2015\)](#) and [Lohr et al. \(2018\)](#) identified new Cepheids as potential members of open clusters. However, no near-infrared (NIR) multi-epoch photometry is available for these Cepheids. Moreover, the [Clark et al. \(2015\)](#) starburst cluster VdBH 222 is not present in the [Cantat-Gaudin et al. \(2018\)](#) catalog. Therefore, we did not include them in our sample.

We find a total of 14 Cepheids that are candidate members of open clusters. They are listed in Table 2, where filled circles stand for the agreement of a parameter at  $1\sigma$  or less. In this table is also provided the separation in arcmin between a Cepheid and the center of its host cluster.

Due to the limited angular size of a cluster, parallaxes of the member stars of a same cluster are highly correlated. Uncertainties provided by [Cantat-Gaudin et al. \(2018\)](#) neglect this effect. Therefore, we revised the open cluster parallax uncertainties by including spatial correlations. We used the approach described in [Lindgren \(2018b\)](#) and retrieved the spatial covariance  $V_\varpi(\theta)$  of parallax errors on the ESA DR2 *Known issues* web page<sup>2</sup>. For each cluster, Table 2 provides the original [Cantat-Gaudin et al. \(2018\)](#) uncertainties, the number of member stars in each cluster, the cluster radius  $r_{50}$ , the averaged  $V_\varpi(\theta)$ , and the

<sup>2</sup> <https://www.cosmos.esa.int/web/gaia/dr2-known-issues>

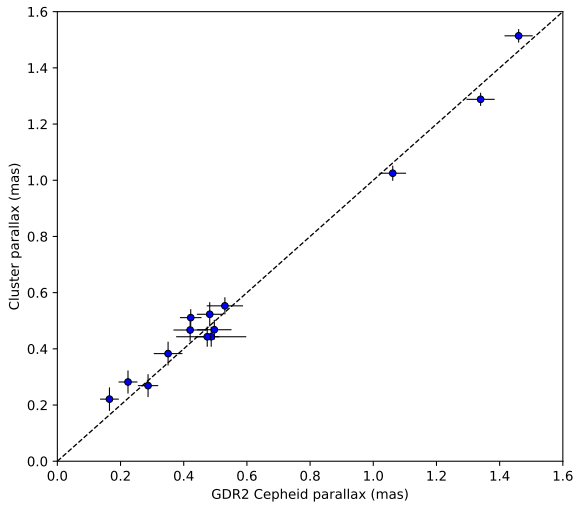


**Table 2.** Sample of cluster Cepheids found by our cross-match selection and in the literature.

Cepheid	Cluster	Cross-match						Cluster parameters				
		$\varpi$	$\mu_\alpha^*$	$\mu_\delta$	Age	Sep (arcmin)	Ref.	$\varpi_{\text{CG18}}$ (mas)	$N_{\text{memb}}$	$r_{50}$ (deg)	$\langle V_{\varpi} \rangle$ ( $\mu\text{as}^2$ )	$\varpi_{\text{adopted}}$ (mas)
CV Mon	vdBergh 1	•	•	•	•	0.9	a, b, c, d	$0.523_{\pm 0.010}$	73	0.03	1741	$0.523_{\pm 0.043}$
S Nor	NGC 6087	•	•	•	•	1.0	a, b, c, e	$1.025_{\pm 0.004}$	251	0.25	708	$1.025_{\pm 0.027}$
U Sgr	IC 4725	•	•	•	•	2.1	a, b, c	$1.514_{\pm 0.003}$	516	0.26	563	$1.514_{\pm 0.024}$
V367 Sct	NGC 6649	•	•	•	•	2.8	a	$0.467_{\pm 0.004}$	560	0.06	1689	$0.467_{\pm 0.041}$
V Cen	NGC 5662	•	•	•	•	25	a, b, c, f	$1.288_{\pm 0.003}$	255	0.33	533	$1.288_{\pm 0.023}$
RS Ori	FSR 0951	•	•	•	$2.4 \sigma$	2.0	PW	$0.553_{\pm 0.004}$	195	0.16	697	$0.553_{\pm 0.027}$
CS Vel	Ruprecht 79	•	•	•	$2.5 \sigma$	2.2	g	$0.221_{\pm 0.004}$	178	0.05	1720	$0.221_{\pm 0.042}$
DL Cas	NGC 129	•	•	$3.4 \sigma$	•	3.4	a, b, c	$0.511_{\pm 0.002}$	392	0.17	904	$0.511_{\pm 0.031}$
EV Sct	NGC 6664	•	$1.1 \sigma$	•	•	2.4	a	$0.468_{\pm 0.004}$	237	0.10	1215	$0.468_{\pm 0.035}$
V340 Nor	NGC 6067	•	$1.3 \sigma$	•	•	0.9	a, c	$0.443_{\pm 0.002}$	995	0.11	1263	$0.443_{\pm 0.036}$
CF Cas	NGC 7790	•	$1.9 \sigma$	•	•	1.3	a, b, c	$0.269_{\pm 0.004}$	200	0.06	1642	$0.269_{\pm 0.041}$
TW Nor	Lyngå 6	•	$2.0 \sigma$	•	$1.4 \sigma$	0.6	a, b, c, h	$0.383_{\pm 0.006}$	79	0.06	1730	$0.383_{\pm 0.042}$
QZ Nor	NGC 6067	•	$1.2 \sigma$	$9 \sigma$	•	18	a	$0.443_{\pm 0.002}$	955	0.11	1263	$0.443_{\pm 0.036}$
CG Cas	Berkeley 58	•	$4.1 \sigma$	$2.0 \sigma$	$1.2 \sigma$	5.5	a, b	$0.282_{\pm 0.004}$	142	0.06	1661	$0.282_{\pm 0.041}$

**Notes.** Full circles stand for an agreement smaller than  $1\sigma$  between the Cepheid and the cluster parameters.

**References.** (a): [Anderson et al. \(2013\)](#); (b): [Chen et al. \(2015\)](#); (c): [An et al. \(2007\)](#); (d): [Turner et al. \(1998\)](#); (e): [Turner \(1986\)](#); (f): [Turner \(1982\)](#); (g): [Turner \(2010\)](#); (h): [Majaess et al. \(2011\)](#); (PW): present work.



**Fig. 2.** Parallaxes of our sample of cluster Cepheids from [Cantat-Gaudin et al. \(2018\)](#) with revised uncertainties, as a function of the corresponding GDR2 Cepheid parallax. The dashed line corresponds to the identity line.

adopted parallax  $\varpi_{\text{adopted}}$  with its revised uncertainty. After this correction the average precision of our cluster parallaxes is  $\sim 8\%$ .

The Cepheid QZ Nor is a particular case; located at 18 arcmin of NGC 6067, it is a peripheral member of this cluster. The  $9\sigma$  difference in  $\mu_\delta$  could be explained by the fact that the Cepheid is leaving the cluster. This membership was identified by [Anderson et al. \(2013\)](#) as bona fide. Moreover, QZ Nor is also present in the sample of companions found by [Kervella et al. \(2019\)](#): the stable star *Gaia* DR2 5932565899990412672 is located at  $16''$  (30 kau) from the Cepheid. Its GDR2 parallax of  $0.452 \pm 0.130$  mas agrees particularly well with the  $0.443 \pm 0.036$  mas parallax of NGC 6067 from [Cantat-Gaudin et al. \(2018\)](#). Therefore, we decided to include this pair.

The cross-match also resulted in potential members that only have 2MASS single epoch photometry available. Since average magnitudes are preferred for the Leavitt law calibration, we discarded these pairs. In that case, we found V379 Cas, GU Nor, and XZ Car to be members of NGC 129, NGC 6067, and NGC 3496 respectively.

A comparison between direct GDR2 Cepheid parallaxes and the corresponding open cluster parallaxes from [Cantat-Gaudin et al. \(2018\)](#) is displayed in Fig. 2. The field charts of each open cluster Cepheid are displayed in Fig. A.1.

### 2.3. Photometry

In order to determine the phase-averaged magnitudes of the CCs in our sample, we searched them in the catalog assembled by [Groenewegen \(2018\)](#). It is a compilation of mean apparent magnitudes in  $J$ ,  $H$ ,  $K$ , and  $V$  bands in different photometric systems, taken from different sources (see Table 3). [Laney & Stobie \(1992\)](#) provide NIR magnitudes in the SAAO system, to which we set the uncertainties to 0.008 mag following [Groenewegen \(2018\)](#). For homogeneity we converted them into the 2MASS system using the equations from [Koen et al. \(2007\)](#):

$$\begin{aligned}
 J_{2\text{MASS}} &= -0.028 + J_{\text{SAAO}} - 0.047(J_{\text{SAAO}} - K_{\text{SAAO}}), \\
 H_{2\text{MASS}} &= +0.014 + H_{\text{SAAO}}, \\
 K_{2\text{MASS}} &= -0.015 + K_{\text{SAAO}} + 0.177(H_{\text{SAAO}} - K_{\text{SAAO}}) \\
 &\quad - 0.082(J_{\text{SAAO}} - H_{\text{SAAO}})^2.
 \end{aligned}$$

The magnitudes given by [Monson & Pierce \(2011\)](#) are in the BIRCAM photometric system, we also adopted uncertainties of 0.008 mag, and the magnitudes taken from [Welch et al. \(1984\)](#) and [Barnes et al. \(1997\)](#) are in the CIT photometric system, with uncertainties of 0.010 mag following [Groenewegen \(2018\)](#). They were all converted into the 2MASS system using the equations from [Monson & Pierce \(2011\)](#):

$$\begin{aligned}
 K_{2\text{MASS}} &= K_{\text{BIRCAM}} + 0.008 (J_{\text{BIRCAM}} - K_{\text{BIRCAM}}) - 0.042, \\
 J_{2\text{MASS}} &= K_{2\text{MASS}} + 1.052 (J_{\text{BIRCAM}} - K_{\text{BIRCAM}}) - 0.002, \\
 H_{2\text{MASS}} &= K_{2\text{MASS}} + 0.993 (H_{\text{BIRCAM}} - K_{\text{BIRCAM}}) + 0.050,
 \end{aligned}$$

**Table 3.** Final sample adopted, combining Cepheids with resolved companions and open cluster Cepheids.

Cepheid	$P$ (days)	$\varpi^{(*)}$ (mas)	$E(B - V)$	$m_V$ (mag)	$m_I$ (mag)	$m_H$ (mag)	$m_{K_s}$ (mag)	$m_H^W (**)$ (mag)	Ref <sub>NIR</sub>
Sample of Cepheids with resolved companions									
DF Cas	3.832	$0.367_{\pm 0.104}$	$0.564_{\pm 0.049}$	$10.880_{\pm 0.030}$	$8.488_{\pm 0.025}$	$8.036_{\pm 0.025}$	$7.879_{\pm 0.025}$	$7.533_{\pm 0.066}$	G14
CM Sct	3.917	$0.518_{\pm 0.056}$	$0.775_{\pm 0.045}$	$11.100_{\pm 0.030}$	$8.300_{\pm 0.025}$	$7.818_{\pm 0.025}$	$7.558_{\pm 0.025}$	$7.240_{\pm 0.066}$	G14
EV Sct	4.396 (*)	$0.481_{\pm 0.040}$	$0.623_{\pm 0.015}$	$10.130_{\pm 0.030}$	$7.608_{\pm 0.008}$	$7.184_{\pm 0.008}$	$7.018_{\pm 0.008}$	$6.658_{\pm 0.061}$	L92
TV CMa	4.670	$0.426_{\pm 0.054}$	$0.574_{\pm 0.029}$	$10.590_{\pm 0.030}$	$8.022_{\pm 0.008}$	$7.582_{\pm 0.008}$	$7.364_{\pm 0.008}$	$7.048_{\pm 0.061}$	M11
V532 Cyg	4.675 (*)	$0.619_{\pm 0.033}$	$0.519_{\pm 0.007}$	$9.090_{\pm 0.030}$	$6.863_{\pm 0.025}$	$6.393_{\pm 0.025}$	$6.250_{\pm 0.025}$	$5.919_{\pm 0.066}$	2MASS
V950 Sco	4.814 (*)	$0.893_{\pm 0.069}$	$0.251_{\pm 0.019}$	$7.310_{\pm 0.030}$	$5.681_{\pm 0.008}$	$5.439_{\pm 0.008}$	$5.295_{\pm 0.008}$	$5.085_{\pm 0.061}$	G18
V350 Sgr	5.154	$1.015_{\pm 0.048}$	$0.308_{\pm 0.008}$	$7.470_{\pm 0.030}$	$5.625_{\pm 0.010}$	$5.245_{\pm 0.010}$	$5.121_{\pm 0.010}$	$4.844_{\pm 0.061}$	W84
VW Cru	5.265	$0.679_{\pm 0.034}$	$0.640_{\pm 0.046}$	$9.600_{\pm 0.030}$	$6.805_{\pm 0.025}$	$6.261_{\pm 0.025}$	$6.051_{\pm 0.025}$	$5.681_{\pm 0.066}$	G14
AX Cir	5.273	$1.725_{\pm 0.527}$	$0.265_{\pm 0.121}$	$5.880_{\pm 0.030}$	$4.299_{\pm 0.025}$	$3.879_{\pm 0.025}$	$3.780_{\pm 0.025}$	$3.524_{\pm 0.066}$	G14
$\delta$ Cep	5.366	$3.364_{\pm 0.049}$	$0.075_{\pm 0.018}$	$3.950_{\pm 0.030}$	$2.683_{\pm 0.010}$	$2.396_{\pm 0.010}$	$2.294_{\pm 0.010}$	$2.104_{\pm 0.061}$	B97
CV Mon	5.379	$0.508_{\pm 0.040}$	$0.705_{\pm 0.018}$	$10.310_{\pm 0.030}$	$7.314_{\pm 0.008}$	$6.781_{\pm 0.008}$	$6.529_{\pm 0.008}$	$6.165_{\pm 0.061}$	M11
QZ Nor	5.401 (*)	$0.452_{\pm 0.132}$	$0.289_{\pm 0.020}$	$8.870_{\pm 0.030}$	$7.085_{\pm 0.008}$	$6.748_{\pm 0.008}$	$6.614_{\pm 0.008}$	$6.360_{\pm 0.061}$	L92
V659 Cen	5.622	$1.355_{\pm 0.448}$	$0.151_{\pm 0.034}$	$6.620_{\pm 0.030}$	$5.177_{\pm 0.025}$	$4.907_{\pm 0.025}$	$4.651_{\pm 0.025}$	$4.583_{\pm 0.066}$	G14
CS Vel	5.905	$0.222_{\pm 0.050}$	$0.716_{\pm 0.027}$	$11.700_{\pm 0.030}$	$8.771_{\pm 0.008}$	$8.246_{\pm 0.008}$	$8.011_{\pm 0.008}$	$7.643_{\pm 0.061}$	L92
RS Nor	6.198	$0.449_{\pm 0.043}$	$0.577_{\pm 0.036}$	$10.000_{\pm 0.030}$	$7.412_{\pm 0.010}$	$6.794_{\pm 0.010}$	$6.683_{\pm 0.010}$	$6.249_{\pm 0.061}$	SPIPS
X Cru	6.220	$0.609_{\pm 0.061}$	$0.294_{\pm 0.019}$	$8.400_{\pm 0.030}$	$6.521_{\pm 0.025}$	$6.125_{\pm 0.025}$	$5.935_{\pm 0.025}$	$5.717_{\pm 0.066}$	G14
AW Per	6.464	$1.046_{\pm 0.349}$	$0.479_{\pm 0.016}$	$7.480_{\pm 0.030}$	$5.213_{\pm 0.008}$	$4.832_{\pm 0.008}$	$4.657_{\pm 0.008}$	$4.354_{\pm 0.061}$	M11
U Sgr	6.745	$1.461_{\pm 0.038}$	$0.408_{\pm 0.007}$	$6.690_{\pm 0.030}$	$4.506_{\pm 0.008}$	$4.100_{\pm 0.008}$	$3.912_{\pm 0.008}$	$3.637_{\pm 0.061}$	M11
ER Car	7.720	$0.889_{\pm 0.210}$	$0.111_{\pm 0.016}$	$6.820_{\pm 0.030}$	$5.310_{\pm 0.008}$	$5.034_{\pm 0.008}$	$4.896_{\pm 0.008}$	$4.698_{\pm 0.061}$	G18
SX Vel	9.550	$0.432_{\pm 0.086}$	$0.237_{\pm 0.014}$	$8.290_{\pm 0.030}$	$6.500_{\pm 0.008}$	$6.133_{\pm 0.008}$	$5.991_{\pm 0.008}$	$5.743_{\pm 0.061}$	L92
SY Nor	12.646	$0.414_{\pm 0.053}$	$0.611_{\pm 0.059}$	$9.500_{\pm 0.030}$	$6.574_{\pm 0.008}$	$6.105_{\pm 0.008}$	$5.865_{\pm 0.008}$	$5.504_{\pm 0.061}$	G18
RS Pup	41.443	$0.503_{\pm 0.045}$	$0.451_{\pm 0.010}$	$7.010_{\pm 0.030}$	$4.365_{\pm 0.008}$	$3.828_{\pm 0.008}$	$3.619_{\pm 0.008}$	$3.276_{\pm 0.061}$	L92
Sample of open cluster Cepheids									
CG Cas	4.365	$0.282_{\pm 0.041}$	$0.667_{\pm 0.009}$	$11.380_{\pm 0.030}$	$8.903_{\pm 0.025}$	$8.299_{\pm 0.025}$	$8.109_{\pm 0.025}$	$7.775_{\pm 0.066}$	G14
EV Sct	4.398 (*)	$0.468_{\pm 0.035}$	$0.623_{\pm 0.015}$	$10.130_{\pm 0.030}$	$7.608_{\pm 0.008}$	$7.184_{\pm 0.008}$	$7.018_{\pm 0.008}$	$6.658_{\pm 0.061}$	L92
CF Cas	4.875	$0.269_{\pm 0.041}$	$0.556_{\pm 0.021}$	$11.060_{\pm 0.030}$	$8.590_{\pm 0.008}$	$8.126_{\pm 0.008}$	$7.900_{\pm 0.008}$	$7.608_{\pm 0.061}$	M11
CV Mon	5.379	$0.523_{\pm 0.043}$	$0.705_{\pm 0.018}$	$10.310_{\pm 0.030}$	$7.314_{\pm 0.008}$	$6.781_{\pm 0.008}$	$6.529_{\pm 0.008}$	$6.165_{\pm 0.061}$	M11
QZ Nor	5.401 (*)	$0.443_{\pm 0.036}$	$0.289_{\pm 0.020}$	$8.870_{\pm 0.030}$	$7.085_{\pm 0.008}$	$6.748_{\pm 0.008}$	$6.614_{\pm 0.008}$	$6.360_{\pm 0.061}$	L92
V Cen	5.495	$1.288_{\pm 0.023}$	$0.265_{\pm 0.016}$	$6.820_{\pm 0.030}$	$5.019_{\pm 0.008}$	$4.642_{\pm 0.008}$	$4.498_{\pm 0.008}$	$4.249_{\pm 0.061}$	L92
CS Vel	5.905	$0.221_{\pm 0.042}$	$0.716_{\pm 0.027}$	$11.700_{\pm 0.030}$	$8.771_{\pm 0.008}$	$8.246_{\pm 0.008}$	$8.011_{\pm 0.008}$	$7.643_{\pm 0.061}$	L92
V367 Sct	6.293	$0.467_{\pm 0.041}$	$1.145_{\pm 0.043}$	$11.610_{\pm 0.030}$	$7.605_{\pm 0.008}$	$6.955_{\pm 0.008}$	$6.651_{\pm 0.008}$	$6.152_{\pm 0.061}$	L92
U Sgr	6.745	$1.514_{\pm 0.024}$	$0.408_{\pm 0.007}$	$6.690_{\pm 0.030}$	$4.506_{\pm 0.008}$	$4.100_{\pm 0.008}$	$3.912_{\pm 0.008}$	$3.636_{\pm 0.061}$	M11
RS Ori	7.567	$0.553_{\pm 0.027}$	$0.332_{\pm 0.010}$	$8.410_{\pm 0.030}$	$6.398_{\pm 0.008}$	$6.020_{\pm 0.008}$	$5.860_{\pm 0.008}$	$5.589_{\pm 0.061}$	M11
DL Cas	8.001	$0.511_{\pm 0.031}$	$0.487_{\pm 0.005}$	$8.970_{\pm 0.030}$	$6.550_{\pm 0.008}$	$6.101_{\pm 0.008}$	$5.892_{\pm 0.008}$	$5.593_{\pm 0.061}$	M11
S Nor	9.754	$1.025_{\pm 0.027}$	$0.182_{\pm 0.008}$	$6.420_{\pm 0.030}$	$4.674_{\pm 0.008}$	$4.288_{\pm 0.008}$	$4.149_{\pm 0.008}$	$3.905_{\pm 0.061}$	L92
TW Nor	10.786	$0.383_{\pm 0.042}$	$1.190_{\pm 0.023}$	$11.670_{\pm 0.030}$	$7.442_{\pm 0.008}$	$6.712_{\pm 0.008}$	$6.375_{\pm 0.008}$	$5.865_{\pm 0.061}$	L92
V340 Nor	11.288	$0.443_{\pm 0.036}$	$0.312_{\pm 0.009}$	$8.370_{\pm 0.030}$	$6.211_{\pm 0.008}$	$5.745_{\pm 0.008}$	$5.573_{\pm 0.008}$	$5.284_{\pm 0.061}$	L92

**Notes.** Parallaxes in the first part of the table are from GDR2 for the companions; parallaxes in the second part are from Cantat-Gaudin et al. (2018) based on GDR2 with revised uncertainties. Reddenings  $E(B - V)$  are taken from the DDO database (Fernie et al. 1995), to which we applied a multiplicative factor of 0.94. Mean apparent magnitudes in  $V, J, H, K_s$  bands are from the catalog compiled by Groenewegen (2018):  $V$  band magnitudes are originally from Mel'nik et al. (2015) and NIR magnitudes are converted in the 2MASS system with the original references provided in the last column. Apparent Wesenheit magnitudes on the WFC3 system ( $m_H^W$ ) are also provided; their uncertainties include the photometric transformation errors. (\*) Cepheid pulsating in the first-overtone mode. In this case the period was converted following the approach described in Sect. 2.4. (\*\*) The parallaxes presented in this table do not include the parallax zero-point offset term. (\*\*)  $m_H^W$  apparent magnitudes presented in this table do not include the addition of the CRNL term.

**References.** (G14) Genovali et al. (2014); (L92) Laney & Stobie (1992); (M11) Monson & Pierce (2011); (2MASS) Skrutskie et al. (2006); (G18) Groenewegen (2018); (W84) Welch et al. (1984); (B97) Barnes et al. (1997); (SPIPS) Light curve fitting with the SPIPS algorithm (Mérand et al. 2015; Trahin 2019).

and

$$\begin{aligned}
 K_{2\text{MASS}} &= K_{\text{CIT}} + 0.001 (J_{\text{CIT}} - K_{\text{CIT}}) - 0.019, \\
 J_{2\text{MASS}} &= K_{2\text{MASS}} + 1.068 (J_{\text{CIT}} - K_{\text{CIT}}) - 0.020, \\
 H_{2\text{MASS}} &= K_{2\text{MASS}} + 1.000 (H_{\text{CIT}} - K_{\text{CIT}}) + 0.034.
 \end{aligned}$$

The NIR magnitudes from Genovali et al. (2014) are derived by template fitting and provided in the 2MASS system. For the

remaining stars the mean magnitude is computed as the median of the available data in Welch et al. (1984), Schechter et al. (1992), and 2MASS (Skrutskie et al. 2006). For RS Nor, the averaged NIR magnitudes were derived by fitting the photometric light curves using the SPIPS algorithm (Mérand et al. 2015). In the  $V$  band, all mean magnitudes are provided in the standard

Johnson system and taken from [Mel'nik et al. \(2015\)](#). An uncertainty of 0.03 mag on those magnitudes is adopted.

Based on apparent magnitudes, we built the reddening-free Wesenheit magnitudes  $m_H^W$  ([Madore 1982](#)), which are a combination of HST-band apparent magnitudes defined by [Riess et al. \(2018b\)](#) as

$$m_H^W = F160W - R(F555W - F814W), \quad (2)$$

where  $R = 0.386$  is derived from the [Fitzpatrick \(1999\)](#) formulation with  $R_V = 3.3$ .

Different formulations for the extinction law are available in the literature ([Savage & Mathis 1979](#); [Cardelli et al. 1989](#)). We adopt the [Fitzpatrick \(1999\)](#) formulation with  $R_V = 3.3$ , which yields  $R_J = 0.86$ ,  $R_H = 0.55$ , and  $R_K = 0.37$ . This allows a direct comparison of our calibration with that of [Riess et al. \(2016\)](#), based on HST Fine Guidance Sensor (FGS) and HST Wide Field Camera 3 (WFC3) measurements (see Sects. 3.2 and 3.3).

[Riess et al. \(2018a\)](#) provides photometric data in the  $F160W$ ,  $F555W$ , and  $F814W$  bands for 50 MW Cepheids. Using the stars in common between this sample and the [Groenewegen \(2018\)](#) catalog, we derive the set of linear transformations between HST system and ground-based apparent magnitudes, with a scatter of 0.06 mag:

$$\begin{aligned} F160W &= H + 0.25(J - H) - 0.030, \\ F555W &= V + 0.28(J - H) + 0.020, \\ F814W &= V - 0.47(V - H) - 0.035. \end{aligned}$$

We note that the transformation from ground-based magnitudes into the HST system requires accounting for the count-rate non-linearity (CRNL) effect ([Riess et al. 2018a](#)). This bias affects the infrared detectors on WFC3, and has the consequence of decreasing the magnitude of faint stars like extragalactic CCs, compared to bright stars like Milky Way CCs. This correction is performed by adding 0.026 mag to HST  $F160W$  apparent magnitudes ([Riess et al. 2019a](#)).

We account for the width of the instability strip (IS) by adding in quadrature an additional term in the photometry errors listed in Table 3. In the  $V$  band, [Macri et al. \(2006\)](#) find a dispersion of 0.23 mag; an intrinsic width of 0.22 mag is obtained after subtracting the estimated measurement errors. In the  $J$  and  $H$  bands, [Madore et al. \(2017\)](#) find a scatter of 0.12 mag, which leaves an intrinsic width of 0.11 mag in NIR bands. In the  $K_S$  band, [Persson et al. \(2004\)](#) find a scatter of 0.084 mag based on a Large Magellanic Cloud (LMC) study, which leaves 0.07 mag for the width of the IS after subtracting error measurements. Finally, [Riess et al. \(2019b\)](#) find a dispersion of 0.075 mag in the  $W_H$  band, yielding an intrinsic width of 0.07 mag for the IS.

In order to compute absolute magnitudes, we need to correct apparent magnitudes from interstellar absorption. We take  $E(B - V)$  values from the DDO database ([Fernie et al. 1995](#)), which is a compilation of various  $E(B - V)$  values from the literature determined in the same system. Following [Groenewegen \(2018\)](#), we apply a multiplicative factor of 0.94 to these reddening values.

#### 2.4. Pulsation modes

The identification of first-overtone (FO) Cepheids is essential for the Leavitt law calibration. These stars belong to a parallel sequence on the PL plane and their pulsation period can be converted into a fundamentalized period ([Feast & Catchpole 1997](#); [Kovtyukh et al. 2016](#)). We reviewed the different pulsation modes found in the literature for the stars in our sample

**Table 4.** Pulsation mode of the Cepheids in our sample.

Cepheid	GDR2	Literature	Adopted
AW Per	FU	FU <sup>(a,b)</sup>	FU
AX Cir	FU	FU <sup>(a,b)</sup>	FU
BP Cir	FO	FU <sup>(b)</sup> , FO <sup>(a,c,d,e)</sup>	★
CF Cas	FU	FU <sup>(a,b)</sup>	FU
CG Cas	FU	FU <sup>(a,b)</sup>	FU
CM Sct	FU	FU <sup>(a,b)</sup>	FU
CS Vel	FU	FU <sup>(a,b)</sup>	FU
CV Mon	–	FU <sup>(b)</sup>	FU
$\delta$ Cep	–	FU <sup>(b)</sup>	FU
DF Cas	FU	FU <sup>(a)</sup>	FU
DL Cas	FU	FU <sup>(a,b)</sup>	FU
DK Vel	FO	FU <sup>(b)</sup> , FO <sup>(a,c)</sup>	★
ER Car	FU	FU <sup>(a,b)</sup>	FU
EV Sct	FO	FO <sup>(a,b)</sup>	FO
QZ Nor	FO	FU <sup>(b)</sup> , FO <sup>(a)</sup>	FO
RS Nor	FU	FU <sup>(a,b)</sup>	FU
RS Ori	FO	FU <sup>(a,b)</sup>	FU
RS Pup	FU	FU <sup>(a,b)</sup>	FU
S Nor	FU	FU <sup>(a,b)</sup>	FU
SX Vel	FU	FU <sup>(a,b)</sup>	FU
SY Nor	FU	FU <sup>(a,b)</sup>	FU
TV CMa	FU	FU <sup>(a,b)</sup>	FU
TW Nor	–	FU <sup>(b)</sup>	FU
U Sgr	FU	FU <sup>(a,b)</sup>	FU
V340 Nor	–	FU <sup>(a,b)</sup>	FU
V350 Sgr	FO	FU <sup>(a,b)</sup>	FU
V367 Sct	–	FU <sup>(f)</sup> , FO <sup>(b)</sup>	FU
V532 Cyg	FO	FU <sup>(b)</sup> , FO <sup>(a)</sup>	FO
V659 Cen	FU	FU <sup>(b)</sup> , FO <sup>(a,c)</sup>	FU
V950 Sco	FO	FU <sup>(b)</sup> , FO <sup>(a)</sup>	FO
V Cen	FU	FU <sup>(a,b)</sup>	FU
VW Cru	FU	FU <sup>(a,b)</sup>	FU
X Cru	FU	FU <sup>(a,b)</sup>	FU

**Notes.** FU = fundamental; FO = first overtone; ★ = excluded because of uncertain pulsation mode.

**References.** (a) [Ripepi et al. \(2019\)](#); (b) [Luck \(2018\)](#); (c) [Zabolotskikh et al. \(2004\)](#); (d) [Evans et al. \(1992\)](#); (e) [Usenko et al. \(2014\)](#); (f) [Anderson et al. \(2013\)](#).

and followed in particular the pulsation modes provided by the reclassification from [Ripepi et al. \(2019\)](#).

The pulsation modes for the Cepheids in our sample are displayed in Table 4. The second and third column of this table give the pulsation mode provided by the GRD2 catalog and by the literature, respectively. The last column gives the adopted pulsation mode.

For BP Cir and DK Vel, different pulsation modes were found: they are both classified as FO Cepheids by GDR2 and other studies ([Zabolotskikh et al. 2004](#); [Ripepi et al. 2019](#)), while they are listed as fundamentals by [Luck \(2018\)](#). The two stars are also consistent with fundamental pulsators in the PL plane. Given the disagreement between the different references about the pulsation mode of BP Cir and DK Vel, we decided to exclude them from the sample.

In order to establish accurate PL and PW relations without excluding the first overtones, we converted their observed periods  $P_{FO}$  into the fundamental mode equivalent period  $P_F$  using

**Table 5.** Period conversion of first overtones into fundamental pulsators.

Cepheid	$P_{FO}$	$P_F$
EV Sct	3.091	4.396
V532 Cyg	3.284	4.675
V950 Sco	3.380	4.814
QZ Nor	3.786	5.401

the equation by Kovtyukh et al. (2016):

$$P_{FO}/P_F = -0.0239_{\pm 0.0031} \log P_F - 0.0404_{\pm 0.0035} [\text{Fe}/\text{H}] + 0.7187_{\pm 0.0017}.$$

Field and cluster Cepheids have similar distributions in the Galactic plane, so they have similar metallicity distributions and both can be assumed close to solar (Romaniello et al. 2008). The first overtones of the sample have periods  $P_{FO}$  comprised between 3 and 4 days. In this range of periods, we can approximate the previous equation by the linear relation:

$$P_F = 1.4459 P_{FO} - 0.0736. \quad (3)$$

The conversion of first overtones into fundamentals is listed in Table 5. The positions of these Cepheids in the PL plane after the transformation are consistent with the distribution of fundamental pulsators.

Even though converting first overtones into fundamentals may introduce a small uncertainty on periods, we decided to include them in the sample for the calibration of the Leavitt law. The periods obtained after conversion with the relations from Feast & Catchpole (1997) and Kovtyukh et al. (2016) only differ by 0.006 days. Gallenne et al. (2018) find a difference of less than 1% between an empirical conversion law and a theoretical one. Including the five first overtones of the sample with their modified periods instead of rejecting them introduces only a very small change on the intercept of the PL relation and improves the precision of the fit.

### 3. Results

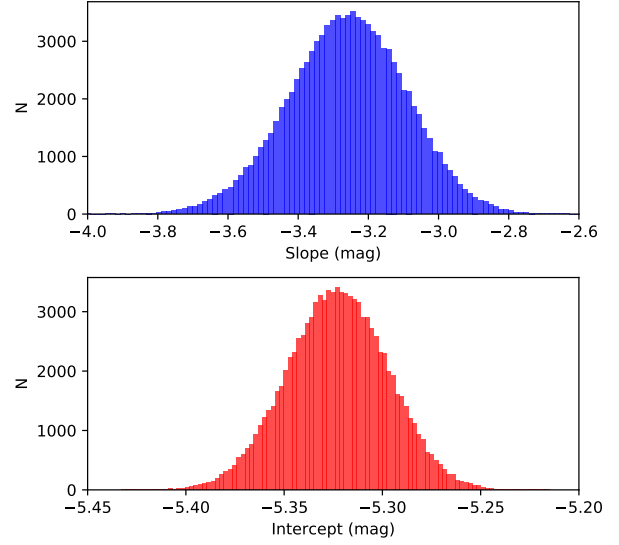
#### 3.1. Calibration of the Leavitt law

In this section we combine the 22 Cepheid companions with the 14 open cluster Cepheids. Their parameters are listed in Table 3. We found five Cepheids present in both samples. For these five stars the companion parallax and the cluster parallax agree within  $1\sigma$  except for U Sgr, which is at  $1.2\sigma$ . In order to avoid any correlation between our two sets of parallaxes, for these five stars we recomputed the Cantat-Gaudin et al. (2018) cluster parallaxes as the median of all stars parallaxes after excluding the companion. We found our new cluster parallaxes to differ by  $0.5 \mu\text{as}$  at most from the original values, so we adopted these new parallax values and considered the two sources of measurement to be independent and non-correlated. For these five Cepheids, both parallax measurements (cluster and companion) are considered independently in the linear fit.

In order to calibrate the PL relations and the Period–Wesenheit (PW) relations, we used the approach introduced by Feast & Catchpole (1997) and Arenou et al. (1999) and we computed the Astrometric Based Luminosity (ABL), defined as

$$ABL = 10^{0.2M_\lambda} = \varpi 10^{0.2m_\lambda - 2}, \quad (4)$$

where  $M_\lambda$  is the absolute magnitude,  $m_\lambda$  is the dereddened apparent magnitude, and  $\varpi$  is the parallax in milliarcseconds. Cali-



**Fig. 3.** Results of the Monte Carlo technique for a PL fit of the form  $K_S = a(\log P - \log P_0) + b$  where  $\log P_0 = 0.84$ . Top and bottom panels: distribution of the slope  $a$  and intercept  $b$ , respectively.

brating the Leavitt Law following this approach is equivalent to determining the coefficients  $a$  and  $b$  in the equation

$$ABL = 10^{0.2[a(\log P - \log P_0) + b]}. \quad (5)$$

We performed a weighted fit of the ABL function by using the `curve_fit` function from the python Scipy library. The robustness of the fit and of the uncertainties is ensured by a Monte Carlo approach, applied with 100 000 iterations. The distributions of the slope and zero-point of our  $K_S$  Leavitt law obtained by this technique are displayed via histograms in Fig. 3.

We used the formalism detailed in Gallenne et al. (2017), i.e., we adopted the linear parameterization

$$M_\lambda = b_\lambda + a_\lambda (\log P - \log P_0), \quad (6)$$

where  $a_\lambda$  and  $b_\lambda$  are respectively the slope and the zero-point of the PL relation. This parameterization removes the correlation between  $a_\lambda$  and  $b_\lambda$  and minimizes their respective uncertainties. The optimum value of  $\log P_0$  depends on the dataset (see Gallenne et al. (2017) for further details)

$$\log P_0 = \frac{\langle \log P_i / e_i^2 \rangle}{\langle 1 / e_i^2 \rangle}, \quad (7)$$

where  $\log P_i$  are the periods of the stars, and  $e_i$  are the uncertainties on their parallax;  $\langle \rangle$  denotes the averaging operator. We find our sample centered around  $\log P_0 = 0.84$ .

GDR2 parallaxes are subject to a zero-point (ZP) offset, whose value was studied extensively but is still debated. Lindgren et al. (2018) used quasars ( $G \sim 19$  mag) to derive that *Gaia* parallaxes are underestimated by 0.029 mas. Arenou et al. (2018) finds a zero-point of  $-0.0319$  mas based on Milky Way Cepheids ( $G \sim 8$  mag), in agreement with the  $-0.031$  mas estimate by Graczyk et al. (2019) from detached eclipsing binaries ( $G \sim 9$  mag) and surface brightness-color relations. Larger values were also found by Ripepi et al. (2019) and Stassun & Torres (2018), who find zero-point offsets of  $-0.070$  mas and  $-0.082$  mas respectively. Intermediary values were derived by

**Table 6.** Zero-point offset for GDR2 parallaxes found in the literature.

ZP <sub>GDR2</sub> (mas)	Reference	Type of sources	Typical $G$ (mag)
−0.029	<a href="#">Lindegren et al. (2018)</a>	Quasars	19
−0.031 $_{\pm 0.011}$	<a href="#">Graczyk et al. (2019)</a>	Eclipsing binaries	9
−0.0319 $_{\pm 0.0008}$	<a href="#">Arenou et al. (2018)</a>	MW Cepheids	8
−0.035 $_{\pm 0.016}$	<a href="#">Sahlholdt &amp; Silva Aguirre (2018)</a>	Dwarf stars	9
−0.041 $_{\pm 0.010}$	<a href="#">Hall et al. (2019)</a>	Red giants	13
−0.046 $_{\pm 0.013}$	<a href="#">Riess et al. (2018a)</a>	MW Cepheids	9
−0.049 $_{\pm 0.018}$	<a href="#">Groenewegen (2018)</a>	MW Cepheids (HST)	8
−0.053 $_{\pm 0.003}$	<a href="#">Zinn et al. (2019)</a>	Red giants	13
−0.054 $_{\pm 0.006}$	<a href="#">Schönrich et al. (2019)</a>	GDR2 RV	12
−0.057 $_{\pm 0.003}$	<a href="#">Muraveva et al. (2018)</a>	RR Lyrae	12
−0.070 $_{\pm 0.010}$	<a href="#">Ripepi et al. (2019)</a>	LMC Cepheids	15
−0.082 $_{\pm 0.033}$	<a href="#">Stassun &amp; Torres (2018)</a>	Eclipsing binaries	9

**Table 7.** Coefficients of the PL relation obtained with GDR2 parallaxes of companions and open clusters (left) and with direct parallaxes of Cepheids (right), for different parallax zero-point offsets.

Band	$a$	$b$	$\rho$	$\chi_r^2$	$\sigma$	$a$	$b$	$\rho$	$\chi_r^2$	$\sigma$	ZP (mas)
Parallaxes of companions and open clusters						Parallaxes of Cepheids					
$V$	−2.486 $_{\pm 0.246}$	−3.782 $_{\pm 0.051}$	0.15	0.27	0.18	−2.093 $_{\pm 0.236}$	−3.888 $_{\pm 0.050}$	0.09	0.58	0.23	−0.031
$J$	−3.079 $_{\pm 0.187}$	−4.964 $_{\pm 0.032}$	0.21	0.38	0.16	−2.680 $_{\pm 0.154}$	−5.040 $_{\pm 0.033}$	0.03	0.97	0.21	−0.031
$H$	−3.223 $_{\pm 0.185}$	−5.263 $_{\pm 0.032}$	0.21	0.34	0.16	−2.799 $_{\pm 0.151}$	−5.331 $_{\pm 0.033}$	0.02	0.91	0.21	−0.031
$K_S$	−3.268 $_{\pm 0.165}$	−5.363 $_{\pm 0.026}$	0.25	0.38	0.14	−2.856 $_{\pm 0.127}$	−5.419 $_{\pm 0.028}$	0.01	1.18	0.22	−0.031
$W_H$	−3.340 $_{\pm 0.180}$	−5.476 $_{\pm 0.030}$	0.23	0.41	0.16	−2.911 $_{\pm 0.141}$	−5.534 $_{\pm 0.031}$	0.01	0.93	0.20	−0.031
$V$	−2.481 $_{\pm 0.244}$	−3.731 $_{\pm 0.050}$	0.15	0.29	0.18	−2.111 $_{\pm 0.236}$	−3.829 $_{\pm 0.050}$	0.09	0.53	0.21	−0.046
$J$	−3.068 $_{\pm 0.184}$	−4.918 $_{\pm 0.032}$	0.21	0.43	0.16	−2.692 $_{\pm 0.153}$	−4.987 $_{\pm 0.033}$	0.03	0.90	0.19	−0.046
$H$	−3.215 $_{\pm 0.185}$	−5.217 $_{\pm 0.031}$	0.22	0.37	0.16	−2.811 $_{\pm 0.151}$	−5.278 $_{\pm 0.033}$	0.03	0.82	0.19	−0.046
$K_S$	−3.257 $_{\pm 0.163}$	−5.323 $_{\pm 0.026}$	0.25	0.44	0.14	−2.865 $_{\pm 0.126}$	−5.370 $_{\pm 0.028}$	0.01	1.09	0.19	−0.046
$W_H$	−3.332 $_{\pm 0.177}$	−5.432 $_{\pm 0.029}$	0.23	0.47	0.17	−2.923 $_{\pm 0.141}$	−5.483 $_{\pm 0.031}$	0.01	0.85	0.18	−0.046
$V$	−2.475 $_{\pm 0.243}$	−3.680 $_{\pm 0.050}$	0.15	0.32	0.19	−2.130 $_{\pm 0.235}$	−3.771 $_{\pm 0.049}$	0.10	0.50	0.21	−0.061
$J$	−3.060 $_{\pm 0.179}$	−4.874 $_{\pm 0.032}$	0.20	0.52	0.17	−2.703 $_{\pm 0.153}$	−4.936 $_{\pm 0.032}$	0.03	0.86	0.18	−0.061
$H$	−3.207 $_{\pm 0.183}$	−5.172 $_{\pm 0.031}$	0.21	0.44	0.17	−2.824 $_{\pm 0.151}$	−5.226 $_{\pm 0.032}$	0.03	0.76	0.17	−0.061
$K_S$	−3.248 $_{\pm 0.162}$	−5.283 $_{\pm 0.025}$	0.24	0.55	0.16	−2.873 $_{\pm 0.125}$	−5.321 $_{\pm 0.027}$	0.01	1.04	0.18	−0.061
$W_H$	−3.322 $_{\pm 0.175}$	−5.389 $_{\pm 0.029}$	0.22	0.58	0.18	−2.934 $_{\pm 0.140}$	−5.433 $_{\pm 0.030}$	0.02	0.81	0.17	−0.061

**Notes.** The equations are of the form  $M = a (\log P - 0.84) + b$ , and  $\rho$  is the correlation between  $a$  and  $b$ .

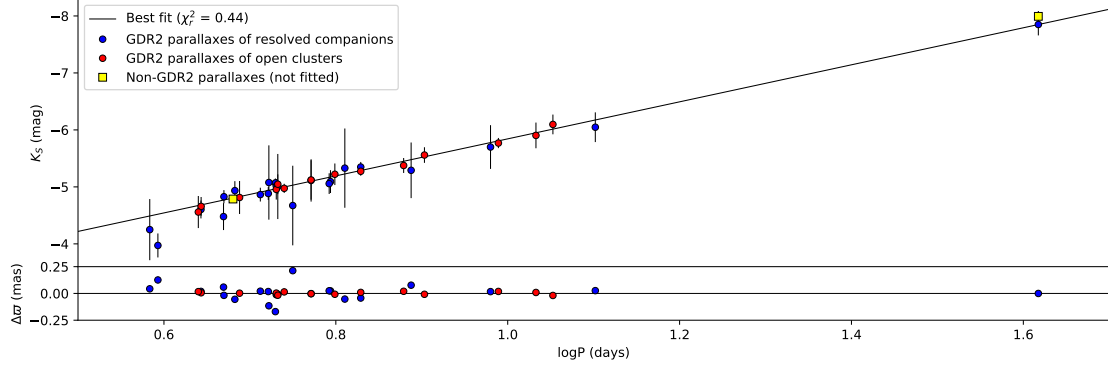
[Riess et al. \(2018a\)](#) and [Groenewegen \(2018\)](#), who estimate −0.046 mas and −0.049 mas respectively. The recent determinations of ZP<sub>GDR2</sub> are listed in Table 6. In the following, we adopt ZP<sub>GDR2</sub> = −0.046 mas ([Riess et al. 2018a](#)) from Cepheids, which is close to the median of all values (see Table 6).

The PL coefficients obtained in different bands are listed in Table 7 for different ZP<sub>GDR2</sub> values. The Leavitt law calibration in the  $K_S$  band is displayed in Fig. 4. The lower panel shows residuals in terms of parallax, computed as the difference between the input parallax and the parallax given by the best fit. This calibration gives a reduced  $\chi^2$  of 0.44 and a dispersion of  $\sigma = 0.14$  mag.

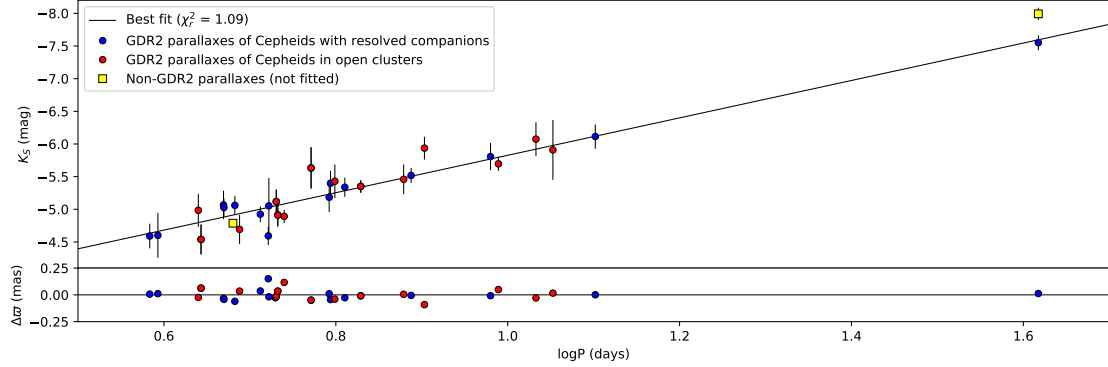
An equivalent calibration, based this time on direct Cepheid parallaxes, is presented in Fig. 5. When the CC parallaxes are adopted, we obtain  $\chi_r^2 = 1.09$  and a dispersion of  $\sigma = 0.19$  mag. The dispersion of the PL relation based on Cepheid parallaxes (Fig. 5) does not appear to be systematic, but rather results in a larger spread not accounted for in the uncertainties. The PL coefficients derived from GDR2 parallaxes of Cepheids are also provided in Table 7.

We note that very accurate distance measurements are available for a few classical Cepheids, independently of *Gaia* DR2. They can be used to check the consistency of GDR2 parallaxes. The Cepheid RS Pup has been studied in detail by [Kervella et al. \(2014\)](#) who estimated its parallax to  $0.524 \pm 0.022$  mas using polarimetric HST images of the light echoes propagating in its circumstellar nebula (see also [Kervella et al. 2017](#)). A second interesting measurement is the distance of the short-period binary Cepheid V1334 Cyg by [Gallenne et al. \(2018\)](#). It is the most precise parallax determination for a Cepheid, with a value of  $1.388 \pm 0.015$  mas. This measurement was obtained by observing the orbit of the system by spectroscopy and optical interferometry. This estimate differs by  $3.6\sigma$  with the GDR2 parallax value ( $1.151 \pm 0.066$  mas). These two independent distance measurements are represented by yellow squares on the PL relations in Figs. 4 and 5, but are not included in the fit since they are not from GDR2. In the case where companion parallaxes and cluster parallaxes are adopted, the two points based on independent measurements agree with the fitted relation at  $1\sigma$ . However, in the case of a PL relation based on direct Cepheid parallaxes, both





**Fig. 4.** Period–luminosity diagram in the  $K_S$  band calibrated with GDR2 parallaxes of Cepheids companions (blue) and open clusters (red). The two yellow squares are V1334 Cyg and RS Pup; they are not included in the fit of the PL relation.



**Fig. 5.** Same as Fig. 4, but using directly GDR2 parallaxes of Cepheids.

absolute magnitudes derived from the independent points differ by  $2.9\sigma$  from the best fit. The Cepheid RS Pup is particularly interesting since it has a resolved companion listed in our sample (see Table 1). We note that the RS Pup independent estimate is in very good agreement with the GDR2 parallax of RS Pup companion ( $0.503 \pm 0.045$  mas), but differs by 0.060 mas from the GDR2 parallax of the Cepheid itself ( $0.584 \pm 0.026$  mas).

### 3.2. Comparison with the literature

In this section, we compare our sample of GDR2 parallaxes with the corresponding parallaxes predicted by a PL calibration based on non-*Gaia* data. Riess et al. (2016; hereafter R16) use ten MW Cepheid parallaxes from HST/FGS (Benedict et al. 2007), three HIPPARCOS measurements and two Cepheids with parallaxes measured by spatial scanning with the HST/WFC3 (Riess et al. 2014; Casertano et al. 2016). These measurements constitute the MW anchor from R16. They combine it with megamasers in NGC 4258 and eight detached eclipsing binaries in the LMC to derive a final Hubble constant  $H_0 = 73.24 \pm 1.74 \text{ km s}^{-1} \text{ Mpc}^{-1}$ , associated with the corresponding PL relation in the Wesenheit HST/WFC3 system:

$$M_H^W = -5.93 - 3.26 (\log P - 1). \quad (8)$$

For the MW anchor only, the  $H_0$  value is  $76.18 \pm 2.37 \text{ km s}^{-1} \text{ Mpc}^{-1}$ . From the ratio of the two  $H_0$  values, we offset Eq. (8) and derive the following PL relation for MW Cepheids only:

$$M_H^W = -5.85 - 3.26 (\log P - 1). \quad (9)$$

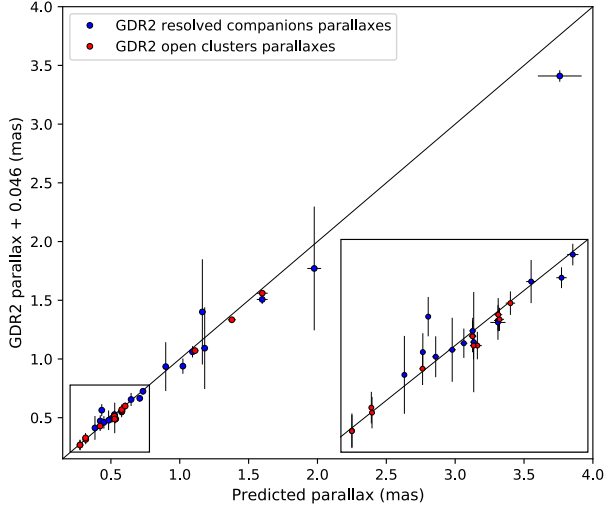
We use this Galactic PL calibration based on the Milky Way anchor to compute the predicted parallaxes  $\varpi_{R16}$  for each star in our sample:

$$5 \log \varpi_{R16} = M_H^W - m_H^W + 10. \quad (10)$$

Here  $m_H^W$  is the apparent magnitude in the Wesenheit system corrected for the CRNL effect (see Sect. 2.3) and  $M_H^W$  is derived from the PL relation given by Eq. (9).

The choice of an  $R$  value in agreement with Riess et al. (2016) (see Sect. 3) ensures the consistency of this comparison. To account for the width of the instability strip ( $\sigma = 0.07$  mag in the  $W_H$  band) and for the photometric transformations from ground to HST system ( $\sigma = 0.06$  mag), we set the apparent magnitudes uncertainties to 0.09 mag. Figure 6 shows the comparison between the GDR2 parallaxes of our sample of stars corrected by a  $-0.046$  mas offset and the predicted parallaxes from R16. The GDR2 parallaxes appear to be slightly underestimated compared with the predicted values, especially for Cepheids with large parallax values.

The prototype  $\delta$  Cep is particularly interesting for this study: it hosts a resolved companion with a GDR2 parallax and it is also present in the sample of HST/FGS parallaxes by Benedict et al. (2007). The GDR2 parallax of its companion is  $3.393 \pm 0.049$  mas, while its HST/FGS parallax is  $3.66 \pm 0.15$  mas. These two measurements differ by  $1.7\sigma$  (7% in relative terms), which agrees with the general trend observed in Fig. 6. We note that  $\delta$  Cep has no valid parallax in GDR2, so its companion parallax is the only possible alternative to HST/FGS measurements.



**Fig. 6.** Comparison of GDR2 parallaxes of resolved companions and open clusters hosting Cepheids with the predicted parallaxes using the MW PL calibration given in Eq. (9). The solid black line corresponds to the identity line.

In Table 8 we present different PL calibrations found in the literature based on various methods and data. [Benedict et al. \(2007\)](#) derive a  $K$ -band PL relation based on HST/FGS parallaxes of seven Galactic Cepheids in the CIT system. We converted this result in the 2MASS system using the relation from [Carpenter \(2001\)](#). The investigation by [Fouqué et al. \(2007\)](#) provides a PL calibration in the  $K_S$  band, based on HST/FGS and HIPPARCOS parallaxes, as well as infrared surface brightness (IRSB) and interferometric Baade-Wesselink parallaxes. Recently, [Gieren et al. \(2018\)](#) derived a calibration of the PL relation using a IRSB Baade-Wesselink-type method to determine individual distances to the Cepheids. The result is in the UKIRT system, but the transformation between UKIRT and 2MASS systems given in [Carpenter \(2001\)](#) shows that this transformation can be neglected. Finally, [Groenewegen \(2018\)](#) established a  $K_S$ -band PL relation based on a large sample of Cepheids parallaxes from GDR2. In Table 8, we report the coefficients obtained after adopting a GDR2 parallax zero-point of  $-0.046$  mas.

We note that our intercept is very similar to that found by [Groenewegen \(2018\)](#), also based on GDR2 data. However, our calibration shows a significant difference ( $\sim 0.1$ – $0.2$  mag) in intercept with previous calibrations based on HST/FGS data ([Benedict et al. 2007](#); [Fouqué et al. 2007](#)).

### 3.3. Implications on the distance scale

The determination of the Hubble constant by [Planck Collaboration VI \(2020\)](#) exhibit a tension at the  $\sim 5\sigma$  level with the latest empirical estimate by [Riess et al. \(2019b\)](#) based on LMC Cepheids combined with masers in NGC 4258 and Milky Way parallaxes measured by the HST/FGS, HST/WFC3, and HIPPARCOS.

Following the method presented in Sect. 4 in [Riess et al. \(2018b\)](#), we translate our previous parallax comparison (see Sect. 3.2) into a comparison in terms of the Hubble constant. We examine the impact of changing the MW anchor alone on the  $H_0$  measurement that depends on three anchors. Therefore, we look at the  $H_0$  value from R16 that pertains only to the MW. We use the relation  $H_{0,\text{GDR2}} = \alpha H_{0,\text{R16}}$ , where  $\alpha = \varpi_{\text{GDR2}}/\varpi_{\text{R16}}$  and  $H_{0,\text{R16}}$  is the value anchored to Milky Way Cepheids only and

**Table 8.** Comparison of our results with other PL relations from the literature.

Reference	$\alpha$	$\beta$
<a href="#">Benedict et al. (2007)</a>	$-3.32_{\pm 0.12}$	$-5.73_{\pm 0.03}$
<a href="#">Fouqué et al. (2007)</a>	$-3.365_{\pm 0.063}$	$-5.647_{\pm 0.066}$
<a href="#">Gieren et al. (2018)</a>	$-3.258_{\pm 0.092}$	$-5.682_{\pm 0.034}$
<a href="#">Groenewegen (2018)</a>	$-3.028_{\pm 0.067}$	$-5.867_{\pm 0.087}$
Present work	$-3.257_{\pm 0.163}$	$-5.844_{\pm 0.037}$

**Notes.** All equations are expressed in the form  $K_S = \alpha(\log P - 1) + \beta$  in the 2MASS system.

**Table 9.** Hubble constant value derived from the comparison between our GDR2 parallax samples and the predicted parallaxes from R16.

	$H_0$ ( $\text{km s}^{-1} \text{Mpc}^{-1}$ ) FU only	$H_0$ ( $\text{km s}^{-1} \text{Mpc}^{-1}$ ) FU + FO
Companions	$72.83 \pm 2.10 \pm 1.89$	$72.49 \pm 2.01 \pm 1.88$
Clusters	$73.11 \pm 2.01 \pm 1.90$	$73.00 \pm 1.99 \pm 1.90$
All Cepheids	$72.99 \pm 1.89 \pm 1.90$	$72.76 \pm 1.86 \pm 1.89$

**Notes.** The first uncertainties are the statistics combined with the systematics, and the second values account for the effect of the GDR2 parallax zero-point. FU = fundamental mode Cepheids; FO = first-overtone mode Cepheids with fundamentalized period.

is equal to  $76.18 \pm 2.37 \text{ km s}^{-1} \text{Mpc}^{-1}$ . The expected parallaxes  $\varpi_{\text{R16}}$  are derived from Eqs. (9) and (10).

For each star of the sample, we derive the corresponding  $\alpha$  value and we adopt a Monte Carlo approach to estimate the final  $\alpha$  value averaged over the sample. We performed this calculation on different subsamples and listed the resulting  $H_0$  values in Table 9. The uncertainties on  $H_0$  include the final error on the R16 estimate excluding the anchors (1.8%), the error on the estimation of  $\alpha$ , and finally the uncertainties on the photometric relations to convert ground-based magnitudes into HST magnitudes (1.5%). Changing the GDR2 parallax offset by 0.015 mas results in a change of 2.6% in the Hubble constant; therefore, we adopted a confidence interval of 0.015 mas around the  $-0.046$  mas zero-point and added a 2.6% uncertainty to account for this effect.

We obtain a final value of  $72.99 \pm 2.68 \text{ km s}^{-1} \text{Mpc}^{-1}$  for fundamental modes only, and  $72.76 \pm 2.65 \text{ km s}^{-1} \text{Mpc}^{-1}$  for all stars included. Both values are very consistent with the LMC and NGC 4258 anchor results derived by [Riess et al. \(2019b\)](#), and also very close to the result by [Reid et al. \(2019\)](#). The last value agrees at the  $1\sigma$  level with that of [Freedman et al. \(2020\)](#) and at the  $2\sigma$  level with the [Planck Collaboration VI \(2020\)](#) measurement.

We note that the CCs used to calibrate the PL relation and  $H_0$  have lower mean periods than most extragalactic Cepheids found by HST. Though there is no evidence of a break in the PL relation at  $\log P = 1$  for the Wesenheit magnitude system ([Bono et al. 1999, 2008](#); [Riess et al. 2016](#)), it remains important to add longer period Cepheids to the parallax calibration to maintain low systematics.

## 4. Conclusions

We presented an original calibration of the Milky Way Leavitt law based on GDR2 parallaxes of resolved Cepheid companions and on GDR2 parallaxes of open clusters hosting Cepheids.



Companion and cluster members are not subject to large amplitude photometric and color variability, which reduces the potential for systematic parallax uncertainties. The comparison of our calibration with previous works based on non-*Gaia* parallaxes indicates a systematic offset between the two measurements. By replacing the trigonometric parallaxes used in R16 by companion and cluster average parallaxes, we render the Milky Way, the LMC, and NGC 4258 Leavitt Laws more consistent with one another: we find a MW estimate of  $73.0 \pm 2.7 \text{ km s}^{-1} \text{ Mpc}^{-1}$  for fundamental modes only and of  $H_0 = 72.8 \pm 2.7 \text{ km s}^{-1} \text{ Mpc}^{-1}$  for all stars included.

The inclusion of the variability of CCs is not expected in the astrometric processing of the third *Gaia* data release. However, the effects of the systematics due to the absence of chromaticity correction on Cepheids parallaxes should be reduced in the next releases thanks to the larger number of measurements. The future developments will help to pursue the community goal to measure  $H_0$  with utmost precision and accuracy.

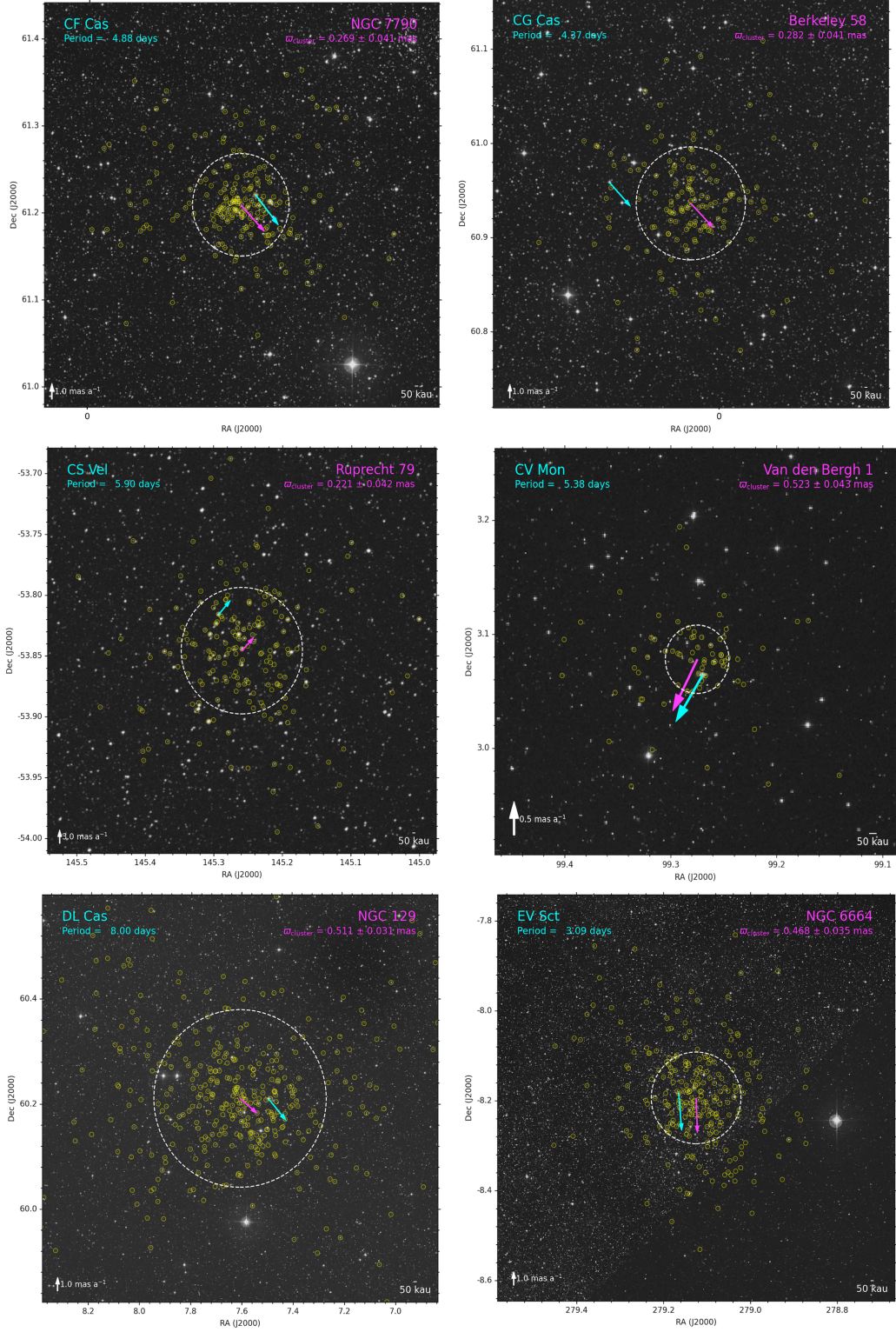
**Acknowledgements.** We gratefully acknowledge D. Graczyk, S. Borgniet and L. Inno for their comments and corrections. We thank T. J. Calderwood from AAVSO for the photometry of Polaris. The research leading to these results has received funding from the European Research Council (ERC) under the European Union's Horizon 2020 research and innovation programme under grant agreement No 695099 (project CepBin). This work has made use of data from the European Space Agency (ESA) mission *Gaia* (<http://www.cosmos.esa.int/gaia>), processed by the *Gaia* Data Processing and Analysis Consortium (DPAC, <http://www.cosmos.esa.int/web/gaia/dpac/consortium>). Funding for the DPAC has been provided by national institutions, in particular the institutions participating in the *Gaia* Multilateral Agreement. The authors acknowledge the support of the French Agence Nationale de la Recherche (ANR), under grant ANR-15-CE31-0012-01 (project Unlock-Cepheids). W.G. and G.P. gratefully acknowledge financial support for this work from the BASAL Centro de Astrofísica y Tecnologías Afines (CATA) AFB-170002. W.G. acknowledges financial support from the Millennium Institute of Astrophysics (MAS) of the Iniciativa Científica Milenio del Ministerio de Economía, Fomento y Turismo de Chile, project IC120009. We acknowledge support from the IdP II 2015 0002 64 and DIR/WK/2018/09 grants of the Polish Ministry of Science and Higher Education and Polish National Science Centre grants MAESTRO UMO-2017/26/A/ST9/00446. This research made use of Astropy7, a community-developed core Python package for Astronomy (Astropy Collaboration 2018). We used the SIMBAD and VIZIER databases and catalog access tool at the CDS, Strasbourg (France), and NASA's Astrophysics Data System Bibliographic Services.

## References

An, D., Terndrup, D. M., & Pinsonneault, M. H. 2007, *ApJ*, **671**, 1640  
 Anderson, R. I. 2018, *A&A*, **611**, L7  
 Anderson, R. I., Eyer, L., & Mowlavi, N. 2013, *MNRAS*, **434**, 2238  
 Anderson, R. I., Saio, H., Ekström, S., Georgy, C., & Meynet, G. 2016, *A&A*, **591**, A8  
 Arenou, F., & Luri, X. 1999, *ASP Conf. Ser.*, **167**, 13  
 Arenou, F., Luri, X., Babusiaux, C., et al. 2018, *A&A*, **616**, A17  
 Astropy Collaboration (Price-Whelan, A. M., et al.) 2018, *AJ*, **156**, 123  
 Barnes, T. G., III, Fernley, J. A., Frueh, M. L., et al. 1997, *PASP*, **109**, 645  
 Benedict, G. F., McArthur, B. E., Feast, M. W., et al. 2007, *AJ*, **133**, 1810  
 Bond, H. E., Nelan, E. P., Remage Evans, N., Schaefer, G. H., & Harmer, D. 2018, *ApJ*, **853**, 55  
 Bono, G., Caputo, F., Castellani, V., & Marconi, M. 1999, *ApJ*, **512**, 711  
 Bono, G., Caputo, F., Fiorentino, G., Marconi, M., & Musella, I. 2008, *ApJ*, **684**, 102  
 Cantat-Gaudin, T., Jordi, C., Vallenari, A., et al. 2018, *A&A*, **618**, A93  
 Cardelli, J. A., Clayton, G. C., & Mathis, J. S. 1989, *ApJ*, **345**, 245  
 Carpenter, J. M. 2001, *AJ*, **121**, 2851  
 Casertano, S., Riess, A. G., Anderson, J., et al. 2016, *ApJ*, **825**, 11  
 Chen, X., de Grijs, R., & Deng, L. 2015, *MNRAS*, **446**, 1268  
 Clark, J. S., Negueruela, I., Lohr, M. E., et al. 2015, *A&A*, **584**, L12  
 Clementini, G., Ripepi, V., Molinaro, R., et al. 2019, *A&A*, **622**, A60  
 Drimmel, R., Bucciarelli, B., & Inno, L. 2019, *Res. Notes Am. Astron. Soc.*, **3**, 79  
 Evans, N. R., Arellano Ferro, A., & Udalska, J. 1992, *AJ*, **103**, 1638  
 Feast, M. W., & Catchpole, R. M. 1997, *MNRAS*, **286**, L1  
 Fernie, J. D., Evans, N. R., Beattie, B., & Seager, S. 1995, *Inf. Bull. Variable Stars*, **4148**

Fitzpatrick, E. L. 1999, *PASP*, **111**, 63  
 Fouqué, P., Arriagada, P., Storm, J., et al. 2007, *A&A*, **476**, 73  
 Freedman, W. L., Madore, B. F., Hoyt, T., et al. 2020, *ApJ*, **891**, 57  
 Gaia Collaboration (Brown, A. G. A., et al.) 2018, *A&A*, **616**, A1  
 Gaia Collaboration (Clementini, G., et al.) 2017, *A&A*, **605**, A79  
 Gallenne, A., Kervella, P., Mérand, A., et al. 2017, *A&A*, **608**, A18  
 Gallenne, A., Kervella, P., Evans, N. R., et al. 2018, *ApJ*, **867**, 121  
 Genovali, K., Lemasle, B., Bono, G., et al. 2014, *A&A*, **566**, A37  
 Gieren, W., Storm, J., Konorski, P., et al. 2018, *A&A*, **620**, A99  
 Graczyk, D., Pietrzyński, G., Gieren, W., et al. 2019, *ApJ*, **872**, 85  
 Groenewegen, M. A. T. 2018, *A&A*, **619**, A8  
 Hall, O. J., Davies, G. R., Elsworth, Y. P., et al. 2019, *MNRAS*, **1036**  
 Kervella, P., Bond, H. E., Cracraft, M., et al. 2014, *A&A*, **572**, A7  
 Kervella, P., Trahin, B., Bond, H. E., et al. 2017, *A&A*, **600**, A127  
 Kervella, P., Gallenne, A., Evans, N. R., et al. 2019, *A&A*, **623**, A117  
 Kharchenko, N. V., Piskunov, A. E., Roeser, S., Schilbach, E., & Scholz, R. D. 2013, *VizieR Online Data Catalog: J/A+A/558/A53*  
 Koen, C., Marang, F., Kilkenny, D., & Jacobs, C. 2007, *MNRAS*, **380**, 1433  
 Kovtyukh, V., Lemasle, B., Chekhonadskikh, F., et al. 2016, *MNRAS*, **460**, 2077  
 Laney, C. D., & Stobie, R. S. 1992, *A&AS*, **93**, 93  
 Leavitt, H. S. 1908, *Ann. Harvard College Observatory*, **60**, 87  
 Leavitt, H. S., & Pickering, E. C. 1912, *Harvard College Obs. Circular*, **173**, 1  
 Lindegren, L. 2018a, *Re-normalising the astrometric chi-square in Gaia DR2*, *Tech. Rep. GAIA-C3-TN-LU-LL-124* (Lund Observatory)  
 Lindegren, L. 2018b, *Gaia DR2 Astrometry*  
 Lindegren, L. 2020, *A&A*, **633**, A1  
 Lindegren, L., Hernández, J., Bombrun, A., et al. 2018, *A&A*, **616**, A2  
 Lohr, M. E., Negueruela, I., Tabernero, H. M., et al. 2018, *MNRAS*, **478**, 3825  
 Luck, R. E. 2018, *AJ*, **156**, 171  
 Macri, L. M., Stanek, K. Z., Bersier, D., Greenhill, L. J., & Reid, M. J. 2006, *ApJ*, **652**, 1133  
 Madore, B. F. 1982, *ApJ*, **253**, 575  
 Madore, B. F., Freedman, W. L., & Moak, S. 2017, *ApJ*, **842**, 42  
 Majaess, D., Turner, D., Moni Bidin, C., et al. 2011, *ApJ*, **741**, L27  
 Mel'nik, A. M., Rautiainen, P., Berdnikov, L. N., Dambis, A. K., & Rastorguev, A. S. 2015, *Astron. Nachr.*, **336**, 70  
 Mérand, A., Kervella, P., Breifelder, J., et al. 2015, *A&A*, **584**, A80  
 Monson, A. J., & Pierce, M. J. 2011, *ApJS*, **193**, 12  
 Muraveva, T., Delgado, H. E., Clementini, G., Sarro, L. M., & Garofalo, A. 2018, *MNRAS*, **481**, 1195  
 Persson, S. E., Madore, B. F., Krzemiński, W., et al. 2004, *AJ*, **128**, 2239  
 Planck Collaboration VI. 2020, *A&A*, **641**, A6  
 Proxauf, B., da Silva, R., Kovtyukh, V. V., et al. 2018, *A&A*, **616**, A82  
 Reid, M. J., Pesce, D. W., & Riess, A. G. 2019, *ApJ*, **886**, L27  
 Riess, A. G. 2019, *Nat. Rev. Phys.*, **2**, 10  
 Riess, A. G., Casertano, S., Anderson, J., MacKenty, J., & Filippenko, A. V. 2014, *ApJ*, **785**, 161  
 Riess, A. G., Macri, L. M., Hoffmann, S. L., et al. 2016, *ApJ*, **826**, 56  
 Riess, A. G., Casertano, S., Yuan, W., et al. 2018a, *ApJ*, **861**, 126  
 Riess, A. G., Casertano, S., Yuan, W., et al. 2018b, *ApJ*, **855**, 136  
 Riess, A. G., Narayan, G., & Calamida, A. 2019a, *Calibration of the WFC3-IR Count-rate Nonlinearity, Sub-percent Accuracy for a Factor of a Million in Flux*, *Tech. Rep.* (Baltimore: Space Telescope Science Institute)  
 Riess, A. G., Casertano, S., Yuan, W., Macri, L. M., & Scolnic, D. 2019b, *ApJ*, **876**, 85  
 Ripepi, V., Molinaro, R., Musella, I., et al. 2019, *A&A*, **625**, A14  
 Romaniello, M., Primas, F., Mottini, M., et al. 2008, *A&A*, **488**, 731  
 Sahlholdt, C. L., & Silva Aguirre, V. 2018, *MNRAS*, **481**, L125  
 Savage, B. D., & Mathis, J. S. 1979, *ARA&A*, **17**, 73  
 Schechter, P. L., Avrukh, I. M., Caldwell, J. A. R., & Keane, M. J. 1992, *AJ*, **104**, 1930  
 Schönrich, R., McMillan, P., & Eyer, L. 2019, *MNRAS*, **487**, 3568  
 Skrutskie, M. F., Cutri, R. M., Stiening, R., et al. 2006, *AJ*, **131**, 1163  
 Stassun, K. G., & Torres, G. 2018, *ApJ*, **862**, 61  
 Trahin, B. 2019, *Theses, Paris Sciences et Lettres; Observatoire de Paris – LESIA ; CNRS*  
 Turner, D. G. 1982, *PASP*, **94**, 1003  
 Turner, D. G. 1986, *AJ*, **92**, 111  
 Turner, D. G. 2010, *Ap&SS*, **326**, 219  
 Turner, D. G., Pedreros, M. H., & Walker, A. R. 1998, *AJ*, **115**, 1958  
 Usenko, I. A., Kniazev, A. Y., Berdnikov, L. N., & Kravtsov, V. V. 2014, *Astron. Lett.*, **40**, 800  
 Verde, L., Treu, T., & Riess, A. G. 2019, *Nat. Astron.*, **3**, 891  
 Welch, D. L., Wieland, F., McAlary, C. W., et al. 1984, *ApJS*, **54**, 547  
 Zabolotskikh, M. V., Rastorguev, A. S., & Egorov, I. E. 2004, *ASP Conf. Ser.*, **316**, 209  
 Zinn, J. C., Pinsonneault, M. H., Huber, D., & Stello, D. 2019, *ApJ*, **878**, 136

## Appendix A: Field charts of open clusters



**Fig. A.1.** Field charts of our candidate Cepheids in their host clusters. The white dashed circles show the radius  $r_{50}$  containing half of the cluster stars, and each yellow circle shows a cluster member. The blue and pink arrows show the Cepheid and cluster proper motion, respectively.



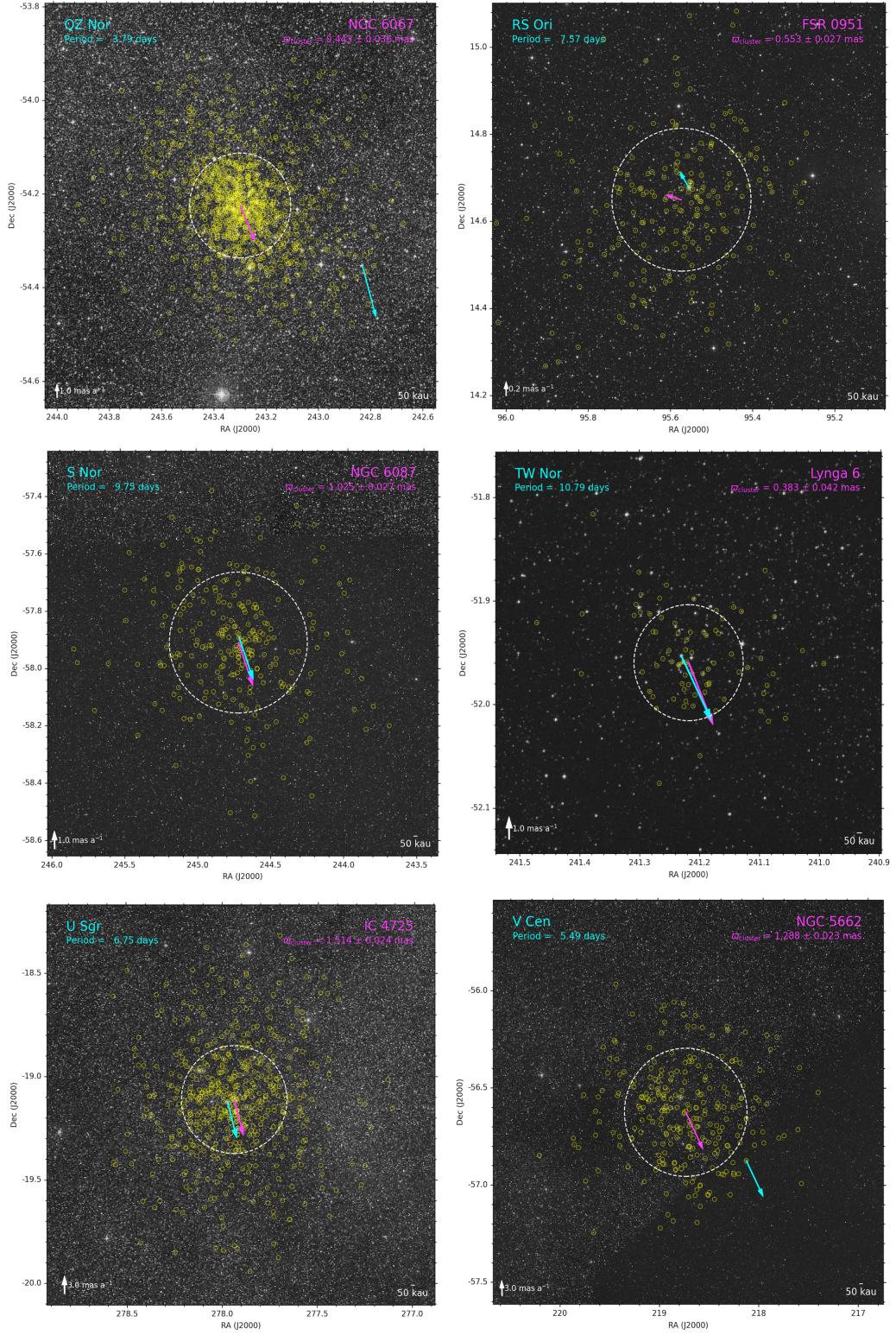


Fig. A.1. continued.

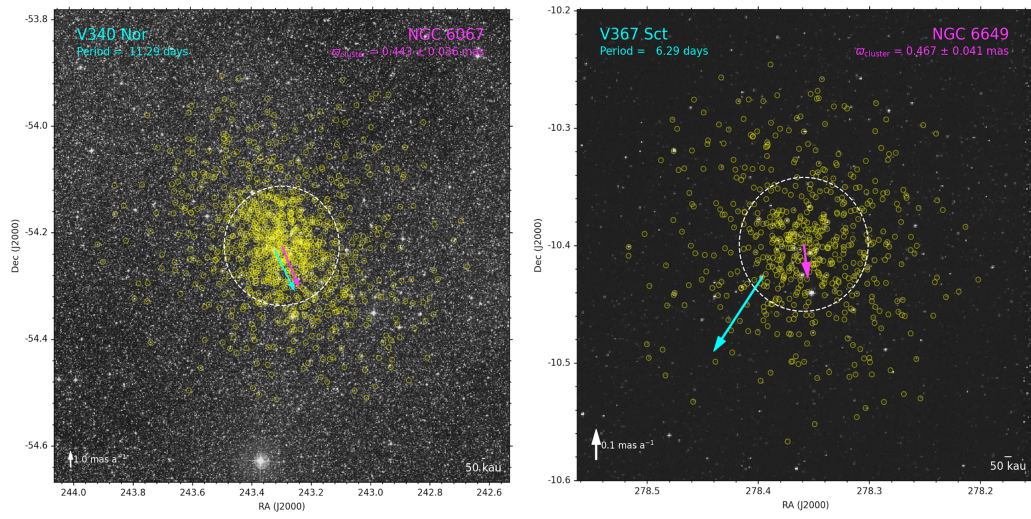


Fig. A.1. continued.

## Chapter 3

# The effect of metallicity on the Leavitt Law

---

<b>3.1</b>	<b>The metallicity effect: definition and values from the literature . . . . .</b>	<b>107</b>
<b>3.2</b>	<b>Photometry . . . . .</b>	<b>111</b>
3.2.1	Photometry for Milky Way Cepheids . . . . .	111
3.2.2	Photometry for Large Magellanic Cloud Cepheids . . . . .	113
3.2.3	Photometry for Small Magellanic Cloud Cepheids . . . . .	114
<b>3.3</b>	<b>Distances . . . . .</b>	<b>115</b>
3.3.1	Gaia EDR3 parallaxes of Milky Way Cepheids . . . . .	115
3.3.2	Distance to Large Magellanic Cloud Cepheids . . . . .	117
3.3.3	Distance to Small Magellanic Cloud Cepheids . . . . .	118
<b>3.4</b>	<b>Metallicity . . . . .</b>	<b>120</b>
3.4.1	Metallicity for Milky Way Cepheids . . . . .	120
3.4.2	Metallicity for LMC and SMC Cepheids . . . . .	122
<b>3.5</b>	<b>Calibration of the P-L relation in the Milky Way and Magellanic Clouds . . .</b>	<b>122</b>
3.5.1	Method . . . . .	123
3.5.1.1	From distances and apparent magnitudes to the P-L coefficients .	123
3.5.1.2	Extinction law and Wesenheit indices . . . . .	123
3.5.1.3	Width of the instability strip . . . . .	124
3.5.1.4	Period cut . . . . .	124
3.5.2	Results . . . . .	124
<b>3.6</b>	<b>Deriving the metallicity effect on the Leavitt law . . . . .</b>	<b>128</b>
3.6.1	The metallicity term in the Milky Way . . . . .	128
3.6.2	The metallicity term from Milky Way and Magellanic Cloud Cepheids . . .	131
3.6.2.1	Method . . . . .	131
3.6.2.2	Results . . . . .	133
3.6.2.3	The effect of CO absorption on <i>Spitzer</i> bands . . . . .	134
3.6.2.4	The dependence of the metallicity effect with wavelength, comparison with the literature . . . . .	135
3.6.2.5	Influence of the radius around the SMC center . . . . .	137
<b>3.7</b>	<b>Conclusion on the metallicity effect . . . . .</b>	<b>139</b>
3.7.1	Summary of the data, method and results . . . . .	139

3.7.2	Limitations and perspectives . . . . .	141
<b>3.8</b>	<b>Publication: <i>The Influence of Metallicity on the Leavitt Law from Geometrical Distances of Milky Way and Magellanic Cloud Cepheids</i>, Breuval et al. 2021, ApJ 913 38 . . . . .</b>	<b>142</b>

---

The calibration of the Cepheid Period-Luminosity relation is constantly improved thanks to the availability of new and more precise distances (e.g. with *Gaia* parallaxes). Yet, the influence of Cepheid chemical composition on the P-L relation is still widely debated. It is responsible for 0.5% of a total of 2.4% in the error budget of the Hubble constant (Riess et al. 2016). A precise calibration of this effect on the Leavitt law, using Cepheids covering a wide range of metallicities, is required to improve the accuracy of the distance scale.

The data necessary to derive this parameter are the same as for the calibration of the P-L relation (i.e. photometry, reddenings and distances) but it additionally requires the information of the metal abundance as well as the use of at least two Cepheid samples of different metallicity. For this purpose, LMC and SMC Cepheids are particularly interesting since they are more metal-poor than their Milky Way counterparts. In this chapter, three Cepheid samples are considered: metal-rich Milky Way Cepheids with precise *Gaia* EDR3 parallaxes, metal-poor LMC Cepheids with a detached eclipsing binary (DEB) distance precise to 1%, and finally metal-poor SMC Cepheids, with a 1.5% precision DEB distance.

First, previous estimations of the metallicity effect from the literature are described in Sect. 3.1. The photometry of the three Cepheid samples is provided in Sect. 3.2. The distances adopted for MW, LMC and SMC Cepheids are described in Sect. 3.3 and the different ranges of metallicity covered by each sample are discussed in Sect. 3.4. The calibration of the period-luminosity relation in our Galaxy and in the Magellanic Clouds is presented in Sect. 3.5. Finally, the effect of metallicity on the Leavitt law is derived and discussed in Sect. 3.6. The analysis described in this chapter was published in Breuval et al. (2021), hereafter B21. This paper is provided in Sect. 3.8. Several improvements and changes are included in this thesis compared with B21, such as the use of more recent reddening values, updated width of the instability strip and photometric zero-points, which result in minor differences with the conclusions of B21. Additional photometry in the *Spitzer* and *Gaia* passbands are included in this analysis and complement the B21 paper.

### 3.1 The metallicity effect: definition and values from the literature

In this chapter, the metallicity of Cepheids and its impact on the P-L relation are investigated. In astronomy, the metallicity is the abundance of elements heavier than hydrogen and helium. It is noted  $Z$  and verifies:

$$X + Y + Z = 1 \quad (3.1)$$

where  $X$  and  $Y$  are the mass fractions of hydrogen and helium respectively. The mass fraction of heavy elements of the Sun is  $Z_{\odot} = 0.0134$ . In this study and many others, the stellar metallicity is approximated by the abundance ratio of iron over hydrogen compared to that of the Sun, defined as:

$$[\text{Fe}/\text{H}]_{\text{star}} = \log_{10} \left( \frac{(N_{\text{Fe}}/N_{\text{H}})_{\text{star}}}{(N_{\text{Fe}}/N_{\text{H}})_{\odot}} \right) \quad (3.2)$$

For example, a star that has a metallicity of  $[\text{Fe}/\text{H}] = -1$  is ten times less metallic than the Sun. The metallicity of Cepheids is usually measured by analysing high resolution spectra and by comparing them with a list of Fe I and Fe II lines (e.g. Romaniello et al. 2008). Oxygen lines are also used in place of iron lines in several studies (with  $(\text{O}/\text{H})_{\odot} = 7.9 \times 10^{-4}$ ), assuming that the oxygen abundance is a good proxy of the iron abundance. This hypothesis is justified by spectroscopic measurements which give  $[\text{O}/\text{Fe}] = 0 \pm 0.14$  dex over the range  $-0.7 < [\text{Fe}/\text{H}] < +0.3$  dex (Luck et al. 2006).



The effect of metallicity on the P-L relation is generally represented as a third term in the Leavitt law, such as:

$$M = \alpha (\log P - \log P_0) + \beta + \gamma [\text{Fe}/\text{H}] \quad (3.3)$$

It is also defined as the variation of distance modulus  $\delta(m - M)$  between two sources that differ by  $\delta [\text{Fe}/\text{H}]$  in metallicity:

$$\gamma = \frac{\delta (m - M)}{\delta [\text{Fe}/\text{H}]} \quad (3.4)$$

Various estimates of the metallicity effect derived in different wavelengths during the past twenty years are listed in Table 3.1. From the theoretical point of view, [Bono et al. \(1999\)](#), [Caputo et al. \(2000\)](#), [Bono et al. \(2008\)](#) and [Fiorentino et al. \(2013\)](#) used masses and luminosities provided by stellar evolutionary calculations as input parameters of nonlinear convecting models and predicted a positive metallicity effect ( $\gamma > 0$ ), which means that metal-rich Cepheids are fainter than metal-poor ones at the same pulsation period. In the NIR, they derived that the P-L relation is almost independent of metallicity, while in the *V* band the effect is positive and relatively strong, with  $\gamma = +0.40$  mag/dex. In the optical Wesenheit index  $W_{VI}$ , [Bono et al. \(2008\)](#) also obtained a positive metallicity effect of  $+0.05$  mag/dex. Similarly, [Marconi et al. \(2005\)](#) discussed the effect of chemical composition on Cepheid properties, not only considering the metal abundance but also the helium-to-metal enrichment ratio. They derive a positive metallicity correction, in agreement with the results by [Bono et al. \(2008\)](#). This positive sign of the metallicity effect is expected, physically, from the fact that a Cepheid of high metallicity would have more lines in its spectra, which would decrease the flux emitted by the star and make it appear fainter. Conversely, [Anderson et al. \(2016b\)](#) used linear non-adiabatic models and derived an opposite trend, with metal-poor Cepheids being fainter.

Empirically, early results by [Kennicutt et al. \(1998\)](#) already indicated an effect of the opposite sign with  $\gamma = -0.24 \pm 0.16$  mag/dex in the optical, obtained by comparing two fields in the nearby galaxy M101. The difference in metallicity between the inner and outer field covered a range of 0.68 dex. The negative sign was confirmed by [Sakai et al. \(2004\)](#) and [Macri et al. \(2006\)](#) a few years later. However, the work by [Romaniello et al. \(2008\)](#) contradicted these empirical studies with a positive metallicity effect in *V* by combining Milky Way and Magellanic Cloud Cepheids with individual metallicities from high resolution spectra.

[Freedman & Madore \(2011\)](#) adopted the Romaniello spectroscopic  $[\text{Fe}/\text{H}]$  abundances and extended the study to mid-infrared wavelengths with *Spitzer* photometry. They derived a negative metallicity effect in mid-infrared bands down to  $-0.39 \pm 0.16$  mag/dex, a dependence consistent with zero in NIR wavelengths and a positive effect up to  $+0.59 \pm 0.49$  mag/dex in *B*. The variation of  $\gamma$  over the wavelength range shows a nearly linear evolution, suggesting that metal-rich Cepheids are fainter than metal-poor ones in the optical, and a reversed effect at longer wavelengths. This result is shown in Fig. 3.1. The value in the *Spitzer*  $[3.6 \mu\text{m}]$  band was updated to  $-0.09 \pm 0.29$  mag/dex by [Freedman et al. \(2011\)](#).

The authors explained this trend by the purely atmospheric line-blanketing effect (see also [Sandage & Eggen 1959](#); [McNamara & Colton 1969](#); [Leitherer 2012](#)). This effect is due to photospheric absorption in the optical, where the spectrum contains a great number of absorption lines: the accumulation of lines appears as a reduction of the continuum level at short wavelengths. The conservation of flux results in a boost of the ionization in the photosphere at longer wavelengths (in NIR) and therefore of the temperature. Hence the emission at longer wavelengths is increased. In summary, a high metallicity enhances the emerging flux in NIR, and therefore the brightness.

Table 3.1: Empirical and theoretical estimations of the metallicity effect ( $\gamma$  in mag/dex) on Cepheid magnitudes taken from the literature between 1998 and 2020.

Band	$\gamma$	Reference	Method	
$W_{VI}$	$-0.24 \pm 0.16$	<a href="#">Kennicutt et al. (1998)</a>	2 fields in M101	[O/H]
$V$	+0.40	<a href="#">Bono et al. (1999)</a>	Nonlinear convecting models	[Fe/H]
$K$	-0.08			
$W_{VI}$	+0.27	<a href="#">Caputo et al. (2000)</a>	Nonlinear convecting models	[Fe/H]
$W_{VI}$	$-0.24 \pm 0.05$	<a href="#">Sakai et al. (2004)</a>	TRGB/Cepheid distances to nearby galaxies	[O/H]
$W_{VI}$	$-0.29 \pm 0.10$	<a href="#">Macri et al. (2006)</a>	2 fields in NGC 4258	[O/H]
$W_{VI}$	$+0.05 \pm 0.03$	<a href="#">Bono et al. (2008)</a>	Nonlinear convecting models	[Fe/H]
$K$	$\sim 0$	<a href="#">Romaniello et al. (2008)</a>	MW, LMC, SMC + HR spectra	[Fe/H]
$V$	$> 0$			
$W_{VI}$	$-0.29 \pm 0.11$	<a href="#">Scowcroft et al. (2009)</a>	4 fields in M33	[O/H]
$B$	$+0.59 \pm 0.49$	<a href="#">Freedman &amp; Madore (2011)</a>	MW, LMC, SMC	[Fe/H]
$V$	$+0.50 \pm 0.31$			
$J$	$+0.14 \pm 0.07$			
$H$	$+0.05 \pm 0.02$			
$K$	$+0.02 \pm 0.03$			
$3.6\mu\text{m}$	$-0.39 \pm 0.16$			
$4.5\mu\text{m}$	$-0.25 \pm 0.18$			
$5.8\mu\text{m}$	$-0.39 \pm 0.17$			
$8.0\mu\text{m}$	$-0.38 \pm 0.16$			
$3.6\mu\text{m}$	$-0.09 \pm 0.29$	<a href="#">Freedman et al. (2011)</a>	MW, LMC, SMC	[Fe/H]
$V$	$+0.09 \pm 0.10$	<a href="#">Storm et al. (2011b)</a>	MW, LMC, SMC + IRSB BW distances	[Fe/H]
$I$	$-0.06 \pm 0.10$		$p = 1.55 - 0.186 \log P$	
$W_{VI}$	$-0.23 \pm 0.10$		( <a href="#">Storm et al. 2011a</a> )	
$J$	$-0.10 \pm 0.10$			
$K$	$-0.11 \pm 0.10$			
$W_{JK}$	$-0.10 \pm 0.10$			
$V$	$+0.23 \pm 0.11$	<a href="#">Groenewegen (2013)</a>	MW, LMC, SMC + IRSB BW distances	[Fe/H]
$K$	$-0.05 \pm 0.10$		$p = 1.50 - 0.24 \log P$	
$W_{VK}$	$+0.04 \pm 0.10$			
$V$	$-0.022 \pm 0.076$	<a href="#">Wielgórski et al. (2017)</a>	LMC, SMC + DEB distances	[Fe/H]
$I$	$-0.015 \pm 0.071$			
$J$	$-0.042 \pm 0.069$			
$H$	$-0.012 \pm 0.069$			
$K$	$-0.017 \pm 0.069$			
$W_{VI}$	$-0.025 \pm 0.067$			
$W_{JK}$	$-0.022 \pm 0.067$			
$V$	$-0.238 \pm 0.186$	<a href="#">Gieren et al. (2018)</a>	MW, LMC, SMC + IRSB BW distances	[Fe/H]
$I$	$-0.293 \pm 0.150$		$p = 1.55 - 0.186 \log P$	
$W_{VI}$	$-0.335 \pm 0.059$		( <a href="#">Storm et al. 2011a</a> )	
$J$	$-0.270 \pm 0.108$			
$K$	$-0.232 \pm 0.064$			
$W_{JK}$	$-0.221 \pm 0.053$			
$V$	$+0.001 \pm 0.258$	<a href="#">Groenewegen (2018)</a>	MW <i>Gaia</i> DR2 parallaxes, ZP = $-0.046$ mas	[Fe/H]
$K$	$-0.090 \pm 0.159$			
$W_{VK}$	$-0.102 \pm 0.156$			
$K$	$-0.039 \pm 0.151$	<a href="#">Ripepi et al. (2020)</a>	MW <i>Gaia</i> DR2 parallaxes, ZP = $-0.049$ mas	[Fe/H]
$W_{JK}$	$-0.084 \pm 0.145$			
$K$	$-0.456 \pm 0.099$	<a href="#">Ripepi et al. (2021)</a>	MW <i>Gaia</i> EDR3 parallaxes + HR spectra	[Fe/H]
$W_{JK}$	$-0.465 \pm 0.071$			
$W_{VK}$	$-0.459 \pm 0.107$			

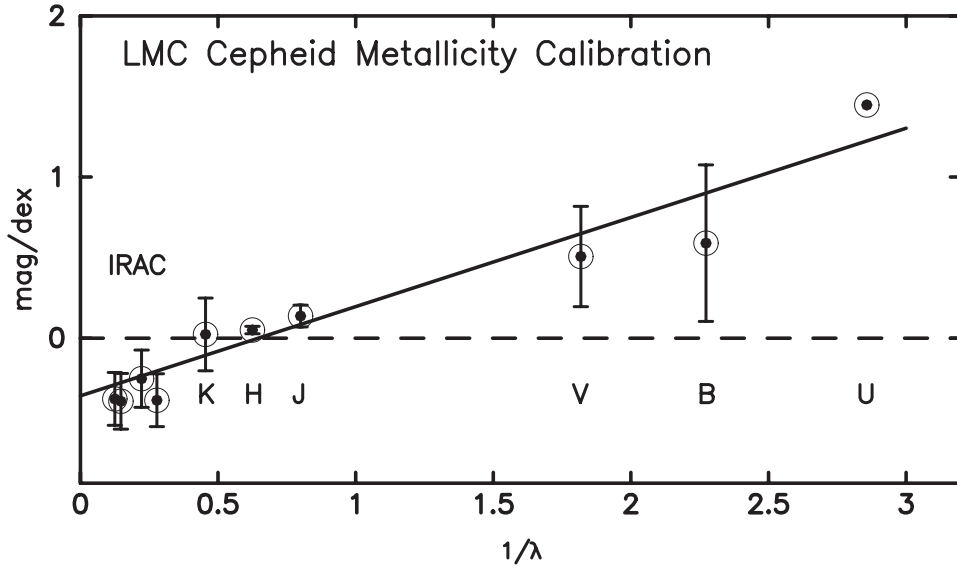


Figure 3.1: Metallicity effect ( $\gamma$ ) as a function of the inverse of the wavelength in  $\mu\text{m}^{-1}$ . The figure is taken from [Freedman & Madore \(2011\)](#).

Using surface brightness relations and the Baade-Wesselink approach to derive distances to Galactic and Magellanic Cloud Cepheids, [Storm et al. \(2011b\)](#) obtained a positive metallicity effect in the optical ( $\gamma_V = +0.09 \pm 0.10$  mag/dex) and a negative effect in the NIR ( $\gamma_K = -0.11 \pm 0.10$  mag/dex). They adopted the projection-factor relation from [Storm et al. \(2011a\)](#),  $p = 1.55 - 0.186 \log P$ , for deriving their distances. These results of the metallicity effect are wavelength dependent and follow the trend identified by [Freedman & Madore \(2011\)](#) but are all consistent with zero within the error bars. Similarly, [Groenewegen \(2013\)](#) used a slightly different  $p$ -factor relation,  $p = 1.50 - 0.24 \log P$ , and derived  $\gamma_V = +0.23 \pm 0.11$  mag/dex and  $\gamma_K = -0.05 \pm 0.10$  mag/dex, confirming the wavelength dependence. With the same method and the  $p$ -factor relation from [Storm et al. \(2011a\)](#), [Gieren et al. \(2018\)](#) find a strong and negative metallicity effect that does not depend on wavelength, with a mean value of  $\gamma \sim -0.25 \pm 0.10$  mag/dex. These studies were limited by the use of the projection factor, which can differ significantly depending on the  $p - P$  relation adopted.

Recently, precise distances to the Magellanic Clouds were published based on detached eclipsing binary systems. [Wielgórski et al. \(2017\)](#) adopted the LMC and SMC distances from [Pietrzyński et al. \(2013\)](#) and [Graczyk et al. \(2014\)](#) respectively and performed a purely differential analysis of the LMC and SMC P-L relations. They obtained a metallicity effect independent of wavelength and consistent with zero ( $\gamma_K = -0.017 \pm 0.069$  mag/dex).

While theoretical works have predicted that high metallicity would flatten the slope of the P-L relation ([Marconi et al. 2010](#); [Fiorentino et al. 2002, 2007](#)), observational studies reported no significant effect of metallicity on the slope of the Leavitt law ([Pietrzyński et al. 2007](#); [Mager et al. 2013](#); [Ripepi et al. 2019](#)).

Finally, *Gaia* DR2 recently provided the distances to hundreds of Milky Way Cepheids: [Groenewegen \(2018\)](#) adopted a parallax zero-point of  $-0.046$  mas and a sample of more than 400 Galactic Cepheids and obtained a null metallicity effect in optical bands ( $\gamma_V = +0.001 \pm 0.258$  mag/dex) and negative but weak effect in NIR ( $\gamma_K = -0.090 \pm 0.159$  mag/dex). [Ripepi et al. \(2020\)](#) confirmed this weak effect in the NIR with  $\gamma_K = -0.039 \pm 0.151$  mag/dex assuming a *Gaia* DR2 parallax

zero-point of  $-0.049$  mag, close to the zero-point adopted by [Groenewegen \(2018\)](#). Recently, [Ripepi et al. \(2021\)](#) published new chemical abundances for 47 Milky Way Cepheids from high resolution spectra: combining these new metallicities with *Gaia* EDR3 parallaxes and with additional data from the literature, they obtained a particularly strong metallicity effect in the near infrared, with  $\gamma_K = -0.456 \pm 0.099$  mag/dex. *Gaia* allows us to improve the precision on Milky Way Cepheid distances, however the metallicity range covered by Galactic Cepheids ( $\sim 0.4$  dex) and their abundance precision are not sufficient to significantly refine the precision of the metallicity effect (see Sect. 3.6.1).

## 3.2 Photometry

The aim of this section is to collect apparent mean magnitudes for Galactic and Magellanic Cloud Cepheids. A great care is taken to use only well covered light curves and a large number of photometric bands. This study covers optical wavelengths in the *V* and *I* bands from ground based telescopes and the *Gaia* passbands in *G*, *BP* and *RP*, NIR wavelengths in *J*, *H*, *K* from ground observatories, and mid-infrared wavelengths with the  $[3.6\ \mu\text{m}]$  and  $[4.5\ \mu\text{m}]$  bands from the *Spitzer* Space Telescope. Wesenheit indices are also derived by combining NIR and optical bands, they are defined in Sect. 3.5. The study in the *Gaia* and *Spitzer* bands is new and complements the [B21](#) paper.

### 3.2.1 Photometry for Milky Way Cepheids

For Milky Way Cepheids, the compilation from [Berdnikov \(2008\)](#) provides well covered light curves in the *V* and *I* bands, respectively in the Johnson and Cousins systems. A total of 272 Cepheids have satisfying light curves in *V* with an average of 168 points per star, and 235 Cepheids have light curves in the *I* band with an average of 128 points per star. All the observations from this catalog were taken by the same author but over a large period of time and with different instruments so a photometric zero-point systematic uncertainty of 0.010 mag is included quadratically to the mean magnitude errors. The photometric zero-points adopted in each band and in each galaxy are listed in Table 3.2.

Optical light curves in the *G*, *BP* and *RP* passbands are taken from the "vari\_cepheid" catalog ([Clementini et al. 2019](#)) of *Gaia* DR2<sup>1</sup>. A total of 238 good quality light curves (no outliers, low dispersion, complete coverage) are available in *G* and *BP* bands and 218 good quality light curves in *RP*, with an average of 35 observations per Cepheid.

In the NIR *J*, *H* and *K* bands, photometry is mostly taken from the catalogs by [Welch et al. \(1984\)](#), [Laney & Stobie \(1992\)](#), [Barnes et al. \(1997\)](#) and [Monson & Pierce \(2011\)](#). The data from these four catalogs are very consistent according to the comparison by [Monson & Pierce \(2011\)](#), with residuals of 0.013, 0.010 and 0.002 mag in the *J*, *H* and *K* bands respectively. These values are adopted as photometric zero-point uncertainties. For a few stars, [Feast et al. \(2008\)](#) provide additional data points in the NIR bands. One can assume that including this source of photometry for a negligible number of stars does not impact the uncertainties. A total of 137, 135 and 126 Cepheids with at least 8 data points are available in *J*, *H* and *K*, with an average of 34 observations per star. Each data point is converted from the original system (CIT, BIRCAM, SAAO) to the 2MASS system using the equations provided in Sect. 2.3.3 in Chapter 2.

Finally, in the mid-IR *Spitzer* bands at  $[3.6\ \mu\text{m}]$  and  $[4.5\ \mu\text{m}]$ , [Monson et al. \(2012\)](#) provides fully covered light curves for 37 Galactic Cepheids, with an average of 24 data points per star.

<sup>1</sup> Full Cepheid light curves are not yet available in *Gaia* EDR3 catalog, only mean magnitudes are provided in the latter.

In all bands, only Cepheids with at least 8 data points are considered. Periods are taken from the VSX catalog (Watson et al. 2006). The data points are phased at the date of the maximum of luminosity and each point of the light curve is transformed from magnitudes ( $m$ ) into fluxes ( $F$ ):

$$F_{\lambda} = F_{\text{Vega}}(\lambda) \times 10^{-m_{\lambda}/2.5} \quad (3.5)$$

where  $F_{\text{Vega}}(\lambda)$  is the passband zero point in the Vega system<sup>2</sup>. The intensity light curve is fitted using Fourier series and the mean magnitude is derived from this fit. The number of Fourier modes adopted for the fit ranges from 3 to 6, depending on the complexity of the light curve shape (e.g. presence of bumps, steep variations).

The statistical uncertainty of a mean magnitude is obtained from the scatter of the points around the light curve fit. When a very large number of points are available for a single light curve, the dispersion becomes very low and the resulting uncertainties are unrealistically small, for this reason a threshold error of 0.006 mag is adopted in these cases. Each light curve is inspected visually in order to exclude possible outliers. Additionally, for long period Cepheids such as RS Pup, SV Vul or GY Sge, the photometric data are spread over 4 decades which introduces significant phase shifts: period changes are taken into account by adopting polynomial models of up to degree 5 for the pulsation period. Fig. 3.2 shows two light curves of different qualities: on the left, the light curve of KN Cen has a very low dispersion and an excellent phase coverage, while the plot on the right of the figure shows the light curve of SW Cas, which is more dispersed and is representative of the minimum quality allowed for the light curves in this sample.

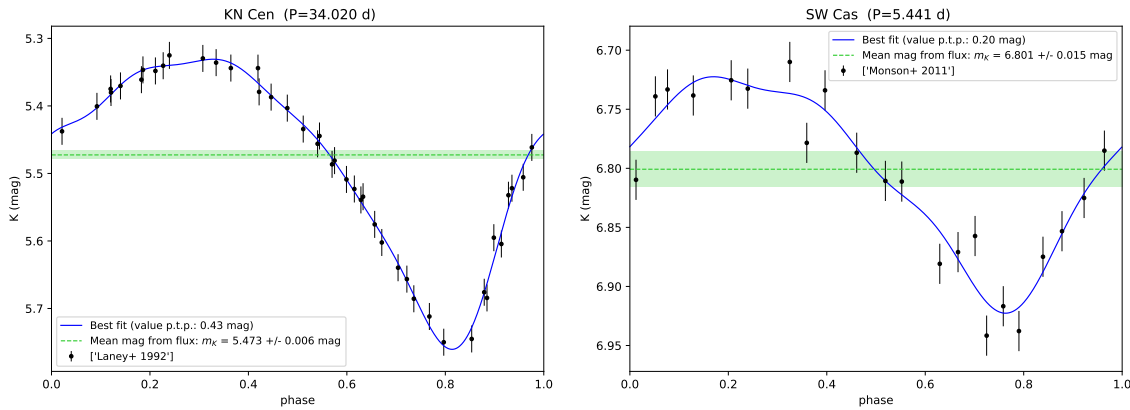


Figure 3.2: Light curves of the Cepheids KN Cen and SW Cas in the  $K$  band. They illustrate respectively a high quality light curve and more dispersed light curve due to a smaller amplitude.

Only fundamental mode Cepheids are considered: since the sample is significantly larger than in Chapter 2, excluding first overtone Cepheids does not impact the size of the sample and avoids possible contamination from misidentified stars. The pulsation modes are taken by order of priority from the reclassification by Ripepi et al. (2019), from the catalog by Groenewegen (2018) and from the VSX database (Watson et al. 2006). As for reddenings, the DDO database by Fernie et al. (1995) is the most complete and homogeneous catalog but is more than 25 years old. Instead of using it for all stars of the sample as in B21, I adopted the catalogs mentioned in Chapter 2, by order of preference: Kovtyukh et al. (2008) with the uncertainties provided in the catalog, Laney & Caldwell (2007) with uncertainties set to 0.03 mag, Sziládi et al. (2007) with uncertainties set to 0.05 mag, Acharova

<sup>2</sup> Taken from the SVO filters database: <http://svo2.cab.inta-csic.es/svo/theory/fps/index.php?mode=browse>

et al. (2012) with uncertainties set to 0.05 mag, and finally the Fernie et al. (1995) database if a star is not present in the previous catalogs.

### 3.2.2 Photometry for Large Magellanic Cloud Cepheids

Large Magellanic Cloud (LMC) Cepheids are more metal-poor than Milky Way Cepheids, therefore they constitute the second sample for the study of the metallicity effect. A total of 1,726 light curves in the *V* band and 1,753 light curves in the *I* band are collected in the OGLE-IV survey by Soszyński et al. (2015), they contain on average 141 and 609 data points per star respectively. The transformation between the *V* filter in the OGLE database and the Johnson system is negligible and the *I* filter from OGLE can be considered as identical to the Cousins system (Udalski et al. 2015). A photometric zero-point uncertainty of 0.01 mag is taken into account.<sup>3</sup>

In the *G*, *BP* and *RP* bands, the photometry is taken from the *Gaia* DR2 "vari\_cepheid" catalog (Clementini et al. 2019): this catalog contains the light curves of LMC Cepheids and provides intensity-averaged apparent magnitudes. Unfortunately, the more recent *Gaia* EDR3 catalog does not provide Cepheid light curves: the magnitudes given in this catalog are not based on light curve fitting but on a simple averaging of the data points. In the *G* band, 1448 light curves are collected and 1167 light curves in *BP* and *RP*, with an average of 27 data points per star.

In the near infrared, the Synoptic Survey by Macri et al. (2015) provides well covered light curves for 887 fundamental mode Cepheids in the LMC, with an average of 42 epochs per light curve. It includes additional Cepheids from Persson et al. (2004). The agreement between both samples is estimated to  $0.018 \pm 0.067$  mag,  $-0.016 \pm 0.058$  mag and  $0.000 \pm 0.054$  mag in *J*, *H*, *K* respectively and is adopted as photometric zero-point uncertainty.<sup>4</sup> Photometric transformations are applied to bring the mean magnitudes from Macri et al. (2015) (noted M15) in better agreement with the 2MASS system (L. Macri 2021, private communication). They were derived by comparing their catalog with the 2MASS Point Source Catalog (Cutri et al. 2003), with  $12 \text{ mag} < H < 13.5 \text{ mag}$ ,  $K > 11.5 \text{ mag}$  and  $-0.5 \text{ mag} < J - K < 1.4 \text{ mag}$ :

$$\begin{aligned} J_{2\text{MASS}} &= J_{\text{M15}} - 0.0167 + 0.0205 (J_{\text{M15}} - K_{\text{M15}} - 0.4) + 0.0101 (J_{\text{M15}} - K_{\text{M15}} - 0.4)^2 \\ H_{2\text{MASS}} &= H_{\text{M15}} + 0.0116 - 0.0054 (J_{\text{M15}} - K_{\text{M15}} - 0.4) - 0.0189 (J_{\text{M15}} - K_{\text{M15}} - 0.4)^2 \\ K_{2\text{MASS}} &= K_{\text{M15}} + 0.0162 + 0.0227 (J_{\text{M15}} - K_{\text{M15}} - 0.4) - 0.0595 (J_{\text{M15}} - K_{\text{M15}} - 0.4)^2 \end{aligned}$$

Finally, a sample of light curves for 85 LMC Cepheids in the *Spitzer* bands at  $[3.6 \mu\text{m}]$  and  $[4.5 \mu\text{m}]$  is taken from Scowcroft et al. (2011), with an average of 24 observations per Cepheid.

Only LMC Cepheids with at least 5 data points are selected and a minimum uncertainty of 10% on the mean magnitudes is adopted as a precision limit. A selection based on the distance between Cepheids and the LMC center is performed in Sect. 3.3.2. A photometric zero-point uncertainty of 0.02 mag is adopted in all bands to account for the possible differences between the various systems used in this study. The reddening values from the Górski et al. (2020) reddening maps are adopted for this sample of LMC Cepheids. The reddening ranges from 0.021 mag to 0.360 mag with a mean value of 0.137 mag.

<sup>3</sup> In B21 the photometric zero-point in *V* and *I* was set to 0.02 which was likely too conservative.

<sup>4</sup> In B21 the photometric zero-point was set to 0.02 mag in all bands which was likely too conservative.



### 3.2.3 Photometry for Small Magellanic Cloud Cepheids

Similarly to the Milky Way and LMC samples, multi-band light curves of SMC Cepheids with the best coverage possible were collected in the literature. A total of 2,195 and 2,315 light curves in the  $V$  and  $I$  bands are taken from the OGLE-IV survey (Soszyński et al. 2015) with an average of 43 and 459 points per star respectively. Similarly to the LMC sample, a photometric zero-point error of 0.01 mag is adopted in the  $V$  and  $I$  bands.

Intensity averaged mean magnitudes in the  $G$ ,  $BP$  and  $RP$  bands are derived from 1,824, 1,643 and 1,643 light curves provided in the *Gaia* DR2 "vari\_cepheid" catalog (Clementini et al. 2019) with an average of 26 points per light curve.

In the near infrared, the VISTA survey for the Magellanic Clouds (VMC) by Ripepi et al. (2016) provides  $J$  and  $K$  band light curves for 1,129 and 2,074 SMC Cepheids, with a mean number of 7 and 17 points per Cepheid. A selection is performed based on the number of epochs available for a given light curve: in the  $J$  band, a large number of Cepheids have less than 8 measurements per light curve (the limit adopted for the MW sample) and excluding them would drastically reduce the sample, therefore a limit of 5 epochs per star is adopted. A minimum uncertainty of 10% on mean magnitudes is adopted as a precision limit. Mean magnitudes in the VISTA system are first converted in a pseudo 2MASS system by applying the transformations from Ripepi et al. (2016):

$$\begin{aligned} J' &= J_{\text{VMC}} + 0.070 (J_{\text{VMC}} - K_{\text{VMC}}) \\ K' &= K_{\text{VMC}} - 0.011 (J_{\text{VMC}} - K_{\text{VMC}}) \end{aligned}$$

An additional correction is derived by matching  $\sim 7000$  stars in common between the VMC survey and the 2MASS Point Source Catalog, with  $J > 12.25$  mag,  $K > 11.5$  mag, and  $-0.5$  mag  $< J - K < 1.4$  mag (L. Macri 2021, private communication):

$$\begin{aligned} J_{2\text{MASS}} &= J' - 0.0087 - 0.0010 (J' - K' - 0.4) \\ K_{2\text{MASS}} &= K' + 0.0011 - 0.0087 (J' - K' - 0.4) \end{aligned}$$

Unfortunately,  $H$  band light curves are not present in this survey. For this reason, in Breuval et al. (2021), only full light curves were considered and the  $H$  band for SMC Cepheids was excluded, which led to a poor calibration of the metallicity effect in this wavelength, based entirely on Milky Way and LMC stars. Here I decided to make an exception and adopt  $H$  band single point photometry from the Kato et al. (2007) Point Source Survey (these data were kindly provided in electronic form by Y. Ita). This catalog covers both Magellanic Clouds. The data were obtained with the SIRIUS camera on the InfraRed Survey Facility (IRSF) 1.4 m telescope at the South African Astronomical Observatory. A total of 2,078 SMC Cepheids are available in this catalog. Additional transformations were applied to the  $H$  band single-point magnitudes and were derived by comparing  $\sim 14,000$  stars in common between the Kato et al. (2007) and the 2MASS surveys (L. Macri 2021, private communication):

$$\begin{aligned} J_{2\text{MASS}} &= J_{\text{K07}} - 0.0081 + 0.0437 (J_{\text{K07}} - K_{\text{K07}} - 0.4) + 0.0112 (J_{\text{K07}} - K_{\text{K07}} - 0.4)^2 \\ H_{2\text{MASS}} &= H_{\text{K07}} - 0.0246 - 0.0228 (J_{\text{K07}} - K_{\text{K07}} - 0.4) + 0.0106 (J_{\text{K07}} - K_{\text{K07}} - 0.4)^2 \\ K_{2\text{MASS}} &= K_{\text{K07}} - 0.0122 + 0.0190 (J_{\text{K07}} - K_{\text{K07}} - 0.4) - 0.0382 (J_{\text{K07}} - K_{\text{K07}} - 0.4)^2 \end{aligned}$$

From the comparison between Kato et al. (2007) and VMC magnitudes, a photometric zero point uncertainty of 0.010 mag is adopted in the  $J$ ,  $H$ ,  $K$  bands. Finally, mid-infrared light curves for 90 SMC Cepheids are provided in Scowcroft et al. (2016) with 12 points per light curve on average.

As for the LMC sample, the reddening values from the Górski et al. (2020) reddening maps are adopted for SMC Cepheids. The reddening ranges from 0.049 mag to 0.171 mag with a mean value

of 0.090 mag. A photometric ZP uncertainty of 0.02 mag is adopted in all bands to account for the possible differences between the various systems used in this study. An additional selection based on the distance between Cepheids and the SMC center is performed in Sect. 3.3.3.

Table 3.2: References for the photometric data and adopted systematics (photometric zero-point). In *Gaia* (*G*, *BP*, *RP*) and *Spitzer* ( $[3.6\ \mu\text{m}]$  and  $[4.5\ \mu\text{m}]$ ) bands, the photometric zero-point is negligible because in the 3 galaxies the data are taken by the same instruments and reduced by the same team.

Band	Milky Way	Large Magellanic Cloud	Small Magellanic Cloud
<i>V, I</i>	<a href="#">Berdnikov (2008)</a> $\sigma_{V,I} = 0.010\ \text{mag}$	<a href="#">Soszyński et al. (2015)</a> $\sigma_{V,I} = 0.010\ \text{mag}$	<a href="#">Soszyński et al. (2015)</a> $\sigma_{V,I} = 0.010\ \text{mag}$
<i>J, H, K</i>	<a href="#">Welch et al. (1984)</a> <a href="#">Laney &amp; Stobie (1992)</a> <a href="#">Barnes et al. (1997)</a> <a href="#">Monson &amp; Pierce (2011)</a> <a href="#">Feast et al. (2008)</a> $\sigma_J = 0.013\ \text{mag}$ $\sigma_H = 0.010\ \text{mag}$ $\sigma_K = 0.002\ \text{mag}$	<a href="#">Macri et al. (2015)</a> <a href="#">Persson et al. (2004)</a> $\sigma_J = 0.018\ \text{mag}$ $\sigma_H = 0.016\ \text{mag}$ $\sigma_K = 0.000\ \text{mag}$	<a href="#">Ripepi et al. (2016) (<i>J</i>, <i>K<sub>S</sub>)</i></a> <a href="#">Kato et al. (2007) (<i>H</i>)</a> $\sigma_{J,H,K} = 0.010\ \text{mag}$
$[3.6\ \mu\text{m}], [4.5\ \mu\text{m}]$	<a href="#">Monson et al. (2012)</a> $\sigma_{[3.6\ \mu\text{m}], [4.6\ \mu\text{m}]} \sim 0$	<a href="#">Scowcroft et al. (2011)</a> $\sigma_{[3.6\ \mu\text{m}], [4.6\ \mu\text{m}]} \sim 0$	<a href="#">Scowcroft et al. (2016)</a> $\sigma_{[3.6\ \mu\text{m}], [4.6\ \mu\text{m}]} \sim 0$
<i>G, BP, RP</i>	<a href="#">Clementini et al. (2019)</a> $\sigma_{G, BP, RP} \sim 0$	<a href="#">Clementini et al. (2019)</a> $\sigma_{G, BP, RP} \sim 0$	<a href="#">Clementini et al. (2019)</a> $\sigma_{G, BP, RP} \sim 0$

### 3.3 Distances

#### 3.3.1 Gaia EDR3 parallaxes of Milky Way Cepheids

In this study, Cepheid parallaxes are taken from the *Gaia* EDR3 catalog ([Gaia Collaboration et al. 2021](#)). Contrary to *Gaia* DR2, the Cepheid parallaxes provided in this recent release can be used directly instead of using companion stars or host open clusters. The effect of chromaticity is still not taken into account in *Gaia* EDR3 parallaxes (see Chap. 2) but due to the large time coverage of the observations (34 months), the noise resulting from the color variation of Cepheids can be considered as globally averaged.

All *Gaia* EDR3 parallaxes are corrected for the zero-point offset, which is computed using the code provided by [Lindgren et al. \(2021a\)](#). As described in Chap. 2, this quantity depends on the magnitude, the color and the position of the sources. It has a mean value of  $-0.026\ \text{mas}$  and ranges from  $-0.003\ \text{mas}$  to  $-0.054\ \text{mas}$  for this sample of MW Cepheids. On average, the *Gaia* EDR3 parallax zero-point is smaller than the *Gaia* DR2 parallax zero-point (estimated between  $-0.029\ \text{mas}$  to  $-0.080\ \text{mas}$ ) and it takes into account the properties and spatial distribution of the sources. [Lindgren et al. \(2021a\)](#) recommended to adopt an uncertainty of a few micro arcsec on the parallax zero-point so I assumed a  $5\ \mu\text{as}$  uncertainty, which is equivalent to including a systematic error of  $\sim 0.020\ \text{mag}$

in terms of distance modulus for my sample of MW Cepheids.<sup>5</sup>

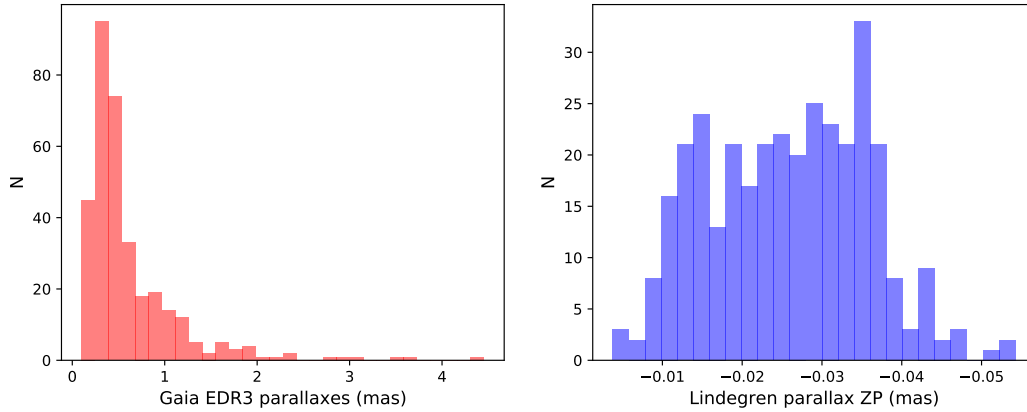


Figure 3.3: Histogram of uncorrected *Gaia* EDR3 parallaxes (left) and *Gaia* EDR3 parallax zero-point correction as suggested by [Lindgren et al. \(2021a\)](#) (right) for the sample of Milky Way Cepheids.

In the range of magnitudes  $10.8 < G < 11.2$ , parallaxes may suffer from additional uncertainties due to a transition of window class (used to avoid saturation for bright stars). For this reason, I included a supplementary uncertainty of  $10\mu\text{as}$  quadratically to the parallax errors for the  $\sim 15$  stars in this range. Finally, I raised all *Gaia* EDR3 parallax errors by 10% by precaution to account for possible additional uncertainties, as suggested by [Riess et al. \(2021b\)](#). This correction is minor compared with *Gaia* DR2 parallax uncertainties which had to be increased by 30%.

Among the initial sample of  $\sim 250$  fundamental-mode Cepheids from [Berdnikov \(2008\)](#), a total of 198 stars have reddening and metallicity values from the literature and verify the quality criterion  $\text{RUWE} < 1.4$  as well. For safety, Cepheids with a RUWE larger than 1.4 were not considered in this analysis.

Obtaining the distance of a star by directly inverting its parallax may be non-trivial due to the nonlinear transformation between both quantities. For this reason, I have compared the distances obtained by inverting *Gaia* EDR3 parallaxes after correcting the parallax zero-point and the distances from [Bailer-Jones et al. \(2021\)](#). In this paper, distances are derived using a probabilistic approach and a prior constructed from a 3D model of the Milky Way. Two different types of distances are derived: first, a "geometric" distance based on the parallax and on the direction on the sky, and secondly a "photo-geometric" distance which also includes the color and apparent magnitude of the star. I inverted *Gaia* EDR3 parallaxes (after applying the zero-point correction) for the present sample of 200 MW Cepheids to obtain the "Gaia-based" distance in parsec. The uncertainty on this Gaia-based distance is obtained by taking the  $\sigma_{\varpi}/\varpi$  ratio (or percentage uncertainty) applied to the distance. Fig. 3.4 shows the comparison between Gaia-based distances and [Bailer-Jones et al. \(2021\)](#) geometric and photo-geometric distances. The agreement is excellent and the uncertainties are similar. In both cases, the dispersion of the distances around the unity line is of 38 pc, which is very low. The largest difference between Gaia-based distances and Bailer-Jones distances is of 230 pc and the mean difference is of 9 pc. This comparison confirms that we can safely invert *Gaia* EDR3 parallaxes in order to obtain Cepheid distances, even for distant ones ( $d > 5$  kpc).

<sup>5</sup> Here the systematic uncertainty on *Gaia* EDR3 parallaxes due to the zero-point is converted in magnitudes for consistency with the LMC and SMC samples (see next section).

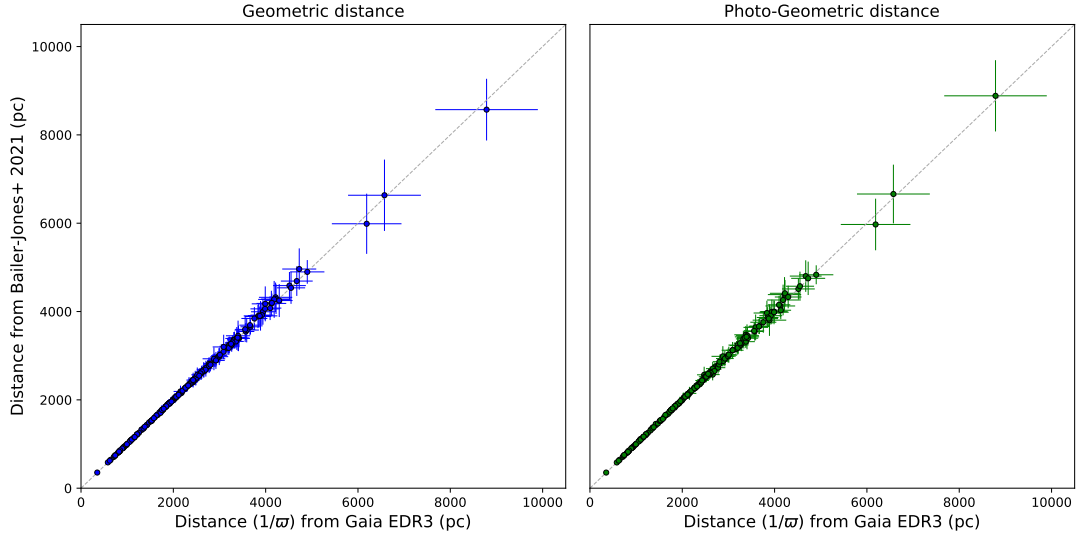


Figure 3.4: Comparison between the Gaia-based distances (obtained by inverting *Gaia* EDR3 corrected parallaxes) and the Bailer-Jones et al. (2021) geometric (left) and photo-geometric (right) distances.

### 3.3.2 Distance to Large Magellanic Cloud Cepheids

The most precise distance to the LMC was measured by Pietrzyński et al. (2019) with a precision of 1.1%: based on 15 detached eclipsing binaries (DEBs), they derive a distance of  $d_{\text{LMC}} = 49.59 \pm 0.09$  (stat.)  $\pm 0.54$  (syst.) kpc. The method for measuring distances from eclipsing binaries is described in Sect. 1.2.2 in Chapter 1. It is based on the geometrical comparison between the angular diameter, derived from surface brightness relations, and the linear diameter of the stars.

At first order, all LMC Cepheids can be considered to be at the same distance  $d_{\text{LMC}}$ . However, for more precision, I took into account the slightly inclined geometry of the LMC disk (Jaczyszyn-Dobrzyniecka et al. 2016) and adopted a corrected distance for each LMC Cepheid noted  $i$ :

$$d_i = \sqrt{x_i^2 + y_i^2 + z_i^2} \quad (3.6)$$

where  $(x_i, y_i, z_i)$  are the Cartesian coordinates and are derived from their equatorial coordinates  $(\alpha_i, \delta_i)$ :

$$\begin{cases} x_i &= -d_{\text{LMC}} \times \cos \delta_i \sin(\alpha_i - \alpha_{\text{LMC}}) \\ y_i &= d_{\text{LMC}} \times [\sin \delta_i \cos \delta_{\text{LMC}} - \cos \delta_i \sin \delta_{\text{LMC}} \cos(\alpha_i - \alpha_{\text{LMC}})] \\ z_i &= d_{\text{LMC}} + c_1 x_i + c_2 y_i \end{cases}$$

where  $(\alpha_{\text{LMC}}, \delta_{\text{LMC}}) = (80.05^\circ, -69.30^\circ)$  are the coordinates of the LMC center and the coefficients  $(c_1, c_2) = (0.395 \pm 0.014, -0.215 \pm 0.013)$  are from Jaczyszyn-Dobrzyniecka et al. (2016). The LMC Cepheids are represented in Fig. 3.5, their color indicate their distance. The yellow stars are the eclipsing binaries used by Pietrzyński et al. (2019) and the red cross is the center of the LMC. The distances of the Cepheids after applying the geometry correction range from 48 kpc to 51.5 kpc, which corresponds to about  $\pm 1.5$  kpc around the LMC center distance.

In order to exclude possible outlier stars such as Cepheids which are far away from the LMC center or have a distance that deviate significantly from the Pietrzyński et al. (2019) value due to the

LMC geometry, only Cepheids within a radius of  $3^\circ$  around the LMC center are considered. This region is represented by the dashed circle in Fig. 3.5. A total of 1,691 Cepheids are in this region, among the initial sample of 1,816 LMC Cepheids. After this selection, other outliers which are not members of the LMC may still be present, especially stars with coordinates close to the LMC center but located at a shorter distance, between the LMC and the Milky Way. The distances attributed to these stars are overestimated and result in brighter absolute magnitudes (i.e. more negative) than they truly are. They will appear as outliers on the P-L plane and will be removed by a sigma clipping procedure.

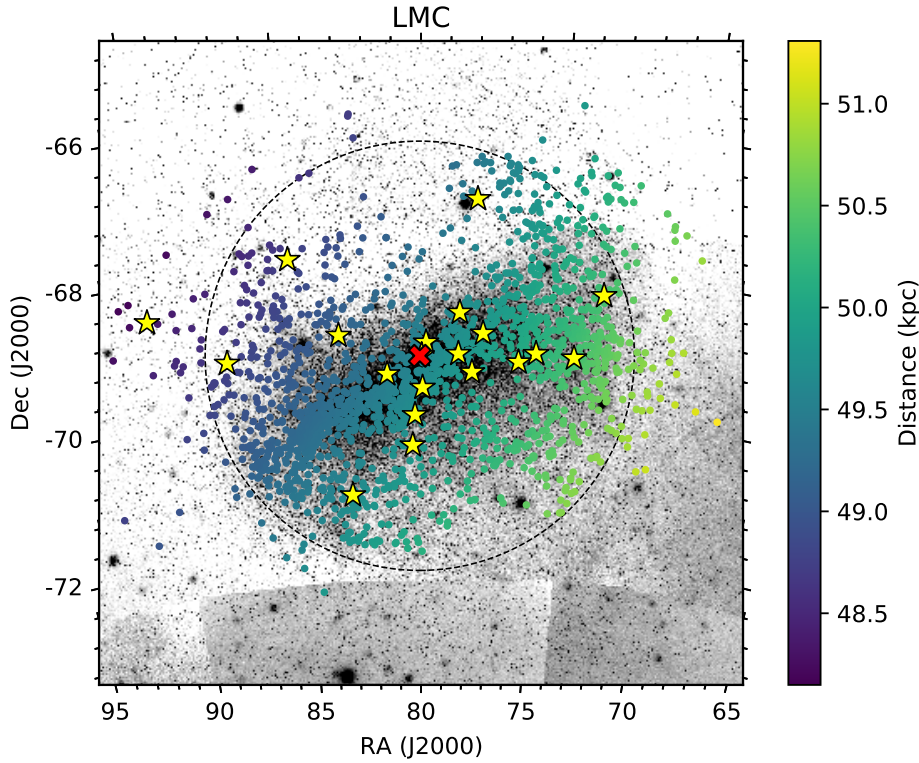


Figure 3.5: Map of fundamental-mode Cepheids in the LMC. The colors represent their distance after correction of the LMC geometry (Jacyszyn-Dobrzniecka et al. 2016), the yellow stars are eclipsing binaries used by Pietrzyński et al. (2019) and the red cross is the center of the LMC. The dashed circle corresponds to a radius of  $3^\circ$  around the LMC center and contains the sample of Cepheids considered in this analysis.

### 3.3.3 Distance to Small Magellanic Cloud Cepheids

The most precise distance to the SMC was derived by Graczyk et al. (2020) with the same method as for the LMC (Pietrzyński et al. 2019). Using 15 eclipsing binaries, they derive  $d_{\text{SMC}} = 62.44 \pm 0.47$  (stat.)  $\pm 0.81$  (syst.) kpc, which is precise to 1.5%. Similarly to the LMC sample, a correction for the SMC inclination can be applied in order to use more precise Cepheid distances, depending on their position in the Cloud. However, the SMC geometry is more complex since this galaxy is very elongated along the line of sight (Subramanian & Subramaniam 2012; Jacyszyn-Dobrzniecka et al. 2016; Ripepi et al. 2017). The true distance to SMC members can therefore show a high dispersion. For each Cepheid noted  $i$  with equatorial coordinates  $(\alpha_i, \delta_i)$ , I derived the Cartesian coordinates



$(x_i, y_i)$ :

$$\begin{cases} x_i &= -d_{\text{SMC}} \times \cos \delta_i \sin(\alpha_i - \alpha_{\text{SMC}}) \\ y_i &= d_{\text{SMC}} \times [\sin \delta_i \cos \delta_{\text{SMC}} - \cos \delta_i \sin \delta_{\text{SMC}} \cos(\alpha_i - \alpha_{\text{SMC}})] \end{cases}$$

where  $(\alpha_{\text{SMC}}, \delta_{\text{SMC}}) = (12.54^\circ, -73.11^\circ)$  is the center of the SMC from [Ripepi et al. \(2017\)](#). For the inclination of the SMC I adopted the equations of the two blue lines in Fig. 4 of [Graczyk et al. \(2020\)](#):

$$\begin{cases} d_i(x) &= d_{\text{SMC}} + (3.086 \pm 0.066) x_i \\ d_i(y) &= d_{\text{SMC}} - (3.248 \pm 0.118) y_i \end{cases}$$

The initial sample of SMC Cepheids is represented in Fig. 3.6. The yellow stars are the 15 eclipsing binaries used by [Graczyk et al. \(2020\)](#) and the distances of Cepheids are represented by their color. They range from 57 to 67 kpc over the full sample, which is  $\pm 5$  kpc around the mean value obtained by [Graczyk et al. \(2020\)](#). Similarly to the LMC sample, I adopted a limiting radius of  $0.6^\circ$  around the SMC center in order to exclude Cepheids which are too far from the center of the galaxy. Due to the significant elongation of the SMC, this radius must be small to ensure that the Cepheids actually belong to the SMC and are not outliers. After this cut, a sample of 841 out of the initial 2,338 Cepheids are found in the central region of the SMC and are adopted for the analysis. Their distances range between 61 and 64 kpc which is  $\pm 1.5$  kpc around the mean distance, which is consistent with the choice of radius adopted for the LMC.

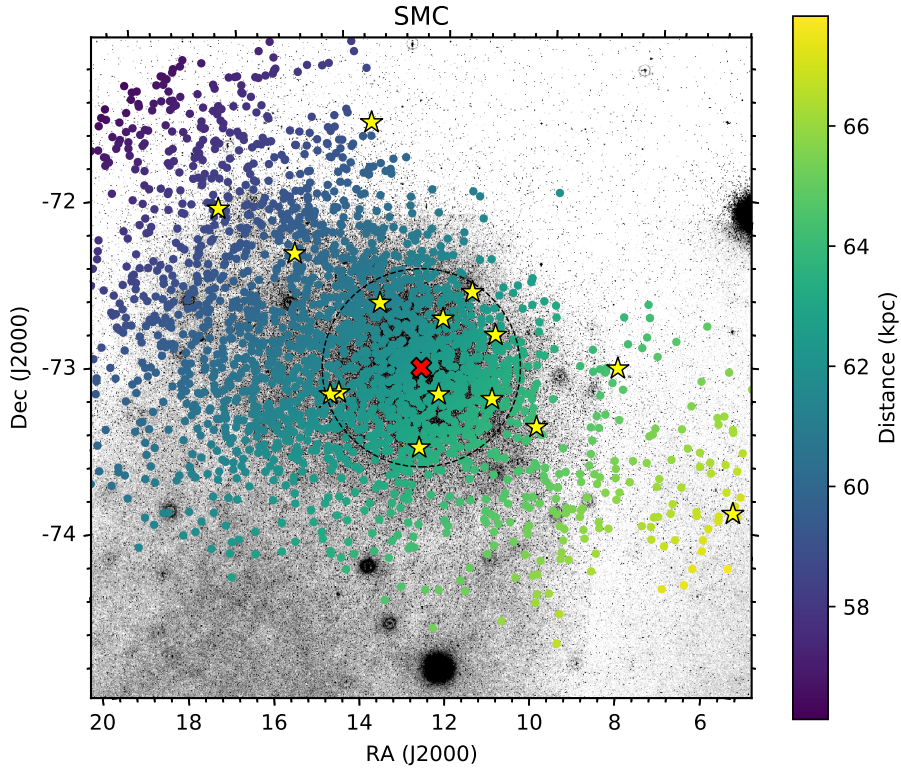


Figure 3.6: Map of fundamental-mode Cepheids in the SMC. The colors represent their distance after correction of the SMC geometry [Graczyk et al. \(2020\)](#), the yellow stars are eclipsing binaries used by [Graczyk et al. \(2020\)](#) and the red cross is the center of the SMC. The dashed circle corresponds to a radius of  $0.6^\circ$  around the SMC center and contains the sample of Cepheids considered in this analysis.



## 3.4 Metallicity

### 3.4.1 Metallicity for Milky Way Cepheids

Several teams have obtained individual metallicities for Galactic Cepheids based on high resolution spectra. One early catalog was by [Fry & Carney \(1997\)](#) who measured iron abundances for 23 MW Cepheids from a spectroscopic study. They found a 0.4 dex spread in  $[\text{Fe}/\text{H}]$  and conclude that it is not due to an observational scatter nor to a metallicity gradient within the galactic disk but is real. [Kovtyukh et al. \(2005\)](#) published metal abundances for 16 additional Cepheids, obtained with the Echelle spectrograph of the Apache Point 3.5 m telescope. [Romaniello et al. \(2008\)](#) complemented the existing measurements and observed 68 Galactic and Magellanic Cepheids with the FEROS and UVES spectrographs, and used high-resolution spectra to derive metallicities. [Luck et al. \(2011\)](#) and [Luck & Lambert \(2011\)](#) increased the number of Galactic Cepheid metallicities to  $\sim 400$  also using the FEROS spectrograph. Recently, [Proxauf et al. \(2018\)](#) collected more than 1,130 high resolution spectra obtained with various spectrographs and derived iron abundances for more than 250 Cepheids. Finally, [Minniti et al. \(2020\)](#) obtained high quality near-infrared spectra with VLT/X-Shooter and provided new metallicities for 45 Cepheids on the far side of the Galactic disk.

In this study, I adopted in priority the catalog of homogeneous and accurate iron abundances for 75 Galactic Cepheids by [Genovali et al. \(2015\)](#), they have a mean uncertainty of 0.08 dex. In complement to these values, I adopted the abundances measured by [Genovali et al. \(2014\)](#) for 42 Galactic Cepheids from 128 high signal-to-noise optical spectra obtained with VLT/UVES, their mean uncertainty is 0.08 dex. This catalog also provides additional abundances from the literature for other 375 Cepheids (for which I set the uncertainty to 0.1 dex). In the literature, the solar metallicity can vary between different studies. For this reason, the catalogs by [Genovali et al. \(2014\)](#) and [Genovali et al. \(2015\)](#) are particularly useful since all metallicity measurements from the literature are rescaled to the same solar abundance,  $A_{\odot} = 7.5$ , where  $A = \log(N/N_H) + 12$  and  $N$  is the abundance by number ([Grevesse et al. 1996](#)).

The metallicity values adopted in this chapter are represented in the histogram in Fig. 3.9, together with the LMC and SMC mean metallicities discussed later in Sect. 3.4.2. The weighted mean metallicity of the sample of Milky Way Cepheids is  $+0.085 \pm 0.022$  dex with a dispersion of 0.123 dex. This value is in good agreement with the average metallicity of  $+0.07 \pm 0.01$  dex obtained by [Gieren et al. \(2018\)](#) using the abundances provided by [Groenewegen \(2013\)](#). Additionally, [Romaniello et al. \(2008\)](#) obtained a mean metallicity of  $+0.00 \pm 0.02$  dex from a sample of 32 Milky Way Cepheids, which is close to our value. The median metallicity of the MW sample is +0.080 dex and the values range between +0.55 dex and  $-0.25$  dex. The typical precision of the individual  $[\text{Fe}/\text{H}]$  measurements available in the literature is of the order of  $\sim 0.1$  dex for Galactic Cepheids and higher for LMC and SMC Cepheids, while the range of metallicities covered by MW, LMC and SMC Cepheids is around 1 dex. Obtaining precise and individual abundances for a large number of Cepheids in the Milky Way and in the Magellanic Clouds is highly desirable for constraining the effect of metallicity on the Leavitt law.

The sample of Milky Way Cepheids adopted in this analysis is also represented on the maps in Fig. 3.7 and 3.8. The metallicity gradient in the Milky Way is particularly visible in Fig. 3.7 with metal-rich Cepheids being located closer to the Galactic center on average, which agrees with previous findings ([Pedicelli et al. 2009](#); [Genovali et al. 2014](#); [Lemasle et al. 2018](#)). Star formation is enhanced around the galactic center, which results in enriching the interstellar medium in heavy elements and in the formation of more metallic stars.

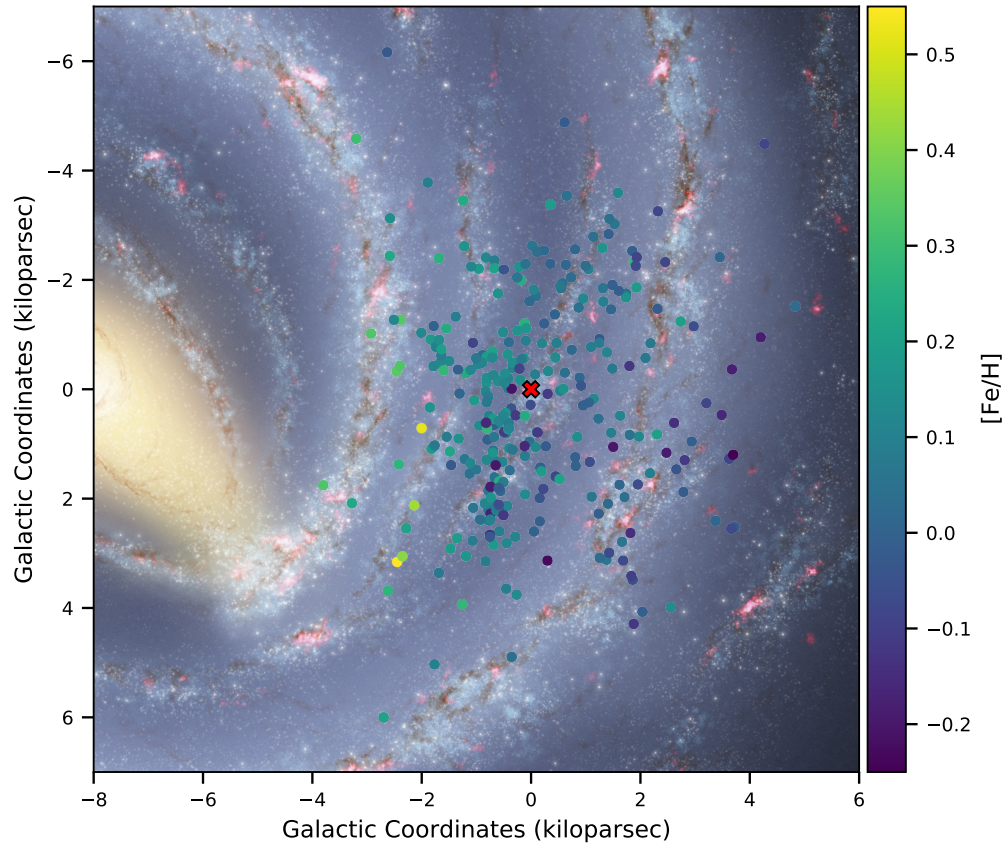


Figure 3.7: Map of the  $\sim 200$  Milky Way Cepheids from [Berdnikov \(2008\)](#) which have a metallicity value from [Genovali et al. \(2014, 2015\)](#), seen from above the disk. The red cross represents the position of the Solar System.

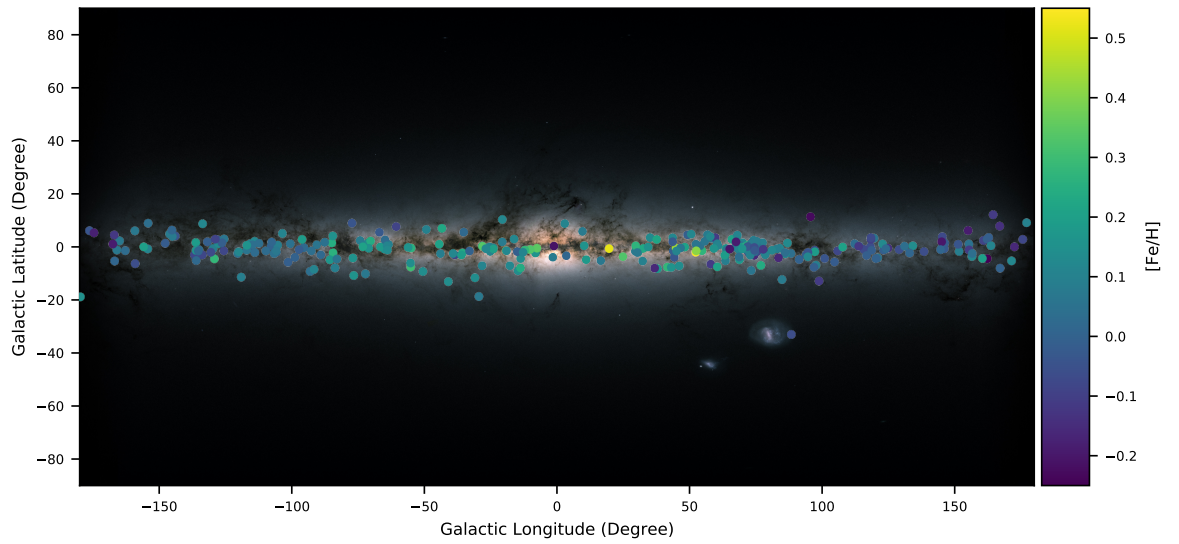


Figure 3.8: Map of the  $\sim 200$  Milky Way Cepheids from [Berdnikov \(2008\)](#) which have a metallicity value from [Genovali et al. \(2014, 2015\)](#), edge-on view.

### 3.4.2 Metallicity for LMC and SMC Cepheids

Very few individual metallicity measurements are available for LMC and SMC Cepheids. From a sample of 22 LMC Cepheids, [Romaniello et al. \(2008\)](#) obtained a mean value of  $[\text{Fe}/\text{H}]_{\text{LMC}} = -0.34 \pm 0.03$  dex with a dispersion of 0.15 dex. From 3 LMC Cepheids in the young blue cluster NGC 1866, [Molinaro et al. \(2012\)](#) derived a slightly less metallic average of  $[\text{Fe}/\text{H}]_{\text{LMC}} = -0.40 \pm 0.04$  dex while [Lemasle et al. \(2017\)](#) confirmed the [Romaniello et al. \(2008\)](#) value with  $-0.33 \pm 0.03$  dex from 6 LMC Cepheids in NGC 1866. Combining these previous estimates, [Gieren et al. \(2018\)](#) adopted a mean metallicity of  $[\text{Fe}/\text{H}]_{\text{LMC}} = -0.34 \pm 0.06$  dex which includes a systematic uncertainty of 0.05 dex to account for possible differences of metallicity scales. I followed [Gieren et al. \(2018\)](#) and adopted this last value for the LMC mean metallicity.

Regarding the SMC sample, [Romaniello et al. \(2008\)](#) obtained an average metallicity of  $-0.75 \pm 0.02$  dex with a dispersion of 0.08 dex from a total of 14 SMC Cepheids. This value is in excellent agreement with the mean metallicity of  $-0.73 \pm 0.02$  dex found by [Lemasle et al. \(2017\)](#) from a sample of 4 SMC Cepheids. As for the LMC, I adopted the final average SMC metallicity provided by [Gieren et al. \(2018\)](#) which takes into account a systematic uncertainty of 0.05 dex for the possible different systems used in the various studies:  $[\text{Fe}/\text{H}]_{\text{SMC}} = -0.75 \pm 0.05$  dex.

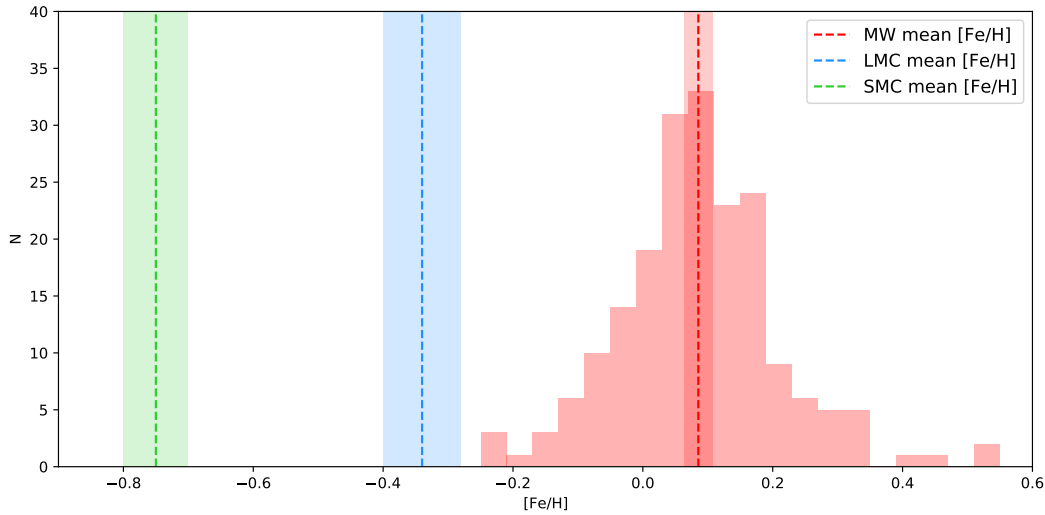


Figure 3.9: Histogram of individual metallicities of MW Cepheids and mean metallicities of LMC and SMC Cepheids.

## 3.5 Calibration of the P-L relation in the Milky Way and Magellanic Clouds

In this section, I first describe the calibration of the P-L relation in the Milky Way, in the LMC and in the SMC without taking into account the metallicity effect. I discuss the slopes and intercepts derived in each of the three galaxies and the dispersion obtained in the various bands. This step will serve as the basis for the calibration of the metallicity effect described in Sect. 3.6.

### 3.5.1 Method

#### 3.5.1.1 From distances and apparent magnitudes to the P-L coefficients

As detailed in Chapter 2, the calibration of the Leavitt law requires to compute absolute magnitudes  $M_\lambda$  from apparent magnitudes  $m_\lambda$  and distances  $d$  in kpc:

$$M_\lambda = m_\lambda - 5 \log d - 10 \quad (3.7)$$

In the Magellanic Clouds, Cepheid distances are directly available but in the Milky Way distances are obtained from *Gaia* EDR3 parallaxes (in mas). The comparison between distances obtained by inverting *Gaia* EDR3 parallaxes and the distances provided by [Bailer-Jones et al. \(2021\)](#) showed that this approach does not introduce significant biases (see Sect. 3.3.1). However, for the Milky Way sample, the P-L coefficients are derived using Astrometric-Based Luminosities (ABL) defined by:

$$ABL = 10^{0.2M_\lambda} = \varpi 10^{0.2(m_\lambda - 10)} \quad (3.8)$$

which avoids issues related to the LKH bias (see Sect. 2.1.1). The calibration of the P-L relation with the ABL approach corresponds to solving the  $a$  and  $b$  coefficients in the equation:

$$ABL = 10^{0.2[a(\log P - \log P_0) + b]} \quad (3.9)$$

where  $\log P_0$  is the pivot period and is set to 0.7 for the present samples. The slope  $a$  and intercept  $b$  are derived by applying a Monte Carlo procedure and by using the `curve_fit` function from the Scipy Python library. The statistical uncertainties on  $a$  and  $b$  are estimated from the 16th and 84th percentiles of the slope and intercept distributions. Two types of systematic uncertainties are added quadratically to the P-L intercept errors: first, the systematic uncertainties of the LMC and SMC distance moduli, 0.026 and 0.032 mag respectively ([Pietrzyński et al. 2019](#); [Graczyk et al. 2020](#)) and the systematic uncertainty of  $\sim 5 \mu\text{as}$  (i.e. 0.020 mag) on the *Gaia* EDR3 parallax zero-point for the MW sample, and secondly the photometric zero-points in each band, due to the use of various systems and references, listed in Table 3.2.

#### 3.5.1.2 Extinction law and Wesenheit indices

For consistency with the LMC and SMC extinction values taken from the [Górski et al. \(2020\)](#) reddening maps, apparent magnitudes are corrected for the reddening using the [Cardelli et al. \(1989\)](#) reddening law with  $R_V = 3.135$  which yields:

$$\begin{cases} R_V &= 3.135 \\ R_I &= 1.894 \\ R_J &= 0.892 \\ R_H &= 0.553 \\ R_K &= 0.363 \end{cases}$$

Following [Scowcroft et al. \(2016\)](#), I adopted the reddening law from [Indebetouw et al. \(2005\)](#) for *Spitzer* bands (based on the [Cardelli et al. \(1989\)](#) reddening law) which gives:

$$\begin{cases} R_{[3.6 \mu\text{m}]} &= 0.203 \\ R_{[4.5 \mu\text{m}]} &= 0.156 \end{cases}$$

Finally, [Wang & Chen \(2019\)](#) provide  $A_\lambda/A_V$  for *Gaia* DR2 bands, with values of 0.789, 1.002 and 0.589 respectively, which gives:

$$\begin{cases} R_G &= 2.473 \\ R_{BP} &= 3.141 \\ R_{RP} &= 1.847 \end{cases}$$

Estimating the extinction law in *Gaia* bands is not trivial and there is currently no universally admitted values (Danielski et al. 2018). For example, Ripepi et al. (2019) obtained higher values for  $R_G$ ,  $R_{BP}$  and  $R_{RP}$ , with 2.90, 3.60, and 2.15 respectively, using Jordi et al. (2010) tables. However, using the SPIPS algorithm (Mérand et al. 2015) with a temperature of 5500 K (which corresponds to the average temperature of Cepheids) returns  $R$  values very similar to Wang & Chen (2019) (2.55, 3.20 and 1.85 respectively, A. Mérand, private communication). In the following I adopt the values from Wang & Chen (2019) but it is important to keep in mind that these values are still uncertain.

In Breuval et al. (2020) the re-evaluation of the  $H_0$  value from Riess et al. (2016) required to adopt the Fitzpatrick (1999) reddening law. However, the reddening law from Cardelli et al. (1989) used in this chapter is different from that adopted in Breuval et al. (2020) which makes the comparison with this previous paper difficult. From these bands, two Wesenheit indices are constructed:

$$W(V, I) = I - 1.526(V - I) \quad (3.10)$$

$$W(J, K) = K - 0.686(J - K) \quad (3.11)$$

### 3.5.1.3 Width of the instability strip

The width of the instability strip is included quadratically in the mean magnitude errors, as explained in the previous chapter (see Sect. 2.3.3). The values in the  $V$  and  $I$  bands are 0.22 mag and 0.14 mag (Macri et al. 2006) and in the  $J$ ,  $H$  and  $K_S$  bands 0.11 mag, 0.09 mag and 0.07 mag respectively (Persson et al. 2004)<sup>6</sup>. For the *Spitzer* bands, I adopted a width of 0.07 mag (Scowcroft et al. 2011; Monson et al. 2012). Finally, it is difficult to estimate the width of the instability strip in *Gaia* bands because most calibrations from the literature either use Wesenheit indices or provide P-L relations without correcting the extinction. Assuming that the  $G$ ,  $BP$  and  $RP$  bands are very similar to the  $V$  band in terms of wavelength and P-L dispersion, the width of the instability strip in *Gaia* bands is set to 0.22 mag. Considering the dispersions obtained in Table 3.3, this hypothesis is slightly conservative.

### 3.5.1.4 Period cut

A non-linearity in the P-L relation was highlighted for short periods around  $\log P \sim 0.4$  (EROS Collaboration et al. 1999; Ngeow & Kanbur 2010). Similarly, Chown et al. (2021) suggested a break in the P-L slope at  $\log P \sim 0.29$  and also at longer periods for  $\log P \sim 1.72$ . Additionally, the presence of misidentified first-overtone at the short-period end can contaminate the P-L relation and increase its dispersion. For these reason, considering extremely short and extremely long period Cepheids is not recommended in this study. The investigation of the P-L slope at longer or shorter periods must be carried out carefully with a large sample. In the following, Cepheids with periods shorter than 2.5 days ( $\log P = 0.4$ ) and longer than 52 days ( $\log P = 1.72$ ) are excluded.

## 3.5.2 Results

The period-luminosity relation is fitted in the Milky Way and in the Magellanic Clouds in the various bands mentioned previously. A few outliers were removed using a  $3 - \sigma$  clipping procedure. Fig. 3.10 shows the  $K$ -band P-L relation in the Milky Way and in the Magellanic Clouds. In this band, the slope is almost identical for the three galaxies. Regarding the intercept, a trend is clearly

<sup>6</sup> In Breuval et al. (2021) we adopted a width of 0.15 mag in  $V$ , 0.09 mag in  $I$  and 0.07 mag in the three NIR bands which was incorrect.



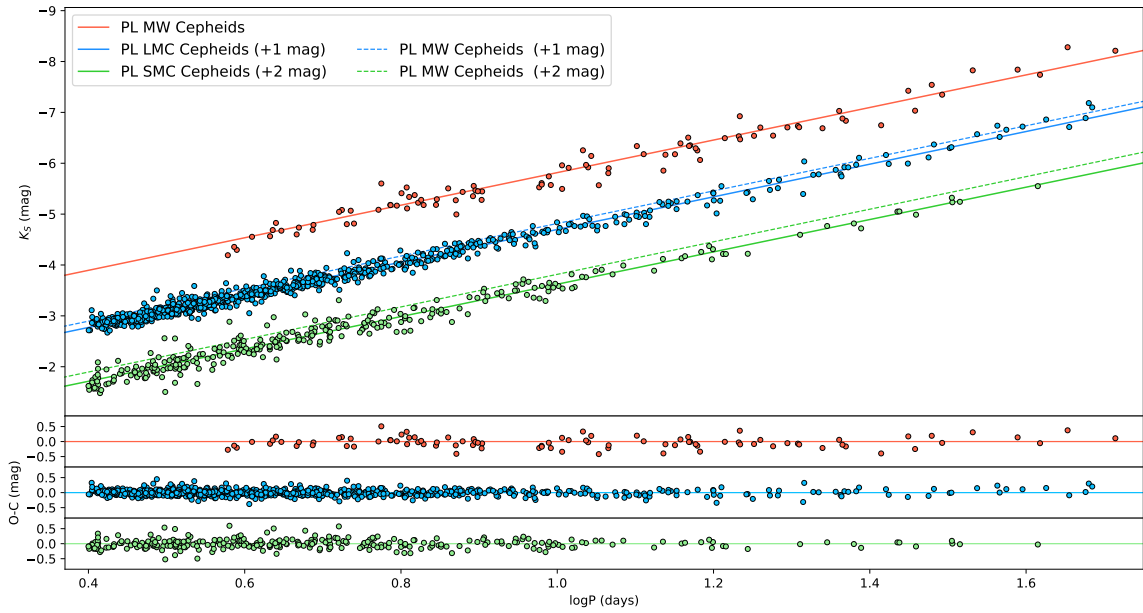


Figure 3.10: Period-luminosity relation in the Milky Way (red), in the LMC (blue) and in the SMC (green). The slope and intercept are both fitted. The LMC and SMC relations were shifted by 1 mag and 2 mag for representation purposes. The two dashed lines show the Milky Way calibration with the same shift as for the LMC and SMC samples. The bottom panels represent the residuals in terms of absolute magnitudes.

visible with SMC Cepheids being fainter than LMC Cepheids, and LMC Cepheids being fainter than Milky Way Cepheids. This trend can be explained by the existence of the metallicity effect discussed in this chapter. In other bands, this trend is not always directly visible because the slopes can slightly differ between the three galaxies. For this reason, in the next section, the metallicity effect is derived by fitting the intercept of the P-L relation in the Milky Way, in the LMC and in the SMC with the same fixed slope. The P-L coefficients and the dispersion as well as the number of stars considered for each sample are listed in Table 3.3.

In the three galaxies, the slope  $\alpha$  of the period-luminosity relation becomes more negative from optical to infrared wavelengths. This quasi-linear trend is represented in Fig. 3.11. Only the slope in the  $[4.5 \mu\text{m}]$  band does not follow the linear behaviour observed for all other bands and is shallower than the slope at  $[3.6 \mu\text{m}]$ . This deviation of the  $[4.5 \mu\text{m}]$  slope was already noticed by [Scowcroft et al. \(2011\)](#) and is represented in their Figure 8. It is explained by the presence of a carbon-monoxide (CO) rotation-vibration band-head at  $4.6 \mu\text{m}$  which is aligned with the *Spitzer*  $[4.5 \mu\text{m}]$  filter. This effect is discussed in detail in Sect. 3.6.2.

Similarly, the intercept of the P-L relation taken at  $\log P = 0.7$  and noted  $\beta$  decreases and becomes more negative from the optical to the infrared (see Fig. 3.12), as expected (see e.g. [Madore & Freedman 2012](#); [Madore et al. 2017](#); [Bhardwaj 2020](#)), which can be considered as a validation of the data and of the approach. The P-L slopes and intercepts derived in this chapter and their uncertainties are not exactly identical to those obtained in [B21](#): the differences are due to several minor changes and improvements in the method, such as the use of more recent reddening values (instead of the [Fernie et al. \(1995\)](#) values adopted in [B21](#)), an update in the photometric zero-point uncertainties (see Sect. 3.2) and in the width of the instability strip (see Sect. 3.5.1.3).



Table 3.3: Results of the fit of the P-L relation of the form  $M = \alpha(\log P - 0.7) + \beta$  in the Milky Way, the Large Magellanic Cloud and the Small Magellanic Cloud. The slope and intercept were both fitted and obtained by applying a Monte-Carlo procedure. The last column gives the number of stars after the sigma-clipping procedure and the period-cut. The results are sorted by wavelength.

Band	$\alpha$	$\beta$	$\sigma$	$N_{\text{stars}}$
Milky Way				
<i>BP</i>	$-2.491 \pm 0.080$	$-3.105 \pm 0.034$	0.31	152
<i>V</i>	$-2.599 \pm 0.078$	$-3.334 \pm 0.034$	0.30	175
<i>G</i>	$-2.739 \pm 0.076$	$-3.452 \pm 0.032$	0.28	162
<i>RP</i>	$-2.734 \pm 0.077$	$-3.910 \pm 0.033$	0.25	142
<i>I</i>	$-2.914 \pm 0.057$	$-3.981 \pm 0.030$	0.24	149
<i>J</i>	$-3.074 \pm 0.057$	$-4.506 \pm 0.032$	0.20	93
<i>H</i>	$-3.182 \pm 0.048$	$-4.763 \pm 0.029$	0.18	93
<i>K</i>	$-3.200 \pm 0.041$	$-4.856 \pm 0.026$	0.18	93
[3.6 $\mu\text{m}$ ]	$-3.533 \pm 0.081$	$-4.805 \pm 0.042$	0.15	19
[4.5 $\mu\text{m}$ ]	$-3.445 \pm 0.078$	$-4.801 \pm 0.041$	0.16	19
<i>W<sub>JK</sub></i>	$-3.295 \pm 0.042$	$-5.095 \pm 0.029$	0.17	93
<i>W<sub>VI</sub></i>	$-3.282 \pm 0.038$	$-5.017 \pm 0.027$	0.18	145
Large Magellanic Cloud				
<i>BP</i>	$-2.552 \pm 0.032$	$-3.091 \pm 0.027$	0.25	979
<i>V</i>	$-2.704 \pm 0.028$	$-3.284 \pm 0.029$	0.23	1446
<i>G</i>	$-2.785 \pm 0.029$	$-3.353 \pm 0.027$	0.19	1214
<i>RP</i>	$-2.874 \pm 0.032$	$-3.849 \pm 0.027$	0.17	974
<i>I</i>	$-2.916 \pm 0.019$	$-3.910 \pm 0.028$	0.15	1460
<i>J</i>	$-3.148 \pm 0.017$	$-4.379 \pm 0.032$	0.12	806
<i>H</i>	$-3.143 \pm 0.014$	$-4.693 \pm 0.031$	0.11	809
<i>K</i>	$-3.210 \pm 0.012$	$-4.735 \pm 0.026$	0.10	807
[3.6 $\mu\text{m}$ ]	$-3.334 \pm 0.038$	$-4.787 \pm 0.035$	0.11	66
[4.5 $\mu\text{m}$ ]	$-3.238 \pm 0.039$	$-4.818 \pm 0.035$	0.11	66
<i>W<sub>JK</sub></i>	$-3.261 \pm 0.014$	$-4.977 \pm 0.032$	0.09	806
<i>W<sub>VI</sub></i>	$-3.281 \pm 0.013$	$-4.877 \pm 0.030$	0.08	1432
Small Magellanic Cloud				
<i>BP</i>	$-2.394 \pm 0.080$	$-3.060 \pm 0.038$	0.28	228
<i>V</i>	$-2.593 \pm 0.074$	$-3.195 \pm 0.038$	0.28	284
<i>G</i>	$-2.707 \pm 0.074$	$-3.274 \pm 0.038$	0.25	251
<i>RP</i>	$-2.763 \pm 0.079$	$-3.791 \pm 0.038$	0.21	229
<i>I</i>	$-2.872 \pm 0.048$	$-3.841 \pm 0.036$	0.22	297
<i>J</i>	$-2.995 \pm 0.037$	$-4.302 \pm 0.035$	0.18	262
<i>H</i>	$-3.184 \pm 0.030$	$-4.602 \pm 0.034$	0.17	288
<i>K</i>	$-3.180 \pm 0.024$	$-4.668 \pm 0.034$	0.15	295
[3.6 $\mu\text{m}$ ]	$-3.227 \pm 0.151$	$-4.732 \pm 0.087$	0.08	21
[4.5 $\mu\text{m}$ ]	$-3.116 \pm 0.151$	$-4.801 \pm 0.083$	0.08	21
<i>W<sub>JK</sub></i>	$-3.324 \pm 0.024$	$-4.901 \pm 0.036$	0.13	261
<i>W<sub>VI</sub></i>	$-3.334 \pm 0.031$	$-4.834 \pm 0.036$	0.12	283

Except for *Spitzer* bands, the dispersion of the P-L relation linearly increases with  $1/\lambda$ . This dependence, represented in Fig. 3.13, indicates that the dispersion obtained here is mostly due to the reddening sensitivity, which is more important in the optical than in the infrared. The two *Spitzer* bands both show a P-L dispersion between 0.10 mag and 0.15 mag but the P-L calibration in these wavelengths is limited by the small number of Cepheids with *Spitzer* light curves. In the LMC, for example, where a very large number of Cepheids are available in most bands except at [3.6  $\mu\text{m}$ ] and

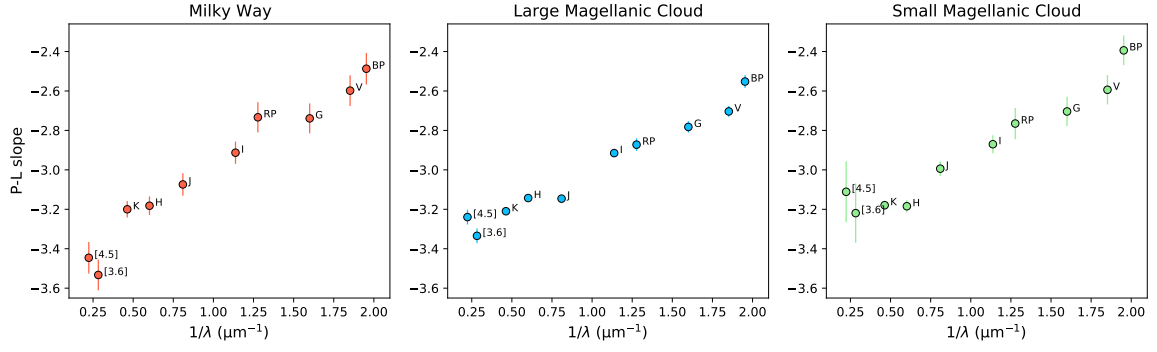


Figure 3.11: Slope of the P-L relation as a function of wavelength in the Milky Way, the Large Magellanic Cloud and the Small Magellanic Cloud.

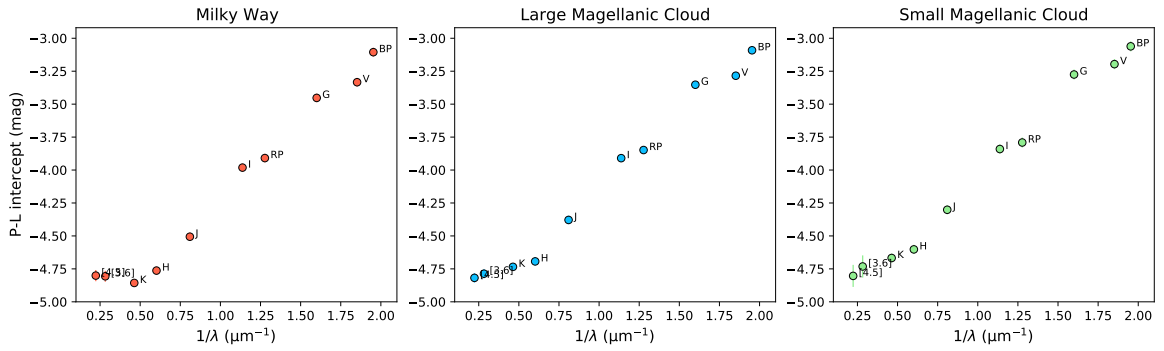


Figure 3.12: Intercept of the P-L relation as a function of wavelength in the Milky Way, the Large Magellanic Cloud and the Small Magellanic Cloud.

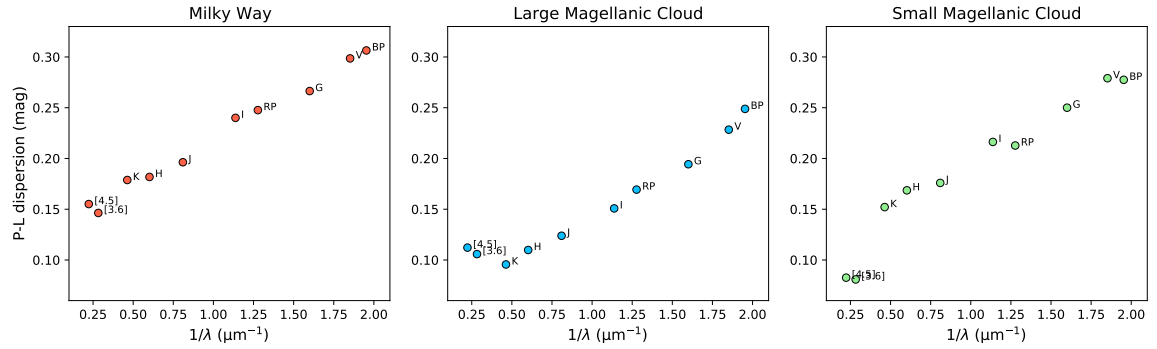


Figure 3.13: Dispersion of the P-L relation (in mag) as a function of wavelength in the Milky Way, the Large Magellanic Cloud and the Small Magellanic Cloud.

[4.5  $\mu\text{m}$ ], the smallest dispersion (apart from Wesenheit indices) is obtained in the  $K_S$  band with a scatter of 0.10 mag. This confirms that the NIR bands  $J$ ,  $H$  and  $K_S$ , with their very large numbers of complete Cepheid light curves available and their low sensitivity to extinction, remain among the best wavelengths to calibrate the Leavitt law (the only limitation being that ground-based systems are not suitable for measuring photometry of extragalactic Cepheids).

In Sect. 3.5.1.2 it is highlighted that the total-to-selective absorption coefficients  $R_\lambda$  are still

poorly defined for *Gaia* DR2 passbands. Adopting the values from [Ripepi et al. \(2019\)](#) instead of those from [Wang & Chen \(2019\)](#) slightly increases the dispersion of the P-L relation (e.g. from 0.27 mag to 0.31 mag in *G*, or from 0.31 mag to 0.34 mag in *BP* in the Milky Way). It is therefore reasonable to adopt the [Wang & Chen \(2019\)](#) values which result in a smaller dispersion.

In [Breuval et al. \(2021\)](#) we did not consider the SMC sample in the *H* band because only single-point photometry was available. However in the present work I adopted the [Kato et al. \(2007\)](#) point-source catalog in this case, in order to complement the Milky Way and LMC samples. In Fig. 3.11, 3.12 and 3.13, the *H* band does not present any suspect behaviour compared with other wavelengths. One can therefore assume that the use of single-point photometry in the *H* band for the SMC sample does not affect the precision and accuracy of the P-L calibration, and consequently that it will not affect the determination of the metallicity effect.

### 3.6 Deriving the metallicity effect on the Leavitt law

This section describes the calibration of the metallicity dependence of the P-L relation. In Sect. 3.6.1, only individual  $[\text{Fe}/\text{H}]$  measurements of Milky Way Cepheids are adopted. Then, the LMC and SMC samples with their mean metallicity are added to the MW sample for a broader metallicity coverage and the results and their dependences with different parameters are discussed in Sect. 3.6.2.

#### 3.6.1 The metallicity term in the Milky Way

Metal abundance measurements are available for a large number of Milky Way Cepheids, thanks to high quality and high resolution spectra collected by various teams (see references in Sect. 3.4.1). Galactic Cepheids cover a relatively wide metallicity range of  $\sim 0.80$  dex, from  $+0.55$  to  $-0.25$  dex. In this section, I determine the effect of metallicity on the Leavitt law in the Milky Way only.

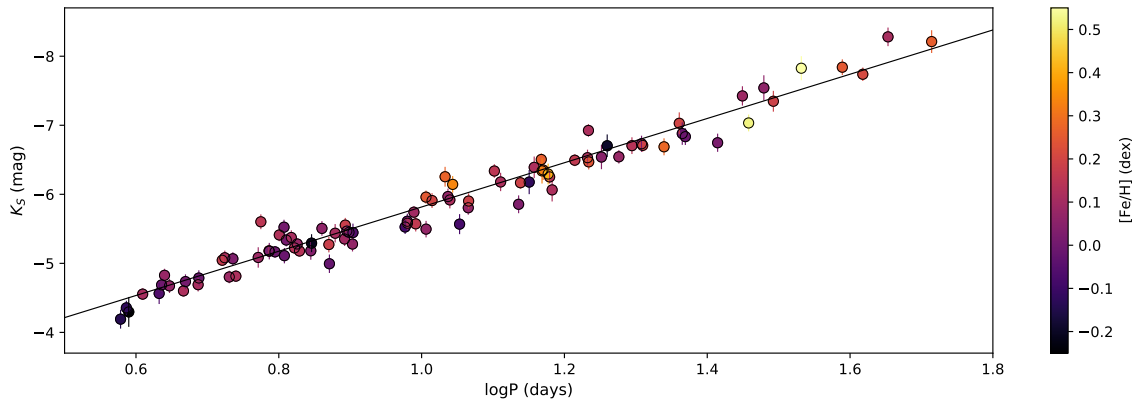


Figure 3.14: Period-Luminosity relation for Milky Way Cepheids in the  $K_S$  band. The color scale represents the metallicity.

Fig. 3.14 shows the distribution of metallic Cepheids (in yellow) and less metallic Cepheids (in dark colors) in the P-L relation in the  $K_S$  band. This band is used as an example because in [B21](#) it is the most sensitive to metallicity, therefore one can expect the trend to be more visible than in other wavelengths. Visually, there is no clear correlation between the brightness of Cepheids and

their metal abundance at a given period. However, on average, long-period Cepheids seem to have higher metallicities than short-period ones. Since they follow the Leavitt law, long-period Cepheids are also brighter than short-period ones, which suggests that metal-rich Cepheids are slightly brighter than metal-poor ones. Fig. 3.15 represents the absolute  $K_S$  band magnitude as a function of the metallicity. The color scale indicates the period of each Cepheid. On this plot, metal-rich Cepheids (on the right-side of the figure) appear on average brighter than metal-poor ones (on the left-side), confirming the trend suggested in Fig. 3.14. This dependence corresponds to a negative sign of the metallicity effect ( $\gamma < 0$ ).

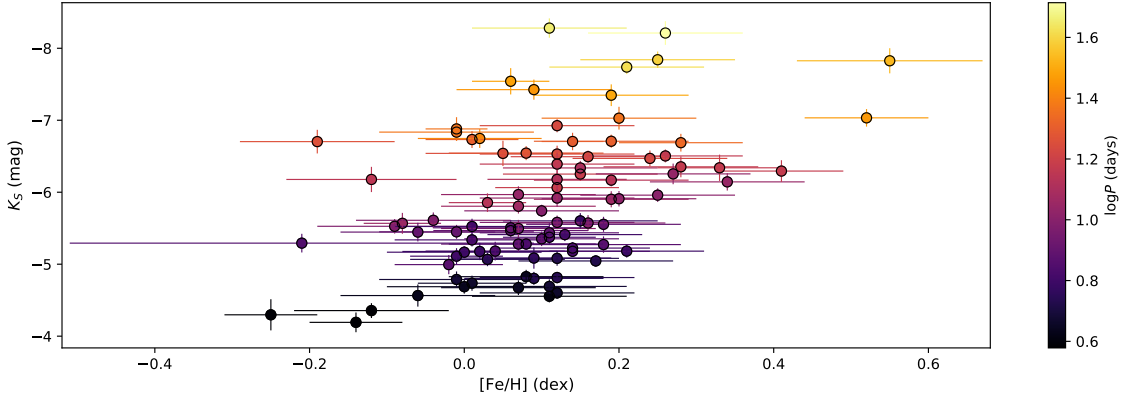


Figure 3.15: Absolute  $K_S$  band magnitude represented against metallicity. The color scale represents the period.

In order to derive the metallicity term in the Milky Way sample, the first step is to calibrate the P-L relation of the form  $M = \alpha(\log P - 0.7) + \beta$ . Then, I searched for a correlation between the brightness of Cepheids at a given period and the metallicity. The equation  $\beta = \gamma [\text{Fe}/\text{H}] + \delta$  is fitted where  $\beta$  are the intercepts of the P-L relations of slope  $\alpha$  verified by each Cepheid. This quantity is obtained by  $\beta = M_{\text{obs}} - \alpha(\log P - 0.7)$ , with  $M_{\text{obs}}$  the absolute magnitude of the star. The errors on the intercepts  $\beta$  include the systematics due to the *Gaia* EDR3 parallax zero-point and to the photometric zero-point. The intercepts  $\beta$  in the  $K_S$  band are represented against  $[\text{Fe}/\text{H}]$  in Fig. 3.16. The points are very dispersed and no clear trend is visible. Fitting the intercept as a function of the metallicity in the  $K_S$  band gives:

$$\beta = -0.185_{\pm 0.107} [\text{Fe}/\text{H}] - 4.817_{\pm 0.016} \quad (3.12)$$

This solution is obtained by applying a Monte Carlo procedure to the intercept and metallicity values. The effect of metallicity is  $\gamma_K = -0.185 \pm 0.107$  mag/dex. In the  $K_S$  band, this effect is expected to be stronger than in other wavelengths (Breuval et al. 2021), however it is still consistent with zero at  $1.7\sigma$ , due to its low precision of 60%. It is however in good agreement with the  $\gamma_K$  value of  $-0.221 \pm 0.051$  mag/dex derived by B21 from the Milky Way and the two Magellanic Clouds, but considerably less precise.

The same procedure is applied to various bands from mid-infrared to the optical. The resulting values of the metallicity effect in mag/dex are listed in Table 3.4 and are represented in Fig. 3.17 as a function of the inverse of the wavelength. The three NIR bands ( $J$ ,  $H$ ,  $K$ ) are very similar and have a metallicity sensitivity between  $-0.150$  and  $-0.190$  mag/dex, which is in good agreement with B21. The ground optical bands  $V$  and  $I$  as well as the *Gaia*  $G$ ,  $BP$  and  $RP$  optical bands are all consistent with a null effect within the uncertainties. In B21 we derived a weak effect of  $-0.048 \pm 0.055$  mag/dex in  $V$  and a slightly stronger effect of  $-0.138 \pm 0.053$  mag/dex in  $I$  which is

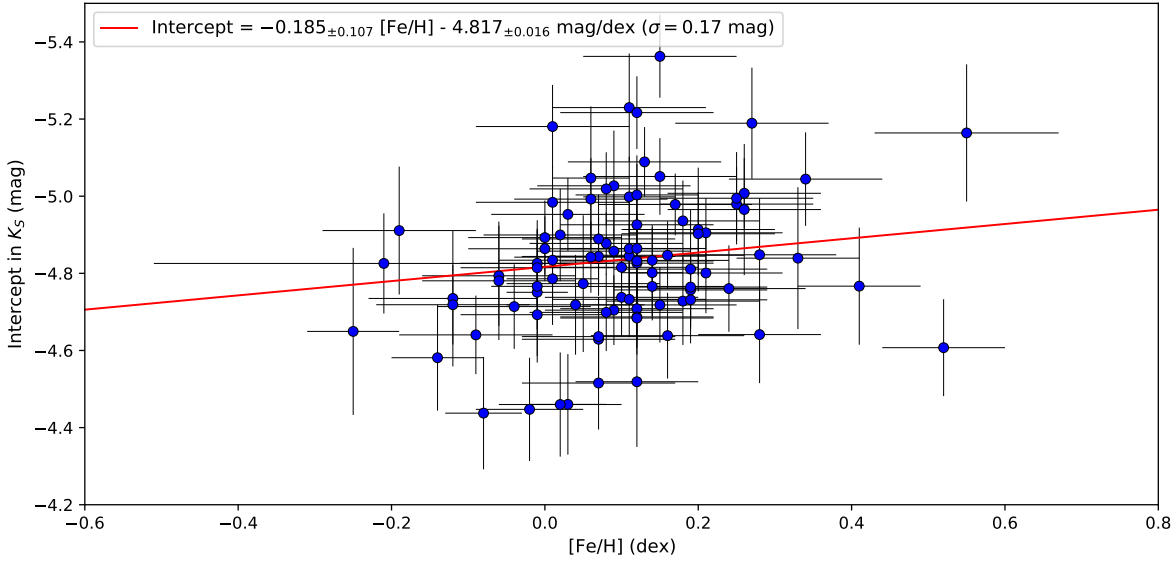


Figure 3.16: Intercept of the P-L relation in the  $K_S$  band for each Cepheid of the MW sample as a function of the metallicity  $[Fe/H]$ .

Table 3.4: Results of the fit of the period-luminosity-metallicity (P-L-Z) relation of the form  $M = \alpha(\log P - 0.7) + \delta + \gamma[Fe/H]$  in the Milky Way sample only.

Band	$\alpha$	$\delta$	$\gamma$	$\sigma$	$N_{\text{stars}}$
<i>BP</i>	$-2.491_{\pm 0.080}$	$-3.049_{\pm 0.026}$	$+0.033_{\pm 0.172}$	0.30	152
<i>V</i>	$-2.599_{\pm 0.078}$	$-3.283_{\pm 0.025}$	$+0.053_{\pm 0.156}$	0.29	175
<i>G</i>	$-2.735_{\pm 0.075}$	$-3.402_{\pm 0.024}$	$-0.037_{\pm 0.155}$	0.27	162
<i>RP</i>	$-2.734_{\pm 0.077}$	$-3.869_{\pm 0.024}$	$-0.045_{\pm 0.161}$	0.24	142
<i>I</i>	$-2.914_{\pm 0.057}$	$-3.946_{\pm 0.019}$	$-0.006_{\pm 0.120}$	0.24	149
<i>J</i>	$-3.076_{\pm 0.054}$	$-4.465_{\pm 0.020}$	$-0.154_{\pm 0.125}$	0.19	93
<i>H</i>	$-3.181_{\pm 0.046}$	$-4.724_{\pm 0.018}$	$-0.179_{\pm 0.113}$	0.18	93
<i>K</i>	$-3.201_{\pm 0.042}$	$-4.817_{\pm 0.016}$	$-0.185_{\pm 0.107}$	0.17	93
$[3.6 \mu\text{m}]$	$-3.533_{\pm 0.081}$	$-4.814_{\pm 0.038}$	$+0.161_{\pm 0.224}$	0.14	19
$[4.5 \mu\text{m}]$	$-3.445_{\pm 0.078}$	$-4.812_{\pm 0.039}$	$+0.199_{\pm 0.235}$	0.15	19
$W_{VI}$	$-3.282_{\pm 0.038}$	$-4.986_{\pm 0.012}$	$-0.142_{\pm 0.085}$	0.18	145
$W_{JK}$	$-3.295_{\pm 0.042}$	$-5.054_{\pm 0.016}$	$-0.213_{\pm 0.104}$	0.17	93

also close to the present values. In the mid-infrared *Spitzer* bands, however, the metallicity term is positive with  $\gamma_{[3.6 \mu\text{m}]} = 0.161 \pm 0.224$  mag/dex and  $\gamma_{[4.5 \mu\text{m}]} = 0.199 \pm 0.235$  mag/dex, although it is consistent with zero due to the important error bars. The uncertainties are particularly large in both *Spitzer* bands because the sample is very limited: only 19 Cepheids of the initial sample have a good quality parallax and a fundamental pulsation mode. For this reason the estimate of the metallicity term in the *Spitzer* bands is too uncertain for a firm conclusion. The NIR Wesenheit index  $W_{JK}$  is strongly affected by metallicity with  $\gamma_{W_{JK}} = -0.213 \pm 0.104$  mag/dex with a negative sign, which indicates that metal-rich Cepheids are brighter. This result is in excellent agreement with B21. Finally, the optical Wesenheit index  $W_{VI}$  is slightly less sensitive to metallicity with  $\gamma_{W_{VI}} = -0.142 \pm 0.085$  mag/dex.

Among the NIR and optical bands, a trend is already visible with NIR bands being more sensitive to metallicity than optical ones. However, the precision is still largely insufficient to claim that there is a correlation between the metallicity effect and the wavelength. As a conclusion, this test shows the absolute necessity to extend the analysis to a larger sample with a broader metallicity range by including LMC and SMC Cepheids, and the importance of collecting more high resolution spectra in order to improve the precision of individual Cepheid metallicity measurements.

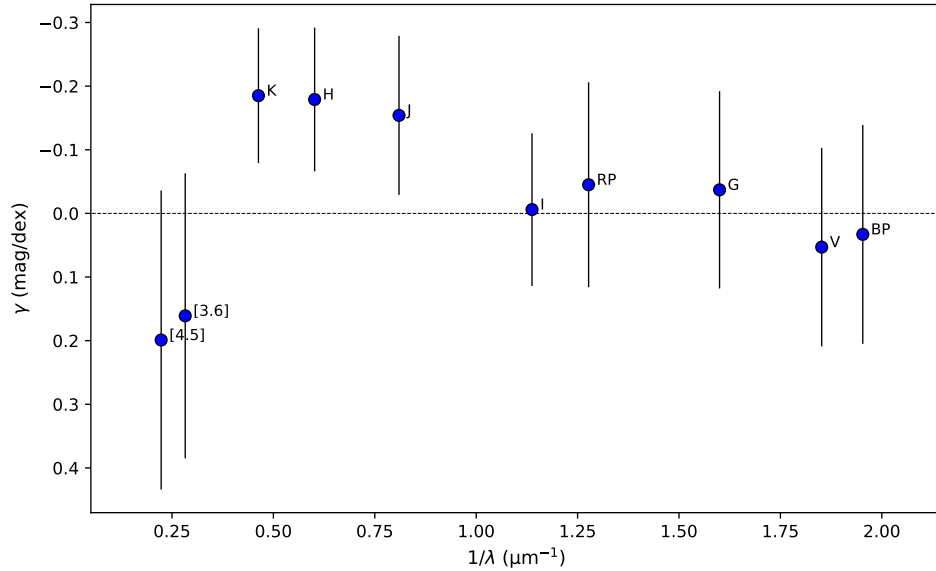


Figure 3.17: Metallicity effect  $\gamma$  (mag/dex) derived from the Milky Way sample only, as a function of wavelength. The values obtained in the *Spitzer* bands ([3.6  $\mu\text{m}$ ], [4.5  $\mu\text{m}$ ]) are based on a very limited number of stars ( $\sim 20$ ) compared with other bands ( $\sim 100 - 150$ ).

### 3.6.2 The metallicity term from Milky Way and Magellanic Cloud Cepheids

#### 3.6.2.1 Method

In the previous section, the effect of metallicity was calibrated in the Milky Way sample with individual Cepheid iron abundances. Unfortunately, the results obtained in the Milky Way are still unprecise due to the limited metallicity range covered by Galactic Cepheids and by the insufficient precision of spectroscopic metallicities. In this section, the LMC and SMC Cepheid samples are included in complement to the MW sample. Mean metallicities of  $-0.34 \pm 0.06$  dex and  $-0.75 \pm 0.05$  dex are adopted for the LMC and SMC samples respectively (see Sect. 3.4.2). For consistency, a mean metallicity of  $+0.085 \pm 0.022$  dex is adopted for the Milky Way sample.

The approach is similar to that described in Sect. 3.6.1. The P-L relation of the form  $M = \alpha(\log P - 0.7) + \beta$  is fitted in the three galaxies. For comparing the intercepts, the slopes must be fixed to the same values for the MW, LMC and SMC samples. In all bands, the LMC has the largest number of stars and provides the most precise P-L slope therefore it is adopted for the MW and SMC samples. Fixing the slope to a given value is not a limitation since the MW, LMC and SMC samples globally have similar slopes. Moreover this strategy is adopted in various works for investigating the intercept of the P-L relation (e.g. [Groenewegen 2018](#); [Ripepi et al. 2019](#); [Riess et al. 2019a](#)). The P-L intercepts  $\beta$  in the Milky Way and Magellanic Clouds include the systematic uncertainties related to



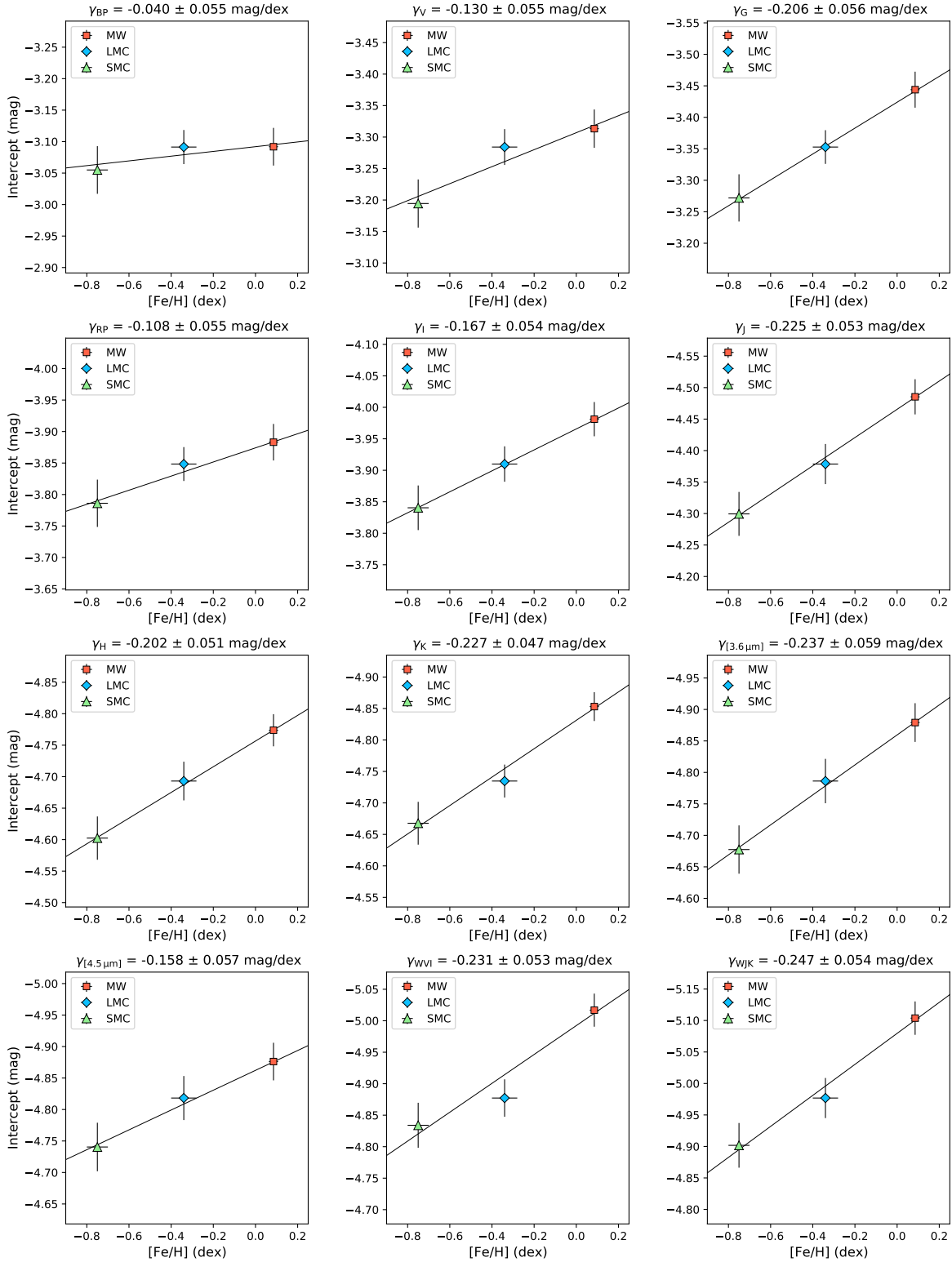


Figure 3.18: Intercept ( $\beta$ ) of the P-L relation in the MW, LMC and SMC represented as a function of the mean metallicity in the three galaxies. The linear fit is realized with a Monte Carlo procedure repeated 10,000 times and the slope gives the metallicity term ( $\gamma$ ) of the P-L relation.

the photometric zero-point and to the distances, they are represented as a function of the mean metallicity of each galaxy in Fig. 3.18 for each band. The relation  $\beta = \delta + \gamma [\text{Fe}/\text{H}]$  is fitted using a Monte Carlo algorithm taking into account the uncertainties on both the intercepts and the mean metallicity values.

### 3.6.2.2 Results

The results obtained for the  $\alpha$ ,  $\delta$  and  $\gamma$  coefficients are listed in Table 3.5. The combination of the Milky Way and Magellanic Cloud samples yields a negative metallicity effect in all bands, meaning that metal-rich Cepheids are intrinsically brighter than metal-poor Cepheids of the same pulsation period. Compared with the metallicity effect determined from Milky Way Cepheids only (see Table 3.4), the results are twice (in the NIR) to four times (at  $[3.6\mu\text{m}]$  and  $[4.5\mu\text{m}]$ ) more precise when the LMC and SMC samples are included. In the near infrared, the effect is strong with  $\gamma_J = -0.225 \pm 0.053$  mag/dex,  $\gamma_H = -0.202 \pm 0.051$  mag/dex,  $\gamma_K = -0.227 \pm 0.047$  mag/dex, and in the  $W_{JK}$  Wesenheit index  $\gamma_{W_{JK}} = -0.247 \pm 0.054$  mag/dex. These values agree perfectly with the results derived in B21 and the precision obtained in the  $H$  band is almost twice better thanks to the inclusion of IRSF single-point photometry from Kato et al. (2007) in the SMC sample. In optical bands, the metallicity effect is more moderate with  $\gamma_V = -0.130 \pm 0.055$  mag/dex and  $\gamma_I = -0.167 \pm 0.054$  mag/dex. In B21 we found that the  $V$  band was significantly less sensitive to metallicity with  $\gamma_V = -0.048 \pm 0.055$  mag/dex: this difference is due to the improvements in the method mentioned in Sect. 3.5.2. In the present study, the intercepts of the MW, LMC and SMC period-luminosity relations in the  $V$  band linearly decrease (in absolute sense) as shown in Fig. 3.18 which was not the case in B21 where the P-L intercept in the LMC was more negative than in the MW and in the SMC.

Table 3.5: Results of the fit of the period-luminosity-metallicity (P-L-Z) relation of the form  $M = \alpha(\log P - 0.7) + \delta + \gamma[\text{Fe}/\text{H}]$  in the Milky Way, LMC and SMC samples.

Band	$\alpha$	$\delta$	$\gamma$	$N_{\text{stars}}$
<i>BP</i>	$-2.552 \pm 0.032$	$-3.091 \pm 0.025$	$-0.040 \pm 0.055$	1360
<i>V</i>	$-2.705 \pm 0.027$	$-3.305 \pm 0.025$	$-0.130 \pm 0.055$	1905
<i>G</i>	$-2.784 \pm 0.029$	$-3.425 \pm 0.024$	$-0.206 \pm 0.056$	1627
<i>RP</i>	$-2.873 \pm 0.031$	$-3.875 \pm 0.024$	$-0.108 \pm 0.055$	1346
<i>I</i>	$-2.916 \pm 0.019$	$-3.967 \pm 0.023$	$-0.167 \pm 0.054$	1906
<i>J</i>	$-3.146 \pm 0.017$	$-4.465 \pm 0.024$	$-0.225 \pm 0.053$	1161
<i>H</i>	$-3.143 \pm 0.014$	$-4.757 \pm 0.022$	$-0.202 \pm 0.051$	1190
<i>K</i>	$-3.210 \pm 0.012$	$-4.831 \pm 0.020$	$-0.227 \pm 0.047$	1195
$[3.6\mu\text{m}]$	$-3.334 \pm 0.039$	$-4.859 \pm 0.026$	$-0.237 \pm 0.059$	106
$[4.5\mu\text{m}]$	$-3.238 \pm 0.038$	$-4.863 \pm 0.026$	$-0.158 \pm 0.057$	106
$W_{VI}$	$-3.280 \pm 0.013$	$-4.992 \pm 0.022$	$-0.231 \pm 0.053$	1860
$W_{JK}$	$-3.261 \pm 0.014$	$-5.080 \pm 0.023$	$-0.247 \pm 0.054$	1160

The effect of metallicity in *Gaia* and *Spitzer* bands is new and was not provided in B21. In *Gaia* passbands, the effect is moderate in *BP* and *RP* with  $\gamma_{BP} = -0.040 \pm 0.055$  mag/dex (consistent with zero) and  $\gamma_{RP} = -0.108 \pm 0.055$  mag/dex. In the *G* band the effect is stronger with  $\gamma_G = -0.206 \pm 0.056$  mag/dex which is comparable to the values obtained in the NIR. At

the *Spitzer* [3.6  $\mu\text{m}$ ] wavelength, the metallicity is consistent with the NIR bands with  $\gamma_{[3.6\mu\text{m}]} = -0.237 \pm 0.059 \text{ mag/dex}$ . However, the effect derived in the [4.5  $\mu\text{m}$ ] band is more moderate with  $\gamma_{[4.5\mu\text{m}]} = -0.158 \pm 0.057 \text{ mag/dex}$ .

### 3.6.2.3 The effect of CO absorption on *Spitzer* bands

Despite the great amount and quality of data, the *Spitzer* [4.5  $\mu\text{m}$ ] P-L relation was so far excluded from studies of the distance scale by the Carnegie Chicago Hubble Program (CCHP, [Scowcroft et al. 2011, 2016](#)), because distance moduli obtained in this band disagreed with measurements made in other wavelengths. As mentioned in Sect. 3.5.2 and confirmed by [Marengo et al. \(2010\)](#) and [Scowcroft et al. \(2011\)](#), the slope of the P-L relation at [4.5  $\mu\text{m}$ ] does not follow the expected linear trend and is  $\sim 0.1 \text{ mag}$  shallower than at [3.6  $\mu\text{m}$ ]. This anomaly is due to the temperature-dependent presence of the CO band between 4 and 6  $\mu\text{m}$ , which is aligned with the [4.5  $\mu\text{m}$ ] filter (Fig. 3.19).

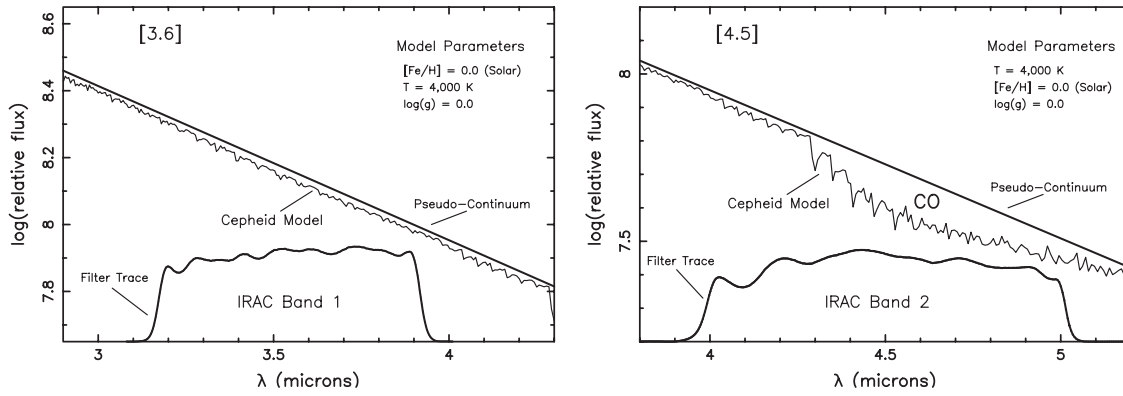


Figure 3.19: Synthetic spectra for supergiants of solar metallicity over a wavelength range that corresponds to the [3.6  $\mu\text{m}$ ] (left) and [4.5  $\mu\text{m}$ ] (right) *Spitzer* passbands, showing the effect of the CO band on the flux in the [4.5  $\mu\text{m}$ ] filter. This figure is taken from [Freedman et al. \(2011\)](#).

The presence of this CO band-head situated around 4.6  $\mu\text{m}$  has been known for many years and was first discussed by [Ayres \(1994\)](#) and [Wiedemann et al. \(1994\)](#). Carbon monoxide is one of the most abundant stellar molecules and is formed in the atmosphere of stars by radiative association:



where  $\gamma$  is a photon emitted by the reaction. For temperatures between 4000 – 6000 K, the CO molecule is destroyed by chemical dissociation:



These reactions occur in a Cepheid's atmosphere which results in a change of opacity and therefore a change of flux in the [4.5  $\mu\text{m}$ ] band. Long-period Cepheids have cooler average temperature and therefore allow the presence of CO molecules in their atmosphere. The CO absorbs some of the flux in the [4.5  $\mu\text{m}$ ] band, making the star appear fainter and bluer. For Cepheids of shorter period, the average temperature is higher and CO molecules are gradually dissociated, making the stars appear redder. This effect is therefore purely temperature-dependent. The variation of flux for long period Cepheids results in a shallower P-L slope in the [4.5  $\mu\text{m}$ ] band compared with the [3.6  $\mu\text{m}$ ] band

which is not affected.

Marengo et al. (2010) first highlighted the effect of the CO band on the  $([3.6\mu\text{m}] - [4.5\mu\text{m}])$  color for a sample of  $\sim 30$  Milky Way Cepheids with *Spitzer* photometry. The authors attribute this feature to a general property of the stars, not only Cepheids but also all supergiants of the temperature and gravity of Cepheids. This effect was confirmed and described by Scowcroft et al. (2011, 2013, 2016).

The relation between the presence of this CO band and the metallicity effect in *Spitzer* wavelengths is still debated. Freedman & Madore (2011) suggested that the mid-infrared P-L relation could be mildly dependent on metallicity with  $\gamma_{[3.6\mu\text{m}]} = -0.39 \pm 0.16$  mag/dex and  $\gamma_{[4.5\mu\text{m}]} = -0.25 \pm 0.18$  mag/dex. They updated the first value to  $\gamma_{[3.6\mu\text{m}]} = -0.09 \pm 0.29$  mag/dex in Freedman et al. (2011). Similarly, Ngeow et al. (2012) concluded that their synthetic mid-infrared P-L relations based on a series of pulsation models likely depend on metallicity. Conversely, Majaess et al. (2013b) found that the slope and intercept of the P-L relation in the *Spitzer* bands are insensitive to metallicity with  $|\gamma| < 0.1$  mag/dex. Finally, Scowcroft et al. (2016) explored in detail the effect of the CO band-head on *Spitzer* photometry and concluded that the  $([3.6\mu\text{m}] - [4.5\mu\text{m}])$  color provides a reliable metallicity indicator, and that the  $[3.6\mu\text{m}]$  band is not contaminated by this temperature dependent effect and is very suitable for distance determination.

#### 3.6.2.4 The dependence of the metallicity effect with wavelength, comparison with the literature

The values of the metallicity effect derived in this study by combining Milky Way, LMC and SMC Cepheids are represented as a function of the inverse of the wavelength in Fig. 3.20 and compared with other estimates from the literature. In *V*, *I*, *J* and *K*, the present findings agree well with the results from Gieren et al. (2018), obtained with a Baade-Wesselink approach assuming the period-projection factor relation from Storm et al. (2011a). However the Gieren et al. (2018) values are less precise (especially in the optical) and systematically more negative. The metallicity effect derived by Wielgórski et al. (2017) from a comparative study of LMC and SMC Cepheid P-L relations is consistent with zero in *V*, *I*, *J*, *H*, *K* and differs from our values at  $1.2\sigma$  to  $2.5\sigma$ . The strong metallicity effect of about  $-0.45$  mag/dex obtained by Ripepi et al. (2021) differs at  $2\sigma$  from our findings but firmly confirms the negative sign in the NIR. Finally, Freedman & Madore (2011) obtained a strong and negative metallicity effect in *Spitzer* bands, which agrees with our results, but a positive effect increasing from the near-infrared to the optical, reaching  $+0.50 \pm 0.31$  mag/dex in *V*, with a crossover occurring near the *K* band.

From the present sample of Galactic and Magellanic Cloud Cepheids, the metallicity effect derived in the various bands shows a trend: although it is always negative, it is generally stronger in infrared than in optical bands. Fitting a linear relation through the blue points in Fig. 3.20 with a Monte-Carlo algorithm gives:

$$\gamma (\text{mag/dex}) = \frac{0.087 \pm 0.031}{\lambda (\mu\text{m})} - (0.268 \pm 0.038) \quad (3.15)$$

for  $0.5\mu\text{m} < \lambda < 3.5\mu\text{m}$  with a dispersion of  $0.040$  mag/dex. The *Spitzer* band at  $[4.5\mu\text{m}]$  was excluded from the fit for the reasons mentioned previously (see Sect. 3.6.2.3). The dependence of the metallicity effect with the wavelength is significant to  $2.8\sigma$ .

While Wielgórski et al. (2017) and Gieren et al. (2018) obtained a metallicity effect independent of wavelength, Freedman & Madore (2011) found a negative effect in the mid-infrared which

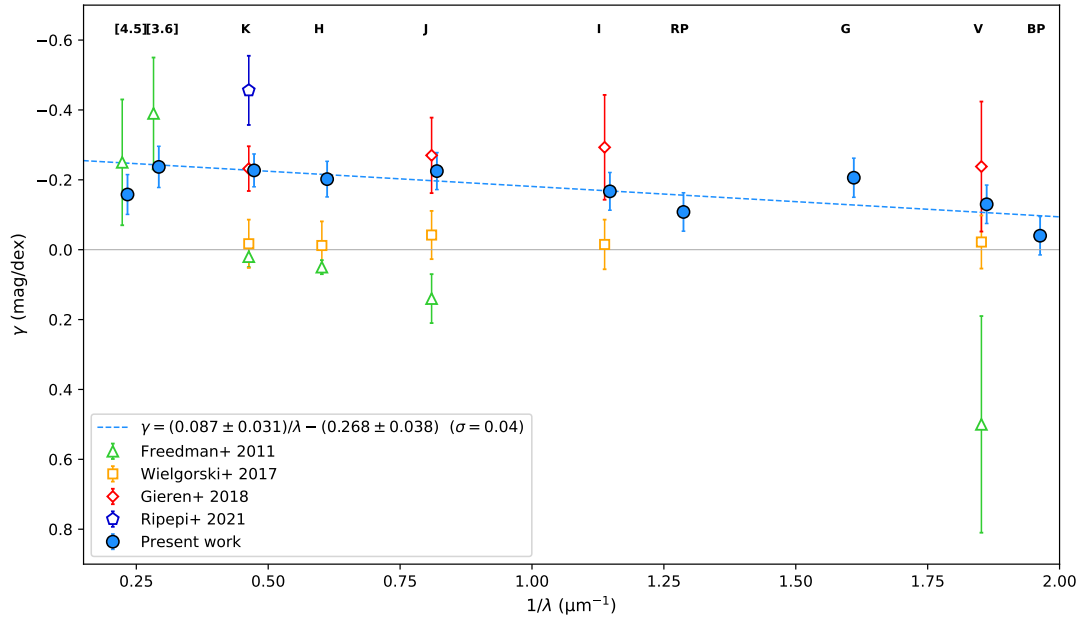


Figure 3.20: Metallicity effect  $\gamma$  represented against the inverse of the wavelength  $1/\lambda$  and comparison with other results from the literature (Freedman & Madore 2011; Wielgórski et al. 2017; Gieren et al. 2018; Ripepi et al. 2021).

becomes positive in near-infrared and increases toward the optical. The line-blanketing effect, mentioned in Sect. 3.1, predicts that the important number of metallic absorption lines in the optical appear as a decrease in the continuum and is re-emitted at longer wavelengths, typically in the near-infrared or mid-infrared. As a consequence, metal-rich stars should be brighter than metal-poor ones in the MIR/NIR, which is what is observed in the present results.

If the metallicity effect is only or mostly due to the line-blanketing effect, the flux in optical bands should be reduced by the presence of the lines, meaning that the metallicity effect would be opposite with metal-rich Cepheids being fainter in the optical. This trend is observed by Freedman & Madore (2011) with  $\gamma$  being negative in *Spitzer* bands and becoming positive in the optical (Fig. 3.20). However in the present work the variation of the metallicity effect with wavelength is monotonic and stays always negative in the range of wavelengths considered. By interpolating Eq. 3.15 further in the optical, it predicts that the metallicity effect becomes consistent with zero in the error bars around  $\lambda \sim 0.510 \mu\text{m}$  (close to the *BP* band) and that the crossover ( $\gamma$  becoming positive) occurs at even shorter wavelengths for  $\lambda = 0.324 \mu\text{m}$  ( $1/\lambda = 3.1 \mu\text{m}^{-1}$ ).

My result agrees very well with the work by Tsang (2019): the author explored the metallicity effect in Sloan Digital Sky Survey (SDSS) *g*, *r* and *i* filters and derived that  $\gamma$  is negative between  $1.3 \mu\text{m}^{-1} < 1/\lambda < 2.2 \mu\text{m}^{-1}$ , with a linear decrease following the relation:

$$\gamma \text{ (mag/dex)} = \frac{0.09}{\lambda \text{ (}\mu\text{m)}} - 0.448 \quad (3.16)$$

This trend, and especially the slope, is in excellent agreement with the linear dependence obtained in Eq. 3.15. This shows that the line blanketing effect does not systematically result in positive  $\gamma$  values in optical bands, as suggested by Freedman & Madore (2011), but that the crossover can be situated at shorter wavelengths.

### 3.6.2.5 Influence of the radius around the SMC center

As mentioned in Sect. 3.3.3, the SMC has a very elongated shape along the line of sight. For this reason, the distance to Cepheids located at a great distance from the SMC center may differ substantially from the distance measured by Graczyk et al. (2020) using eclipsing binaries. As represented in Fig. 3.6, using the equations of the two lines in Figure 4 of Graczyk et al. (2020) to correct for the SMC geometry yields distances between 58 kpc and 67 kpc for Cepheids located in a radius of  $\sim 2^\circ$  around the SMC center. This range of distances corresponds to  $\pm 4.5$  kpc around the DEB distance, which corresponds to  $\sim 15\%$  of the SMC distance by Graczyk et al. (2020).

In order to avoid contamination from outlier stars, which is very likely considering the SMC structure, the SMC sample was limited to a radius of  $0.6^\circ$  around its center. With a smaller radius, the size of the SMC sample becomes limiting and insufficient for a precise P-L-Z calibration. On the other hand, including Cepheids beyond a radius of  $0.6^\circ$  increases the number of outliers and of Cepheids which distance may not correspond to the distance of the SMC core region. In this section, the radius around the SMC center is successively set to  $0.5^\circ$ ,  $0.6^\circ$  and  $0.7^\circ$  and the effect of metallicity is derived following the same method as previously (Sect. 3.6.2.1). The coefficients of the P-L-Z relation of the form  $M = \alpha(\log P - 0.7) + \delta + \gamma[\text{Fe}/\text{H}]$  are listed in Table 3.6 and the effect of metallicity is represented as a function of  $1/\lambda$  in Fig. 3.21. The  $[4.5 \mu\text{m}]$  *Spitzer* band is excluded from the linear fit for the reasons explained in Sect. 3.6.2.3.

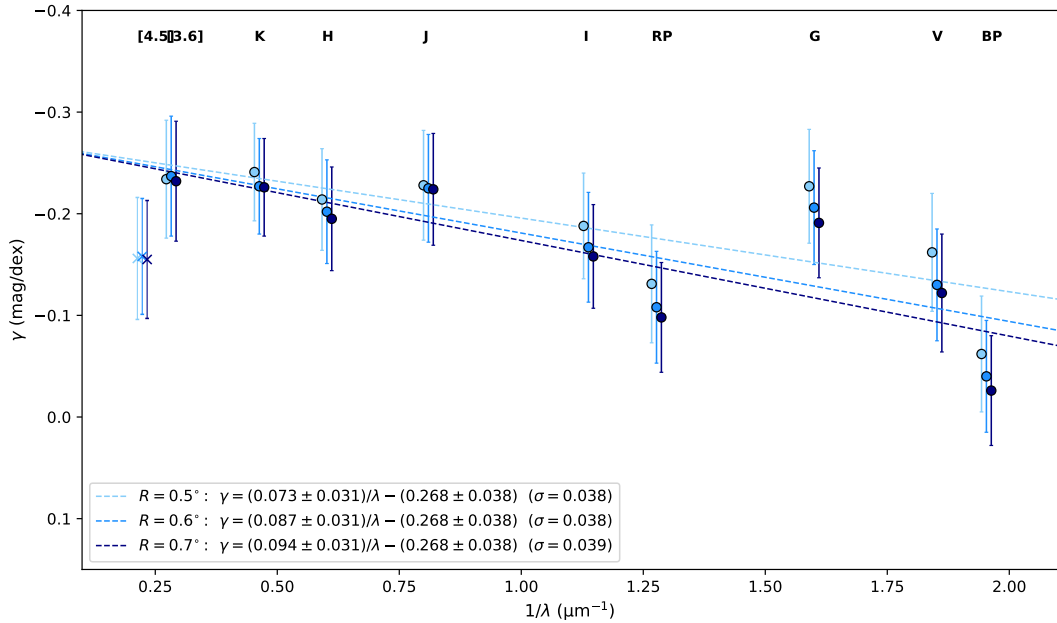


Figure 3.21: Metallicity effect  $\gamma$  represented against the inverse of the wavelength  $1/\lambda$  when the SMC sample is limited to a radius of  $0.5^\circ$  (light blue),  $0.6^\circ$  (medium blue) and  $0.7^\circ$  (dark blue) around the SMC center. The *Spitzer*  $[4.5 \mu\text{m}]$  band is not fitted. In each band, the three points are slightly offset along the horizontal axis for more readability.

While the slope ( $\alpha$ ) and intercept ( $\delta$ ) are very stable under this test, the effect of metallicity ( $\gamma$ ) slightly depends on the radius considered around the SMC center. In mid-infrared and near infrared, the variation is minor ( $\Delta\gamma = 0.020$  mag/dex between  $R = 0.5^\circ$  and  $R = 0.5^\circ$ ) but it reaches  $\Delta\gamma = 0.040$  mag/dex in V. Increasing the radius of the SMC region yields a shallower metallicity



effect in all bands. The relations between  $\gamma$  and the wavelength are fitted in each of the three situations in Fig. 3.21 and the equations are provided in the legend. The trend is similar, no matter the radius of the region:  $\gamma$  decreases (in absolute sense) towards shorter wavelengths. This test shows that the effect of metallicity is not completely insensitive to the sample of SMC Cepheids considered. Adopting a larger sample with Cepheids more distant from the SMC central region apparently results in a weaker effect in all wavelengths. Refined studies of the SMC and of its structure are crucial and would allow us to strengthen the role of this galaxy in the distance ladder and for the determination of the metallicity effect.

Table 3.6: Results of the fit of the P-L-Z relation of the form  $M = \alpha(\log P - 0.7) + \delta + \gamma[\text{Fe}/\text{H}]$  in the Milky Way, LMC and SMC samples, for a radius of  $0.5^\circ$ ,  $0.6^\circ$  and  $0.7^\circ$  around the SMC center.

Band	$\alpha$	$\delta$	$\gamma$	$N_{\text{stars}}$	Radius
<i>BP</i>	$-2.552 \pm 0.032$	$-3.090 \pm 0.025$	$-0.062 \pm 0.057$	1306	$0.5^\circ$
<i>V</i>	$-2.705 \pm 0.027$	$-3.304 \pm 0.025$	$-0.162 \pm 0.058$	1842	$0.5^\circ$
<i>G</i>	$-2.783 \pm 0.028$	$-3.424 \pm 0.024$	$-0.227 \pm 0.056$	1570	$0.5^\circ$
<i>RP</i>	$-2.872 \pm 0.031$	$-3.874 \pm 0.025$	$-0.131 \pm 0.058$	1292	$0.5^\circ$
<i>I</i>	$-2.917 \pm 0.019$	$-3.966 \pm 0.023$	$-0.188 \pm 0.052$	1841	$0.5^\circ$
<i>J</i>	$-3.146 \pm 0.017$	$-4.464 \pm 0.024$	$-0.228 \pm 0.054$	1118	$0.5^\circ$
<i>H</i>	$-3.143 \pm 0.014$	$-4.756 \pm 0.022$	$-0.214 \pm 0.050$	1125	$0.5^\circ$
<i>K</i>	$-3.210 \pm 0.012$	$-4.830 \pm 0.020$	$-0.241 \pm 0.048$	1128	$0.5^\circ$
[3.6 $\mu\text{m}$ ]	$-3.335 \pm 0.038$	$-4.858 \pm 0.026$	$-0.234 \pm 0.058$	103	$0.5^\circ$
[4.5 $\mu\text{m}$ ]	$-3.238 \pm 0.039$	$-4.864 \pm 0.026$	$-0.156 \pm 0.060$	103	$0.5^\circ$
<i>W<sub>VI</sub></i>	$-3.281 \pm 0.013$	$-4.993 \pm 0.022$	$-0.232 \pm 0.054$	1796	$0.5^\circ$
<i>W<sub>JK</sub></i>	$-3.261 \pm 0.013$	$-5.080 \pm 0.022$	$-0.251 \pm 0.054$	1117	$0.5^\circ$
<i>BP</i>	$-2.552 \pm 0.032$	$-3.091 \pm 0.025$	$-0.040 \pm 0.055$	1360	$0.6^\circ$
<i>V</i>	$-2.705 \pm 0.027$	$-3.305 \pm 0.025$	$-0.130 \pm 0.055$	1905	$0.6^\circ$
<i>G</i>	$-2.784 \pm 0.029$	$-3.425 \pm 0.024$	$-0.206 \pm 0.056$	1627	$0.6^\circ$
<i>RP</i>	$-2.873 \pm 0.031$	$-3.875 \pm 0.024$	$-0.108 \pm 0.055$	1346	$0.6^\circ$
<i>I</i>	$-2.916 \pm 0.019$	$-3.967 \pm 0.023$	$-0.167 \pm 0.054$	1906	$0.6^\circ$
<i>J</i>	$-3.146 \pm 0.017$	$-4.465 \pm 0.024$	$-0.225 \pm 0.053$	1161	$0.6^\circ$
<i>H</i>	$-3.143 \pm 0.014$	$-4.757 \pm 0.022$	$-0.202 \pm 0.051$	1190	$0.6^\circ$
<i>K</i>	$-3.210 \pm 0.012$	$-4.831 \pm 0.020$	$-0.227 \pm 0.047$	1195	$0.6^\circ$
[3.6 $\mu\text{m}$ ]	$-3.334 \pm 0.039$	$-4.859 \pm 0.026$	$-0.237 \pm 0.059$	106	$0.6^\circ$
[4.5 $\mu\text{m}$ ]	$-3.238 \pm 0.038$	$-4.863 \pm 0.026$	$-0.158 \pm 0.057$	106	$0.6^\circ$
<i>W<sub>VI</sub></i>	$-3.280 \pm 0.013$	$-4.992 \pm 0.022$	$-0.231 \pm 0.053$	1860	$0.6^\circ$
<i>W<sub>JK</sub></i>	$-3.261 \pm 0.014$	$-5.080 \pm 0.023$	$-0.247 \pm 0.054$	1160	$0.6^\circ$
<i>BP</i>	$-2.553 \pm 0.031$	$-3.091 \pm 0.024$	$-0.026 \pm 0.054$	1394	$0.7^\circ$
<i>V</i>	$-2.704 \pm 0.028$	$-3.305 \pm 0.025$	$-0.122 \pm 0.058$	1948	$0.7^\circ$
<i>G</i>	$-2.784 \pm 0.029$	$-3.426 \pm 0.023$	$-0.191 \pm 0.054$	1666	$0.7^\circ$
<i>RP</i>	$-2.874 \pm 0.031$	$-3.875 \pm 0.024$	$-0.098 \pm 0.054$	1379	$0.7^\circ$
<i>I</i>	$-2.916 \pm 0.019$	$-3.967 \pm 0.022$	$-0.158 \pm 0.051$	1950	$0.7^\circ$
<i>J</i>	$-3.147 \pm 0.017$	$-4.465 \pm 0.024$	$-0.224 \pm 0.055$	1186	$0.7^\circ$
<i>H</i>	$-3.143 \pm 0.014$	$-4.757 \pm 0.022$	$-0.195 \pm 0.051$	1234	$0.7^\circ$
<i>K</i>	$-3.210 \pm 0.011$	$-4.831 \pm 0.020$	$-0.226 \pm 0.048$	1240	$0.7^\circ$
[3.6 $\mu\text{m}$ ]	$-3.334 \pm 0.039$	$-4.859 \pm 0.026$	$-0.232 \pm 0.059$	107	$0.7^\circ$
[4.5 $\mu\text{m}$ ]	$-3.238 \pm 0.038$	$-4.863 \pm 0.025$	$-0.155 \pm 0.058$	107	$0.7^\circ$
<i>W<sub>VI</sub></i>	$-3.281 \pm 0.013$	$-4.993 \pm 0.022$	$-0.229 \pm 0.054$	1903	$0.7^\circ$
<i>W<sub>JK</sub></i>	$-3.261 \pm 0.014$	$-5.080 \pm 0.023$	$-0.244 \pm 0.053$	1185	$0.7^\circ$

## 3.7 Conclusion on the metallicity effect

### 3.7.1 Summary of the data, method and results

In this chapter, I described the calibration of the metallicity effect on the Leavitt law carried out in [Breuval et al. \(2021\)](#). Cepheids in the Milky Way and in the Magellanic Clouds cover a wide range of metallicity of about 0.9 dex and therefore constitute an ideal sample for this study. Distances to hundreds of Galactic Cepheids are now available in *Gaia* EDR3 and precise distances to the LMC and SMC were recently measured by [Pietrzyński et al. \(2019\)](#) and [Graczyk et al. \(2020\)](#) using a sample of detached eclipsing binaries. I obtained the distance to each Magellanic Cloud Cepheid by including geometric corrections to account for the shape of these galaxies.

Full light curves are adopted in priority to derive mean magnitudes in various bands. Exceptionally, single-point photometry is adopted in the *H* band for the SMC sample, which was ignored in the [B21](#) paper. Additionally to the *V*, *I*, *J*, *H* and *K<sub>S</sub>* passbands adopted in the paper, I also included light curves in the *Spitzer* bands [3.6  $\mu$ m] and [4.5  $\mu$ m], and in *Gaia* *G*, *BP* and *RP* bands. The study covers a range of wavelengths from 500 nm to 4.5  $\mu$ m, which is particularly suitable for investigating the dependence of the metallicity effect on wavelength.

Several other improvements are made with respect to the [B21](#) paper: the width of the instability strip is more correctly incorporated to the magnitude errors (Sect. 3.5.1.3), the photometric zero-point systematics are re-evaluated to lower values (Table 3.2) and the reddenings of Milky Way Cepheids are taken from catalogs more recent than [Fernie et al. \(1995\)](#) when available (Sect. 3.2.1). These slight changes explain the differences between the results of this chapter and the results given in [B21](#), especially in optical bands. The method, however, remains unchanged. Figure 3.22 gives a summary of the data and method adopted for each sample in order to derive the metallicity effect.

A first calibration of the metallicity effect is performed using only Milky Way Cepheids with individual spectroscopic metallicities. In the NIR, the effect is significant to  $1.7\sigma$  and negative with a value close to [B21](#), meaning that metal-rich Cepheids are brighter than metal-poor ones. In optical bands the effect is consistent with zero. Finally in mid-infrared bands the metallicity effect is positive ( $\gamma > 0.160$  mag/dex) but still consistent with zero due to very large uncertainties resulting from a small sample of only 19 Cepheids with *Spitzer* photometry. In both Wesenheit indices the metallicity effect is negative and significant to  $2\sigma$ , in agreement with [B21](#). However, the precision obtained from the sample of Milky Way Cepheids is very limited: the metallicity range covered by Galactic Cepheids is too small for a precise determination of the metallicity effect, and the individual spectroscopic metallicities show no obvious correlation with the intercept of the P-L relation.

Combining the LMC and SMC samples with Galactic Cepheids yields a more precise value of the metallicity effect. For consistency, the mean metallicity of the Milky Way sample is adopted. The intercept of the P-L relation clearly correlates with the mean metallicity of the MW, LMC and SMC samples, as seen in Fig. 3.18: the more metal-rich is the sample, the more negative is the intercept. In NIR bands, the metallicity effect is negative and significant from  $4\sigma$  to  $5\sigma$ , in excellent agreement with [B21](#). In optical bands, the effect is more moderate but still negative. The *Spitzer* band [4.5  $\mu$ m] is very sensitive to the absorption by the CO molecule in the Cepheid atmosphere, which likely explains the shallower metallicity effect in this band. The [3.6  $\mu$ m] band, which is insensitive to this CO absorption, shows a very strong and negative metallicity effect, similar to that obtained in the NIR.

A linear relation is fitted between the metallicity and the wavenumber ( $1/\lambda$ ) after excluding the [4.5  $\mu$ m] band, which yields  $\gamma \propto 0.087/\lambda$  where  $\gamma$  is in mag/dex and  $\lambda$  is in  $\mu$ m. This trend resembles

		Milky Way	LMC	SMC
SAMPLE	Distance	Gaia EDR3 parallaxes + ZP correction (Lindegren+ 2021)	DEB distance (Pietrzyński+ 2019) 49.59 ± 0.09 ± 0.54 kpc + geometry correction (Jacyszyn-Dobrzyniecka+ 2016)	DEB distance (Graczyk+ 2020) 62.44 ± 0.47 ± 0.81 kpc + geometry correction (Graczyk+ 2020)
	Photometry	V, I: Berdnikov+ 2008 (Johnson/Cousins systems)	V, I: Soszynski+ 2015 (OGLE system)	V, I: Soszynski+ 2015 (OGLE system)
		NIR: Monson+ 2011, Laney+ 1992, Welch+ 1984, Barnes+ 1997 (converted to 2MASS)	NIR: Persson+ 2004, Macri+ 2015 (2MASS)	NIR: VMC (Ripepi+ 2016), Kato+ 2007 (2MASS)
		MIR: Monson+ 2012 (Spitzer/IRAC)	MIR: Scowcroft+ 2011 (Spitzer/IRAC)	MIR: Scowcroft+ 2016 (Spitzer/IRAC)
		Gaia: Clementini+ 2019	Gaia: Clementini+ 2019	Gaia: Clementini+ 2019
Reddening	Kovtyukh+ 2008, Laney & Caldwell 2007, Sziládi+ 2007, Acharova+ 2012, Fernie+ 1995	Górski+ 2020 reddening maps	Górski+ 2020 reddening maps	
Metallicity	Genovali+ 2014, 2015 and references therein Mean metallicity: [Fe/H] = +0.085 ± 0.022 dex	Gieren+ 2018 Mean metallicity: [Fe/H] = -0.34 ± 0.06 dex	Gieren+ 2018 Mean metallicity: [Fe/H] = -0.75 ± 0.05 dex	
ABSOLUTE MAG.	$M_\lambda = m_\lambda - 5 \log(d_{\text{kpc}}) - 10 - R_\lambda E(B-V)$			
	Width of the instability strip (added quadratically to mean magnitude errors): V: 0.22 mag, I: 0.14 mag, J: 0.11 mag, H: 0.09 mag, K: 0.07 mag, [3.6]/[4.5]: 0.07 mag, G/BP/RP: 0.22 mag			
	Reddening law: $R_V=3.135, R_I=1.894, R_J=0.892, R_H=0.553, R_K=0.363$ (Cardelli et al. 1989) $R_{[3.6]}=0.203, R_{[4.5]}=0.156$ (Indebetouw et al. 2005) $R_G=2.473, R_{BP}=3.141, R_{RP}=1.847$ (Wang & Chen 2019)			
P-L-Z	Step 1: P-L relation (slope fixed to LMC value) $M = \alpha (\log P - 0.7) + \beta$		Step 2: P-L-Z relation $\beta = \delta + \gamma [\text{Fe}/\text{H}]$	

Figure 3.22: Summary of the data and method adopted in this chapter for the calibration of the metallicity effect on the Leavitt law.

the decrease observed by [Freedman & Madore \(2011\)](#), however in the latter paper the metallicity effect becomes positive towards shorter wavelengths, which is not the case in the present study. [Tsang \(2019\)](#) similarly observed a negative metallicity effect using SDSS bands, with a decrease towards optical wavelengths. The line-blanketing effect, which results in capturing energy from the spectrum in optical wavelengths and redistributing it in the NIR, likely explains the trend observed in Fig. 3.20. The values of the metallicity effect derived in this chapter agree well with the results by [Gieren et al. \(2018\)](#) but are more precise, and are stronger than the effect obtained by [Wielgórski et al. \(2017\)](#) from a comparative study of LMC and SMC Cepheids. Finally, the metallicity effect measured in [Breuval et al. \(2021\)](#) is one of the most precise estimates in the literature, based on 3 Cepheid samples of distinct metallicities and on the best distances available.

In summary, most theoretical studies predict that metal-rich Cepheids would be fainter than metal-poor ones, corresponding to a positive sign of the  $\gamma$  term of the P-L relation, while the large majority of empirical studies observed that metal-rich Cepheids are brighter than metal-poor ones ( $\gamma < 0$ ). This disagreement between the predictions of models and most empirical studies is still an open question. However, it should be noted that both methods are very different. Theoretical studies are based on models in which it is possible to change the chemical abundance of a given Cepheid, and to measure the influence of this change on the physical parameters of the Cepheid. Empirically, since it is not possible to change the metallicity of a Cepheid, we can only compare different P-L relation calibrated with Cepheids of different metallicities, such as in the Milky Way and in the Magellanic Clouds. Additionally, a change in the P-L intercept, as observed in the present work, may not be only due to a variation of brightness, but also possibly to a change in period, along the horizontal axis of the P-L relation. This change in period would be stronger for larger slopes of the P-L relation (i.e. in the NIR). However, it is currently impossible to disentangle the changes in brightness and in period when comparing several P-L relations. In conclusion, the influence of metallicity should be considered not only on the photosphere of Cepheids but also on the physics inside of the stars.

### 3.7.2 Limitations and perspectives

Covering a sufficiently large metallicity range by combining Galactic Cepheids with metal-poor Cepheid samples such as the LMC and the SMC is essential to derive precisely the effect of metallicity on the Leavitt law. However, combining and comparing Cepheids from different galaxies often imply the use of inhomogeneous data, given in different systems. Photometry and reddenings are especially sensitive to the large diversity of filters and instruments.

Individual spectroscopic metallicities have been measured for a large number of Milky Way Cepheids but the uncertainties are still relatively large and the relation between metallicity and the P-L intercept in the Milky Way is not clearly visible (see Fig. 3.16). Individual metallicities in the LMC and SMC are available for a few Cepheids only ([Romaniello et al. 2008](#)): the next generation of telescopes and instruments (ELT/HIRES, JWST/NIRSpec) will certainly improve the precision of Cepheid metallicities, although these measurements require a lot of observing time. The assumption of a metallicity gradient from the central parts to the outer regions of galaxies have been used to estimate the metallicity effect outside of the Local Group ([Kennicutt et al. 1998](#); [Macri et al. 2006](#); [Scowcroft et al. 2009](#); [Tsang 2019](#)), but these indirect estimates of the metal abundance are not ideal and introduce significant uncertainties. Additionally, the use of mean metallicity for LMC and SMC Cepheids is particularly limiting.

The choice of reddening law has an influence on the results, especially in optical bands, it is therefore important to choose it carefully and consistently with the data. Finally, the distances to Milky

Way Cepheids have reached a great precision thanks to *Gaia*, and even the parallax zero-point is now better estimated ([Lindegren et al. 2021a](#)). The detached eclipsing binaries study has also improved the LMC and SMC distances to 1% and 2% respectively.

### **3.8 Publication: *The Influence of Metallicity on the Leavitt Law from Geometrical Distances of Milky Way and Magellanic Cloud Cepheids*, Breuval et al. 2021, ApJ 913 38**

This section presents my second paper, [Breuval et al. \(2021\)](#). It describes the calibration of the metallicity effect on the Cepheid Leavitt law, from a combination of the most precise distance available and of the wide range of metallicities covered by Milky Way and Magellanic Cloud Cepheids.



# The Influence of Metallicity on the Leavitt Law from Geometrical Distances of Milky Way and Magellanic Cloud Cepheids

Louise Breuval<sup>1</sup>, Pierre Kervella<sup>1</sup>, Piotr Wielgórski<sup>2</sup>, Wolfgang Gieren<sup>3</sup>, Dariusz Graczyk<sup>4</sup>, Boris Trahin<sup>1</sup>,  
Grzegorz Pietrzyński<sup>2</sup>, Frédéric Arenou<sup>5</sup>, Behnam Javanmardi<sup>1</sup>, and Bartłomiej Zgierski<sup>2</sup>  
<sup>1</sup> LESIA, Observatoire de Paris, Université PSL, CNRS, Sorbonne Université, Université de Paris, 5 place Jules Janssen, F-92195 Meudon, France  
[louise.breuval@obspm.fr](mailto:louise.breuval@obspm.fr)

<sup>2</sup> Nicolaus Copernicus Astronomical Centre, Polish Academy of Sciences, Bartycka 18, 00-716 Warszawa, Poland

<sup>3</sup> Universidad de Concepción, Departamento de Astronomía, Casilla 160-C, Concepción, Chile

<sup>4</sup> Centrum Astronomiczne im. Mikołaja Kopernika, Polish Academy of Sciences, Rabiańska 8, 87-100, Toruń, Poland

<sup>5</sup> GEPI, Observatoire de Paris, Université PSL, CNRS, 5 place Jules Janssen, F-92190 Meudon, France

Received 2021 January 29; revised 2021 March 18; accepted 2021 March 18; published 2021 May 21

## Abstract

The Cepheid period–luminosity (PL) relation is the key tool for measuring astronomical distances and for establishing the extragalactic distance scale. In particular, the local value of the Hubble constant ( $H_0$ ) strongly depends on Cepheid distance measurements. The recent Gaia Data Releases and other parallax measurements from the Hubble Space Telescope (HST) already enabled us to improve the accuracy of the slope ( $\alpha$ ) and intercept ( $\beta$ ) of the PL relation. However, the dependence of this law on metallicity is still largely debated. In this paper, we combine three samples of Cepheids in the Milky Way (MW), the Large Magellanic Cloud (LMC), and the Small Magellanic Cloud (SMC) in order to derive the metallicity term (hereafter  $\gamma$ ) of the PL relation. The recent publication of extremely precise LMC and SMC distances based on late-type detached eclipsing binary systems provides a solid anchor for the Magellanic Clouds. In the MW, we adopt Cepheid parallaxes from the early third Gaia Data Release. We derive the metallicity effect in  $V$ ,  $I$ ,  $J$ ,  $H$ ,  $K_S$ ,  $W_{VI}$ , and  $W_{JK}$ . In the  $K_S$  band we report a metallicity effect of  $-0.221 \pm 0.051$  mag dex<sup>-1</sup>, the negative sign meaning that more metal-rich Cepheids are intrinsically brighter than their more metal-poor counterparts of the same pulsation period.

*Unified Astronomy Thesaurus concepts:* Cepheid distance (217); Parallax (1197); Metallicity (1031); Magellanic Clouds (990); Milky Way Galaxy (1054)

*Supporting material:* machine-readable tables

## 1. Introduction

The Cepheid period–luminosity (PL) relation, discovered by Henrietta Leavitt (Leavitt & Pickering 1912) about a century ago, is an essential tool for measuring astronomical distances since it represents the first rung of the extragalactic distance ladder. This law is used to measure distances to Type Ia supernovae (SNe Ia) host galaxies and thus plays a key role in the determination of the Hubble constant ( $H_0$ ). This parameter currently exhibits a tension of at least  $\sim 4\sigma$  between its measurement in the early universe by Planck Collaboration et al. (2020) assuming a  $\Lambda$ CDM cosmology and the local estimate based on Cepheid distances (Riess et al. 2021). The precise calibration of the PL relation is therefore of paramount importance to reach a 1% determination of the Hubble constant.

While the slope ( $\alpha$ ) and intercept ( $\beta$ ) of the Leavitt law are generally consistent between various studies, the value and even the sign of the metallicity term ( $\gamma$ , defined as  $M = \alpha \log P + \beta + \gamma[\text{Fe}/\text{H}]$ ) are still debated and constitute 0.5% of the error budget of  $H_0$  (Riess et al. 2016). Some empirical studies report a metallicity dependence consistent with  $\gamma \sim 0$  mag dex<sup>-1</sup>: Udalski et al. (2001) conclude with a null effect from the study of a metal-poor galaxy in optical bands, Storm et al. (2011b) find a null effect in all bands except in  $W_{VI}$ , and Wielgórski et al. (2017) derive a gamma value consistent with zero in optical and near-IR (NIR) bands. Still, a large majority of the analysis investigating the metallicity effect derived a negative sign, with values ranging between  $-0.2$  and

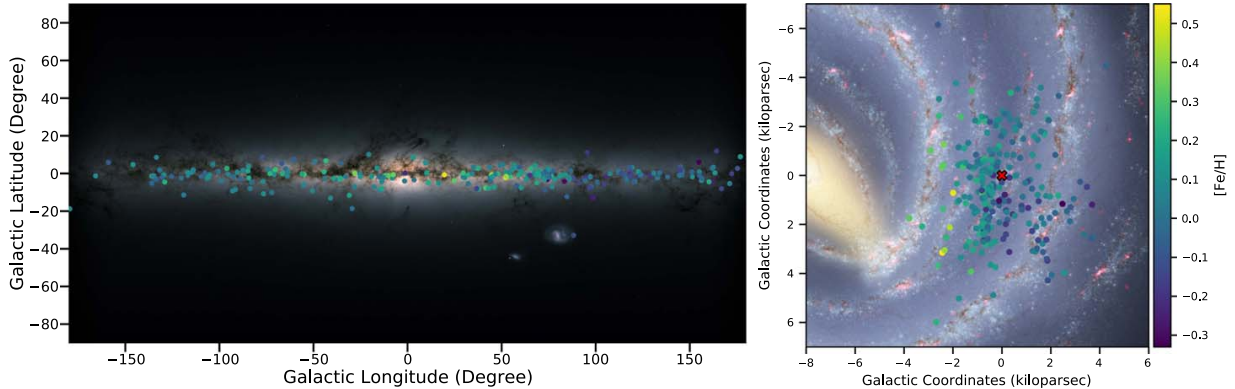
$-0.5$  mag dex<sup>-1</sup> (Freedman & Madore 1990; Macri et al. 2006; Saha et al. 2006; Gieren et al. 2018; Groenewegen 2018). This trend would indicate that metal-rich Cepheids are brighter than metal-poor ones. However, the study by Romaniello et al. (2008) yielded a metallicity effect of the opposite sign, confirming the theoretical predictions (Caputo et al. 2000; Bono et al. 2008; Fiorentino et al. 2013).

In this paper, we aim at determining the effect of metallicity on the PL relation by combining samples of Cepheids in the Milky Way (MW) and in the Magellanic Clouds (MCs), taking advantage of the large range of metallicity covered by the Cepheids in these three galaxies (from  $+0.08$  to  $-0.75$  dex). Most of the Cepheids located in distant galaxies hosting SNe Ia have metallicities within this range; therefore, our results are directly applicable to extragalactic studies of the distance scale (e.g., Javanmardi et al. 2021).

Recently, Pietrzyński et al. (2019) and Graczyk et al. (2020) measured the most precise distances to date for the Large Magellanic Cloud (LMC) and Small Magellanic Cloud (SMC), respectively, based on enhanced samples of late-type detached eclipsing binaries (DEBs). These distances allow us to obtain a precise calibration of the PL relation in the LMC and SMC. For MW Cepheids, we use the early third Gaia Data Release (EDR3), which recently provided parallaxes of unprecedented precision for hundreds of galactic Cepheids.

In Section 2 we present our samples of Cepheids in the three galaxies, and in Section 3 we provide the distances we adopted for each sample. Then, in Section 4 we estimate the metallicity effect by fitting the period–luminosity–metallicity (PLZ)





**Figure 1.** Galactic maps projected on the sky (left) and on the galactic plane (right) showing the distribution of the MW Cepheid sample. The color scale represents the metallicity  $[Fe/H]$ , and the red cross is the position of the solar system.

relation in the three galaxies. We discuss the results in Section 5.

## 2. Samples of Cepheids

### 2.1. MW Cepheids

We gather a sample of MW Cepheids for which well-covered light curves are available. In the NIR  $J$ ,  $H$ , and  $K$  bands, we combine the catalogs by Welch et al. (1984), Laney & Stobie (1992), Barnes et al. (1997), and Monson & Pierce (2011). The data from these four studies are found to be in close agreement, with residuals of 0.013, 0.010, and 0.002 mag in  $J$ ,  $H$ , and  $K$ , respectively (Monson & Pierce 2011). We adopt these values as photometric zero-point (ZP) uncertainties for the NIR photometry. Additional NIR data were also found in Feast et al. (2008); we consider that including this source of data does not impact the homogeneity and the dispersion of the data since it only affects four stars of the sample. In the optical  $V$  and  $I$  bands, we use the catalog from Berdnikov (2008) that provides photometry in the Johnson–Cousins system for a large number of Cepheids. Since it is a compilation of data from various catalogs by the same author, we adopt a photometric ZP uncertainty of 0.010 mag.

For each star and in each filter, we phase the data at the date of maximum luminosity and obtain intensity-averaged mean apparent magnitudes by performing light-curve fitting using Fourier series. Depending on the properties of the different light curves (such as the presence of bumps, steep variations, or to prevent the introduction of unphysical oscillations when the data are too dispersed or not dense enough), we adapt the number of Fourier modes, and thus of free parameters, in order to obtain a satisfactory representation of the light curve. A Fourier decomposition of order 3 is generally sufficient for an usual Cepheid light curve such as  $\delta$  Cep and is up to order 6 for a more complex star such as RS Pup. We derived the statistical uncertainties on the mean magnitudes from the scatter of each light curve. In a few cases, a very large number of data points are available ( $>300$ ) and result in unrealistic small errors; in these cases we adopt a minimum error of 0.006 mag.

For long-period Cepheids, large phase shifts may degrade the quality of the fit, the photometry being spread over four decades. Therefore, period changes were taken into account for

the phasing of long-period stars such as SV Vul, GY Sge, or RS Pup (Kervella et al. 2017). We adopted a polynomial model of up to degree 5 for the pulsation period.

We carefully analyze the light curves: we exclude Cepheids for which fewer than eight data points are available (MW Cepheids have on average 35 data points in NIR and 160 in optical) and Cepheids that have poor-quality photometry or insufficient phase coverage. Finally, we convert all the NIR data in the Two Micron All Sky Survey (2MASS) system using the transformations from Monson & Pierce (2011). The systematics related to these transformations are negligible. Examples of a well-covered light curve and of a poor-quality light curve are provided in Figures 8 and 9 in Appendix A.

We select Cepheids pulsating in the fundamental mode according to the reclassification by Riipepi et al. (2019). For stars that were not available in this catalog, we adopted by order of priority the pulsation modes from Groenewegen (2018), from the Variable Star index (VSX; Watson et al. 2006), and from Luck (2018).

We adopt reddening values from Fernie et al. (1995) with a 0.94 scaling factor as suggested by Groenewegen (2018), and from Acharova et al. (2012) if not available in the latter. We adopt an uncertainty of 0.05 if it is not provided.

For MW Cepheids, we search for individual metallicities in Genovali et al. (2015). This catalog provides mean abundances based on high-resolution spectra for 75 Cepheids. For stars that are not available in this catalog, we adopt the values from Genovali et al. (2014); they provide homogeneous Cepheid metallicities from their group and compiled from the literature, rescaled to their solar abundance. The individual metallicities are represented in Figure 1 by colored points; they range from  $-0.33$  to  $+0.55$  dex. The gradient of metallicity in the MW is particularly visible, with metal-rich Cepheids located closer to the galactic center than metal-poor ones. These individual metallicities have a weighted mean value of  $0.083 \pm 0.019$  dex with a scatter of 0.14 dex. In the following, we adopt this weighted mean value for all MW Cepheids for consistency and homogeneity with the LMC and SMC samples that only have a mean metallicity, but also because the current precision of the individual metallicities is not sufficient for a thorough calibration of the metallicity effect.

The Cepheids of our MW sample are represented in Figure 1, and their main parameters are listed in Tables 3 and 4 in Appendix B.

## 2.2. LMC Cepheids

We build a sample of LMC Cepheids by combining the OGLE-IV photometry in  $V$  and  $I$  bands (Soszyński et al. 2015) with the multiepoch observations from the LMC Near-Infrared Synoptic Survey by Macri et al. (2015) taken with the CPAPIR camera on the 1.5 m CTIO telescope. We update their NIR mean magnitudes to bring them into better agreement with the 2MASS system using the following relations (L. Macri 2021, private communication). These were derived by matching  $\sim 34,000$  stars in common between their Table 1 and the 2MASS Point Source Catalog (Cutri et al. 2003), with  $12 \text{ mag} < H < 13.5 \text{ mag}$ ,  $K > 11.5 \text{ mag}$ , and  $-0.5 \text{ mag} < J - K < 1.4 \text{ mag}$ :

$$\begin{aligned} J_{2\text{MASS}} &= J_{\text{M15}} - 0.0167 + 0.0205 (J_{\text{M15}} - K_{\text{M15}} - 0.4) \\ &\quad + 0.0101 (J_{\text{M15}} - K_{\text{M15}} - 0.4)^2 \\ H_{2\text{MASS}} &= H_{\text{M15}} + 0.0116 - 0.0054 (J_{\text{M15}} - K_{\text{M15}} - 0.4) \\ &\quad - 0.0189 (J_{\text{M15}} - K_{\text{M15}} - 0.4)^2 \\ K_{2\text{MASS}} &= K_{\text{M15}} + 0.0162 + 0.0227 (J_{\text{M15}} - K_{\text{M15}} - 0.4) \\ &\quad - 0.0595 (J_{\text{M15}} - K_{\text{M15}} - 0.4)^2. \end{aligned}$$

We adopt a photometric ZP uncertainty of 0.02 mag in all bands. Since some Cepheids exhibit large brightness variations during a pulsation cycle, we consider that single-epoch photometry is not precise enough to derive reliable mean magnitudes; therefore, we discarded the mean magnitudes derived by Inno et al. (2016) from template fitting on 2MASS single-point data and IRSF measurements.

We perform a quality check on this initial sample: we reject stars with magnitude uncertainties larger than 1% and with fewer than five data points (LMC Cepheids have on average 43 data points in NIR and 147 in optical), and we only consider fundamental mode Cepheids. We reject Cepheids located outside a radius of  $3^\circ$  around the LMC center in order to avoid outliers such as stars that do not belong to the LMC or that are strongly affected by its geometrical effects (see Section 3.2). We adopt reddening values from the Górski et al. (2020) reddening map. The final sample of LMC Cepheids contains 1446 stars in the  $V$  band and 807 stars in  $K_S$ ; it is listed in Table 5 in Appendix C and provided as supplementary material online. A map of the final sample of LMC Cepheids is represented in Figure 2. For LMC Cepheids, we adopt the mean metallicity used by Gieren et al. (2018), which compiles several estimates from various studies:  $[\text{Fe}/\text{H}]_{\text{LMC}} = -0.34 \pm 0.06 \text{ dex}$ . The uncertainties take into account the homogenization of the different measurements.

## 2.3. SMC Cepheids

We assemble a sample of SMC Cepheids by taking the mean magnitudes from the VISTA survey of the Magellanic Clouds (VMC; Ripepi et al. 2016) cross-matched with OGLE-IV photometry by Soszyński et al. (2015). Unfortunately, we do not have  $H$ -band photometry for SMC Cepheids because we rejected data from single-epoch photometry and template fitting. Results in the  $H$  band are therefore derived from the

combination of MW and LMC Cepheids only. Magnitudes in the VISTA system were converted into the 2MASS system using the equations from Ripepi et al. (2016):

$$\begin{aligned} J' &= J_{\text{VMC}} + 0.070 (J_{\text{VMC}} - K_{\text{VMC}}) \\ K' &= K_{\text{VMC}} - 0.011 (J_{\text{VMC}} - K_{\text{VMC}}). \end{aligned}$$

We perform an additional correction (L. Macri 2021, private communication) derived by matching  $\sim 7000$  stars in common between the VMC DR4 and the 2MASS Point Source Catalog, with  $J > 12.25 \text{ mag}$ ,  $K > 11.5 \text{ mag}$ , and  $-0.5 \text{ mag} < J - K < 1.4 \text{ mag}$ :

$$\begin{aligned} J_{2\text{MASS}} &= J' - 0.0087 - 0.0010 (J' - K' - 0.4) \\ K_{2\text{MASS}} &= K' + 0.0011 - 0.0087 (J' - K' - 0.4). \end{aligned}$$

We adopt a photometric ZP uncertainty of 0.02 mag for all bands. As we did for the LMC sample, we also reject SMC Cepheids with magnitude uncertainties larger than 1%, with fewer than five data points (SMC Cepheids have on average 17 data points in NIR and 46 in optical), and we only keep Cepheids pulsating in the fundamental mode. As for the LMC sample, we adopt reddening values from the Górski et al. (2020) reddening map.

While the LMC has a rather simple geometry, the SMC is very elongated along the line of sight: we select Cepheids located in a region of  $0.6^\circ$  around the SMC center, which covers an area of 1.3 kpc width. Since the SMC distance is derived from DEBs, this selection ensures that the Cepheids are located in the same region as these DEBs. The final SMC sample has 284 stars in the  $V$  band and 295 stars in  $K_S$ ; it is listed in Table 6 in Appendix D and provided as supplementary material. A map of our final sample of SMC Cepheids is presented in Figure 3.

For SMC Cepheids, we adopt the mean metallicity used by Gieren et al. (2018), which compiles several estimates from various studies:  $[\text{Fe}/\text{H}]_{\text{SMC}} = -0.75 \pm 0.05 \text{ dex}$ . Similar to the LMC value, the uncertainty takes into account the homogenization of the different measurements.

## 3. Distances

In order to calibrate the Leavitt law, one needs to derive the absolute magnitude of each Cepheid from its apparent luminosity and from its distance.

### 3.1. Distances to Milky Way Cepheids

Recently, the early third Gaia Data Release provided new parallaxes for MW Cepheids (Gaia Collaboration 2020). We perform a first quality check of Gaia EDR3 parallaxes based on the renormalized unit weight error (RUWE) provided in the catalog. This parameter reflects the quality of the parallax of a star compared to other stars of the same color and brightness. Its value is expected to be close to 1 for well-behaved sources (Lindgren et al. 2021b). In particular, the RUWE is sensitive to the photocentric motion of unresolved objects; therefore, it can be used to detect possible astrometric binaries. We discard the Cepheids of our sample that have an  $\text{RUWE} > 1.4$ ; this selection corresponds to approximately 13% of our MW sample and removes the stars that are possibly affected by saturation or contamination by a bright neighbor companion. In particular, all the outliers noticed by eye on the PL relation are

affected by a large RUWE; therefore, the quality check based on this parameter appears to be relevant for our purposes.

Riess et al. (2021) use a different indicator: they identify stars with a goodness of fit (GOF) larger than 12.5 as having a compromised parallax. We find the GOF and the RUWE selections to have a very similar effect on our sample: adopting this GOF criterion for the quality check instead of the RUWE leads to rejecting exactly the same stars, except T Mon, V0496 Aql, and VW Pup, which have an RUWE of 1.72, 1.56, and 1.41 and a GOF of 12.11, 10.90, and 11.36, respectively. The RUWE criterion seems slightly more selective than the GOF limit adopted by Riess et al. (2021). Adopting a threshold of  $\text{RUWE} < 1.4$  corresponds to a limit GOF of 10.

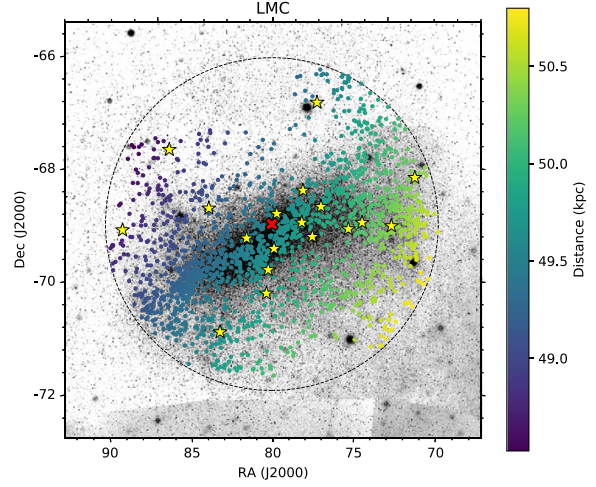
One method to check whether a Cepheid is an astrometric binary is to look for proper-motion anomalies between the observations by Hipparcos and Gaia. Using the approach described in Kervella et al. (2019), we find 20 Cepheids with a high-proper-motion anomaly signal. However, none of them were identified by their high RUWE or GOF, and they do not appear as outliers; therefore, we do not exclude them.

Cepheids are variable stars, and therefore their brightness and color can change significantly during a pulsation cycle. This effect was not taken into account in the processing of Gaia DR2 astrometry and resulted in additional systematics, noise, and dispersion for variable star parallaxes (Breuval et al. 2020). The correction for this chromatic effect on Cepheid parallaxes is still absent from Gaia EDR3 (Lindgren et al. 2021b). However, the number of observations obtained for each star increased consequently between Gaia DR2 (~22 months) and Gaia EDR3 (~34 months). We assume in this paper that the noise induced by this effect is negligible for Gaia EDR3 parallaxes.

For each Cepheid we correct for the parallax ZP by using the Python tool<sup>6</sup> described in Lindgren et al. (2021b). This ZP correction takes into account the ecliptic latitude, magnitude, and color of each star. Our MW Cepheids cover a range of magnitudes from  $G = 3$  to 12 mag. For our sample of MW Cepheids, we find the ZP to vary between  $-4$  and  $-54 \mu\text{as}$  with a median value of  $-27 \mu\text{as}$  ( $\sigma = 10 \mu\text{as}$ ), which is very similar to the median parallax offset derived by Riess et al. (2021). Following Lindgren et al. (2021b), who recommend to include an uncertainty of a few microarcseconds in the ZP, we adopt a systematic error of  $5 \mu\text{as}$  on this quantity. Considering our sample of Cepheids, this error is equivalent to an average systematic uncertainty of  $0.020 \text{ mag}$  in distance modulus. In Section 5.1, we discuss the influence of adopting this individual ZP correction compared with the uniform ZP of  $-17 \mu\text{as}$  derived from quasars.

We find 13 Cepheids to fall in the range between  $G = 10.8$  and  $11.2 \text{ mag}$ , where a transition of window classes occurs (Figure 1 in Lindgren et al. 2021a). In this particular range, the value of the parallax ZP can possibly be affected, so we quadratically add  $10 \mu\text{as}$  to the parallax uncertainty.

Finally, we increase all Gaia EDR3 parallax uncertainties by 10%, following Riess et al. (2021) to account for potential excess uncertainty. This correction has significantly reduced since Gaia DR2, where it was recommended to increase parallax uncertainties by 30%.



**Figure 2.** Map of the LMC Cepheids considered in our study. Yellow stars are the eclipsing binaries from Pietrzyński et al. (2019), and the red cross is the center of the LMC. The dashed circle represents a radius of  $3^\circ$  around the LMC center.

### 3.2. Distances to LMC Cepheids

Recently, Pietrzyński et al. (2019) estimated the distance to the LMC with a 1% precision based on DEBs:  $d_{\text{LMC}} = 49.59 \pm 0.09 \text{ (stat.)} \pm 0.54 \text{ (syst.) kpc}$ . This method for measuring distances is independent from Cepheids and relies on surface brightness relations, established by precise interferometric measurements. We use this value as the initial distance to our Cepheids, and we add a corrective term depending on the position of each Cepheid in the LMC, assuming the disk geometry derived by OGLE from Cepheids by Jacyszyn-Dobrzyniecka et al. (2016). First, we compute the Cartesian coordinates ( $x_i, y_i, z_i$ ) of each Cepheid from their equatorial coordinates ( $\alpha_i, \delta_i$ ) using the transformations

$$\begin{cases} x_i = -d_{\text{LMC}} \cos \delta_i \sin(\alpha_i - \alpha_{\text{LMC}}) \\ y_i = d_{\text{LMC}} [\sin \delta_i \cos \delta_{\text{LMC}} \\ \quad - \cos \delta_i \sin \delta_{\text{LMC}} \cos(\alpha_i - \alpha_{\text{LMC}})] \\ z_i = c_1 x_i + c_2 y_i + d_{\text{LMC}} \end{cases}$$

where  $(\alpha_{\text{LMC}}, \delta_{\text{LMC}}) = (80.05^\circ, -69.30^\circ)$  are the coordinates of the LMC center and the coefficients  $(c_1, c_2) = (0.395 \pm 0.014, -0.215 \pm 0.013)$  are from Jacyszyn-Dobrzyniecka et al. (2016). The corrected distance of each LMC Cepheid is

$$d_i = \sqrt{x_i^2 + y_i^2 + z_i^2}.$$

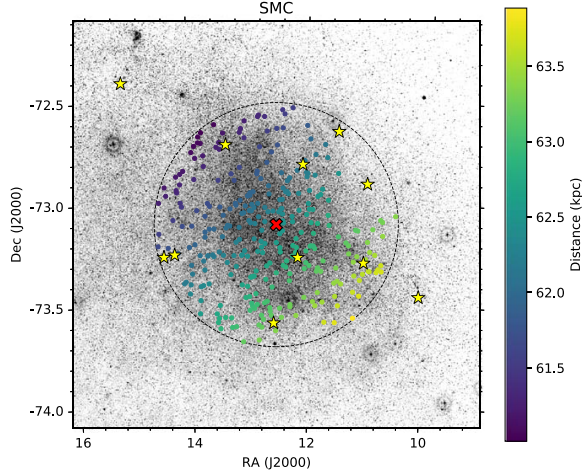
The distances of each LMC Cepheid derived with this correction are located in a range of  $\pm 1.5 \text{ kpc}$  around the mean LMC distance from Pietrzyński et al. (2019). They are represented by the colors in Figure 2.

### 3.3. Distances to SMC Cepheids

The distance to the SMC was recently measured by Graczyk et al. (2020) with a precision of 1.5% using the same method as used in Pietrzyński et al. (2019) for the LMC: from a sample of 15 DEBs, a distance of  $d_{\text{SMC}} = 62.44 \pm 0.47 \text{ (stat.)} \pm 0.81 \text{ (syst.) kpc}$  is derived. However, the SMC has a large

<sup>6</sup> <https://www.cosmos.esa.int/web/gaia/edr3-code>





**Figure 3.** Map of the SMC Cepheids considered in our study. Yellow stars are the eclipsing binaries from Graczyk et al. (2020), and the red cross is the center of the SMC. The dashed circle represents a radius of  $0.6^\circ$  around the SMC center.

extension along the line of sight (Subramanian & Subramanian 2012; Jacyszyn-Dobrzeńska et al. 2016; Ripepi et al. 2017), which makes the distance to its core region particularly difficult to measure, contrary to the LMC, which has a rather simple geometry. In this section, we take into account the SMC elongated shape in order to derive corrected distances to each of its Cepheids. For each SMC Cepheid of coordinates  $(\alpha_i, \delta_i)$ , we compute the Cartesian coordinates  $(x_i, y_i)$  such that

$$\begin{cases} x_i = -d_{\text{SMC}} \cos \delta_i \sin(\alpha_i - \alpha_{\text{SMC}}) \\ y_i = d_{\text{SMC}} [\sin \delta_i \cos \delta_{\text{SMC}} - \cos \delta_i \sin \delta_{\text{SMC}} \cos(\alpha_i - \alpha_{\text{SMC}})] \end{cases},$$

where  $(\alpha_{\text{SMC}}, \delta_{\text{SMC}}) = (12^\circ 54', -73^\circ 11')$  (Ripepi et al. 2017). Then, we used the equations corresponding to the blue lines in Figure 4 of Graczyk et al. (2020):

$$\begin{cases} d_i(x) = (3.086 \pm 0.066) x_i + d_{\text{SMC}} \\ d_i(y) = (-3.248 \pm 0.118) y_i + d_{\text{SMC}}. \end{cases}$$

We adopt the mean value of  $d_i(x)$  and  $d_i(y)$  as the final distance of each Cepheid. The elongated shape of the SMC is highlighted by the dispersion of the derived distances between  $+5$  and  $-6$  kpc around the mean value  $d_{\text{SMC}}$ , which represents almost 10% of the mean value. The distances of our sample of SMC Cepheids are represented on the map in Figure 3. A discussion about the elongated shape of the SMC and its impact on our results is provided in Section 5.2.

#### 4. The Metallicity Effect from Milky Way and Magellanic Cloud Cepheids

In this section, we aim at estimating the metallicity term  $\gamma$  of the Leavitt law. In Section 4.1, we start by fitting the  $\alpha$  and  $\beta$  coefficients of the PL relation in each of the three galaxies, without considering the metallicity term. In Section 4.2, we include the metallicity for each galaxy and derive the third term of the PLZ relation by combining the three galaxies.

##### 4.1. The Period–Luminosity Relation

We adopt the Cepheid samples described in Section 2. In the first place, we correct apparent magnitudes for the extinction by adopting the reddening law from Cardelli et al. (1989) and O’Donnell (1994) assuming  $R_V = 3.135$ , which yields  $A_\lambda = R_\lambda E(B - V)$  with  $R_I = 1.894$ ,  $R_J = 0.892$ ,  $R_H = 0.553$ , and  $R_{K_S} = 0.363$ . We also derive optical and NIR Wesenheit indices (Madore 1982) as defined by  $W_{VI} = I - 1.526(V - I)$  and  $W_{JK} = K_S - 0.686(J - K_S)$ . Wesenheit magnitudes are particularly convenient for calibrating the PL relation since they are independent of reddening.

We account for the width of the instability strip by adding quadratically to the photometry uncertainties the intrinsic scatter in each band: this quantity is obtained by subtracting quadratically the measurement errors (photometric inhomogeneities, differential extinction, geometrical effects, phase corrections, etc.) from the scatter of the PL relation: we adopt a width of the instability strip of 0.07 mag in NIR bands ( $J$ ,  $H$ ,  $K_S$ , and  $W_{JK}$ ) from Persson et al. (2004), 0.15 mag in  $V$  and 0.09 mag in  $I$  from Macri et al. (2006), and finally 0.08 mag in  $W_{VI}$  from Madore et al. (2017). We derive the absolute magnitude  $M_\lambda$  of each Cepheid from their distance  $d$  (in kpc) and dereddened apparent magnitude  $m_\lambda$ :

$$M_\lambda = m_\lambda - 5 \log d - 10. \quad (1)$$

In the MW, the distance is obtained at the first order by taking the inverse of the parallax. In order to avoid biases due to this inversion, we adopt the approach introduced by Feast & Catchpole (1997) and Arenou & Luri (1999), consisting in fitting the astrometric-based luminosity (ABL) function instead of absolute magnitudes:

$$\text{ABL} = \pi_{(\text{mas})} 10^{0.2m_\lambda - 2} = 10^{M_\lambda/5} \quad (2)$$

where:

$$M_\lambda = \alpha_\lambda (\log P - \log P_0) + \beta_\lambda. \quad (3)$$

We adopt a pivot period of  $\log P_0 = 0.7$ , which represents the median period of our Cepheid sample. This approach ensures minimum correlations between the fitted coefficients. We perform a  $3\sigma$  clipping procedure on the PL relation to remove possible outliers.

A nonlinearity in the SMC PL relation was highlighted at the short-period end ( $\log P < 0.4$ ; EROS Collaboration et al. 1999). For LMC and SMC Cepheids, Chown et al. (2021) detect a break in the PL relation at  $\log P = 0.29$  and also at very long periods ( $\log P = 1.72$ ). Cepheids beyond these limits are found to deviate from the global PL fit and can affect both the slope and the ZP. Additionally, the short-period edge of the PL relation is potentially affected by first-overtone contamination. In the following, we exclude all Cepheids with periods shorter than 2.5 days ( $\log P = 0.4$ ) and longer than 52 days ( $\log P = 1.72$ ). Finally, we include the systematics on the LMC and SMC distance moduli (0.026 and 0.032 mag, respectively) and the photometric ZPs provided in Section 2 on the intercept error. We use the `curve_fit` function from the `scipy` Python library in a Monte Carlo algorithm to derive the PL coefficients and the 16th and 84th percentiles of the distribution to derive the uncertainties. The PL relations derived for each galaxy are provided in Table 1, where both the slope and intercept are fitted.

In each band, the intercept increases with decreasing metallicity, i.e., it becomes less negative from the MW to the

**Table 1**  
Results of the PL Fit of the Form  $M = \alpha(\log P - 0.7) + \beta$  in the Milky Way, the Large Magellanic Cloud, and the Small Magellanic Cloud

Band	$\alpha$	$\beta$	$\sigma$	$N^a$
MW <sup>b</sup>				
<i>V</i>	$-2.443 \pm 0.031$	$-3.296 \pm 0.024$	0.25	178
<i>I</i>	$-2.780 \pm 0.028$	$-3.981 \pm 0.024$	0.23	150
<i>W<sub>VI</sub></i>	$-3.289 \pm 0.026$	$-5.030 \pm 0.025$	0.21	149
<i>J</i>	$-3.050 \pm 0.029$	$-4.498 \pm 0.026$	0.18	97
<i>H</i>	$-3.160 \pm 0.028$	$-4.762 \pm 0.024$	0.17	97
<i>K<sub>S</sub></i>	$-3.207 \pm 0.028$	$-4.848 \pm 0.022$	0.17	97
<i>W<sub>JK</sub></i>	$-3.317 \pm 0.028$	$-5.086 \pm 0.026$	0.17	97
LMC <sup>c</sup>				
<i>V</i>	$-2.704 \pm 0.007$	$-3.284 \pm 0.033$	0.23	1446
<i>I</i>	$-2.916 \pm 0.005$	$-3.910 \pm 0.033$	0.15	1460
<i>W<sub>VI</sub></i>	$-3.281 \pm 0.008$	$-4.877 \pm 0.038$	0.08	1432
<i>J</i>	$-3.127 \pm 0.005$	$-4.385 \pm 0.033$	0.12	805
<i>H</i>	$-3.160 \pm 0.005$	$-4.696 \pm 0.033$	0.11	808
<i>K<sub>S</sub></i>	$-3.217 \pm 0.005$	$-4.737 \pm 0.033$	0.10	807
<i>W<sub>JK</sub></i>	$-3.272 \pm 0.008$	$-4.974 \pm 0.039$	0.10	806
SMC <sup>d</sup>				
<i>V</i>	$-2.594 \pm 0.012$	$-3.196 \pm 0.038$	0.28	284
<i>I</i>	$-2.871 \pm 0.008$	$-3.841 \pm 0.038$	0.22	297
<i>W<sub>VI</sub></i>	$-3.334 \pm 0.014$	$-4.834 \pm 0.043$	0.12	283
<i>J</i>	$-2.956 \pm 0.004$	$-4.317 \pm 0.038$	0.17	294
<i>H</i>	...	...	...	...
<i>K<sub>S</sub></i>	$-3.163 \pm 0.002$	$-4.670 \pm 0.038$	0.15	295
<i>W<sub>JK</sub></i>	$-3.326 \pm 0.002$	$-4.916 \pm 0.043$	0.14	295

**Notes.**

<sup>a</sup> The number of stars is given after the sigma clipping procedure and the period cuts.

<sup>b</sup> Mean  $[\text{Fe}/\text{H}] = +0.083 \pm 0.019$  dex.

<sup>c</sup> Mean  $[\text{Fe}/\text{H}] = -0.34 \pm 0.06$  dex.

<sup>d</sup> Mean  $[\text{Fe}/\text{H}] = -0.75 \pm 0.05$  dex.

LMC and in turn to the SMC. In the NIR, the intercept changes by  $\sim 0.18$  mag between the MW and the SMC, possibly indicating a strong dependence with metallicity. We note that our  $K_S$ -band calibration in the MW is in good agreement with the result by Breuval et al. (2020) based on Gaia DR2 parallaxes. The fit of the PL relation in the  $K_S$  band performed in each of the three galaxies is represented in Figure 4.

#### 4.2. The Period–Luminosity–Metallicity Relation

In this section, we now calibrate the dependence of the PL intercept  $\beta$  with metallicity. First, we fit the PL relation of the form  $M = \alpha(\log P - 0.7) + \beta$  in each of the three galaxies separately with a common slope fixed to the LMC value. As in the previous section, the systematics due to the LMC and SMC distance and to the photometric ZP are included in quadrature to the intercept random error. The intercept  $\beta$  contains the metallicity term such that

$$\beta = \gamma [\text{Fe}/\text{H}] + \delta. \quad (4)$$

In Figure 5 are represented the intercepts of the PL relations in the MW, LMC, and SMC as a function of metallicity. We fit Equation (4) with a Monte Carlo algorithm to derive the  $\gamma$  and  $\delta$  coefficients, and we adopt the 16th and 84th percentiles of the distribution to derive the random errors. A histogram

representing the distribution of the  $\gamma$  values obtained with the Monte Carlo algorithm is represented in Figure 6.

The results of the fit are listed in Table 2. In the NIR, we report a strong metallicity effect of  $-0.208 \pm 0.051$  mag dex<sup>-1</sup> in *J*,  $-0.152 \pm 0.092$  mag dex<sup>-1</sup> in *H*, and  $-0.221 \pm 0.050$  mag dex<sup>-1</sup> in  $K_S$ . The NIR Wesenheit index  $W_{JK}$  shows a similar dependence with  $-0.214 \pm 0.057$  mag dex<sup>-1</sup>. These results agree by  $1\sigma$  with Gieren et al. (2018), who used the Infrared Surface Brightness Technique (Fouqué & Gieren 1997; Storm et al. 2011a) to derive the distances to the Cepheids in their MW, LMC, and SMC samples, an approach different and independent from the one used in the present study. In the NIR Wesenheit index  $W_H$ , Riess et al. (2019) find an effect of  $-0.170 \pm 0.060$  mag dex<sup>-1</sup>, which is also close to our results in the NIR. In optical bands, we derive a weaker effect than in the NIR with  $-0.048 \pm 0.051$  mag dex<sup>-1</sup> in *V* and  $-0.138 \pm 0.051$  mag dex<sup>-1</sup> in *I*. These values also agree at  $1\sigma$  with Gieren et al. (2018), and the value in *V* is also consistent at  $1\sigma$  with the differential study of LMC and SMC PL relations by Wielgórski et al. (2017). On average, our results are located between the values by Wielgórski et al. (2017), consistent with a null metallicity effect, and the work by Gieren et al. (2018), who derive a strong negative effect. In the *H* band, we derive a metallicity effect weaker than in other NIR bands, likely because it is derived from the MW and LMC samples only (due to the lack of *H*-band photometry for SMC Cepheids). We conclude with the general trend being that the sensitivity to metallicity increases in the absolute sense and becomes more negative from optical to NIR wavelengths. This trend is particularly visible in Figure 7.

We note that the PL slope was fixed to the LMC value because this sample contains significantly more stars than the two other ones. However, if the slope is fixed to the value found in the MW or in the SMC, the intercepts agree by 0.2% in NIR and by 1.4% in optical. Similarly, the  $\gamma$  values agree at  $0.2\sigma$  and  $0.8\sigma$  in NIR and optical, respectively.

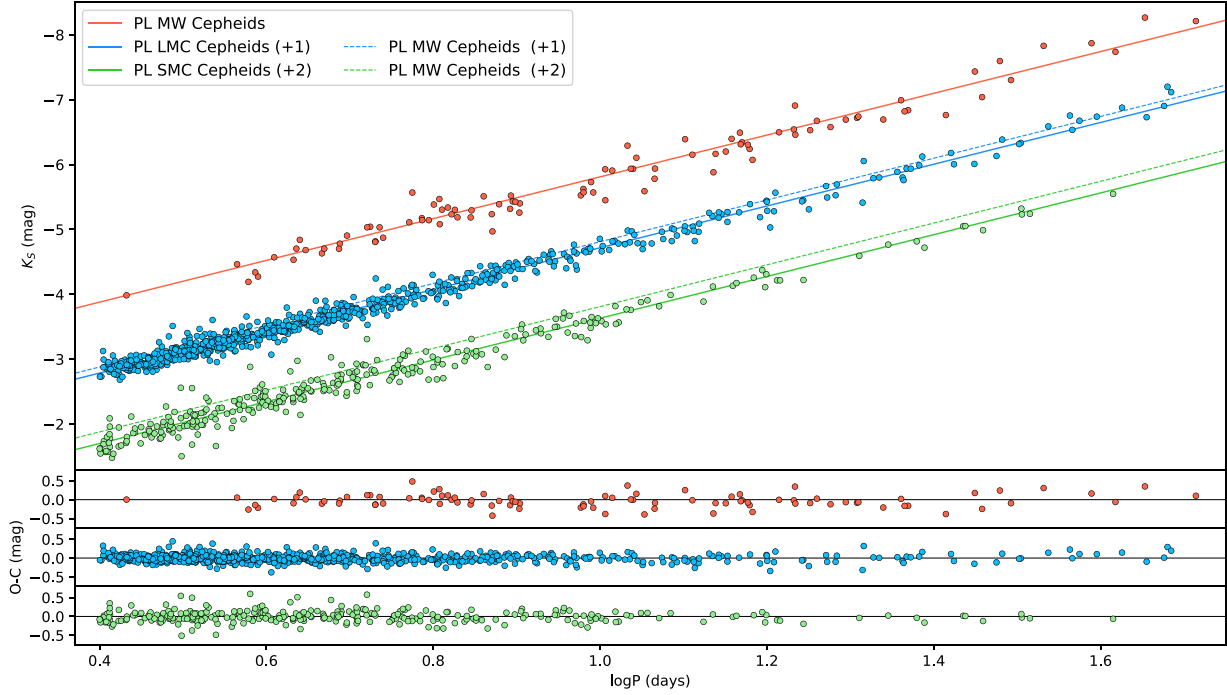
## 5. Discussion

The metallicity term of the PL relation can be sensitive to many different effects. In this section we study the stability  $\gamma$  after varying some parameters.

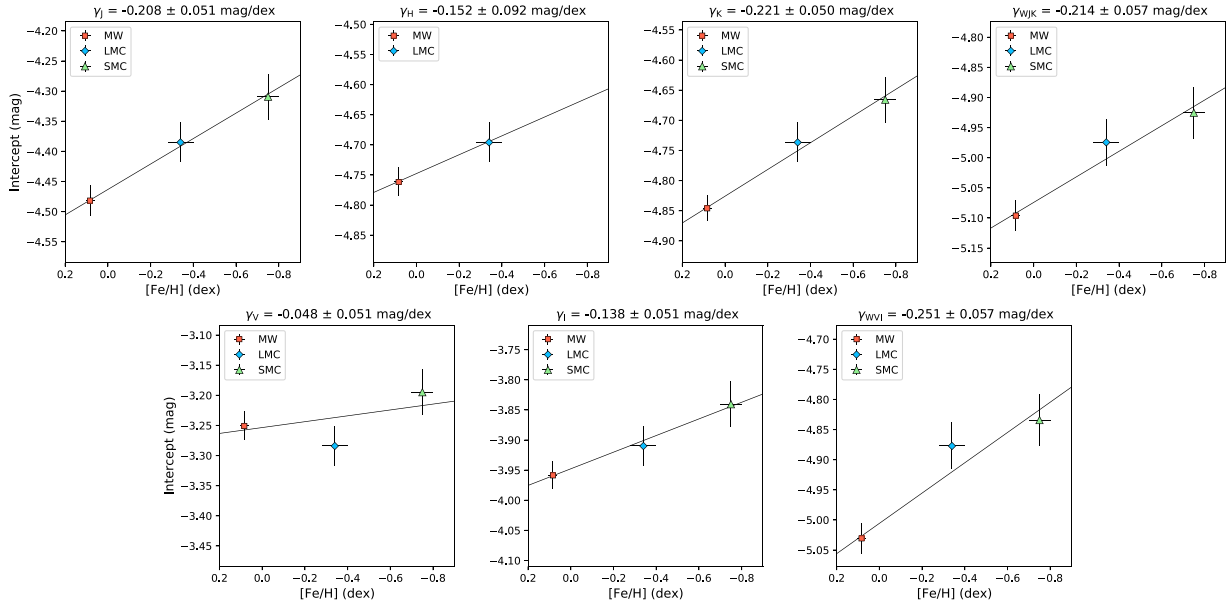
### 5.1. Influence of Gaia EDR3 Parallax ZP

In Section 3.1, we corrected each Gaia EDR3 parallax for their individual ZP by using the Python tool described in Lindegren et al. (2021b). However, in Lindegren et al. (2021a), a uniform parallax ZP of  $-17 \mu\text{as}$  is derived from quasars. The results of the PLZ fit obtained after adopting this uniform ZP are provided in the second part of Table 7 in Appendix E. They are consistent at the  $1\sigma$  level with the values derived using the individual ZP, although it gives a slightly more negative metallicity effect in each band. For example, in  $K_S$  we obtain  $\gamma = -0.271 \pm 0.051$  mag dex<sup>-1</sup>, compared with  $\gamma = -0.221 \pm 0.050$  mag dex<sup>-1</sup> with individual ZPs. This effect can be explained by the individual ZPs being on average more negative than  $-17 \mu\text{as}$  for our sample of MW Cepheids.

We also investigate whether the individual ZP correction by Lindegren et al. (2021b) is adapted to the most distant Cepheids: we remove from our sample the Cepheids with a parallax smaller than  $0.3$  mas and derive the PL relation in  $K_S$  without these stars. Using this PL relation, we compute



**Figure 4.** Fit of the PL relation in  $K_s$  for MW, LMC, and SMC Cepheids. The bottom panel shows the residual between the Cepheid absolute magnitudes and the corresponding PL fit for each of the three galaxies. The LMC and SMC relations were offset by +1 and +2 mag, respectively, for visualization purposes.



**Figure 5.** Intercept of the PL relation represented as a function of metallicity in  $J$ ,  $H$ ,  $K$ ,  $V$ ,  $I$ , and Wesenheit bands.

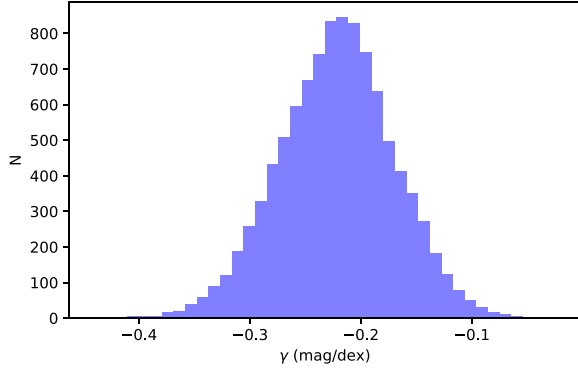
the expected parallax of the most distant Cepheids and compare it with the Gaia EDR3 parallax corrected by the individual ZP. We find a good agreement between the predicted parallaxes and the values from Gaia EDR3 with the Lindegren et al. (2021b) individual correction. From this study, we confirm that the individual ZP correction from

Lindegren et al. (2021b) is adapted to the most distant MW Cepheids of our sample.

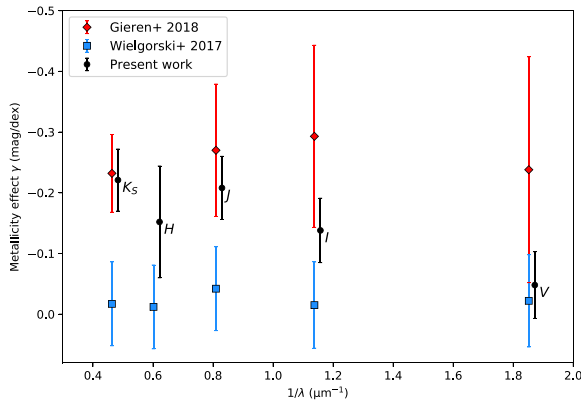
### 5.2. Influence of the SMC Sample

As mentioned in Sections 2.3 and 3.3, the distance to the core region of the SMC is particularly difficult to measure.





**Figure 6.** Histogram of the  $\gamma$  values obtained in the  $K_S$  band by the Monte Carlo algorithm iterated 10,000 times.



**Figure 7.** Metallicity effect as a function of wavelength, compared with values from the literature. The error bars include the systematics discussed in Section 5.2. For visualization purposes, the X-axis was slightly shifted for our values so that the error bars do not overlap, but they correspond to the same wavelength as the literature values.

**Table 2**  
Final Results of the PLZ Fit of the Form  
 $M = \alpha(\log P - 0.7) + \delta + \gamma [\text{Fe}/\text{H}]$  and Associated Uncertainties

Band	$\alpha$	$\sigma$	$\delta$	$\sigma$	$\gamma$	$\sigma$
V	-2.704	0.007	-3.252	0.020	-0.048	0.055
I	-2.916	0.005	-3.948	0.020	-0.138	0.053
$W_{VI}$	-3.281	0.008	-5.005	0.022	-0.251	0.057
J	-3.127	0.005	-4.463	0.022	-0.208	0.052
H	-3.160	0.005	-4.748	0.020	-0.152	0.092
$K_S$	-3.217	0.004	-4.826	0.019	-0.221	0.051
$W_{JK}$	-3.273	0.008	-5.075	0.022	-0.214	0.057

**Note.** The uncertainties include the systematics discussed in Section 5.2.

From their sample of DEBs, Graczyk et al. (2020) derive an uncertainty of about 2% for the distance to the SMC core region. These DEB systems are unevenly distributed in the central region of the galaxy, and their individual distances show a large dispersion around the mean value, ranging from 57 to 67 kpc (see their Figure 3), which corresponds to  $\sim 16\%$  of the SMC distance. In order to avoid including Cepheids

located too far away from the SMC center, we restricted our sample to a region of radius  $0.6^\circ$  around the SMC center. With a smaller radius, the contribution of the SMC sample in the PLZ fit becomes smaller than the MW contribution; therefore, we consider that the number of retained SMC Cepheids is insufficient. On the other hand, if we assume a radius larger than  $0.6^\circ$  around the SMC center, the number of outlier stars increases and the distance of some Cepheids may not correspond to the distance of the SMC core region. In order to test the validity of our hypothesis, we perform the same PLZ fit with a radius of  $0.5^\circ$  and  $0.7^\circ$  around the SMC center and report the coefficients in Table 7 in Appendix E.

After extending the SMC sample to a radius of  $0.7^\circ$  around the galaxy center, we find  $\gamma$  values in very good agreement (better than  $1\sigma$ ) with the values derived in the initial conditions. When the radius is reduced to  $0.5^\circ$ , the metallicity effect still agrees at  $1\sigma$  with the initial conditions in all bands. Considering a smaller region around the SMC center results in a slightly stronger (i.e., more negative) metallicity effect. These results highlight the sensitivity of the metallicity effect with respect to the adopted SMC sample, and in particular to the spatial distribution of the Cepheids considered. Moreover, it emphasizes the necessity to correct each Cepheid distance according to their position in the SMC plane, as we did in Section 3.3.

We consider the variation of  $\gamma$  within a region of  $0.5^\circ < R < 0.7^\circ$  around the SMC center as an additional source of systematic uncertainties: this source of error is at the level of  $0.02 \text{ mag dex}^{-1}$  in optical bands and of  $0.01 \text{ mag dex}^{-1}$  in NIR (see Table 7 in Appendix E). We adopt the same additional source of uncertainty for the intercept  $\delta$ , although the latter coefficient is particularly stable when the radius around the SMC center is changed. These systematics are included in the results presented in Table 2.

## 6. Conclusions

We build large samples of Cepheids in the MW and in the MCs and make use of the most recent and precise distances available to estimate the metallicity effect on the Cepheid PL relation. In the  $K_S$  band we derive an effect of  $\gamma = -0.221 \pm 0.051 \text{ mag dex}^{-1}$ , in agreement with the value found by Gieren et al. (2018) but more precise. In the V band we derive a weaker effect of  $\gamma = -0.048 \pm 0.055 \text{ mag dex}^{-1}$ , which is consistent with both Wielgorski et al. (2017) and Gieren et al. (2018) within the error bars. We conclude with a nonzero dependence of Cepheid magnitude with metallicity, and we confirm its negative sign: metal-rich Cepheids are brighter than metal-poor ones.

The improved precision reached in this work was made possible thanks to the high quality of Gaia EDR3 parallaxes and the new distances of the two MCs obtained by the Araucaria Project. Combining MW and MC Cepheids also allows us to reach a better precision than previous studies based on MCs only, by the larger range of metallicities they cover. A refined analysis of each light curve ensures the use of accurate mean magnitudes. However, the elongated shape of the SMC in the line of sight remains a source of systematic uncertainty in our study, despite continuous efforts to improve our knowledge of its structure. In this study, we assumed a linear dependence of the PL relation with metallicity, but it might as well be nonlinear (Gieren et al. 2018). Additional high-resolution spectroscopic metallicity measurements of both MW and MC

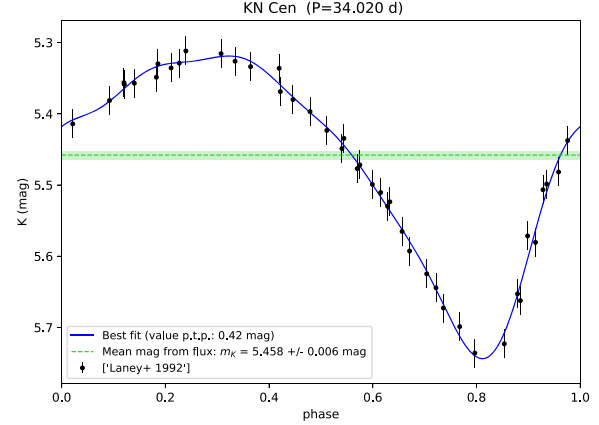
Cepheids should be carried out in the future to even better constrain the metallicity effect, particularly in the NIR, in our effort to further reduce the systematic uncertainty on the determination of the Hubble constant from the Cepheid-SN Ia method.

We thank the anonymous referee for the very constructive comments that helped us to improve the manuscript. We are grateful to Lucas Macri for providing the photometric transformations. The research leading to these results has received funding from the European Research Council (ERC) under the European Union's Horizon 2020 research and innovation program under grant agreement No. 695099 (project CepBin). This work has made use of data from the European Space Agency (ESA) mission Gaia (<http://www.cosmos.esa.int/gaia>), processed by the Gaia Data Processing and Analysis Consortium (DPAC, <http://www.cosmos.esa.int/web/gaia/dpac/consortium>). Funding for the DPAC has been provided by national institutions, in particular the institutions participating in the Gaia Multilateral Agreement. The authors acknowledge the support of the French Agence Nationale de la Recherche (ANR), under grant ANR-15-CE31-0012-01 (project UnlockCepheids). W.G. and G.P. gratefully acknowledge financial support for this work from the BASAL Centro de Astrofísica y Tecnologías Afines (CATA) AFB- 170002. W.G. and D.G. acknowledge financial support from the Millennium Institute of Astrophysics (MAS) of the Iniciativa Científica Milenio del Ministerio de Economía, Fomento y Turismo de Chile, project IC120009. This research made use of Astropy7, a community-developed core Python package for Astronomy (Astropy Collaboration et al. 2018). Support from the Polish National Science Centre grants MAESTRO UMO-2017/26/A/ST9/00446 and from the IdP11 2015 0002 64 and DIR/WK/2018/12 grants of the Polish Ministry of Science and Higher Education is also acknowledged. We used the SIMBAD and VIZIER databases and catalog access tool at the CDS, Strasbourg (France), and NASA's Astrophysics Data System Bibliographic Services.

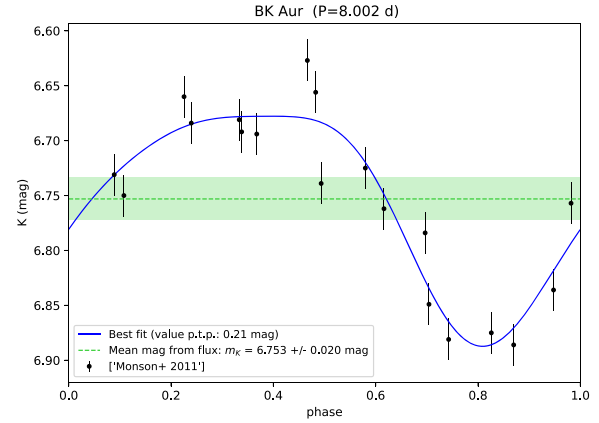
## Appendix A

### Examples of Light Curves of Milky Way Cepheids

Here we present examples of a well-covered light curve (Figure 8) and of a poor-quality light curve (Figure 9). The solid blue line represents the best fit of the light curve, the dashed green line is the mean magnitude derived from the best fit, and the green region is the uncertainty on the intensity-averaged mean magnitude. The method used to fit the light curves is described in Section 2.1.



**Figure 8.** Example of a well-covered light curve in the  $K$  band for the Galactic Cepheid KN Cen. The solid blue line represents the best fit of the light curve, the dashed green line is the mean magnitude derived from the best fit, and the green region is the uncertainty on the intensity-averaged mean magnitude.



**Figure 9.** Example of a poor-quality light curve in the  $K$  band for the Galactic Cepheid BK Aur. The solid blue line represents the best fit of the light curve, the dashed green line is the mean magnitude derived from the best fit, and the green region is the uncertainty on the intensity-averaged mean magnitude.

## Appendix B

### Data for the Sample of Milky Way Cepheids

Here we detail the sample of Milky Way Cepheids. In Table 3, we provide the period, parallax, and RUWE from Gaia EDR3, reddening, and metallicity for each Cepheid. In Table 4 are listed the apparent magnitudes in  $V$ ,  $I$ ,  $J$ ,  $H$ , and  $K$  for each Milky Way Cepheid, along with the references.

**Table 3**  
Sample of Milky Way Cepheids and Main Parameters

Star	Period (days)	$\pi_{\text{EDR3}}$ (mas)	RUWE	$E(B - V)$ (mag)	Reference	[Fe/H] (dex)	Reference
AA Gem	11.302	$0.311 \pm 0.018$	1.25	$0.345 \pm 0.036$	F95	$-0.08 \pm 0.05$	G15
AC Mon	8.014	$0.383 \pm 0.019$	1.38	$0.507 \pm 0.033$	F95	$-0.03 \pm 0.06$	G14b
AD Gem	3.788	$0.370 \pm 0.020$	0.97	$0.206 \pm 0.048$	F95	$-0.14 \pm 0.06$	G15
AD Pup	13.596	$0.254 \pm 0.017$	1.36	$0.363 \pm 0.020$	F95	$-0.20 \pm 0.15$	G14b
AE Vel	7.134	$0.369 \pm 0.012$	0.97	$0.691 \pm 0.055$	F95	$0.14 \pm 0.06$	G14b
AG Cru	3.837	$0.758 \pm 0.020$	1.02	$0.242 \pm 0.020$	F95	$0.08 \pm 0.06$	G14b
AP Pup	5.084	$0.924 \pm 0.020$	1.05	$0.250 \pm 0.034$	F95	$-0.16 \pm 0.15$	G14b
AP Sgr	5.058	$1.217 \pm 0.024$	0.88	$0.184 \pm 0.015$	F95	$0.10 \pm 0.08$	G14b
AQ Car	9.769	$0.361 \pm 0.016$	1.07	$0.168 \pm 0.013$	F95	$-0.30 \pm 0.15$	G14b
AQ Pup	30.149	$0.294 \pm 0.023$	1.18	$0.531 \pm 0.017$	F95	$0.06 \pm 0.05$	G15
AS Per	4.973	$0.650 \pm 0.016$	1.08	$0.684 \pm 0.041$	F95	$0.14 \pm 0.06$	G14b
AT Pup	6.665	$0.604 \pm 0.016$	1.04	$0.166 \pm 0.011$	F95	$-0.22 \pm 0.15$	G14b
AV Sgr	15.415	$0.404 \pm 0.025$	0.84	$1.238 \pm 0.027$	F95	$0.35 \pm 0.17$	G15
AW Per	6.464	$1.093 \pm 0.029$	1.16	$0.479 \pm 0.016$	F95	$0.04 \pm 0.06$	G14b
AY Cas	2.872	$0.414 \pm 0.019$	1.07	$0.760 \pm 0.049$	F95	$0.02 \pm 0.06$	G14b
AY Cen	5.310	$0.574 \pm 0.014$	0.95	$0.357 \pm 0.066$	F95	$0.08 \pm 0.06$	G14b
AY Sgr	6.570	$0.546 \pm 0.019$	0.85	$0.840 \pm 0.009$	F95	$0.11 \pm 0.06$	G15
BB Her	7.508	$0.280 \pm 0.015$	1.06	$0.392 \pm 0.039$	A12	$0.26 \pm 0.06$	G14b
BB Sgr	6.637	$1.188 \pm 0.024$	0.82	$0.285 \pm 0.011$	F95	$0.08 \pm 0.08$	G14b
BE Mon	2.706	$0.504 \pm 0.017$	1.17	$0.549 \pm 0.036$	F95	$0.05 \pm 0.09$	G15
BF Oph	4.068	$1.189 \pm 0.024$	0.84	$0.261 \pm 0.016$	F95	$0.14 \pm 0.06$	G14b
BG Vel	6.924	$1.045 \pm 0.017$	0.99	$0.434 \pm 0.011$	F95	$-0.10 \pm 0.15$	G14b
BK Aur	8.002	$0.426 \pm 0.015$	1.01	$0.393 \pm 0.026$	F95	$-0.07 \pm 0.15$	G14b
BM Per	22.952	$0.334 \pm 0.022$	0.99	$0.919 \pm 0.059$	F95	$0.23 \pm 0.06$	G14b
BM Pup	7.199	$0.302 \pm 0.013$	1.18	$0.575 \pm 0.058$	F95	$-0.07 \pm 0.08$	G15
BN Pup	13.673	$0.301 \pm 0.015$	1.25	$0.422 \pm 0.017$	F95	$0.03 \pm 0.05$	G15
BP Cas	6.273	$0.442 \pm 0.013$	1.02	$0.864 \pm 0.014$	F95	$0.09 \pm 0.06$	G14b
BZ Cyg	10.142	$0.500 \pm 0.014$	1.14	$0.832 \pm 0.018$	F95	$0.19 \pm 0.08$	G14b
CD Cas	7.801	$0.412 \pm 0.014$	1.06	$0.745 \pm 0.012$	F95	$0.13 \pm 0.06$	G14b
CD Cyg	17.074	$0.394 \pm 0.016$	1.01	$0.512 \pm 0.021$	F95	$0.15 \pm 0.06$	G14b
CE Pup	49.326	$0.114 \pm 0.014$	0.82	$0.740 \pm 0.074$	A12	$-0.04 \pm 0.09$	G14
CF Cas	4.875	$0.316 \pm 0.012$	1.04	$0.556 \pm 0.021$	F95	$0.02 \pm 0.06$	G14b
CG Cas	4.366	$0.296 \pm 0.017$	1.03	$0.667 \pm 0.009$	F95	$0.09 \pm 0.06$	G14b
CK Sct	7.415	$0.490 \pm 0.020$	0.97	$0.816 \pm 0.024$	F95	$0.21 \pm 0.06$	G14b
CN Car	4.933	$0.342 \pm 0.014$	0.96	$0.438 \pm 0.049$	F95	$0.21 \pm 0.06$	G14b
CP Cep	17.859	$0.279 \pm 0.021$	1.01	$0.681 \pm 0.045$	F95	$-0.01 \pm 0.08$	G14b
CR Cep	6.233	$0.699 \pm 0.013$	1.06	$0.704 \pm 0.009$	F95	$-0.06 \pm 0.08$	G14b
CR Ser	5.301	$0.578 \pm 0.020$	1.19	$0.974 \pm 0.017$	F95	$0.12 \pm 0.08$	G15
CS Mon	6.732	$0.324 \pm 0.014$	1.04	$0.528 \pm 0.032$	F95	$-0.08 \pm 0.06$	G14b
CS Ori	3.889	$0.257 \pm 0.022$	1.33	$0.373 \pm 0.030$	F95	$-0.25 \pm 0.06$	G15
CS Vel	5.905	$0.272 \pm 0.016$	0.91	$0.716 \pm 0.027$	F95	$0.12 \pm 0.06$	G14b
CV Mon	5.379	$0.601 \pm 0.015$	1.10	$0.705 \pm 0.018$	F95	$0.09 \pm 0.09$	G15
CY Car	4.266	$0.427 \pm 0.011$	0.93	$0.409 \pm 0.043$	F95	$0.11 \pm 0.06$	G14b
CY Cas	14.377	$0.255 \pm 0.019$	1.07	$0.952 \pm 0.008$	F95	$0.06 \pm 0.08$	G14b
CZ Cas	5.664	$0.292 \pm 0.016$	0.96	$0.761 \pm 0.030$	F95	$0.07 \pm 0.06$	G14b
DD Cas	9.812	$0.346 \pm 0.013$	1.05	$0.486 \pm 0.016$	F95	$0.10 \pm 0.08$	G14b
DF Cas	3.832	$0.374 \pm 0.014$	1.05	$0.564 \pm 0.049$	F95	$0.13 \pm 0.08$	G14b
DW Per	3.650	$0.296 \pm 0.019$	1.31	$0.620 \pm 0.033$	F95	$-0.05 \pm 0.06$	G14b
EK Mon	3.958	$0.376 \pm 0.021$	1.16	$0.547 \pm 0.003$	F95	$-0.05 \pm 0.15$	G14b
ER Car	7.719	$0.869 \pm 0.015$	0.82	$0.111 \pm 0.016$	F95	$0.15 \pm 0.06$	G14b
EX Vel	13.234	$0.204 \pm 0.015$	0.94	$0.728 \pm 0.052$	F95	$0.07 \pm 0.06$	G14b
FI Car	13.458	$0.242 \pm 0.019$	0.99	$0.694 \pm 0.007$	F95	$0.31 \pm 0.06$	G14b
FM Aql	6.114	$1.014 \pm 0.026$	1.26	$0.635 \pm 0.019$	F95	$0.24 \pm 0.06$	G14b
FN Aql	9.482	$0.736 \pm 0.025$	1.12	$0.486 \pm 0.008$	F95	$-0.06 \pm 0.06$	G14b
GH Cyg	7.818	$0.417 \pm 0.014$	1.07	$0.608 \pm 0.023$	F95	$0.21 \pm 0.06$	G14b
GI Cyg	5.783	$0.273 \pm 0.017$	1.01	$0.734 \pm 0.073$	F95	$0.27 \pm 0.06$	G14b
GQ Ori	8.616	$0.408 \pm 0.021$	0.87	$0.224 \pm 0.013$	F95	$0.20 \pm 0.08$	G15
GU Nor	3.453	$0.565 \pm 0.015$	0.87	$0.683 \pm 0.029$	F95	$0.08 \pm 0.06$	G15
GX Car	7.197	$0.459 \pm 0.013$	1.02	$0.380 \pm 0.008$	F95	$0.14 \pm 0.06$	G14b
GY Sge	51.790	$0.342 \pm 0.023$	0.95	$1.183 \pm 0.111$	F95	$0.29 \pm 0.06$	G14b
HW Car	9.199	$0.397 \pm 0.012$	0.94	$0.181 \pm 0.018$	F95	$0.09 \pm 0.06$	G14b
IQ Nor	8.220	$0.535 \pm 0.018$	0.97	$0.676 \pm 0.044$	F95	$0.22 \pm 0.07$	G15

**Table 3**  
(Continued)

Star	Period (days)	$\pi_{\text{EDR3}}$ (mas)	RUWE	$E(B - V)$ (mag)	Reference	[Fe/H] (dex)	Reference
IT Car	7.533	$0.702 \pm 0.020$	1.08	$0.212 \pm 0.016$	F95	$0.14 \pm 0.06$	G14b
KK Cen	12.180	$0.152 \pm 0.018$	1.03	$0.555 \pm 0.033$	F95	$0.24 \pm 0.06$	G14b
KN Cen	34.020	$0.251 \pm 0.018$	1.03	$0.728 \pm 0.040$	F95	$0.55 \pm 0.12$	G15
KQ Sco	28.705	$0.472 \pm 0.021$	0.91	$0.852 \pm 0.041$	F95	$0.52 \pm 0.08$	G15
LS Pup	14.147	$0.214 \pm 0.016$	1.25	$0.452 \pm 0.009$	F95	$-0.12 \pm 0.11$	G15
MW Cyg	5.955	$0.542 \pm 0.019$	1.21	$0.651 \pm 0.039$	F95	$0.09 \pm 0.08$	G14b
MZ Cen	10.354	$0.221 \pm 0.017$	0.84	$0.782 \pm 0.077$	F95	$0.27 \pm 0.10$	G15
QY Cen	17.752	$0.293 \pm 0.021$	1.02	$1.213 \pm 0.216$	F95	$0.24 \pm 0.06$	G14b
R Cru	5.826	$1.078 \pm 0.028$	1.16	$0.156 \pm 0.012$	F95	$0.13 \pm 0.06$	G14b
R Mus	7.510	$1.076 \pm 0.018$	1.07	$0.149 \pm 0.030$	F95	$-0.08 \pm 0.06$	G14b
R TrA	3.389	$1.560 \pm 0.016$	0.89	$0.167 \pm 0.025$	F95	$0.19 \pm 0.06$	G14b
RR Lac	6.416	$0.424 \pm 0.015$	1.10	$0.267 \pm 0.023$	F95	$0.04 \pm 0.06$	G14b
RS Nor	6.198	$0.472 \pm 0.017$	0.94	$0.577 \pm 0.036$	F95	$0.18 \pm 0.08$	G15
RS Ori	7.567	$0.589 \pm 0.030$	1.12	$0.332 \pm 0.010$	F95	$0.11 \pm 0.09$	G15
RS Pup	41.480	$0.581 \pm 0.017$	1.16	$0.451 \pm 0.010$	F95	$0.07 \pm 0.15$	G14b
RU Sct	19.704	$0.526 \pm 0.024$	0.87	$0.914 \pm 0.017$	F95	$0.14 \pm 0.04$	G15
RV Sco	6.061	$1.257 \pm 0.021$	0.81	$0.343 \pm 0.007$	F95	$0.11 \pm 0.06$	G14b
RW Cas	14.795	$0.335 \pm 0.019$	1.26	$0.440 \pm 0.032$	F95	$0.22 \pm 0.08$	G14b
RX Aur	11.624	$0.654 \pm 0.021$	0.98	$0.254 \pm 0.020$	F95	$0.10 \pm 0.06$	G14b
RY CMa	4.678	$0.825 \pm 0.029$	1.29	$0.238 \pm 0.016$	F95	$0.00 \pm 0.15$	G14b
RY Sco	20.323	$0.764 \pm 0.032$	0.73	$0.654 \pm 0.044$	F95	$0.01 \pm 0.06$	G15
RY Vel	28.136	$0.376 \pm 0.021$	1.07	$0.539 \pm 0.012$	F95	$-0.05 \pm 0.15$	G14b
RZ Vel	20.398	$0.661 \pm 0.017$	1.24	$0.301 \pm 0.011$	F95	$0.05 \pm 0.15$	G14b
S Cru	4.690	$1.342 \pm 0.024$	0.94	$0.172 \pm 0.014$	F95	$0.11 \pm 0.06$	G14b
S Nor	9.754	$1.099 \pm 0.022$	0.88	$0.182 \pm 0.008$	F95	$0.02 \pm 0.09$	G14b
S TrA	6.324	$1.120 \pm 0.022$	1.04	$0.086 \pm 0.010$	F95	$0.21 \pm 0.06$	G14b
SS CMa	12.361	$0.307 \pm 0.013$	1.11	$0.551 \pm 0.012$	F95	$0.06 \pm 0.04$	G15
SS Sct	3.671	$0.934 \pm 0.023$	0.84	$0.340 \pm 0.022$	F95	$0.14 \pm 0.06$	G14b
ST Tau	4.034	$0.916 \pm 0.034$	1.35	$0.328 \pm 0.006$	F95	$-0.14 \pm 0.15$	G14b
ST Vel	5.858	$0.384 \pm 0.015$	1.19	$0.530 \pm 0.024$	F95	$-0.14 \pm 0.15$	G14b
SV Mon	15.233	$0.464 \pm 0.032$	1.01	$0.264 \pm 0.021$	F95	$0.12 \pm 0.08$	G15
SV Vel	14.097	$0.434 \pm 0.018$	1.02	$0.376 \pm 0.024$	F95	$0.12 \pm 0.06$	G14b
SV Vul	44.993	$0.402 \pm 0.021$	1.20	$0.474 \pm 0.024$	F95	$0.05 \pm 0.08$	G14b
SW Cas	5.441	$0.461 \pm 0.012$	1.12	$0.475 \pm 0.027$	F95	$-0.03 \pm 0.08$	G14b
SW Vel	23.407	$0.413 \pm 0.018$	1.05	$0.338 \pm 0.009$	F95	$-0.15 \pm 0.15$	G14b
SX Car	4.860	$0.515 \pm 0.022$	1.25	$0.323 \pm 0.026$	F95	$0.05 \pm 0.06$	G14b
SX Per	4.290	$0.313 \pm 0.019$	1.19	$0.537 \pm 0.046$	F95	$-0.03 \pm 0.06$	G14b
SX Vel	9.550	$0.501 \pm 0.019$	1.02	$0.237 \pm 0.014$	F95	$-0.18 \pm 0.15$	G14b
SY Aur	10.145	$0.462 \pm 0.020$	1.08	$0.386 \pm 0.040$	F95	$-0.07 \pm 0.15$	G14b
SZ Aql	17.141	$0.525 \pm 0.020$	0.94	$0.553 \pm 0.022$	F95	$0.18 \pm 0.08$	G14b
SZ Cas	13.639	$0.407 \pm 0.017$	1.01	$0.713 \pm 0.060$	F95	$0.07 \pm 0.06$	G14b
SZ Cyg	15.110	$0.445 \pm 0.012$	0.96	$0.594 \pm 0.004$	F95	$0.09 \pm 0.08$	G14b
T Ant	5.898	$0.312 \pm 0.014$	1.18	$0.300 \pm 0.030$	A12	$-0.20 \pm 0.06$	G14b
T Cru	6.733	$1.222 \pm 0.014$	0.82	$0.191 \pm 0.022$	F95	$0.14 \pm 0.06$	G14b
T Vel	4.640	$0.940 \pm 0.016$	0.93	$0.282 \pm 0.018$	F95	$-0.02 \pm 0.15$	G14b
T Vul	4.435	$1.719 \pm 0.058$	1.20	$0.092 \pm 0.017$	F95	$0.01 \pm 0.08$	G14b
TT Aql	13.755	$0.997 \pm 0.023$	1.08	$0.487 \pm 0.024$	F95	$0.22 \pm 0.06$	G14b
TV CMa	4.670	$0.420 \pm 0.015$	1.20	$0.574 \pm 0.029$	F95	$0.01 \pm 0.07$	G15
TV Cam	5.295	$0.237 \pm 0.018$	1.11	$0.560 \pm 0.023$	F95	$0.04 \pm 0.06$	G14b
TW CMa	6.995	$0.384 \pm 0.019$	1.15	$0.374 \pm 0.033$	F95	$0.04 \pm 0.09$	G15
TW Nor	10.786	$0.360 \pm 0.020$	0.89	$1.190 \pm 0.023$	F95	$0.27 \pm 0.10$	G15
TX Cen	17.098	$0.332 \pm 0.018$	0.94	$0.941 \pm 0.038$	F95	$0.44 \pm 0.12$	G15
TX Cyg	14.710	$0.829 \pm 0.019$	0.95	$1.123 \pm 0.005$	F95	$0.20 \pm 0.08$	G14b
TY Sct	11.053	$0.371 \pm 0.016$	0.91	$0.930 \pm 0.017$	F95	$0.37 \pm 0.06$	G14b
TZ Mon	7.428	$0.298 \pm 0.015$	1.24	$0.434 \pm 0.023$	F95	$-0.02 \pm 0.07$	G15
TZ Mus	4.945	$0.266 \pm 0.020$	1.00	$0.676 \pm 0.020$	F95	$0.10 \pm 0.06$	G14b
U Car	38.829	$0.561 \pm 0.023$	1.23	$0.276 \pm 0.013$	F95	$0.17 \pm 0.09$	G14b
U Nor	12.644	$0.625 \pm 0.019$	0.98	$0.868 \pm 0.038$	F95	$0.07 \pm 0.09$	G14b
U Sgr	6.745	$1.605 \pm 0.023$	0.85	$0.408 \pm 0.007$	F95	$0.08 \pm 0.08$	G14b
UU Mus	11.636	$0.306 \pm 0.012$	1.01	$0.431 \pm 0.041$	F95	$0.11 \pm 0.09$	G14b
UX Car	3.682	$0.653 \pm 0.019$	1.02	$0.102 \pm 0.023$	F95	$-0.10 \pm 0.15$	G14b
UX Per	4.566	$0.162 \pm 0.020$	1.17	$0.462 \pm 0.024$	F95	$-0.05 \pm 0.06$	G14b

**Table 3**  
(Continued)

Star	Period (days)	$\pi_{\text{EDR3}}$ (mas)	RUWE	$E(B - V)$ (mag)	Reference	[Fe/H] (dex)	Reference
UY Car	5.544	$0.455 \pm 0.014$	0.94	$0.188 \pm 0.017$	F95	$0.13 \pm 0.06$	G14b
UY Per	5.365	$0.415 \pm 0.015$	1.17	$0.888 \pm 0.013$	F95	$0.18 \pm 0.06$	G14b
UZ Car	5.205	$0.401 \pm 0.013$	0.95	$0.213 \pm 0.034$	F95	$0.13 \pm 0.06$	G14b
UZ Cas	4.259	$0.251 \pm 0.020$	1.23	$0.469 \pm 0.034$	F95	$-0.05 \pm 0.06$	G14b
UZ Sct	14.744	$0.324 \pm 0.025$	0.91	$0.959 \pm 0.023$	F95	$0.33 \pm 0.08$	G15
V Car	6.697	$0.797 \pm 0.014$	1.04	$0.164 \pm 0.013$	F95	$-0.06 \pm 0.15$	G14b
V Cen	5.494	$1.409 \pm 0.022$	1.06	$0.265 \pm 0.016$	F95	$0.04 \pm 0.09$	G14b
V Lac	4.983	$0.496 \pm 0.016$	1.09	$0.293 \pm 0.034$	F95	$0.06 \pm 0.06$	G14b
V Vel	4.371	$0.953 \pm 0.017$	1.03	$0.225 \pm 0.021$	F95	$-0.30 \pm 0.15$	G14b
V0339 Cen	9.466	$0.568 \pm 0.021$	0.89	$0.426 \pm 0.016$	F95	$0.06 \pm 0.03$	G15
V0340 Ara	20.814	$0.239 \pm 0.020$	0.93	$0.548 \pm 0.008$	F95	$0.33 \pm 0.09$	G15
V0340 Nor	11.289	$0.491 \pm 0.025$	0.92	$0.312 \pm 0.050$	F95	$0.07 \pm 0.07$	G15
V0378 Cen	6.460	$0.524 \pm 0.019$	0.99	$0.374 \pm 0.049$	F95	$0.08 \pm 0.06$	G14b
V0381 Cen	5.079	$0.818 \pm 0.020$	1.06	$0.206 \pm 0.013$	F95	$0.02 \pm 0.06$	G14b
V0386 Cyg	5.258	$0.894 \pm 0.013$	0.95	$0.907 \pm 0.033$	F95	$0.11 \pm 0.08$	G14b
V0402 Cyg	4.365	$0.410 \pm 0.011$	0.92	$0.455 \pm 0.062$	F95	$0.02 \pm 0.08$	G14b
V0459 Cyg	7.251	$0.382 \pm 0.014$	1.09	$0.775 \pm 0.024$	F95	$0.09 \pm 0.06$	G14b
V0470 Sco	16.261	$0.534 \pm 0.029$	0.97	$1.550 \pm 0.124$	F95	$0.16 \pm 0.06$	G15
V0493 Aql	2.988	$0.472 \pm 0.017$	1.12	$0.730 \pm 0.087$	F95	$0.03 \pm 0.06$	G14b
V0496 Cen	4.424	$0.563 \pm 0.013$	0.94	$0.579 \pm 0.031$	F95	$0.09 \pm 0.06$	G14b
V0520 Cyg	4.049	$0.437 \pm 0.012$	1.03	$0.754 \pm 0.075$	F95	$0.08 \pm 0.06$	G14b
V0538 Cyg	6.119	$0.394 \pm 0.017$	0.99	$0.656 \pm 0.021$	F95	$0.05 \pm 0.06$	G14b
V0600 Aql	7.239	$0.523 \pm 0.019$	1.13	$0.812 \pm 0.007$	F95	$0.03 \pm 0.08$	G14b
V0609 Cyg	31.088	$0.295 \pm 0.017$	1.12	$1.243 \pm 0.124$	F95	$0.22 \pm 0.06$	G14b
V0636 Cas	8.377	$1.372 \pm 0.018$	1.02	$0.593 \pm 0.065$	F95	$0.07 \pm 0.08$	G14b
V0636 Sco	6.797	$1.180 \pm 0.034$	1.15	$0.227 \pm 0.017$	F95	$0.10 \pm 0.06$	G14b
V0733 Aql	6.179	$0.244 \pm 0.015$	0.98	$0.106 \pm 0.011$	A12	$0.08 \pm 0.08$	G14b
V0737 Cen	7.066	$1.213 \pm 0.019$	0.92	$0.227 \pm 0.022$	F95	$0.14 \pm 0.06$	G14b
V1154 Cyg	4.925	$0.442 \pm 0.012$	1.04	$0.315 \pm 0.031$	F95	$-0.10 \pm 0.08$	G14b
V1162 Aql	5.376	$0.823 \pm 0.023$	0.95	$0.184 \pm 0.011$	F95	$0.01 \pm 0.08$	G14b
VW Cen	15.036	$0.260 \pm 0.016$	1.06	$0.424 \pm 0.022$	F95	$0.41 \pm 0.08$	G15
VW Cru	5.265	$0.738 \pm 0.016$	0.85	$0.640 \pm 0.046$	F95	$0.19 \pm 0.06$	G15
VY Car	18.890	$0.565 \pm 0.017$	0.92	$0.270 \pm 0.019$	F95	$-0.06 \pm 0.15$	G14b
VY Cyg	7.857	$0.485 \pm 0.012$	1.07	$0.596 \pm 0.021$	F95	$0.00 \pm 0.08$	G14b
VY Per	5.532	$0.485 \pm 0.017$	1.15	$0.948 \pm 0.018$	F95	$0.04 \pm 0.06$	G14b
VY Sgr	13.557	$0.412 \pm 0.025$	0.81	$0.903 \pm 0.243$	F95	$0.33 \pm 0.12$	G15
VZ Cyg	4.864	$0.545 \pm 0.016$	1.31	$0.291 \pm 0.015$	F95	$0.05 \pm 0.08$	G14b
VZ Pup	23.175	$0.220 \pm 0.015$	1.24	$0.433 \pm 0.018$	F95	$-0.01 \pm 0.04$	G15
W Gem	7.914	$1.006 \pm 0.028$	1.23	$0.264 \pm 0.011$	F95	$0.02 \pm 0.06$	G14b
WW Pup	5.517	$0.212 \pm 0.016$	1.14	$0.334 \pm 0.017$	F95	$0.13 \pm 0.16$	G15
WX Pup	8.937	$0.387 \pm 0.015$	1.06	$0.306 \pm 0.018$	F95	$-0.15 \pm 0.15$	G14b
WY Pup	5.251	$0.258 \pm 0.013$	1.02	$0.259 \pm 0.031$	F95	$-0.10 \pm 0.08$	G15
WZ Pup	5.027	$0.281 \pm 0.017$	1.35	$0.196 \pm 0.022$	F95	$-0.07 \pm 0.06$	G15
WZ Sgr	21.851	$0.612 \pm 0.028$	0.94	$0.457 \pm 0.025$	F95	$0.28 \pm 0.08$	G15
X Cru	6.220	$0.654 \pm 0.019$	0.95	$0.294 \pm 0.019$	F95	$0.15 \pm 0.06$	G14b
X Cyg	16.386	$0.910 \pm 0.020$	1.28	$0.251 \pm 0.010$	F95	$0.10 \pm 0.08$	G14b
X Pup	25.973	$0.397 \pm 0.020$	1.04	$0.396 \pm 0.015$	F95	$0.02 \pm 0.08$	G15
X Sct	4.198	$0.634 \pm 0.019$	0.80	$0.581 \pm 0.030$	F95	$0.12 \pm 0.09$	G15
X Sgr	7.013	$2.843 \pm 0.141$	1.22	$0.189 \pm 0.020$	F95	$-0.21 \pm 0.30$	G14b
X Vul	6.320	$0.864 \pm 0.022$	1.06	$0.775 \pm 0.021$	F95	$0.07 \pm 0.08$	G14b
XX Cen	10.953	$0.570 \pm 0.026$	1.24	$0.245 \pm 0.012$	F95	$0.04 \pm 0.09$	G14b
XX Mon	5.456	$0.242 \pm 0.013$	0.86	$0.586 \pm 0.014$	F95	$0.01 \pm 0.08$	G15
XX Sgr	6.424	$0.724 \pm 0.027$	1.10	$0.493 \pm 0.016$	F95	$-0.01 \pm 0.06$	G15
XX Vel	6.985	$0.308 \pm 0.013$	0.88	$0.530 \pm 0.007$	F95	$0.11 \pm 0.06$	G14b
XZ Car	16.651	$0.473 \pm 0.018$	1.05	$0.372 \pm 0.026$	F95	$0.19 \pm 0.06$	G14b
Y Aur	3.859	$0.541 \pm 0.017$	1.12	$0.384 \pm 0.031$	F95	$-0.26 \pm 0.15$	G14b
Y Lac	4.324	$0.431 \pm 0.013$	1.05	$0.212 \pm 0.020$	F95	$0.03 \pm 0.06$	G14b
Y Oph	17.125	$1.348 \pm 0.036$	1.03	$0.606 \pm 0.030$	F95	$0.06 \pm 0.08$	G14b
Y Sct	10.342	$0.558 \pm 0.020$	0.94	$0.792 \pm 0.021$	F95	$0.23 \pm 0.06$	G14b
YZ Aur	18.193	$0.233 \pm 0.016$	0.99	$0.548 \pm 0.055$	F95	$-0.33 \pm 0.15$	G14b
YZ Car	18.168	$0.358 \pm 0.018$	1.17	$0.324 \pm 0.039$	F95	$0.00 \pm 0.06$	G14b
YZ Sgr	9.554	$0.860 \pm 0.024$	0.95	$0.289 \pm 0.007$	F95	$0.06 \pm 0.08$	G14b

**Table 3**  
(Continued)

Star	Period (days)	$\pi_{\text{EDR3}}$ (mas)	RUWE	$E(B - V)$ (mag)	Reference	[Fe/H] (dex)	Reference
Z Lac	10.886	$0.510 \pm 0.021$	1.05	$0.352 \pm 0.015$	F95	$0.10 \pm 0.06$	G14b
Z Sct	12.901	$0.357 \pm 0.018$	0.90	$0.535 \pm 0.039$	F95	$0.12 \pm 0.09$	G15

**Note.** Parallaxes from Gaia EDR3 include ZP correction. Stars with an RUWE parameter larger than 1.4 were marked with a star and excluded from the sample. **References.** (F95): reddening from Fernie et al. (1995) multiplied by 0.94; (A12): reddening from Acharova et al. (2012), (G14): metallicity from Genovali et al. (2014); (G14b): metallicity from the literature (Yong et al. 2006; Lemasle et al. 2007; Sziládi et al. 2007; Romaniello et al. 2008; Pedicelli et al. 2010; Luck et al. 2011; Luck & Lambert 2011; Genovali et al. 2013) rescaled to Genovali et al. (2014) solar abundance; (G15): metallicity from Genovali et al. (2015).

(This table is available in machine-readable form.)

**Table 4**  
Optical and NIR Mean Apparent Magnitudes for the Sample of Milky Way Cepheids

Star	$V$ (mag)	$I$ (mag)	$J$ (mag)	$H$ (mag)	$K_s$ (mag)	Reference NIR
AA Gem	$9.735 \pm 0.008$	...	$7.647 \pm 0.011$	$7.206 \pm 0.010$	$7.069 \pm 0.020$	M11
AC Mon	$10.100 \pm 0.016$	$8.708 \pm 0.012$	$7.590 \pm 0.013$	$7.072 \pm 0.011$	$6.867 \pm 0.012$	M11
AD Gem	...	...	$8.453 \pm 0.006$	$8.154 \pm 0.006$	$8.043 \pm 0.007$	B97, M11
AD Pup	$9.898 \pm 0.006$	$8.716 \pm 0.006$	...	...	...	...
AE Vel	$10.257 \pm 0.009$	$8.730 \pm 0.007$	...	...	...	...
AG Cru	$8.228 \pm 0.006$	$7.346 \pm 0.006$	...	...	...	...
AP Pup	$7.385 \pm 0.006$	$6.463 \pm 0.006$	...	...	...	...
AP Sgr	$6.967 \pm 0.006$	$6.053 \pm 0.006$	...	...	...	...
AQ Car	$8.892 \pm 0.023$	$7.895 \pm 0.020$	...	...	...	...
AQ Pup	$8.690 \pm 0.006$	$7.153 \pm 0.006$	$6.000 \pm 0.006$	$5.484 \pm 0.008$	$5.256 \pm 0.009$	L92
AS Per	...	...	$6.941 \pm 0.014$	$6.482 \pm 0.007$	$6.279 \pm 0.017$	M11
AT Pup	$7.985 \pm 0.006$	$7.080 \pm 0.006$	...	...	...	...
AV Sgr	$11.331 \pm 0.021$	$8.851 \pm 0.013$	...	...	...	...
AW Per	$7.473 \pm 0.140$	...	$5.222 \pm 0.010$	$4.836 \pm 0.009$	$4.676 \pm 0.010$	M11
AX Cir	$5.887 \pm 0.006$	$4.987 \pm 0.006$	...	...	...	...
AY Cas	$11.543 \pm 0.024$	...	...	...	...	...
AY Cen	$8.818 \pm 0.006$	$7.701 \pm 0.006$	...	...	...	...
AY Sgr	$10.559 \pm 0.012$	$8.729 \pm 0.009$	$7.140 \pm 0.008$	$6.534 \pm 0.010$	$6.282 \pm 0.016$	M11
BB Her	$10.093 \pm 0.007$	$8.941 \pm 0.010$	...	...	...	...
BB Sgr	$6.952 \pm 0.006$	$5.848 \pm 0.006$	$5.025 \pm 0.006$	$4.643 \pm 0.007$	$4.496 \pm 0.008$	L92, W84
BE Mon	$10.574 \pm 0.008$	$9.243 \pm 0.008$	$8.265 \pm 0.014$	$7.857 \pm 0.011$	$7.701 \pm 0.024$	M11
BF Oph	$7.342 \pm 0.006$	$6.367 \pm 0.006$	$5.626 \pm 0.008$	$5.298 \pm 0.007$	$5.147 \pm 0.009$	L92, W84
BG Lac	$8.897 \pm 0.006$	$7.811 \pm 0.014$	$7.023 \pm 0.006$	$6.655 \pm 0.006$	$6.500 \pm 0.006$	B97, M11
BG Vel	$7.653 \pm 0.006$	$6.342 \pm 0.006$	...	...	...	...
BK Aur	$9.445 \pm 0.015$	...	$7.300 \pm 0.015$	$6.890 \pm 0.019$	$6.735 \pm 0.021$	M11
BM Per	$10.428 \pm 0.028$	...	$6.680 \pm 0.015$	$6.007 \pm 0.012$	$5.724 \pm 0.018$	M11
BM Pup	$10.846 \pm 0.006$	$9.414 \pm 0.006$	...	...	...	...
BN Pup	$9.907 \pm 0.016$	$8.585 \pm 0.020$	$7.534 \pm 0.008$	$7.079 \pm 0.009$	$6.880 \pm 0.008$	L92
BP Cas	$10.951 \pm 0.021$	...	...	...	...	...
BZ Cyg	$10.221 \pm 0.006$	$8.327 \pm 0.018$	$6.774 \pm 0.014$	$6.153 \pm 0.010$	$5.879 \pm 0.014$	M11
$\beta$ Dor	$3.737 \pm 0.006$	$2.939 \pm 0.006$	$2.365 \pm 0.006$	$2.038 \pm 0.006$	$1.925 \pm 0.006$	F08, L92
CD Cas	$10.782 \pm 0.009$	...	$7.644 \pm 0.006$	$7.093 \pm 0.012$	$6.878 \pm 0.012$	M11
CD Cyg	$8.963 \pm 0.009$	$7.498 \pm 0.028$	$6.363 \pm 0.015$	$5.853 \pm 0.012$	$5.668 \pm 0.011$	W84, M11
CE Pup	$11.832 \pm 0.010$	$9.968 \pm 0.007$	...	...	...	...
CF Cas	$11.138 \pm 0.006$	$9.756 \pm 0.012$	$8.606 \pm 0.010$	$8.136 \pm 0.012$	$7.923 \pm 0.012$	W84, M11
CG Cas	$11.378 \pm 0.010$	...	...	...	...	...
CK Sct	...	...	$7.393 \pm 0.006$	$6.822 \pm 0.010$	$6.610 \pm 0.014$	M11
CN Car	$10.684 \pm 0.008$	$9.355 \pm 0.009$	...	...	...	...
CP Cep	$10.588 \pm 0.012$	$8.766 \pm 0.024$	$7.348 \pm 0.010$	$6.726 \pm 0.012$	$6.492 \pm 0.012$	M11
CR Cep	$9.646 \pm 0.008$	$7.979 \pm 0.020$	$6.654 \pm 0.006$	$6.101 \pm 0.007$	$5.890 \pm 0.007$	M11
CR Ser	$10.857 \pm 0.009$	$8.899 \pm 0.026$	$7.353 \pm 0.007$	$6.763 \pm 0.007$	$6.503 \pm 0.012$	M11
CS Mon	$11.005 \pm 0.006$	$9.651 \pm 0.006$	...	...	...	...
CS Ori	$11.399 \pm 0.037$	$10.261 \pm 0.019$	$9.341 \pm 0.011$	$8.960 \pm 0.009$	$8.810 \pm 0.017$	M11
CS Vel	$11.702 \pm 0.007$	$10.069 \pm 0.007$	$8.735 \pm 0.010$	$8.228 \pm 0.014$	$7.973 \pm 0.011$	L92, W84
CV Mon	$10.291 \pm 0.006$	$8.645 \pm 0.006$	$7.323 \pm 0.011$	$6.790 \pm 0.007$	$6.545 \pm 0.007$	L92, W84, M11
CY Car	$9.755 \pm 0.007$	$8.712 \pm 0.006$	...	...	...	...
CY Cas	$11.643 \pm 0.020$	...	$7.876 \pm 0.028$	$7.180 \pm 0.018$	$6.915 \pm 0.023$	M11



**Table 4**  
(Continued)

Star	<i>V</i> (mag)	<i>I</i> (mag)	<i>J</i> (mag)	<i>H</i> (mag)	<i>K<sub>S</sub></i> (mag)	Reference NIR
CZ Cas	11.752 ± 0.009	10.059 ± 0.021	...	...	...	...
DD Cas	9.888 ± 0.007	8.561 ± 0.025	7.537 ± 0.008	7.073 ± 0.011	6.909 ± 0.014	M11
DF Cas	10.879 ± 0.006	...	...	...	...	...
DL Cas	8.971 ± 0.006	...	6.560 ± 0.014	6.106 ± 0.011	5.912 ± 0.015	W84, M11
DW Per	11.577 ± 0.008	...	...	...	...	...
δ Cep	3.930 ± 0.010	...	2.676 ± 0.006	2.393 ± 0.006	2.291 ± 0.006	F08, B97
EK Mon	11.062 ± 0.006	9.617 ± 0.006	...	...	...	...
ER Car	6.828 ± 0.006	5.961 ± 0.006	...	...	...	...
EX Vel	11.573 ± 0.007	9.775 ± 0.006	...	...	...	...
EY Car	10.359 ± 0.010	9.260 ± 0.008	...	...	...	...
Eta Aql	3.878 ± 0.006	3.024 ± 0.006	2.386 ± 0.006	2.067 ± 0.006	1.951 ± 0.006	B97, W84
FI Car	11.626 ± 0.010	9.855 ± 0.009	...	...	...	...
FM Aql	8.278 ± 0.006	6.780 ± 0.010	5.681 ± 0.006	5.217 ± 0.006	5.026 ± 0.006	B97, W84, M11
FN Aql	8.383 ± 0.006	6.992 ± 0.006	5.965 ± 0.006	5.495 ± 0.006	5.315 ± 0.006	B97, W84, M11
FN Vel	10.303 ± 0.006	8.830 ± 0.007	...	...	...	...
GH Cyg	9.904 ± 0.006	8.432 ± 0.011	7.262 ± 0.011	6.804 ± 0.006	6.598 ± 0.016	M11
GI Cyg	11.745 ± 0.012	...	...	...	...	...
GQ Ori	8.965 ± 0.011	7.885 ± 0.007	...	...	...	...
GU Nor	10.354 ± 0.006	8.799 ± 0.007	...	...	...	...
GX Car	9.344 ± 0.009	8.137 ± 0.006	...	...	...	...
GY Sge	10.163 ± 0.006	...	5.604 ± 0.008	4.887 ± 0.007	4.546 ± 0.006	L92, W84
HW Car	9.136 ± 0.006	8.028 ± 0.006	...	...	...	...
IQ Nor	9.665 ± 0.019	8.115 ± 0.020	...	...	...	...
IT Car	8.102 ± 0.006	7.070 ± 0.006	...	...	...	...
KK Cen	11.452 ± 0.036	9.934 ± 0.026	...	...	...	...
KN Cen	9.865 ± 0.006	7.994 ± 0.006	6.399 ± 0.007	5.747 ± 0.008	5.440 ± 0.006	L92
KQ Sco	9.835 ± 0.006	7.659 ± 0.006	5.909 ± 0.012	5.215 ± 0.010	4.901 ± 0.013	L92, W84
ℓCar	3.723 ± 0.006	2.554 ± 0.006	1.679 ± 0.006	1.218 ± 0.006	1.054 ± 0.006	L92
LS Pup	10.462 ± 0.007	9.073 ± 0.008	7.999 ± 0.006	7.521 ± 0.007	7.312 ± 0.006	L92
MW Cyg	9.483 ± 0.006	...	6.700 ± 0.006	6.209 ± 0.009	5.998 ± 0.014	M11
MZ Cen	11.553 ± 0.007	9.786 ± 0.010	...	...	...	...
QY Cen	11.784 ± 0.006	9.350 ± 0.007	...	...	...	...
R Cru	6.771 ± 0.006	5.901 ± 0.006	...	...	...	...
R Mus	6.313 ± 0.006	5.497 ± 0.006	...	...	...	...
R TrA	6.656 ± 0.006	5.843 ± 0.006	...	...	...	...
RR Lac	8.846 ± 0.006	7.814 ± 0.015	6.977 ± 0.008	6.628 ± 0.010	6.488 ± 0.011	M11
RS Nor	10.019 ± 0.018	8.541 ± 0.013	...	...	...	...
RS Ori	8.410 ± 0.011	7.282 ± 0.012	6.408 ± 0.016	6.027 ± 0.017	5.880 ± 0.019	M11
RS Pup	7.008 ± 0.006	5.478 ± 0.006	4.341 ± 0.009	3.830 ± 0.007	3.605 ± 0.008	L92, W84
RT Aur	5.469 ± 0.076	4.811 ± 0.043	4.236 ± 0.008	3.998 ± 0.007	3.906 ± 0.006	B97, M11
RU Sct	...	...	5.909 ± 0.008	5.298 ± 0.007	5.036 ± 0.009	L92, W84, M11
RV Sco	7.046 ± 0.006	5.907 ± 0.006	...	...	...	...
RW Cam	8.657 ± 0.010	...	5.828 ± 0.012	5.291 ± 0.013	5.093 ± 0.010	M11
RW Cas	9.248 ± 0.019	7.871 ± 0.020	6.841 ± 0.024	6.372 ± 0.011	6.194 ± 0.026	M11
RX Aur	7.670 ± 0.007	...	5.737 ± 0.008	5.363 ± 0.011	5.233 ± 0.017	M11
RX Cam	7.670 ± 0.012	...	5.178 ± 0.023	4.732 ± 0.020	4.561 ± 0.012	M11
RY CMa	8.109 ± 0.006	7.133 ± 0.006	...	...	...	...
RY Sco	7.999 ± 0.006	6.253 ± 0.006	4.899 ± 0.006	4.368 ± 0.006	4.102 ± 0.007	L92, W84
RY Vel	8.376 ± 0.006	6.827 ± 0.006	5.604 ± 0.008	5.124 ± 0.007	4.886 ± 0.006	L92, W84
RZ CMa	9.702 ± 0.007	8.504 ± 0.007	...	...	...	...
RZ Gem	10.048 ± 0.249	...	7.612 ± 0.010	7.169 ± 0.009	6.970 ± 0.015	M11
RZ Vel	7.089 ± 0.006	5.862 ± 0.006	4.889 ± 0.012	4.463 ± 0.007	4.267 ± 0.006	L92
S Cru	6.601 ± 0.006	5.732 ± 0.006	...	...	...	...
S Mus	6.133 ± 0.006	5.199 ± 0.006	4.473 ± 0.006	4.135 ± 0.006	3.983 ± 0.008	L92, W84
S Nor	6.427 ± 0.006	5.428 ± 0.006	4.652 ± 0.006	4.286 ± 0.006	4.131 ± 0.008	L92, W84
S Sge	5.612 ± 0.006	4.772 ± 0.010	4.155 ± 0.006	3.847 ± 0.006	3.732 ± 0.006	W84, B97
S TrA	6.391 ± 0.006	5.592 ± 0.006	...	...	...	...
SS CMa	...	8.480 ± 0.010	...	...	...	...
SS Sct	...	...	6.299 ± 0.008	5.938 ± 0.006	5.807 ± 0.008	W84, M11
ST Tau	8.243 ± 0.014	7.171 ± 0.016	...	...	...	...
ST Vel	9.699 ± 0.006	8.286 ± 0.006	...	...	...	...
SU Cyg	6.855 ± 0.007	6.198 ± 0.013	5.638 ± 0.007	5.397 ± 0.007	5.295 ± 0.008	W84, M11
SV Mon	8.266 ± 0.008	7.139 ± 0.006	6.262 ± 0.015	5.835 ± 0.010	5.691 ± 0.017	M11

**Table 4**  
(Continued)

Star	<i>V</i> (mag)	<i>I</i> (mag)	<i>J</i> (mag)	<i>H</i> (mag)	<i>K<sub>S</sub></i> (mag)	Reference NIR
SV Per	8.977 ± 0.011	...	6.802 ± 0.021	6.360 ± 0.016	6.198 ± 0.018	M11
SV Vel	8.583 ± 0.006	7.329 ± 0.006	...	...	...	...
SV Vul	7.216 ± 0.006	5.697 ± 0.009	4.571 ± 0.006	4.077 ± 0.006	3.887 ± 0.006	W84, L92, B97, M11
SW Cas	9.713 ± 0.007	8.438 ± 0.020	7.412 ± 0.009	6.987 ± 0.013	6.820 ± 0.015	M11
SW Vel	8.137 ± 0.014	6.850 ± 0.008	5.852 ± 0.018	5.407 ± 0.012	5.203 ± 0.011	L92
SX Car	9.082 ± 0.006	8.039 ± 0.006	...	...	...	...
SX Per	11.223 ± 0.104	...	8.769 ± 0.010	8.352 ± 0.007	8.187 ± 0.013	M11
SX Vel	8.278 ± 0.006	7.262 ± 0.006	6.474 ± 0.006	6.127 ± 0.006	5.965 ± 0.006	L92
SY Aur	9.069 ± 0.009	...	6.923 ± 0.009	6.530 ± 0.012	6.367 ± 0.014	M11
SY Nor	9.520 ± 0.023	7.949 ± 0.030	...	...	...	...
SZ Aql	8.636 ± 0.011	7.082 ± 0.015	5.865 ± 0.008	5.351 ± 0.006	5.138 ± 0.006	B97, W84, L92, M11
SZ Cas	9.843 ± 0.006	8.110 ± 0.008	...	...	...	...
SZ Cyg	9.435 ± 0.011	7.798 ± 0.026	6.530 ± 0.009	5.960 ± 0.007	5.732 ± 0.014	M11
T Ant	9.331 ± 0.006	8.523 ± 0.006	...	...	...	...
T Cru	6.570 ± 0.006	5.608 ± 0.006	...	...	...	...
T Mon	6.138 ± 0.006	4.987 ± 0.006	4.092 ± 0.009	3.648 ± 0.009	3.487 ± 0.008	W84, L92, M11
T Vel	8.029 ± 0.006	6.964 ± 0.006	6.143 ± 0.006	5.775 ± 0.006	5.605 ± 0.006	L92
T Vul	5.750 ± 0.006	5.077 ± 0.015	4.532 ± 0.006	4.272 ± 0.006	4.174 ± 0.006	W84, B97
TT Aql	7.141 ± 0.006	5.732 ± 0.009	4.671 ± 0.009	4.194 ± 0.007	4.017 ± 0.006	W84, M11, B97
TV CMa	10.587 ± 0.011	9.173 ± 0.011	8.035 ± 0.008	7.588 ± 0.011	7.386 ± 0.014	M11
TV Cam	11.729 ± 0.018	...	...	...	...	...
TW CMa	9.573 ± 0.007	8.458 ± 0.007	7.577 ± 0.010	7.183 ± 0.009	7.029 ± 0.017	M11
TW Nor	11.670 ± 0.007	9.306 ± 0.010	7.406 ± 0.022	6.705 ± 0.013	6.358 ± 0.029	L92, W84
TX Cen	10.527 ± 0.006	8.618 ± 0.006	...	...	...	...
TX Cyg	9.490 ± 0.012	7.225 ± 0.030	5.342 ± 0.020	4.633 ± 0.018	4.323 ± 0.018	M11
TX Mon	10.960 ± 0.010	9.634 ± 0.008	8.581 ± 0.013	8.121 ± 0.013	7.943 ± 0.017	M11
TY Sct	10.821 ± 0.013	8.811 ± 0.016	7.247 ± 0.011	6.637 ± 0.009	6.386 ± 0.021	M11
TZ Mon	10.793 ± 0.008	9.472 ± 0.006	8.458 ± 0.012	8.009 ± 0.014	7.815 ± 0.016	M11
TZ Mus	11.690 ± 0.006	10.144 ± 0.008	...	...	...	...
U Aql	6.432 ± 0.006	5.271 ± 0.010	4.389 ± 0.012	3.999 ± 0.009	3.844 ± 0.010	W84, M11
U Car	6.284 ± 0.006	5.052 ± 0.006	4.104 ± 0.007	3.674 ± 0.006	3.483 ± 0.006	L92, W84
U Nor	...	...	5.825 ± 0.006	5.236 ± 0.006	4.944 ± 0.006	L92
U Sgr	6.697 ± 0.006	5.436 ± 0.006	4.512 ± 0.006	4.100 ± 0.006	3.933 ± 0.007	W84, L92, M11
U Vul	7.122 ± 0.006	5.602 ± 0.011	4.528 ± 0.009	4.093 ± 0.007	3.912 ± 0.006	B97, M11
UU Mus	...	...	7.439 ± 0.007	6.994 ± 0.006	6.788 ± 0.006	L92
UW Car	9.424 ± 0.008	8.218 ± 0.013	...	...	...	...
UX Car	8.295 ± 0.006	7.554 ± 0.006	...	...	...	...
UX Per	11.650 ± 0.018	...	...	...	...	...
UY Car	8.948 ± 0.006	8.007 ± 0.010	...	...	...	...
UY Per	11.319 ± 0.013	9.493 ± 0.016	...	...	...	...
UZ Car	9.327 ± 0.006	8.365 ± 0.006	...	...	...	...
UZ Cas	11.379 ± 0.007	...	...	...	...	...
UZ Sct	11.289 ± 0.022	9.148 ± 0.035	7.418 ± 0.010	6.741 ± 0.010	6.485 ± 0.016	M11
V Car	7.368 ± 0.006	6.433 ± 0.006	5.728 ± 0.006	5.396 ± 0.006	5.249 ± 0.006	L92
V Cen	6.830 ± 0.006	5.794 ± 0.006	4.995 ± 0.006	4.638 ± 0.006	4.479 ± 0.009	L92, W84
V Lac	8.932 ± 0.007	...	...	...	...	...
V Vel	7.586 ± 0.006	6.691 ± 0.006	...	...	...	...
V0339 Cen	8.714 ± 0.013	7.384 ± 0.010	...	...	...	...
V0340 Ara	10.228 ± 0.014	8.580 ± 0.007	...	...	...	...
V0340 Nor	8.403 ± 0.008	7.167 ± 0.008	...	...	...	...
V0350 Sgr	7.481 ± 0.006	6.435 ± 0.006	5.627 ± 0.011	5.256 ± 0.011	5.130 ± 0.008	W84
V0378 Cen	8.479 ± 0.006	7.260 ± 0.006	...	...	...	...
V0381 Cen	7.675 ± 0.006	6.791 ± 0.006	...	...	...	...
V0386 Cyg	9.624 ± 0.007	...	6.375 ± 0.007	5.809 ± 0.007	5.540 ± 0.015	M11
V0395 Cas	10.748 ± 0.019	9.447 ± 0.035	...	...	...	...
V0402 Cyg	9.864 ± 0.006	...	7.809 ± 0.006	7.416 ± 0.006	7.263 ± 0.015	M11
V0459 Cyg	10.576 ± 0.033	8.881 ± 0.019	7.613 ± 0.011	7.075 ± 0.010	6.859 ± 0.016	M11
V0470 Sco	11.005 ± 0.008	8.246 ± 0.007	...	...	...	...
V0493 Aql	11.046 ± 0.006	...	...	...	...	...
V0496 Aql	7.769 ± 0.006	6.489 ± 0.008	...	...	...	...
V0496 Cen	9.945 ± 0.006	8.539 ± 0.006	...	...	...	...
V0508 Mon	10.502 ± 0.006	9.461 ± 0.006	...	...	...	...
V0520 Cyg	10.852 ± 0.006	9.306 ± 0.029	...	...	...	...

**Table 4**  
(Continued)

Star	<i>V</i> (mag)	<i>I</i> (mag)	<i>J</i> (mag)	<i>H</i> (mag)	<i>K<sub>S</sub></i> (mag)	Reference NIR
V0538 Cyg	10.449 ± 0.009	8.971 ± 0.049	7.803 ± 0.007	7.311 ± 0.006	7.119 ± 0.008	M11
V0600 Aql	10.034 ± 0.006	8.281 ± 0.011	...	...	...	...
V0609 Cyg	11.026 ± 0.017	8.683 ± 0.015	6.832 ± 0.013	6.128 ± 0.010	5.800 ± 0.017	M11
V0636 Cas	7.183 ± 0.006	...	...	...	...	...
V0636 Sco	6.654 ± 0.006	5.649 ± 0.006	...	...	...	...
V0733 Aql	9.976 ± 0.006	9.040 ± 0.012	...	...	...	...
V0737 Cen	6.724 ± 0.006	5.701 ± 0.006	...	...	...	...
V1154 Cyg	9.186 ± 0.006	8.180 ± 0.018	...	...	...	...
V1162 Aql	7.806 ± 0.006	6.850 ± 0.007	6.143 ± 0.008	5.814 ± 0.017	5.682 ± 0.020	M11
VV Cas	10.768 ± 0.016	9.432 ± 0.018	8.328 ± 0.008	7.885 ± 0.006	7.719 ± 0.008	M11
VW Cen	10.263 ± 0.007	8.783 ± 0.006	7.555 ± 0.007	7.015 ± 0.006	6.775 ± 0.006	L92
VW Cru	9.597 ± 0.009	7.977 ± 0.006	...	...	...	...
VW Pup	11.393 ± 0.007	10.091 ± 0.006	...	...	...	...
VY Car	7.460 ± 0.006	6.283 ± 0.006	5.375 ± 0.015	4.943 ± 0.010	4.760 ± 0.010	L92, W84
VY Cyg	9.594 ± 0.006	8.127 ± 0.019	7.009 ± 0.006	6.552 ± 0.009	6.355 ± 0.010	M11
VY Per	11.221 ± 0.014	9.297 ± 0.026	...	...	...	...
VY Sgr	11.469 ± 0.012	9.129 ± 0.013	...	...	...	...
VZ Cyg	8.970 ± 0.008	7.966 ± 0.015	7.201 ± 0.007	6.864 ± 0.006	6.721 ± 0.006	B97, W84, M11
VZ Pup	9.657 ± 0.009	8.302 ± 0.006	7.277 ± 0.007	6.830 ± 0.006	6.626 ± 0.006	L92
W Gem	7.012 ± 0.049	...	5.129 ± 0.033	4.771 ± 0.026	4.656 ± 0.021	M11
W Sgr	4.664 ± 0.006	3.850 ± 0.006	...	...	...	...
WW Car	9.750 ± 0.010	8.644 ± 0.007	...	...	...	...
WW Pup	10.599 ± 0.010	9.525 ± 0.007	...	...	...	...
WX Pup	9.070 ± 0.007	7.968 ± 0.006	...	...	...	...
WY Pup	10.599 ± 0.013	9.662 ± 0.008	...	...	...	...
WZ Pup	10.320 ± 0.006	9.424 ± 0.006	...	...	...	...
WZ Sgr	8.046 ± 0.011	6.544 ± 0.010	5.282 ± 0.008	4.761 ± 0.006	4.538 ± 0.008	L92, W84, M11
X Cru	8.404 ± 0.006	...	...	...	...	...
X Cyg	6.385 ± 0.009	5.236 ± 0.028	4.383 ± 0.008	3.960 ± 0.006	3.799 ± 0.006	W84, B97
X Pup	8.517 ± 0.011	7.161 ± 0.006	6.077 ± 0.023	5.599 ± 0.011	5.386 ± 0.011	L92
X Sct	10.031 ± 0.017	8.613 ± 0.033	...	...	...	...
X Sgr	4.548 ± 0.006	3.652 ± 0.006	2.950 ± 0.007	2.635 ± 0.007	2.505 ± 0.010	F08, W84
X Vul	8.834 ± 0.006	7.198 ± 0.020	5.928 ± 0.010	5.433 ± 0.008	5.214 ± 0.015	M11
XX Cen	7.824 ± 0.006	6.743 ± 0.006	5.914 ± 0.008	5.541 ± 0.006	5.375 ± 0.007	L92, W84
XX Mon	11.914 ± 0.007	10.505 ± 0.009	...	...	...	...
XX Sgr	8.869 ± 0.006	7.506 ± 0.006	6.412 ± 0.033	5.964 ± 0.018	5.799 ± 0.022	W84
XX Vel	10.676 ± 0.006	9.302 ± 0.006	...	...	...	...
XZ Car	8.597 ± 0.006	7.248 ± 0.006	...	...	...	...
Y Aur	9.809 ± 0.044	...	7.660 ± 0.007	7.291 ± 0.008	7.133 ± 0.026	M11
Y Lac	9.159 ± 0.007	8.308 ± 0.026	7.626 ± 0.006	7.316 ± 0.006	7.201 ± 0.008	B97, M11
Y Oph	6.148 ± 0.006	4.533 ± 0.006	3.349 ± 0.006	2.874 ± 0.006	2.662 ± 0.008	W84, L92
Y Sct	...	...	6.472 ± 0.009	5.897 ± 0.011	5.646 ± 0.014	M11
Y Sgr	5.739 ± 0.006	4.790 ± 0.006	...	...	...	...
YZ Aur	10.346 ± 0.009	...	7.498 ± 0.015	6.905 ± 0.011	6.689 ± 0.024	M11
YZ Car	8.714 ± 0.006	7.438 ± 0.006	...	...	...	...
YZ Sgr	7.351 ± 0.006	6.226 ± 0.006	5.379 ± 0.007	5.004 ± 0.009	4.861 ± 0.010	M11, W84
Z Lac	8.417 ± 0.006	7.198 ± 0.043	6.235 ± 0.009	5.811 ± 0.006	5.653 ± 0.008	B97, M11
Z Sct	...	...	6.962 ± 0.017	6.483 ± 0.016	6.282 ± 0.017	M11
ζ Gem	3.889 ± 0.006	3.096 ± 0.006	2.538 ± 0.006	2.210 ± 0.006	2.096 ± 0.006	F08

**Note.** The magnitudes do not include the reddening correction. The uncertainties are only the random errors and do not include photometric ZP errors.

**References.** (B97): Barnes et al. (1997); (F08): Feast et al. (2008); (L92): Laney & Stobie (1992); (M11): Monson & Pierce (2011); (W84): Welch et al. (1984). All magnitudes in *V* and *I* are from Berdnikov (2008).

(This table is available in machine-readable form.)

### Appendix C

#### *Data for the Sample of LMC Cepheids*

In Table 5 we provide the period, distance, coordinates, photometry, and reddening of the Cepheids in our LMC sample. The sample is described in Section 2.2.

**Table 5**  
Sample of Large Magellanic Cloud Cepheids and Their Main Parameters

Cepheid	$P$ (days)	$\alpha$ (J2000)	$\delta$ (J2000)	$d$ (kpc)	$V$ (mag)	$I$ (mag)	$J$ (mag)	$H$ (mag)	$K_S$ (mag)	$E(B - V)$ (mag)
0107	8.739	72.214	−69.356	$50.63 \pm 0.56$	14.761	13.947	$13.332 \pm 0.018$	$13.027 \pm 0.015$	$12.941 \pm 0.014$	0.182
0174	15.863	72.719	−69.316	$50.55 \pm 0.56$	14.739	13.666	$12.876 \pm 0.022$	$12.454 \pm 0.020$	$12.312 \pm 0.019$	0.174
0328	34.460	73.599	−70.902	$50.68 \pm 0.56$	13.124	12.088	$11.460 \pm 0.031$	$11.111 \pm 0.027$	$11.001 \pm 0.024$	0.133
0467	22.718	74.301	−67.383	$50.06 \pm 0.55$	13.704	12.775	$12.113 \pm 0.033$	$11.767 \pm 0.031$	$11.668 \pm 0.029$	0.112
0473	2.634	74.331	−68.821	$50.25 \pm 0.56$	16.335	15.590	$15.093 \pm 0.082$	$14.856 \pm 0.116$	$14.641 \pm 0.114$	0.141
0478	2.764	74.355	−69.567	$50.36 \pm 0.56$	16.160	15.471	$14.961 \pm 0.057$	$14.666 \pm 0.073$	$14.624 \pm 0.076$	0.150
0480	4.035	74.364	−69.355	$50.33 \pm 0.56$	16.865	15.779	$15.107 \pm 0.049$	$14.513 \pm 0.052$	$14.515 \pm 0.080$	0.161
0482	7.466	74.370	−69.227	$50.31 \pm 0.56$	15.655	14.661	$13.977 \pm 0.081$	$13.439 \pm 0.031$	$13.315 \pm 0.030$	0.151
0487	3.109	74.422	−69.406	$50.33 \pm 0.56$	16.221	15.469	$15.002 \pm 0.124$	$14.614 \pm 0.041$	$14.488 \pm 0.090$	0.165
0488	3.647	74.422	−68.800	$50.24 \pm 0.56$	16.535	15.608	$14.921 \pm 0.037$	$14.517 \pm 0.045$	$14.451 \pm 0.066$	0.140
0494	2.727	74.441	−69.062	$50.27 \pm 0.56$	16.973	16.013	$15.441 \pm 0.087$	$14.953 \pm 0.100$	$14.658 \pm 0.091$	0.134
0498	3.630	74.455	−68.720	$50.22 \pm 0.56$	15.914	15.154	$14.617 \pm 0.071$	$14.295 \pm 0.059$	$14.286 \pm 0.061$	0.139
0514	3.504	74.554	−69.203	$50.28 \pm 0.56$	16.276	15.458	$14.879 \pm 0.063$	$14.458 \pm 0.055$	$14.381 \pm 0.068$	0.152
0518	3.249	74.577	−69.367	$50.30 \pm 0.56$	16.550	15.589	$14.988 \pm 0.044$	$14.565 \pm 0.044$	$14.543 \pm 0.046$	0.174
0529	2.856	74.637	−69.041	$50.24 \pm 0.56$	16.603	15.777	$15.168 \pm 0.087$	$14.746 \pm 0.084$	$14.698 \pm 0.087$	0.134
0539	3.455	74.672	−68.865	$50.21 \pm 0.55$	16.064	15.320	$14.758 \pm 0.056$	$14.373 \pm 0.069$	$14.299 \pm 0.054$	0.131
0540	3.750	74.673	−69.526	$50.31 \pm 0.56$	15.841	15.069	$14.574 \pm 0.061$	$14.198 \pm 0.058$	$14.188 \pm 0.056$	0.160
...	...	...	...	...	...	...	...	...	...	...

**Note.** The Cepheid names in the first column are of the form OGLE-LMC-CEP-XXXX. The uncertainties on  $V$ - and  $I$ -band mean magnitudes are 0.02 mag, and the uncertainty on  $E(B - V)$  values is 0.017 mag. The distances listed in Column (5) are corrected for their position in the LMC by the equations provided in Section 3.2. Apparent magnitudes in this table are not corrected for the reddening.

(This table is available in its entirety in machine-readable form.)

## Appendix D

### *Data for the Sample of SMC Cepheids*

In Table 6 we provide the period, distance, coordinates, photometry, and reddening of the Cepheids in our SMC sample. The sample is described in Section 2.3.

**Table 6**  
Sample of Small Magellanic Cloud Cepheids and Their Main Parameters

Cepheid	$P$ (days)	$\alpha$ (J2000)	$\delta$ (J2000)	$d$ (kpc)	$V$ (mag)	$I$ (mag)	$J$ (mag)	$K_S$ (mag)	$E(B - V)$ (mag)
0443	4.037	10.525	-73.061	$63.36 \pm 0.95$	16.443	15.671	$15.139 \pm 0.018$	$14.742 \pm 0.006$	0.096
0489	3.242	10.734	-73.160	$63.42 \pm 0.95$	16.493	15.822	$15.096 \pm 0.006$	$14.492 \pm 0.010$	0.101
0494	4.758	10.742	-73.335	$63.72 \pm 0.96$	15.884	15.025	$14.447 \pm 0.006$	$14.030 \pm 0.004$	0.103
0495	6.312	10.743	-73.092	$63.30 \pm 0.95$	16.038	15.217	$14.604 \pm 0.012$	$14.164 \pm 0.004$	0.097
0499	6.229	10.751	-73.304	$63.66 \pm 0.96$	15.986	15.258	$14.740 \pm 0.004$	$14.374 \pm 0.006$	0.108
0514	2.542	10.774	-73.082	$63.27 \pm 0.95$	16.842	16.145	$15.687 \pm 0.010$	$15.306 \pm 0.010$	0.097
0518	15.773	10.802	-73.326	$63.67 \pm 0.96$	15.184	14.173	$13.449 \pm 0.002$	$12.948 \pm 0.004$	0.108
0524	10.527	10.828	-73.339	$63.68 \pm 0.96$	15.383	14.536	$13.934 \pm 0.008$	$13.492 \pm 0.006$	0.105
0533	3.909	10.859	-73.254	$63.52 \pm 0.95$	16.122	15.390	$14.895 \pm 0.006$	$14.489 \pm 0.010$	0.105
0551	3.262	10.905	-73.129	$63.28 \pm 0.95$	16.473	15.807	$15.302 \pm 0.006$	$14.954 \pm 0.016$	0.101
0570	10.883	10.947	-73.241	$63.45 \pm 0.95$	15.213	14.354	$13.738 \pm 0.010$	$13.294 \pm 0.004$	0.112
0571	4.897	10.948	-73.335	$63.62 \pm 0.95$	15.872	15.178	$14.662 \pm 0.006$	$14.297 \pm 0.008$	0.104
0576	14.426	10.963	-73.333	$63.61 \pm 0.95$	15.110	14.122	$13.470 \pm 0.016$	$12.923 \pm 0.018$	0.104
0584	4.654	10.989	-73.192	$63.35 \pm 0.95$	16.058	15.296	$14.777 \pm 0.006$	$14.418 \pm 0.006$	0.111
0596	3.072	11.013	-73.277	$63.48 \pm 0.95$	17.170	16.282	$15.673 \pm 0.006$	$15.184 \pm 0.012$	0.120
...	...	...	...	...	...	...	...	...	...

**Note.** The Cepheid names in the first column are of the form OGLE-SMC-CEP-XXXX. The uncertainties on  $V$ - and  $I$ -band mean magnitudes are 0.02 mag, and the uncertainty on  $E(B - V)$  values is 0.015 mag. The distances listed in Column (5) are corrected for their position in the SMC by the equations provided in Section 3.3. Apparent magnitudes in this table are not corrected for the reddening.

(This table is available in its entirety in machine-readable form.)

## Appendix E

### Results of the PLZ Fit in Different Conditions

In Table 7 we provide the coefficients of the PLZ relation fitted under different conditions. The various tests are described in Sections 5.1 and 5.2.

**Table 7**










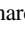
Results of the PLZ Linear Fit of the Form  $M = \alpha(\log P - 0.7) + \delta + \gamma [\text{Fe}/\text{H}]$  for Milky Way, Large Magellanic Cloud, and Small Magellanic Cloud Cepheids Fitted Together for Different Conditions

Band	$\delta$	$\gamma$	$N$	Comments
<i>V</i>	$-3.252 \pm 0.020$	$-0.048 \pm 0.051$	1908	Initial conditions <sup>a</sup>
<i>I</i>	$-3.948 \pm 0.020$	$-0.138 \pm 0.051$	1907	Initial conditions
<i>W<sub>VI</sub></i>	$-5.005 \pm 0.022$	$-0.251 \pm 0.057$	1864	Initial conditions
<i>J</i>	$-4.463 \pm 0.022$	$-0.208 \pm 0.051$	1196	Initial conditions
<i>H</i>	$-4.748 \pm 0.020$	$-0.152 \pm 0.092$	905	Initial conditions
<i>K<sub>S</sub></i>	$-4.826 \pm 0.019$	$-0.221 \pm 0.050$	1199	Initial conditions
<i>W<sub>JK</sub></i>	$-5.075 \pm 0.022$	$-0.214 \pm 0.057$	1198	Initial conditions
<i>V</i>	$-3.274 \pm 0.020$	$-0.084 \pm 0.051$	1908	Gaia EDR3 parallax ZP = $-17 \mu\text{s}$
<i>I</i>	$-3.966 \pm 0.020$	$-0.165 \pm 0.050$	1907	Gaia EDR3 parallax ZP = $-17 \mu\text{s}$
<i>W<sub>VI</sub></i>	$-5.020 \pm 0.022$	$-0.275 \pm 0.058$	1864	Gaia EDR3 parallax ZP = $-17 \mu\text{s}$
<i>J</i>	$-4.495 \pm 0.022$	$-0.258 \pm 0.052$	1196	Gaia EDR3 parallax ZP = $-17 \mu\text{s}$
<i>H</i>	$-4.778 \pm 0.020$	$-0.241 \pm 0.099$	905	Gaia EDR3 parallax ZP = $-17 \mu\text{s}$
<i>K<sub>S</sub></i>	$-4.857 \pm 0.019$	$-0.271 \pm 0.051$	1199	Gaia EDR3 parallax ZP = $-17 \mu\text{s}$
<i>W<sub>JK</sub></i>	$-5.106 \pm 0.022$	$-0.263 \pm 0.058$	1198	Gaia EDR3 parallax ZP = $-17 \mu\text{s}$
<i>V</i>	$-3.252 \pm 0.020$	$-0.036 \pm 0.052$	1952	$R = 0.7^\circ$ around SMC center
<i>I</i>	$-3.948 \pm 0.020$	$-0.130 \pm 0.052$	1951	$R = 0.7^\circ$ around SMC center
<i>W<sub>VI</sub></i>	$-5.005 \pm 0.022$	$-0.252 \pm 0.058$	1908	$R = 0.7^\circ$ around SMC center
<i>J</i>	$-4.464 \pm 0.022$	$-0.206 \pm 0.052$	1241	$R = 0.7^\circ$ around SMC center
<i>K<sub>S</sub></i>	$-4.826 \pm 0.019$	$-0.218 \pm 0.051$	1244	$R = 0.7^\circ$ around SMC center
<i>W<sub>JK</sub></i>	$-5.075 \pm 0.022$	$-0.208 \pm 0.058$	1242	$R = 0.7^\circ$ around SMC center
<i>V</i>	$-3.250 \pm 0.020$	$-0.077 \pm 0.051$	1845	$R = 0.5^\circ$ around SMC center
<i>I</i>	$-3.947 \pm 0.020$	$-0.160 \pm 0.053$	1842	$R = 0.5^\circ$ around SMC center
<i>W<sub>VI</sub></i>	$-5.005 \pm 0.022$	$-0.251 \pm 0.059$	1800	$R = 0.5^\circ$ around SMC center
<i>J</i>	$-4.462 \pm 0.022$	$-0.225 \pm 0.054$	1132	$R = 0.5^\circ$ around SMC center
<i>K<sub>S</sub></i>	$-4.825 \pm 0.019$	$-0.234 \pm 0.050$	1132	$R = 0.5^\circ$ around SMC center
<i>W<sub>JK</sub></i>	$-5.075 \pm 0.022$	$-0.222 \pm 0.057$	1132	$R = 0.5^\circ$ around SMC center

**Note.** The slope values are the same as in Table 2.

<sup>a</sup> Initial conditions correspond to Gaia EDR3 parallaxes corrected for individual ZP and SMC Cepheids limited to a radius of  $0.6^\circ$  around the SMC center.

## ORCID iDs

Louise Breuval  <https://orcid.org/0000-0003-3889-7709>  
 Pierre Kervella  <https://orcid.org/0000-0003-0626-1749>  
 Piotr Wielgórski  <https://orcid.org/0000-0002-1662-5756>  
 Wolfgang Gieren  <https://orcid.org/0000-0003-1405-9954>  
 Dariusz Graczyk  <https://orcid.org/0000-0002-7355-9775>  
 Boris Trahin  <https://orcid.org/0000-0001-5875-5340>  
 Grzegorz Pietrzyński  <https://orcid.org/0000-0002-9443-4138>  
 Frédéric Arenou  <https://orcid.org/0000-0003-2837-3899>  
 Behnam Javanmardi  <https://orcid.org/0000-0002-9317-6114>  
 Bartłomiej Zgierski  <https://orcid.org/0000-0003-1515-6107>

## References

- Acharova, I. A., Mishurov, Y. N., & Kovtyukh, V. V. 2012, *MNRAS*, **420**, 1590
- Arenou, F., & Luri, X. 1999, in ASP Conf. Ser. 167, Harmonizing Cosmic Distance Scales in a Post-HIPPARCOS Era, ed. D. Egret & A. Heck (San Francisco, CA: ASP), 13
- Astropy Collaboration, Price-Whelan, A. M., Sipőcz, B. M., et al. 2018, *AJ*, **156**, 123
- Barnes, T. G. I., Fernley, J. A., Frueh, M. L., et al. 1997, *PASP*, **109**, 645
- Berdnikov, L. N. 2008, *yCat*, **2285**, 0
- Bono, G., Caputo, F., Fiorentino, G., Marconi, M., & Musella, I. 2008, *ApJ*, **684**, 102
- Breuval, L., Kervella, P., Anderson, R. I., et al. 2020, *A&A*, **643**, A115
- Caputo, F., Marconi, M., Musella, I., & Santolamazza, P. 2000, *A&A*, **359**, 1059
- Cardelli, J. A., Clayton, G. C., & Mathis, J. S. 1989, *ApJ*, **345**, 245
- Chown, A. H., Scowcroft, V., & Wuyts, S. 2021, *MNRAS*, **500**, 817
- Cutri, R. M., Skrutskie, M. F., van Dyk, S., et al. 2003, The IRSA 2MASS All-Sky Point Source Catalog, NASA/IPAC Infrared Science Archive, <http://irsa.ipac.caltech.edu/applications/Gator/>
- EROS Collaboration, Bauer, F., Afonso, C., et al. 1999, *A&A*, **348**, 175
- Feast, M. W., & Catchpole, R. M. 1997, *MNRAS*, **286**, L1
- Feast, M. W., Laney, C. D., Kinman, T. D., van Leeuwen, F., & Whitelock, P. A. 2008, *MNRAS*, **386**, 2115
- Fernie, J. D., Evans, N. R., Beattie, B., & Seager, S. 1995, *IBVS*, **4148**, 1
- Fiorentino, G., Musella, I., & Marconi, M. 2013, *MNRAS*, **434**, 2866
- Fouqué, P., & Gieren, W. P. 1997, *A&A*, **320**, 799
- Freedman, W. L., & Madore, B. F. 1990, *ApJ*, **365**, 186
- Gaia Collaboration 2020, *yCat*, **1350**, 0
- Genovali, K., Lemasle, B., Bono, G., et al. 2013, *A&A*, **554**, A132
- Genovali, K., Lemasle, B., Bono, G., et al. 2014, *A&A*, **566**, A37
- Genovali, K., Lemasle, B., da Silva, R., et al. 2015, *A&A*, **580**, A17



- Gieren, W., Storm, J., Konorski, P., et al. 2018, [A&A](#), **620**, [A99](#)
- Górski, M., Zgierski, B., Pietrzyński, G., et al. 2020, [ApJ](#), **889**, [179](#)
- Graczyk, D., Pietrzyński, G., Thompson, I. B., et al. 2020, [ApJ](#), **904**, [13](#)
- Groenewegen, M. A. T. 2018, [A&A](#), **619**, [A8](#)
- Inno, L., Bono, G., Matsunaga, N., et al. 2016, [ApJ](#), **832**, [176](#)
- Jacyszyn-Dobrzeńicka, A. M., Skowron, D. M., Mróz, P., et al. 2016, [AcA](#), **66**, [149](#)
- Javanmardi, B., Mérand, A., Kervella, P., et al. 2021, [ApJ](#), **911**, [12](#)
- Kervella, P., Arenou, F., Mignard, F., & Thévenin, F. 2019, [A&A](#), **623**, [A72](#)
- Kervella, P., Trahin, B., Bond, H. E., et al. 2017, [A&A](#), **600**, [A127](#)
- Laney, C. D., & Stobie, R. S. 1992, [A&AS](#), **93**, [93](#)
- Leavitt, H. S., & Pickering, E. C. 1912, [HarCi](#), **173**, [1](#)
- Lemasle, B., François, P., Bono, G., et al. 2007, [A&A](#), **467**, [283](#)
- Lindgren, L., Bastian, U., Biermann, M., et al. 2021a, [A&A](#), **649**, [A4](#)
- Lindgren, L., Klioner, S. A., Hernández, J., et al. 2021b, [A&A](#), **649**, [A2](#)
- Luck, R. E. 2018, [AJ](#), **156**, [171](#)
- Luck, R. E., Andrievsky, S. M., Kovtyukh, V. V., Gieren, W., & Graczyk, D. 2011, [AJ](#), **142**, [51](#)
- Luck, R. E., & Lambert, D. L. 2011, [AJ](#), **142**, [136](#)
- Macri, L. M., Ngeow, C.-C., Kanbur, S. M., Mahzooni, S., & Smitka, M. T. 2015, [AJ](#), **149**, [117](#)
- Macri, L. M., Stanek, K. Z., Bersier, D., Greenhill, L. J., & Reid, M. J. 2006, [ApJ](#), **652**, [1133](#)
- Madore, B. F. 1982, [ApJ](#), **253**, [575](#)
- Madore, B. F., Freedman, W. L., & Moak, S. 2017, [ApJ](#), **842**, [42](#)
- Monson, A. J., & Pierce, M. J. 2011, [ApJS](#), **193**, [12](#)
- O'Donnell, J. E. 1994, [ApJ](#), **422**, [158](#)
- Pedicelli, S., Lemasle, B., Groenewegen, M., et al. 2010, [A&A](#), **518**, [A11](#)
- Persson, S. E., Madore, B. F., Krzemiński, W., et al. 2004, [AJ](#), **128**, [2239](#)
- Pietrzyński, G., Graczyk, D., Gallenne, A., et al. 2019, [Natur](#), **567**, [200](#)
- Planck Collaboration, Aghanim, N., Akrami, Y., et al. 2020, [A&A](#), **641**, [A6](#)
- Riess, A. G., Casertano, S., Yuan, W., et al. 2021, [ApJL](#), **908**, [L6](#)
- Riess, A. G., Casertano, S., Yuan, W., Macri, L. M., & Scolnic, D. 2019, [ApJ](#), **876**, [85](#)
- Riess, A. G., Macri, L. M., Hoffmann, S. L., et al. 2016, [ApJ](#), **826**, [56](#)
- Ripepi, V., Cioni, M.-R. L., Moretti, M. I., et al. 2017, [MNRAS](#), **472**, [808](#)
- Ripepi, V., Marconi, M., Moretti, M. I., et al. 2016, [ApJS](#), **224**, [21](#)
- Ripepi, V., Molinaro, R., Musella, I., et al. 2019, [A&A](#), **625**, [A14](#)
- Romaniello, M., Primas, F., Mottini, M., et al. 2008, [A&A](#), **488**, [731](#)
- Saha, A., Thim, F., Tammann, G. A., Reindl, B., & Sandage, A. 2006, [ApJS](#), **165**, [108](#)
- Soszyński, I., Udalski, A., Szymański, M. K., et al. 2015, [AcA](#), **65**, [297](#)
- Storm, J., Gieren, W., Fouqué, P., et al. 2011a, [A&A](#), **534**, [A94](#)
- Storm, J., Gieren, W., Fouqué, P., et al. 2011b, [A&A](#), **534**, [A95](#)
- Subramanian, S., & Subramaniam, A. 2012, [ApJ](#), **744**, [128](#)
- Sziládi, K., Vinkó, J., Poretti, E., Szabados, L., & Kun, M. 2007, [A&A](#), **473**, [579](#)
- Udalski, A., Wyrzykowski, L., Pietrzyński, G., et al. 2001, [AcA](#), **51**, [221](#)
- Watson, C. L., Henden, A. A., & Price, A. 2006, [SASS](#), **25**, [47](#)
- Welch, D. L., Wieland, F., McAlary, C. W., et al. 1984, [ApJS](#), **54**, [547](#)
- Wielgórski, P., Pietrzyński, G., Gieren, W., et al. 2017, [ApJ](#), **842**, [116](#)
- Yong, D., Carney, B. W., Teixeira de Almeida, M. L., & Pohl, B. L. 2006, [AJ](#), **131**, [2256](#)

## Chapter 4

# Conclusions and perspectives

---

<b>4.1</b>	<b>Results of the thesis . . . . .</b>	<b>164</b>
<b>4.2</b>	<b>Main limitations in the Cepheid distance scale . . . . .</b>	<b>165</b>
<b>4.3</b>	<b>Perspectives . . . . .</b>	<b>166</b>
4.3.1	Cluster Cepheid photometry in HST system . . . . .	166
4.3.2	Uncrowding extragalactic Cepheids in SN Ia hosts with JWST . . . . .	167
4.3.3	Other perspectives . . . . .	169

---

## 4.1 Results of the thesis

The Cepheid period-luminosity relation is a key tool for measuring extragalactic distances and must be calibrated with great precision for deriving the Hubble constant to 1%. In this thesis, I developed an original method based on companion stars and host open clusters for the calibration of the Cepheid Leavitt law. This technique allows us to bypass saturation and variability issues that affect *Gaia* parallaxes of Cepheids and provides an alternative method to obtain reliable Cepheid distances.

The approach adopted in [Breuval et al. \(2020\)](#) is described in chapter 2 and the analysis carried out in this paper is updated: the P-L calibration based on Cepheid companions and host clusters is repeated after replacing *Gaia* DR2 by *Gaia* EDR3 parallaxes and new cluster memberships from the literature are included. The results are consistent with the conclusions of [Breuval et al. \(2020\)](#), which confirms the robustness and reliability of the method. Thanks to the larger period of time covered by the third *Gaia* data release, the noise introduced by the variability of pulsating stars is globally averaged and apparently no longer deteriorates Cepheid parallaxes. Additionally, due to their faint nature, Cepheid companions are no longer competitive with Cepheids in terms of parallax precision. However they serve as an important cross-check for Cepheid astrometry. On the other hand, using mean cluster parallaxes in place of Cepheids reduces the P-L scatter by half and improves by up to a factor 3 the parallax precision. The [Breuval et al. \(2020\)](#) sample is enlarged with additional cluster Cepheids from the literature ([Zhou & Chen 2021](#)) that are re-analyzed and validated in this thesis. From this enhanced and updated sample, a revised value of  $73.47 \pm 1.77$  km/s/Mpc (for fundamental modes only) and  $73.10 \pm 1.76$  km/s/Mpc (including first-overtone modes) is obtained for the Hubble constant anchored to Galactic Cepheids, in good agreement with the other distance indicators from [Riess et al. \(2016\)](#), and slightly more precise than the value obtained in [Breuval et al. \(2020\)](#) based on *Gaia* DR2.

The effect of metallicity on the Leavitt law was investigated in chapter 3. The recent publication of Cepheid parallaxes from the *Gaia* Early Data Release 3 provides a strong anchor in the Milky Way. Additionally, new distances to both Magellanic Clouds were recently estimated by the Araucaria Project ([Pietrzyński et al. 2019](#); [Graczyk et al. 2020](#)). The three galaxies, in which Cepheid distances are precisely measured, cover a large range of  $\sim 1$  dex in metallicity, allowing for a robust estimation of the metallicity effect. My second paper ([Breuval et al. 2021](#)) is described in Chapter 3 as well as the data and method adopted. This analysis is complemented by additional magnitudes in the *Gaia* and *Spitzer* bands, enlarging the study further in optical and mid-infrared wavelengths. In particular, the effect of metallicity is derived for the first time in *Gaia* passbands. This chapter also reveals that the metallicity term likely depends on wavelength: while it is moderate in the optical with  $\gamma \sim -0.100$  mag/dex, it is stronger in the near infrared with  $\gamma \sim -0.200$  mag/dex. This trend is consistent with the line-blanketing effect, which removes a fraction of the flux in optical wavelengths and redistributes it around the NIR. The negative sign indicates that metal-rich Cepheids are brighter than metal-poor ones at a given pulsation period.

## 4.2 Main limitations in the Cepheid distance scale

Several issues and systematic effects are still limiting the calibration of the Cepheid distance scale. A few of them are listed in this section. They directly affect the P-L relation and therefore have significant consequences on the extragalactic distance scale and on the Hubble constant.

The period-luminosity coefficients and the metallicity effect are sensitive to the reddening law adopted. Most studies are based either on the [Cardelli et al. \(1989\)](#) reddening law or on the [Fitzpatrick \(1999\)](#) one. The two formulations slightly differ, which results in a small difference of extinction correction for apparent magnitudes, especially in optical bands. While Wesenheit indices are used extensively in the literature to avoid reddening corrections, they still depend on the reddening law: they should hence be constructed consistently.

Thanks to the surveys published by [Welch et al. \(1984\)](#), [Laney & Stobie \(1992\)](#), [Barnes et al. \(1997\)](#) and [Monson & Pierce \(2011\)](#), full light curves are available for a few dozens of Galactic Cepheids. However, many Cepheids with precise *Gaia* EDR3 parallaxes have a poor phase coverage or only a single-point apparent magnitude. A large photometric survey of Milky Way Cepheids should be carried out to provide a new complete and homogeneous catalog of apparent mean magnitudes.

So far, Cepheids located in SN Ia host galaxies can only be observed with space telescopes such as the HST. However, the P-L relation is often calibrated in the Milky Way using ground-based instruments: measuring the distance to extragalactic Cepheids by applying the Leavitt law requires the transformation from ground-based magnitudes to the HST system, which is an important source of systematics. Photometry in the HST system was recently measured for a sample of 75 Galactic Cepheids ([Riess et al. 2021b](#)). Yet, only single-point measurements are available in this system, which can also limit the precision of the derived mean magnitudes. Calibrating the Cepheid P-L relation with HST photometry from a larger number of Cepheids would greatly benefit the precision of the distance scale. In particular, the measurement of HST photometry for Cepheids in open clusters will be possible in the near future and should improve the P-L calibration (see Sect. 4.3.1).

A major improvement of *Gaia* EDR3 compared with *Gaia* DR2 is that the parallax zero-point is reduced and now includes the magnitude, colour, and ecliptic latitude of the source ([Lindgren et al. 2021a](#)). However, this systematic bias still requires correction and may also depend on additional parameters. Several authors attempted to provide a recipe for computing this quantity but there is no universal method to derive it precisely. In future *Gaia* data releases, the parallax zero-point should be better determined and hopefully will have a limited influence on parallax values. Additionally, the consideration of the variability of pulsating stars, as well as the larger period of time covered by future *Gaia* data releases, should improve the reliability of Cepheid parallaxes.

The effect of metallicity on the Leavitt law and its dependence with wavelength were estimated in this study based on the Milky Way and the two Magellanic Clouds. This system is particularly suitable for studying this effect thanks to the relatively large range of metallicity covered by the three galaxies. However, the results presented in this thesis still need confirmation from different samples. Unfortunately, the presence of strong CO absorption bands prevents the precise determination of the metallicity effect in the *Spitzer* [4.5  $\mu$ m] filter. Extending the metallicity range by including more metal-poor galaxies would be interesting. So far, only mean metallicities have been used for the LMC and SMC samples: measuring individual abundances for Magellanic Cloud Cepheids would also contribute to a better determination of the metallicity effect.

## 4.3 Perspectives

### 4.3.1 Cluster Cepheid photometry in HST system

Open clusters hosting Cepheids provide a very promising method to obtain their distance. In chapter 2, the P-L relation calibrated with mean parallaxes of cluster Cepheids showed a reduced scatter and a better precision compared with directly using Cepheid parallaxes. Since each cluster has 70 to 1000 members (Cantat-Gaudin et al. 2018), their mean parallax is more precise than the individual members, including its Cepheid. The main limitation of *Gaia* EDR3 open cluster parallaxes is the angular correlation between the cluster members, which are closely spaced on the sky. This effect is included when deriving mean cluster parallaxes by using the covariance function described in Chapter 2, Sect. 2.3.2.1, and yields a floor uncertainty of  $\sim 10 \mu\text{as}$ .

In Breuval et al. (2020), we identified 14 high confidence open cluster Cepheids, among which 13 are pulsating in the fundamental mode. In this thesis, this initial sample is complemented by 6 additional memberships from the literature. However the P-L calibration based on cluster Cepheids was obtained in ground-based filters only. As mentioned in the previous section, Cepheids located in SN Ia host galaxies are observed in the HST system exclusively: for this reason, calibrating the Leavitt law in the Milky Way using the same photometric system as for extragalactic Cepheids is very advantageous since it cancels the systematics due to photometric transformations.

In order to fully exploit open cluster Cepheids and *Gaia* EDR3 parallaxes to calibrate the distance scale, we proposed to measure HST/WFC3 photometry for 10 Cepheids of this sample: we obtained a total of 10 HST orbits to fulfill this project<sup>1</sup>.

Observing Galactic Cepheids, which are significantly brighter than their extragalactic counterparts, requires very short exposure times to avoid saturation. For this purpose, the spatial scanning technique already mentioned for parallax measurements will be implemented: the telescope is drifted during the observation, so that the position of the source is varying with time and creates a trail over the detector. The fast scan speed enables us to reach the equivalent of a much shorter exposure time than that proposed for the WFC3 instrument.

Figure 4.1 shows the improvements enabled by using mean cluster parallaxes and expected from the HST fluxes of cluster Cepheids. The upper left panel represents the P-L relation obtained in the ground-based  $K_S$  band from *Gaia* EDR3 parallaxes of Cepheids, and the lower left panel is the same but Cepheid parallaxes are replaced by mean cluster parallaxes. Substituting the Cepheid parallax for its mean cluster value improves the parallax precision by a factor of  $\sim 3$  and reduces the P-L scatter to half (from  $\sigma = 0.15 \text{ mag}$  to  $\sigma = 0.08 \text{ mag}$ ), approaching the intrinsic width of the instability strip in the NIR. On the upper right panel, the P-L relation is calibrated using mean open cluster parallaxes in the HST Wesenheit index ( $W_H$ ) by synthetically combining ground-based magnitudes. The zero-point error due to photometric transformation reaches 0.04 mag which yields an error of 0.047 mag in  $H_0$ . The expected P-L relation obtained from the proposed HST observations is represented in the lower right panel, where the empty markers are the Cepheids requested in the proposal. Adopting HST/WFC3 spatial scanning magnitudes will cancel the photometric zero-point and is expected to reduce the  $H_0$  error to 0.020 mag. Three of the 13 fundamental-mode Cepheids from the Breuval et al. (2020) sample were already observed by Riess et al. (2021b) in the HST system (DL Cas, U Sgr, and XZ Car). They are represented in green in the lower right panel: their dispersion

<sup>1</sup> I am co-investigator of the Hubble Space Telescope Proposal "A 1% Calibration of the Distance Ladder from Cepheids Using High Precision Cluster Parallaxes to Reveal the Origin of the Hubble Tension", Cycle 29, GO 16676 (PI: A. Riess). For more information: <https://www.stsci.edu/cgi-bin/get-proposal-info?id=16676&observatory=HST>

appears small as they have the best possible combination of parallax and photometry precision.

As stated in the conclusion of the proposal: *"Together, Gaia and HST, each doing what they do best, can achieve what neither can do alone."* These new observations will continue to improve the precision of the Cepheid distance scale, hopefully allowing for a 1% determination of the Hubble constant and a better understanding of the current  $\sim 4\sigma$  tension.

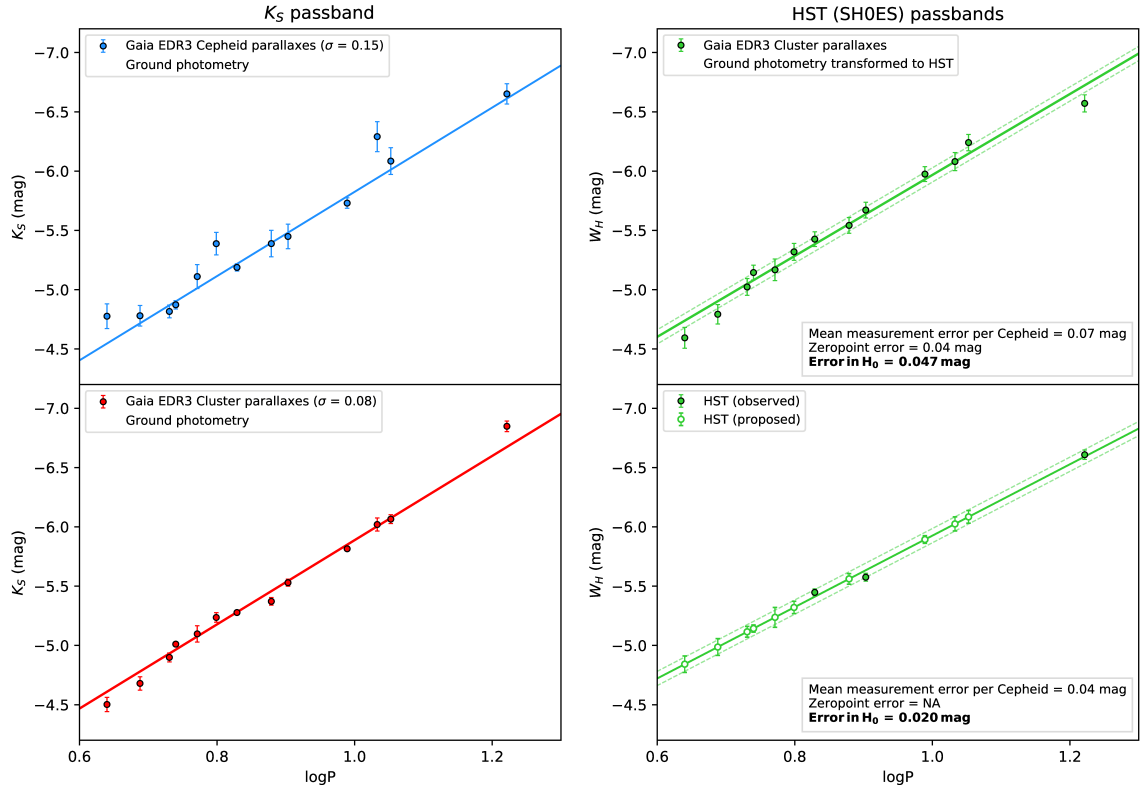


Figure 4.1: Improvements in the calibration of the Milky Way Cepheid period-luminosity relation using *Gaia* EDR3 parallaxes and HST system photometry. **Upper left:** P-L relation in the  $K_S$  band from *Gaia* EDR3 parallaxes of 13 Cepheids in open clusters. **Lower left:** Same as upper left but replacing Cepheid parallaxes with the mean of their host cluster. **Upper right:** P-L relation in the HST system obtained from transformed ground-based magnitudes. **Lower right:** Obtaining HST photometry for Cepheids in clusters (empty markers) is expected to reduce the scatter of the P-L relation and eliminate the zero point uncertainty between the ground and HST systems. This figure is taken from the HST Proposal GO 16676 (PI: A. Riess) and was made by me.

#### 4.3.2 Uncrowding extragalactic Cepheids in SN Ia hosts with JWST

Once the Cepheid P-L relation is calibrated locally using geometrical distances, the second step of the distance ladder is to observe Cepheids in SN Ia host galaxies. Although Cepheids are very bright stars, it is often difficult to separate their flux contribution from their stellar background in crowded regions of nearby galaxies, even at the resolution of HST. The unresolved and diffuse background flux adds noise to Cepheid measurements and dominates the scatter of the P-L relation.



In [Riess et al. \(2016\)](#), Cepheid backgrounds are estimated by randomly placing artificial stars in the neighbourhood of each Cepheid. The unbiased Cepheid photometry is obtained after correcting the overestimate of the Cepheid flux based on the measured photometry of artificial stars added to simulate blending. The unprecedented resolution of *James Webb* Space Telescope (JWST) will allow us to bypass this correction and to directly resolve the Cepheid backgrounds, providing uncontaminated photometric measurements for Cepheids in SN Ia host galaxies.

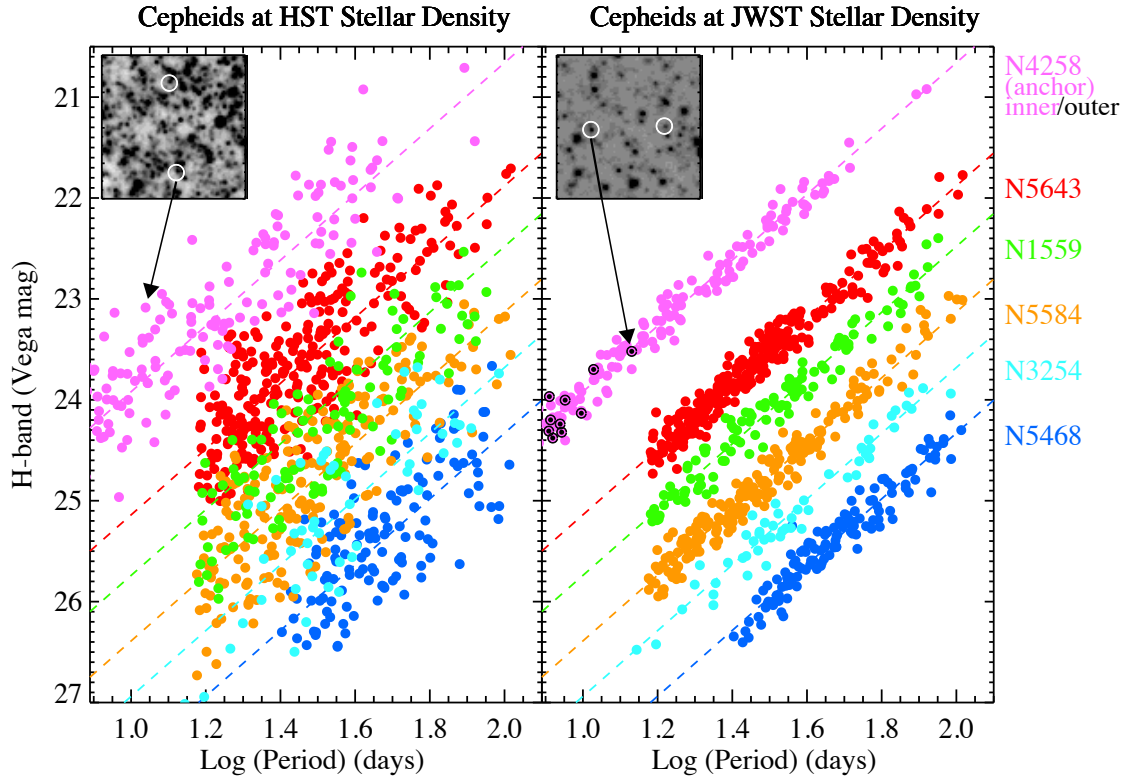


Figure 4.2: **Left:** Observed Cepheid P-L relations in the five SN Ia host galaxies and in the maser-host NGC 4258 with HST/WFC3 F160W filter. The typical 0.45 mag scatter is dominated by background fluctuations due to crowding. **Right:** Expected P-L relation at JWST resolution. The background and its fluctuations are reduced by a factor of 8 over HST, reducing the simulated P-L scatter by a factor of 3 in F150W. **Image stamps:** The inner (left plot) and outer (right plot) fields of NGC 4258 are a good proxy for the proposed JWST imaging as they benefit from a similar factor of 6 background reduction. This figure is taken from the JWST Proposal GO 1685 (PI: A. Riess) and was made by A. Riess.

We proposed a JWST program<sup>2</sup> dedicated to observe with the NIRCAM instrument 1500 known Cepheids in five galaxies hosting seven SNe Ia and in the maser host galaxy NGC 4258, which has a 1.5% geometric distance, in three NIR colors and two epochs. The high resolution of JWST will separate the contribution of Cepheids from that of their background by a factor of 8 compared with what is currently possible with HST, which will tighten the P-L relation. Figure 4.2 compares the scatter of the observed P-L relation at HST resolution and the expected dispersion with JWST.

<sup>2</sup> I am co-investigator of the James Webb Space Telescope Proposal "Uncrowding the Cepheids for an Improved Determination of the Hubble Constant", Cycle 1, GO 1685 (PI: A. Riess). For more information: <https://www.stsci.edu/cgi-bin/get-proposal-info?observatory=JWST&id=1685&pi=1>

The background noise is expected to decrease from 0.45 to 0.06 mag and should reveal potential remaining systematics. The proposed two epochs of observations will reduce the error from the random phase by 40% and will be compared with non-variable stars to test the accuracy of JWST photometry.

Additionally, with the same observations of these six galaxies, two other independent primary distance indicators will be observed: the infrared TRGB and Oxygen-rich Mira variables. The parallel modules of NIRCAM can simultaneously observe one field in the disk, hosting Cepheids and Mira stars, and less crowded halo fields where the infrared tip of the red giant branch can be detected. In the infrared, TRGB stars are 1.5 mag to 2 mag brighter than in the *I* band, where it is usually studied (Freedman et al. 2019), and are also ten times less affected by extinction. Finally, blue Oxygen-rich Mira stars follow a tight P-L relation which provides an additional primary distance indicator (White-lock et al. 2008; Yuan et al. 2017; Huang et al. 2020), but they first need to be separated from redder Carbon-rich Miras by studying their position in a color-color diagram. The JWST imaging will provide this color information and decontaminate the Mira P-L relation, allowing for an independent calibration of SNe Ia.

Observing three independent distance indicators in six SN Ia or maser host galaxies with JWST will hopefully unravel differences between methods connecting both ends of the distance ladder, address the remaining systematics between the Milky Way and extragalactic Cepheid P-L relation and demonstrate whether the  $H_0$  tension is a robust feature of the Universe.

### 4.3.3 Other perspectives

In the near future, the publication of the final *Gaia* Data Release will provide full astrometric and photometric data with unprecedented precision for more than one billion stars. *Gaia* DR4 parallaxes will refine the calibration of the Cepheid Leavitt law to the highest level of precision ever reached. The *Gaia* mission has already enabled major improvements in the determination of the distance scale and is the cornerstone for a 1% precision measurement of the Hubble constant.

As demonstrated in this thesis, Cepheid metallicities have a non-negligible influence on the P-L relation, and consequently on the Hubble constant. However, the precision and the number of metal abundances available for Milky Way and Magellanic Cloud Cepheids is still insufficient to conclude about a firm value of the metallicity effect in each band, although most empirical studies (including the present work) suggest a negative sign, meaning that metal-rich Cepheids are intrinsically brighter than their metal-poor counterparts of the same pulsation period. In the Magellanic Clouds, individual metallicity measurements are very few and even the most recent works are based on mean metallicities in these galaxies. Measuring individual metal abundances from high-resolution spectra for Milky Way and Magellanic Cloud Cepheids is paramount for the calibration of the metallicity effect and its wavelength dependence. Ground telescopes such as the Very Large Telescope (VLT) or the Magellan telescope at Las Campanas Observatory have been widely used to obtain earlier metallicity measurements. In the next decade, the operation of the Extremely Large Telescope, currently under construction by the European Southern Observatory (ESO), should provide more precise abundances for a larger number of Cepheids, especially with the HIRES high-resolution spectrograph or the MOSAIC multi-object spectrograph.

Several systematic effects are still poorly calibrated and may significantly impact the first rung of the distance ladder. For instance, many Cepheids are known to be in binary systems (Kervella et al. 2019a). Close companions could potentially bias the brightness of their parent Cepheid: Gallenne et al. (2018) showed that correcting the photometric bias due to the companion of V1334 Cyg gives a

better agreement of the star with the P-L relation. However [Anderson & Riess \(2018\)](#) showed that the effects of wide binaries on the Hubble constant are at the level of 0.004 % only. Similarly, blending due to cluster populations has previously resulted in a minor overestimate of 0.23% of  $H_0$ .

Additionally, the presence of circumstellar envelopes was observed around several Cepheids ([Kervella et al. 2006](#); [Mérand et al. 2006, 2007](#); [Marengo et al. 2010](#); [Gallenne et al. 2013](#); [Nardetto et al. 2016](#); [Hocdé et al. 2021](#)). These envelopes can be responsible for an infrared excess on apparent brightnesses, which would necessarily affect the P-L relation by increasing its dispersion and biasing the slope and zero-point. The mass-loss of Cepheids is therefore interesting to understand the physics behind the P-L relation and its scatter.

Asides from Cepheids, the calibration of other primary distance indicators will undoubtedly be refined thanks to the *James Webb* Space Telescope: for example, Mira stars and TRBG provide powerful independent methods to calibrate SN Ia distances and complement Cepheid measurements. The recent estimates of the Hubble constant based on the TRGB are particularly interesting since they seem to constantly yield lower  $H_0$  values compared with Cepheids and other anchors, decreasing the tension to  $\sim 1 - 2\sigma$  ([Freedman et al. 2019](#); [Freedman 2021](#); [Anand et al. 2021](#)).

The second step of the distance ladder, which is observing Cepheids in SN Ia host galaxies and applying the P-L relation to measure their distance, will also be improved: so far, only 19 SNe Ia were detected in nearby galaxies ([Riess et al. 2016](#)). This sample will soon be doubled to reach  $\sim 40$  SNe Ia within a redshift of  $z < 0.01$ , bringing the error on  $H_0$  close to 1%. Regarding the third step of the distance ladder, a sample of about 300 SNe Ia were measured in the Hubble flow between redshifts of 0.02 and 0.05, where they trace the accelerated expansion of the Universe ([Scolnic et al. 2015](#); [Scolnic & Kessler 2016](#)).

Within the next years, the *Nancy Grace Roman* Telescope will be launched with the primary goal to measure the expansion of the Universe, study the effects of dark energy and test the consistency of general relativity. New independent distance indicators have recently been used to derive the Hubble constant, such as gravitational waves or gravitational lensing and should be further developed in the next years. The ESA *Euclid* mission will be focused on mapping dark matter and deriving properties of dark energy, characterizing the accelerating expansion of the Universe. All these mutual efforts will soon result in a better understanding of the distance scale and should indicate whether the tension on the Hubble constant between the locally-measured and the CMB-inferred value is a robust feature of the Universe.

# Bibliography

- Acharova, I. A., Mishurov, Y. N., & Kovtyukh, V. V. 2012, MNRAS, 420, 1590
- Alcock, C., Allsman, R. A., Axelrod, T. S., et al. 1995, AJ, 109, 1653
- Alonso-Santiago, J., Negueruela, I., Marco, A., Tabernero, H. M., & Castro, N. 2020, A&A, 644, A136
- An, D., Terndrup, D. M., & Pinsonneault, M. H. 2007, ApJ, 671, 1640
- Anand, G. S., Tully, R. B., Rizzi, L., Riess, A. G., & Yuan, W. 2021, arXiv e-prints, arXiv:2108.00007
- Anders, F., Khalatyan, A., Chiappini, C., et al. 2019, A&A, 628, A94
- Anderson, R. I. 2018, A&A, 611, L7
- Anderson, R. I., Casertano, S., Riess, A. G., et al. 2016a, ApJS, 226, 18
- Anderson, R. I., Eyer, L., & Mowlavi, N. 2013, MNRAS, 434, 2238
- Anderson, R. I. & Riess, A. G. 2018, ApJ, 861, 36
- Anderson, R. I., Saio, H., Ekström, S., Georgy, C., & Meynet, G. 2016b, A&A, 591, A8
- Arenou, F. & Luri, X. 1999, in Astronomical Society of the Pacific Conference Series, Vol. 167, Harmonizing Cosmic Distance Scales in a Post-HIPPARCOS Era, ed. D. Egret & A. Heck, 13–32
- Ayres, T. R. 1994, in Astronomical Society of the Pacific Conference Series, Vol. 57, Stellar and Circumstellar Astrophysics, a 70th birthday celebration for K. H. Bohm and E. Bohm-Vitense, ed. G. Wallerstein & A. Noriega-Crespo, 124
- Baade, W. 1948, PASP, 60, 230
- Bailer-Jones, C. A. L., Rybizki, J., Fouesneau, M., Demleitner, M., & Andrae, R. 2021, AJ, 161, 147
- Baker, N. & Kippenhahn, R. 1962, ZAp, 54, 114
- Barnes, T. G., I., Fernley, J. A., Frueh, M. L., et al. 1997, Publications of the Astronomical Society of the Pacific, 109, 645
- Behr, A. 1951, Astronomische Nachrichten, 279, 97
- Benedict, G. F., McArthur, B., Chappell, D. W., et al. 1999, AJ, 118, 1086
- Benedict, G. F., McArthur, B. E., Feast, M. W., et al. 2011, AJ, 142, 187
- Benedict, G. F., McArthur, B. E., Feast, M. W., et al. 2007, AJ, 133, 1810

- Benedict, G. F., McArthur, B. E., Franz, O. G., Wasserman, L. H., & Henry, T. J. 2000, *AJ*, 120, 1106
- Benedict, G. F., McArthur, B. E., Franz, O. G., et al. 2001, *AJ*, 121, 1607
- Benedict, G. F., McArthur, B. E., Fredrick, L. W., et al. 2002, *AJ*, 124, 1695
- Benedict, G. F., McArthur, B. E., Napiwotzki, R., et al. 2009, *AJ*, 138, 1969
- Bennett, C. L., Larson, D., Weiland, J. L., et al. 2013, *ApJS*, 208, 20
- Berdnikov, L. N. 2008, *VizieR Online Data Catalog*, 2285, 0
- Berdnikov, L. N., Dambis, A. K., & Vozyakova, O. V. 2000, *A&AS*, 143, 211
- Bhardwaj, A. 2020, *Journal of Astrophysics and Astronomy*, 41, 23
- Blakeslee, J. P., Jensen, J. B., Ma, C.-P., Milne, P. A., & Greene, J. E. 2021, *ApJ*, 911, 65
- Bono, G., Caputo, F., Castellani, V., & Marconi, M. 1999, *ApJ*, 512, 711
- Bono, G., Caputo, F., Fiorentino, G., Marconi, M., & Musella, I. 2008, *ApJ*, 684, 102
- Bradley, A., Abramowicz-Reed, L., Story, D., Benedict, G., & Jefferys, W. 1991, *PASP*, 103, 317
- Bradley, L., Sipocz, B., Robitaille, T., et al. 2019, *astropy/photutils: v0.6*
- Breitfelder, J., Kervella, P., Mérand, A., et al. 2015, *A&A*, 576, A64
- Breitfelder, J., Mérand, A., Kervella, P., et al. 2016, *A&A*, 587, A117
- Breuval, L., Kervella, P., Anderson, R. I., et al. 2020, *A&A*, 643, A115
- Breuval, L., Kervella, P., Wielgórski, P., et al. 2021, *ApJ*, 913, 38
- Cantat-Gaudin, T., Anders, F., Castro-Ginard, A., et al. 2020, *A&A*, 640, A1
- Cantat-Gaudin, T., Jordi, C., Vallenari, A., et al. 2018, *A&A*, 618, A93
- Caputo, F., Marconi, M., Musella, I., & Santolamazza, P. 2000, *A&A*, 359, 1059
- Cardelli, J. A., Clayton, G. C., & Mathis, J. S. 1989, *ApJ*, 345, 245
- Carpenter, J. M. 2001, *AJ*, 121, 2851
- Casertano, S., Riess, A. G., Anderson, J., et al. 2016, *ApJ*, 825, 11
- Challouf, M., Nardetto, N., Mourard, D., et al. 2014, *A&A*, 570, A104
- Chen, X., de Grijs, R., & Deng, L. 2015, *MNRAS*, 446, 1268
- Chen, X., de Grijs, R., & Deng, L. 2017, *MNRAS*, 464, 1119
- Chown, A. H., Scowcroft, V., & Wuyts, S. 2021, *MNRAS*, 500, 817
- Clark, J. S., Negueruela, I., Lohr, M. E., et al. 2015, *A&A*, 584, L12
- Clementini, G., Gratton, R., Bragaglia, A., et al. 2003, *AJ*, 125, 1309
- Clementini, G., Ripepi, V., Molinaro, R., et al. 2019, *A&A*, 622, A60

- Cox, J. P. 1963, *ApJ*, 138, 487
- Crowley, C., Kohley, R., Hambly, N. C., et al. 2016, *A&A*, 595, A6
- Curtis, H. D. 1920, *JRASC*, 14, 317
- Cutri, R. M., Skrutskie, M. F., van Dyk, S., et al. 2003, 2MASS All Sky Catalog of point sources.
- Danielski, C., Babusiaux, C., Ruiz-Dern, L., Sartoretti, P., & Arenou, F. 2018, *A&A*, 614, A19
- De Grijs, R. 2011, *An Introduction To Distance Measurement In Astronomy* (Wiley-Blackwell Academic Publishers)
- de Sitter, W. 1930, *Bull. Astron. Inst. Netherlands*, 5, 157
- de Vaucouleurs, G. 1970, *ApJ*, 159, 435
- de Vaucouleurs, G., ed. 1977, *Décalage vers le rouge et expansion de l'univers*, IAU Coll. 37, (paris: Ed. CNRS), 301
- de Vaucouleurs, G. & Peters, W. L. 1986, *ApJ*, 303, 19
- Di Valentino, E., Mena, O., Pan, S., et al. 2021, arXiv e-prints, arXiv:2103.01183
- Drimmel, R., Bucciarelli, B., & Inno, L. 2019, *Research Notes of the American Astronomical Society*, 3, 79
- Dyson, Frank, S. 1926, *MNRAS*, 86, 686
- Eddington, A. S. 1913, *MNRAS*, 73, 359
- Eddington, A. S. 1917, *The Observatory*, 40, 290
- Eddington, A. S., S. 1941, *MNRAS*, 101, 182
- EROS Collaboration, Bauer, F., Afonso, C., et al. 1999, *A&A*, 348, 175
- ESA, ed. 1997, *ESA Special Publication*, Vol. 1200, *The HIPPARCOS and TYCHO catalogues. Astrometric and photometric star catalogues derived from the ESA HIPPARCOS Space Astrometry Mission*
- Fabrizius, C., Luri, X., Arenou, F., et al. 2021, *A&A*, 649, A5
- Feast, M. W. & Catchpole, R. M. 1997, *MNRAS*, 286, L1
- Feast, M. W., Laney, C. D., Kinman, T. D., van Leeuwen, F., & Whitelock, P. A. 2008, *MNRAS*, 386, 2115
- Fernie, J. D., Evans, N. R., Beattie, B., & Seager, S. 1995, *Information Bulletin on Variable Stars*, 4148
- Fiorentino, G., Caputo, F., Marconi, M., & Musella, I. 2002, *ApJ*, 576, 402
- Fiorentino, G., Marconi, M., Musella, I., & Caputo, F. 2007, *A&A*, 476, 863
- Fiorentino, G., Musella, I., & Marconi, M. 2013, *MNRAS*, 434, 2866
- Fitzpatrick, E. L. 1999, *PASP*, 111, 63



- Fitzpatrick, E. L., Ribas, I., Guinan, E. F., Maloney, F. P., & Claret, A. 2003, *ApJ*, 587, 685
- Fouqué, P., Arriagada, P., Storm, J., et al. 2007, *A&A*, 476, 73
- Fouqué, P. & Gieren, W. P. 1997, *A&A*, 320, 799
- Freedman, W. L. 2021, arXiv e-prints, arXiv:2106.15656
- Freedman, W. L. & Madore, B. F. 2011, *ApJ*, 734, 46
- Freedman, W. L., Madore, B. F., Gibson, B. K., et al. 2001, *ApJ*, 553, 47
- Freedman, W. L., Madore, B. F., Hatt, D., et al. 2019, *ApJ*, 882, 34
- Freedman, W. L., Madore, B. F., Hoyt, T., et al. 2020, *ApJ*, 891, 57
- Freedman, W. L., Madore, B. F., Rigby, J., Persson, S. E., & Sturch, L. 2008, *ApJ*, 679, 71
- Freedman, W. L., Madore, B. F., Scowcroft, V., et al. 2012, *ApJ*, 758, 24
- Freedman, W. L., Madore, B. F., Scowcroft, V., et al. 2011, *AJ*, 142, 192
- Fry, A. M. & Carney, B. W. 1997, *AJ*, 113, 1073
- Gaia Collaboration, Brown, A. G. A., Vallenari, A., et al. 2018, *A&A*, 616, A1
- Gaia Collaboration, Brown, A. G. A., Vallenari, A., et al. 2021, *A&A*, 649, A1
- Gaia Collaboration, Clementini, G., Eyer, L., et al. 2017, *A&A*, 605, A79
- Gaia Collaboration, Eyer, L., Rimoldini, L., et al. 2019, *A&A*, 623, A110
- Gallenne, A., Kervella, P., Evans, N. R., et al. 2018, *ApJ*, 867, 121
- Gallenne, A., Kervella, P., Mérand, A., et al. 2017, *A&A*, 608, A18
- Gallenne, A., Mérand, A., Kervella, P., et al. 2013, *A&A*, 558, A140
- Gallenne, A., Mérand, A., Kervella, P., et al. 2021, *A&A*, 651, A113
- Garnavich, P. M., Kirshner, R. P., Challis, P., et al. 1998, *ApJ*, 493, L53
- Genovali, K., Lemasle, B., Bono, G., et al. 2014, *A&A*, 566, A37
- Genovali, K., Lemasle, B., da Silva, R., et al. 2015, *A&A*, 580, A17
- Gieren, W., Storm, J., Konorski, P., et al. 2018, *A&A*, 620, A99
- Górski, M., Zgirski, B., Pietrzyński, G., et al. 2020, *ApJ*, 889, 179
- Gouguenheim, L., Bottinelli, L., Fouque, P., Paturel, G., & Teerikorpi, P. 1990, in *The Quest for the Fundamental Constants in Cosmology*, ed. J. Audouze & J. Tran Thanh Van, Vol. 9, 3–17
- Graczyk, D., Pietrzyński, G., Thompson, I. B., et al. 2014, *ApJ*, 780, 59
- Graczyk, D., Pietrzyński, G., Thompson, I. B., et al. 2020, *ApJ*, 904, 13
- Grevesse, N., Noels, A., & Sauval, A. J. 1996, in *Astronomical Society of the Pacific Conference Series*, Vol. 99, *Cosmic Abundances*, ed. S. S. Holt & G. Sonneborn, 117

- Groenewegen, M. 2021, arXiv e-prints, arXiv:2106.08128
- Groenewegen, M. A. T. 2013, A&A, 550, A70
- Groenewegen, M. A. T. 2018, A&A, 619, A8
- Groenewegen, M. A. T. & Oudmaijer, R. D. 2000, A&A, 356, 849
- Gudehus, D. H. 1973, AJ, 78, 583
- Guinan, E. F., Fitzpatrick, E. L., DeWarf, L. E., et al. 1998, ApJ, 509, L21
- Hanson, R. B. 1979, MNRAS, 186, 875
- Hershey, J. L. & Taff, L. G. 1998, AJ, 116, 1440
- Hertzsprung, E. 1913, *Astronomische Nachrichten*, 196, 201
- Hertzsprung, E. 1924, *Bull. Astron. Inst. Netherlands*, 2, 83
- Hertzsprung, E. 1926, *Bull. Astron. Inst. Netherlands*, 3, 115
- Hinshaw, G., Weiland, J. L., Hill, R. S., et al. 2009, ApJS, 180, 225
- Hocdé, V., Nardetto, N., Lagadec, E., et al. 2020, A&A, 633, A47
- Hocdé, V., Nardetto, N., Matter, A., et al. 2021, A&A, 651, A92
- Hoffmann, S. L., Macri, L. M., Riess, A. G., et al. 2016, ApJ, 830, 10
- Holmberg, E. 1958, *Meddelanden fran Lunds Astronomiska Observatorium Serie II*, 136, 1
- Huang, C. D., Riess, A. G., Hoffmann, S. L., et al. 2018, ApJ, 857, 67
- Huang, C. D., Riess, A. G., Yuan, W., et al. 2020, ApJ, 889, 5
- Hubble, E. 1929, *Proceedings of the National Academy of Science*, 15, 168
- Hubble, E. P. 1936, *Realm of the Nebulae* (Yale University Press)
- Humphreys, E. M. L., Reid, M. J., Moran, J. M., Greenhill, L. J., & Argon, A. L. 2013, ApJ, 775, 13
- Indebetouw, R., Mathis, J. S., Babler, B. L., et al. 2005, ApJ, 619, 931
- Jacyszyn-Dobrzaniecka, A. M., Skowron, D. M., Mróz, P., et al. 2016, *Acta Astron.*, 66, 149
- Jang, I. S. & Lee, M. G. 2017, ApJ, 835, 28
- Jarosik, N., Bennett, C. L., Dunkley, J., et al. 2011, ApJS, 192, 14
- Javanmardi, B., Mérand, A., Kervella, P., et al. 2021, ApJ, 911, 12
- Jha, S., Riess, A. G., & Kirshner, R. P. 2007, ApJ, 659, 122
- Jordi, C., Gebran, M., Carrasco, J. M., et al. 2010, A&A, 523, A48
- Kanbur, S. M., Marconi, M., Ngeow, C., et al. 2010, MNRAS, 408, 695
- Kato, D., Nagashima, C., Nagayama, T., et al. 2007, PASJ, 59, 615

- Kennicutt, Robert C., J., Stetson, P. B., Saha, A., et al. 1998, *ApJ*, 498, 181
- Kervella, P., Arenou, F., Mignard, F., & Thévenin, F. 2019a, *A&A*, 623, A72
- Kervella, P., Bond, H. E., Cracraft, M., et al. 2014, *A&A*, 572, A7
- Kervella, P., Fouqué, P., Storm, J., et al. 2004, *ApJ*, 604, L113
- Kervella, P., Gallenne, A., Evans, N. R., et al. 2019b, *A&A*, 623, A117
- Kervella, P., Mérand, A., & Gallenne, A. 2009, *A&A*, 498, 425
- Kervella, P., Mérand, A., Perrin, G., & Coudé du Foresto, V. 2006, *A&A*, 448, 623
- Kervella, P., Mérand, A., Szabados, L., et al. 2008, *A&A*, 480, 167
- Kervella, P., Trahin, B., Bond, H. E., et al. 2017, *A&A*, 600, A127
- Klagyivik, P. & Szabados, L. 2009, *A&A*, 504, 959
- Koen, C. & Laney, D. 1998, *MNRAS*, 301, 582
- Koen, C., Marang, F., Kilkeny, D., & Jacobs, C. 2007, *MNRAS*, 380, 1433
- Kourkchi, E., Tully, R. B., Anand, G. S., et al. 2020, *ApJ*, 896, 3
- Kovtyukh, V., Lemasle, B., Chekhonadskikh, F., et al. 2016, *MNRAS*, 460, 2077
- Kovtyukh, V. V., Soubiran, C., Luck, R. E., et al. 2008, *MNRAS*, 389, 1336
- Kovtyukh, V. V., Wallerstein, G., & Andrievsky, S. M. 2005, *PASP*, 117, 1173
- Lacy, C. H. 1977, *ApJ*, 213, 458
- Lallement, R., Capitanio, L., Ruiz-Dern, L., et al. 2018, *A&A*, 616, A132
- Laney, C. D. & Caldwell, J. A. R. 2007, *MNRAS*, 377, 147
- Laney, C. D. & Stobie, R. S. 1992, *Astronomy and Astrophysics Supplement Series*, 93, 93
- Lanoix, P., Paturel, G., & Garnier, R. 1999, *MNRAS*, 308, 969
- Leavitt, H. S. 1908, *Annals of Harvard College Observatory*, 60, 87
- Leavitt, H. S. & Pickering, E. C. 1912, *Harvard College Observatory Circular*, 173, 1
- Leitherer, C. 2012, in *Astronomical Society of India Conference Series*, Vol. 6, *Astronomical Society of India Conference Series*, ed. P. Prugniel & H. P. Singh, 79
- Lemaître, G. 1927, *Annales de la Société Scientifique de Bruxelles*, 47, 49
- Lemasle, B., Groenewegen, M. A. T., Grebel, E. K., et al. 2017, *A&A*, 608, A85
- Lemasle, B., Hajdu, G., Kovtyukh, V., et al. 2018, *A&A*, 618, A160
- Lindgren, L. 2018a, *Gaia DR2 astrometry*, IAU 30 GA - Division A: Fundamental Astronomy [https://www.iau.org/static/science/scientific\\_bodies/divisions/a/2018/Lindgren.pdf](https://www.iau.org/static/science/scientific_bodies/divisions/a/2018/Lindgren.pdf)

- Lindegren, L. 2018b, Gaia DR2 astrometry
- Lindegren, L. 2018c, Re-normalising the astrometric chi-square in Gaia DR2, Tech. Rep. GAIA-C3-TN-LU-LL-124, Lund Observatory
- Lindegren, L. 2020, A&A, 633, A1
- Lindegren, L., Bastian, U., Biermann, M., et al. 2021a, A&A, 649, A4
- Lindegren, L., Hernández, J., Bombrun, A., et al. 2018, A&A, 616, A2
- Lindegren, L., Klioner, S. A., Hernández, J., et al. 2021b, A&A, 649, A2
- Lindegren, L., Lammers, U., Bastian, U., et al. 2016, A&A, 595, A4
- Lindemann, F. A. 1918, MNRAS, 78, 639
- Lohr, M. E., Negueruela, I., Tabernero, H. M., et al. 2018, MNRAS, 478, 3825
- Longmore, A. J., Fernley, J. A., & Jameson, R. F. 1986, MNRAS, 220, 279
- Luck, R. E. 2018, AJ, 156, 171
- Luck, R. E., Andrievsky, S. M., Kovtyukh, V. V., Gieren, W., & Graczyk, D. 2011, AJ, 142, 51
- Luck, R. E., Kovtyukh, V. V., & Andrievsky, S. M. 2006, AJ, 132, 902
- Luck, R. E. & Lambert, D. L. 2011, AJ, 142, 136
- Lutz, T. E. & Kelker, D. H. 1973, Publications of the Astronomical Society of the Pacific, 85, 573
- MacConnell, D. J., Osborn, W. H., & Miller, R. J. 1997, AJ, 114, 1268
- Macri, L. M., Ngeow, C.-C., Kanbur, S. M., Mahzooni, S., & Smitka, M. T. 2015, AJ, 149, 117
- Macri, L. M., Stanek, K. Z., Bersier, D., Greenhill, L. J., & Reid, M. J. 2006, ApJ, 652, 1133
- Madore, B. F. 1982, ApJ, 253, 575
- Madore, B. F. & Freedman, W. L. 1991, Publications of the Astronomical Society of the Pacific, 103, 933
- Madore, B. F. & Freedman, W. L. 1998, ApJ, 492, 110
- Madore, B. F. & Freedman, W. L. 2012, ApJ, 744, 132
- Madore, B. F., Freedman, W. L., & Moak, S. 2017, ApJ, 842, 42
- Madore, B. F., Freedman, W. L., Rigby, J., et al. 2009, ApJ, 695, 988
- Madore, B. F., Hoffman, D., Freedman, W. L., et al. 2013, ApJ, 776, 135
- Mager, V. A., Madore, B. F., & Freedman, W. L. 2013, ApJ, 777, 79
- Maíz Apellániz, J., Pantaleoni González, M., & Barbá, R. H. 2021, A&A, 649, A13
- Majaess, D., Sturch, L., Moni Bidin, C., et al. 2013a, Ap&SS, 347, 61
- Majaess, D., Turner, D. G., & Gieren, W. 2013b, ApJ, 772, 130

- Marconi, M., Coppola, G., Bono, G., et al. 2015, *ApJ*, 808, 50
- Marconi, M., Musella, I., & Fiorentino, G. 2005, *ApJ*, 632, 590
- Marconi, M., Musella, I., Fiorentino, G., et al. 2010, *ApJ*, 713, 615
- Marengo, M., Evans, N. R., Barmby, P., et al. 2010, *ApJ*, 725, 2392
- McGonegal, R., McAlary, C. W., McLaren, R. A., & Madore, B. F. 1983, *ApJ*, 269, 641
- McNamara, D. H. & Colton, D. J. 1969, *PASP*, 81, 826
- McQuinn, K. B. W., Boyer, M., Skillman, E. D., & Dolphin, A. E. 2019, *ApJ*, 880, 63
- Medina, G. E., Lemasle, B., & Grebel, E. K. 2021, arXiv e-prints, arXiv:2104.14565
- Mel'nik, A. M., Rautiainen, P., Berdnikov, L. N., Dambis, A. K., & Rastorguev, A. S. 2015, *Astronomische Nachrichten*, 336, 70
- Mérand, A., Aufdenberg, J. P., Kervella, P., et al. 2007, *ApJ*, 664, 1093
- Mérand, A., Kervella, P., Breielfelder, J., et al. 2015, *A&A*, 584, A80
- Mérand, A., Kervella, P., Coudé du Foresto, V., et al. 2006, *A&A*, 453, 155
- Mérand, A., Kervella, P., Coudé du Foresto, V., et al. 2005, *A&A*, 438, L9
- Minniti, J. H., Sbordone, L., Rojas-Arriagada, A., et al. 2020, *A&A*, 640, A92
- Molinaro, R., Ripepi, V., Marconi, M., et al. 2011, *MNRAS*, 413, 942
- Molinaro, R., Ripepi, V., Marconi, M., et al. 2012, *ApJ*, 748, 69
- Monson, A. J., Freedman, W. L., Madore, B. F., et al. 2012, *ApJ*, 759, 146
- Monson, A. J. & Pierce, M. J. 2011, *ApJS*, 193, 12
- Mowlavi, N., Lecoœur-Taïbi, I., Lebzelter, T., et al. 2018, *A&A*, 618, A58
- Muraveva, T., Delgado, H. E., Clementini, G., Sarro, L. M., & Garofalo, A. 2018, *MNRAS*, 481, 1195
- Muraveva, T., Palmer, M., Clementini, G., et al. 2015, *ApJ*, 807, 127
- Nardetto, N., Fokin, A., Fouqué, P., et al. 2011, *A&A*, 534, L16
- Nardetto, N., Fokin, A., Mourard, D., et al. 2004, *A&A*, 428, 131
- Nardetto, N., Gieren, W., Kervella, P., et al. 2009, *A&A*, 502, 951
- Nardetto, N., Mathias, P., Fokin, A., et al. 2013, *A&A*, 553, A112
- Nardetto, N., Mérand, A., Mourard, D., et al. 2016, *A&A*, 593, A45
- Nardetto, N., Mourard, D., Mathias, P., Fokin, A., & Gillet, D. 2007, *A&A*, 471, 661
- Nardetto, N., Poretti, E., Rainer, M., et al. 2017, *A&A*, 597, A73
- Neeley, J. R., Marengo, M., Bono, G., et al. 2017, *ApJ*, 841, 84

- Negueruela, I., Chené, A. N., Tabernero, H. M., et al. 2021, MNRAS
- Negueruela, I., Dorda, R., & Marco, A. 2020, MNRAS, 494, 3028
- Nelan, E. 2001, *Fine Guidance Sensor Instrument Handbook*, Version 10 (Baltimore, STScI)
- Nelan, E. P. & Bond, H. E. 2013, ApJ, 773, L26
- Ngeow, C. & Kanbur, S. M. 2008, ApJ, 679, 76
- Ngeow, C.-C. & Kanbur, S. M. 2010, ApJ, 720, 626
- Ngeow, C.-C., Marconi, M., Musella, I., Cignoni, M., & Kanbur, S. M. 2012, ApJ, 745, 104
- Oort, J. H. 1931, *Bull. Astron. Inst. Netherlands*, 6, 155
- Oudmaijer, R. D., Groenewegen, M. A. T., & Schrijver, H. 1998, MNRAS, 294, L41
- Pedicelli, S., Bono, G., Lemasle, B., et al. 2009, A&A, 504, 81
- Perlmutter, S., Aldering, G., Goldhaber, G., et al. 1999, ApJ, 517, 565
- Persson, S. E., Madore, B. F., Krzemiński, W., et al. 2004, AJ, 128, 2239
- Pesce, D. W., Braatz, J. A., Reid, M. J., et al. 2020, ApJ, 891, L1
- Phillips, M. M. 1993, ApJ, 413, L105
- Pietrzyński, G., Gieren, W., Udalski, A., et al. 2007, AJ, 134, 594
- Pietrzyński, G., Graczyk, D., Gallenne, A., et al. 2019, *Nature*, 567, 200
- Pietrzyński, G., Graczyk, D., Gieren, W., et al. 2013, *Nature*, 495, 76
- Pilecki, B., Graczyk, D., Pietrzyński, G., et al. 2013, MNRAS, 436, 953
- Planck Collaboration, Ade, P. A. R., Aghanim, N., et al. 2014, A&A, 571, A1
- Planck Collaboration, Ade, P. A. R., Aghanim, N., et al. 2016, A&A, 594, A13
- Planck Collaboration, Aghanim, N., Akrami, Y., et al. 2020, A&A, 641, A6
- Pourbaix, D., Platais, I., Detournay, S., et al. 2003, A&A, 399, 1167
- Proxauf, B., da Silva, R., Kovtyukh, V. V., et al. 2018, A&A, 616, A82
- Reid, M. J., Pesce, D. W., & Riess, A. G. 2019, ApJ, 886, L27
- Riess, A., Anderson, R. I., Breuval, L., et al. 2021a, *Uncrowding the Cepheids for an Improved Determination of the Hubble Constant*, JWST Proposal. Cycle 1
- Riess, A. G., Casertano, S., Anderson, J., MacKenty, J., & Filippenko, A. V. 2014, ApJ, 785, 161
- Riess, A. G., Casertano, S., Yuan, W., et al. 2021b, ApJ, 908, L6
- Riess, A. G., Casertano, S., Yuan, W., et al. 2018a, ApJ, 855, 136
- Riess, A. G., Casertano, S., Yuan, W., et al. 2018b, ApJ, 861, 126
- Riess, A. G., Casertano, S., Yuan, W., Macri, L. M., & Scolnic, D. 2019a, ApJ, 876, 85



- Riess, A. G., Filippenko, A. V., Challis, P., et al. 1998a, *AJ*, 116, 1009
- Riess, A. G., Macri, L., Casertano, S., et al. 2011, *ApJ*, 730, 119
- Riess, A. G., Macri, L., Casertano, S., et al. 2009, *ApJ*, 699, 539
- Riess, A. G., Macri, L. M., Hoffmann, S. L., et al. 2016, *ApJ*, 826, 56
- Riess, A. G., Narayan, G., & Calamida, A. 2019b, Calibration of the WFC3-IR Count-rate Nonlinearity, Sub-percent Accuracy for a Factor of a Million in Flux, Tech. rep., STScI
- Riess, A. G., Nugent, P., Filippenko, A. V., Kirshner, R. P., & Perlmutter, S. 1998b, *ApJ*, 504, 935
- Ripepi, V., Catanzaro, G., Molinaro, R., et al. 2021, *MNRAS*
- Ripepi, V., Catanzaro, G., Molinaro, R., et al. 2020, *A&A*, 642, A230
- Ripepi, V., Cioni, M.-R. L., Moretti, M. I., et al. 2017, *MNRAS*, 472, 808
- Ripepi, V., Marconi, M., Moretti, M. I., et al. 2016, *ApJS*, 224, 21
- Ripepi, V., Molinaro, R., Musella, I., et al. 2019, *A&A*, 625, A14
- Romaniello, M., Primas, F., Mottini, M., et al. 2008, *A&A*, 488, 731
- Sakai, S., Ferrarese, L., Kennicutt, Robert C., J., & Saha, A. 2004, *ApJ*, 608, 42
- Salsi, A., Nardetto, N., Mourard, D., et al. 2021, *A&A*, 652, A26
- Sandage, A. 1958, *ApJ*, 127, 513
- Sandage, A. 1962, *ApJ*, 136, 319
- Sandage, A. 1996, *AJ*, 111, 18
- Sandage, A. 2002, *AJ*, 123, 1179
- Sandage, A. & Tammann, G. A. 1975, *ApJ*, 197, 265
- Sandage, A. & Tammann, G. A. 1982, *ApJ*, 256, 339
- Sandage, A., Tammann, G. A., & Reindl, B. 2004, *A&A*, 424, 43
- Sandage, A., Tammann, G. A., Saha, A., et al. 2006, *ApJ*, 653, 843
- Sandage, A. R. 1954, *AJ*, 59, 180
- Sandage, A. R. & Eggen, O. J. 1959, *MNRAS*, 119, 278
- Schechter, P. L., Avruch, I. M., Caldwell, J. A. R., & Keane, M. J. 1992, *AJ*, 104, 1930
- Schmidt, B. P., Suntzeff, N. B., Phillips, M. M., et al. 1998, *ApJ*, 507, 46
- Scolnic, D., Casertano, S., Riess, A., et al. 2015, *ApJ*, 815, 117
- Scolnic, D. & Kessler, R. 2016, *ApJ*, 822, L35
- Scowcroft, V., Bersier, D., Mould, J. R., & Wood, P. R. 2009, *MNRAS*, 396, 1287
- Scowcroft, V., Freedman, W. L., Madore, B. F., et al. 2016, *ApJ*, 816, 49

- Scowcroft, V., Freedman, W. L., Madore, B. F., et al. 2013, *ApJ*, 773, 106
- Scowcroft, V., Freedman, W. L., Madore, B. F., et al. 2011, *ApJ*, 743, 76
- Serenelli, A., Weiss, A., Cassisi, S., Salaris, M., & Pietrinferni, A. 2017, *A&A*, 606, A33
- Shapley, H. 1918a, *ApJ*, 48, 89
- Shapley, H. 1918b, *ApJ*, 48, 154
- Shapley, H. 1919, *JRASC*, 13, 438
- Skrutskie, M. F., Cutri, R. M., Stiening, R., et al. 2006, *AJ*, 131, 1163
- Slipher, V. M. 1914, *Popular Astronomy*, 22, 19
- Soltis, J., Casertano, S., & Riess, A. G. 2021, *ApJ*, 908, L5
- Soszyński, I., Gieren, W., & Pietrzyński, G. 2005, *PASP*, 117, 823
- Soszyński, I., Udalski, A., Szymański, M. K., et al. 2015, *Acta Astron.*, 65, 297
- Spergel, D. N., Bean, R., Doré, O., et al. 2007, *ApJS*, 170, 377
- Spergel, D. N., Verde, L., Peiris, H. V., et al. 2003, *ApJS*, 148, 175
- Stassun, K. G. & Torres, G. 2018, *ApJ*, 862, 61
- Stetson, P. B. 1987, *PASP*, 99, 191
- Storm, J., Gieren, W., Fouqué, P., et al. 2011a, *A&A*, 534, A94
- Storm, J., Gieren, W., Fouqué, P., et al. 2011b, *A&A*, 534, A95
- Subramanian, S. & Subramaniam, A. 2012, *ApJ*, 744, 128
- Sziládi, K., Vinkó, J., Poretti, E., Szabados, L., & Kun, M. 2007, *A&A*, 473, 579
- Tammann, G. A. 2006, *Reviews in Modern Astronomy*, 19, 1
- Tammann, G. A. & Leibundgut, B. 1990, *A&A*, 236, 9
- Terndrup, D. M. 1988, in *Astronomical Society of the Pacific Conference Series*, Vol. 4, *The Extragalactic Distance Scale*, ed. S. van den Bergh & C. J. Pritchet, 211
- Tonry, J. & Schneider, D. P. 1988, *AJ*, 96, 807
- Trahin, B. 2019, PhD thesis, Observatoire de Paris
- Tsang, K.-J. 2019, PhD thesis, Liverpool John Moores University
- Tully, R. B. & Fisher, J. R. 1977, *A&A*, 500, 105
- Turner, D. G. 2010, *Ap&SS*, 326, 219
- Udalski, A., Szymański, M. K., & Szymański, G. 2015, *Acta Astron.*, 65, 1
- van Altena, W. F., Lee, J. T., & Hoffleit, E. D. 1995, *The general catalogue of trigonometric [stellar] parallaxes*

- Van Den Bergh, S. 1960, *JRASC*, 54, 49
- Van Den Bergh, S., ed. 1988, *The Extragalactic Distance Scale: Proceedings of the ASP 100th Anniversary Symposium*, Vol. 4
- van Leeuwen, F. 2007, *A&A*, 474, 653
- Vasiliev, E. & Baumgardt, H. 2021, arXiv e-prints, arXiv:2102.09568
- Verde, L., Treu, T., & Riess, A. G. 2019, *Nature Astronomy*, 3, 891
- Wang, S. & Chen, X. 2019, *ApJ*, 877, 116
- Watson, C. L., Henden, A. A., & Price, A. 2006, *Society for Astronomical Sciences Annual Symposium*, 25, 47
- Welch, D. L., Wieland, F., McAlary, C. W., et al. 1984, *ApJS*, 54, 547
- Wesselink, A. J. 1946, *Bull. Astron. Inst. Netherlands*, 10, 91
- Whitlock, P. A., Feast, M. W., & Van Leeuwen, F. 2008, *MNRAS*, 386, 313
- Wiedemann, G., Ayres, T. R., Jennings, D. E., & Saar, S. H. 1994, *ApJ*, 423, 806
- Wielgórski, P., Pietrzyński, G., Gieren, W., et al. 2017, *ApJ*, 842, 116
- Wong, K. C., Suyu, S. H., Chen, G. C. F., et al. 2020, *MNRAS*, 498, 1420
- Yoachim, P., McCommas, L. P., Dalcanton, J. J., & Williams, B. F. 2009, *AJ*, 137, 4697
- Yuan, W., He, S., Macri, L. M., Long, J., & Huang, J. Z. 2017, *AJ*, 153, 170
- Zhevakin, S. A. 1963, *ARA&A*, 1, 367
- Zhou, X. & Chen, X. 2021, *MNRAS*, 504, 4768
- Zinn, J. C. 2021, *AJ*, 161, 214
- Zwicky, F. 1962, in *Problems of Extra-Galactic Research*, ed. G. C. McVittie, Vol. 15, 347

## Appendix A

# Contribution to Trahin et al. (2021), accepted in A&A

### Inspecting the Cepheid parallax-of-pulsation using Gaia EDR3 parallaxes - Projection factor, Period-Luminosity and Period-Radius relations

Distances to Classical Cepheids can be obtained independently from the other techniques mentioned in this thesis, by applying the parallax-of-pulsation method (PoP). This approach consists in comparing the variation of linear radius  $\Delta R$  of a Cepheid, derived from the integration of its pulsation velocity, with the variation of angular diameter  $\Delta\theta$ , either measured directly by interferometry or derived using surface brightness color relations. In the latter case, this implementation of the PoP technique is called the Baade-Wesselink method (Baade 1948; Wesselink 1946). The distance is then obtained from the equation:

$$\theta(t) - \theta(t = 0) = -\frac{2}{d} \int_0^t v_{puls}(\tau) d\tau \quad (\text{A.1})$$

However, as shown in Fig. A.1, the true pulsational velocity of a star  $v_{puls}$  is derived by multiplying the disk-integrated radial velocities  $v_{rad}$  measured by spectroscopy by a geometrical factor called the projection factor (hereafter the  $p$ -factor).

The  $p$ -factor was extensively studied by the Araucaria collaboration and other authors (e.g. Nardetto et al. 2004, 2007, 2009, 2011, 2013, 2017; Storm et al. 2011a; Ngeow et al. 2012; Groenewegen 2013; Pilecki et al. 2013; Mérand et al. 2015; Breitfelder et al. 2016; Gallenne et al. 2017; Kervella et al. 2017; Trahin 2019). There are many contributors to the  $p$ -factor, such as the sphericity of the star or the limb-darkening due to the stellar atmosphere structure, and the exact value of this parameter is still poorly calibrated, as well as its dependence with other quantities. The assumptions behind the PoP method may introduce important sources of error on the derived distances, which is why it is still not competitive with other methods, especially with *Gaia* parallaxes, for the determination of the Hubble constant (Riess et al. 2009).

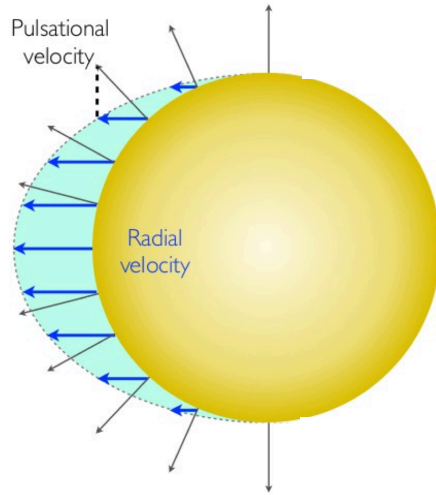


Figure A.1: Schematic view of the projection factor of Cepheids, which is defined as the ratio between the true pulsational velocity and the spectroscopic radial velocity. (Figure courtesy: P. Kervella)

In a paper that we recently submitted for publication and of which I am second author (Trahin, Breuval et al. 2021, accepted in A&A), we apply the Spectro-Photo-Interferometry for Pulsating Stars (SPIPS) modeling tool: this method, developed by [Mérand et al. \(2015\)](#), is a variant implementation of the PoP technique which makes use of atmospheric models and reproduces an observational dataset that combines spectroscopic radial velocities, photometric data in any filter and optical interferometric measurements. The data are adjusted simultaneously altogether using a standard multi-parameter  $\chi^2$  minimization in order to obtain a realistic estimate of the statistical uncertainties, as opposed to a method that would fit consecutive sets of parameters. In the paper, we present the application of the SPIPS algorithm to a sample of Galactic Cepheids for which we dispose of the best and most complete data, in combination with the new *Gaia* EDR3 parallaxes used as an input parameter. We derive precise and consistent parameters such as the radius, reddening, multi-band mean magnitudes, effective temperature, period changes, infrared excess and  $p$ -factor. An example of SPIPS fit for the Cepheid RS Pup is given in Fig. A.2.

The robustness of the SPIPS method and the accuracy of the derived parameters are tested by calibrating the period-luminosity and period-radius (P-R) relations. Using the mean apparent magnitudes and color excesses derived by the SPIPS models, we obtained:

$$K_S = -5.529_{\pm 0.015} - 3.141_{\pm 0.050} (\log P - 0.9) \quad (\text{A.2})$$

with a dispersion of 0.18 mag, which is in excellent agreement with previous calibrations of the P-L relation based on *Gaia* DR2 ([Breuval et al. 2020](#)) and *Gaia* EDR3 parallaxes ([Breuval et al. 2021](#)). Similarly, we use the radius of each Cepheid, derived from the angular diameter curves modeled by the SPIPS algorithm to calibrate the P-R relation. This relation plays an important role in the determination of the masses and various physical parameters of Cepheids. We obtain:

$$\log R = 1.763_{\pm 0.003} + 0.653_{\pm 0.012} (\log P - 0.9) \quad (\text{A.3})$$

with a low dispersion of 0.04. This relation is in good agreement with the red and blue edges of the instability strip defined by [Anderson et al. \(2016b\)](#). It is also compatible with the relation calibrated by [Molinaro et al. \(2011\)](#) at short periods ( $\log P < 1$ ) and with the relation by [Gallenne et al. \(2017\)](#) established for LMC Cepheids.

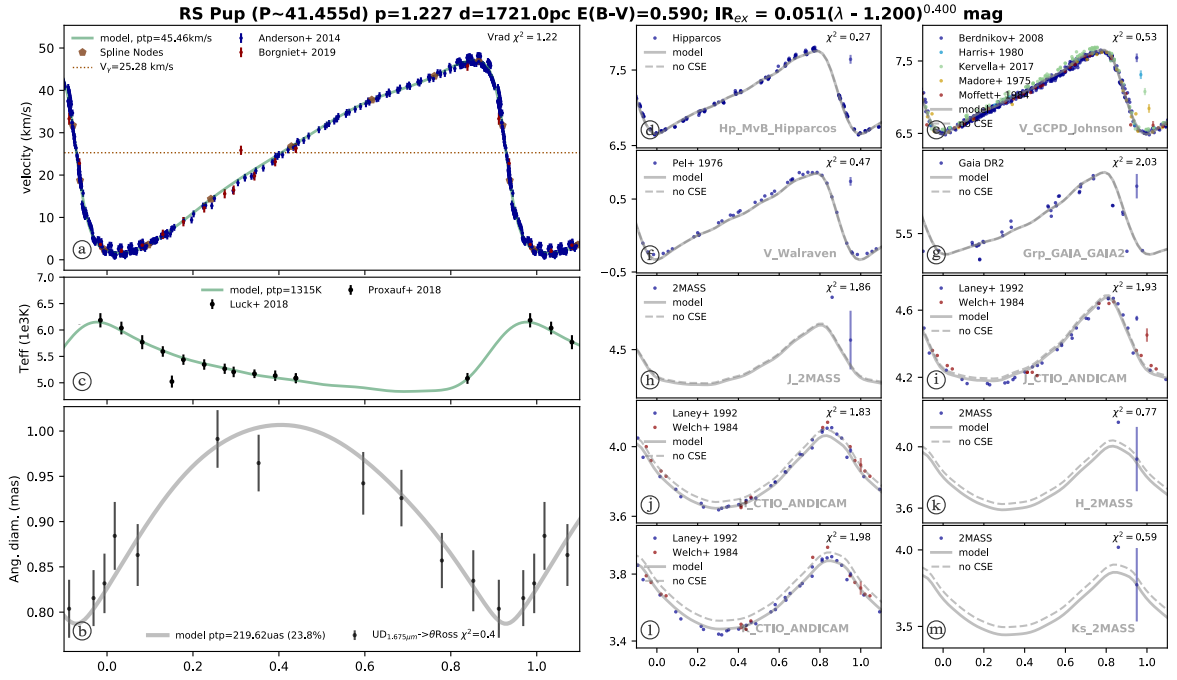


Figure A.2: SPIPS model of the Cepheid RS Pup taken from Trahin et al. (2021, submitted). **(a):** Spectroscopic radial velocities; **(b):** Interferometric angular diameters; **(c):** Spectroscopic effective temperatures; **(d)-(m):** multi-band photometry.

In the past decade, a great effort was made to calibrate a relation between the projection-factor and the pulsation period (hereafter the  $p - P$  relation). The limb-darkening effect is more important for the most massive stars, which also have the longest periods: this may explain why most studies derived a linear dependence of this parameter and a negative slope. However, the various studies of this parameter did not converge to a consistent dependence of the  $p$ -factor with period. Using the SPIPS implementation of the PoP technique with *Gaia* EDR3 parallaxes as an input parameter, we computed the value of the projection factor for each star of our sample. They are represented in Fig. A.3 as a function of the period.

We noticed a large dispersion of the  $p$ -factor values and also the presence of some unexpected values with  $p > 1.5$  (area delimited in grey in Fig. A.3). Such values would physically correspond to a limb-brightening effect or a reverse atmospheric velocity gradient which are highly unlikely. To explain these values, we cannot firmly exclude any residual bias in the parallaxes as well as imperfect data, or an effect related to the circumstellar envelopes of Cepheids. Values lower than  $p = 1$  would be physically possible if we consider that long-period Cepheids (and therefore of large radius) have stronger dynamics and an intense atmospheric velocity gradient. Finally, no clear dependence with period is visible. Fitting a linear relation through the points in Fig. A.3 gives the following equation:

$$p = 1.251_{\pm 0.008} - 0.097_{\pm 0.024} (\log P - 0.9) \quad (\text{A.4})$$

with a large dispersion of 0.15. The dispersion of the  $p$ -factor values and the presence of values outside of the expected range suggest potential additional dependencies of the  $P - p$  relation, or physics of the projection factor that is still not well understood. After investigation, we did not find any correlation between the projection factor and any other physical parameter such as effective temperature, metallicity, parallax or radial velocity amplitude.



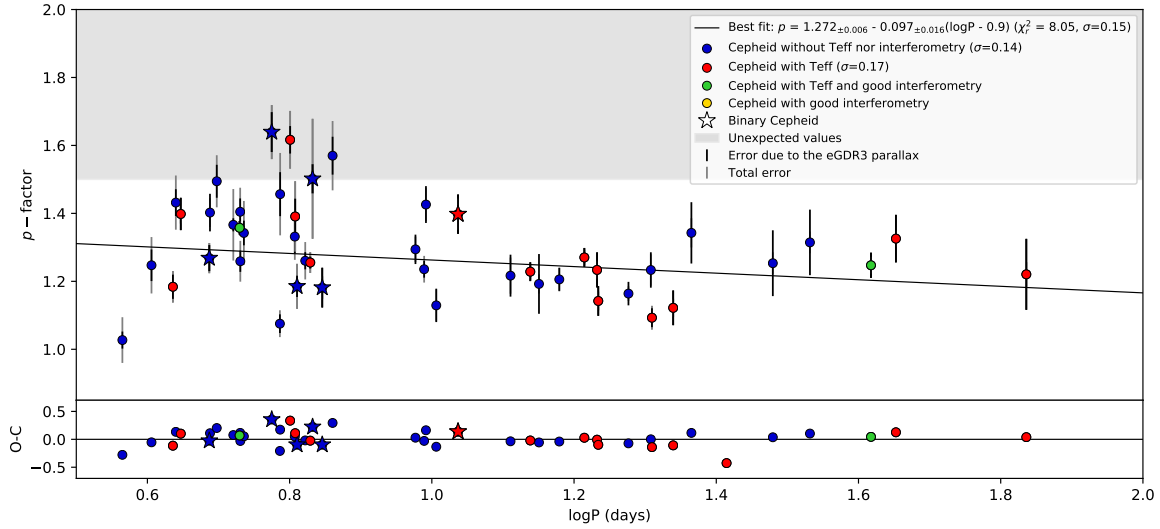


Figure A.3: Projection factor as a function of the period, derived from the application of the SPIPS algorithm with *Gaia* EDR3 parallaxes adopted as input parameter. This figure is taken from Trahin et al. (2021, submitted).

We conclude that the  $p$ -factor is consistent with a constant value of  $p = 1.26 \pm 0.07$  with a significant dispersion of 0.15. Additionally, this study suggests that the period- $p$ -factor relation may have an intrinsic width, similar to that of the instability strip but apparently uncorrelated with the basic stellar parameters. Recent studies of close circumstellar envelopes of Cepheid variables (Hocdé et al. 2020, 2021; Gallenne et al. 2021) have revealed a much more complex physics that could partly explain the dispersion observed in the  $p$ -factor values. An on-going effort is made by the Araucaria Project in order to study this effect. Moreover, parallel independent applications of the PoP technique would allow us to understand in more detail the physics of pulsating stars in order to conclude on the reliability of this method for the calibration of the extragalactic distance scale.

## Appendix B

# Contribution to Javanmardi et al. (2021), ApJ, 911, 12

### Inspecting the Cepheid Distance Ladder: the Hubble Space Telescope Distance to the SN Ia Host Galaxy NGC 5584

The tension on the Hubble constant between the direct measurement and the inferred value from the CMB assuming a  $\Lambda$ -CDM model has recently reached a significance of at least  $4\sigma$  (Riess et al. 2021b). If it is confirmed, this tension would have deep consequences on the standard model of cosmology (see the review of solutions by Di Valentino et al. 2021). Therefore, each step of the distance ladder must be inspected carefully, from the first geometric calibrations of nearby stars to the SNe Ia in the Hubble flow, in order to conclude or rule out whether the  $H_0$  tension is caused by a measurement error.

The spiral galaxy NGC 5584 played a key role in the local measurement of  $H_0$ : since it has time-series observations of Cepheids in several HST bands, the SH0ES project used the Cepheids of this galaxy to establish a relation between the periods and ratios of their amplitudes in different HST bands. Then, assuming that these relations derived from NGC 5584 also hold in other galaxies, they applied them in around half of the current sample of local SN Ia host galaxies to correct for the effect of random phase observations of the Cepheids in the galaxies with few observations. Therefore, the Cepheids in NGC 5584 played a key role in obtaining the periods and mean magnitudes of the Cepheids in almost half of the current SH0ES sample of SN Ia host galaxies and, in turn, in the final measurement of  $H_0$ . In the recent paper by Javanmardi et al. (2021), to which I contributed as a co-author, we reanalyzed the SH0ES distance to NGC 5584 and, where possible, we intentionally explored different tools and numerical methods in order to provide an independent insight into the  $H_0$  problem. This work was carried out totally independently of any input from the SH0ES team.

To enable direct comparison and evaluation of the methods, we did not re-observe NGC 5584 but we made use the raw data from the HST observations made by the SH0ES team (PI: A. Riess, Cycle 17, Proposal ID 11570), publicly available on the MAST database. Riess et al. (2016) present NIR observations of Cepheids in the 19 host galaxies, whereas Hoffmann et al. (2016) reports the

optical counterparts of the observations. The NGC 5584 galaxy has been observed in 13 epochs in the F555W filter (equivalent to  $V$ ), 6 epochs in F814W (equivalent to  $I$ ), 12 epochs in the wide band F350LP filter, and 2 epochs in F160W (equivalent to  $H$ ). To measure the brightness of the Cepheids at each epoch, we used the point spread function (PSF) photometry routines of the `Photutils` package of `Astropy` (Bradley et al. 2019), which provides tools similar to DAOPHOT (Stetson 1987), which is used by Hoffmann et al. (2016). We also internally tested different algorithms for model fitting and sky subtraction and the differences between their results is very small and negligible. Finally, we obtained the flux of 82 Cepheids in NGC 5584 at various epochs, which forms the light curves.

At large distances such as that of NGC 5584 ( $\sim 23$  Mpc), the light of Cepheids is often difficult to separate from the background stellar crowds, despite their large luminosity. For example, at the distance of NGC 5584, each pixel of the WFC3/UVIS camera spans around 4 pc: it is therefore very likely that the pixel that contains a given Cepheid also encompasses other stellar sources, either physically near the Cepheid or along the line of sight. This crowding bias is one of the most significant challenges for Cepheid measurements at large distances. A typical method used by the SH0ES team to correct for it is to simulate and add artificial stars to the immediate surroundings of each Cepheid on an image, retrieve their flux using the same PSF photometry approach applied to the Cepheids, and measure the difference between the input and output fluxes. In Javanmardi et al. (2021), we used a similar approach to Riess et al. (2016) and Hoffmann et al. (2016), but we correct for the crowding bias estimated locally at the position of each Cepheid on the measured magnitudes of that Cepheid before template light-curve fitting, rather than averaging over the whole galaxy as done by SH0ES for the optical observations. We also reject the artificial stars that are blended with another bright source by applying a  $2\sigma$ -clipping procedure, while the SH0ES team directly removed bright stars. We then measure the mean magnitude difference as the crowding bias estimate for each Cepheid.

In order to derive the pulsation period and mean magnitudes in each band from these time-series observations, we built template light curves using the Spectro-Photo-Interferometry for Pulsating Stars (SPIPS) algorithm, developed by Mérand et al. (2015) and described in Appendix A. In Hoffmann et al. (2016), this was done using template light curves from Yoachim et al. (2009) which have been generated from a sample of Cepheids in the Milky Way, the LMC, and the SMC. We built template light curves for 28 Galactic Cepheids with periods ranging from 12 to  $\sim 90$  days, a similar period range of that in SN Ia galaxies, and we apply it to derive periods and mean magnitudes in each band. Contrary to the fitting method adopted in Hoffmann et al. (2016), in the SPIPS algorithm all bands are analyzed simultaneously and fitted together at once.

The Cepheid light curves obtained in NGC 5584 by Hoffmann et al. (2016) were then used to derive relations between the amplitude ratios with respect to the HST F350LP band and the period. Assuming that this relation holds for all Cepheids in SN Ia host galaxies, they applied it to estimate photometry in F555W and F814W bands for Cepheids in about half of the 19 host galaxies. An accurate and precise calibration of these relations can potentially impact the final  $H_0$  measurements. We revisit this amplitude ratios relation and derive:

$$A_{F555W}/A_{F350LP} = 1.167 + 0.073 (\log P - 1.5) \quad (\sigma = 0.014) \quad (\text{B.1})$$

$$A_{F814W}/A_{F350LP} = 0.757 + 0.090 (\log P - 1.5) \quad (\sigma = 0.022) \quad (\text{B.2})$$

The amplitude ratios of the Cepheids in NGC 5584 are represented in Fig. B.1 as a function of the period. The grey symbols are the amplitudes obtained by the SH0ES team (Hoffmann et al. 2016) while our results are in blue and red for the F555W ( $V$ ) and F814W ( $I$ ) bands respectively. The fit only considers NGC 5584 Cepheids but also passes through the Milky Way Cepheids, represented as black circles. The relations that we find are significantly tighter than the relations found by SH0ES,

the standard deviations of the fits are an order of magnitude smaller, which means that our amplitude ratio measurement is less noisy and indicates a high-quality light-curve modeling approach. Indeed, SH0ES fitted the F555W and F814W light curves separately, while in our approach the light curves of all bands are fitted simultaneously: our amplitudes are therefore not estimated independently from one another, leading to a lower scatter. These amplitude ratio relations do not affect the distance of NGC 5584 because good Cepheid light curves are available for this galaxy, however the relations are applied to the 9 other galaxies and therefore may potentially affect their distance.

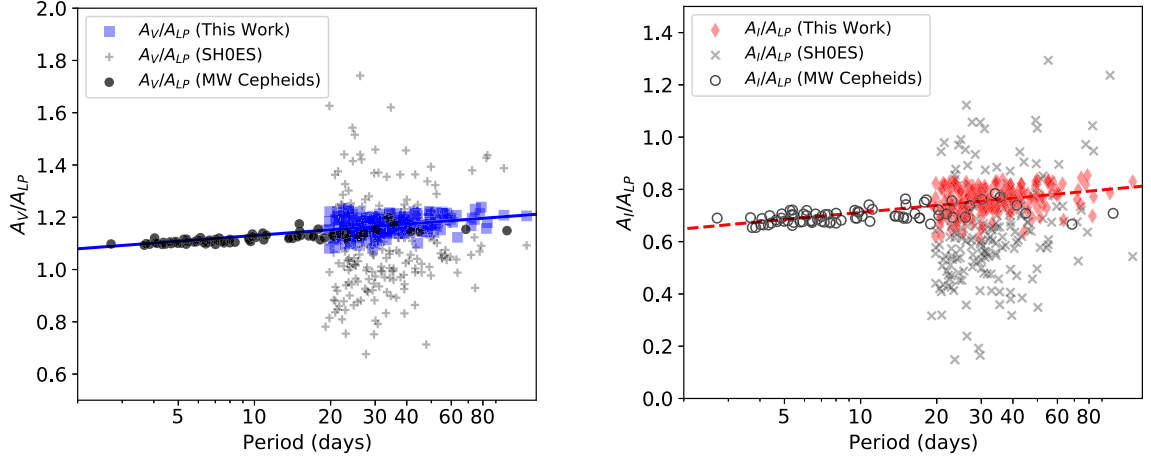


Figure B.1: Amplitude ratios in F555W ( $V$ ) and F814W ( $I$ ) bands with respect to F350LP filter against the period. The fit only considers NGC 5584 Cepheids but also fortuitously passes through the Milky Way Cepheids of shorter periods. (Figure taken from [Javanmardi et al. 2021](#)).

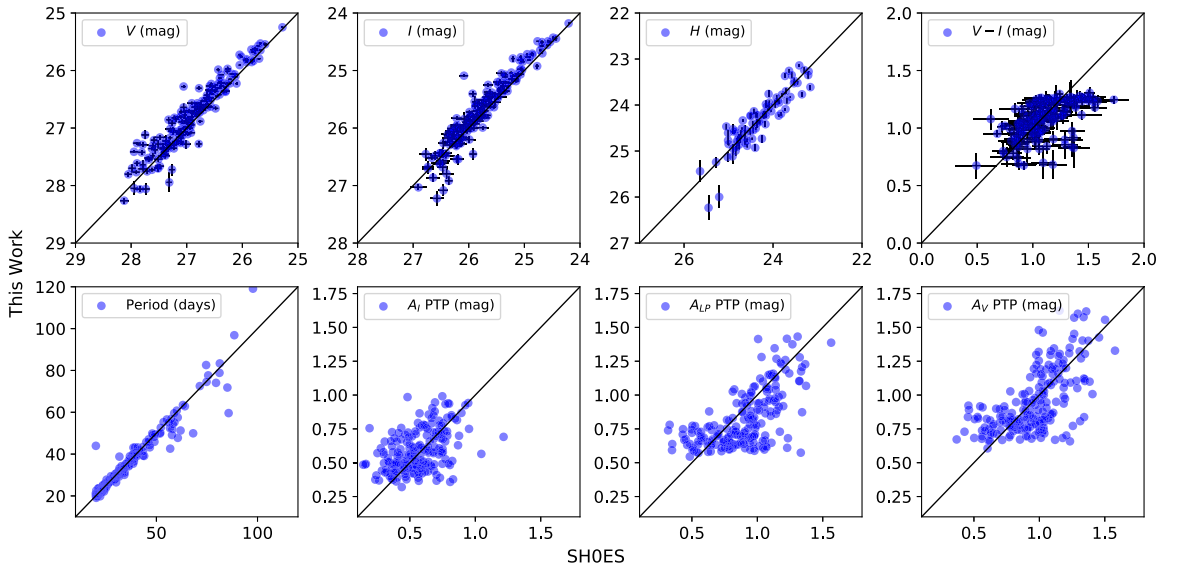


Figure B.2: Comparison between the [Javanmardi et al. \(2021\)](#) results (vertical axis) and the SH0ES ([Hoffmann et al. 2016](#)) results (horizontal axis): mean magnitudes,  $(V - I)$  color, period and light-curve amplitudes. (Figure taken from [Javanmardi et al. 2021](#)).

Using the light-curve template fitting obtained with the SPIPS algorithm, we derive the periods and the mean magnitudes for all the identified Cepheids in the four HST bands. Fig. B.2 compares our results with those of SH0ES (Hoffmann et al. 2016). The top row provides comparisons for the mean magnitude measurements in the  $V$ ,  $I$ , and  $H$  bands, as well as the  $(V - I)$  color. A generally good agreement can be seen between the two results, especially for the  $H$  band and the  $(V - I)$  color, both of which directly contribute to the distance measurement. The leftmost panel on the bottom row of Fig. B.2 provides a comparison for period measurements. As can be seen, although we use a different approach for template fitting and hence the period measurements, the two results are in general agreement with only a few exceptions. We found no systematic difference in our mean magnitudes, colors, periods and amplitudes compared with the SH0ES analysis, although we used different tools and methods.

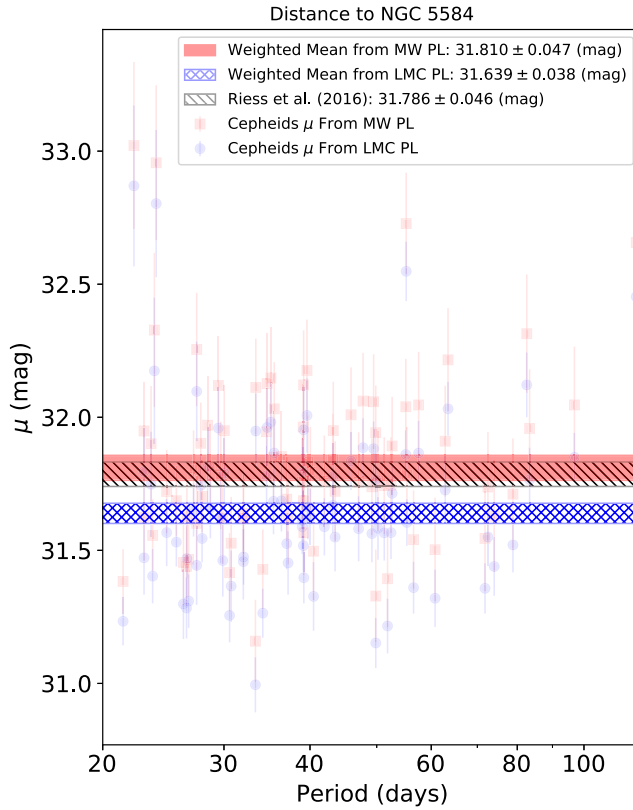


Figure B.3: Distance modulus of NGC 5584 obtained from a sample of 82 Cepheids using two different P-L relations calibrated in the Wesenheit  $W_H$  index. The horizontal filled rectangles show the  $1\sigma$  confidence regions for measured distances. The red and blue regions represent our measurements based on the MW and LMC PL relations, respectively, and are the weighted means of the  $\mu$  values measured for individual identified Cepheids. The black hatched region represents the estimated distance reported by Riess et al. (2016). (Figure taken from Javanmardi et al. 2021).

In order to derive the distance modulus of NGC 5584, we first calculated apparent magnitudes in the Wesenheit  $W_H$  index for each Cepheid of this galaxy:

$$W_H = F160W - 0.386(F555W - F814W) \quad (\text{B.3})$$

By applying an existing P-L relation in the  $W_H$  band to the Cepheids of known period of our sample, one can derive their absolute magnitude  $M_H^W$  and finally their individual distance modulus  $\mu =$

$W_H - M_H^W$ . We performed this calculation using two different P-L relations: one calibrated in the Milky Way (Breuval et al. 2020) and another calibration from the LMC (Riess et al. 2019a), to which we subtract the LMC distance modulus as measured by Pietrzyński et al. (2019). For both P-L relations, the individual distance moduli obtained for each Cepheid are represented in Fig. B.3. The Galactic P-L relation yields a weighted mean distance modulus of  $31.810 \pm 0.047$  mag, in good agreement with the value of  $31.786 \pm 0.046$  mag obtained by SH0ES, while the LMC calibration results in a slightly lower value of  $31.639 \pm 0.038$  mag. This difference is consistent with the lower metallicity of LMC Cepheids. Since SN Ia host galaxies are similar to the Milky Way in terms of metallicity, the Galactic P-L relation is more appropriate to derive the distance to NGC 5584. We reported a final distance of  $23.01 \pm 0.05$  Mpc.

In Javanmardi et al. (2021), we provided an independent and detailed re-analysis of the HST data from NGC 5584. Where possible, we intentionally used methods and tools different from those used by SH0ES. This allowed the investigation of the possible influence of these methods on distance measurements. We found no systematic difference in our mean magnitudes, which directly influence the distance measurements, compared to SH0ES, and finally we obtained a significantly tighter amplitude ratio versus period relation compared to the one derived by SH0ES. While it is important to seek alternative ideas on the theoretical side, the improvement of current observational methods as well as the development of new independent ones are necessary for progress toward a solution to the  $H_0$  tension.



## Appendix C

# List of publications

### Refereed publications

#### As first author

- *The influence of metallicity on the Leavitt law from geometrical distances of Milky Way and Magellanic Cloud Cepheids.* **Breuval L.**, Kervella P., Wielgórski P., Gieren W. et al., ApJ 913, 38 (2021)
- *The Milky Way Cepheid Leavitt law based on Gaia DR2 parallaxes of companion stars and host open cluster populations.* **Breuval L.**, Kervella P., Anderson, R. I., Riess, A. G. et al., A&A 643, A115 (2020)

#### As co-author

- *Inspecting the Cepheid parallax-of-pulsation using Gaia EDR3 parallaxes.* Trahin B., **Breuval L.**, Kervella P., A. Mérand, et al., accepted in A&A (2021)
- *Extended envelopes around Galactic Cepheids. V. Multi-wavelength and time-dependent analysis of IR excess.* Gallenne A., Mérand A., ..., **Breuval L.** et al., A&A 651, 113 (2021)
- *Mid-infrared circumstellar emission of the long-period Cepheid  $\iota$  Carinae resolved with VLTI/MATISSE.* Hocdé V., Nardetto N., ..., **Breuval L.** et al., A&A 651, 92 (2021)
- *Inspecting the Cepheid distance ladder: The Hubble Space Telescope distance to SNIa host galaxy NGC 5584.* Javanmardi B., Mérand A., Kervella P., **Breuval L.** et al., ApJ 911, 12 (2021)
- *Pulsating chromosphere of classical Cepheids. Calcium infrared triplet and H $\alpha$  profile variations.* Hocdé V., Nardetto N., ..., **Breuval L.** et al., A&A 641, A74 (2020)
- *A thin shell of ionized gas as the explanation of infrared excess among classical Cepheids.* Hocdé V., Nardetto N., ..., **Breuval L.** et al., A&A 633, A47 (2020)
- *Testing systematics of Gaia DR2 parallaxes with empirical surface brightness: color relations applied to eclipsing binaries.* Graczyk D., Pietrzyński G., ..., **Breuval L.**, ApJ 872, 85 (2019)

- 
- *Consistent radial velocities of classical Cepheids from the cross-correlation technique.* Borgniet S., Kervella P., ..., **Breuval L.** et al., A&A 613, A37 (2019)

## Proceeding publications

- *Calibrating the Cepheid distance scale with Gaia.* **Breuval L.**, Proceedings of the Hypatia Colloquium for Early Career Astronomers, European Southern Observatory (2021).
- *The Galactic Leavitt Law from Gaia DR2 Visual Binaries: Implications on the Distance Scale.* **Breuval L.** & Kervella P., Proceedings of the conference *RR Lyrae/Cepheid 2019: Frontiers of Classical Pulsators* held (13-18 October 2019) at Cloudcroft, New Mexico, USA. Edited by Karen Kinemuchi, Catherine Lovekin, Hilding Neilson, and Kathy Vivas. San Francisco: Astronomical Society of the Pacific Conference Series, Vol. 529, p.279 (2021).
- *Galactic Cepheids with Gaia DR2: Period-Luminosity relations and implications on  $H_0$ .* **Breuval L.** & Kervella P., Proceedings of the French Society for Astronomy and Astrophysics (SF2A) (2019).

## Appendix D

# Oral presentations, conferences, seminars

### **The Araucaria Project Group Meeting, Concepción, Chile**

5 March 2019 - Oral presentation: *The Galactic Cepheid P-L relation from visual binaries.*

At this meeting, I presented the preliminary results of my calibration of the P-L relation with *Gaia* DR2 parallaxes of Cepheid companions. I met the members of the Araucaria group for the first time and I had interesting discussions with Giuseppe Bono, Wolfgang Gieren, Grzegorz Pietrzyński, Jesper Storm and Dariusz Graczyk, among others. I was invited to visit Jesper Storm in Potsdam for further discussions.

### **Annual Meeting of the French Society for Astronomy and Astrophysics (SF2A), Nice, France**

15 May 2019 - Oral presentation: *The Galactic Cepheid P-L relation from Gaia DR2 visual binaries.*<sup>1</sup>

I presented my work on the P-L calibration using *Gaia* DR2 at the S03 session: "Stellar physics and *Gaia*". The results presented at this conference were significantly improved and some corrections were performed. For the final version of this study, we refer the reader to [Breuval et al. \(2020\)](#).

### **Visit at the Leibniz Institut für Astrophysik, Potsdam, Germany**

22 May 2019 - Oral presentation: *The Galactic Cepheid P-L relation from Gaia visual binaries.*

During my stay at the Leibniz Institut für Astrophysik in Potsdam, I worked with Jesper Storm on the improved *Gaia* parallaxes by [Anders et al. \(2019\)](#). I discussed the impact of metallicity on Cepheid magnitudes and started investigating this effect. I presented my work to the stellar group and received constructive comments from Ralf-Dieter Scholz.

---

<sup>1</sup> The proceeding paper of this talk is available at this link: <http://sf2a.eu/proceedings/2019/2019sf2a.conf..0129B.pdf>

## **Cosmic Controversies Conference, Kavli Institute for Cosmological Physics, Chicago, IL, USA**

8 October 2019 - Poster presentation: *The Cepheid Leavitt law from Gaia DR2 parallaxes of resolved companions.*<sup>2</sup>

The poster that I presented at this conference was **selected as one of the best posters** and I was awarded the possibility to give a 10-minute oral presentation. I had the opportunity to discuss with Wendy Freedman and Barry Madore, who shared with me their experience in the calibration of the Cepheid P-L relation. The last day, I was contacted by Adam Riess who had questions on my poster. We started a long series of emails and he helped me to improve my paper significantly, in particular for the determination of the Hubble constant from my ground-based P-L relation.

## **RRL/Cep - Frontiers of Classical Pulsators, Cloudcroft, NM, USA**

18 October 2019 - Oral presentation: *The Cepheid Leavitt law from Gaia DR2 parallaxes of resolved companions.*<sup>3</sup>

During this conference, I presented my results on the P-L relation and the rescale of the Hubble constant, after including the first suggestions of Adam Riess. I met Lucas Macri and Richard I. Anderson. I had interesting discussions with Richard and I also received helpful advice from Katrien Kolenberg and Massimo Marengo for my oral presentation.

## **Dark Energy Colloquium, Institut Henri Poincaré, Paris, France**

20 November 2019 - **Invited** by Alain Blanchard to give a talk. Oral presentation: *The Cepheid Leavitt law from Gaia DR2 parallaxes of resolved companions.*<sup>4</sup>

## **Frontiers of Stellar Physics: the Theory-Observation Interface, Workshop MW-Gaia, Zagreb, Croatia**

21 January 2020 - **Invited** by Lovro Palaversa to give a talk. Oral presentation: *The Galactic Leavitt Law from Gaia DR2 Visual Binaries: Implications on the Distance Scale.*<sup>5</sup>

During this workshop, I first met Gisella Clementini who commented my presentation. I also had a very constructive discussion with Richard I. Anderson. He kindly answered my questions about the crossmatch of Open Clusters with Milky Way Cepheids.

## **Annual Conference of the PhD students in Astrophysics in Paris**

26 February 2020 - Oral presentation: *The Cepheid Leavitt Law from Gaia DR2 parallaxes of resolved companions.*

<sup>2</sup> Website of the Cosmic Controversies conference: <https://kicp-workshops.uchicago.edu/2019-COSMIC/index.php>

<sup>3</sup> Website of the RRL/Cep conference: <https://rrl2019.nmsu.edu>

<sup>4</sup> Website of the Dark Energy Colloquium: <https://indico.in2p3.fr/event/18900/overview>

<sup>5</sup> Website of the Gaia Workshop: <https://www.mw-gaia.org/participate/zagreb-wg2/>

### Early Career Poster Exhibition, Royal Astronomical Society (online)

1 September 2020 - Poster presentation: *Measuring Astronomical Distances with Pulsating Stars: From Cepheids in the Milky Way to the Hubble constant*.<sup>6</sup>

The poster I presented at the Early Career Poster Exhibition described the results of my first paper ([Breuval et al. 2020](#)).

### Seminar at the Nuclear and High Energy Physics Laboratory, Paris, France

28 September 2020 - **Invited** by Luc Poggioni to give a talk. Oral presentation: *The Cepheid distance scale: from the local Gaia calibration to distant galaxies*.

At this seminar, I presented my research on the Cepheid distance scale to a public of scientists specialized in cosmology and high energy physics. I received interesting feedback and suggestions on the Hubble tension.

### Gaia EDR3 Day, Presentation of Gaia DR2 scientific results, Paris, France (online)

3 December 2020 - Oral presentation: *The Cepheid period-luminosity relation from Gaia DR2 parallaxes*.<sup>7</sup>

On the publication day of the *Gaia* Early Data Release 3, an online event was hosted by Paris Observatory. I presented my results based on *Gaia* DR2 and the expectations of the community regarding *Gaia* EDR3 parallaxes.

### Meeting of the High Angular Resolution Group at LESIA, Paris Observatory (online)

21 January 2021 - Oral presentation: *Improving the Cepheid distance scale with High Angular Resolution*.

The LESIA is one of the 5 laboratories of Paris Observatory: it is specialized in space science and instrumentation. In this laboratory, I belong to the High Angular Resolution (HAR) group. During this meeting, I presented the advantages of interferometry for the study of Cepheids and the calibration of the distance scale.

### International Space Science Institute (ISSI) SHoT Team (online)

4 March 2021 - Oral presentation: *Improving the calibration of the Leavitt law with Gaia*.

I was **invited** by Gisella Clementini and Richard Anderson to give a talk at this meeting, as a nominated young scientist. The ISSI SHoT team<sup>8</sup> is led by Gisella Clementini and includes experts in stellar physics, variable star distances, the Hubble constant measurement and *Gaia* data.

<sup>6</sup> Link to my poster presentation: <https://ras.ac.uk/poster-contest/louise-breuval>

<sup>7</sup> Link to my oral presentation (in french): <https://www.youtube.com/watch?v=nRwza7OabSo>

<sup>8</sup> Website of the ISSI SHoT team: <https://www.issibern.ch/teams/shot/>

### **Hypatia Colloquium, European Southern Observatory (online)**

8 June 2021 - Oral presentation: *Calibrating the Cepheid distance scale with Gaia*.<sup>9</sup>

The seminars given at the Hypatia Colloquium<sup>10</sup> are presented by astronomers at the early stages of their career, who were selected after a very competitive process. During this talk, I summarize the work I achieved during the three years of my PhD thesis<sup>11</sup>.

### **European Astronomical Society - Annual Meeting (online)**

29 June 2021 - Oral presentation: *Period-luminosity-metallicity relation of Cepheids from Gaia parallaxes*.<sup>12</sup>

I presented the results of my two papers at the session S15: *Gaia: The (two) billion star galaxy census: The Science of EDR3 and the promise of DR3*.

### **MIAPP Workshop on the Hubble Tension (online)**

29 September 2021 - Oral presentation: *The Cepheid period-luminosity relation and its calibration*.<sup>13</sup>

I was **invited** by Stéphane Blondin to present the results of my thesis. I discussed the calibration of the P-L relation with *Gaia* DR2 and EDR3 parallaxes, and the calibration of the metallicity effect from geometrical distances of Cepheids in the Milky Way and in the Magellanic Clouds.

<sup>9</sup> Link to my oral presentation (in english): <https://www.youtube.com/watch?v=eLmnnDJH-cM>

<sup>10</sup> Webpage of the Hypatia Colloquium: <https://www.eso.org/sci/meetings/garching/hypatia-colloquium.html>

<sup>11</sup> Proceedings of the Hypatia Colloquium: <https://www.eso.org/sci/activities/garching/Hypatia/2021/ESOHypatia2021.pdf>

<sup>12</sup> Abstract of my presentation: <https://eas.kuoni-congress.info/2021/programme/abstract/2017>

<sup>13</sup> Website of the MIAPP workshop on the Hubble tension: <https://indico.ph.tum.de/event/6895/>

## Appendix E

### List of acronyms

Table E.1: List of acronyms used in this thesis.

Acronym	Definition
ABL	Astrometric Based Luminosity
BAM	Basic Angle Monitor (for Gaia detector)
BW	Baade-Wesselink method
CC	Classical Cepheid
CCHP	Carnegie Chicago Hubble Program
CMB	Cosmic Microwave Background
CRNL	Count Rate Non-Linearity (effect)
DEB	Detached Eclipsing Binary
FO	First Overtone (pulsation mode)
FGS	Fine Guidance Sensor
Gaia DR1	Gaia Data Release 1
Gaia DR2	Gaia Data Release 2
Gaia EDR3	Gaia Early Data Release 3
GoF	Goodness of Fit
HR	Hertzsprung-Russell (diagram)
HST	Hubble Space Telescope
JWST	James Webb Space Telescope
OC	Open Cluster
$\Lambda$ -CDM	$\Lambda$ - Cold Dark Matter (model)
LKH	Lutz-Kelker bias ( <a href="#">Lutz &amp; Kelker 1973</a> ) as modified by <a href="#">Hanson (1979)</a>
LMC	Large Magellanic Cloud
MW	Milky Way
NIR	Near InfraRed
PSF	Point Spread Function
P-L	Period-Luminosity
P-W	Period-Wesenheit
PoP	Parallax of Pulsation
RUWE	Renormalized Unit Weight Error

...



**Table E.1** (continued)

Acronym	Definition
SBCR	Surface Brightness Color Relation
SH0ES	Supernova $H_0$ for the Equation of State
SMC	Small Magellanic Cloud
SN Ia	Type Ia supernova
SPIPS	Spectro-Photo-Interferometry for Pulsating Stars
TDI	Time Delayed Integration
TRGB	Tip of the Red Giant Branch
VLBI	Very Long Baseline Interferometry
VLT	Very Large Telescope
VLTI	Very Large Telescope Interferometer
WFC3	Wide Field Camera 3
WMAP	Wilkinson Microwave Anisotropy Probe
ZP	Zero-point

## RÉSUMÉ

---

Les Céphéides sont des étoiles variables pulsantes qui jouent un rôle clé comme indicateurs primaires de distance grâce à la relation empirique entre leur période de pulsation et leur luminosité intrinsèque, la relation période-luminosité. Cette loi est utilisée pour étalonner la luminosité des supernovæ de type Ia dans les galaxies proches, qui est à son tour utilisée pour mesurer la distance aux galaxies dans le flot de Hubble, fournissant une estimation du taux d'expansion actuel de l'Univers: la constante de Hubble ( $H_0$ ). Ces dernières années, une tension significative d'au moins  $4\sigma$  est apparue entre la mesure de  $H_0$  dans l'univers primitif par le satellite Planck, en supposant un modèle  $\Lambda$ CDM, et les mesures directes dans l'univers local basées sur les distances des Céphéides. La confirmation de cette tension pourrait impliquer une nouvelle physique au delà du modèle standard : il est donc essentiel d'améliorer l'étalonnage de la relation période-luminosité grâce à des distances précises et fiables de Céphéides. La collaboration *Gaia* a récemment publié les parallaxes trigonométriques de plus d'1.7 milliard d'étoiles, permettant une amélioration remarquable de la précision de l'échelle des distances. Cependant, les parallaxes des Céphéides sont affectées par des problèmes de calibration en raison de leur variabilité et de leur importante luminosité. Dans cette thèse, je présente une méthode alternative pour étalonner la relation période-luminosité en utilisant des compagnons de Céphéides et des amas ouverts hôtes, qui ne sont pas soumis à ces problèmes. En utilisant ces compagnons proches non biaisés pour déterminer la distance des Céphéides, j'étalonne la relation période-luminosité dans la Voie Lactée et je réévalue la valeur locale de la constante de Hubble. Enfin, j'étudie le lien entre les magnitudes absolues des Céphéides et leur abondance en métaux en comparant les Céphéides de la Voie Lactée et celles des Nuages de Magellan. J'en déduis que les Céphéides riches en métaux sont plus brillantes que celles qui en sont pauvres, avec un effet plus fort en infrarouge proche qu'en optique. Cet effet peut avoir un impact sur la mesure de la constante de Hubble et devra être pris en compte plus précisément à l'avenir, afin de mieux contraindre l'étalonnage de l'échelle des distances extragalactiques.

## MOTS CLÉS

---

Étoiles variables, Échelle des distances, Astrométrie, Analyse de données, Observations astronomiques, Métallicité, Voie Lactée, Nuages de Magellan, Constante de Hubble

## ABSTRACT

---

Cepheids are pulsating variable stars which play a key role as primary distance indicators thanks to the empirical relation between their pulsation period and intrinsic luminosity, the period-luminosity relation. This law is used to calibrate the brightness of type-Ia supernovæ in nearby galaxies, which is in turn used to measure the distance to galaxies in the Hubble flow. This provides an estimate of the current expansion rate of the Universe, known as the Hubble constant ( $H_0$ ). In recent years, a significant tension of at least  $4\sigma$  has arisen between the early universe measurement of  $H_0$  from the Planck satellite, assuming a  $\Lambda$ CDM model, and the late universe direct measurements based on Cepheid distances. The persistence of this tension would imply new physics beyond the standard model of cosmology: it is therefore critical to improve the period-luminosity calibration with precise and reliable Cepheid distance measurements. The *Gaia* Collaboration recently published trigonometric parallaxes for 1.7 billion stars, allowing for a remarkable improvement in the precision of the distance scale. However, Cepheid parallaxes suffer from calibration issues due to their variability and important brightness. In this thesis, I present an alternative method for calibrating the period-luminosity relation using Cepheid companions and host open clusters, which are not subject to these issues. By adopting these close and unbiased companion stars to determine the distance to Cepheids, I calibrate the period-luminosity relation in the Milky Way and re-evaluate the local value of the Hubble constant. Finally, I study the relation between Cepheid magnitudes and their metal abundance by comparing the Cepheids of the Milky Way and those of the Magellanic Clouds. I conclude that metal-rich Cepheids are brighter than metal-poor ones, with a stronger effect in near-infrared than in optical. This effect may impact the measurement of the Hubble constant and will have to be taken into account more precisely in the future, to better constrain the calibration of the extragalactic distance scale.

## KEYWORDS

---

Variable stars, Distance scale, Astrometry, Data Analysis, Astronomical observations, Metallicity, Milky Way, Magellanic Clouds, Hubble Constant